Imperial College of Science, Technology and Medicine
University of London

Analysis of Heart Rate Variability and Blood Pressure Variation by Nonlinear Modelling Techniques

By:

Saeid Reza Seydnejad

This thesis is submitted in partial fulfillment of the requirements
for the **Degree of Doctor of Philosophy (Ph.D.)**
and the **Diploma of Imperial College (D.I.C)**

Department of Electrical and Electronic Engineering
Imperial College of Science Technology and Medicine
University of London

June 1998

BIBL
LONDON

To My Parents

ABSTRACT

The thesis is concerned with analysis of Heart Rate Variability (HRV) and Blood Pressure Variation (BPV) by nonlinear modelling techniques. Rhythmical fluctuations in heart rate and blood pressure are believed to convey valuable information about performance of the neuro-cardiovascular system. Linear analysis of these variability signals, however, is known to be inadequate.

A new method for real time detection of HRV based on Integral Pulse Frequency Modulation (IPFM) model and its similarity to pulse position modulation is presented. The new method has a firm mathematical basis but is simple to implement and is fast in operation. The method is then utilised for system identification between a spike series signal and a continuous signal. By comparing with the existing methods, superiority of the new HRV detection method for identification purposes in frequency domain and by parametric analysis is also demonstrated.

A novel approach for detection of input-output nonlinearity in the neuro-cardiovascular system, based on cyclostationary analysis of signals, is presented. Metronome-type breathing is employed to provide a sinusoidal input to the neuro-cardiovascular system in which HRV and BPV are considered as its outputs. The presence of coupled harmonics in the variability signals reveals involvement of the Volterra type nonlinearity in the actual system.

To model the mechanical stretching effect of the SA node, the threshold level of the IPFM model is allowed to vary with time. Through a rigorous mathematical analysis a parametric solution is derived for the modified model to separate the mechanical modulation of the SA node from the autonomic influence.

Interaction between HRV, BPV and respiration is studied by proposing and implementing a new closed loop model based on the underlying physiological system. A nonlinear identification method using Laguerre expansion technique for Volterra series representation is invoked to investigate the contribution of HRV and respiration on BPV in random breathing pattern. The new model is validated by comparing its results with the experimental observations.

Statement of Originality

The following aspects of this thesis are considered to be original in this area of application:

1- Finding a new real time algorithm for detection of HRV based on the IPFM model and pulse position modulation technique.

2- Obtaining a proper set of signal descriptors for relating a spike series signal to continuous signals for identification purposes.

3- Developing the cyclostationary nonlinear detection technique for the system analysis and demonstrating the presence of input-output nonlinearity in HRV and BPV through this technique.

4- Analysis of the IPFM model and Time Varying Threshold IPFM (TVTIPFM) model by a parametric method and deriving a new HRV detection technique based on vector space theory.

5- Presenting a new HRV-BPV-ILV nonlinear closed loop model for analysis of the variability signals and describing their origins.

Acknowledgments

To Professor Richard I. Kitney, my supervisor for guidance, enthusiasm and encouragement throughout the highs and lows of PhD research and introducing me to the field of heart rate variability. Also, supporting me with his vast experience in this field.

To Dr. Giovanni Calcagnini, Department of Information and System, University of Rome 'La Sapienza', Italy, for generously gathering the majority of the clinical data used in this work. Also, for enlightening discussions into several aspects of the research.

To Dr. Jonathon Chambers, Electrical Engineering Department, Imperial College, and Dr. Nezam Mahdavi Amiri, Department of Mathematics, Sharif University of Technology, Tehran, Iran, for their constructive criticism and support during the writing of Chapters 5 and 6 of this thesis.

To Dr Stanley Head, St Mary's Medical School, Imperial College, and Dr. Stefano Lino, Clinical Pathophysiology Unit, University of Rome, 'La Sapienza', Rome, Italy, for spending many hours discussing the physiological aspects of this work and for assisting in the gathering of additional clinical data.

To Dr. Rebecca Claesen-Finn, Department of Biological and Medical Systems, Imperial College, for her invaluable suggestions and devoting a lot of time for the grammatical correction of the whole thesis.

To Dr Peter Cashman and Dr. Anil Bharath, Department of Biological and Medical Systems, Imperial College, for many helpful conversations and comments and also their kind support.

To Mr Mattew Liptrot in guiding me in the various aspects of English writing throughout the whole period of my PhD.

To Mrs. Frances Gibson, Secretary to Prof. Kitney, without whom life at Imperial is impossible to imagine.

The Following papers have, so far, been published/written on the work presented in this thesis

1- "Real-Time Heart Rate Variability Extraction Using the Kaiser Window", *IEEE Trans. Biomed. Eng.*, Vol. 44, pp. 990-1005, Oct. 1997.

2- "Investigation of HRV by Model Analysis", in the book entitled: *Frontiers of Blood Pressure and Heart Rate Analysis,* M. Di Rienzo *et. al.* Eds. pp. 67-88, IOS Press, 1997

3- "Detection of Nonlinearity in Heart Rate Variability and Blood PressureVariation by Cyclostationary analysis", Submitted to *IEEE Trans. Biomed. Eng.*, Feb. 1998.

4- "Modelling of the SA Node by the Time Varying IPFM Model", Submitted to *IEEE Trans. Biomed. Eng*, March 1998.

5- "Heart Rate Variability System Identification Using Different Signal Descriptors", *Proc. IEEE Computers in Cardiology*, pp. 101-104, Sept. 1996.

6- "Analysis of Heart Rate Variability and Blood Pressure Variation by Nonlinear Closed Loop Modelling", *Proc. World Congress on Biophysics and Biomedical Engineering,* Nice France pp. 241, Sept. 1997.

7- "Cardiovascular Variability Modelling: Some Fundamental Concepts", will be presented in *IEEE Annual International Conference in Engineering in Medicine and Biology,* Hong Kong, Nov. 1998.

8- "The Nonlinear Closed Loop Mechanism Underlying the LF Oscillation in Blood Pressure" will be presented in *IEEE Annual International Conference in Engineering in Medicine and Biology*, Hong Kong, Nov. 1998.

Contents

1 Introduction **24**

2 Real-Time HRV Signal Extraction **31**

2.1 Introduction 31

2.2 IPFM Model 34

2.3 The French-Holden Algorithm 35

2.4 Pulse Position Modulation and its Relation to the IPFM Model 39

2.5 Real Time HRV Signal Extraction 44

2.5.1 The New Method 44

2.5.2 Simulation Results 47

2.6 Real Time Band Pass Filtering of the R-wave Signal 51

2.7 Experimental Results 53

2.8 Conclusion 56

2.9 APPENDIX A 58

3 Heart Rate Variability System Identification Using Different Signal Descriptors **59**

3.1 Introduction 60

3.2 Model Structure 61

3.3 Different Signal Descriptors 63

3.3.1 Beat-to-Beat Method 64

3.3.2 Interpolation Method 64

3.3.3 Berger-Saul Method 65

3.3.4 The Proposed Method 66

3.4 System Identifier 66

3.4.1 Identification by Spectral Analysis 66

3.4.2 Identification by Parametric Methods 67

3.5 Simulation Results 68

3.5.1 Simulation Results with Spectral Analysis Method 70

3.5.2 Simulation Results with Parametric Identification 74

3.6 Experimental Results 77

3.7 Discussion 82

3.8 Conclusion 85

3.9 Appendix A: Berger-Saul Method 87

4 Investigation of HRV and BPV by Model Analysis **88**

4.1 Introduction 88

4.2 The Physiological Basis of the Rhythmical Fluctuations in HRV and BPV 89

4.2.1 Respiratory Sinus Arrhythmia 90

4.2.2 Respiratory Oscillation in Arterial Blood Pressure 92

4.2.3 Low Frequency Oscillations 94

4.2.4 Dominant Factors in Producing the Rhythmical Fluctuations in HRV and BPV 97

4.3 Model Review 98

4.3.1 Saul (S) Model 98

4.3.2 Baselli (B) Model 100

4.3.3 TenVoorde (T) Model 103

4.3.4 Kitney (K) Model 106

4.4 Small Signal and Large Signal Modelling 108

4.5 The Proposed Model 111

4.6 Conclusion 117

4.7 Appendix A: Baselli Model 119

5 Detection of Nonlinearity in Neuro-cardiovascular System 121

5.1 Introduction 121

5.2 Overview 123

5.3 Phase and Frequency Coupling 124

5.4 Frequency and Phase Coupling Detection Using Higher Order Spectra 126

5.5 k-th Order Self Phase and Self Frequency Coupling 128

5.6 Amplitude Modulated Signals Through Nonlinear Systems 130

5.7 The Cyclostationary Approach to Harmonic Retrieval 132

5.8 Systemic Analysis of Nonlinearity Using Cyclo-stationary Properties . 134

5.8.1 Self Frequency and Self Phase Coupling Detection 134

5.8.2 Phase and Frequency Coupling Detection 137

5.8.3 Detection of Higher Order Nonlinearities 141

5.9 Simulation Results 142

5.10 Experimental Results 146

5.11 Discussion and Conclusion 154

5.12 Appendix A: Relation Between Higher Order Moment Spectra and Cyclic Spectra 157

5.13 Appendix B: Proof of Equation (5.43) 158

6 Time Varying Threshold Integral Pulse Frequency Modulation 160

6.1 Introduction 160

6.2 TVTIPFM model 164

6.3 Parametric Solution of the TVTIPFM Model 166

6.3.1 Basic Concepts 166

6.3.2 Selection of the Basis Functions 172

6.3.3 Properties of the Parametric Solution 174

6.4 Computational Aspects 179

6.5 Simulation Results 180

6.5.1 Zero Threshold Signal 180

6.5.2 Zero Modulating Signal 189

6.5.3 Nonzero Signals 192

6.6 Experimental Results 194

6.7 TVTIPFM Model with Small Threshold Signal 202

6.8 Conclusion 206

6.9 Appendix A: Uniqueness of the Parametric Solution 208

7 Theoretical Development of the Proposed Model 212

7.1 Introduction 212

7.2 The SA Node 213

7.2.1 Autonomic Response 213

7.2.2 Mechanical Stretching Effect of the SA Node 219

7.2.3 Overall Representation 221

7.3 Cardiopulmonary Baroreceptors 222

7.4 Phrenic Nerves and the Diaphragm Transfer Functions 227

7.5 Mayer Waves Generation Mechanisms 228

7.5.1 Feedback Mechanism 228

7.5.2 Centrogenic Mechanism 235

7.5.3 The VLF Component 237

7.6 Overall Model 239

7.7 Nonlinear Identification Methodology 245

7.7.1 Simulation Results 249

7.8 Conclusion 257

8 Validation of the Proposed Model by Comparison with Experimental Results 259

8.1 Introduction 259

8.2 Experimental Procedure and Data Collection and Analysis 260

8.3 Identifying the Experimental Kernels 263

8.4 Respiratory Sinus Arrhythmia in the Model 273

8.5 The LF Component in the Model 279

8.6 Simulation of the Model with the Actual ILV Signal 287

8.7 Performance of the Model in Spectral Domain 287

8.8 Influence of HRV on BPV in the Respiratory Band 295

8.9 Discussion and Conclusion 296

9 Overall Conclusions and Future Work **301**

List of Figures

2.1 (a) ECG, (b) the corresponding R-wave signal obtained by replacing each R peak with a unit sample function. 34

2.2 (a) IPFM model, (b) output power spectrum for a sinusoidal excitation at frequency f_m. 35

2.3 (a) Generation of the sampled R-wave signal from the ECG. $x_{cs}(t)$ denotes the sampled ECG and $x_{crs}(t)$ represents the R-wave signal. (b) Generation of the sampled R-wave signal from the presumed continuous time R-wave signal $x_r(t)$. 37

2.4 Pulse position and pulse duration modulation. (a) The message signal, (b) the corresponding PPM signal, (c) the corresponding PDM signal. 40

2.5 (a),(b) Detecting the message signal from PPM, (c) from IPFM output signals. . . 42

2.6 Detection of signal $0.2sin(2\pi 0.15t)$. (a) Input signal. (b) The detected signal using the F-H algorithm. (c) The detected signal using the KLPF method. (d) PSD of the detected signal using the F-H algorithm. (e) PSD of the detected signal using the KLPF method. 48

2.7 Detection of signal $0.3sin(2\pi 0.3t)$. (a) Input signal. (b) The detected signal using the F-H algorithm. (c) The detected signal using the KLPF method. (d) PSD of the detected signal using the F-H algorithm. (e) PSD of the detected signal using the KLPF method. 49

2.8 Detection of signal $0.4sin(2\pi 0.15t) + 0.4sin(2\pi 0.3t)$. (a) Input signal. (b) The detected signal using the F-H algorithm. (c) The detected signal using the KLPF method. (d) PSD of the detected signal using the F-H algorithm. (e) PSD of the detected signal using the KLPF method. 50

2.9 Performance of the F-H and the proposed algorithms for transient signals. (a) IPFM input signal. (b) The detected signal using the F-H algorithm, (c) The detected signal using the KLPF method. 51

2.10 Bandpass filtering of the IPFM output signal by the proposed KBPF algorithm, (a) Input signal $0.2sin(2\pi 0.1t) + 0.2sin(2\pi 0.25t)$. (b) Output signal. (c) PSD of the output signal. 53

2.11 (a) ECG. (b) Respiration. (c) R-wave signal. (d) The HRV signal using the KLPF algorithm. (e) PSD of the HRV signal. (f) KBPF of the R-wave signal with $f_l = 0.15Hz$, $f_h = 0.21Hz$. (g) KBPF of the R-wave signal with $f_l = 0.05Hz$, $f_h = 0.14Hz$. (h) PSD of the signal of part (f). (i) PSD of the signal of part (g). . . . 55

2.12 Real-time monitoring of the HRV in inspiratory breath hold experiment. The top trace shows pulmonary ventilation and the bottom one HRV. 56

3.1 Minimum order Wiener modelling. (a) First order MOW, threshold trigger (TT): $s(n) = 0\ if\ v(n) \leq \theta, s(n) = 1\ if\ v(n) > \theta$, θ =threshold value. (b) Second order MOW, ZMN: zero memory nonlinearity. 62

3.2 The general model of an unknown system in series with the IPFM model. 63

3.3 Beat-to-Beat method. (a) R-R intervals ($T1 - T4$) are extracted from the ECG (R-wave signal). (b) The corresponding respiratory samples are highlighted on the respiratory signal. 65

3.4 (a),(b) Bode plot of equation (3.3) with $t_0 = 2.5sec$ and $a = 1.9rad/sec$, (c),(d) Spectral estimation of $G(s)$, (e),(f) result of the beat-to-beat method, (g),(h) spline-spline method, (i),(j) spline-decimate method, (k),(l) the B-S method, (m),(n) the proposed method. 72

3.5 Input-output signals in the presence of noise, (a) $u(t)$, (b) $z(t)$. 74

3.6 Spectral estimation of $G(s)$ in the presence of noise (a),(b) the beat-to-beat method, (c),(d) spline-spline method, (e),(f) spline-decimate method, (g),(h) the B-S method, (i),(j) the proposed method, ... 76

3.7 Random breathing experiment. (a) Respiratory signal, (b) PSD of the respiratory signal. 78

3.8 The estimated transfer function between the respiratory movement and HRV. (a),(b) beat-to-beat method, (c),(d) spline-spline method, (e),(f) spline-decimate method, (g),(h) the B-S method, (i),(j) the proposed method. 80

3.9 The estimated transfer function between respiration and HRV using the beat-to-beat method with the alternative protocol. 80

3.10 Berger-Saul method. 87

4.1 Tracing from top to bottom: aortic pressure(mmHg), pulmonary artery pressure, superior vena cava and intrathoracic pressures (mmH2O), pulmonary arterial and superior vena caval flows (ml/min). A denotes beginning of respiration. Stroke volume (ml) is shown below pulmonary arterial flow curve. Volume (ml) through superior vena cava during each cardiac cycle is shown at bottom (de Burgh Daly, 1986) 93

4.2 (a) Saul (S) model, (b) its systematic diagram. 99

4.3 (a) Baselli (B) model. (b) An alternative version of the B model. 101

4.4 TenVoorde (T) model. 104

4.5 Kitney (K) model. 107

4.6 A simple sketch of the cardiovascular controlling system. 108

4.7 The eight segment model as an example of the circulatory model. 109

4.8 A transistor amplifier circuit as an example of the small and large signal modelling in system science. (a) Large signal model, (b) small signal model. The same concept can be extended to cardiovascular modelling. 110

4.9 A physiological layout of the problem. 111

4.10 The proposed model. 113

4.11 Superimposed slow variations on the instantaneous blood pressure signal. 117

4.12 (a) The B model. (b) Alternative version of the B model which is used for identification of the neuro-cradiovascular system. 119

5.1 The nonlinear model when frequency coupling is accompanied by phase coupling. . 125

5.2 Random variation in respiratory amplitude in the metronome breathing pattern (12 breaths/min experiment). 131

5.3 Magnitude of the cyclic correlation of signal $sin(2\pi 0.25t)$. 143

5.4 Normalized magnitude of the cyclic mean (left hand column) and cyclic correlation (right hand column) of the simulated signals. For the descriptions of the figures refer to the text. 145

5.5 (a) Respiratory signal with 12 breaths/min, (b) the corresponding HRV signal. . . 147

5.6 Cyclic mean (left hand column) and cyclic correlation (right hand column) of respiration (top panel) and HRV (bottom panel) in 12 breaths/min experiment (subject 1). 147

5.7 Cyclic mean (left hand column) and cyclic correlation (right hand column) of respiration (top panel) and HRV (bottom panel) in 15 breaths/min experiment (subject 2). 148

5.8 Cyclic mean (left hand column) and cyclic correlation (right hand column) of respiration (top panel) and HRV (bottom panel) in 12 breaths/min experiment (subject 2). 149

5.9 Cyclic mean (left hand column) and cyclic correlation (right hand column) of respiration (top panel) and HRV (bottom panel) in 8 breaths/min experiment (subject 2). 150

5.10 Cyclic mean (left hand column) and cyclic correlation (right hand column) of respiration (top panel) and BPV (bottom panel) in 8 breaths/min experiment (subject 3). 152

5.11 Cyclic mean (a) and cyclic correlation (b) of the HRV from a subject in 12 breaths/min experiment (subject 2). 152

5.12 Cyclic mean (a) and cyclic correlation (b) of the BPV from a subject in 10 breaths/min experiment (subject 4). 153

5.13 Cyclic mean (a) and cyclic correlation (b) of the HRV for a subject who showed prominent LF component in the 10 breaths/min experiment (subject 5). 154

6.1 In an isolated blood-perfused SA node the sinus rate increases with increase in the nodal stretch. The degree of acceleration is directly related to the magnitude of stretch (Chiba, 1977). 162

6.2 TVTIPFM model is the IPFM model with a varying threshold level. 164

6.3 (a) The modulating signal $\lambda_{ac}(t)$. (b) Zero threshold signal $a_{ac}(t) = 0$. (c) The R-wave signal ($\lambda_{dc} = a_{dc} = 1$). 165

6.4 (a) Zero modulating signal $\lambda_{ac}(t) = 0$. (b) The threshold signal $a_{ac}(t)$. (c) The R-wave signal ($\lambda_{dc} = a_{dc} = 1$). 165

6.5 (a) The modulating signal $\lambda_{ac}(t)$. (b) The threshold signal $a_{ac}(t)$. (c) The R-wave signal ($\lambda_{dc} = a_{dc} = 1$). 166

6.6 True and reconstructed signals for $\lambda_{ac} = 0.3sin(2\pi 0.3t)$ and $f_{low} = 0.2Hz$, $f_{high} = 0.4Hz, \Delta f = 0.02Hz$. 181

6.7 True and reconstructed signals for $\lambda_{ac} = 0.3sin(2\pi 0.3t)$ and $f_{low} = 0.2+0.01Hz$, $f_{high} = 0.4 + 0.01Hz, \Delta f = 0.02Hz$. 182

6.8 True and the reconstructed signals for $\lambda_{ac} = 0.3sin(2\pi 0.3t)$ and $f_{low} = 0.12Hz$, $f_{high} = 0.52Hz, \Delta f = 0.04Hz$, (b) the reconstructed signal plotted over a longer length, (c) Fourier transform of the reconstructed signal. 183

6.9 True and reconstructed signals for $\lambda_{ac} = 0.2sin(2\pi 0.1t) - 0.15cos(2\pi 0.25t) + 0.1cos(2\pi 0.35t - \pi/4)$ and $f_{low} = 0.08Hz$, $f_{high} = 0.4Hz, \Delta f = 0.02Hz$. 184

6.10 (a) The actual signal $\lambda_{ac}(t) = 0.3sin(2\pi 0.15t)$, (b) the reconstructed signal using the parametric method ($f_{low} = 0.04Hz$, $f_{high} = 0.4Hz$, $\Delta f = 0.02Hz$), (c) the reconstructed signal using the KLPF method ($f_c = 0.4Hz$, $\beta = 4.5$, $d = 5sec$). . . 185

6.11 (a) The actual signal $\lambda_{ac}(t) = 0.8sin(2\pi 0.29t)$, (b) the reconstructed signal using the parametric method ($f_{low} = 0.1Hz$, $f_{high} = 0.5Hz$, $\Delta f = 0.02Hz$), (c) the reconstructed signal using the KLPF method ($f_c = 0.45Hz$, $\beta = 4.5$, $d = 5sec$). . 186

6.12 (a) The actual signal $\lambda_{ac}(t) = 0.4sin(2\pi 0.85t)$, (b) the reconstructed signal using the parametric method ($f_{low} = 0.45Hz$, $f_{high} = 0.95Hz$, $\Delta f = 0.02Hz$), (c) the reconstructed signal using the KLPF method ($f_c = 0.45Hz$, $\beta = 4.5$, $d = 5sec$), (d) Fourier transform of the actual signal, (e) Fourier transform of the signal of part (b), (f) Fourier transform of the signal of part (c). 187

6.13 (a) The actual signal $\lambda_{ac}(t) = 0.8sin(2\pi 0.85t)$, (b) the reconstructed signal using the parametric method ($f_{low} = 0.45Hz$, $f_{high} = 0.95Hz$, $\Delta f = 0.02Hz$), (c) the reconstructed signal using the KLPF method ($f_c = 0.45Hz$, $\beta = 4.5$, $d = 5sec$), (d) Fourier transform of the actual signal, (e) Fourier transform of the signal of part (b), (f) Fourier transform of the signal of part (c). 188

6.14 (a) True and reconstructed signals with a random input in the range $[0.1 \;\; 0.4]Hz$, (b) Fourier transform of the random signal. 189

6.15 True and reconstructed signals for a transient input. 190

6.16 True and reconstructed signals for $a_{ac}(t) = 0.5sin(2\pi 0.3t)$ and $f_{low}(t) = 0.2Hz, f_{high} = 0.4Hz, \Delta f = 0.02Hz$. 190

6.17 True and reconstructed signals for $a_{ac}(t) = 0.2cos(2\pi 0.5t) - 0.5sin(2\pi 0.75t - \pi/3)$ and $f_l(t) = 0.4Hz, f_h = 0.8Hz, \Delta f = 0.02Hz$. 191

6.18 True and reconstructed signals for a random threshold input in the range $[0.1 \;\; 0.4]Hz$. 191

6.19 True and reconstructed signals with $f_{low} = 0.2Hz, f_{high} = 0.44Hz, \Delta f = 0.02Hz$, (a) $\lambda_{ac}(t) = 0.4cos(2\pi 0.4t + \pi/4)$, (b) $a_{ac}(t) = 0.3sin(2\pi 0.24t - \pi/3)$. 192

6.20 True and reconstructed signals with (a) $\lambda_{ac}(t) = 0.25cos(2\pi 0.4t + \pi/4) - 0.6sin(2\pi 0.6t)$, (b) $a_{ac}(t) = 0.3sin(2\pi 0.21t - \pi/3) + 0.5cos(2\pi 0.45t)$. 193

6.21 True and reconstructed signals for a TVTIPFM model with random signals at both inputs. 193

6.22 Spontaneous breathing experiment in resting supine position (subject 1). (a) $\lambda_{ac}(t)$, (b) $a_{ac}(t)$, (c) PSD of $\lambda_{ac}(t)$, (d) PSD of $a_{ac}(t)$. 195

6.23 12 breaths per minute experiment in resting supine position (subject 1). (a) $\lambda_{ac}(t)$, (b) $a_{ac}(t)$, (c) PSD of $\lambda_{ac}(t)$, (d) PSD of $a_{ac}(t)$. 196

6.24 7 breaths per minute experiment in resting supine position (subject 1). (a) $\lambda_{ac}(t)$, (b) $a_{ac}(t)$, (c) PSD of $\lambda_{ac}(t)$, (d) PSD of $a_{ac}(t)$. 198

6.25 Random breathing experiment in resting supine position (subject 2). (a) $\lambda_{ac}(t)$, (b) $a_{ac}(t)$, (c) PSD of $\lambda_{ac}(t)$, (d) PSD of $a_{ac}(t)$. 199

6.26 15 breaths per minute experiment in resting supine position (subject 2). (a) $\lambda_{ac}(t)$, (b) $a_{ac}(t)$, (c) PSD of $\lambda_{ac}(t)$, (d) PSD of $a_{ac}(t)$. 200

6.27 8 breaths per minute experiment in resting supine position (subject 2). (a) $\lambda_{ac}(t)$, (b) $a_{ac}(t)$, (c) PSD of $\lambda_{ac}(t)$, (d) PSD of $a_{ac}(t)$. 201

6.28 Small signal analysis of the TVTIPFM model. (a) $\lambda_{ac}(t)+a_{ac}(t) = 0.3cos(2\pi 0.25t)+0.1sin(2\pi 0.15t)$, (b) Fourier transform of $\lambda_{ac}(t) + a_{ac}(t)$, (c) result of the KLPF method on t_i of the TVTIPFM model, (d) Fourier transform of the signal of part (c), (e) result of the KLPF method on t_i of the TVTIPFM model when $\lambda_{ac}(t) = 0$ and $a_{ac}(t) = 0.1sin(2\pi 0.15t)$, (f) Fourier transform of the signal of part (e). . . . 205

7.1 The proposed model. 214

7.2 (a) Magnitude, (b) phase of the SA node vagal transfer function given by equation (7.3). 217

7.3 (a) Magnitude, (b) phase of the SA node sympathetic transfer function given by equation (7.4). 218

7.4 (a) Transfer function between respiration and nonautonomic response of the SA node, (b) frequency response of the transfer function. 220

7.5 Complete model of the SA node. 222

7.6 The feedback regulatory mechanism of the arterial blood pressure. 228

7.7 (a) Modified Kitney model, (b) modified nonlinear element. 231

7.8 Analysis of the limit cycle in the modified K model with different selection of the parameters. The left hand column shows the Nyquist plot of $G(s)$ and $-\frac{1}{N}$. The amplitude and frequency of the oscillation can be determined by finding the intersection of these plots. The middle and the right hand columns illustrate the time behaviour and frequency analysis of the K model with the modified nonlinear element, respectively. (a),(b),(c) $M = 2, \alpha = 1, T_0 = 2.5, g = 3.0$, (d),(e),(f) $M = 2, \alpha = 1, T_0 = 4.0, g = 3.0$, (g),(h),(i) $M = 2, \alpha = 1, T_0 = 2.5, g = 6.0$, (j),(k),(l) $M = 4, \alpha = 1, T_0 = 2.5, g = 3.0$, (m),(n),(o) $M = 2, \alpha = 2, T_0 = 2.5, g = 3.0$ 233

7.9 Frequency entrainment in the modified K model by increasing the amplitude and decreasing the frequency of the respiratory input. Left hand column shows respiration, middle blood pressure and the right hand column shows the normalised Fourier transform of the blood pressure. From top to bottom, zero respiratory input, respiration at $0.25Hz$, and respiration at $0.19Hz$, respectively. 234

7.10 Model of the LF centrogenic oscillator and its influence on the autonomic nervous system. 237

7.11 A detailed illustration of the proposed model. 240

7.12 A sketch of the mechanical effect of respiration on intrathoracic circulation. . . . 242

7.13 (a) The model of the individual influence and the interaction between Symp, HRV and ILV on BPV. Each input has a direct effect as well as a joint effect with the other inputs on BPV. (b) The equivalent mathematical representation of the model of part (a) in the nonlinear system identification context. 243

7.14 The final model of the neuro-cardiovascular system for variability analysis. 244

7.15 The original kernels used for evaluating the nonlinear identification procedure. . . 250

7.16 The identified kernels with $x(t)$, $u(t)$, and $w(t)$ three independent white noise signals. 251

7.17 The estimated kernels with actual HRV, ILV and Symp. signals as inputs. 253

7.18 The simulated model for the closed loop experiment. 254

7.19 Power spectral density of the signals ($u(t)$, $w(t)$) which were used for the simulation in the closed loop condition (Fig. 7.18). 254

7.20 The estimated kernels in the closed loop experiment without additive output noise. 255

7.21 The estimated kernels in the closed loop experiment with additive output noise. . 256

8.1 The final model of the neuro-cardiovascular system. 261

8.2 Time behaviour (left hand column) and power spectral density (right hand column) of the variability signals for subject 1. 262

8.3 Time behaviour (left hand column) and power spectral density (right hand column) of the variability signals for subject 5. 263

8.4 Extraction of the sympathetic influence from the blood pressure variability signal. 264

8.5 The identified kernels for subject 1. 265

8.6 The identified kernels for subject 2. 266

8.7 The identified kernels for subject 3. 267

8.8 The identified kernels for subject 4. 268

8.9 The identified kernels for subject 5. 269

8.10 Phase relationship between ILV (top trace) and BPV (bottom trace) for two different breathing rates if a pure delay (two seconds) system is assumed. 271

8.11 The actual and the predicted BPV for two subjects, (a) subject 1, (b) subject 5. . 272

8.12 The assumed model for determining the central respiratory gain G_4 to the cardiac control centres. 276

8.13 Simulation results of Fig. 8.12 with different values of G_4 for subject 1. 277

8.14 Simulation results of Fig. 8.12 with different values of G_4 for subject 5. 278

8.15 The simulated model for observing the LF component ($M = 2, \alpha = 1$ for the NL). . 279

8.16 The LF oscillation in the model. Right hand column subject 1 and left hand column subject 5. (a),(b) time behaviour (c),(d) power spectral density. 280

8.17 The LF oscillation for subject 3, (a) in time and, (b) in frequency domain. 281

8.18 Augmentation of the LF oscillation by increasing the open loop static gain for subject 5 ($g_5 = 2.8$). 282

8.19 Presence of the HF, LF and VLF components in the simulated variability signals of the model of subject 1. Left hand column time behaviour, right hand column PSD. From top to bottom HRV, ILV and BPV. 283

8.20 Presence of the HF, LF and VLF components in the simulated variability signals of the model of subject 5. Left hand column time behaviour, right hand column PSD. From top to bottom HRV, ILV and BPV. 283

8.21 Time behaviour (left hand column) and PSD (right hand column) of the actual variability signals when subject 1 was breathing with rate 15 breaths/min. From top to bottom HRV, ILV and BPV. 284

8.22 Time behaviour (left hand column) and PSD (right hand column) of the actual variability signals when subject 5 was breathing with rate 15 per minute. From top to bottom HRV, ILV and BPV. 284

8.23 Time behaviour (left hand column) and PSD (right hand column) of the simulated signals for subject 1 when the centrogenic LF oscillator is active. From top to bottom HRV, ILV and BPV. 286

8.24 Time behaviour (left hand column) and PSD (right hand column) of the simulated signals for subject 5 when the centrogenic LF oscillator is active. From top to bottom HRV, ILV and BPV. 286

8.25 Simulation of the proposed model with the actual ILV signal. Left hand column subject 1, right hand column subject 5. From top to bottom ILV, HRV, BPV. . . 288

8.26 Time behaviour and power spectral density of the synthetic respiratory signal used for the simulation in spectral domain. 289

8.27 Predicted transfer functions for subject 1. Left hand column magnitude, middle column phase and right hand column coherence function. From top to bottom (ILV to HRV), (ILV to BPV), (BPV to HRV). 290

8.28 Actual transfer functions for subject 1. Left hand column magnitude, middle column phase and right hand column coherence function. From top to bottom (ILV to HRV), (ILV to BPV), (BPV to HRV). 291

8.29 Predicted transfer functions for subject 5. Left hand column magnitude, middle column phase and right hand column coherence function. From top to bottom (ILV to HRV), (ILV to BPV), (BPV to HRV). 292

8.30 Actual transfer functions for subject 5. Left hand column magnitude, middle column phase and right hand column coherence function. From top to bottom (ILV to HRV), (ILV to BPV), (BPV to HRV). 293

8.31 Fixing the heart rate in the model causes a reduction in the respiratory fluctuation of the BPV. (a) Subject 1, (b) subject 5. 295

Chapter 1

Introduction

Modelling is a fundamental procedure in the human understanding of the breadth and depth of the surrounding world. Although there are countless modelling approaches and many levels of modelling complexity, the common feature of phenomenological models is that they somehow represent our perception of the relationships between observed events, exogenous factors and endogenous features.

Developments in systems science and cybernetics have allowed significant progress in the mathematical modelling of physiological organs, their interconnections and functional performance. Coupled with a deeper understanding, these representations have numerous clinical applications. In this context, respiration and the cardiovascular system have engaged considerable attention for more than a century. Respiration is regulated to maintain the correct arterial blood gas partial pressures and the circulatory system is responsible for the transport of these gases to and from the tissues. The respiratory and cardiovascular systems must act in unison to transfer gases between the air and the cells, and hence their control system must be dependent to ensure that the metabolic needs of the tissues are met under varying conditions according to their demands.

Interestingly, the cardiovascular parameters exhibit synchronous fluctuations with respiration. The cyclic variation of arterial blood pressure with respiration was noted by Hales as early as 1733. It is well known that respiration mechanically perturbs the venous return and the pulmonary vascular and aortic pressures through intrathoracic pressure changes, resulting in the corresponding fluctuations in blood pressure. Accompanied by central modulation, the resultant cyclic variation in blood pressure im-

pinges on the heart rate *via* the autonomically mediated baroreceptor reflex. Heart rate is continuously regulated by the sympathetic and parasympathetic nervous systems. The autonomic nervous system senses, through a variety of receptors, fluctuations in cardiovascular parameters including arterial and venous pressures and O_2 and CO_2 concentration. The afferent information is transmitted to the controlling centres in the brain stem. The controller comprises the pools of neurons in the central nervous system that provide the output to the effectors which include heart rate, myocardial contractility, peripheral resistance and venous return.

The electrical stimulation that starts the heartbeat and controls its natural rhythm originates in the sinoatrial (SA) node. In the absence of external disturbance the intrinsic rhythm of the SA node is constant, whilst a rise or a fall in the firing rate is normally a result of sympathetic or parasympathetic excitation. Therefore, heart rate fluctuations can reflect the regulatory activity of the autonomic nervous system. Consequently, it should not come as a surprise if fluctuations in heart rate provide diagnosis information in various cases.

It is well known that even in stationary conditions, such as supine resting position, the heart rate exhibits regular fluctuations around its mean value. This so_called Heart Rate Variability (HRV) is believed to convey useful information about the autonomic nervous system. Apparently, fluctuations in the respiratory band are not the only rhythmical fluctuations in heart rate. Investigation in the spectral domain has revealed the presence of three major components in heart rate variability:

i) The High Frequency (HF) component around $0.25Hz$, in synchrony with respiratory rate which is considered to be an expression of the respiratory influence, mediated mostly by vagal activity.

ii) The Low Frequency (LF) component, generally centred around $0.1Hz$, which is attributed to the sympathetic activity and the closed loop controlling action of the cardiovascular regulation.

iii) The Very Low Frequency (VLF) component around $0.04Hz$, which is probably due to the vasorhythmicity, thermoregulatory system or humoral regulations.

Correspondingly, the same frequency components can be observed in the power spectral density of Blood Pressure Variation (BPV). Superimposed on the instanta-

neous blood pressure signal, regular fluctuations of systolic, diastolic and mean blood pressure can be observed even in stationary conditions. The baroreflex is known to be a fast and powerful reflex to buffer the blood pressure fluctuations, yet relatively large rhythmical variations in synchrony with respiration and in the LF and VLF bands can be observed in the blood pressure signal. Is the baroreflex an ineffective controller or is it not meant to attenuate these variations?

Finding appropriate explanations for the observed VLF, LF and HF fluctuations in heart rate and blood pressure under normal conditions is the primary objective of the present study. This is to be achieved by developing a mathematical model based on the physiological system involved with the variability signals; namely, heart rate variability (HRV), blood pressure variation (BPV) and instantaneous lung volume (ILV).

Finding a comprehensive model to describe, interpret and even predict the behaviour of the cardiovascular system has always been an important subject in biomedical engineering. Specifically, a great amount of effort has been made to present a mathematical model for depicting the blood pressure regulatory mechanism in the form of a feedback system and then to explain cardiovascular haemostasis and regulation based on this model. More recently a new avenue in cardiovascular system analysis has appeared which focusses on the study of the rhythmical fluctuations in the cardiovascular parameters. This so-called cardiovascular variability modelling or neuro-cardiovascular modelling tries to explain the presence of the observed cyclic variation in the HF, LF and VLF bands in heart rate, blood pressure, blood flow, etc, and to elucidate their variations under different physiological and pathological conditions. Simply stated, in cardiovascular variability modelling the main concern is variations in heart rate, fluctuations in blood pressure, etc, around an operating point (mean heart rate, mean blood pressure, etc). From this point of view, cardiovascular variability modelling can be categorised as a sub-class in the larger group of cardiovascular system modelling. While the latter concentrates on the global behaviour of the cardiovascular system and its regulation, the emphasis of the former is on the origin and consequences of the observed rhythmical fluctuations in the cardiovascular parameters.

The cardiovascular system is an extremely complex system; however, the developed mathematical model should represent the reality with reduced complexity. Relative simplicity is a paramount feature of the model construction. On the other

hand oversimplification may cause severe performance degradation. A critical element in cardiovascular variability modelling is the appropriate definition of the variability signals (HRV, BPV, ILV). While the instantaneous blood pressure and the respiratory signal are continuous state continuous time [1] (time series) signals, heart rate is expressed as a discrete quantity (beats per minute). Therefore, the process of defining a unified approach for treating the variability signals and analysing their joint relationships encounters methodological limitations; one has to relate a continuous state time series signal such as respiration to a series of interval variations (HRV).

In the general context of cardiovascular system modelling the dominant approach has been to use a set of differential equations for expressing the haemodynamic part of the model based on the pressure-flow-volume relationships under the influence of the neuronal control part. However, in the specific domain of cardiovascular variability modelling the beat-to-beat definition together with an identification procedure has been the prevalent approach. In the beat-to-beat method a single value is attributed to each cardiovascular parameter over each cardiac cycle. Then the mean of each set of the collected samples is subtracted to obtain the corresponding variability signal (variation around zero) for the relevant parameter. Finally, the variability signals are employed to model the variability features (rhythmical fluctuations) of the cardiovascular system.

While the beat-to-beat approach offers great simplicity in extracting the variability signals and the modelling procedure, it sacrifices the reality of the model and its direct implications. What exists in reality is the contraction of the heart in a short time with a subsequent increase in blood pressure, blood flow, etc., and then relaxation of the heart and decrease in blood pressure, blood flow, etc. From this viewpoint all the variability signals, superimposed on the absolute values, can be defined as continuous state time series signals not as single quantities in each cardiac cycle.

Indeed, the major incentive for employing the beat-to-beat approach for cardiovascular variability analysis, apart from the simplicity in definition and ease of implementation, has been the methodological problems that are encountered when an event series signal like the heart beat must be related to a continuous signal such as respiration or instantaneous blood pressure which predominantly consists of a pulsatile component. On the other hand if the more realistic continuous state time series repre-

[1] No jump in the signal (continuous state) and well defined on a time basis (continuous time).

sentation is to be selected for defining the variability signals then appropriate techniques for connection of an event series signal (such as R-R intervals) to continuous signals (such as respiration), suitable for model analysis, must be found. Such a solution can be achieved by realising that the variation in the R-R intervals (variation in heart rate) is nothing but a specific coding scheme, imposed by the SA node on the continuous based sympathovagal drive signal. In other words it is assumed that a continuous state time series signal is behind the variations in the R-R intervals. This continuous signal is converted (coded) to the R-R interval variations by the spike generation mechanism of the SA node. Hence, extraction of this original continuous signal will be possible if the underlying coding mechanism is recognised. Clarifying this coding mechanism and finding a suitable decoding algorithm motivates us to begin this study with the basic steps of the extraction of the HRV signal from the R-R intervals and its relationship with the other variability signals in Chapters 2 and 3.

The spike generation mechanism of the SA node is addressed in Chapter 2. The Integral Pulse Frequency Modulation (IPFM) model is selected as a suitable physiological model to represent the coding characteristics of the SA node. Although the IPFM model has been used for many years for analysing the spike generation mechanism of excitable neurons and then the SA node, there are only a few comprehensive reports describing its coding and decoding mechanism in a practical framework. By noting the similarity between the IPFM model and the pulse position modulation technique for which strong theoretical studies exist, this chapter will elaborate on the functional performance of the IPFM model. It will be shown that by simple lowpass filtering, the sympathovagal drive signal of the SA node can be faithfully extracted. Then by using the Kaiser windowed lowpass filtering method a real-time algorithm for detection of HRV will be introduced. It will be shown that the definition of the HRV as a continuous state continuous time signal is not only feasible and realistic but also exceedingly simple and useful. This definition will also allow us to decompose the HRV signal into its constituent components in real time.

The problem of relating the R-R interval variations to the continuous signals is disentangled in Chapter 3. The idea that the SA node can be fitted into the class of continuous input spike output systems and, regardless of its physiological properties, can be treated as a nonlinear system by the Wiener series representation is discussed first. It is shown, however, that the IPFM model can still play a vital role for iden-

tifying the presumed systems between the HRV and the relevant physiological signals and therefore it can extricate us from the intricate computational work required for obtaining the Wiener kernels. Using this assumption, a new method for connecting a point series signal to the other signals based on the continuous state continuous time representation is introduced and its results are compared with the beat-to-beat approach for identifying an unknown system using parametric methods and spectral analysis.

The essential concepts of cardiovascular variability modelling are considered in Chapter 4. The discussion begins with a comprehensive description of the relevant physiological phenomena with emphasis on the possible origins of the variability signals. This is followed by an investigation into the structure of some of the existing models and examination of their restrictions and their concluding remarks. Preceded by a conceptual discussion about large signal and small signal cardiovascular modelling, a new model for describing the HRV-BPV-ILV relationships is presented. The prominent features of the model are highlighted but no mathematical representation is attempted until its linearity or nonlinearity features are discussed in Chapter 5.

In Chapter 5 the presence of input-output nonlinearity in the underlying physiological system is studied. This is accomplished through a novel approach based on cyclostationarity. Due to its robustness, the cyclostationary analysis of signals and systems has flourished recently. Although detection of nonlinearity in a given signal by cyclostationary methods is well documented, these methods are not suitable for system analysis. By theoretical development of the existing cyclostationary methods, employing the respiratory signal as an exogenous input in a set of metronome breathing experiments, and examining the variability signals by cyclic tools, it is shown that the neuro-cardiovascular system exhibits input-output nonlinearity even in the small signal regime. This conclusion prompts us to use nonlinear modelling techniques for further investigation into cardiovascular variability modelling in Chapters 7 and 8.

Further development of the IPFM representation of the SA node is the subject of Chapter 6. By adding the stretching effect, a more complete model of the SA node, namely the Time Varying Threshold IPFM (TVTIPFM) model, is obtained. An innovative approach for finding the solution of the TVTIPFM model based on vector space theory is presented. This theory, for the first time, gives a parametric insight

into the coding scheme of the IPFM model. The accuracy, flexibility and versatility of the new approach, particularly for the IPFM model as a special case of the TVTIPFM model, hold considerable promise for future analysis of the HRV.

Depicting the detailed structure of the new HRV-BPV-ILV model, already sketched in Chapter 4, constitutes the major part of Chapter 7. By invoking the available physiological data each individual part of the proposed model finds a mathematical foundation. For the unknown parts, the required theory is also expounded and an appropriate analysis technique is presented. Finally, the proposed model is simplified in order to allow a feasible mathematical treatment.

Chapter 8 is entirely devoted to the validation of the new HRV-BPV-ILV model by comparing experimental data with simulation results. The performance of the model is examined under different conditions by qualitative and quantitative comparison between the actual and the simulated variability signals over the important frequency bands. The close resemblance of the actual signals and the signals predicted by the model in different cases clearly justifies the plausibility of the new model. Specifically, the model offers convincing explanations for some of the fundamental features which are observed experimentally in the variability signals such as the LF oscillation.

The procedures employed and the results obtained during this study present a new approach to the clarification of heart rate variability and blood pressure variation. Further ideas for future work, together with an overview of what has been achieved, are discussed in Chapter 9 which concludes the thesis.

Chapter 2

Real-Time HRV Signal Extraction

Objectives of the Chapter

The vast majority of signal processing and system identification methods assume continuous state time series signals (e.g. a sinusoidal function such as $sin(2\pi 0.2t)$) for their treatments. However, the observed fluctuation in heart rate cannot be directly expressed as a well defined time series signal unless a proper operation is employed. That is because heart rate variability should be measured from interval variations in each cardiac cycle. The objective of this chapter is to determine how to obtain a well defined heart rate variability signal from the interval variations of the cardiac cycles. It is shown that by using a lowpass filter in an appropriate manner a continuous state HRV signal can be satisfactorily obtained. The presented method is further developed to extract the HRV signal in real-time from the ECG.

2.1 Introduction

The cells of the SA node (normally) initiate the sequence of excitation in the heart, and their repetitive discharge consequently determines the heart rate. In the absence of external disturbances, the membrane potential of an SA nodal fibre depolarizes at approximately constant rate. When the membrane potential of a fibre reaches a certain value (the threshold potential), an action potential is generated. The generation of these action potentials in the SA node eventually causes excitation of the heart muscles.

The firing rate of the SA node depends upon the time required for the membrane

potential of the nodal fibres to move from their initial resting values to the threshold level for generation of the action potential. Changes in rate are consequently mediated by alterations in (Milnor, 1990),

(i) the magnitude of the initial resting potential,

(ii) the rate of depolarization,

(iii) the threshold level.

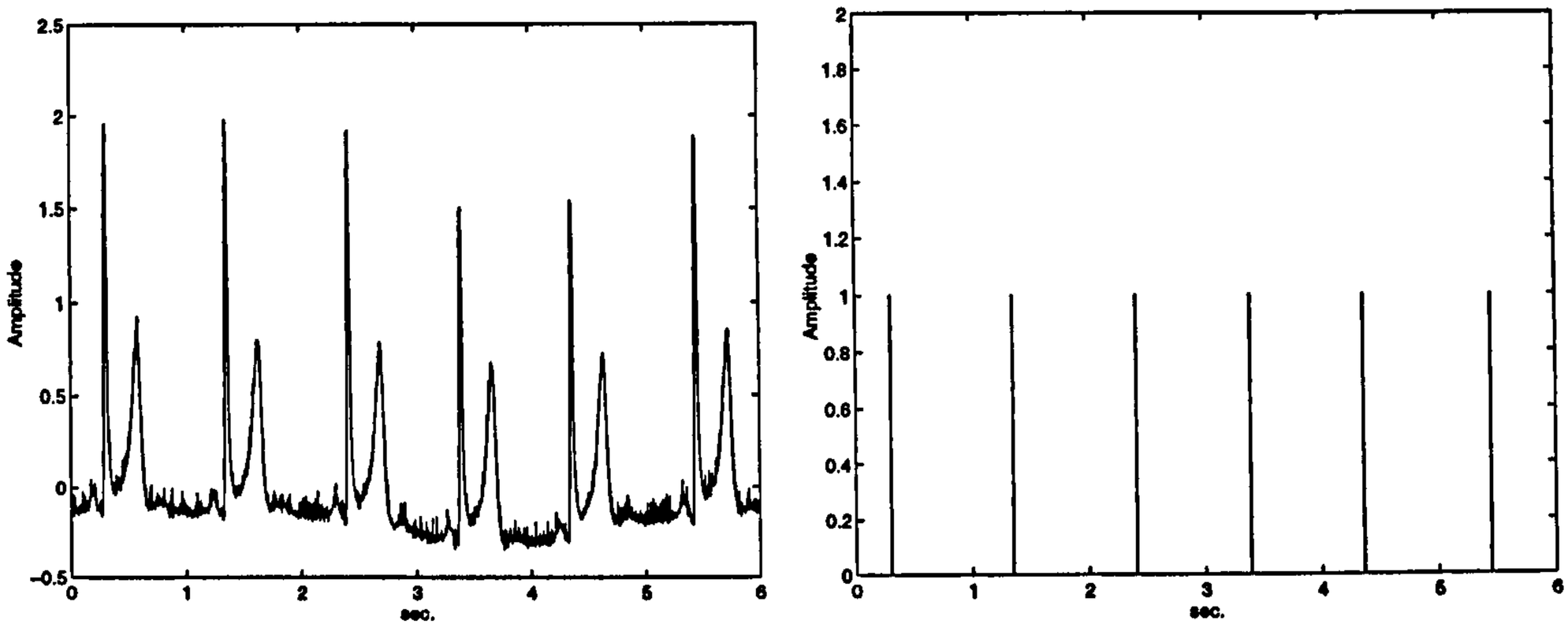
The SA node is innervated by sympathetic and parasympathetic fibres of the autonomic nervous system. Sympathetic and parasympathetic nerves both exhibit tonic activity under normal conditions; that is, they transmit impulses at some rate all the time. The sympathetic excitation of the heart increases its intrinsic rate whereas the parasympathetic excitation decreases the heart rate. It is known that the sympathetic activity increases the slope of the depolarization rate of the SA nodal cells whilst parasympathetic activity causes a decrease in the slope (Milnor, 1990; Guyton, 1996; Hyndman & Mohen, 1975). At any instant of time the resultant heart rate depends upon the balance between the incoming sympathetic and parasympathetic excitations. It is well known that even in the resting condition the heart rate is not constant. Spontaneous fluctuations in heart rate are caused mainly by the continuous activity of the autonomic nervous system. This activity modulates the natural rhythm of the SA node which is finally reflected in the interval variations between successive R peaks of the ECG and is known as heart rate variability (HRV).

Modern signal processing techniques have been used, extensively, for processing the HRV and describing its relationship with the other physiological signals. However, a problem not yet satisfactorily resolved concerns the correct detection of HRV from interval variations. In this chapter this problem is investigated and a real-time method for HRV detection is proposed.

There are two common approaches for the HRV detection. The first method looks at the R-wave signal on a beat-by-beat basis and tries to extract the hidden information directly from the interval variations (Pagani, Lombardi, Guzetti, Rimoldi, Furlan, 1986; Rimoldi, Pierini, Ferrari, Cerutti, Pagani, Malliani, 1990). The second method assumes a physiological based model for the generation of the so-called R-wave signal (Section 2.2) and utilises the characteristics of this model for defining the HRV signal (Hyndman & Mohen, 1975; Rompelman, Coenen, Kitney, 1977). Of the two methods,

the latter is considered to be better for system analysis and the popular Integral Pulse Frequency Modulation (IPFM) model (Section 2.2) has been accepted as a plausible physiological basis for deriving the HRV (Hyndman & Mohen, 1975; Rompelman, Snijders, Van Spronsen, 1982). IPFM has several advantages in this context. Indeed its definition is an adequate mathematical description of what physiologists believe to be the process of spike generation at the membrane level. Furthermore, the behaviour of this model corresponds to some of the important experimental findings and is relatively easy to handle mathematically (Hyndman & Mohen, 1975; Bruckstein & Zeevi, 1979). Throughout this study it is assumed that the SA node can be described as a localised anatomical area whose function is represented by the IPFM model. This, moreover, facilitates the analysis of the whole neuro-cardiovascular system by replacing the SA node with a tractable mathematical model. IPFM has also been used as a suitable model for the generation of neuronal spikes (Bayly, 1968; Gestri, 1971; Coggshall, 1973). From this standpoint there is much in common between this area and HRV signal analysis.

Bayly (1968) has derived the expression of the IPFM output signal in the case of a single sinusoidal excitation. He has shown that, with certain conditions, extraction of the excitation signal is possible by lowpass filtering. In a separate study French and Holden (1971) proposed the lowpass filtering method for conversion of a spike series signal to equispaced samples suitable for estimation of Power Spectral Density PSD *via* Fourier Transform (FT) algorithm, irrespective of the IPFM model. The French-Holden (F-H) algorithm thereafter was employed for HRV signal extraction from the R-wave signal and it was called the Low Pass Filtered Event Series (LPFES) method (Rompelman *et. al.*, 1977). Many investigators since then tried to present a new method for extraction of the coded information from the R-wave signal (Section 2.4). They used the IPFM model for confirmation of their proposed methods regardless of its characteristics. In this chapter the coding characteristic of the IPFM model is explored based on its similarity to pulse position modulation. Using this similarity a new method for real-time HRV extraction from the R-wave signal is proposed. This method can also be used for off-line HRV analysis in both the time and frequency domains. Real-time bandpass filtering as a new HRV investigation method and as a by-product of the proposed algorithm is also introduced. Furthermore, the discrete time domain version of the French-Holden algorithm is developed and it is shown that



(a) (b)

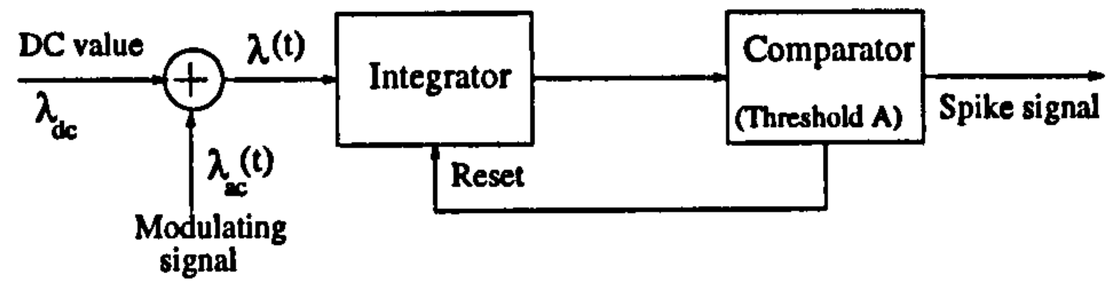
Figure 2.1: (a) ECG, (b) the corresponding R-wave signal obtained by replacing each R peak with a unit sample function.

lowpass filtering is an appropriate method for detection of HRV.

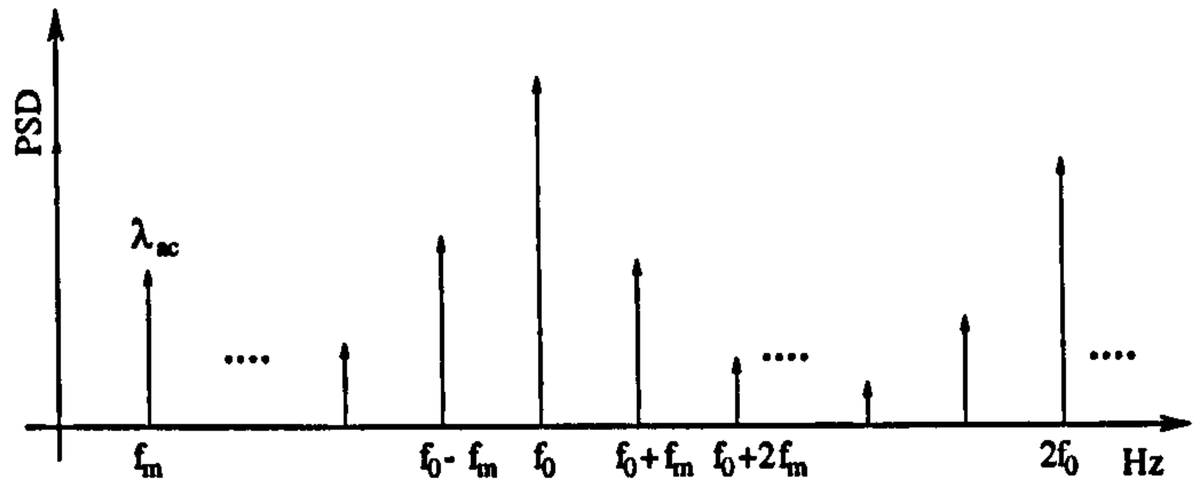
2.2 IPFM Model

The R peaks in the ECG signal are considered to be reliable indicators of the depolarization rate of the SA node (Hyndman & Mohen, 1975). In order to detect the R peaks, the ECG is first digitised and then, using a peak detection algorithm, their times of occurrence are determined. The location of the R peaks is normally shown by straight lines of unit amplitude (or impulse functions as described later). Hence, the R-wave signal comprises straight lines at the occurrence of the R peaks and zero elsewhere (Fig. 2.1). The sampling frequency of the ECG determines the resolution in the locations of the R peaks and therefore the amount of error in HRV (Merri, Farden, Mottley, Titlebaum, 1990). For credible HRV detection the sampling frequency is usually selected to be more than 300 Hz. The digitised R-wave signal is then used as the basic signal for HRV investigation.

Theoretically, the R-wave signal can be produced by the IPFM model as shown in Fig. 2.2(a). Referring to the figure, the excitation signal, $\lambda(t)$, consists of a constant (dc) component, λ_{dc}, and a time varying (ac) part, $\lambda_{ac}(t)$. The integral of $\lambda(t)$ is compared with the threshold level A. Whenever these two values become equal, a spike, which corresponds to an R peak, is produced at the output and the integrator



(a)



(b)

Figure 2.2: (a) IPFM model, (b) output power spectrum for a sinusoidal excitation at frequency f_m.

resets simultaneously. Both λ_{dc} and A are assumed to be positive numbers, hence when $\lambda_{ac}(t)$ is equal to zero the intervals between spikes remain the same. Therefore, in the case of variable intervals, estimation of $\lambda_{ac}(t)$ will be the objective. $\lambda_{ac}(t)$ in fact represents the sympathovagal excitation to the SA node.

Clearly, the IPFM is a nonlinear model. Bayly (1968) has shown that in the case of a sinusoidal excitation, the PSD of the output signal (Fig. 2.2(b)) comprises one frequency component at the frequency of excitation, f_m, and an infinite number of components at $kf_0 \pm nf_m$, where f_0 is the free-running frequency of the IPFM ($\lambda_{ac}(t) = 0$, interspike interval=$1/f_0$). He also argued that if the free running frequency is high enough and the modulation depth ($|\lambda_{ac}(t)|/\lambda_{dc}$) sufficiently low then the modulating signal, $\lambda_{ac}(t)$, can be recovered by lowpass filtering. This is discussed in the following section.

2.3 The French-Holden Algorithm

Analysis of the HRV signal has been of particular interest both in the frequency domain, such as investigation into the power spectral density and system identification by spectral analysis, (Akselrod, Gordon, Madwed, 1985; Saul, Berger Albrecht, Stein, Chen, Cohen, 1991; Cerutti, Bianchi, Mainardi, 1995) and in the time domain which can be used, for example, for the parametric system identification of the cardiovascu-

lar system (Baselli, Cerutti, Civardi, 1988; Mainardi, Bianchi, Barbieri, Di Virgilio, Piazza, Fulran, Baselli, Cerutti, 1997). As previously stated, French and Holden described the implementation of an ideal lowpass filter for estimation of the PSD of a spike series signal. To formulate the F-H algorithm a typical R-wave signal shown in Fig. 2.1(b) is assumed. If this signal is passed through an ideal lowpass filter with cutoff frequency of f_c, the output will be given by

$$x_l(t) = x_r(t) * sinc(2f_c t), \tag{2.1}$$

in which $*$ denotes the convolution operator, $x_r(t)$ is the R-wave signal,

$$x_r(t) = \sum_i \delta(t - t_i), \tag{2.2}$$

t_i is the occurrence time of the ith peak and $\delta(t)$ is the unit impluse function. Therefore,

$$x_l(t) = \sum_i sinc(2f_c(t - t_i)). \tag{2.3}$$

By choosing a suitable value for f_c, $x_l(t)$ will be the modulating signal of the interspike intervals, $\lambda_{ac}(t)$, plus a dc term. This is so since lowpass filtering in the form of equation (2.3) removes all the undesired components ($f > f_m$ in Fig. 2.2(b)) of the spike series signal of equation (2.2) whilst preserving the desired low frequency components (f_m in Fig. 2.2(b)). Although equation (2.3) results in a very simple detection technique, it is computationally inefficient because frequency components of the modulating signal, namely the HRV signal, are less than a hertz while the sampling frequency of the ECG and therefore the R-wave signal is much higher, for instance 300 Hz. A considerable amount of data reduction can be obtained by employing a down sampling method in the discrete time domain or sampling at a lower frequency in the continuous time domain (Oppenheim & Schafer, 1989). Since after lowpass filtering the highest possible frequency is f_c, a sampling frequency $2f_c$ or higher would be appropriate to satisfy the Nyquist limit. In the case of $2f_c$ a simple result is obtained,

$$x_s(t) = x_l(t) \cdot \sum_k \delta(t - \frac{k}{2f_c}) = \sum_i sinc(2f_c(t - t_i)) \cdot \sum_k \delta(t - \frac{k}{2f_c}) =$$
$$\sum_k \sum_i \frac{sin(\pi k - 2\pi f_c t_i)}{\pi k - 2\pi f_c t_i} \delta(t - \frac{k}{2f_c}) = \sum_k \sum_i \frac{(-1)^{k+1} sin(2\pi f_c t_i)}{\pi(k - 2f_c t_i)} \delta(t - \frac{k}{2f_c}) \tag{2.4}$$

where $x_s(t)$ denotes the sampled signal. Therefore the magnitude of the kth sample is

$$\sum_i \frac{(-1)^{k+1} sin(2\pi f_c t_i)}{\pi(k - 2f_c t_i)}. \tag{2.5}$$

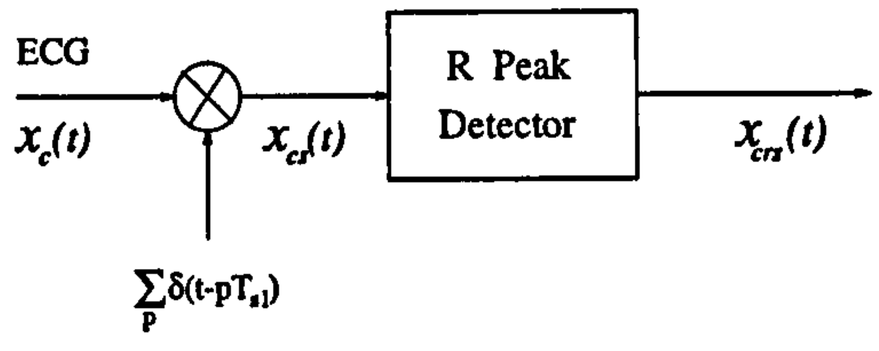


Figure 2.3: (a) Generation of the sampled R-wave signal from the ECG. $x_{cs}(t)$ denotes the sampled ECG and $x_{crs}(t)$ represents the R-wave signal. (b) Generation of the sampled R-wave signal from the presumed continuous time R-wave signal $x_r(t)$.

Expression (2.5) is the usual form used in the F-H algorithm.

Although the above equations were presented in the continuous time domain, all the intermediate stages are processed in the discrete time domain. In the following, the discrete time domain counterpart of the F-H algorithm is illustrated. This will be of importance when real-time lowpass filtering is considered later.

As previously stated, the R-wave signal is obtained from the sampled version of the ECG signal (Fig. 2.3(a)). This conversion can be described as the sampling of a presumed continuous time R-wave signal ($x_r(t)$ in Fig. 2.3(b)) on condition that all the R peaks can be accurately located by regular samples. The sampled R-wave signal, $x_{crs}(t)$, can be expressed as,

$$x_{crs}(t) = \sum_{p=-\infty}^{+\infty} x_r(pT_{s1})\delta(t - pT_{s1}), \tag{2.6}$$

where

$$x_r(pT_{s1}) = \begin{cases} 1 & \text{at R peaks} \\ 0 & \text{otherwise} \end{cases} \tag{2.7}$$

In the discrete time domain $x[n]$ is defined as,

$$x[n] \triangleq x_r(nT_{s1}). \tag{2.8}$$

In the frequency domain this transformation divides all the true frequency components by f_{s1}, where $f_{s1} = 1/T_{s1}$ is the sampling frequency of the ECG signal. In the simple

case of the sinusoidal excitation, f_m is now converted to f_m/f_{s1}. By passing $x[n]$ through a lowpass filter, $h_l[n]$, it follows that,

$$x_l[n] = x[n] * h_l[n] = \sum_{m=-\infty}^{+\infty} x[m]h_l[n-m]. \tag{2.9}$$

While f_{s1} may be as large as 1000 Hz (sampling frequency of ECG), f_m can be as small as 0.1 Hz (e.g. LF component in HRV). Since after lowpass filtering the area of interest occupies only a very small portion of the entire spectrum, $x_l[n]$ can be sampled with sampling frequency f_{s2}, provided that the Nyquist criterion is satisfied. If $N \triangleq f_{s1}/f_{s2}$ then the sampled signal can be represented by

$$x_{ls}[n] = \sum_{k=-\infty}^{+\infty} x_l[kN]\delta[n-kN]. \tag{2.10}$$

Finally, by decimation (Oppenheim & Schafer, 1989) the number of samples can be reduced by N if it is defined

$$x_{lsd}[n] \triangleq x_{ls}[Nn]. \tag{2.11}$$

All the previous stages can be summarised as:

$$x_{lsd}[n] = x_{ls}[Nn] = \sum_{k=-\infty}^{+\infty} x_l[kN]\delta[Nn-kN] = \sum_{k=-\infty}^{+\infty} \left\{ \sum_{m=-\infty}^{+\infty} x[m]h_l[kN-m] \right\}$$

$$\delta[Nn-kN] = \sum_{k=-\infty}^{+\infty} \left\{ \sum_{m=-\infty}^{+\infty} x_r(mT_{s1})h_l[kN-m] \right\} \delta[n-k]. \tag{2.12}$$

Thus, the kth sample is equal to

$$\sum_{m=-\infty}^{+\infty} x_r(mT_{s1})h_l[kN-m]. \tag{2.13}$$

The lowpass filter in the F-H algorithm is assumed to be ideal with cutoff frequency f_c. In the discrete time domain f_c becomes f_c/f_{s1}, but the *sinc* shape of the impulse response of the lowpass filter does not change. Hence,

$$x_{lsd}[n] = \sum_{k=-\infty}^{+\infty} \left\{ \sum_{m=-\infty}^{+\infty} x_r(mT_{s1}) sinc\left(\frac{2f_c}{f_{s1}}(kN-m)\right) \right\} \delta[n-k]. \tag{2.14}$$

Therefore, the kth sample will be given by

$$\sum_{m-\infty}^{+\infty} x_r(mT_{s1}) sinc\left(\frac{2f_c}{f_{s1}}(kN-m)\right), \tag{2.15}$$

where

$$x_r(mT_{s1}) = \begin{cases} 1 & \text{at R peaks} \\ 0 & \text{otherwise} \end{cases} \tag{2.16}$$

Now by choosing $N = \frac{f_{s1}}{2f_c}$, which corresponds to the sampling of the continuous time lowpass signal with frequency $2f_c$, the kth sample will be equal to,

$$\sum_{\substack{m=-\infty \\ m \text{ at } R \text{ peaks}}}^{+\infty} sinc(k - \frac{2f_c}{f_{s1}}m) = \sum_{\substack{m=-\infty \\ m \text{ at } R \text{ peaks}}}^{+\infty} \frac{(-1)^{k+1} sin(\frac{2\pi f_c}{f_{s1}}m)}{\pi(k - \frac{2f_c}{f_{s1}}m)}, \tag{2.17}$$

which is identical to equation (2.5). Therefore, the above procedure is an alternative way to describe HRV signal detection using the F-H algorithm. Equations (2.12) and (2.13) will be used for the new algorithm in Section 2.5.

2.4 Pulse Position Modulation and its Relation to the IPFM Model

The similarity between the base-band pulse position modulation signal and the IPFM output signal will now be discussed and used as the basis for developing a more general scheme for HRV signal detection.

In Pulse Position Modulation (PPM) the message signal changes the location of a sequence of impulse functions (Rowe, 1965). If the message signal is zero the modulator generates a series of impulses with equal intervals as depicted on the left-hand side of Fig. 2.4(b). By injection of the message signal the position of each impulse function varies according to the amplitude of the message signal as shown in the right-hand side of Fig. 2.4(b). There are two kinds of pulse position modulation techniques; uniform sampling and natural sampling. If $s(t)$ denotes the message signal, the natural sampling PPM is defined as,

$$x(t) = \sum_k \delta(t - t_k) = \sum_k \delta(t - kT - s(t_k)), \tag{2.18}$$

$$s'(t) < 1$$

where T is the free running period (no message signal). This equation is identical to the describing equation of the R-wave signal, expressed by equation (2.2). Zeevi (1977) and Bruckstein (1979) have considered this similarity in detail. They concluded that the output signal from a PPM modulator is exactly equal to the R-wave signal

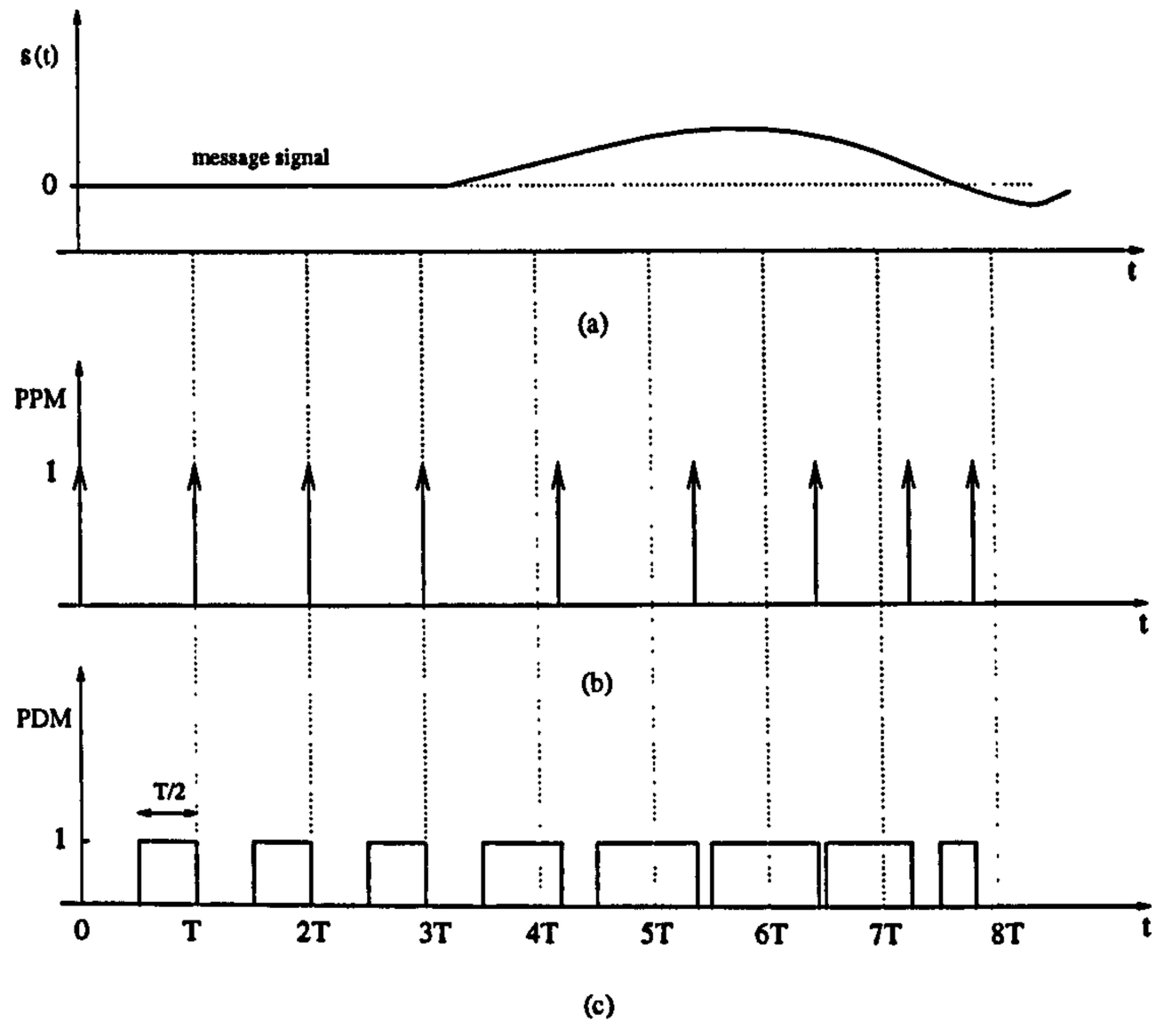


Figure 2.4: Pulse position and pulse duration modulation. (a) The message signal, (b) the corresponding PPM signal, (c) the corresponding PDM signal.

generated by the IPFM model provided that,

$$\lambda(t) = \frac{A}{T}\left[1 - \frac{ds(t)}{dt}\right], \tag{2.19}$$

and $T = \frac{1}{f_0}$. From this identity it follows that,

$$\lambda_{dc} = \frac{A}{T}, \tag{2.20}$$

$$\lambda_{ac}(t) = -\frac{A}{T}s'(t)\cdot \tag{2.21}$$

Regarding the similarity between the IPFM model and pulse position modulation, for which comprehensive theoretical studies exist, the functional performance of the IPFM model can now be elucidated and an appropriate HRV detection method can be derived.

It is shown in Appendix A at the end of chapter that equation (2.18) can be written as:

$$x(t) = (1 - s'(t))\sum_k \delta(t - kT - s(t)) =$$

$$\frac{1}{T}(1 - s'(t))\sum_k e^{jk2\pi f_0(t-s(t))} = \frac{1}{T}(1 - s'(t)) + \frac{1}{T}\frac{d}{dt}\sum_{\substack{k=-\infty \\ k\neq 0}}^{+\infty} \frac{1}{jk2\pi f_0} e^{jk2\pi f_0(t-s(t))}\ , \tag{2.22}$$

$$s'(t) < 1$$

Equation (2.22) reveals that $x(t)$ comprises three terms; a dc component, a term proportional to $s'(t)$, and the derivative of a series of phase modulated signals. The phase modulated signals are with carrier frequencies kf_0, $k \neq 0$ and with the modulating signals proportional to $s(t)$ and the order of harmonic. It can be shown that in the case of a sinusoidal modulating signal the frequency spectrum of $x(t)$ will be equal to the results obtained by Bayly (1968) providing that equations (2.20) and (2.21) hold.

In communication theory demodulation of the PPM signal is achieved by conversion to the corresponding Pulse Duration Modulation (PDM) signal and then lowpass filtering. The natural PDM signal is defined as (Rowe, 1965),

$$\ell(t) = \sum_k \Big(u(t - kT + \frac{T}{2}) - u(t - kT - s(t_k)) \Big) \cdot \tag{2.23}$$

in which $u()$ is the unit step function. This equation implies that in PDM the message signal modulates the width of a series of rectangular pulses as illustrated in Fig. 2.4(c). It is easy to show that PDM and PPM signals are related by:

$$\frac{d\ell(t)}{dt} = \sum_k \delta(t - kT + \frac{T}{2}) - x(t) \cdot \tag{2.24}$$

Using equations (2.22) and (2.24) it is proved in Appendix A that

$$\ell(t) = \frac{1}{T}s(t) + \frac{1}{2} + \frac{1}{T}\sum_{\substack{k=-\infty \\ k\neq 0}}^{+\infty} \frac{(-1)^k}{jk2\pi f_0} e^{jk2\pi f_0 t} - \frac{1}{T}\sum_{\substack{k=-\infty \\ k\neq 0}}^{+\infty} \frac{1}{jk2\pi f_0} e^{jk2\pi f_0 (t - s(t))}, \tag{2.25}$$

$$s'(t) < 1 \quad , \quad |s(t)| < \tfrac{T}{2} \cdot$$

Equation (2.25) shows that the PDM signal is the sum of the modulating signal, a dc component, discrete sinusoidal components at the pulse repetition frequency and its harmonics, and phase modulated carriers at the pulse repetition frequency and its harmonics, with phase modulation proportional to the message signal and the order of harmonic. Now suppose that $s'(t) \ll 1$ and that $s(t)$ is essentially confined to a band W where $W \ll f_0$. Then the spectral densities of the phase modulated signals (the final summation of equation (2.25)) will be essentially confined to narrow regions around kf_0, $k \neq 0$ (Rowe, 1965). Bearing in mind that the frequency components of the first summation of equation (2.25) only exist at kf_0, $k \neq 0$, it is concluded that $s(t)$ is recoverable by passing the PDM signal through a lowpass filter with a suitable cutoff frequency. Consequently, equation (2.24) can be written as:

$$x(t) = \frac{-d\ell(t)}{dt} + x(t)\Big|_{s(t_k)=\frac{-T}{2}} \tag{2.26}$$

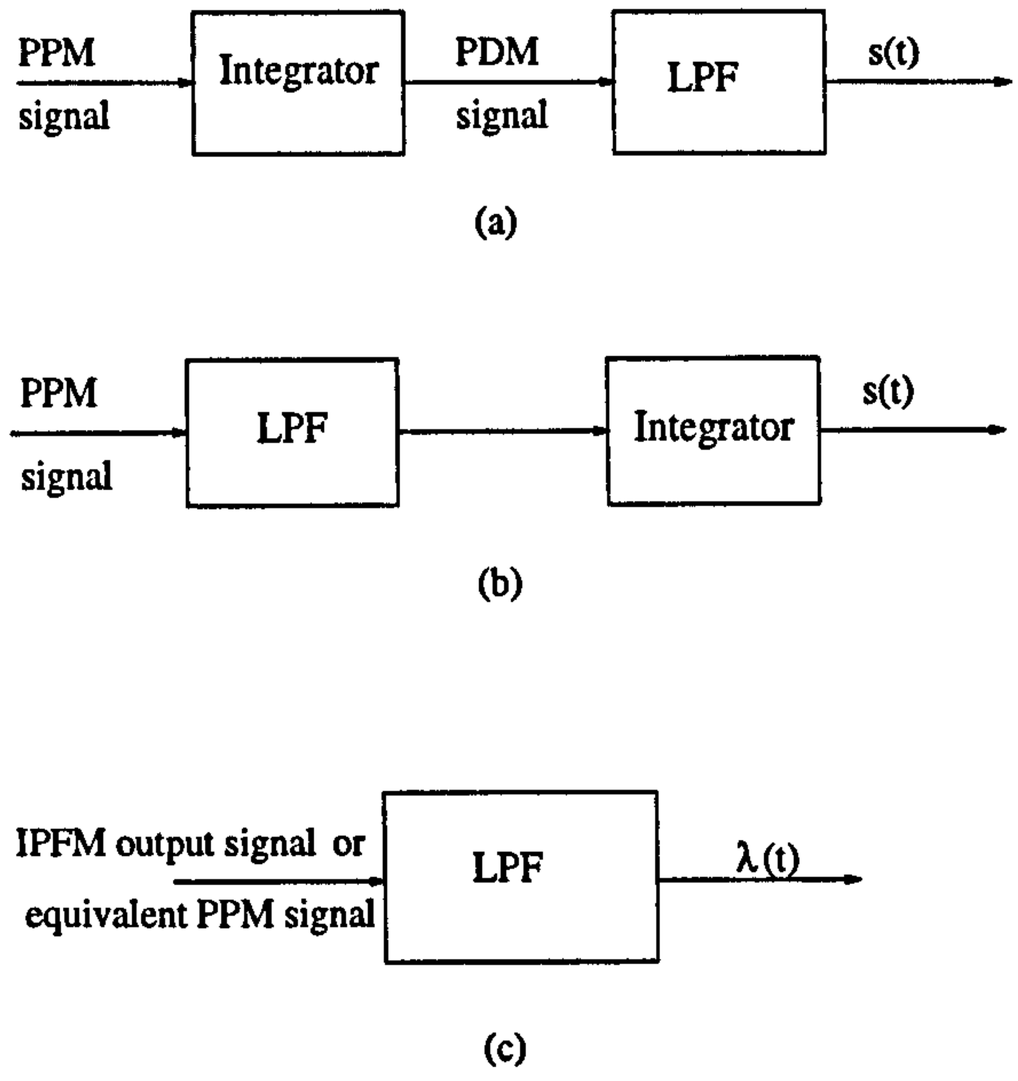


Figure 2.5: (a),(b) Detecting the message signal from PPM, (c) from IPFM output signals.

Using equation (2.22) the frequency components of the second term of the right side of equation (2.26) comprises the terms at kf_0. Hence, for frequencies less than the free running frequency, $\ell(t)$ can be viewed as the integration of $x(t)$. Therefore, the demodulation algorithm can be summarised as shown in Fig. 2.5(a). It is also possible to change the integration and lowpass filtering stages as shown in Fig. 2.5(b). However, according to equation (2.19), $\lambda(t)$ is equal to the derivative of the PPM modulating signal except for a dc value. Thus extraction of the HRV signal, $\lambda_{ac}(t)$, can be accomplished by using an appropriate lowpass filter as illustrated in Fig. 2.5(c). This is the crucial point for correct detection of the HRV. This filter should retain the desired signal, $\lambda_{ac}(t)$, while removing all the higher components. To do so it needs to have a flat response up to the highest frequency of $\lambda_{ac}(t)$ and maximum attenuation for the disturbing components. The cutoff frequency is chosen according to the value of the free running frequency and the maximum frequency of $\lambda_{ac}(t)$ (Fig. 2.2(b) and equation (2.22)). In practical applications half of the free running frequency is usually a desired selection.

In fact equation (2.22) is the generalised form of the Bayly (1965) equation. Evidently, implementation of an ideal lowpass filter is impossible and a realizable filter is involved with constructional errors. Lowpass filtering can also be interpreted, roughly, as the time averaging of the signal. Indeed many of the other HRV detection methods

from the R-wave signal (as well as from neuronal spikes) use a kind of time averaging algorithm (Kitney, Rompelman 1980; Berger, Akselrod, Gordon, Cohen, 1986; de Boer 1985a, 1985b; Paulin, 1992). Convolution with a rectangular window in the time domain is the common point of many of these algorithms. deBoer *et. al.* (1984, 1985b) have compared the F-H algorithm with two other methods and concluded that lowpass filtering gives a better result. The same conclusion has been obtained by Rompelman *et. al.* (1977) by comparing the LPFES algorithm with interval tachogram, instantaneous heart rate variability and interval function methods. To present a better HRV detection method Berger *et. al.* (1986) have presented an algorithm based on counting the number of events in a bin which is not causal and can be considered as convolution with a rectangular function (Appendix A of Chapter 3). Coenen, Rompelman and Kitney (1977) have proposed a real-time method on the basis of the IPFM model and the F-H algorithm. They used a squared cosine filter instead of a rectangular shape filter, hence they had to reduce the cut off frequency of the filter or define dummy pulses which results in a frequency dependent filter. Also they do not introduce any criterion for the selection of the filter delay. More recently Noguchi, Hataoka, Sugimoto, Kobayashi and Kobayashi (1987) have proposed a very simple method which is also real-time. However, their approach is only a rough approximation of the lowpass filtering. To obtain a fast algorithm for obtaining the PSD of HRV, Rompelman *et. al.* (1982) have also used convolution of the spike series signal with a rectangular function and resampling with a low sampling rate. But, as they have mentioned, this method shifts the position of the R peaks and therefore causes distortion in the final estimations.

It should be pointed out here, that the IPFM model has been used by these authors for justification of their proposed HRV detection algorithms. However, the equivalence between PPM and IPFM outputs and the above analysis implies that ideal lowpass filtering of the R-wave signal gives the true HRV signal. By applying this fact and noting the sparse property of the R-wave signal, the Kaiser windowed lowpass filter is employed in the next section in the proposal of a real-time technique for extraction of the HRV.

2.5 Real Time HRV Signal Extraction

2.5.1 The New Method

The existing algorithms for HRV signal detection suffer either from being non-causal methods (they need the future values of the R-wave signal) or they have poor recovering features. As already stated, the R-wave signal is available in the form of a discrete time signal. In view of this fact and the concepts presented in previous sections, a new method is now developed for HRV detection based on the Finite Impulse Response (FIR) lowpass filtering. Using FIR filter can also prevent the phase distortion which arises in other real-time algorithms.

In FIR filter design, the windowing method is very straightforward. Even though employing conventional windows such as Hanning or Hamming may seem easier, the Kaiser window, because of its behaviour in side lobe reduction and maximally flat characteristic in the pass band is an optimum selection among windowed type FIR filters (Oppenheim & Schafer, 1989). Nevertheless, delineation of this filter, as will be shown later, is very convenient so it does not increase the complexity of detection.

Equation (2.12) presents a general expression for HRV signal extraction and equation (2.13) gives the magnitude of the kth sample. Here it is sufficient to replace $h_l[n]$ with the impulse response of the Kaiser windowed lowpass filter which is (Oppenheim & Schafer, 1989),

$$h_l[n] = \begin{cases} \frac{sin(\frac{2\pi f_c}{f_{s1}}(n-\alpha))}{\frac{2\pi f_c}{f_{s1}}(n-\alpha)} \cdot \frac{I_0[\beta(1-[(n-\alpha)/\alpha]^2)^{\frac{1}{2}}]}{I_0(\beta)} & 0 \leq n \leq \Upsilon \\ 0 & \text{otherwise} \end{cases} \tag{2.27}$$

where $I_0(\cdot)$ denotes the zeroth-order modified Bessel function of the first kind. Υ is the width of the window and β is the shape parameter. Increasing Υ decreases the main lobe width but increases the output delay which is equal to $\alpha = \Upsilon/2$. On the other hand increasing β decreases the sidelobe amplitudes but increases the main lobe width. If the peak amplitude of the Fourier transform of the Kaiser window in the stopband region is represented by σ and $\mathcal{A} \triangleq -20log_{10}\sigma$ then the empirical value of β and Υ are

given by (Oppenheim & Schafer, 1989),

$$\beta = \begin{cases} 0.1102(\mathcal{A} - 8.7) & \mathcal{A} > 50 \\ 0.5842(\mathcal{A} - 21)^{0.4} + 0.07886(\mathcal{A} - 21) & 21 \leq \mathcal{A} \leq 50 \\ 0 & \mathcal{A} < 21 \end{cases} \tag{2.28}$$

and

$$\Upsilon = \frac{\mathcal{A} - 8}{14.357 \frac{\Delta f}{f_{s1}}} \tag{2.29}$$

in which Δf denotes the transition band in Hz. In real-time HRV extraction the delay of the filter is of importance. If d represents the delay time in seconds then,

$$d = \frac{\Upsilon}{2} \frac{1}{f_{s1}} \tag{2.30}$$

A number of choices for parameter selection can be thought of, but some compromises should also be kept in mind. Firstly, better performance of the filter can be obtained by choosing larger values of d but this increases the number of filter coefficients and hence, the amount of computation. It also degrades the on-line characteristic of the filter. Secondly, $\mathcal{A}$ and Δf are conflicting factors, however they are not critical in the filter design. Considering the PSD of the HRV signal (Fig. 2.2(b) and equation (2.22)), $40dB$ for the minimum attenuation in the stopband region will be a reasonable choice. This attenuation corresponds to $\beta = 3.4$ (equation (2.28)). Next, by substituting the value of Υ from equation (2.30) into (2.29) it follows that

$$\Delta f = \frac{1.11}{d} \approx \frac{1}{d}. \tag{2.31}$$

Equation (2.31) imposes higher delay time for getting lower transition band. Further, equation (2.27) can be expressed as:

$$h_l[n] = \begin{cases} \frac{sin(\frac{2\pi f_c}{f_{s1}}(n - df_{s1}))}{\frac{2\pi f_c}{f_{s1}}(n - df_{s1})} K(n, d) & 0 \leq n \leq 2df_{s1} \\ 0 & \text{otherwise} \end{cases} \tag{2.32}$$

in which, for notational brevity, $K(n, d)$ denotes the Kaiser window (the second fraction of equation (2.27)).

Using equation (2.13) the kth interpolation function will be,

$$\frac{sin(\frac{2\pi f_c}{f_{s1}}(kN - m) - 2\pi f_c d)}{\frac{2\pi f_c}{f_{s1}}(kN - m - df_{s1})} K(kN - m, d). \tag{2.33}$$

If analogous to the F-H algorithm $N = f_{s1}/2f_c$ is chosen then equation (2.33) becomes,

$$\frac{sin(\pi k - \frac{2\pi f_c}{f_{s1}}m - 2\pi f_c d)}{\pi(k - \frac{2f_c}{f_{s1}}m - 2df_c)} K(\frac{f_{s1}k}{2f_c} - m, d)\cdot \tag{2.34}$$

and the kth sample will be,

$$\sum_{\substack{m=-\infty \\ m \text{ at } R \text{ peaks}}}^{+\infty} \frac{(-1)^{k+1} sin(2\pi(\frac{f_c}{f_{s1}}m + f_c d))}{\pi(k - \frac{2f_c}{f_{s1}}m - 2df_c)} \cdot K(\frac{kf_{s1}}{2f_c} - m, d) \tag{2.35}$$

Once the Kaiser window coefficients are calculated, they can be replaced by $K(\cdot,\cdot)$ in equation (2.35), thus implementation of the proposed algorithm is exceedingly simple. Moreover, according to equation (2.17), calculation of the kth sample in the F-H algorithm needs to be accomplished on all R peaks whereas the kth sample of equation (2.35) includes the R peaks only, in the vicinity of the kth sample. It should be pointed out that only Υ must be an integer number, therefore selection of d by equation (2.30) should preserve this property. The number of coefficients in the FIR filter, represented by equation (2.32), is $2df_{s1}$ which is very large. But the R-wave signal is sparse, its value is often equal to zero (Fig. 2.1(b)). Hence, in the whole length of the FIR filter only a few nonzero points of the R-wave signal may take place. Therefore, the number of calculations for each output sample reduces to a few additions. The sparse property is of great value in real-time HRV signal detection.

To recapitulate, the main steps involved in the proposed algorithm are as follows:
(i) Assume a real-time ECG signal that is being sampled at frequency f_{s1}. Select a desired value for f_c, the highest frequency component of the HRV signal (e.g. $f_c = 0.4Hz$).
(ii) Select an appropriate value for d (e.g. $d = 5sec$).
(iii) Calculate the coefficients of the filter $h_l[n]$ using equations (2.30), (2.32) and place them in a look-up table. The number of coefficients is equal to Υ. Since the filter is symmetrical, only half of the coefficients are in fact required.
(iv) Pass the sampled ECG signal through the R peak detector algorithm (Section 2.7).
(v) Follow the samples of the R-wave signal while they are coming out of the R peak detector algorithm. Whenever a non-zero value (R peak) is detected, select the first row of the look-up table. With each new input sample select the next row and deselect the existing one (a shift down procedure). Each output sample is obtained by summation of the selected rows of the look-up table.
(vi) Keep every Nth sample of the output samples. This is the HRV signal. Note that

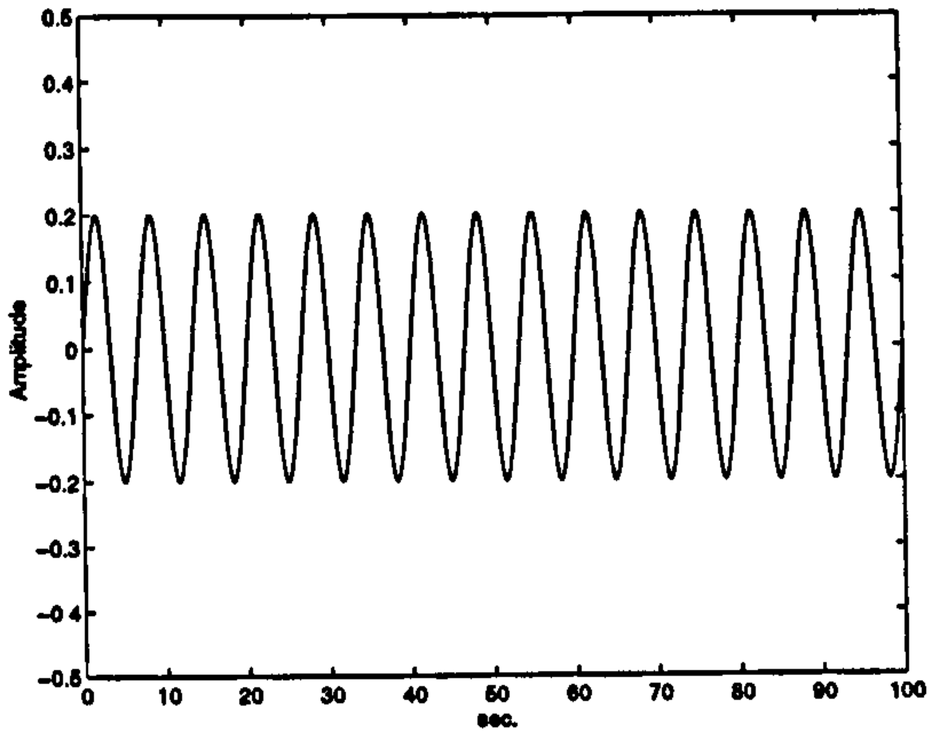
for time monitoring, $N = 1$ is the best selection because it gives a very smooth time series signal whereas for frequency or time analysis $\frac{f_{s1}}{4f_c} \leq N < \frac{f_{s1}}{2f_c}$ is recommended because it gives a small number of samples to decrease the computational effort.
For convenience this HRV detection method is called the KLPF method hereafter.

2.5.2 Simulation Results

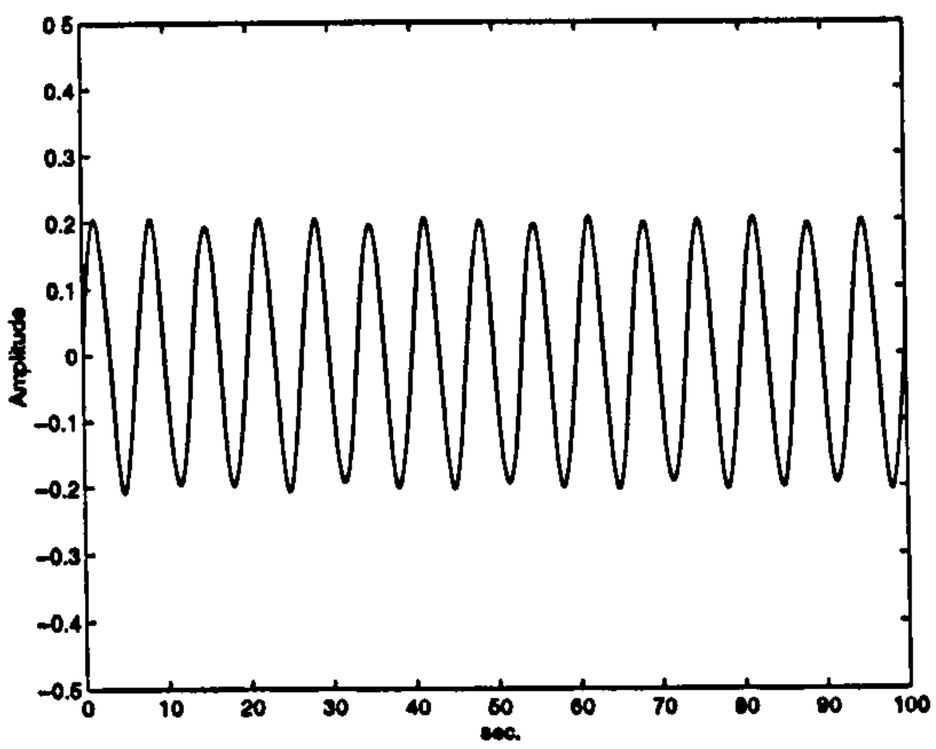
The validity of the KLPF method is examined in this section by considering four different cases and comparing the results with the F-H method. In all cases the R-wave signal was produced by the IPFM model with threshold $A = 1$, sampling frequency 300 Hz and data length $400sec$. For the F-H method $f_c = 0.4Hz$ and for the proposed method $f_c = 0.4Hz$ and $d = 5sec$ were employed. For the sake of comparison the transient period and the delay in the detected signals have been removed from all the figures.

In the first case a single sinusoidal excitation in the form of $\lambda(t) = 1+0.2sin(2\pi 0.15t)$ is assumed. Figures 2.6(a), 2.6(b) and 2.6(c) illustrate the ac part of the input signal, $\lambda_{ac}(t)$, the detected signal using the F-H algorithm and the detected signal using the KLPF method, respectively. Figures 2.6(d) and 2.6(e) depict the normalised PSD of the demodulated signal using the F-H and the new algorithm, respectively. Both methods reconstruct the original signal quite well. Figure 2.7 plots similar results but for $\lambda(t) = 1 + 0.3sin(2\pi 0.3t)$. Because of the higher input frequency, spurious components can now be observed in the detected signal ($f \approx 0.4Hz$). This is due to the nonlinear operation of the IPFM model as predicted by equation (2.22). The input signal at $0.3Hz$ is recovered quite well by both methods, slightly better by the KLPF method. Figure 2.8 presents the simulation results for the two sinusoidal function $\lambda(t) = 1 + 0.4sin(2\pi 0.15t) + 0.4sin(2\pi 0.3t)$. Now the intermodulation frequencies of the main components also exist due to the nonlinear operation of the IPFM model. The price paid for having a lower spurious component at 0.4 Hz in the proposed KLPF algorithm is a slight decrease in the magnitude of the main component at 0.3 Hz (Figs. 2.8(d),(e))

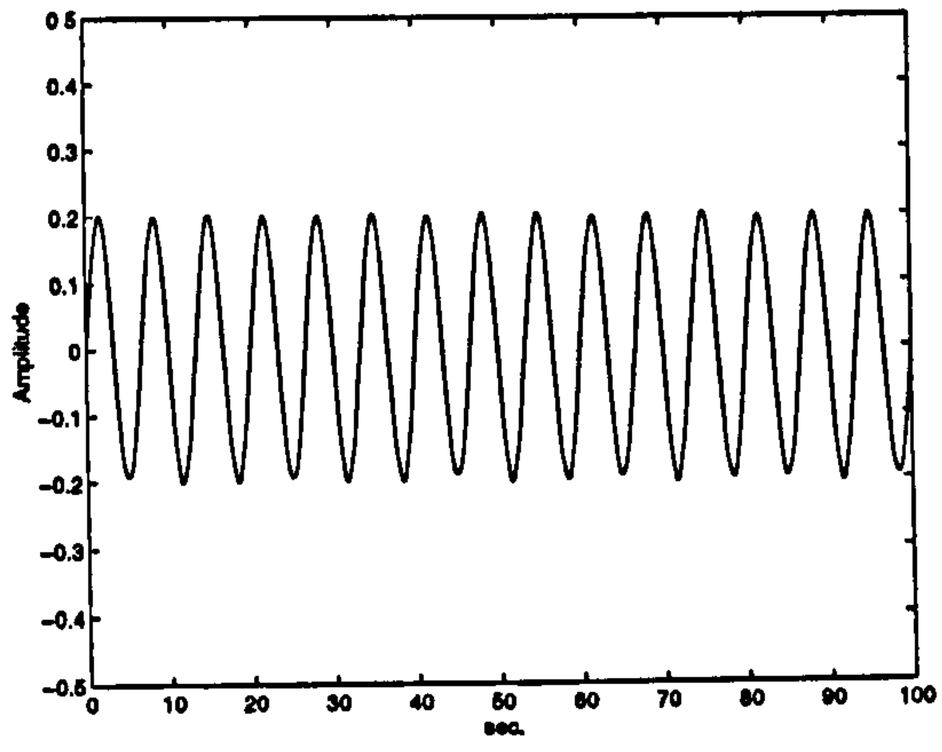
An interesting result is illustrated in Fig. 2.9. Figure 2.9(a) shows the ac part of the input signal. Here a transient signal instead of pure sinusoids has been assumed



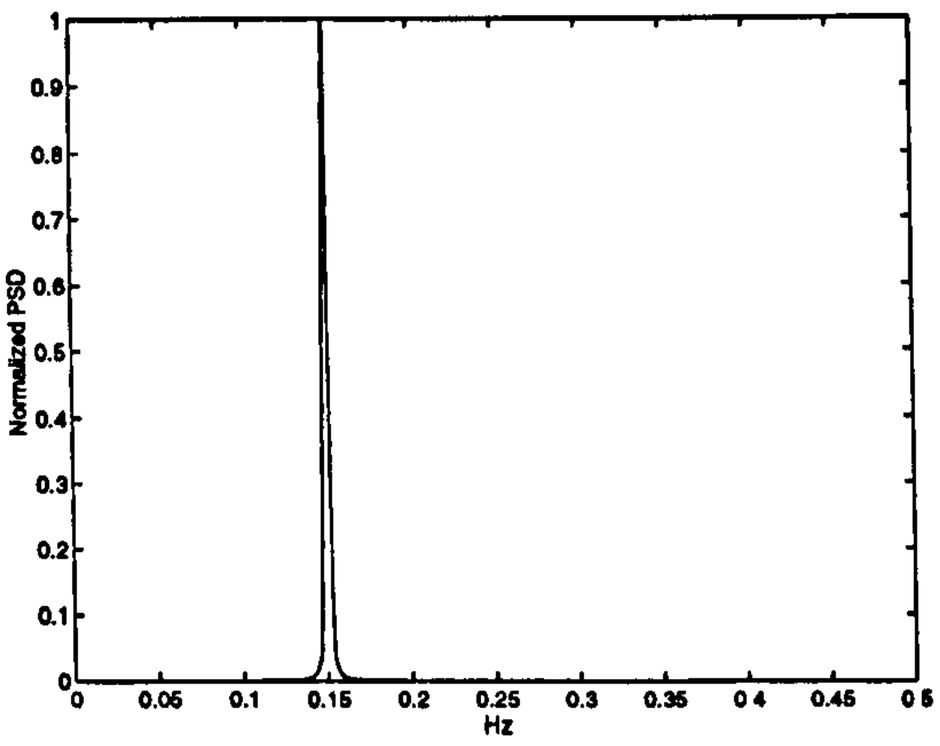
(a)



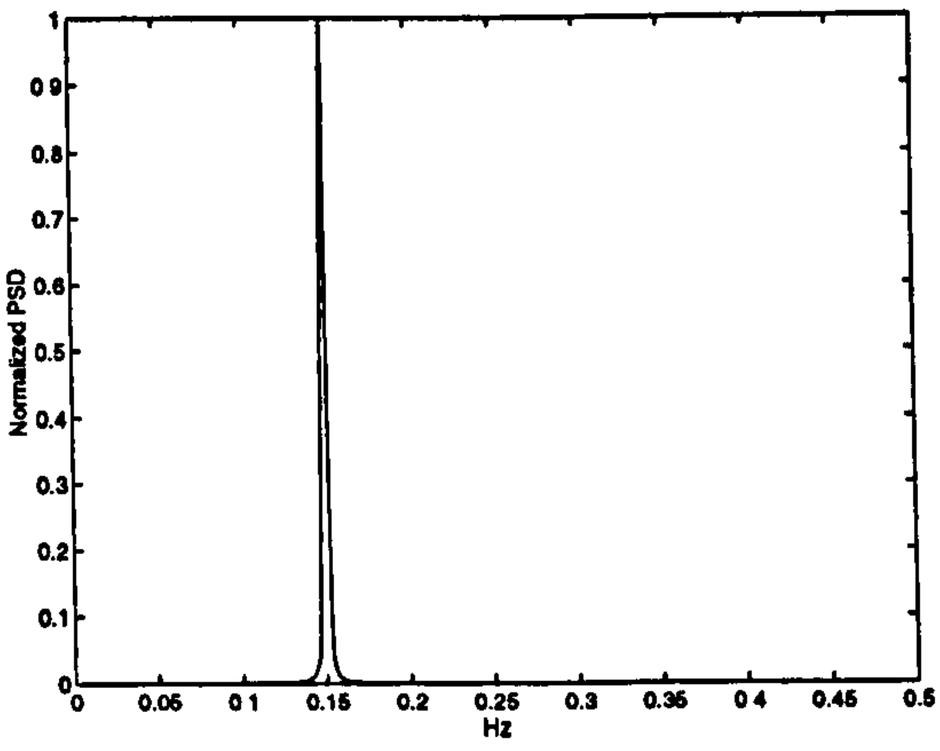
(b)



(c)

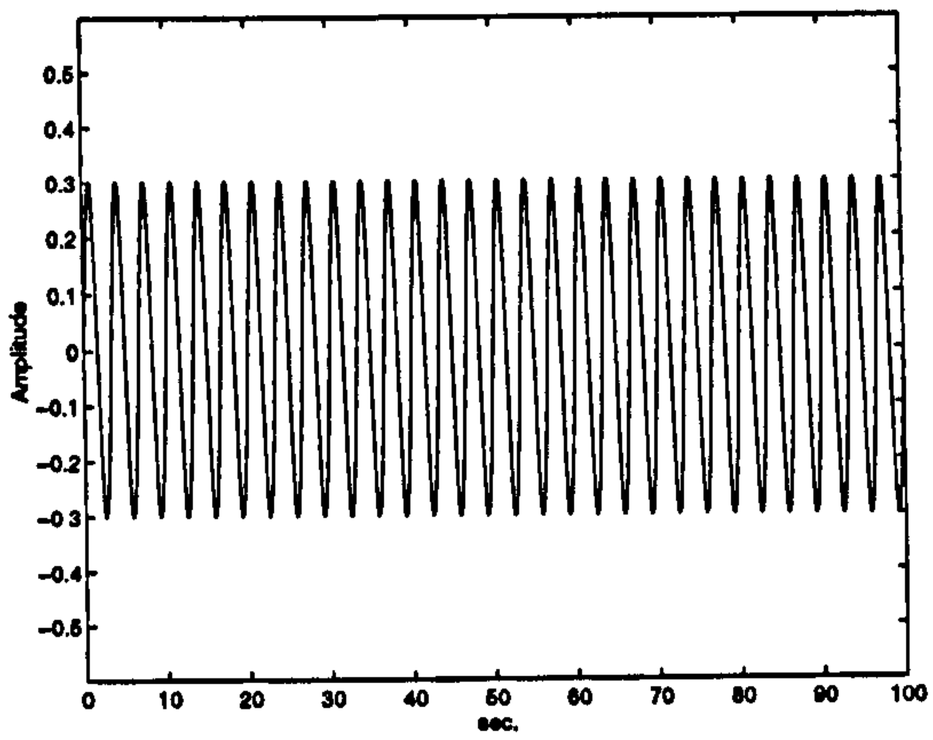


(d)

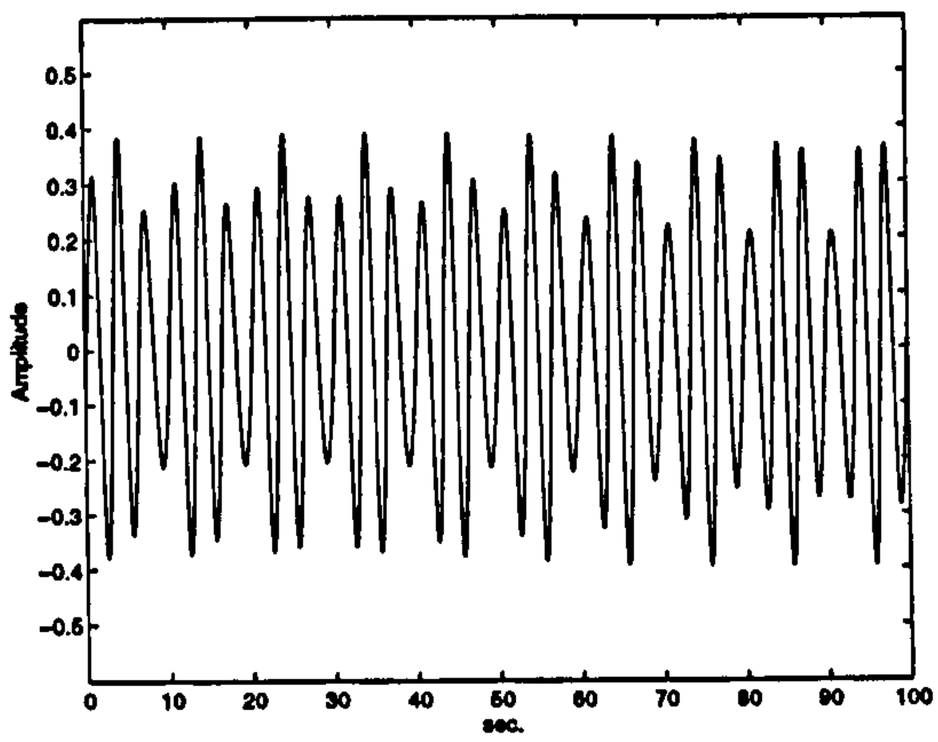


(e)

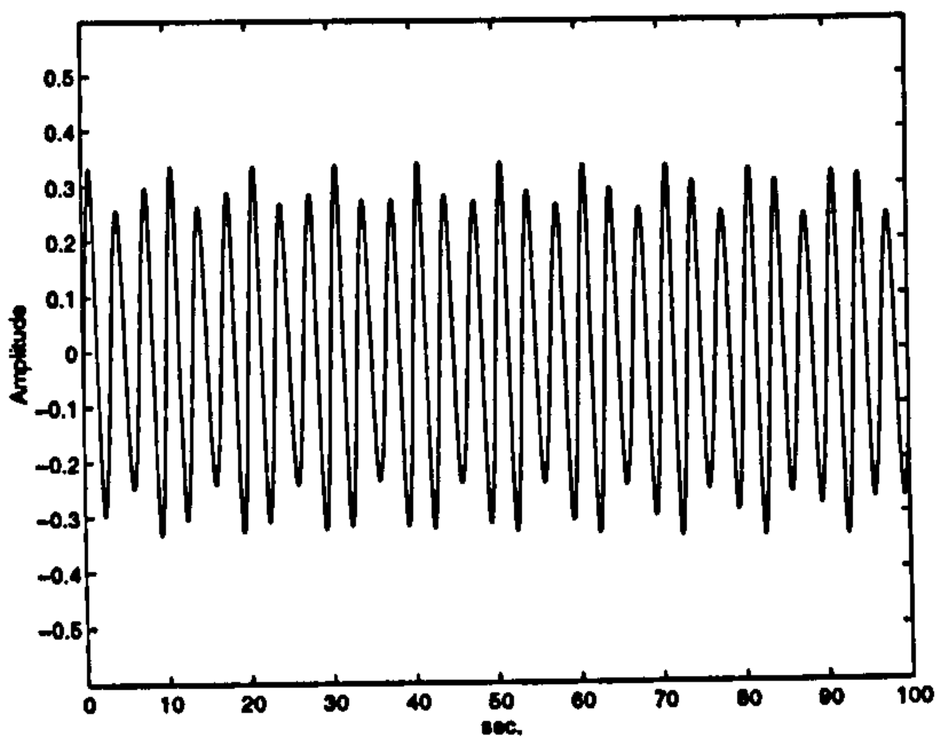
Figure 2.6: Detection of signal $0.2sin(2\pi 0.15t)$. (a) Input signal. (b) The detected signal using the F-H algorithm. (c) The detected signal using the KLPF method. (d) PSD of the detected signal using the F-H algorithm. (e) PSD of the detected signal using the KLPF method.



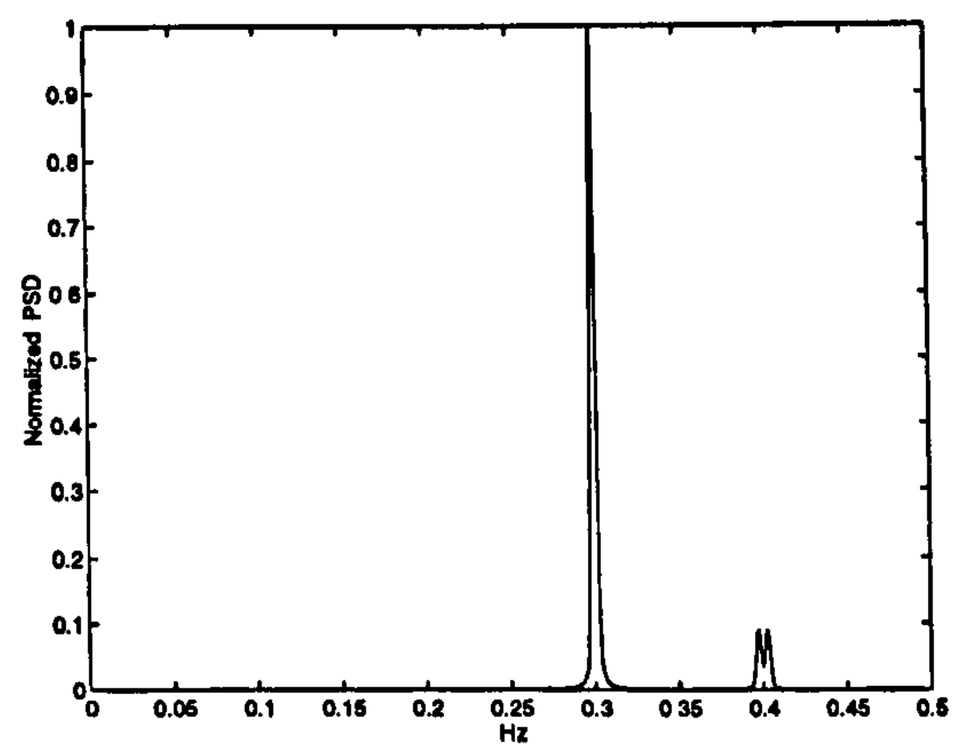
(a)



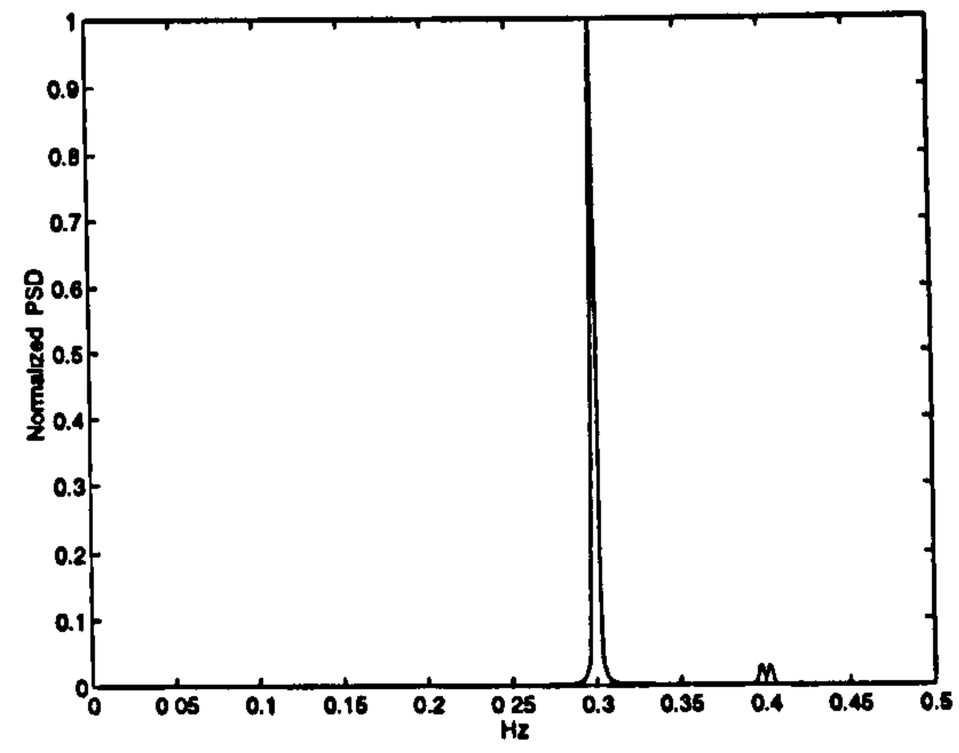
(b)



(c)



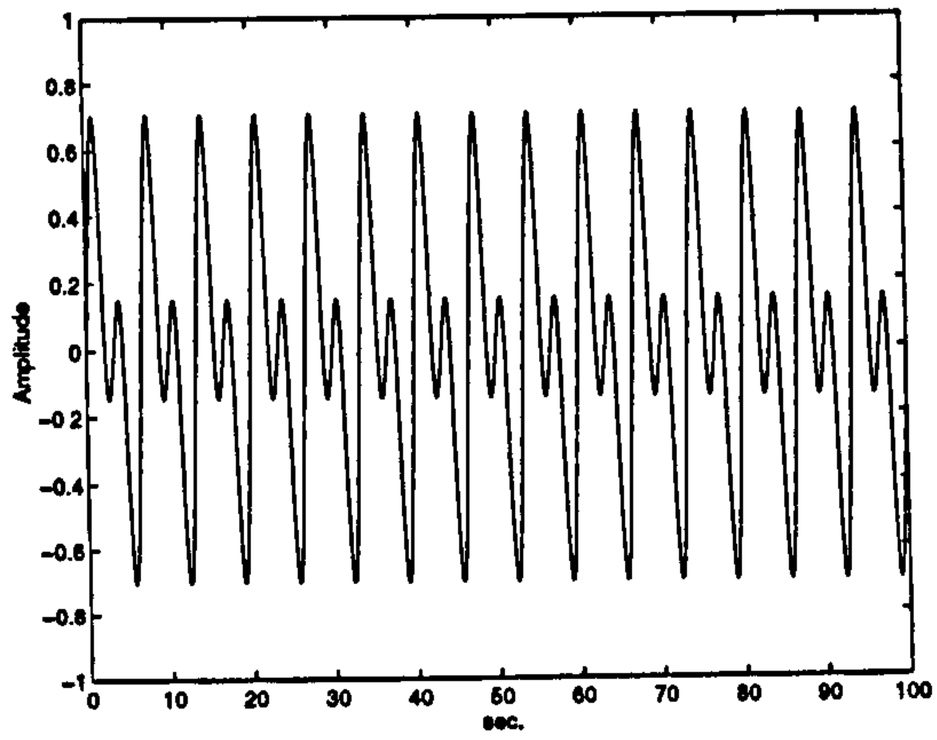
(d)



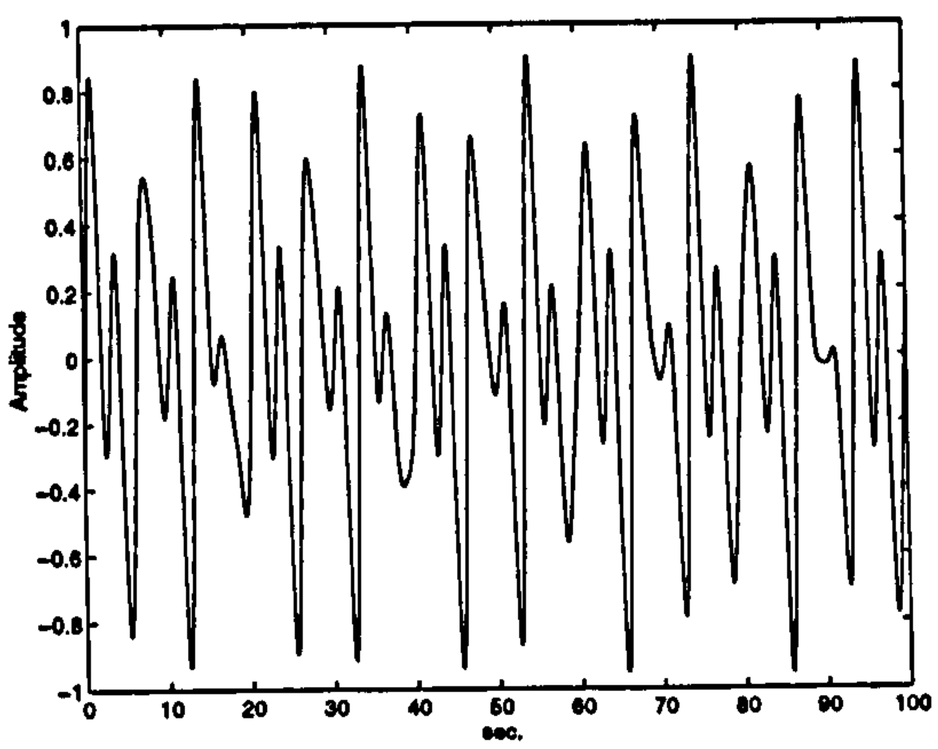
(e)

Figure 2.7: Detection of signal $0.3sin(2\pi 0.3t)$. (a) Input signal. (b) The detected signal using the F-H algorithm. (c) The detected signal using the KLPF method. (d) PSD of the detected signal using the F-H algorithm. (e) PSD of the detected signal using the KLPF method.

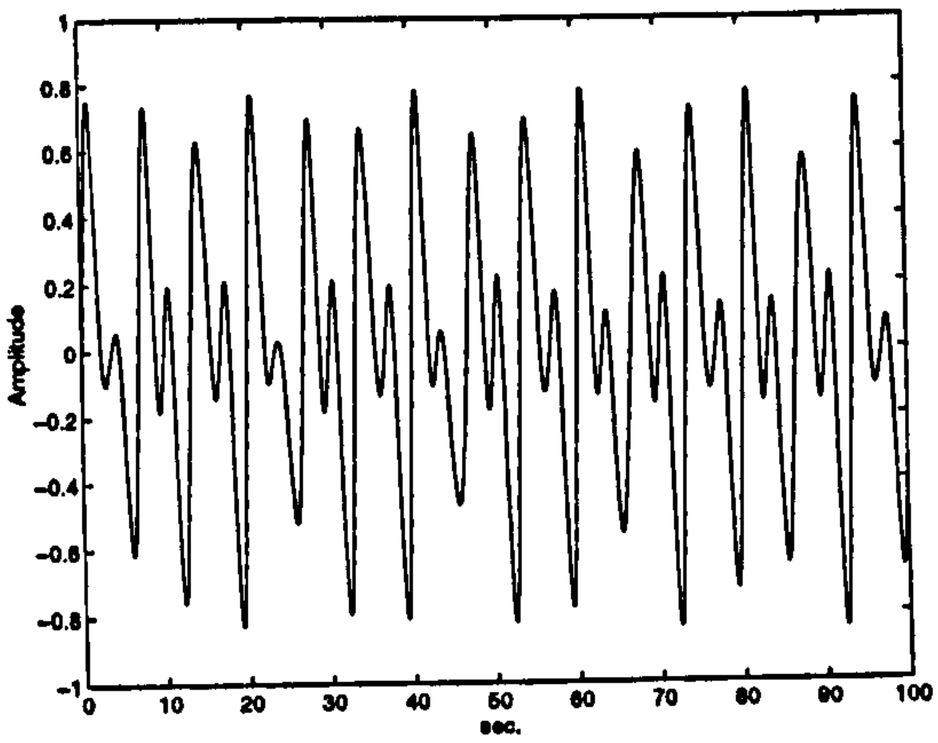
BIBL
LONDON
UNIV.



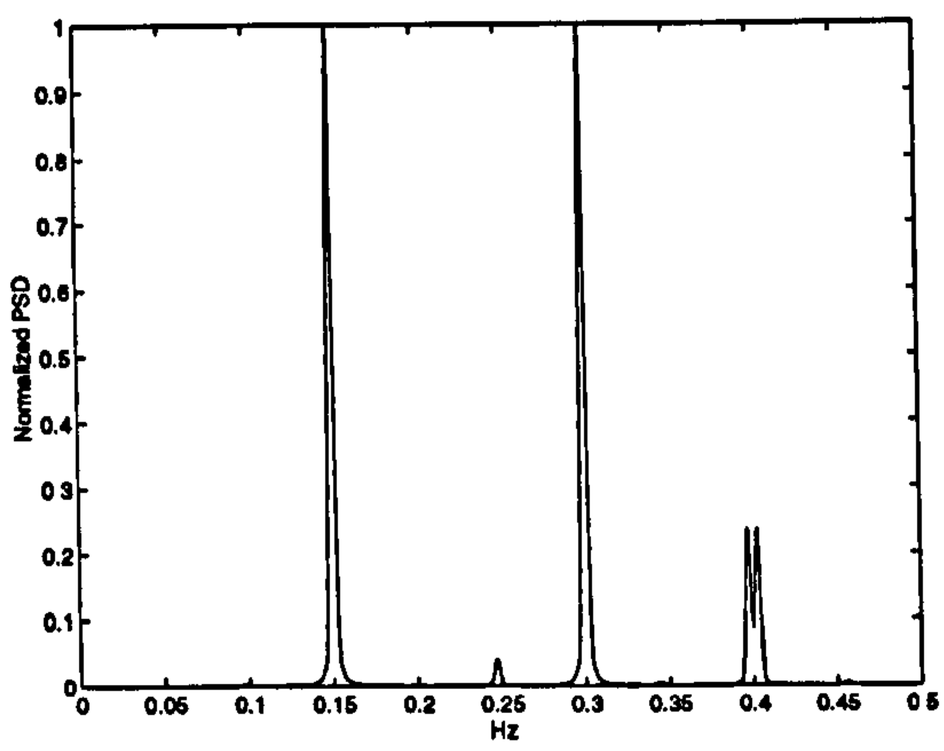
(a)



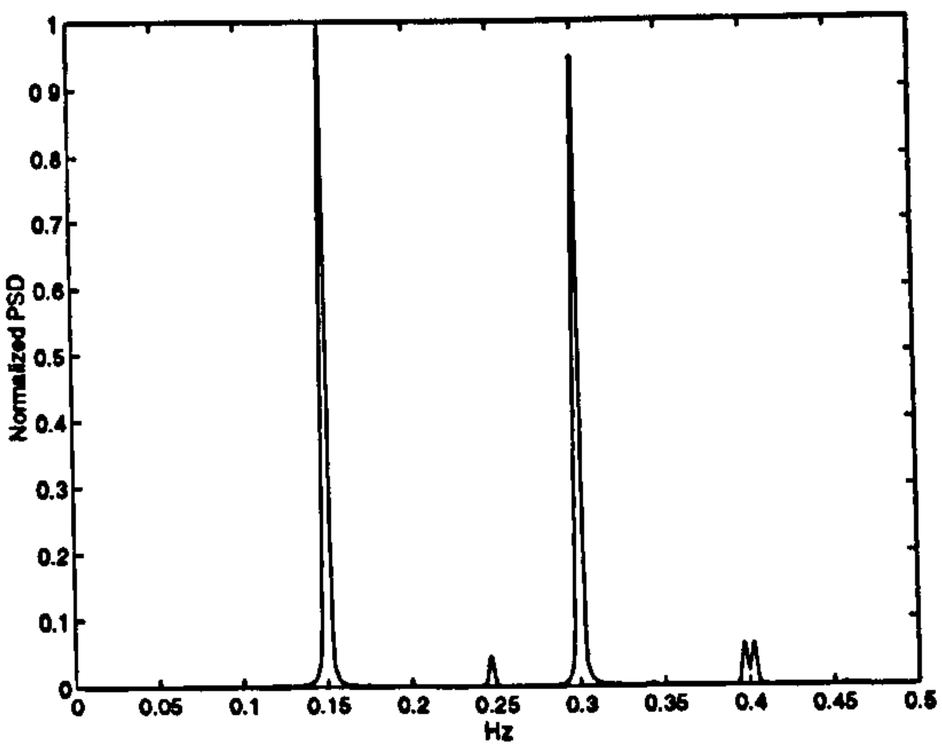
(b)



(c)

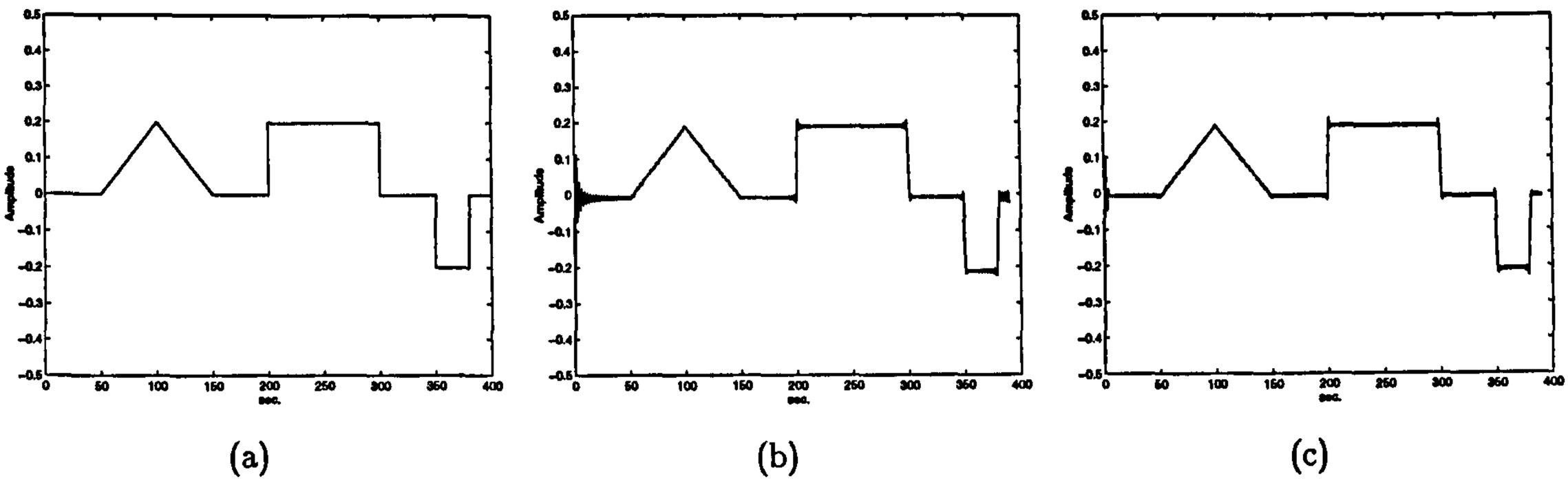


(d)



(e)

Figure 2.8: Detection of signal $0.4sin(2\pi 0.15t) + 0.4sin(2\pi 0.3t)$. (a) Input signal. (b) The detected signal using the F-H algorithm. (c) The detected signal using the KLPF method. (d) PSD of the detected signal using the F-H algorithm. (e) PSD of the detected signal using the KLPF method.



(a) (b) (c)

Figure 2.9: Performance of the F-H and the proposed algorithms for transient signals. (a) IPFM input signal. (b) The detected signal using the F-H algorithm, (c) The detected signal using the KLPF method.

to evaluate the performance of the KLPF algorithm for a more complex modulating signal. Figures 2.9(b) and 2.9(c) present the detected signals obtained by the F-H and the KLPF algorithms, respectively. The ringing effect due to the Gibbs phenomenon (Oppenheim & Schafer, 1989) is clearly observed in Fig. 2.9(b) while Fig. 2.9(c) gives a closer output in transients to the real one. In all the simulations, closeness of the results from the new algorithm to the original signals can easily be seen.

It is worthwhile noting that a more reliable reconstructed signal can be obtained if a higher value for the resampling frequency, f_{s2}, is selected. Since the lowpass filters in both the F-H algorithm and the proposed method are not ideal, choosing $N = f_{s1}/2f_c$, which is suggested by the F-H algorithm, would be the extreme case and may cause aliasing error. Hence, decreasing N, for instance $N = f_{s1}/4f_c$, gives more reliable results. Specifically, reducing N does not increase the amount of computation in the KLPF algorithm. However, estimation of the PSD now requires additional calculations for both methods.

2.6 Real Time Band Pass Filtering of the R-wave Signal

It is believed that each frequency component of HRV represents the activity of a specific phenomenon in the neuro-cardiovascular system (Kitney & Rompelman, 1987; Pagani *et. al.*, 1986). The three frequency components which are normally considered are

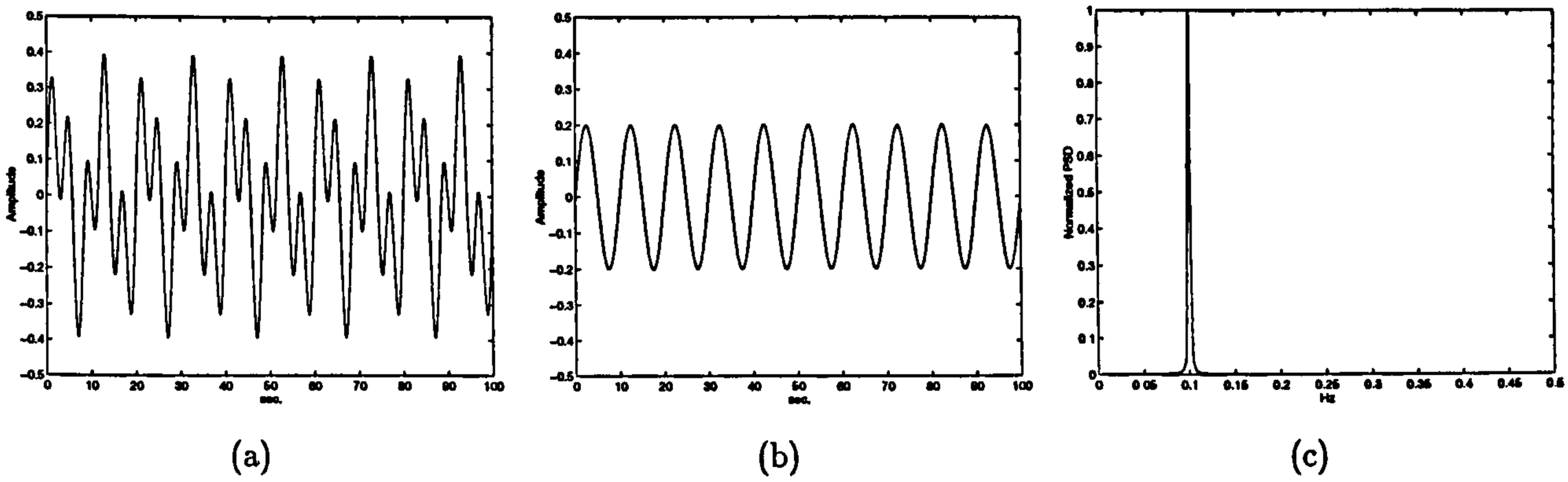
vasorhythmicity around $0.04Hz$, blood pressure oscillating frequency around $0.1Hz$ and respiratory related frequency around $0.25Hz$ (Chapters 4 and 7). The proposed method can easily be extended to separate the important narrow band frequency regions in real-time, directly from the R-wave signal, if $h_l[n]$ is replaced with the impulse response of a suitable bandpass filter. Looking at the variation of each specific frequency region of the HRV is of paramount importance because it can illustrate the variation of the physiologically related phenomena such as considering the sympatho-vagal balance.

The impulse response of an appropriate bandpass filter (BPF) can simply be obtained by a frequency shift in the lowpass filter of equation (2.32) through multiplication with a sinusoidal function,

$$h_b[n] = \begin{cases} cos\left\{\pi(f_l + f_h)(n - df_{s1})\right\} \cdot \frac{sin\left(\frac{\pi(f_h - f_l)}{f_{s1}}(n - df_{s1})\right)}{\frac{\pi(f_h - f_l)}{f_{s1}}(n - df_{s1})} K(n,d) & 0 \leq n \leq 2df_{s1} \\ 0 & \text{otherwise} \end{cases} \tag{2.36}$$

where f_h, f_l are high and low cutoff frequencies of the BPF, respectively. Implementation of equation (2.36) is the same as equation (2.32); only the values of the coefficients must be modified in step (iii) in the KLPF algorithm. Once more the sparse property of the R-wave signal reduces the amount of computation to a few additions for each output sample. Although N can be selected to be equal to $f_{s1}/2f_h$, due to nonideality of the BPF a lower value is recommended especially when a narrow band filter is employed. Alternatively, a combination of lowpass and bandpass filters can also be used. The value of the new coefficients is obtained by the convolution of the coefficients of the individual filters.

To illustrate the application of the bandpass filtering method a composite sinusoidal signal is assumed. Figure 2.10 illustrates the simulation results carried out by the Kaiser windowed bandpass filter (KBPF) method for this case. In this example it is assumed that two sinusoids are injected into the IPFM model and we are interested in investigating only one of them. Figure 2.10(a) shows the input signal $\lambda_{ac}(t) = 0.2sin(2\pi 0.1t) + 0.2sin(2\pi 0.25t)$. Figures 2.10(b) and 2.10(c) plot the detected signal and its PSD using the KBPF method with cut off frequencies $f_l = 0.05Hz$, $f_h = 0.15Hz$, $N = f_{s1}/(2 \times 0.4)$ and $d = 10\ sec.$ It is clear from the figure that the frequency component at 0.25 Hz has been completely removed.



(a) (b) (c)

Figure 2.10: Bandpass filtering of the IPFM output signal by the proposed KBPF algorithm, (a) Input signal $0.2sin(2\pi 0.1t) + 0.2sin(2\pi 0.25t)$. (b) Output signal. (c) PSD of the output signal.

The performance of the bandpass filtering can be improved by increasing the value of d, particularly when detection in a narrow band region is of interest. Needless to say, several BPF at different bands can be used simultaneously, to discern the relationship between interconnected physiological phenomena. The number of filters is restricted by the speed of the installed software and hardware.

It is useful to note here that the complex demodulation technique has been used by Shin, Tapp, Resiman and Natelson (1989) for the same purpose. These authors have utilised multiplication by an exponential function and then lowpass filtering. However, their method is not real-time and is also more complicated than the method described here.

2.7 Experimental Results

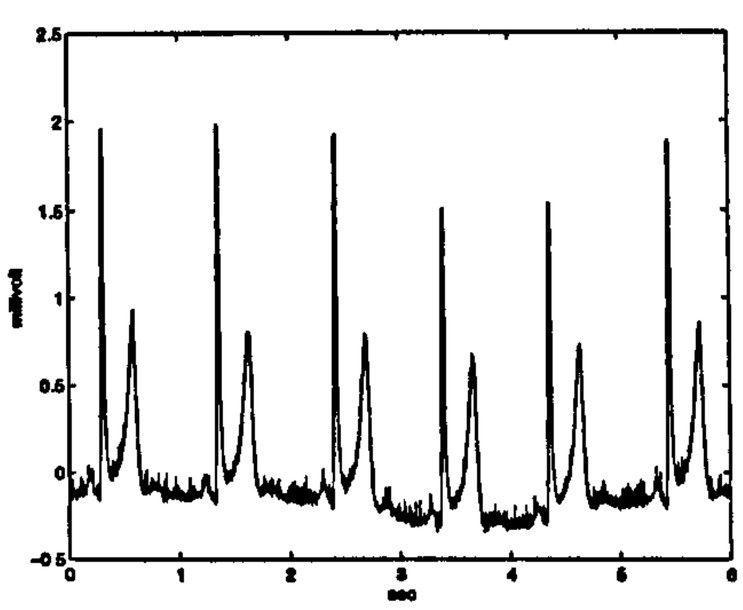
The proposed KLPF and KBPF algorithms are perfect substitutes for the other HRV detection methods. Therefore, they can be used whenever extraction of the HRV from the R-wave signal is required. In this section two examples are considered to show the application of this method in practical cases. In both cases, ECG and respiratory activity were sent to the computer *via* an interface board with sampling frequency $500Hz$ and 12 bit resolution.

Employing a real-time R peak detection algorithm is the first step in obtaining the HRV in an actual experiment. Usually the use of a simple causal sliding averager

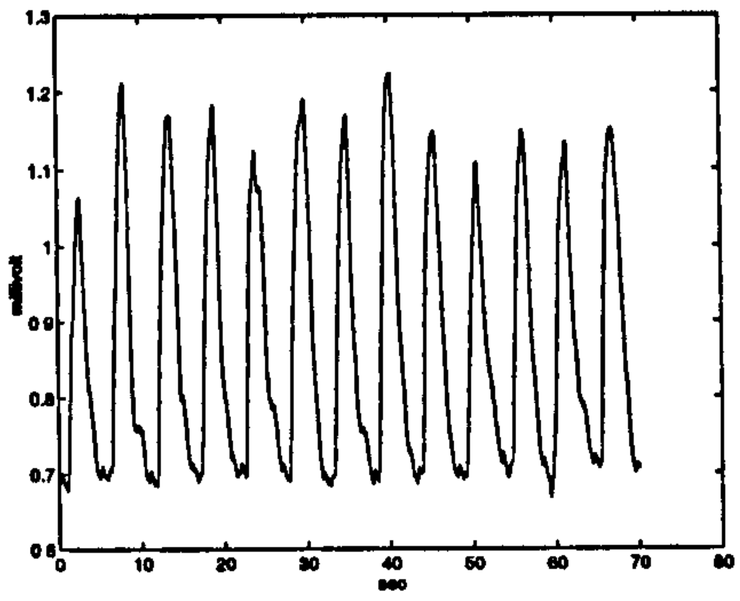
(Oppenheim & Schafer, 1989) for reducing the noise, differentiating and thresholding are adequate. These stages, of course, will impose more calculations and time delay. However, these are not time demanding tasks. Furthermore, the amount of the imposed delay is negligible in comparison with d.

Figures 2.11(a) and 2.11(b) show a part of ECG and respiratory movement obtained from a young healthy subject in the supine position who was constrained to breath according to the beep sounds generated by a computer at the rate of 12 breaths per minute. Chest movement was measured by the strain gauge plethysmography method. To obtain the R-wave signal which is shown in Fig. 2.11(c) a three point causal sliding averager and a simple differentiating algorithm were used. Figures 2.11(d) and 2.11(e) present the detected HRV signal and its PSD using the proposed KLPF algorithm with $f_c = 0.4Hz$ and $d = 5sec$. For convenience in comparison the delay of the signals is not shown in the figures. Fluctuations of the HRV with respiration can be observed clearly from Fig. 2.11(d). As would be expected HRV increases during inspiration and decreases with expiration. The high frequency (HF) component at 0.18 Hz (due to respiration) and low frequency (LF) component around 0.1 Hz (due to blood pressure oscillation) are completely dominant in the PSD shown in Figure 2.11(e). Figure 2.11(f) depicts the output signal of the KBPF of the R-wave signal with $f_l = 0.15Hz$ and $f_h = 0.21Hz$. This range corresponds to the respiratory region of the HRV signal. Figure 2.11(g) pictures the similar result but for $f_l = 0.05Hz$ and $f_h = 0.14Hz$ which coincides with the blood pressure oscillatory region (LF) of the spectrum. The PSDs of these two signals which are illustrated in Figs. 2.11(h) and 2.11(i) respectively, clearly show that the KBPF algorithm can segregate the desired components in the HRV directly from the R-wave signal.

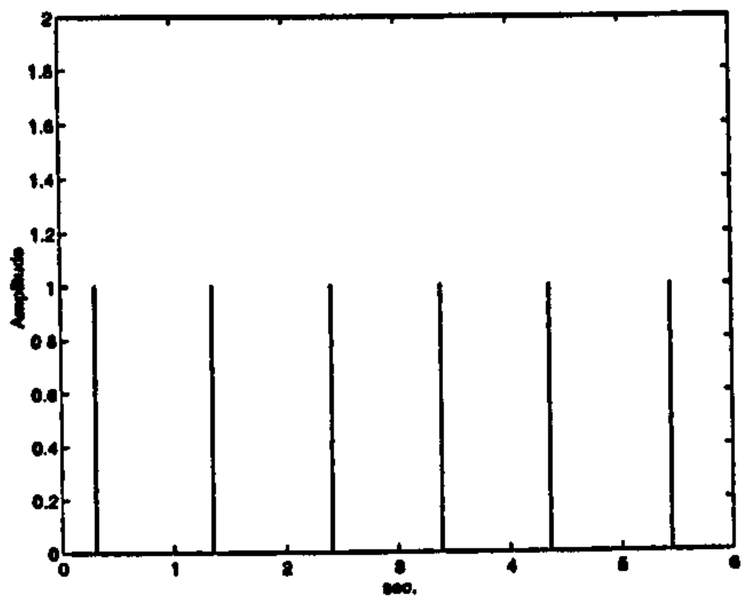
The second practical example demonstrates real-time detection of the HRV in the inspiratory breath hold experiment (Hirsch & Bishop, 1981; de Burgh Daly, 1986). In this experiment ECG and pulmonary ventilation were measured simultaneously. The subject started free breathing through a water-sealed spirometer filled with oxygen until receiving a signal to stop his breathing following a deep inspiration. Heart rate variability was monitored by the KLPF algorithm with the same parameters as those of the previous experiment. The HRV is shown in Fig. 2.12 along with the respiratory signal (tidal volume). In the period of free breathing, marked by A-B, synchronous fluctuations of the HRV with respiration is quite clear. Deep inspiration at the begin-



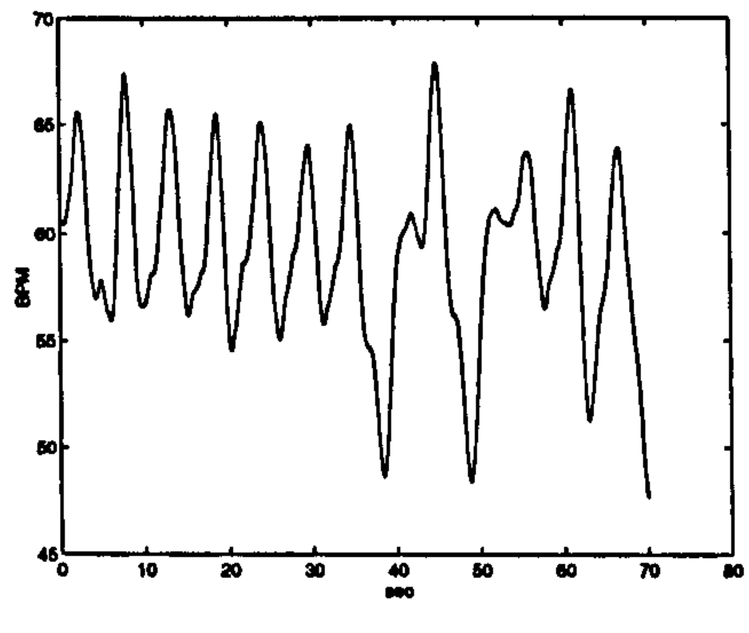
(a)



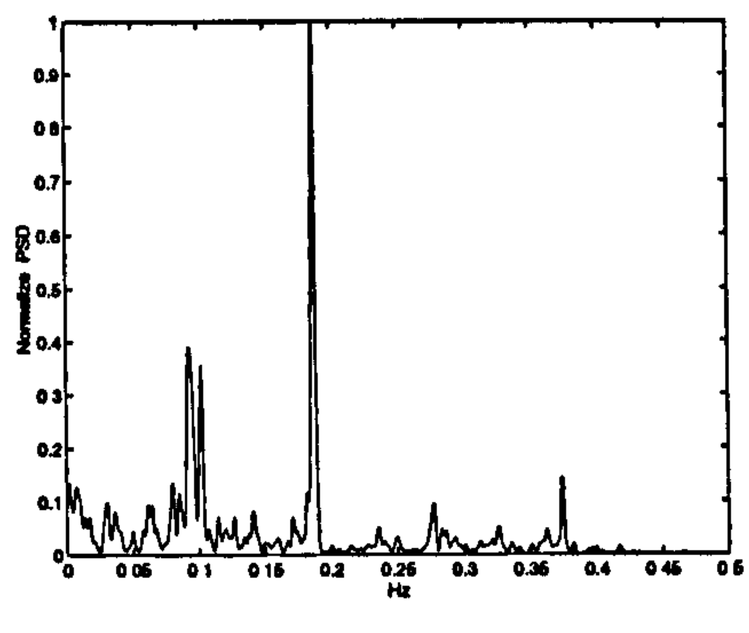
(b)



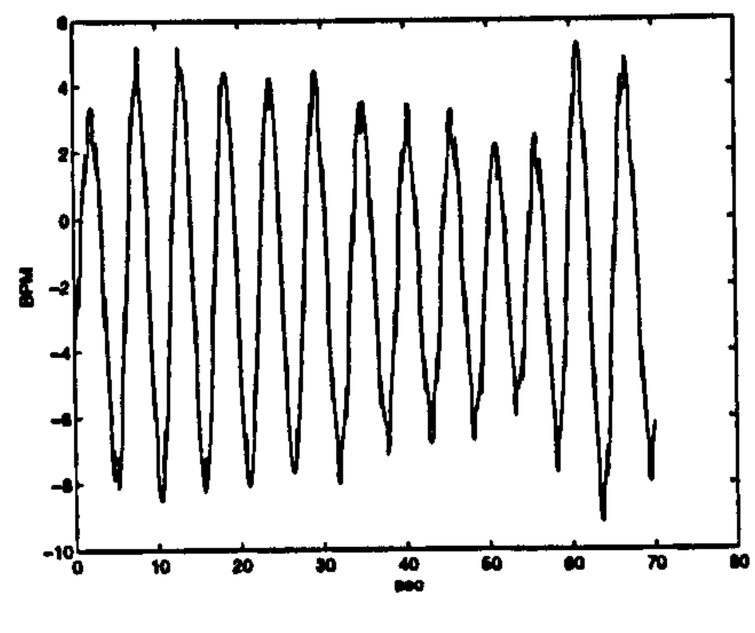
(c)



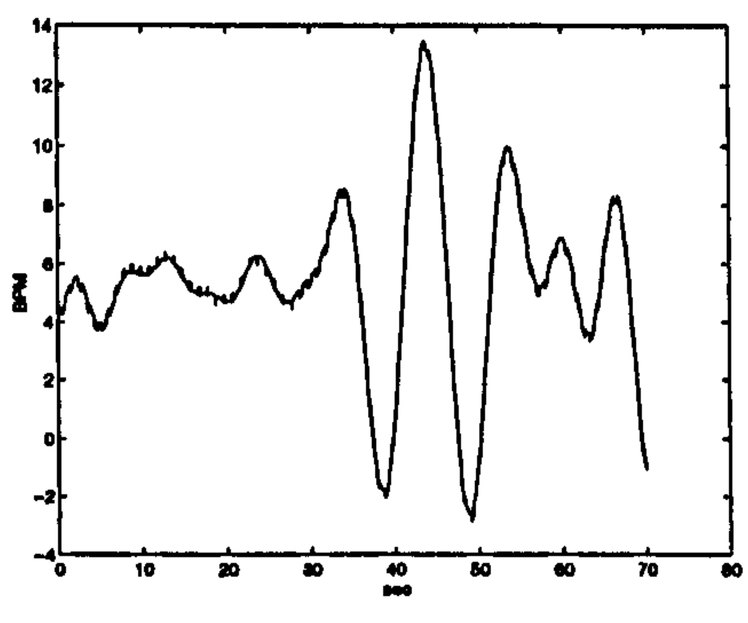
(d)



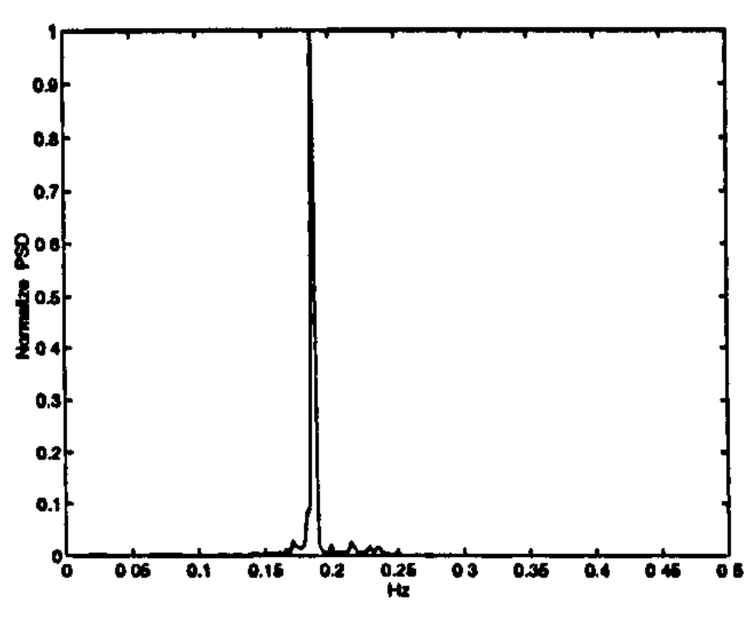
(e)



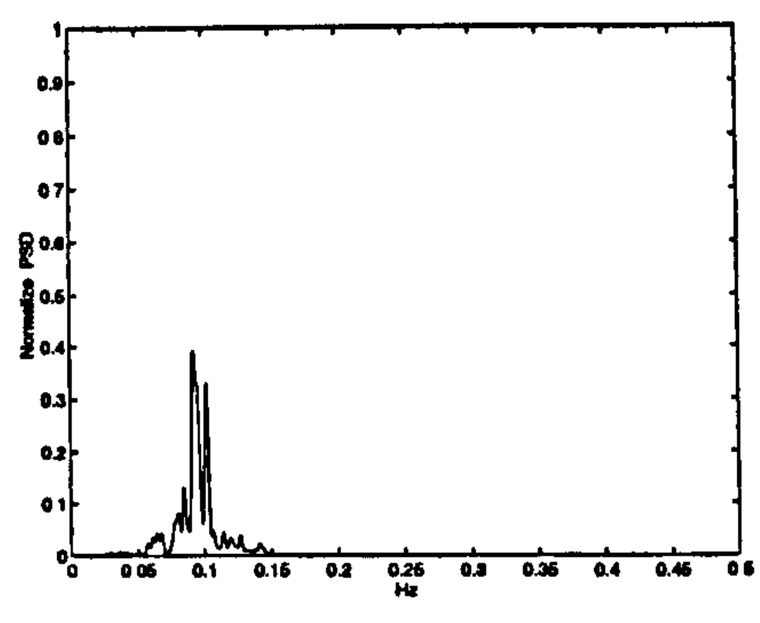
(f)



(g)



(h)



(i)

Figure 2.11: (a) ECG. (b) Respiration. (c) R-wave signal. (d) The HRV signal using the KLPF algorithm. (e) PSD of the HRV signal. (f) KBPF of the R-wave signal with $f_l = 0.15Hz$, $f_h = 0.21Hz$. (g) KBPF of the R-wave signal with $f_l = 0.05Hz$, $f_h = 0.14Hz$. (h) PSD of the signal of part (f). (i) PSD of the signal of part (g).

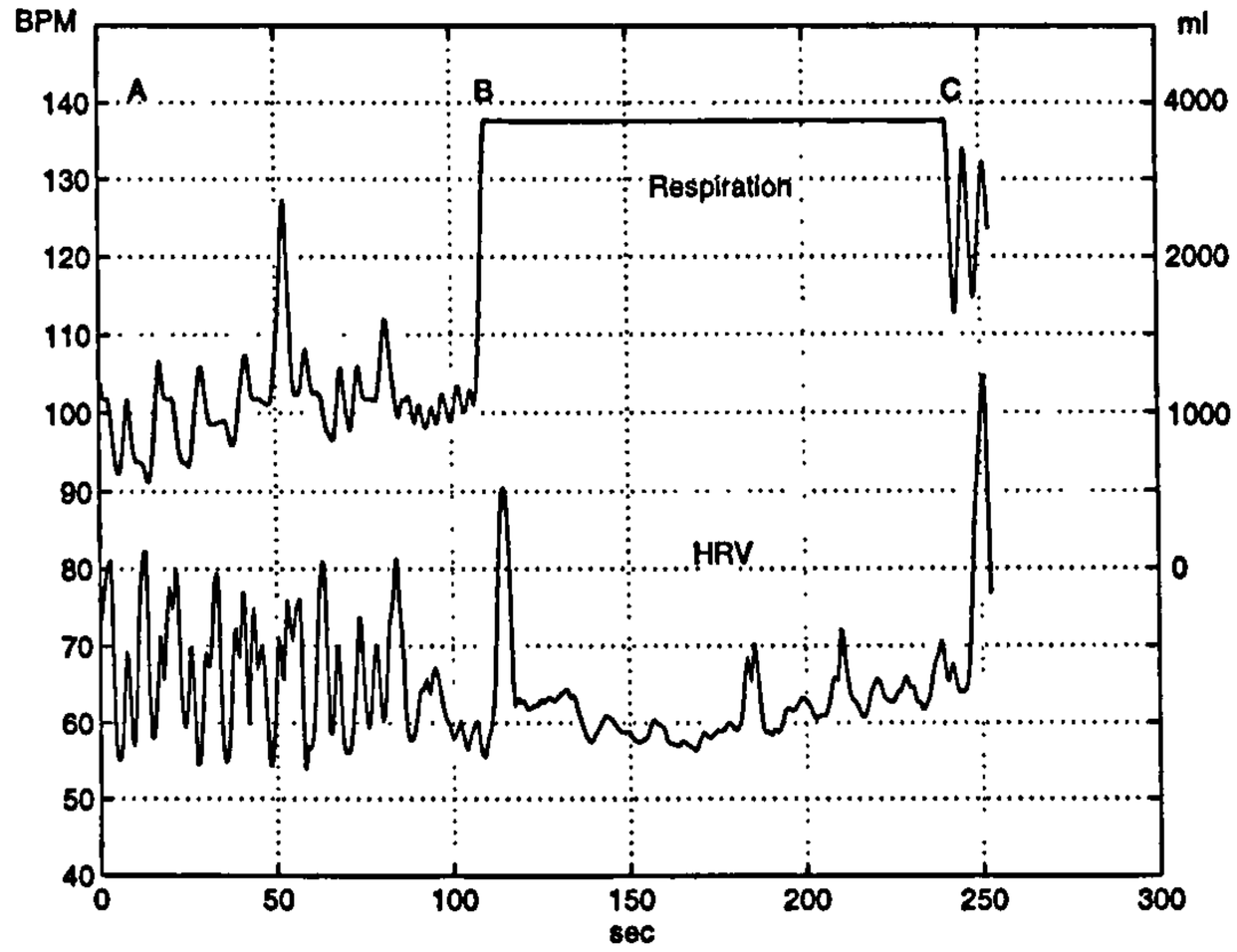


Figure 2.12: Real-time monitoring of the HRV in inspiratory breath hold experiment. The top trace shows pulmonary ventilation and the bottom one HRV.

ning of the breath hold period induces a significant change in HRV which appears with 5 seconds delay with respect to the inspiration. Stopping the breathing in the period marked by B-C greatly diminishes the heart rate variability. A sudden rise in the HRV and then oscillation with the respiratory rate again with 5 seconds delay indicates the end of the breath hold period and returning to the normal position (Hirsch & Bishop, 1981). All these changes in the HRV can be presented as a well defined signal by the KLPF algorithm.

It is worthwhile here to emphasise that an important advantage accruing from the proposed KLPF algorithm is the clear definition of HRV and its constituent parts as continuous state time series signals so that relating the HRV to other physiological signals, particularly for system identification purposes, becomes very straightforward. This, for example, can be observed in Figs. 2.11(d), 2.11(f) and 2.11(g) or Fig. 2.12 for relating the HRV to respiration. This point will be clarified with much more details in the next chapter.

2.8 Conclusion

The proposed KLPF method presents a powerful yet simple tool, for extraction of the HRV signal and its analysis both in the time and frequency domains. This method

stems from the IPFM model and the result that the HRV signal can be extracted by lowpass filtering from the R-wave signal. The filter is based on the Kaiser window which is an optimum choice among windowed type FIR filters. It also guarantees real-time behaviour, ease of implementation and phase linearity.

Even without the basic assumption of the IPFM model, the new algorithm can still be used similar to the LPFES method (Rompelman *et. al.* 1977), on-line and with higher performance. Obviously, it can also be employed for off-line processing of the HRV with better characteristics than that of the existing algorithms. It is also an appropriate method for following rapid changes over time as well as time frequency analysis of the HRV. The BPF version of the new method allows more careful consideration of the HRV signal. Similarly, a band stop filter (BSF) can be designed using an identical procedure. Hence, a combination of LPF and BSF will remove undesired frequency bands for observing weaker, but desired, frequency components. In all cases the bulk of the calculations are independent of the type of filter and are limited to a few additions for each output sample. Due to its prominent features, the KLPF method will be the core algorithm for extraction of the HRV throughout this study.

Summary of the Chapter

A well defined time series HRV signal is simply obtained by passing the R-wave signal, obtained from the ECG, through a lowpass filter. The lowpass filter can be constructed as a look up table and can be implemented as a real-time or nonreal-time algorithm. Importantly, the presented algorithm is not limited to using the Kaiser windowed LPF implemented here, any kind of similar operation can be used in an analogous way. Although the lowpass filtering method has already been used by many authors, our results present a rigourous reason and a simple implementation algorithm.

2.9 APPENDIX A

In this appendix derivation of equations (2.22) through (2.25) is illustrated by employing a similar approach to that of Rowe (1965).

Suppose a function $g(t)$ has a single, simple zero at $t = t_0$. Then by using the properties of the impulse function it follows

$$\delta(g(t)) = \frac{\delta(t - t_0)}{|g'(t_0)|}. \tag{2.37}$$

By applying the above result for the PPM signal of equation (2.18) the following is obtained

$$x(t) = \delta(t - t_k) = |1 - s'(t)|\ \delta(t - kT - s(t)). \tag{2.38}$$

If $s'(t) < 1$ is assumed then

$$x(t) = \delta(t - t_k) = [1 - s'(t)]\ \ \delta(t - kT - s(t)). \tag{2.39}$$

This restriction on $s'(t)$, in addition to permitting us to drop the absolute magnitude sign, is a sufficient condition for $t - kT - s(t) = 0$ to have a single, simple zero. Moreover, from equations (2.20) and (2.21) we get $s'(t) = -\lambda_{ac}(t)/\lambda_{dc}$, therefore $s'(t) < 1$ is equivalent to the low modulation depth condition in the IPFM model. Further, if $c(t)$ is defined as $c(t) = \sum_{k=-\infty}^{+\infty} \delta(t - kT)$ then $x(t)$ will be given by

$$x(t) = [1 - s'(t)]\ \ c(t - s(t)). \tag{2.40}$$

Using Fourier series expansion, $c(t)$ can be written as $c(t) = \frac{1}{T} \sum_{k=-\infty}^{+\infty} e^{j\frac{2k\pi t}{T}}$ which brings about equation (2.22).

To reach (2.25), equation (2.24) can be written as

$$\frac{d\ell(t)}{dt} = \frac{1}{T} \sum_{k=-\infty}^{+\infty} e^{jk2\pi f_0(t+\frac{T}{2})} - x(t) = \frac{1}{T} + \frac{1}{T}\frac{d}{dt} \sum_{\substack{k=-\infty \\ k\neq 0}}^{+\infty} \frac{(-1)^k}{jk2\pi f_0} e^{jk2\pi f_0 t} - x(t). \tag{2.41}$$

Substituting $x(t)$ from (2.22) and then integrating yields

$$\ell(t) = \frac{1}{T}s(t) + \frac{1}{T} \sum_{\substack{k=-\infty \\ k\neq 0}}^{+\infty} \frac{(-1)^k}{jk2\pi f_0} e^{jk2\pi f_0 t} - \frac{1}{T} \sum_{\substack{k=-\infty \\ k\neq 0}}^{+\infty} \frac{1}{jk2\pi f_0} e^{jk2\pi f_0(t-s(t))} + constant \tag{2.42}$$

Integration of $\ell(t)$ over $[0, T]$ with $s(t) = 0$ fixes the constant value to $\frac{1}{2}$ and completes the proof.

Chapter 3

Heart Rate Variability System Identification Using Different Signal Descriptors

Objectives of the Chapter

On various occasions, physiologists encounter a phenomenon which shows up as a modulatory effect on a series of intervals (e.g. variation in neuronal discharge pattern or heart rate variability) and want to relate it to another phenomenon which has a well defined time series representation (e.g. blood flow, lung volume). Since these two phenomena exhibit two different informational schemes (time series versus spike series), determining their relationship will entail methodological difficulties. As an example in the current study, we wish to identify the system which relates the lung volume to the heart rate variability; while the former is a well defined continuous state time series signal, the latter is originally in the form of a series of interval variations, and the majority of system identification methods are appropriate for continuous state time series signals. The objective of this chapter is to determine how to identify a system which relates a continuous signal to a spike series signal in the context of heart rate variability.

3.1 Introduction

In the study of the neuro-cardiovascular system, joint analysis of heart rate variability and the relevant physiological signals such as respiration or blood pressure has been more highly regarded than the individual analysis of HRV. This issue, however, has always encountered methodological limitations. Respiration, for example, is a well-defined continuous state time series signal whereas HRV should be extracted from interspike interval variations. Therefore, it will be of considerable importance to find a method to properly connect a spike series signal to a continuous signal, a matter which in our view has been under-emphasised so far.

This problem can be treated in two different ways. The first method, comprehensive but extremely complex, looks at the SA node as a black box whose input is the continuous signal and whose output is the spike series signal, namely fitting the problem into the class of Continuous Input Spike Output (CISO) systems (Marmarelis, Citron, Vivo, 1986). For complete modelling of the CISO systems one has to employ a nonlinear methodology such as the Volterra-Wiener nonlinear modelling technique. This is because the conversion of a continuous input signal to a spike series output is a nonlinear operation. This methodology, however, brings about a tremendous amount of computation and intricacy.

The second approach defines two sets of signal descriptors, one for the HRV, in the form of a continuous state time series signal extracted from the spike series signal, and the other for the given input signal. These sets of signal descriptors are then used for modelling and identification purposes. Finding proper sets of signal descriptors will be the major concern in this chapter.

Four different sets of signal descriptors which are currently used for connecting the heart rate variability to other physiological signals are investigated together with a new method based on the KLPF algorithm of the previous chapter. Performance of these descriptors is compared through identification of an unknown system in the parametric domain and by spectral analysis. It will be shown that identification of the systems and physiological interpretation of the outcomes can be biased for the currently-employed signal descriptors, whereas the proposed method is able to elicit the correct result. Experimental illustrations at the end of chapter will underscore the

practical significance of the theoretical achievements and will emphasise the role of the signal descriptors in physiological deductions.

3.2 Model Structure

In developing the mathematical model, we seek a compromise between mathematical complexity and biological relevance in order to obtain tractable mathematical formulations of the problem while preserving the essential functional features that are observed experimentally. As considered in the previous chapter, the information of the HRV is coded into interspike intervals. Transmission of the variability signal from the autonomic nerves and generation of the R peaks are accomplished through complex biophysical mechanisms of the excitable tissues (ionic currents arising from changing membrane permeabilities, release of neurotransmitters and their effects, etc). If the SA node is conceptualised as a black box that receives a continuous input signal and produces the R-wave signal it allows us to bypass the complex biophysical mechanisms involved with the problem. Therefore, one only confronts the question of appropriate mathematical representation of the system function and its input-output signals. This categorises the SA node in the class of CISO systems. Nonlinearity imposed by signal transformation and spike generation of the SA node can then be treated by the Wiener series representation as (Sakai, 1992; Marmarelis, 1978) :

$$s(t) = h_0 + \sum_m h_1(m)y(t-m) + \sum_{m_1}\sum_{m_2} h_2(m_1,m_2)y(t-m_1)y(t-m_2) - \sigma_y^2 \sum_{m_1} h_2(m_1,m_1) + \ldots\ldots \tag{3.1}$$

where σ_y^2 is the variance of the discrete input Gaussian white sequence $y(t)$, $h_l(m_1,...,m_l)$ are the Wiener kernels and $s(t)$ is the spike output signal. The Wiener kernels can be estimated through the cross-correlation technique as (Marmarelis, 1986):

$$h_l(m_1,\cdots,m_l) = \frac{1}{l!\sigma_y^{2l}}\left\{\frac{1}{N}\sum_{k=1}^{K} y(t_k-m_1)\cdots y(t_k-m_l) - \sum_{i=0}^{l-1}\frac{1}{N}\sum_{t=1}^{N} G_i[h_i, x(t'),\ \ t'\le t]\cdot y(t-m_1)\cdots y(t-m_l)\right\}, \tag{3.2}$$

in which G_i represents the lower order discrete Wiener functional, N is the total number of points in the input-output data and K denotes the total number of spikes in the

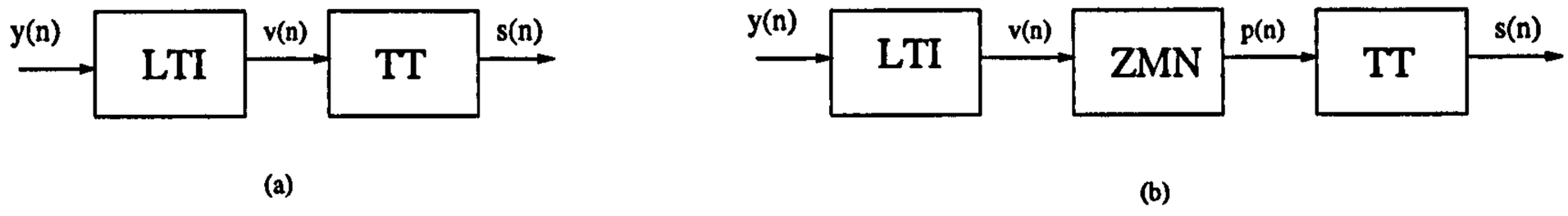


Figure 3.1: Minimum order Wiener modelling. (a) First order MOW, threshold trigger (TT): $s(n) = 0\ if\ v(n) \leq \theta, s(n) = 1\ if\ v(n) > \theta$, θ =threshold value. (b) Second order MOW, ZMN: zero memory nonlinearity.

output. The dynamic characteristics of the path connecting the given continuous signal to the spike series signal is therefore reflected in the computed kernels.

Although the Wiener series approach is theoretically exact and accurate modelling in the whole frequency band would be possible through this method, calculations of the Wiener kernels are very cumbersome. Furthermore, the presence of hard nonlinearity, required for generation of the spike series from a continuous signal, necessitates the use of higher order nonlinear terms which complicates the identification procedure.

In order to reduce the number of the required terms in the Wiener series expansion, the Minimum Order Wiener (MOW) approach has been suggested for the analysis of the CISO systems (Marmarelis, 1986, 1987a). In MOW, a first and/or second order system followed by a threshold trigger element for converting the continuous signal to a series of spikes is used to represent a CISO system (Fig. 3.1). The advantage of the MOW is that mere presence of the threshold trigger mechanism does not give rise to essential nonlinearities from the standpoint of modelling and still the dynamic performance of the SA node can be represented by a low order (first or second order) system for the entire frequency band. However, the threshold level still has to be estimated.

In the variability analysis of the cardiovascular system, the frequency band of interest is limited to $f < 0.5Hz$. This motivates us to employ a simpler model for identification purposes in the low frequency band $f < 0.5Hz$. The IPFM representation as an appropriate model for the spike generation mechanism of the SA node was studied in the previous chapter. It was stated that reconstruction of the coded information in the form of a continuous state time series signal is possible if certain conditions are met in the model. By employing this model, it will be shown in the upcoming sections that identification of an unknown system in the low frequency band is possible if proper definitions for the input/output signals (signal descriptors) are selected. This is performed through the model structure shown in Fig. 3.2. $G(s)$ in

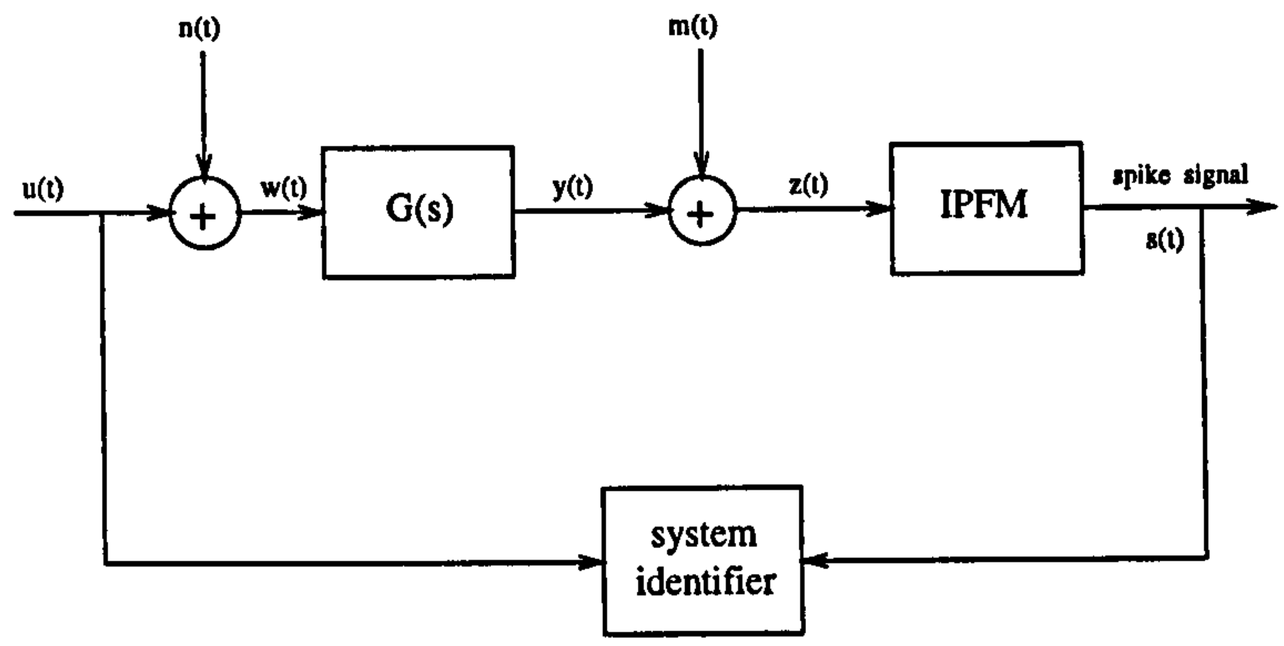


Figure 3.2: The general model of an unknown system in series with the IPFM model.

the figure represents the unknown continuous time system relating the input signal $u(t)$, such as the respiratory movement, to the R-wave signal $s(t)$, generated by the IPFM model. $n(t)$ and $m(t)$ are assumed to be zero mean stationary additive noise sources to consider the effect of external disturbances. Our objective is finding $G(s)$ by introducing an appropriate definition for the signals (signal descriptors) and a suitable method for the system identifier. It is postulated that $G(s)$ in its simplest form is a linear system with delay as:

$$G(s) = \frac{e^{-st_0}}{s+a}. \tag{3.3}$$

This is a reasonable assumption since the majority of physiological systems exhibit lowpass characteristics with a constant delay (Linkens, 1979a).

3.3 Different Signal Descriptors

Continuous information at the input of the IPFM is converted to interval variations of the spike series signal $s(t)$ represented by

$$s(t) = \sum_k \delta(t - t_k). \tag{3.4}$$

The influence of the different signal definitions (descriptors) for extracting the HRV from interval variations on time behaviour and spectral estimation has been considered by de Boer *et. al.* (1984, 1985a, 1985b) in detail. These authors introduced different methods (such as delayed heart rate signal, instantaneous interbeat intervals, etc.) to construct a well-defined time series signal from the event series of equation (3.4). de Boer *et. al.* divided their proposed methods into time tracking and frequency

analysis methods. They showed specifically that in the strict case of sinusoidally excited event series all of their proposed descriptors clearly detect the major components of the excitation signals, but with considerable differences in the rest of the spectrum. Obviously, this scenario becomes more complex if finding a relationship between the event series and another physiological signal is requested. Literally, this is the first task in modelling and identification of HRV, BPV and ILV relationships.

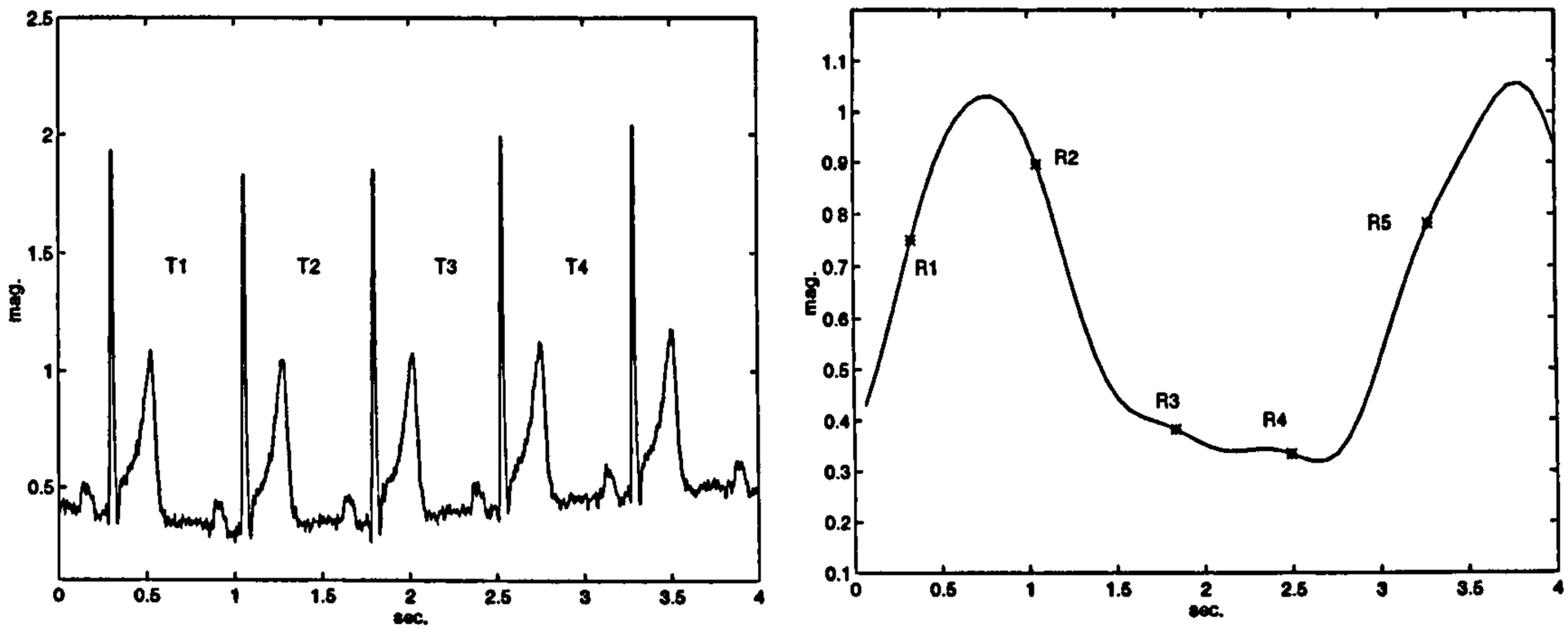
Each research group so far has employed a specific set of signal descriptors for relating the heart rate, respiration and blood pressure. However, the authenticity of the identified systems, emerging from these diverse definitions, has not yet been considered. Subsequently, popular signal descriptors which are currently used for neuro-cardiovascular system identification are presented. Without loss of generality we focus on the respiratory signal as the given continuous signal for the identification procedure.

3.3.1 Beat-to-Beat Method

Amongst the various possible definitions of the signals for describing the HRV and respiration, the simplest method is the direct beat-to-beat measurement of the interval tachogram and the respiratory samples. This approach, which has been used by many research groups (de Boer, Karemaker, Strackee, 1987; Baselli, *et. al.* 1988; Pagani, *et. al.* 1986; Ponikowski, Chua, Piepoli, Amadi, Harrington, Webb-Peploe, Volterrani, Colombo, Mazzeuero, Giordano, Coats, 1997) is shown in Fig. 3.3. In the beat-to-beat method, the interval tachogram is measured between two successive R peaks and the respiratory amplitude is determined at the location of the first R peak in each interval. Consequently, two sets of data, one corresponding to HRV as the output signal $z(t)$, and the other to respiration as the input signal $u(t)$, will be provided $([T_1, T_2, T_3, \cdots]\ [R_1, R_2, R_3, \cdots])$.

3.3.2 Interpolation Method

Time interpolation of the interval tachogram $([T_1, T_2, T_3, \cdots])$ for producing a uniform sampled time series signal has also been employed to a large extent for analysis of the neuro-cardiovascular signals (Shin, *et. al.* 1989; Saul, *et. al.* 1991; Christini, Bennete, Lutchen, Ahmed, Hansdorff, Oriol, 1995). Due to its simplicity, zero order interpolation



(a) (b)

Figure 3.3: Beat-to-Beat method. (a) R-R intervals ($T1-T4$) are extracted from the ECG (R-wave signal). (b) The corresponding respiratory samples are highlighted on the respiratory signal.

is usually selected. In the present study, cubic spline interpolation is exploited since it has a better fitting property and more satisfactory results (Saul, *et. al.* 1991; Taylor & Eckberg, 1986). For the associated respiratory signal, either decimation of the original respiratory signal or interpolation of the respiratory samples (interpolation between $R_1, R_2, R_3, \cdots$) can be thought of. Both methods are considered here.

3.3.3 Berger-Saul Method

A specific method for conversion of the nonuniform R-wave signal to uniform samples of HRV, synchronised with the respiratory movement, has been presented by Berger *et. al.* (1986). Appendix A at the end of chapter explains the details of this method. This method has been extensively used by the MIT (Massachusetts Institute of Technology) group, particularly by Saul and Berger, for neuro-cardiovascular system identification by spectral analysis as well as the parametric methods (Saul, *et. al.* 1989, 1991; Berger, Saul, Cohen, 1989b; Triedman & Saul, 1994; Mullen, Apple, Mukkamala, Matias, Cohen, 1997). The decimated signal of the respiratory movement is used in this method as the input signal. For convenience this method is called Berger-Saul (B-S) method hereafter.

3.3.4 The Proposed Method

In the previous chapter an appropriate method for extraction of the HRV from the R-wave signal was presented. It was shown that the proposed KLPF method can be used either on-line or off-line, for time or frequency analysis. As a new set of signal descriptors, it is now assumed that the HRV is extracted from the KLPF method and the respiratory signal is obtained by the decimation of the original respiratory signal.

3.4 System Identifier

The next step after definition of the signals is identification of $G(s)$. The R-wave signal $s(t)$ and the input signal $u(t)$ are fed to the system identifier block. The output of this block is an estimate of $G(s)$. Based on the different signal descriptors, explained above, and using appropriate system identification algorithms, described below, different estimates of $G(s)$ are obtained. In this study two identification methods which are frequently used in neuro-cardiovascular system identification are considered. They are identification by parametric methods and identification by spectral analysis. In an actual application, spectral analysis can be selected as the first trial, followed by the parametric method for a more accurate estimation. The discretized counterpart of $G(s)$ using the bilinear transformation (Oppenheim & Schafer, 1989) has been employed for the computer implementation.

3.4.1 Identification by Spectral Analysis

For the linear system $G(s)$ shown in Fig. 3.2 the output is given by

$$y(t) = \sum_{\tau} g(\tau)w(t-\tau), \tag{3.5}$$

where $g(t)$ is the impulse response of $G(s)$. The cross-correlation between $y(t)$ and $w(t)$ is defined as:

$$R_{yw}(\tau) = E[y(t+\tau)w(t)]. \tag{3.6}$$

In the frequency domain it follows that,

$$\Phi_{yw}(e^{jw}) = G(e^{jw})\Phi_{ww}(e^{jw}), \tag{3.7}$$

in which $\Phi_{yw}(e^{jw})$ and $\Phi_{ww}(e^{jw})$ are Fourier transforms of cross- and auto-correlation functions, respectively:

$$\Phi_{yw}(e^{jw}) = \mathcal{F}(R_{yw}(\tau)), \tag{3.8}$$

$$\Phi_{ww}(e^{jw}) = \mathcal{F}(R_{ww}(\tau)). \tag{3.9}$$

In practical applications only an estimation of $G(e^{jw})$ can be obtained (Gardner, 1988; Ljung, 1987; Broersen, 1995),

$$\hat{G}(e^{jw}) = \frac{\hat{\Phi}_{yw}(e^{jw})}{\hat{\Phi}_{ww}(e^{jw})}, \tag{3.10}$$

where $\hat{\Phi}_{yw}(e^{jw})$ and $\hat{\Phi}_{ww}(e^{jw})$ are estimates of $\Phi_{yw}(e^{jw})$ and $\Phi_{ww}(e^{jw})$, respectively. Within the present study, the frequency-smoothed spectrum method with a Hamming window has been used for analysis in the spectral domain (Gardner, 1988).

3.4.2 Identification by Parametric Methods

The difficulties of estimation through parametric identification methods are manifold. Model structure and order determination, local minimas, initial conditions, time delays and drifts are some of them. In the analysis of this chapter, however, the general characteristics of the unknown system are known in advance (equation 3.3). Consequently, the output error method (Ljung, 1987; Söderstrom & Stoica, 1989) is employed here in the form of:

$$y(t) = \frac{B(q^{-1})}{F(q^{-1})} w(t - n_k) + \epsilon(t), \tag{3.11}$$

where $B(q^{-1})$ and $F(q^{-1})$ are finite order polynomials,

$$B(q^{-1}) = b_1 + b_2 q^{-1} + ... + b_{nb} q^{-nb+1}, \tag{3.12}$$

$$F(q^{-1}) = 1 + f_1 q^{-1} + ... + f_{nf} q^{-nf}, \tag{3.13}$$

n_k denotes the number of the delayed samples from input to output and $\epsilon(t)$ is the prediction error. The unknown parameters b_i and f_i are found by minimising the total power of the prediction error,

$$min V_N(\Theta) \triangleq min \frac{1}{N} \sum_{t=1}^{N} \epsilon^2(t), \tag{3.14}$$

$$\epsilon(t) = y(t) - \frac{B(q^{-1})}{F(q^{-1})} w(t - n_k), \tag{3.15}$$

where $\Theta = [b_1\ b_2\ ....\ b_{nb}\ f_1\ f_2\ ....\ f_{nf}]^T$ and N is the data length.

For the $G(s)$ of equation (3.3), $B(q^{-1})$ and $F(q^{-1})$ are first order polynomials. Transportation lag t_0 is reflected in n_k of the discrete time model (3.11) by the sampling frequency (Söderstrom & Stoica, 1989).

3.5 Simulation Results

To evaluate the performance of the different signal descriptors, discussed in Section 3.3, in identifying an unknown system, the model of Fig. 3.2 is subjected to a simulation procedure. Referring to this figure, $w(t)$, consisting of input signal $u(t)$ and input noise $n(t)$, excites the linear system $G(s)$. The output signal $y(t)$ is added to the output noise $m(t)$ and then it excites the IPFM model to generate the R-wave signal $s(t)$. The input signal $u(t)$ and the R-wave signal $s(t)$ are used by the system identifier to estimate the transfer function $G(s)$.

The input signal, used in an identification experiment, can have a significant influence on the identification result. If the input signal is persistently exciting (Söderstrom & Stoica, 1989) with enough order then consistent estimation of the parameters can be guaranteed. While for parametric identification an input signal with order two is sufficient (because $G(s)$ is of order one), in spectral analysis a rich signal should be used to cover the whole spectral region. This is opposed, however, by the limitations imposed by the IPFM model on the frequency content of the input signal *i.e.,* zeroness beyond half of the free running frequency (Chapter 2). Thus a zero mean coloured Gaussian process with cutoff frequency $0.35Hz$ (FIR, Hamming, order 30) and a suitable power was chosen for $u(t)$ (low modulation depth). Two independent noise sources $n(t)$ and $m(t)$ with the same characteristics to that of the input signal and with $SNR = 10dB$ [1] were also employed for the simulations in the presence of noise. $G(s)$ was selected according to equation (3.3) with $2.5sec$ delay and a pole at $0.3Hz$. These values were selected as typical physiological parameters in the cardiovascular system (Saul *et. al.*, 1991; TenVoorde, Faes, Janssen, Scheffer, Rompelman, 1995). An IPFM model with the same parameters to that of the previous chapter was also selected here. The sam-

[1]Simulation with different values of SNR from $6dB$ to $13dB$ gave rise to the same conclusions. For SNR less than $5dB$ the estimations were quite unreliable.

pling frequency of the entire system was fixed at $100Hz$. This value is high enough to prevent any significant error which may arise in discretizing the IPFM model yet low enough so as to prevent any computational error in discretizing $G(s)$ (Söderstrom & Stoica, 1989).

$u(t)$ and $s(t)$ in the form of two discrete time signals with sampling frequency 100 Hz and length 36000 points ($6min$) for spectral analysis and 18000 points ($3min$) for the parametric method were fed to the identifier block. A shorter length for the parametric identification was used because parametric methods need less samples for estimation than spectral methods. The identifier extracts two signals as input and output from $u(t)$ and $s(t)$, respectively. The extracted input signal is represented by $U(t)$ and the extracted output signal by $Z(t)$ (after mean removal).

For the beat-to-beat method, R-R intervals and the respiratory samples at the locations of the spikes were collected from $s(t)$ and $u(t)$ by the identifier. It was expected to observe the mean length of 360 (180) samples for $U(t)$ and $Z(t)$ for the selected length of data, noting that the free running frequency of the IPFM model was $1Hz$. This is indeed the least number of data samples among different signal descriptors.

For the interpolation methods, two approaches were examined. In the spline-spline approach the cubic spline interpolation of the signals $U(t)$ and $Z(t)$, obtained from the beat-to-beat method, was used for identification. $U(t)$ and $Z(t)$ were interpolated by factor 10 which increases the data length to 3600 (1800) samples (sampling frequency $10Hz$). In the spline-decimate approach, spline interpolation of $Z(t)$ and the decimated version of $u(t)$ with reduction rate 10 were employed for the identification procedure.

Sampling frequency $10Hz$ and window width 6 bins were chosen for $Z(t)$ in the B-S method (Appendix A). The decimated version of $u(t)$ with reduction rate 10 was also selected for extracting the $U(t)$.

For the proposed method the KLPF algorithm with $d = 10$, $\beta = 4.5$, $N = 10$ and $f_c = 0.45Hz$ was selected. The above parameters were employed in order to achieve a narrow width transition region and an adequate stop band attenuation. $U(t)$ was obtained by decimating the input signal $u(t)$ with reduction rate 10.

Decimation or interpolation by the factor 10 provides the same data lengths for all the methods (apart from the beat-to-beat method). This factor yields a $0.1sec$ time resolution in the estimation of the delay in the parametric method which is a reasonable selection for neuro-cardiovascular modelling.

3.5.1 Simulation Results with Spectral Analysis Method

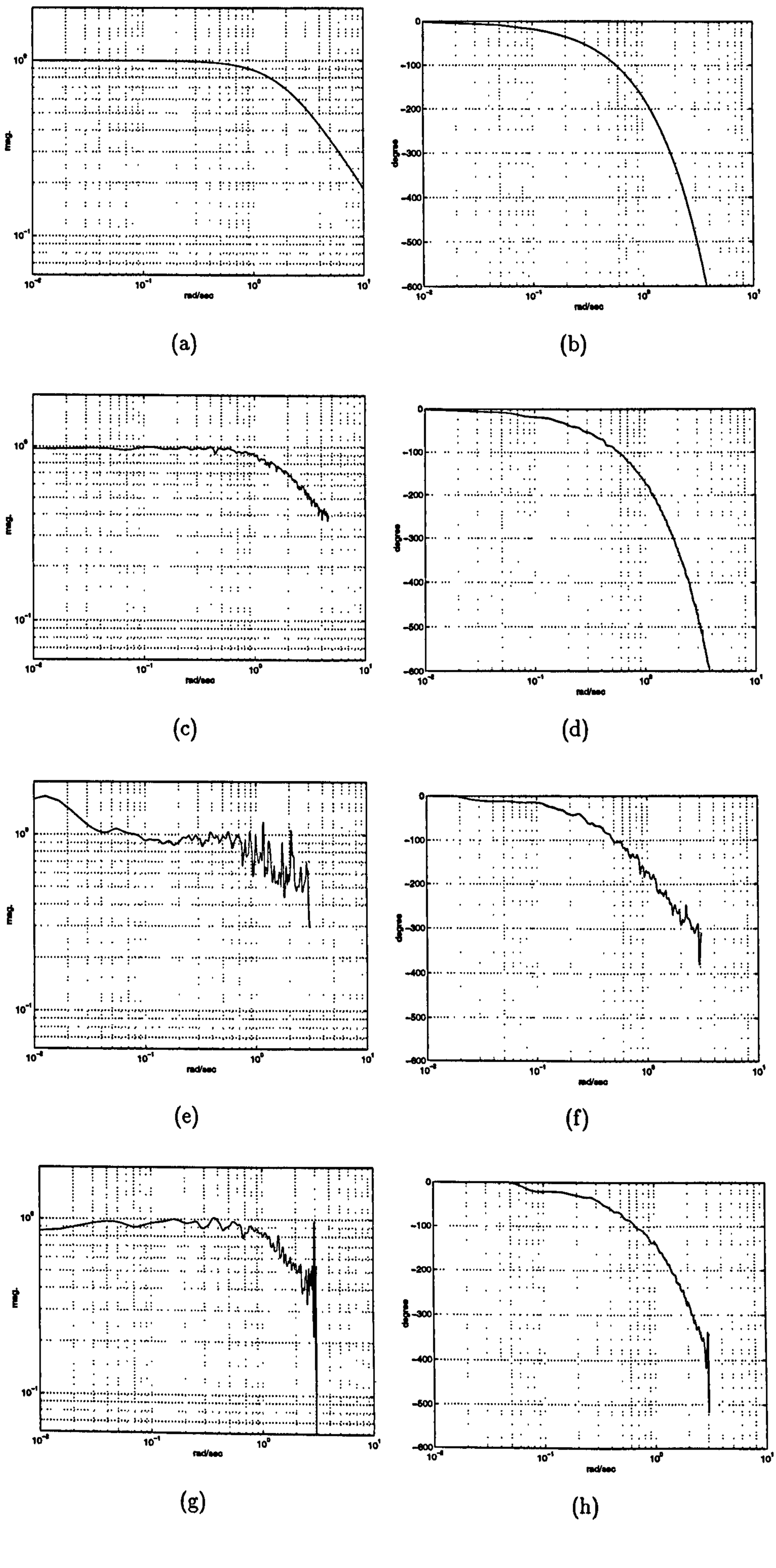
The output signal of the linear system $G(s)$ passes through the nonlinear system IPFM. Identification by spectral analysis gives the best linear estimation of $G(s)$ based on the defined signal descriptors. The Bode plot of the continuous time transfer function $G(s)$ is illustrated in Figs. 3.4(a) and 3.4(b). However, the estimate of $G(s)$ is accompanied by some fluctuating behaviour due to the finite data lengths as shown in Figs. 3.4(c) and 3.4(d) (frequency resolution $= 0.01Hz$). The depicted estimate has been obtained by using the decimated signals of $y(t)$ and $w(t)$ with reduction rate 10 ($10Hz$ sampling frequency) and employing the estimator of equation (3.10). This estimation reveals the performance of the employed estimator without having the interference of the IPFM model and the corrupting noise.

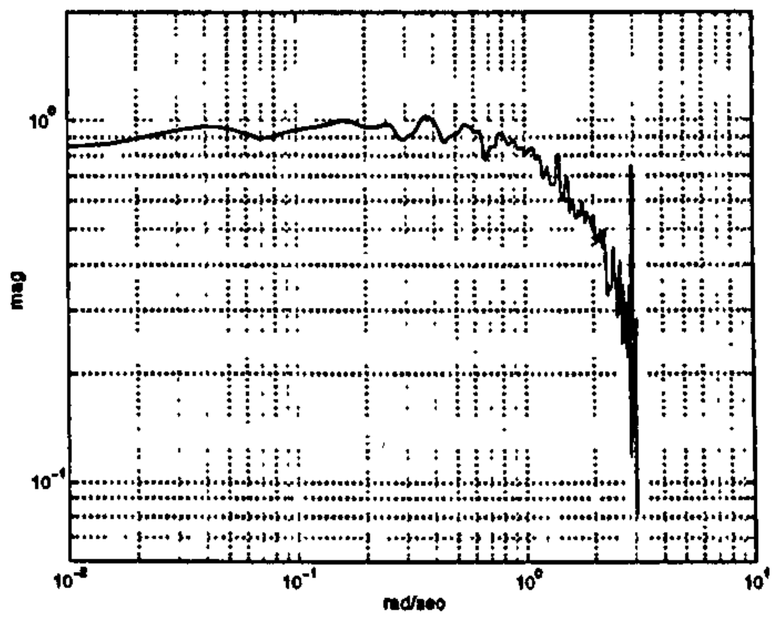
Noise Free Results

Initially the noise sources m(t) and n(t) are assumed to be zero. Figures 3.4(e) and 3.4(f) depict the estimation of the magnitude and phase of $G(s)$ using the beat-to-beat algorithm [2]. Comparison of Figs. 3.4(c),(d) and 3.4(e),(f) illustrates that the beat-to-beat method cannot be an appropriate algorithm for faithful estimation of $G(s)$. The phase estimate (absolute value) is less than the true value and the magnitude estimate demonstrates rapid declination and erratic behaviour.

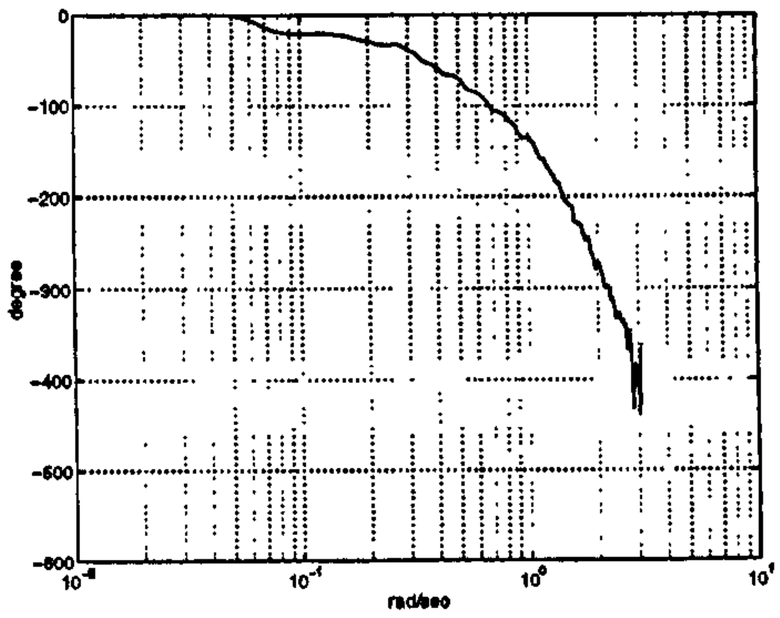
The results obtained with the spline-spline method and spline-decimate method are shown in Figs. 3.4(g) through 3.4(j). No significant difference between these two methods can be observed. Both the estimated phase and magnitude values (pole estimations) are less than the true ones. However, these results are better than those of the beat-to-beat method.

[2]For the beat-to-beat and interpolation methods $-Z(t)$ has been used for estimations instead of $Z(t)$.

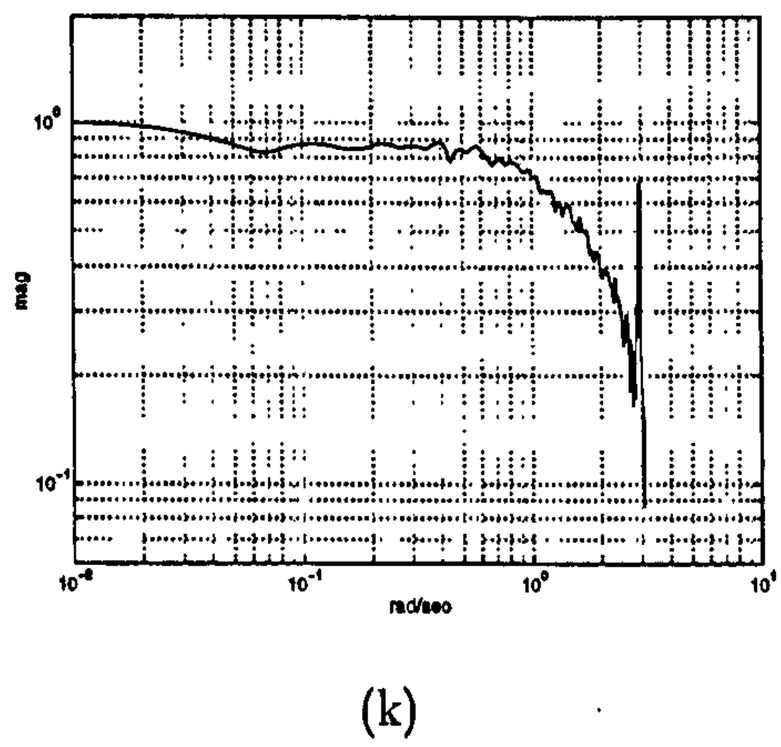

mag.
degree
rad/sec
(a)
(b)
(c)
(d)
(e)
(f)
(g)
(h)



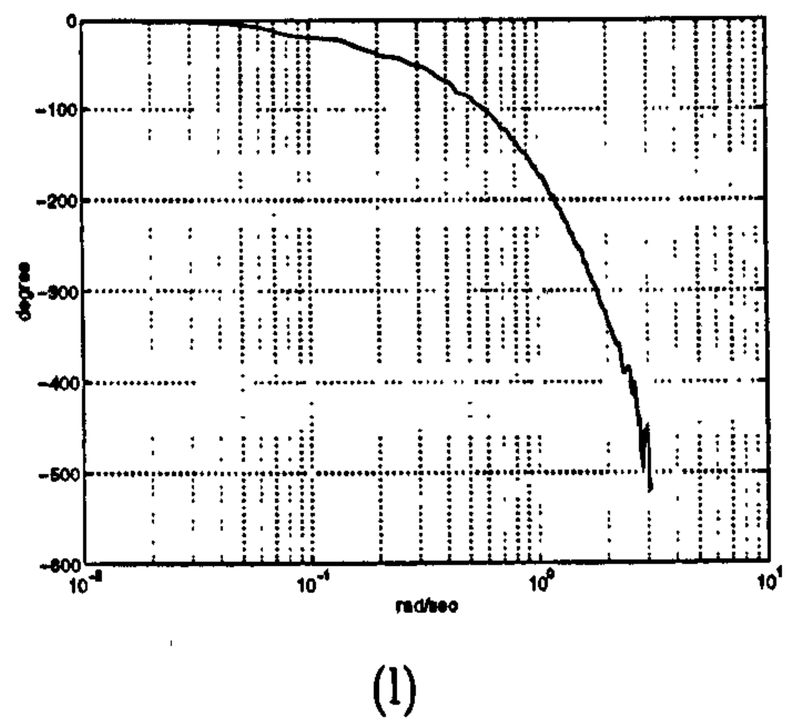
(i)



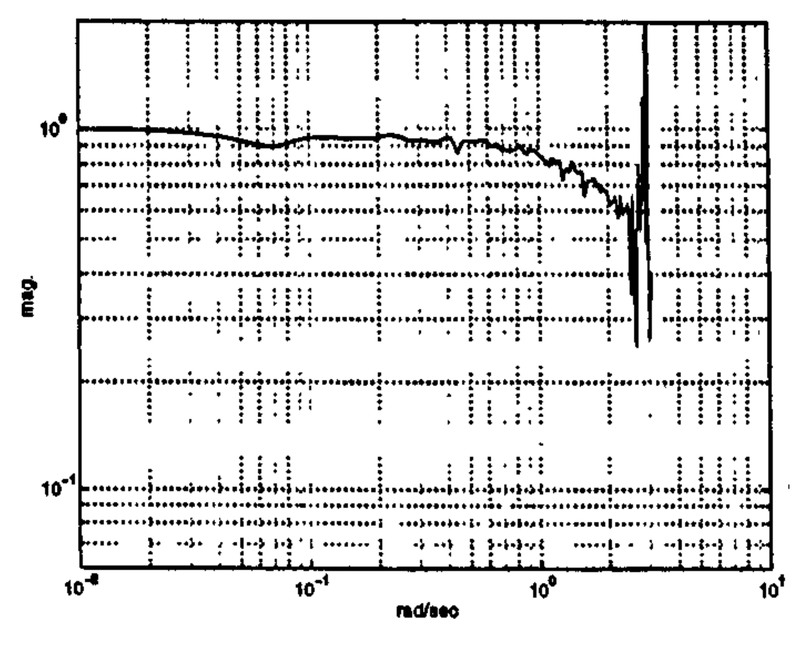
(j)



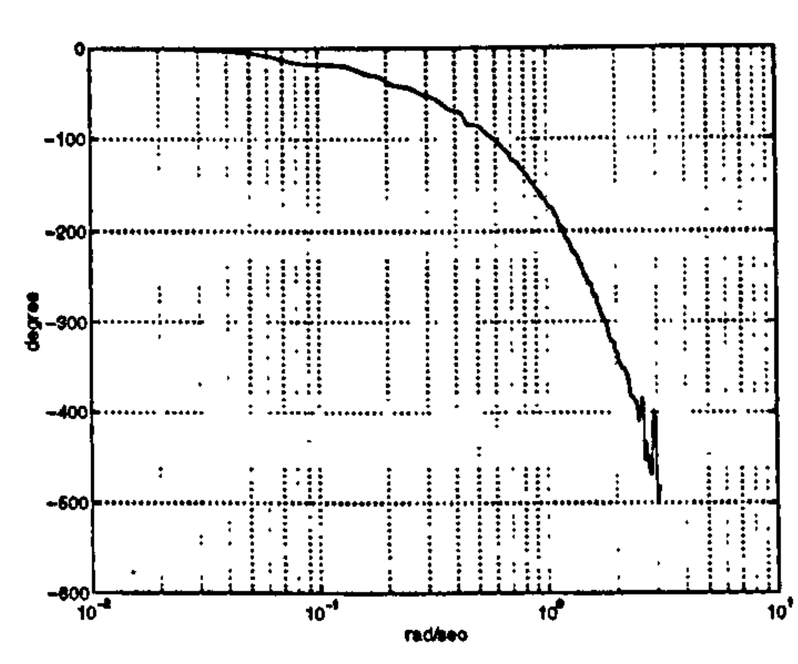
(k)



(l)



(m)



(n)

Method	Beat-to-Beat	Interpolation I	Interpolation II	Berger-Saul	Proposed
Cut Off Frequency	Hard to Determine	0.25 Hz	0.25 Hz	0.2 Hz	0.28 Hz

Figure 3.4: (a),(b) Bode plot of equation (3.3) with $t_0 = 2.5sec$ and $a = 1.9rad/sec$, (c),(d) Spectral estimation of $G(s)$, (e),(f) result of the beat-to-beat method, (g),(h) spline-spline method, (i),(j) spline-decimate method, (k),(l) the B-S method, (m),(n) the proposed method. The estimated cut off frequencies are illustrated in the tabel for all the methods.

The transfer function estimation using the B-S method is shown in Figs. 3.4(k) and 3.4(l). According to these figures correct phase estimation is obtained but curve of the magnitude estimate rapidly decreases which results in a lower value for the pole estimation.

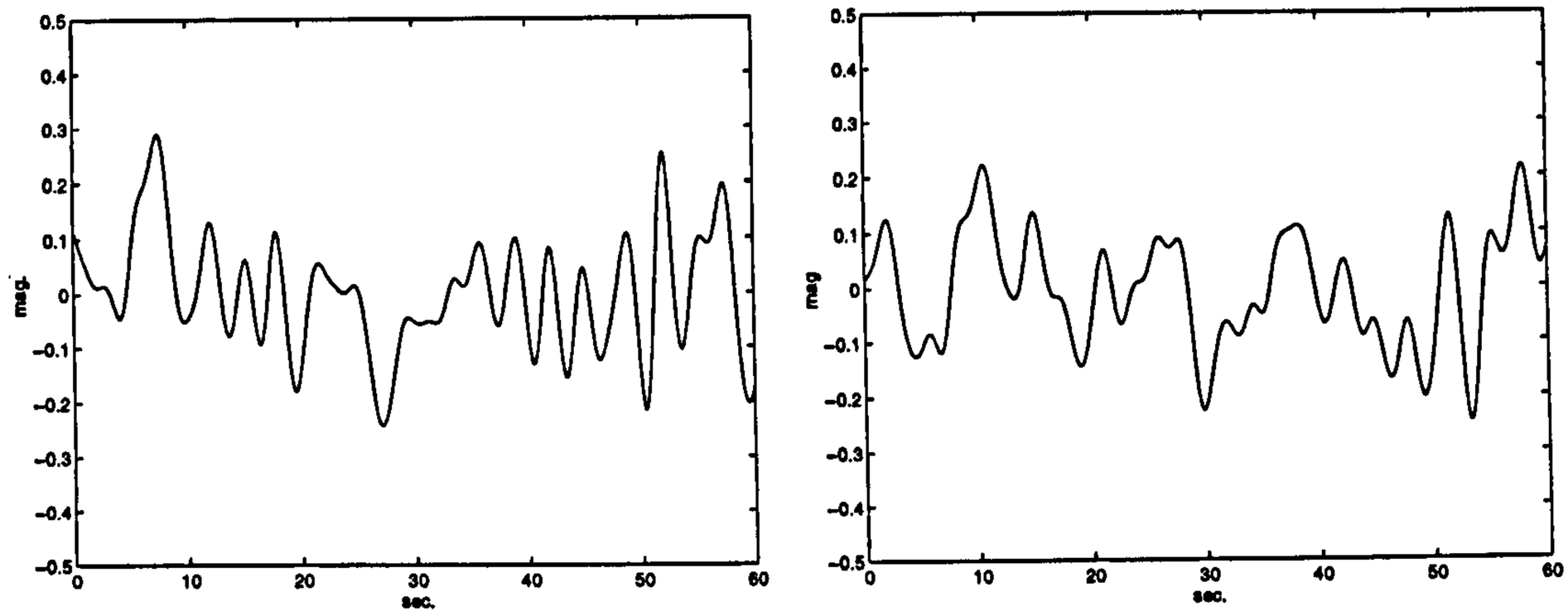
The results of the proposed method are plotted in Figs. 3.4(m) and 3.4(n). In contrast to the previous methods, a good estimation, in magnitude as well as phase, is obtained by this method. This means that a satisfactory estimation of the pole and the transportation lag is possible if the proposed method is used for the spectral analysis. It will be shown shortly that this conclusion remains valid even in the presence of noise.

It is worthwhile here to point out that the coherence function for all the methods was around 0.9 for the frequency band of interest. This shows that using the coherence function is not beneficial in comparing the different signal descriptors.

A quick scan of the obtained estimates reveals that above the frequency $0.4Hz$ ($2.5rad/sec$), a large amount of fluctuations appear in all the methods. These fluctuations arise as a result of the nonlinear behaviour of the IPFM model and overlap of the frequency components as described in previous chapter. It also implies that the identification fails beyond half of the free running frequency of the IPFM model.

Simulation in the Presence of Noise

We will show now that the better performance of the proposed method is preserved even with the injection of noise. As already stated, two independent noise sources with SNR=$10dB$ were fed to the model shown in Fig. 3.2. After injection of the noise, $z(t)$ does not resemble the ideal output anymore (Fig. 3.5), but still the best linear approximation is elicited by the spectral analysis method. Figures 3.6(a) through 3.6(j) illustrate the estimated transfer functions by spectral analysis for all sets of signal descriptors. Clearly, the noise sources have a deteriorating effect on $\hat{G}(s)$. However, the trend of the curves show that the proposed method still gives a closer result to the original plots of Figs. 3.4(c),(d) than the other methods.



(a) (b)

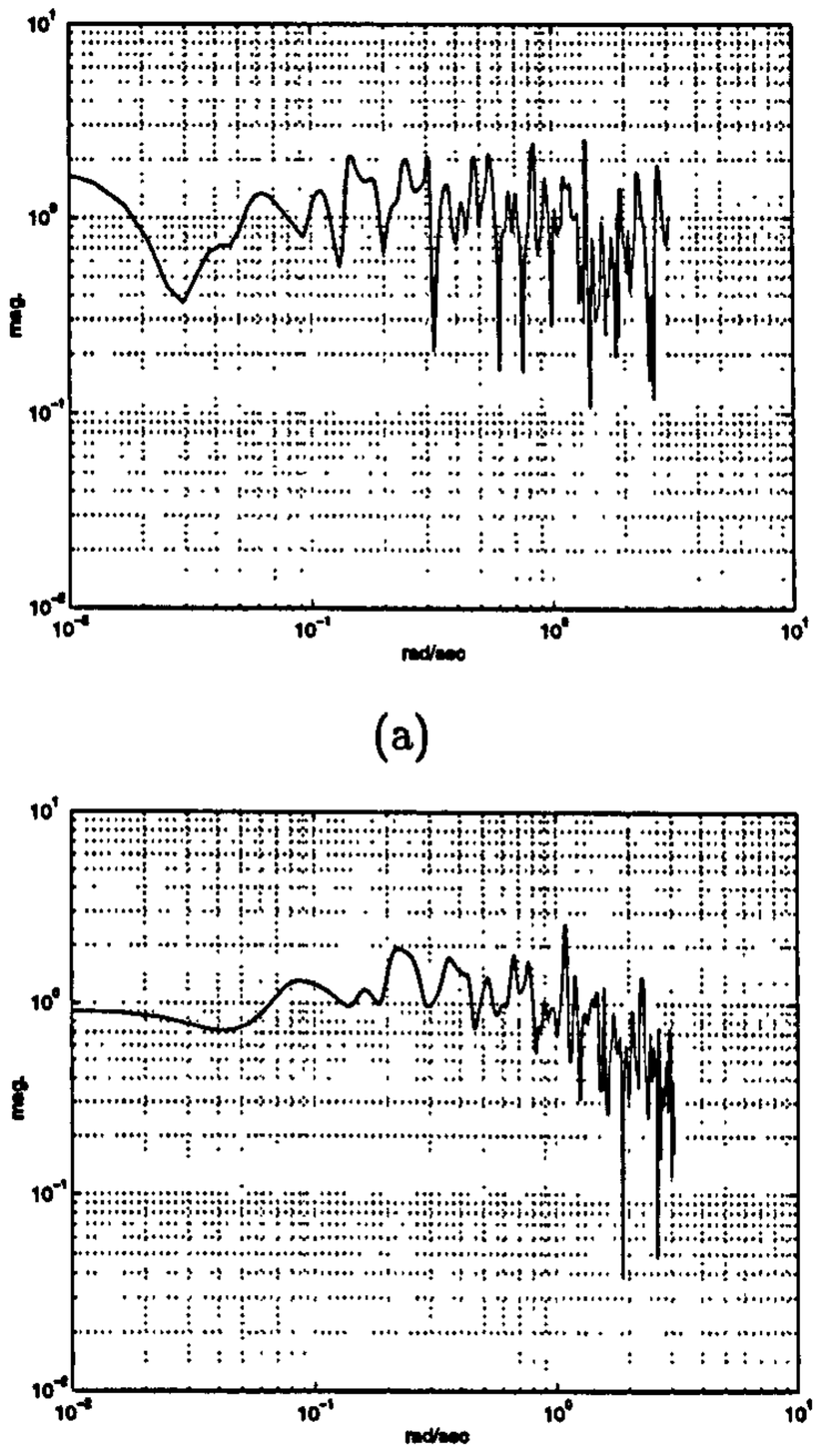
Figure 3.5: Input-output signals in the presence of noise, (a) $u(t)$, (b) $z(t)$.

3.5.2 Simulation Results with Parametric Identification

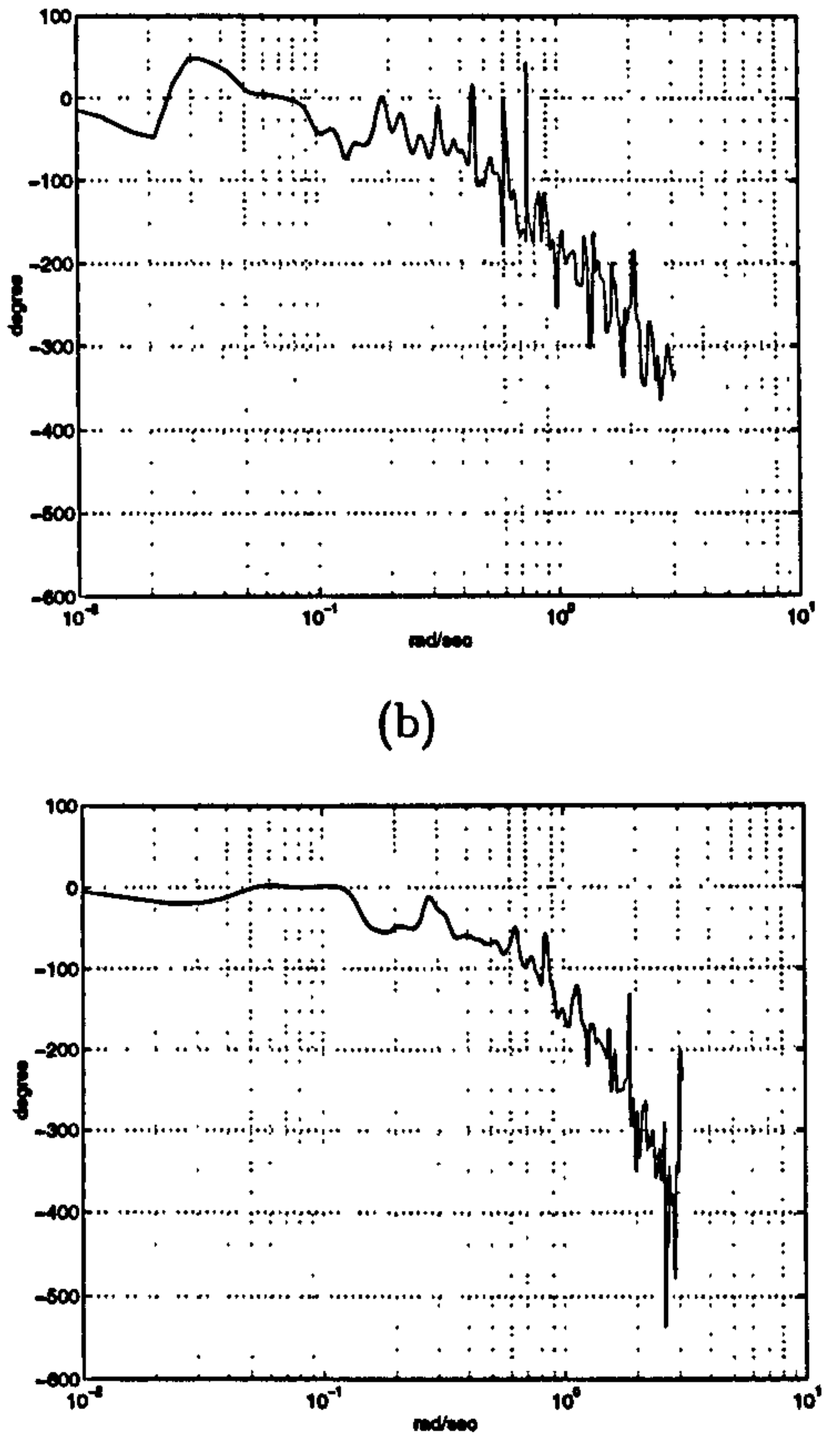
For the presumed system $G(s)$, two parameters, the delay and the pole, must be estimated. The assumed delay of $2.5sec$ corresponds to 250 samples delay between $w(t)$ and $y(t)$. For the extracted signals with reduction rate 10, the delay reduces to 25 samples between $U(t)$ and $Z(t)$. This value is valid for all the presented methods except the beat-to-beat algorithm. In the beat-to-beat method definition of the delay is ambiguous. This is because extraction of the signals is based on the beat-to-beat definition and not on the base of time samples. To clarify, assume that the mean interspike interval is $1sec$. Then $2.5sec$ delay corresponds to two and half samples which is undefined on a beat by beat basis. This is another major deficiency in the beat-to-beat method and will create biased estimates of the unknown parameters, as will be shown subsequently.

As concluded from Figs. 3.4(h) and 3.4(j), in the interpolation methods the estimated delay is less than the true one. Therefore, one would expect to estimate a lower value for n_k in equation (3.11) for these methods. On the other hand, according to Figs. 3.4(l) and 3.4(n), correct estimation of the delay can be possible in the B-S and the proposed methods.

Before presenting the estimated values it is recalled that for estimation of the delay the critical point is to not consider a parametrised model having a larger time delay than the true one (Söderstrom & Stoica, 1989). Underestimated delays (n_k too


mag.
rad/sec

(a)


degree
rad/sec

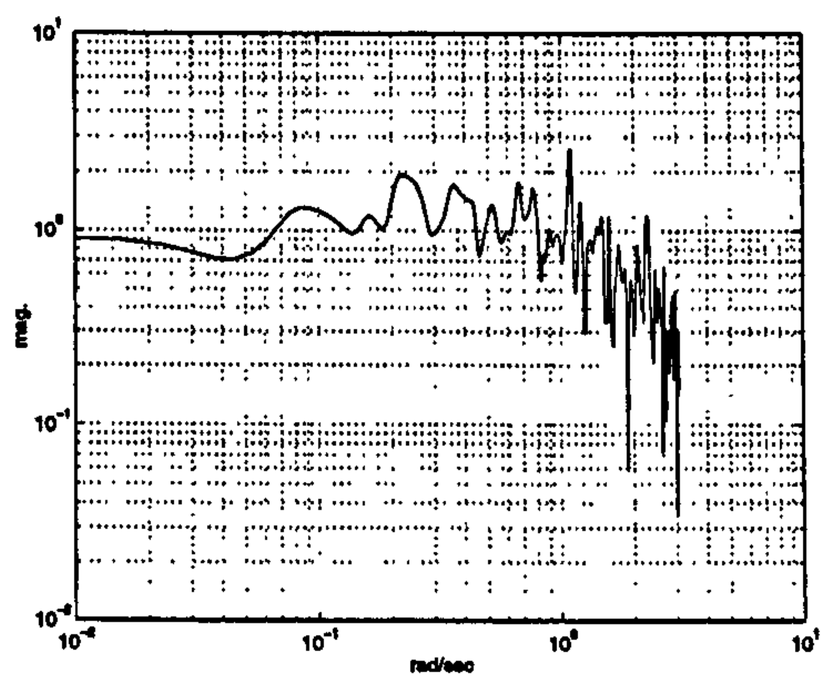
(b)

mag.
rad/sec

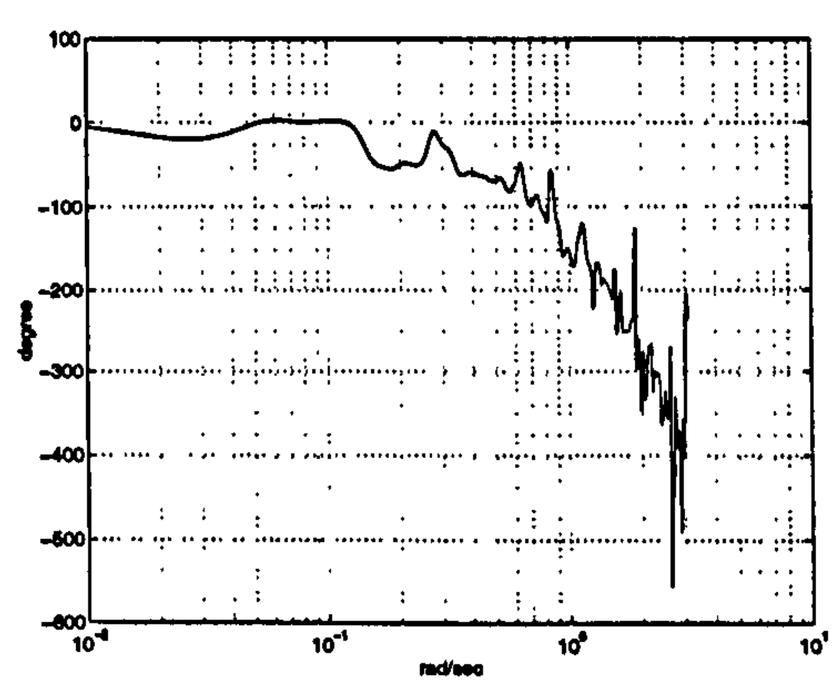
(c)

degree
rad/sec

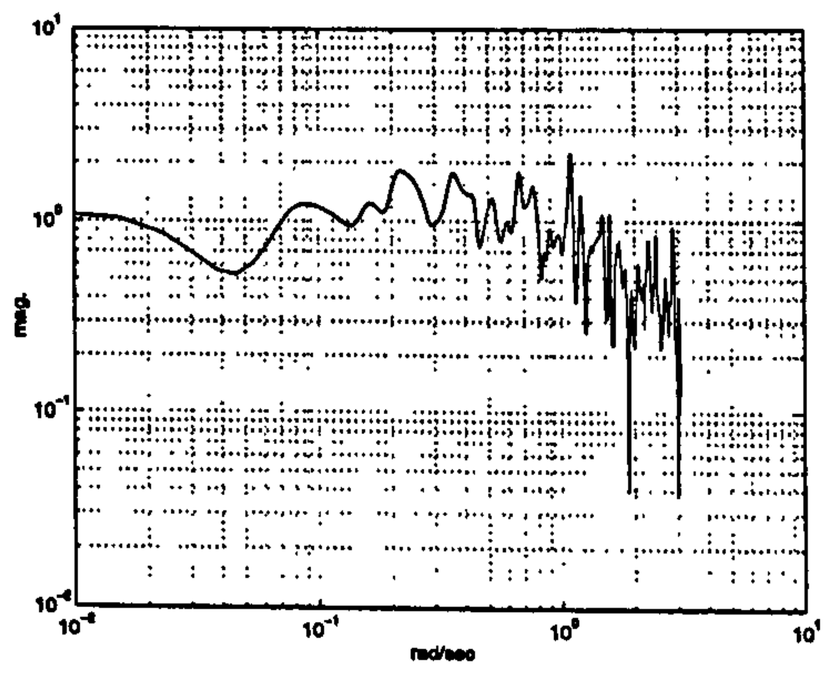
(d)


mag.
rad/sec

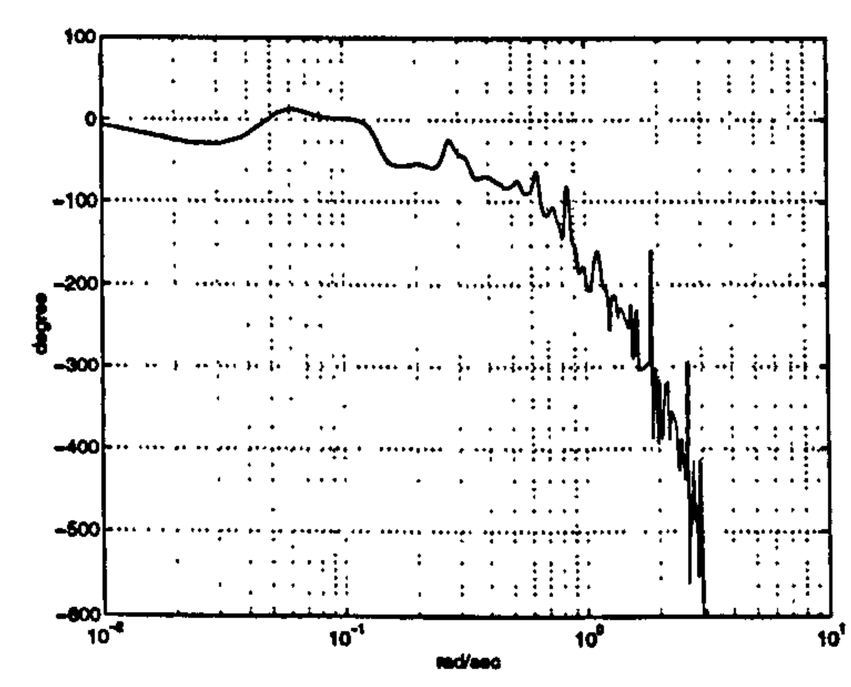
(e)


degree
rad/sec

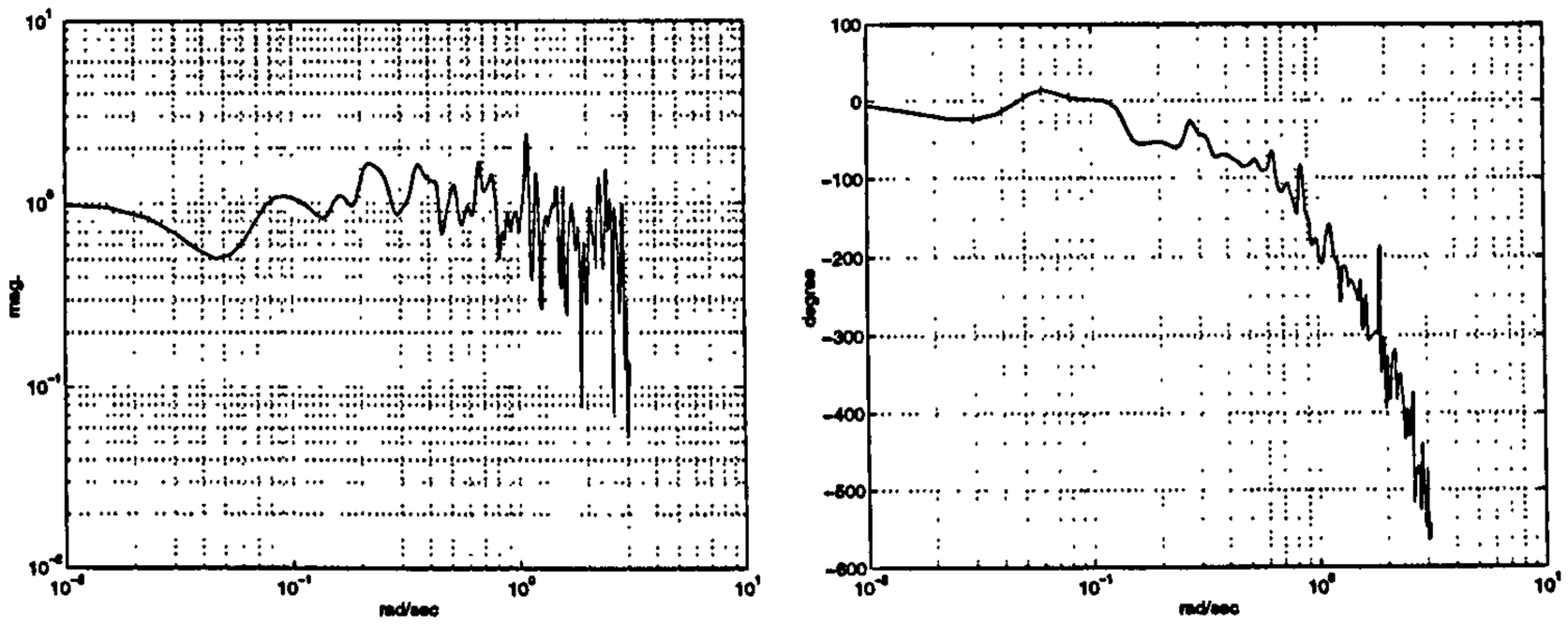
(f)


mag.
rad/sec

(g)


degree
rad/sec

(h)



(i) (j)

Figure 3.6: Spectral estimation of $G(s)$ in the presence of noise (a),(b) the beat-to-beat method, (c),(d) spline-spline method, (e),(f) spline-decimate method, (g),(h) the B-S method, (i),(j) the proposed method,

small) show up as small values of leading b_k estimates. The pole estimate can be obtained by proper selection of the delay samples and minimising the penalty function $V_N(\epsilon)$ as described earlier.

Table 3.1 presents the simulation results obtained by considering 30 different experiments (different random input realizations) in the noise free situation using the MATLAB system identification toolbox (Mathworks Inc.). Mean, variance and mean squared error (MSE) of the pole estimate are shown in the table for the different methods. Clearly, the best result is given by the proposed method whereas the other methods exhibit biased estimation in the parameters. Interestingly, the results are consistent with those of the spectral estimation method. The worst result belongs to the beat-to-beat method. Not only does the pole estimate differ markedly from the true value but the delay estimate also shows a drastic deviation. Both spline methods again behave similarly. Although estimation of the delay is biased, a close estimation for the pole is obtained. Correct estimation of the delay is possible by the B-S method. However, estimation of the pole is not satisfactory enough.

Table 3.2 presents similar results but in the presence of noise. The characteristics of the noise sources were selected as described for the spectral estimation. Table 3.2 reveals that the injection of noise causes a positive change in the estimated poles in all the methods. It also causes a large increase in the variance and MSE of the pole estimates. As would be expected the beat-to-beat method once more exhibits a large

	Mean($\hat{pole}$)	Var($\hat{pole}$)	$1/N\|\|pole - \hat{pole}\|\|^2$	$Delay_{(sec)}$
Beat-to-Beat Method	-0.4593	4.8074×10^{-4}	0.0258	1.0
Spline-Spline Method	-0.2868	8.6485×10^{-5}	2.5833×10^{-4}	2.0
Spline-Decimate Method	-0.2803	8.9131×10^{-5}	4.7479×10^{-4}	2.0
B-S Method	-0.2604	7.7477×10^{-5}	0.0016	2.5
Proposed Method	-0.3029	4.0309×10^{-5}	4.7409×10^{-5}	2.5

Table 3.1: Results of the parametric identification without noise $(n(t), m(t) = 0)$. Actual value of the pole $= -0.3$ and delay $= 2.5sec$.

	Mean($\hat{pole}$)	Var($\hat{pole}$)	$1/N\|\|pole - \hat{pole}\|\|^2$	$Delay_{(sec)}$
Beat-to-Beat Method	-0.5227	0.0428	0.0698	1.0
Spline-Spline Method	-0.2937	0.0017	0.0017	2.0
Spline-Decimate Method	-0.2878	0.0016	0.0017	2.0
B-S Method	-0.2701	0.0014	0.0023	2.5
Proposed Method	-0.3074	0.0015	0.0015	2.5

Table 3.2: Results of the parametric identification in the presence of noise. Actual value of the pole $= -0.3$ and delay $= 2.5sec$.

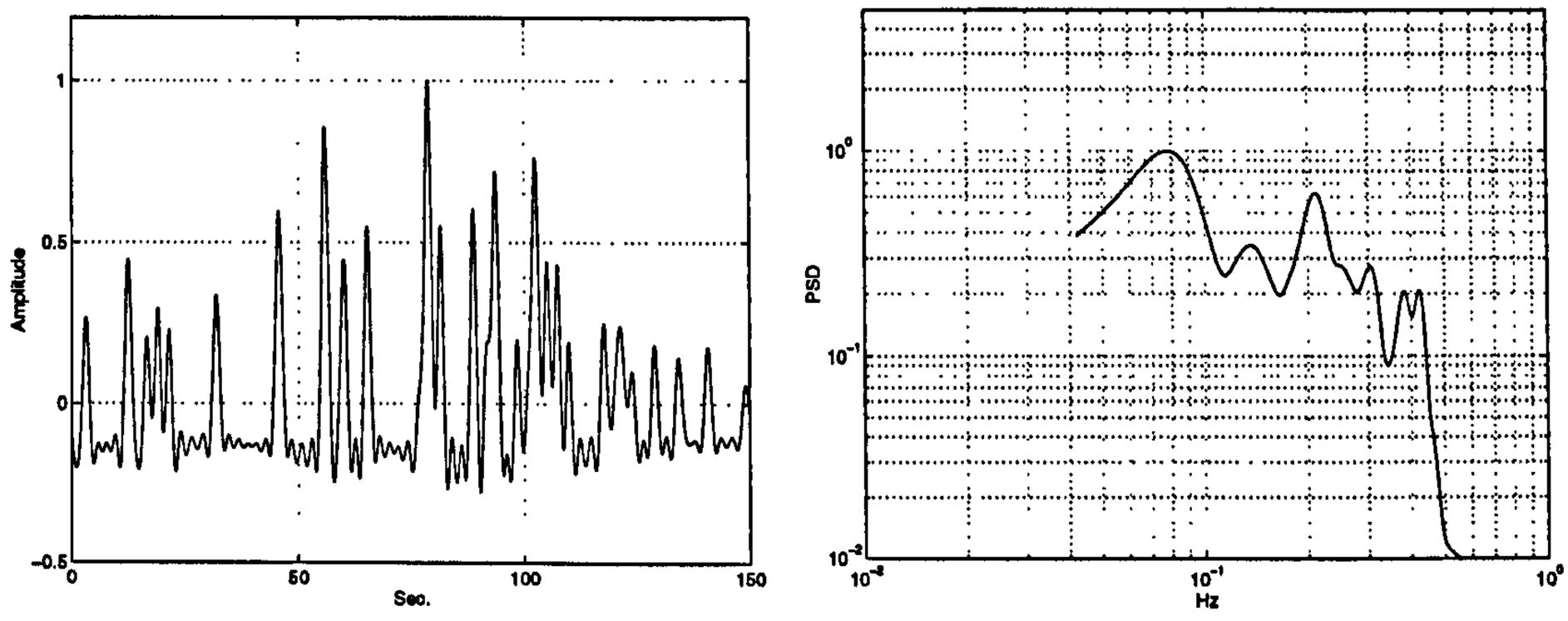
bias.

In the next section performance of the different signal descriptors with actual data is considered. It will be seen that the results obtained in the simulations can also be observed in practical conditions.

3.6 Experimental Results

One limitation in cardio-respiratory system identification is that under normal conditions the respiratory rate is relatively fixed, thereby limiting the frequency content of the pertinent signals and the identified systems. For broadening the frequency content of the respiratory signal, needed for system identification, Berger, Saul and Cohen (1989a) have introduced a random breathing pattern according to a Poisson process. The same procedure has been used here for whitening the power spectrum of the signals and comparison of the different signal descriptors in actual conditions.

The computer was programmed to produce random Poisson auditory tones based



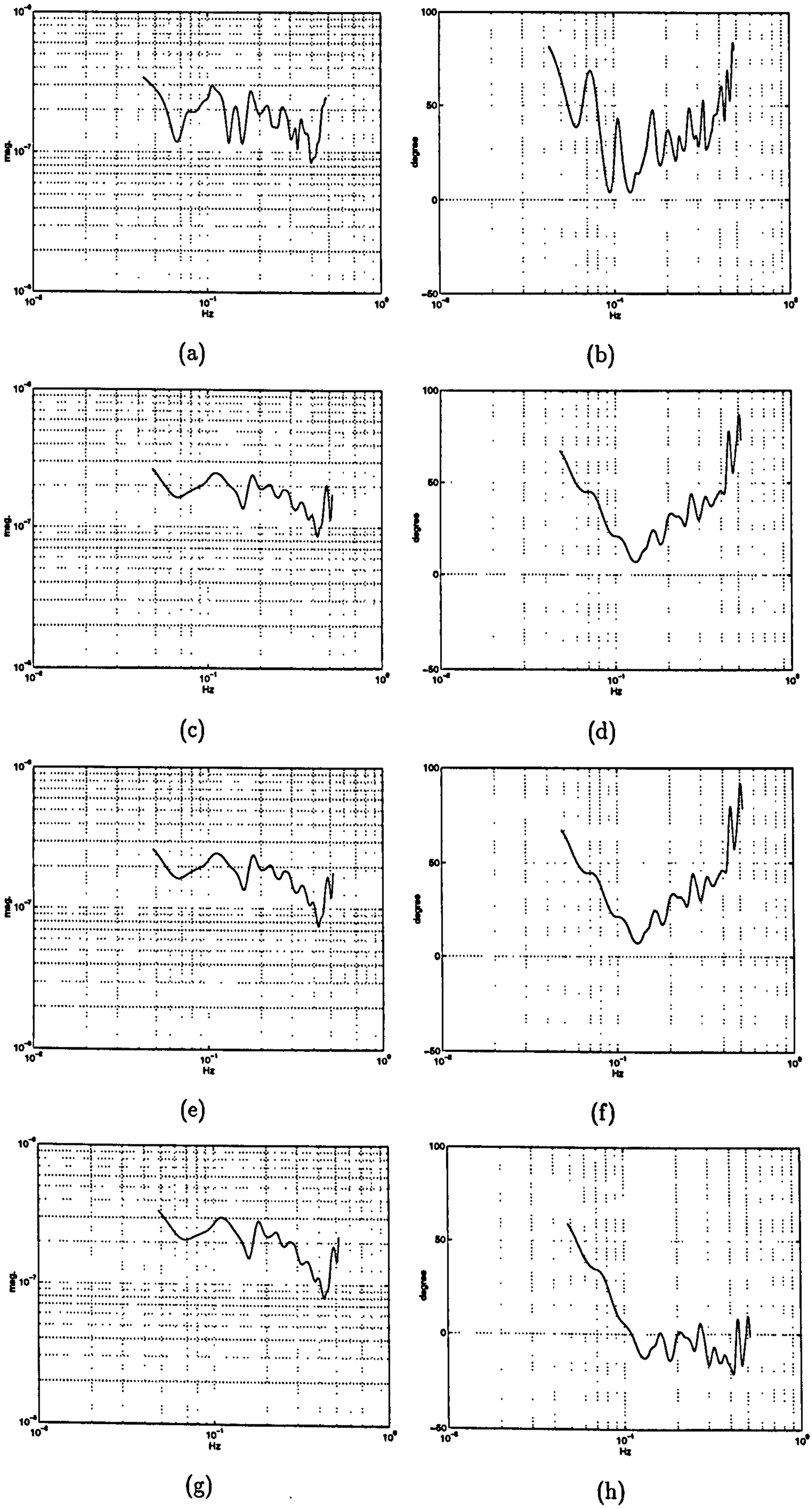
(a) (b)

Figure 3.7: Random breathing experiment. (a) Respiratory signal, (b) PSD of the respiratory signal.

on the Berger algorithm with mean, minimum and maximum intervals of 5, 2 and 14 seconds, respectively. Seven healthy adult subjects in the supine resting position were examined and for each of them, eight minutes of data (chest movement *via* a strain gauge transducer, and ECG) were collected (sampling frequency $500Hz$, 12 bit resolution). Subjects were instructed to initiate a breath with each tone. Although the respiratory intervals were controlled, the subjects were allowed to comfortably control the depth and shape of each breath throughout the experiment to preserve normal ventilation. Figure 3.7 displays the time behaviour and PSD of the respiratory signal for one subject (frequency resolution $= 0.04Hz$). Broadening of the spectrum can be seen in Fig. 3.7(b). Similar to the results obtained by Saul, Berger *et. al.* (1991) the PSD of the respiratory signal shows a decay with increasing the frequency.

After preliminary processing of the signals (R-wave detection, checking for the absence of artifacts), the magnitude and phase of the transfer function between the respiratory movement and HRV were estimated by different signal descriptors. The procedure described in Section 3.5 for the simulations was exactly used here to extract the input-output pairs. As a typical illustration the results obtained from one subject are depicted in Figs. 3.8(a) through 3.8(j) (similar results were observed for the other subjects).

It is inferred from these figures that the illustrated transfer functions demonstrate a lowpass filter characteristic. However, similar to the simulation results the estimated


mag.
degree
Hz
(a)
(b)
(c)
(d)
(e)
(f)
(g)
(h)

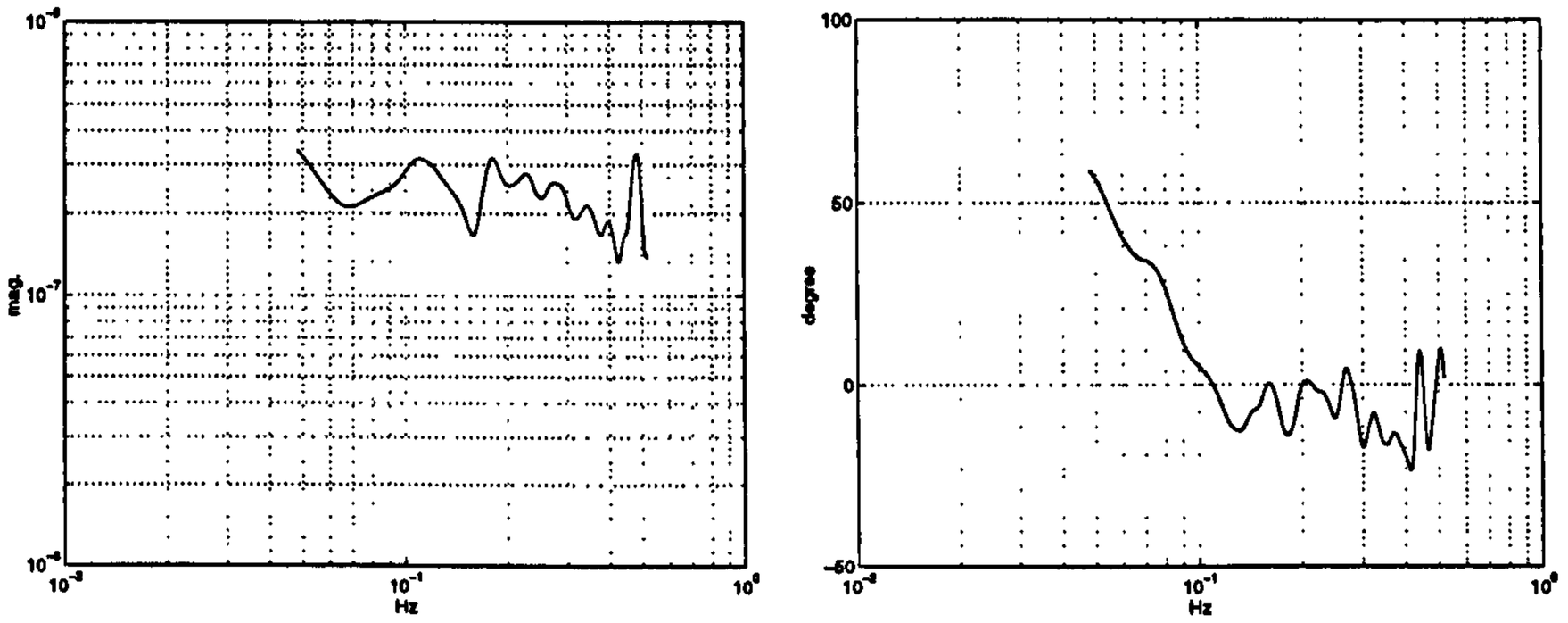


Figure 3.8: The estimated transfer function between the respiratory movement and HRV. (a),(b) beat-to-beat method, (c),(d) spline-spline method, (e),(f) spline-decimate method, (g),(h) the B-S method, (i),(j) the proposed method.

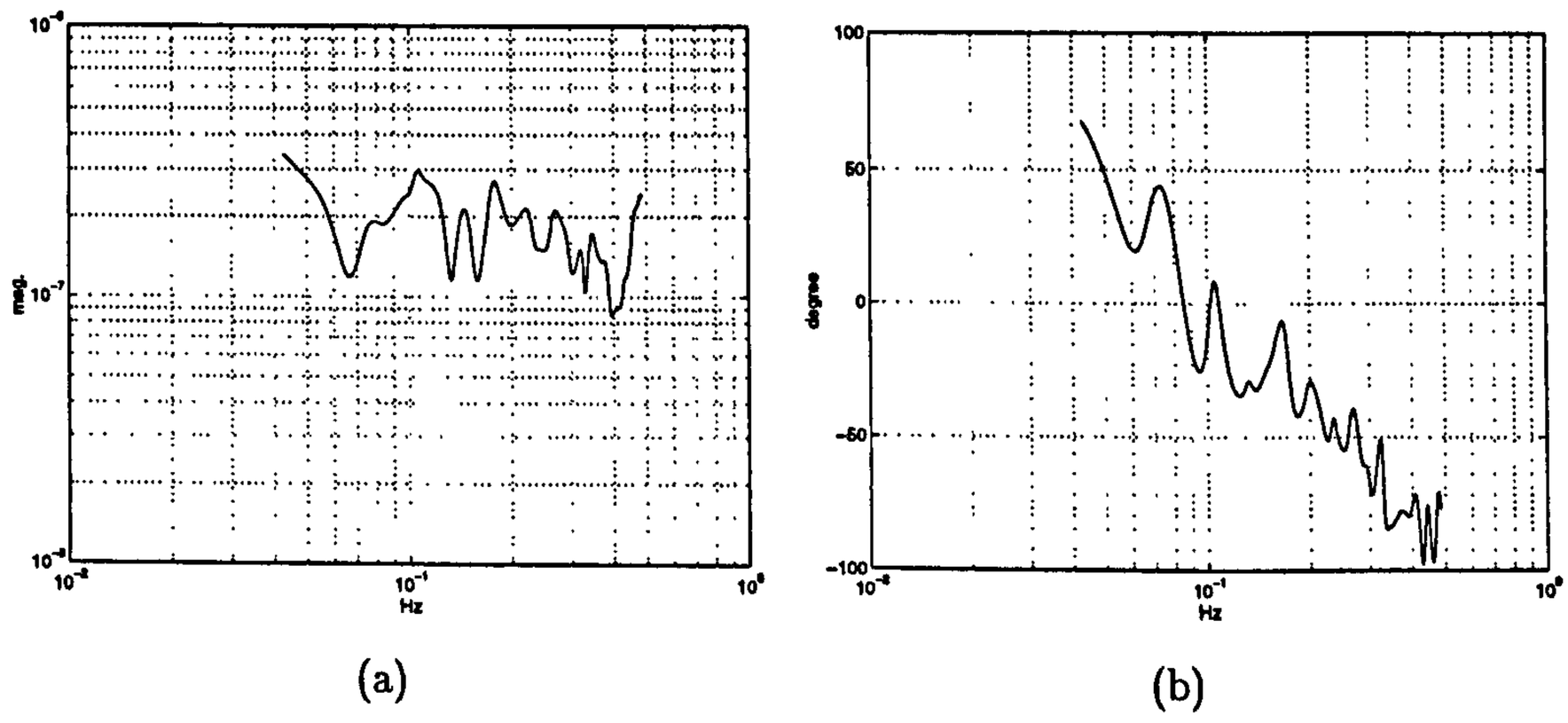


Figure 3.9: The estimated transfer function between respiration and HRV using the beat-to-beat method with the alternative protocol.

cutoff frequency of the system depends on the chosen sets of signal descriptors. The B-S method gives the lowest cutoff frequency whereas the highest (and perhaps the correct one) belongs to the proposed method. As would be expected the most fluctuating result is given by the beat-to-beat method. The discrepancy between phase estimates of the different methods, however, is more striking than the magnitude estimates. While for the beat-to-beat and spline methods a progressive positive phase for $f > 0.15Hz$ is observed, for the B-S and the proposed method a negative phase close to zero is estimated. Based on the simulation results it can be concluded that correct phase values (regarding the IPFM model assumption) can be extracted using either the B-S method or the proposed method. The reason for observing different phase estimations will be discussed in detail in the following section.

Transfer function estimation between tidal volume and HRV has also been considered by other investigators (Saul *et. al.*, 1991; Eckberg, 1983; Hirsch & Bishop, 1981). The lowpass characteristic of the transfer function has been confirmed by all of these authors. However, there is only a partial agreement between the cutoff frequencies of their estimations. This could be a result of the different experimental procedures and/or different signal descriptors. Saul *et. al.*, (1991) have employed the B-S method for their derivations. Our experimental results most closely resemble their results. Eckberg (1983) has measured the phase relationship between respiration and the interval tachogram. His results are close to the results of Fig. 3.9 (see Discussion). A detailed discussion of these results is not presented here, since the aim of this chapter is to evaluate the influence of the different signal descriptors on the obtained results rather than comparing the individual experiments or interpreting their physiological outcomes.

Even though the difference in the magnitude behaviour of the estimated transfer functions using different signal descriptors might not be very important, the phase characteristic must be carefully estimated because of its significant physiological meaning. While a negative phase indicates the existence of a delay between input and output, a positive phase implies the presence of a noncausal system. The results presented here enlighten the discrepancies between different signal descriptors for estimating the experimental transfer functions.

3.7 Discussion

The illustrated results in the preceding sections demonstrate that the issue of connecting a point event series to a continuous state time series signal is quite speculative. At first sight, constructing two sets of signals by measuring the interspike intervals and the corresponding samples of the continuous signal might be seen as a remedy. The rationale behind this construction is the belief that the heart rate and consequently the heart rate variability are essentially event series signals. This view, although it might be useful in individual analysis of the heart rate, is problematic in the joint analysis of the signals. To overcome this methodological inconsistency, de Boer (1985b) has recommended an *ad hoc* solution. He argues that if HRV is to be related to a continuous signal such as respiration, the event series should be converted to a time series signal whereas if it is to be related to another variable that is defined on a beat-to-beat basis such as systolic or diastolic pressure then the beat-to-beat protocol should be adopted. de Boer describes how to extract time series and beat-to-beat sets from interval variations in different ways. Although he analyses the performance of the different HRV descriptors, he does not give attention to the joint analysis of the signals.

In a rather different view of the problem we take note of the fact that the discrete events, associated with the occurrence times of the R-peaks, can be clearly and exactly defined on a continuous time basis (Chapter 2). By adding to this the fact that the actual HRV is a continuous signal which is coded (modulated) into the interspike interval variations, one can reach the original continuous-state continuous-time HRV signal by properly decoding (demodulating) this hidden information. This signal can be easily connected afterwards to any other signal. Fitting the problem into this realistic framework will extricate us from the maze of the improper relationship of the signals by producing a well-defined HRV signal using the KLPF method.

Let us now consider the disparity between the illustrated results by first scrutinising the beat-to-beat method. Owing to the random location of the R peaks, the beat-to-beat method imposes nonuniform sampling on the respiratory signal. TenVoorde (1994) and Rompelman (1995) have studied the power spectrum of the nonuniform samples of a sinusoidal signal, sampled with the spike series output of a sinusoidally modulated IPFM model. They have shown that the Fourier transform of the nonuni-

form samples ($R_1, R_2, R_3, \cdots$ in Fig. 3.3(b)) is given by

$$U(f) = A(f) + B(f) + C(f), \tag{3.16}$$

where,

$$A(f) = \frac{A_u}{2T_0}\delta(f \mp f_u)e^{j\theta_u},$$

$$B(f) = \frac{A_u\lambda_{ac}}{4T_0\lambda_{dc}}\delta[f \mp (f_p + f_u)]e^{\pm(\theta_p+\theta_u)} + \frac{A_u\lambda_{ac}}{4T_0\lambda_{dc}}\delta[f \mp (f_p - f_u)]e^{\mp(\theta_u-\theta_p)},$$

$$C(f) = \frac{A_u}{2T_0}\sum_{k=1}^{\infty}\sum_{n=-\infty}^{+\infty} B_{k,n}\delta[f \mp (kf_0 + nf_p) + f_u]e^{j(\theta_u \pm \Phi_{k,n})}$$

$$+\frac{A_u}{2T_0}\sum_{k=0}^{\infty}\sum_{n=-\infty}^{+\infty} B_{k,n}\delta[f \mp (kf_0 + nf_p) - f_u]e^{-j(\theta_u \mp \Phi_{k,n})},$$

$$B_{k,n} = J_n\left(\frac{k\lambda_{ac}f_0}{f_p\lambda_{dc}}\right)\left(1 + \frac{nf_p}{kf_0}\right),$$

$$\Phi_{k,n} = n\theta_p - \frac{k\lambda_{ac}f_0}{f_p\lambda_{dc}}sin(\theta_p),$$

(A_u, f_u, θ_u) and $(\lambda_{ac}, f_p, \theta_p)$ are amplitude, frequency and phase of the input sinusoidal signal and IPFM modulating signal (sinusoidal), respectively and J_n is the Bessel function of the first kind of the order n. In the ideal case the Fourier transform in the low frequency band ($|f| < f_0/2$) should contain only the desired frequency component (f_u). However, equation (3.16) illustrates that the interfering components, arising from the intermodulation between IPFM modulating signal f_p, the IPFM free running frequency f_0, and the input signal f_u, penetrate into the desired frequency band [3]. The presence of these components may cause distortion in the result of the identification. The amount of distortion depends on the parameters of the IPFM model, its modulating signal and the desired input signal.

The reason for having a positive progressive phase in the beat-to-beat method originates from the accepted protocol which relates the next R-R interval to the current respiratory sample ($(R1, T1), (R2, T2), \ldots$, in Fig. 3.3). This is because the current variation of the R-R interval in each cycle is pulled back towards the respiratory sample (positive phase shift). If the protocol is changed so that the current interval is related to the next respiratory sample ($(R2, T1), (R3, T2), \ldots$) then a negative phase value

[3]It is useful to note that for an arbitrary input and IPFM modulating signal, the generalised form of equation (3.16) can be obtained through equation (2.22).

is estimated. This is confirmed by using this alternative protocol on the previous experimental data as shown in Fig. 3.9. Although by using this protocol the phase curve shows a negative trend, its shape is still different from that obtained by the proposed method or the B-S method.

Further, the spline algorithm is based on the beat-to-beat method. That is why the phase estimates in both methods look alike. Now the question is: why do the spline methods exhibit less erratic results? The reason lies in the statistical estimation of the probabilistic parameters. While the number of the data points for the estimation in the beat-to-beat method is limited to the number of the R-peaks in the given length of data, it is markedly increased to any arbitrary value for the interpolation methods, thereby decreasing the variance of the estimations. Furthermore, the HRV descriptor in the interpolation method is a well-defined continuous signal.

It is also worthwhile to point out that the error in phase estimation in the interpolation method, although it appeared significantly in the experimental results presented here, might not be in general a critical factor in systems with large values of delay. This can be understood from the simulation results presented earlier. It is, however, much safer to use always the proposed method for the purpose of system identification.

The reason that all other methods estimate a lower value for the pole than the actual one is that these methods use a rough approximation of the lowpass filtering method for extracting the HRV from the spike series signal as described in Chapter 2. The influence of this approximation manifests itself as a lower value for the pole estimate.

Although the respiratory signal was considered here as the given continuous signal, an analogous discussion can be raised if heart rate variability is to be related to blood pressure variation, albeit with more controversy. The beat-to-beat blood pressure indices (descriptors) are: systolic blood pressure, diastolic blood pressure, pulse pressure and mean blood pressure. Importantly, each of these indices has a special physiological meaning. However, according to the presented results, if a beat-to-beat approach is employed for the system identification, estimation of the parameters, and therefore physiological interpretations can be biased. The instantaneous blood pressure signal, unlike the R-R interval, is a well-defined continuous state time series signal. Hence, attributing an associated continuous state blood pressure variability signal

(BPV) extracted from the instantaneous blood pressure signal will not be a formidable task. Further discussion on this subject is postponed until the concept of small signal and large signal variations is described in Chapter 4 and it is only remarked here that passing the instantaneous blood pressure signal through a lowpass filter will elicit an appropriate blood pressure variability (BPV) signal, suitable for system analysis.

Finally, we would like to emphasise that the results of this chapter can be applied analogously to the analysis of the neuronal discharge. Because of the complexity involved in the Volterra-Wiener approach, there has been a great tendency towards the use of the IPFM representation for the modelling of excitable neurons (Paulin, 1992, 1993; Sanderson, 1980). Consequently, the prevalent but inaccurate, rate histogram method can be replaced by the method introduced in this chapter for the joint analysis of the neuronal discharge and the relevant physiological signals.

3.8 Conclusion

The demonstrated results reveal that identification of a linear system followed by an IPFM model, is possible in the low frequency region. This achievement is of particular benefit in HRV system analysis since it promises the correct identification of any possible system between respiration or blood pressure and the SA node in spite of its nonlinear operation.

The major contribution of this chapter, however, was devoted to determining the appropriate sets of signal descriptors for faithful identification of an unknown system. It was shown that the current methods for relating the spike series signal to a continuous signal should be used with care, whereas the correct result can be given by the proposed method. Particularly, the simulation results demonstrated that the true phase estimate can be obtained by the proposed method. By considering the experimental results it was shown that the physiological interpretation should be accompanied with careful attention to the method chosen for extracting the involved signals.

The proposed method also appears to be a suitable tool for a large group of problems dealing with spike series signals. Finding time delays in the baroreflex loop (Pickering & Davies, 1973; Borst & Karemaker, 1983), searching for a relationship

between excitatory inputs and neuronal discharge (Katona, Poitras, Barnett, Terry, 1970), and even obtaining the connection between vagal and sympathetic rhythmical fluctuations (sympathovagal balance) (Koizumi, Terui, Kollai, 1984) can be fulfilled by this method.

Summary of the Chapter

Applying the KLPF method, and in general the lowpass filtering method, to the R-wave signal not only elicits a well defined time series HRV signal but also guarantees the ability to find the correct relationship between a spike series signal, generated by the IPFM model, and a continuous state time series signal. This result gives enough confidence to take further steps towards the identification of HRV-BPV-ILV relationships in the next chapters. Importantly, extraction of the signals based on the proposed algorithm is exceedingly simple.

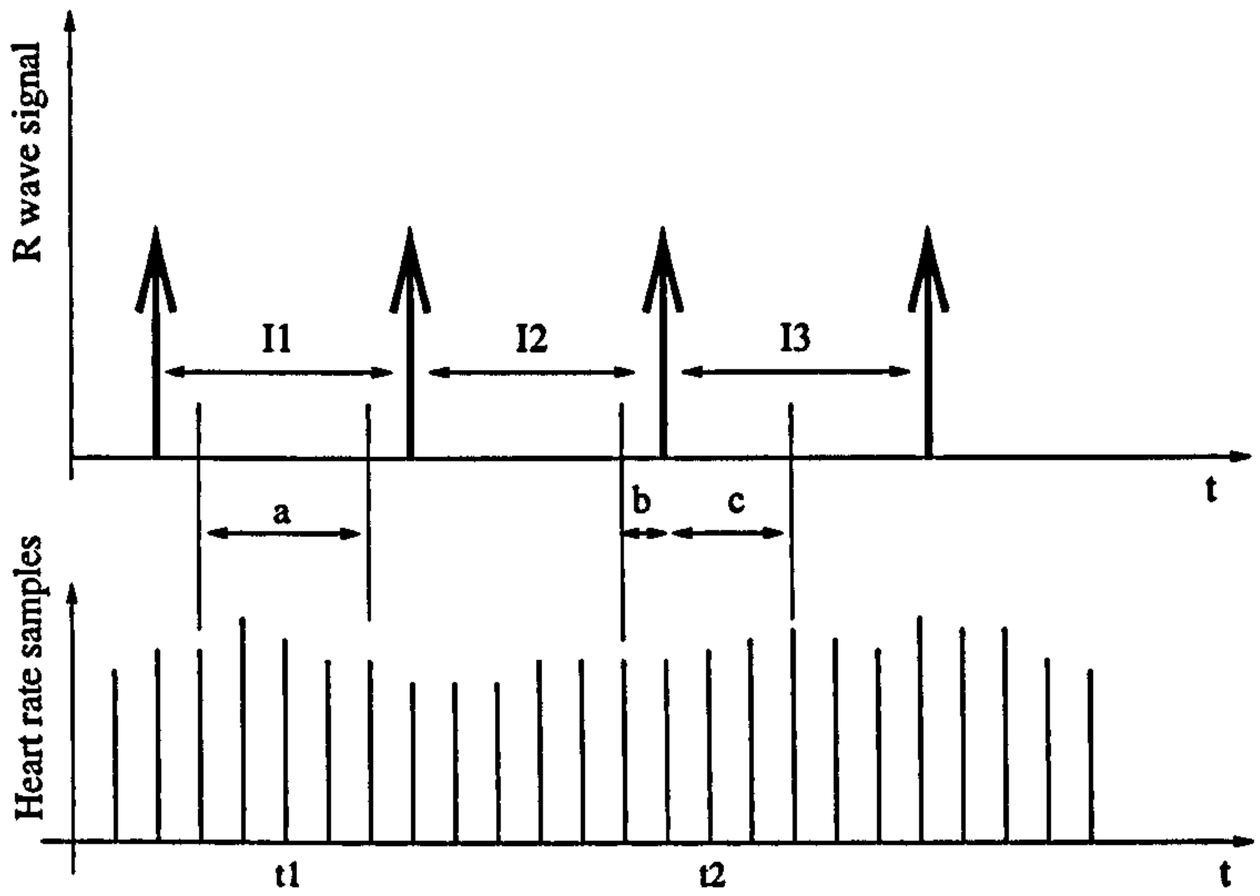


Figure 3.10: Berger-Saul method.

3.9 Appendix A: Berger-Saul Method

The steps involved in the the B-S method are as follows. First, the ECG is sampled at a sufficiently high rate to determine the time locations of the R peaks to whatever accuracy is desired. Next, a sampling rate for the heart rate signal is chosen. This is a true frequency (i.e., the heart rate samples will be evenly spaced in time at this frequency), and may be chosen arbitrarily, without regard to the mean heart rate or the frequency at which the ECG is sampled. A local window is then defined at each heart rate sample point as the time interval extending from the previous sample to the next. We then count the number of RR intervals (including fractions thereof) that occur within this local window. For example the number of RR intervals for the sample point at t_1 in Fig. 3.10 is a/I_1 and at sample point t_2 is $b/I_2 + c/I_3$. The value of heart rate at each sample point is taken to be the number of intervals that fell within the local window centred at that point multiplied by the sampling frequency and divided by the width of the window. More details can be found in Berger *et. al.* (1986).

Chapter 4

Investigation of HRV and BPV by Model Analysis

Objectives of the Chapter

It was shown in Chapters 2 and 3 how to obtain a well defined heart rate variability signal in the form of a continuous state time series signal. Furthermore, it was demonstrated that by this treatment correct identification of an unknown system and consequently a joint relationship between the neuro-cardiovascular signals would be possible. In the current chapter the objective is first to describe the physiological relationships between the variability signals and their origins by considering different hypotheses and secondly to show how these physiological relationships can be drawn in the form of a block diagram and mathematical representation. A comprehensive model is finally proposed which will form a basis for further investigation into the HRV and BPV.

4.1 Introduction

Fluctuations in blood pressure and heart rate are consequences of perpetual interactions between several complex physiological systems working in unison. To draw a correct systematic picture of these interconnections a thorough study of the underlying physiological phenomena is needed. Therefore, the first part of this chapter is allocated to those lines of physiological evidence which are believed to have significant contributions to the rhythmical fluctuations in heart rate and blood pressure. This is followed by a review of some of the pertinent mathematical models, their advantages

and their drawbacks, to give insight into a deeper understanding of the overall problem. In order to successfully delineate a comprehensive HRV-BPV-ILV model, a conceptual discussion about large signal and small signal cardiovascular modelling is presented next. This discussion specifically helps to determine a suitable approach for analysis of the variability signals. Finally, in the last section of this chapter a new model is depicted and its prominent features are highlighted. This model forms the basis for further analysis of HRV and BPV in the succeeding chapters.

4.2 The Physiological Basis of the Rhythmical Fluctuations in HRV and BPV

The activity of the autonomic nervous system in response to an ever-changing internal environment goes on without our awareness or voluntary control. These autonomic functions involve heart rate, blood pressure, respiratory rate and body temperature. Interestingly, control of these systems is accomplished in an interactive manner. Specifically, interdependency between different effectors and their governing centres complicate the study of the functional aspects of the autonomic nervous system. Related to this point is the oscillating behaviour of blood pressure and respiration. Research on the rhythmic fluctuations of systemic arterial blood pressure or blood pressure waves has now been ongoing for more than two centuries (Hales 1733 [1]). Blood pressure regulation is also closely connected with fluctuations of the heart rate. It is well-known that respiration has a significant effect on heart rate. This so-called Respiratory Sinus Arrhythmia (RSA) has also been the centre of attention for many years and has been described as a window on autonomic regulation (Akselrod *et. al.*, 1985; Mathias & Bannister, 1992).

In addition to the respiratory related phenomena, other rhythmic oscillations can also be observed in the heart rate and blood pressure. Although the origin of these fluctuations is much less clear than the respiratory related fluctuations the ultimate model of the entire system must include satisfactory explanations for at least the significant components. In the succeeding sections the widely-accepted mechanisms for origins of the different fluctuations in heart rate and blood pressure are presented.

[1] As described by de Burgh Daly (1986).

4.2.1 Respiratory Sinus Arrhythmia

Heart rate increases with inspiration and decreases with expiration and the magnitude of this respiratory sinus arrhythmia depends on tidal volume and breathing rate (Saul *et. al.*, 1991; Hirsch & Bishop, 1981; Eckberg, 1983). It is well-known that a variety of direct neural controls through sympathetic and parasympathetic innervations in conjunction with indirect mechanisms modulate the heart rate. Blockade of the autonomic nervous system and especially the vagus branch to the heart causes a marked reduction in heart rate variability (Saul *et. al.*, 1991; Perlini, Solda, Piepoli, Salla-Galllini, Calciati, Finardi, Bernardi, 1995a; Triedman & Saul, 1994). Also, observation of respiratory fluctuations in cardiac sympathetic and parasympathetic neuronal spikes has been used as a further evidence (Polosa, 1984a; Katona *et. al.*, 1970; Barman & Gebber, 1976). It is believed that direct central influence of the respiratory related neurones on the cardiac control centres in the brain stem has a significant role in producing the RSA. This view is based on experiments in which respiratory sinus arrhythmia persists in the paralysed animal with open or closed chest on stopping artificial respiration. This direct respiratory modulation of heart rate was first observed by Traube (Traube-Hering experiment) and confirmed then by other researchers (Levy, Degeest, Zieske, 1966; McCrady, Vallbona, Hoff, 1966; de Burgh Daly, 1986 and references therein). Traube demonstrated [2] that RSA persisted after curarization of the animal and concluded that the variations in heart rate were central in origin and due to transmission of impulses from the respiratory centres to the cardio-inhibitory centre, thereby diminishing vagal tone. Acceleration of the heart accompanies inspiratory movement of the ribs and inspiratory activity in fibres of the phrenic nerve (Gebber, 1980). In addition, the cessation of vagal efferent activity during the inspiratory phase of natural, but not artificial, ventilation strongly suggests a medullary connection from the respiratory to cardiovascular centre as the predominant origin of RSA (Katona *et. al.*, 1970).

One of the important mechanisms by which respiration affects the cardiovascular system is through modulation of the autonomic reflexes that control heart rate and peripheral vascular resistance. These reflexes are initiated by baroreceptors which are located in the walls of the large systemic arteries, mainly in the carotid arteries and the

[2] As described by Koepchen (1984), Polosa (1984a) and de Burgh Daly (1986).

aortic arch. A rise in the blood pressure stretches the baroreceptors and causes them to transmit signals into the central nervous system. Then feedback signals are sent back through the autonomic nervous system to the circulation to reduce arterial pressure downward toward the normal level. Baroreceptors send their signals to the medulla to inhibit the vasoconstrictor centre of the medulla and excite the vagal centre (Guyton, 1996; Milnor, 1990). Inhibitory signals are then transmitted through the vagus nerve to decrease the heart rate. At the same time decrease in sympathetic stimulation causes a decelerating effect on the heart rate. Therefore, any change in arterial blood pressure due to respiratory activity (or any other rhythmic fluctuation in blood pressure) can be reflected in sinus rhythm.

In addition to the arterial baroreceptors, the heart and the pulmonary arteries are richly innervated with afferent fibres. The cardiopulmonary afferents can be divided into three main functional classes: (i) mechanoreceptors around the right and left veno-atrial junctions connected to myelinated vagal fibres, (ii) mechanoreceptors which are scattered diffusely throughout the atria, ventricles and pulmonary arteries and are connected to the vagus and cardiac sympathetic nerves, (iii) chemosensitive fibres travelling in the vagus and cardiac sympathetic nerves (Levic, 1991). Of these, the veno-atrial receptors are normally the most active (Levic, 1991). The mechanical effect of respiration directly influences the central venous and atrial pressure. Although the explicit role of the cardioplumonary receptors is still unclear, their contribution in cardiovascular regulation is beyond dispute (Mark & Mancia, 1986; Hainsworth, 1991).

In addition to the reflexes just described, an analogous role is also given to the Hering-Breuer reflex. Pulmonary stretch receptors located in the smooth muscle of the walls of the bronchi and bronchioles are activated when stretched by lung inflation (de Burgh Daly, 1986). Afferent fibres in the vagus nerve travel to the inspiratory centre to inhibit inspiration. It is believed that this reflex also reinforces a vagal inhibition and slows down the heart (Hainsworth, 1974; Saul & Cohen, 1994; de Burgh Daly, 1995).

The direct mechanical effect of respiration on heart rate is also of importance. Although RSA is markedly attenuated by autonomic blockade, a small RSA still remains (Saul *et. al.*, 1989; Triedman & Saul, 1994; Perlini *et. al.*, 1995a) suggesting that at least part of HRV originates from an intracardiac mechanism; either by an intracardiac reflex, or mechanical stretching of the SA node. It is known that direct stretch of the

SA node can increase the heart rate, in the isolated situation, by as much as 15 per cent (Chapter 6).

4.2.2 Respiratory Oscillation in Arterial Blood Pressure

Unlike heart rate variability, there appears to be no fixed relationship between blood pressure and respiration. During spontaneous breathing the arterial pressure falls during inspiration but conversely at low breathing rates blood pressure rises with inspiration (Laude, Goldman, Escourrou, Elghozi, 1993; Dornhorst, Howard, Leathart, 1952). Increase in tidal volume, however, increases the corresponding fluctuations in arterial blood pressure over all breathing rates.

An important contribution to the respiratory fluctuations of blood pressure belongs to the direct mechanical influence of respiration. Under normal conditions the cardiac output is controlled mainly by peripheral factors that determine the venous return. Respiration induces phasic changes in venous return and pulmonary arterial blood flow, *i.e.*, an increase with inspiration and a decrease with expiration. Each time inspiration occurs the pressure in the thoracic cavity becomes more negative, causing the blood vessels in the chest to expand. This reduces the quantity of blood returning to the left side of the heart and thereby momentarily decreases the stroke volume and arterial pressure. As the pressure in the thorax becomes more negative there is an increase in the pressure gradient between the peripheral veins and the right atrium. Therefore, blood flow into the chest is accelerated. The additional blood comes from the extrathoracic large veins. Hence, the filling of the right heart from the extrathoracic veins increases. The right ventricular outflow mirrors the venous return with a delay of one beat. Thus, right ventricular stroke volume increases. After a lag of about two cardiac cycles the pressure in the pulmonary veins rises and the filling of the left heart increases. This leads to increased left ventricular stroke volume and cardiac output (Lindqvist, 1990). Figure 4.1 illustrates intrathoracic pressure and flow variations during spontaneous respiration.

Besides the respiratory modulation of venous return, respiration can have a direct mechanical effect on left ventricular loading and the thoracic arteries. Some authors believe that the central venous pressure fluctuations for $f > 0.1Hz$ are transmitted

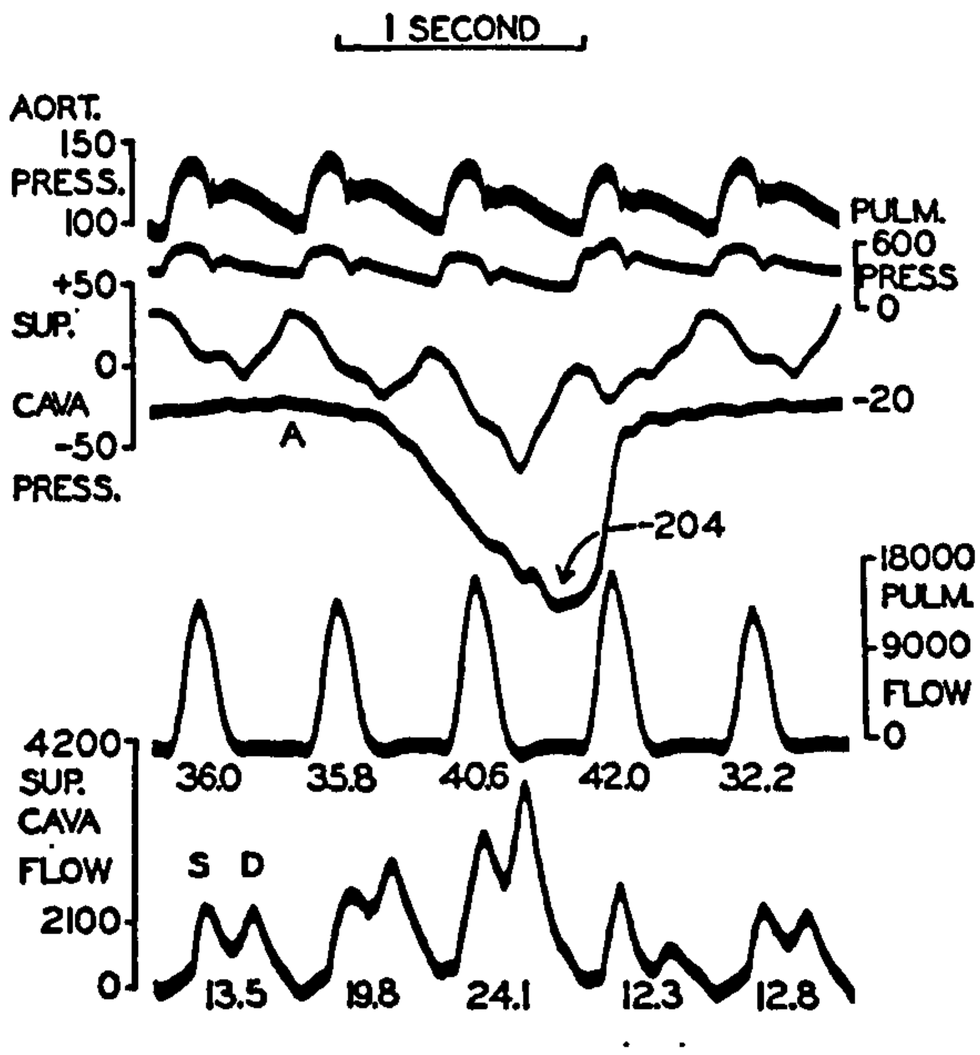


Figure 4.1: Tracing from top to bottom: aortic pressure(mmHg), pulmonary artery pressure, superior vena cava and intrathoracic pressures (mmH2O), pulmonary arterial and superior vena caval flows (ml/min). A denotes beginning of respiration. Stroke volume (ml) is shown below pulmonary arterial flow curve. Volume (ml) through superior vena cava during each cardiac cycle is shown at bottom (de Burgh Daly, 1986).

with a marked reduction in magnitude to the arterial side (Triedman & Saul, 1994). Hence, it can be concluded that the mechanical effect of respiration for $f > 0.1Hz$ is mainly due to the direct arterial modulation.

It is believed that the respiratory fluctuations in heart rate have a significant effect on the corresponding fluctuations in blood pressure. However, whether the RSA has only a buffering effect on blood pressure, conducted through baroreceptors and blood pressure regulatory mechanism, or it has a direct effect, which is imposed by the central respiratory oscillator, still is a debatable matter (Parati, Pomidossi, Casadei, Gropelli, Trazzi, Di Rienzoi, 1987; Taylor & Eckberg 1996; Saul *et. al.*, 1991). If the change in arterial blood pressure is the major determinant in producing RSA, blood pressure would have to fall with inspiration. Detailed analysis has revealed that there is no consistent relationship between blood pressure and heart rate in respiratory band (de Burgh Daly, 1986, 1995).

A direct link between the respiratory centre and the vasomotor centre in the brain stem might also be involved (de Burgh Daly, 1995; Barman, 1976; Gebber, 1980). The vasomotor origin of this rhythmic fluctuation is again confirmed by the Traube-Hering experiment which shows that the respiratory fluctuations of blood pressure still

persists in curarized, vagotomized dogs after cessation of artificial ventilation and even after temporary exclusion of the heart (Polosa, 1984a). Although at higher breathing rates, the centrogenic respiratory modulation may be largely attenuated by the vascular smooth muscle response (Rosenbaum & Race, 1968), it can play a significant role at lower breathing rates.

In addition to the baroreceptors, blood pressure is regulated by the activity of the chemoreceptors. Chemoreceptors of the large arteries are mostly scattered in the carotid sinus and the aortic arch close to the baroreceptors. When blood pressure falls below a critical level the chemoreceptors become stimulated because of the diminished blood flow and excess build up of CO_2 and H^+. The afferent signals from the chemoreceptors enter the brain stem and excite the vasomotor centre. However, chemoreceptors play an important role in the control of respiration and are thought to be of relatively minor importance in the control of circulation and inducing the respiratory fluctuation to the cardiovascular parameters (Guyton, 1996).

4.2.3 Low Frequency Oscillations

Respiratory fluctuation is not the only rhythmic oscillation in heart rate and blood pressure. Investigation by spectral analysis has revealed that a large part of the spectrum is also occupied by fluctuations around $0.1Hz$ and also at values less than $0.05Hz$ (Pagani *et. al.*, 1986; Kitney & Rompelman, 1980). These two regions plus the respiratory fluctuation are called Low Frequency (LF), Very Low Frequency (VLF) and High Frequency (HF) oscillations, respectively[3].

With regard to the origin of blood pressure waves of the third order (LF and VLF) there is still considerable controversy. They can be observed during heart rhythms other than normal sinus, such as atrial fibrillation, ventricular fibrillation and ventricular pacing, indicating their independence from specific variations in heart rate (Craelius, 1986; Akselrod *et. al.*, 1985). It is believed that under normal conditions the existence of at least three oscillatory systems are responsible for the generation of the third order waves (Koepchen, 1984) namely;

[3]In the study of blood pressure waves, respiratory and low frequency (Mayer waves) components are termed second order and third order blood pressure waves, respectively. The basic rhythmic oscillation of blood pressure with each heart beat is called the first order blood pressure wave (Koepchen, 1984).

(i) centrogenic rhythm in the brain stem with interconnection to respiratory oscillator,
(ii) the baroreceptor or chemoreceptor feedback system,
(iii) the autorhythmicity of the vascular smooth muscle.

The first hypothesis means that there is a central vasomotor oscillator in its own right generating the Mayer waves. These waves are then transmitted, *via* the sympathetic nerves, to the vascular system producing the third order blood pressure waves. This assumption is strengthened by the observation of reticular neuronal activity; the discharge sequences of the reticular neurons in the lower brain stem has revealed that the activities of these neurons show oscillations with period 4-10*sec* (Langhorst, Schulz, Lambertz, 1984; Montano, Gnecchi-Ruscone, Porta, Lombardi, Malliani, Barman, 1996). If this is the case, independent activity of the endogenous generator of the third order waves does not seem to be possible without interaction with other endogenous generators such as neurones of the respiratory centre. This assumption also provides a basis for explanation of the so-called sliding coordination between LF and HF oscillators. Sliding coordination means that two independent and variable rhythms interact. More recently the concept of sliding coordination was adopted for respiratory, cardiovascular and other central sympathetic rhythms and was described both physiologically and mathematically (Gebber, 1980; Kitney, 1975; Kitney & Rompleman, 1987). Observation of simultaneous HF and LF components in the medullary neurones in vagotomized, sinoaortic denervated animals in coherence with blood pressure oscillations has strengthened this belief (Montano *et. al.*, 1996).

The picture of several central rhythms appearing, disappearing and interfering with each other in a sliding manner also delineates the theory of common rhythmicity and a common brainstem network as described by Langhorst *et. al.* (1984). On one hand, the reticular neurons have reciprocal relations with the neurons of the respiratory oscillator and on the other hand their discharge behaviour is influenced by afferents from the lungs and blood vessels (Barman, 1976; Gebber, 1980). Pronounced rhythmic oscillations, in the sense of resonance, may be observed when the rhythmic signals of the afferents are in the same frequency range as the endogenous frequencies of the brain stem oscillators (Langhorst *et. al.*, 1984).

The second hypothesis for Mayer waves generation mechanism is based on feedback theory of the circulatory control system (Section 7.5.1). The receptors responsible

for the feedback are either in the periphery *i.e.*, carotid and/or aortic baro- or chemoreceptors or within the central nervous system (medullary chemoreceptors). Thus any reflex pressure control mechanism can oscillate if the intensity of feedback is strong enough and there is also an appropriate delay between excitation of the pressure receptors and the subsequent pressure response (Hosomi & Hayashida, 1984). It has also been argued that oscillation based on linear feedback theory is not sufficient for the occurrence of the sustained and regular blood pressure oscillation but should be explained by nonlinearity in the circulatory system and the limit cycle theory (Kitney & Rompelman, 1987; Kanoh, 1984).

Although Mayer waves usually stop after opening the closed loop of the blood pressure control system by pharmacological agents or receptor destruction, rhythmic fluctuations at the Mayer frequencies can still be seen in the efferent sympathetics, suggesting a centrogenic origin (Section 7.5.2). One question which may arise here is, if Mayer waves have a central origin then what is the possible role of the feedback mechanism? Perhaps the effect of peripheral receptors is additional synchronisation or wave shaping upon the central oscillator without entering into the actual rhythm generating mechanism as described by Koepchen (1984). Shifting of the Mayer waves to higher frequencies with injection of Beta sympathetic blocking agents supports this conjecture (Craelius, 1986).

The third possibility for the origin of the blood pressure waves in the low, and particularly in very low frequency (VLF) region, is based on the rhythmic properties of vascular smooth muscle. Hence, the third order oscillations are not necessarily pressure dependent or of central origin but may also arise from an endogenous oscillator located in the peripheral vessels (Section 7.5.3). Periodic fluctuations of systemic arterial pressure are possible only when a considerable part of peripheral vascular musculature performs synchronous, rhythmic contractions where synchronisation, perhaps, is guided by central nervous innervation, whereas the time course of contraction and relaxation is determined by the intrinsic properties of the vascular smooth muscle cells (Siegel, Ebeling, Hofer, Nolte, Roedel, Klubandorf, 1984; Rosenbaum & Race, 1968). Consequently, the absence of peaks in this frequency band may not decisively exclude vascular endogenic activity- because the contractile activity of the smooth muscle cells may be out of phase (Janssen, Oosting, Sloaf, Persson, Struijker-Boudier, 1995). The thermoregulatory control system may also contribute to the generation of very low fre-

quency components. It has been shown that the VLF generation mechanism, based on nonlinear oscillating theory for controlling the thermoregulatory system, can be verified by experimental results (Kitney, 1974). This hypothesis also provides satisfactory reasons for observing the associated oscillation in HRV (Kitney & Rompelman, 1980).

Bearing all the above points in mind, it is difficult to validate only one of the LF generating mechanisms. Since the existence of each of the different mechanisms has been proved under certain experimental conditions, it is much more likely that the third order waves have a multiple origin. The fact that each of the oscillators can develop different frequencies with different phase lag or lead can explain the existence or disappearance of the waves in an unpredictable manner and synchronisation and resonance between oscillators as described by Koepchen (1984).

4.2.4 Dominant Factors in Producing the Rhythmical Fluctuations in HRV and BPV

In addition to the factors discussed so far, many other phenomena inside the body may interact with the cardiovascular-respiratory system in producing the rhythmical fluctuations in HRV and BPV. However, in the resting state and in short term studies (which is assumed here) it is postulated that they have negligible effects.

To recapitulate, the important mechanisms in the generation of the heart rate and blood pressure waves can be summarised as follows:

(i) Respiratory fluctuations in heart rate:

- Direct central linkage between respiratory and cardiac control centres.
- Reflex action of the baroreceptors.
- Mechanical stretching of the SA node.
- The effects of lung stretch receptors.

(ii) Respiratory fluctuations in blood pressure:

- Direct central linkage between the respiratory and vasomotor centres.

- Mechanical action on heart and intrathoracic vessels.
- Respiratory fluctuation in heart rate.

(iii) Mayer waves in blood pressure:

- An endogenous oscillator in the brainstem.
- Feedback through the baroreceptors and/or chemoreceptors.
- Vasorhythmicity.

(iv) Mayer waves in HRV:

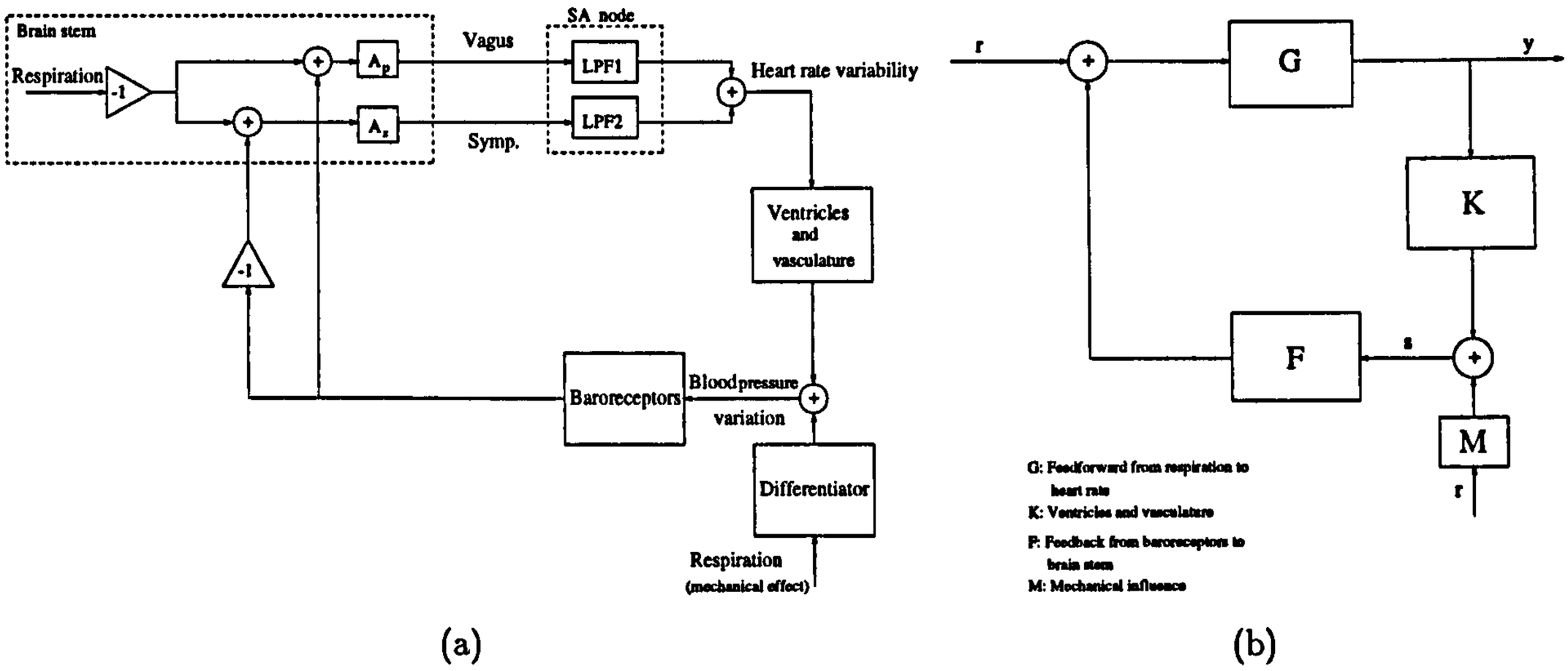
- Closed loop interaction between blood pressure and heart rate.
- Central linkage between the vasomotor and the cardiac centres.

4.3 Model Review

It would be advantageous here to see how the physiological descriptions cited above can be fitted in a system representation. Consequently, the eligibility of four popular models is investigated. This consideration will give us a broad insight into different views and different treatments of the mathematical modelling of the rhythmical fluctuations in heart rate and blood pressure and therefore cardiovascular variability modelling.

4.3.1 Saul (S) Model

A closed loop model based on identification by spectral analysis has been presented by Saul *et. al.* (1989, 1991). Figure 4.2(a) shows the S model and Figure 4.2(b) illustrates its systemic diagram. The model of the SA node is the major building block in the S model. It comprises two parallel lowpass filters which represent the dynamic behaviour of the SA node to the sympathetic and parasympathetic excitations. By random stimulation of the cardiac autonomic nerves, Berger, Saul and Cohen (1989b) showed that the SA node demonstrates a lowpass characteristic to the vagal and sympathetic excitations. Because of the sluggish nature of the sympathetic response an



(a) (b)

Figure 4.2: (a) Saul (S) model, (b) its systematic diagram.

appropriate delay is also included in the corresponding branch of the model. The sympathetic and parasympathetic transfer functions are allowed to change with posture and pharmacological blockade.

In the S model heart rate variability passes through the heart and induces similar fluctuations in the arterial blood pressure. The transfer function between HRV and BPV has been modelled by a constant magnitude and a fixed time lag system. The magnitude, however, can alter with postural change.

After modulation by mechanical effect of respiration, arterial blood pressure variation is transmitted to the brain stem by baroreceptors. A pure time delay has also been employed for representing the transfer characteristics of baroreceptors. Afferent signals enter the brain stem where they interfere with the central respiratory oscillator. A simple summation has been used to illustrate the interaction between afferent signals and the respiratory oscillator in the brain stem. A_p and A_s display the transfer relations between respiratory drive and the modulation depth of the vagal and sympathetic efferent activities. They are assumed to be constants and are allowed to change with the state of autonomic balance.

For broadening the spectral band, the random respiratory pattern has been selected in the S model for data collection as described in Chapter 3. The B-S signal descriptor method has been employed by Saul and Berger for system identification

by spectral analysis (Chapter 3). For definition of the BPV signal, these authors have used time interpolation of the different blood pressure indices (systolic, diastolic, mean, pulse). In spite of the simplicity of the model, the general trend of the experimental transfer functions can be held by the S model with postural change and autonomic blockades. However, a number of questions remain unanswered in regard to this model.

First, many aspects of the cardiovascular control system are not reflected in the model. For example, vascular innervation by the sympathetics and their functions have been ignored in the model. Also complex performance of the ventricles and vasculature has been represented by a simple lag. The model of the SA node constructs the back bone of the S model while pure lag systems are employed for all others. Even by opening the loop no significant change can be observed in the HRV-ILV transfer function, meaning that the feedback loop in the S model has little functional significance.

Second, and in accordance with their experimental results, heart rate variability can still be observed with autonomic blockade whereas the S model is not able to exhibit the same phenomenon.

The model does not take into account the LF or VLF generation mechanism nor does it consider their presence. In fact, broadening of the spectrum by a random respiratory pattern hides the existence of the Mayer waves. Interestingly, the coherence function of Saul *et. al.*'s experimental results decreases for $f < 0.1Hz$, indicating that the correlation between respiration and HRV diminishes in this region.

4.3.2 Baselli (B) Model

A more complete model than the S model has been presented by Baselli, Cerutti, *et. al.*, (1988,1994,1995). Figure 4.3(a) illustrates the B model and Appendix A at the end of chapter provides details of the blocks and the pertinent hypotheses.

The B model is the first comprehensive parametric model which covers many aspects of the HRV-BPV-ILV relationships in an appropriate manner. In contrast to the S model, the B model is able to explain the origin of the LF component. However, it suffers from other problems as discussed below.

For the identification of the model beat-to-beat signal descriptors have been

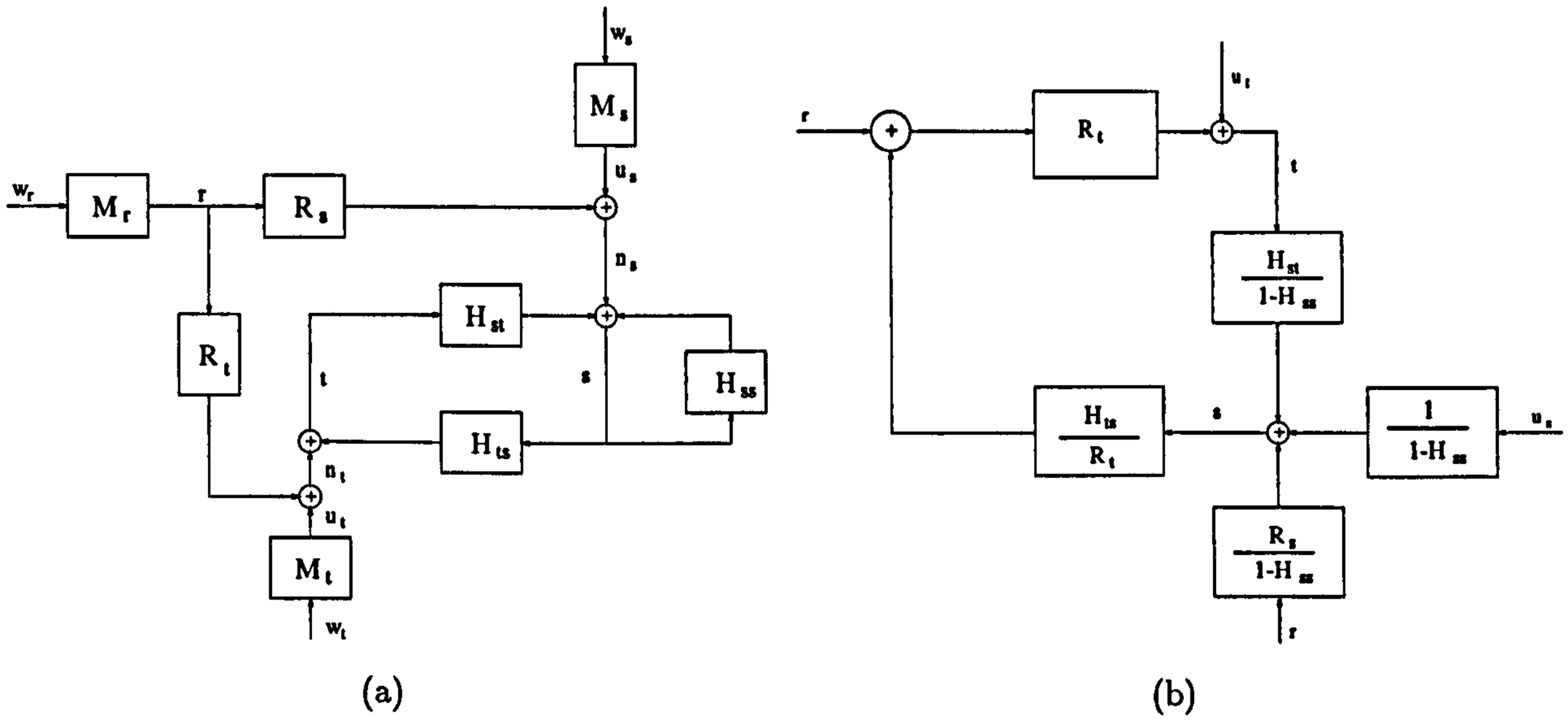


Figure 4.3: (a) Baselli (B) model. (b) An alternative version of the B model.

used. As demonstrated in Chapter 3 the beat-to-beat method is not an appropriate method for identification purposes. Therefore, interpretation of the identified parameters should be considered with caution. Furthermore, quantised values of the delays to the integer multiples of the mean heart interval, imposed by the beat-to-beat method, restricts the ability of the identification procedure to determine the true transfer functions.

The blocks of the model aggregate many different physiological phenomena, hence, finding explicit links between the identified blocks and their physiological counterparts is difficult. For example, H_{ss} covers all the pressure regulatory mechanisms through peripheral resistance, venous return, heart contractility, etc. As another problem, it is shown in some subjects that the LF component has to be injected through M_t or M_s to the system (Baselli *et. al.*, 1994). Since t in Fig. 4.3(a) illustrates the fluctuations in heart rate (which is generated by the SA node) and based on the previous discussion about LF generation mechanisms, it is difficult to accept an individual LF generation mechanism which only affects the heart rate *via* M_t. On the other hand inasmuch as H_{ss} represents the reflex regulating mechanisms through sympathetic pathways, entrance of the LF component through M_s and out of the sympathetic control loop is not a sound assumption and cannot be easily attributed to the centrogenic oscillator.

The LF generation mechanism in the B model is basically described by a reso-

nance system ($s - s$ loop) rather than a spontaneous oscillator. Therefore, it does not admit a stable oscillation and needs external inputs to maintain the LF fluctuations (Baselli *et. al.*, 1988).

Some further objections can be raised if the B model is recast in the form of Fig. 4.3(b). This model can be readily obtained by noting that the $s - s$ loop through H_{ss} has the transfer function $1/(1 - H_{ss})$. This transfer function can be moved to the adjacent branches by the linear property of the model.

Because t and s exhibit two major components at HF and LF, the identification procedure, based on the generalised least square minimisation, tries to adjust the poles and zeros of each block of the model to satisfy the observed peaks of the PSD. Specifically, the blood pressure variability signal s is surrounded by three all pole transfer functions $1/(1 - H_{ss})$. Consequently, there is a tendency for the identification procedure to allocate the LF peak to $1/(1 - H_{ss})$ (also refer to Fig. 4.12(b) in appendix A at the end of chapter). This is particularly true for hypertensive subjects which show a dominant LF peak in the spectral estimation of s and t. In this case even by omitting w_s and w_t, a pronounced LF peak can be observed in the PSD of s or t (Baselli *et. al.*, 1988) indicating that the LF component is generated by the respiratory signal. This is because the respiratory signal is a random process and, therefore, has components at lower frequency bands, albeit small, are still amplified in the resonance circuit $1/(1 - H_{ss})$ and demonstrated in s. The LF component is then transmitted through the H_{ts} block, which behaves as a mild lowpass filter, to t. But the LF inducing mechanism through the respiratory excitation cannot be physiologically acceptable. Baselli *et. al.* have shown that in this case R_s plays an important role for inducing respiratory fluctuations in s and t whereas R_t has only a minor effect. However, it seems that importance of R_s ensues following the resonance feature of $1/(1 - H_{ss})$ at LF and the requirement of a very large respiratory input for inducing a large LF component through $R_s/(1 - H_{ss})$ to the system. Moreover, if the same requirement is supposed to be offered by $H_{st}/(1 - H_{ss})$, an excessively large HF component ought to be imposed on t which is not observed practically. In contrast to hypertensive subjects, in supine dogs the HF component is dominant and it has been shown that, now, R_t has the major role for inducing the respiratory fluctuation but not R_s. Similar objections can be found for other experimental subjects. Succinctly stated, it is the specific structure of the B model which dictates the particular assignment to each block rather than the

physiological bases.

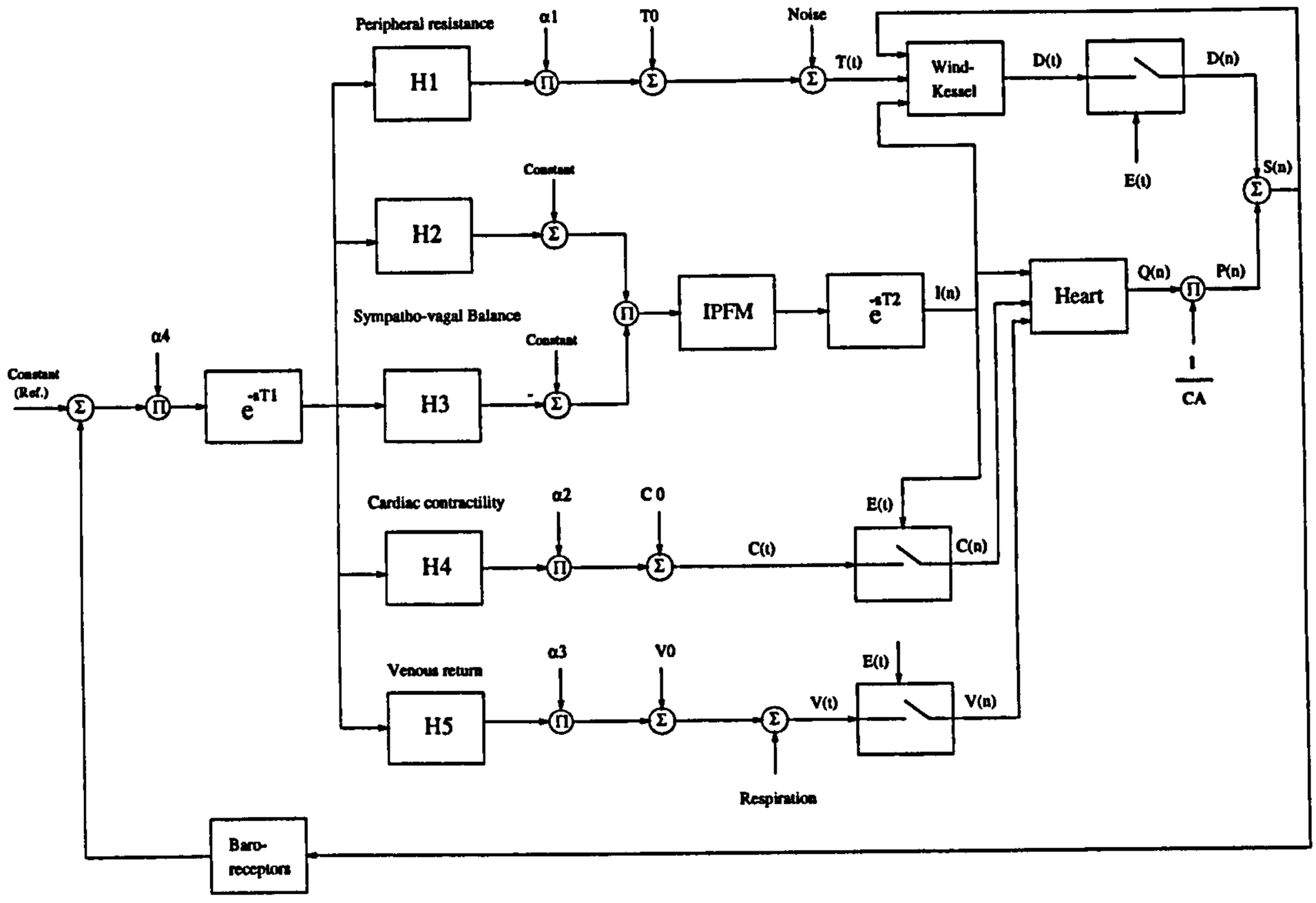
An interesting remark arises by comparison of Fig. 4.3(b) and the S model of Fig. 4.2(b). Ignoring the influence of u_s and u_t in the B model, a one-to-one correspondence can be observed between R_t and G, $H_{st}/(1-H_{ss})$ and K, H_{ts}/R_t and F, $R_s/(1-H_{ss})$ and M. Aside from this connection, there is little resemblance between the B and the S constituting blocks. $H_{st}/(1-H_{ss})$ and $R_s/(1-H_{ss})$ exhibit resonance peaks at LF whilst K and M represent pure delay and differentiating property, respectively. G and F represent a lowpass characteristic and pure delay, respectively, whereas R_t and H_{ts}/R_t show different behaviour. The author believes that this inconsistency arises from oversimplification of the original physiological system and should be avoided for further modelling.

4.3.3 TenVoorde (T) Model

The TenVoorde (1995) model has been constructed on the basis of the baroreflex control model and in contrast to the S and B models exerts absolute values of physiological parameters instead of their small signal variations. As shown in Fig. 4.4 different branches have been allocated in the T model to represent the peripheral resistance, sympathovagal balance, cardiac contractility and venous return. Each branch is modelled by a first order lag system plus a constant value which renders the mean value of the related quantity. Sympathovagal balance comprises two parallel paths for modelling the sympathetic and parasympathetic control of the heart. The T model is in fact a hybrid model; it connects a continuous neural control part with a beat-to-beat implemented hemodynamic part. This connection is facilitated through the IPFM model which generates the cardiac event series. The generated event series is used for conversion of the continuous physiological quantities to their beat-to-beat counterparts by exploiting a series of sample and hold blocks.

Starling and Windkessel equations are utilised for modelling of the hemodynamic part. Stroke volume Q_n in the model is produced by a one chamber Starling heart and is dependent on the heart interval length I_n, venous return V_n and contractility term C_n,

$$Q_n = \delta_n V_n + C_n. \tag{4.1}$$



H1-H5 : First order lag systems with stauration elements

α1 - α4 : Constant multipliers

Figure 4.4: TenVoorde (T) model.

The factor δ_n is a left ventricle filling factor, linearly dependent on heart interval I_n,

$$\delta_n = 0.5 + \frac{0.5}{1000} I_n. \tag{4.2}$$

On the other hand stroke volume and pulse pressure are related by arterial compliance C_A,

$$P_n = \frac{Q_n}{C_A}. \tag{4.3}$$

The relation between systolic and diastolic pressures is given by,

$$D_n = (D_{n-1} + \frac{1}{2} P_{n-1}) e^{-\frac{I_n}{T_n}}. \tag{4.4}$$

which is slightly different from the standard Windkessel equation. The time constant of equation (4.4) is controlled by the product of the total peripheral resistance and arterial compliance $T(t) = R(t)C_A(t)$. Systolic blood pressure S_n is sensed by the baroreceptors and the afferent signal is compared with a set point in the brain stem. The error signal which is elicited from this comparison regulates the whole controlling system after the central processing delay T_1.

Respiration is supposed to primarily modulate the venous return, and hence stroke volume, and consequently arterial pressure. Respiratory modulation of the blood pressure then affects the cardiac event series through afferent-efferent neural pathways, causing the RSA.

The T model exhibits a light resonance at $0.1Hz$ which is highly dependent on the gain and time delay of the resistance control loop. This model exhibits the general features of the experimental results obtained in the postural change from supine to upright by decreasing the venous return. This case is simulated by diminishing the venous return, increasing respiratory venous return modulation and decreasing vagus inhibition by lowering the corner frequency of the corresponding lowpass filter from $\tau_{supine} = 0.1sec$ to $\tau_{standing} = 1.5sec$. Despite these satisfactory features, however, the T model suffers from the following problems.

Firstly, the respiratory signal is assumed to affect the system solely through the venous return modulation and there is no central link between the respiratory centre and the cardiovascular control centres. TenVoorde *et. al.* have reasoned that a twofold increase of RSA and blood pressure modulation for $f < 0.12Hz$ with respiration in the change from supine to the upright position cannot be explained in the central link framework, since it needs 5 to 10 times higher feedforward hemodynamic gain from RSA to blood pressure modulation which is not physiological. However, the central link can always be functioning while the postural change may markedly increase the respiratory modulation of the venous return. At the same time the central link influence can also rise moderately and invigorates the total respiratory modulation. Moreover, employing a different form of the Windkessel equation in the TenVoorde derivation, which results in a smaller hemodynamic feedforward gain, might be another factor in their inference. Nevertheless, as already mentioned, there is strong physiological evidence to affirm the direct central link between the respiratory pacemaker and cardiovascular centres; mere mechanical respiratory modulation cannot be acceptable.

In a similar manner to the B model, the LF wave in the T model does not have an intrinsic origin. It is described by the resonance of the system and hence, it requires external inputs for a sustained oscillation. Nonetheless, the resonance frequency at $0.1Hz$ needs fine tuning of the system and is quite sensitive to the selected parameters (TenVoorde *et. al.*, 1995). Specifically, the resonance disappears in the upright

position in contrast to the conspicuous increase in the LF component observed in the practical data (Pagani *et. al.*, 1986). Since the respiratory input in the model is a pure sinusoid coupled with the fact that the resonance of the system strongly depends on the peripheral resistance, it can be concluded that the observed LF component in the PSD of the HRV and blood pressure variation is a result of the external noise in the resistance path. This assumption, however, is not consistent with physiological evidence.

The corner frequency of the lowpass filter ($\approx 1.6Hz$) illustrating the transfer characteristic of the vagal branch is far beyond the physiological values ($0.1 - 0.2Hz$) (Berger *et. al.*, 1989b; Mokrane, LeBlanc, Nadeau, 1995). Also, changing the corner frequency by as much as a factor of 15 ($0.1sec$ to $1.5sec$) during postural change does not seem to correlate with physiological observations.

4.3.4 Kitney (K) Model

All the models considered so far are based on linear dynamics. There is, however, abundant evidence for the presence of nonlinearity in the performance of the organs in the cardiovascular system, although it is argued by many authors that in the normal operating range linear analysis is adequate. This argument will be examined by a nonlinearity test in the next chapter. But before that, it should be noted that at least the presence of sliding coordination in the physiological oscillators is beyond doubt. Specifically, investigation by spectral analysis has shown the presence of nonlinear phenomena such as frequency entrainment and pulling in HRV and BPV (Kitney & Rompelman, 1987). If a periodic force of frequency w_s is applied to a system capable of exhibiting a limit cycle of frequency w_0 then the beating phenomenon is observed. As the difference between the two frequencies decreases the frequency w_0 is entrained by the forcing frequency w_s within a certain band of frequencies. This is called frequency entrainment. In variability signal analysis, frequency entrainment plus other nonlinear behaviours such as frequency pulling and nonlinear modulation can be observed in both the BPV and HRV signals (Kitney, 1975, 1979). It has been shown that the LF component can be entrained by the respiratory component if the tidal volume and respiratory frequency are selected appropriately. Kitney (1975, 1979) has presented a nonlinear model for explanation of these phenomena which is illustrated in Fig. 4.5.

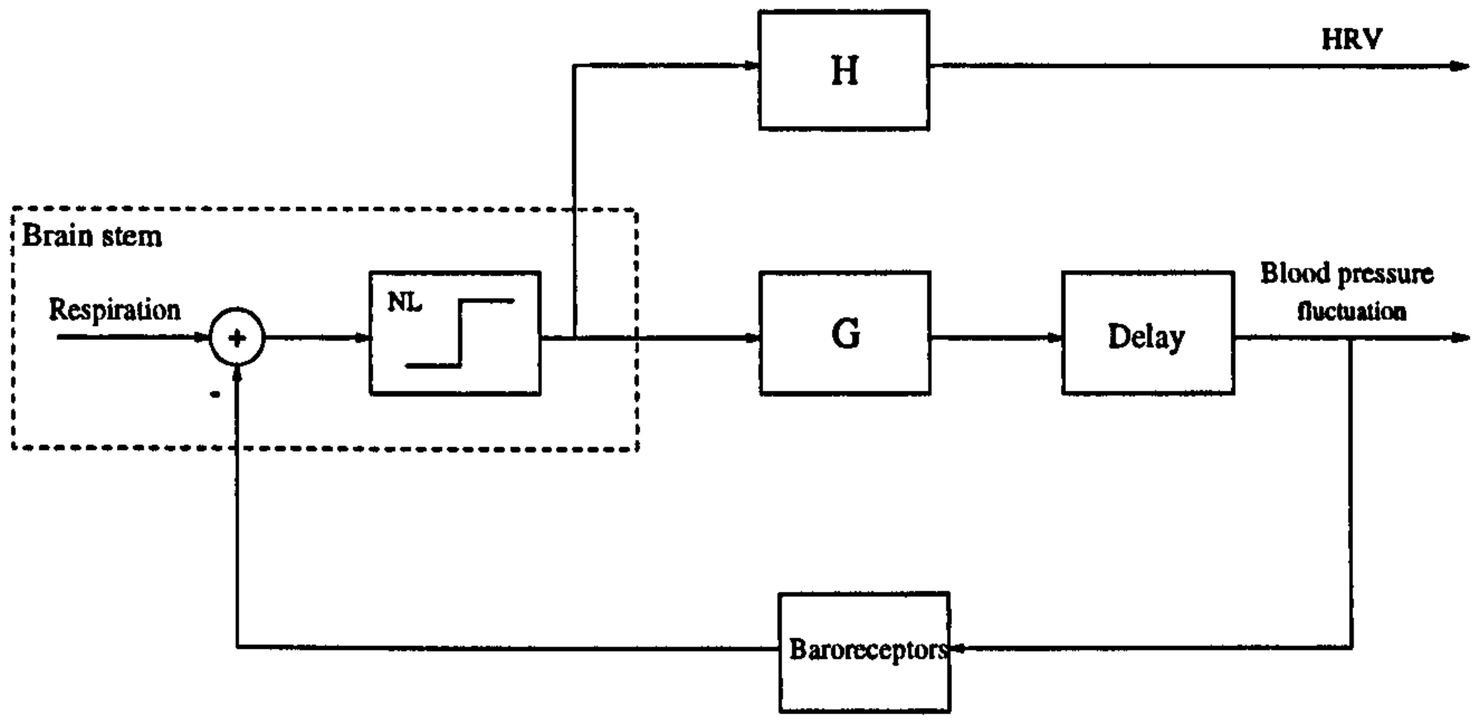


Figure 4.5: Kitney (K) model.

A nonlinear closed loop system including a bang-bang element guarantees the existence of a sustained oscillation in the LF band. Block G and the following delay represent the transfer characteristic (linear) of the peripheral vascular response. The afferent signals of the baroreceptors transmit the blood pressure information to the brain stem where it interacts with the respiratory oscillator. Respiratory signal may emanate from the central pacemaker or may be a feedback signal through mechanical respiratory effect. It has been shown that the K model can exhibit the frequency entrainment and pulling phenomena quite well. Furthermore, the same events can be transfered to the SA node *via* block H in the model which integrates the transfer function between the brain stem and the SA node.

In spite of satisfactory performance in describing the observed nonlinear phenomena, the physical presence of the bang-bang element in the brain stem has not been justified yet. Importantly, employing a very mild nonlinearity such as a soft sigmoid does not give rise to the same phenomena. On the other hand the K model mainly focusses on elaborating a nonlinear model to explain the frequency entrainment and the LF generation mechanism rather than a model covering all aspects of the neuro-cardiovascular system. Therefore, many preliminary features of the fluctuations in BPV and HRV as described in Section 4.2 are missing in the K model. Still this model is promising because it provides a basis for developing the LF part of our detailed model described in the next sections.

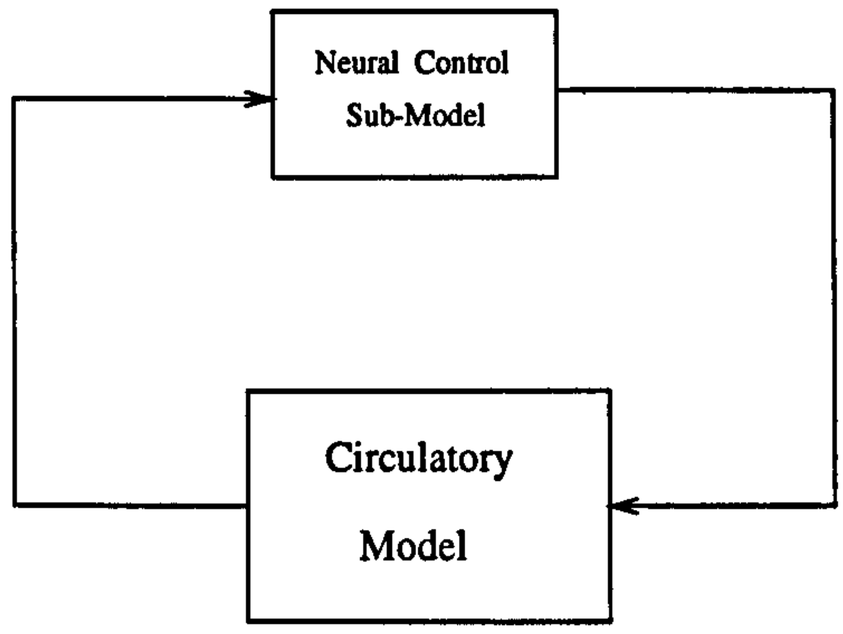


Figure 4.6: A simple sketch of the cardiovascular controlling system.

4.4 Small Signal and Large Signal Modelling

Before proceeding further it is worthwhile describing an important concept which in the view of the author has not been highlighted yet; namely small signal versus large signal cardiovascular modelling. Cardiovascular modelling is not a new subject. Over the years great attention has been paid to evolve a comprehensive mathematical model to describe, interpret, and even predict the corresponding physiological observations. Primarily, all these traditional models have the following common factors: the relationships between blood volume, flow and pressure in different segments of the body under a central regulatory mechanism (Fig. 4.6). The circulatory part of the model comprises different segments of the circulation (Fig. 4.7). The neural sub-model part constitutes autonomic control of heart rate, contractility, compliance, and peripheral resistance. The pressure, volume, flow, resistance and compliance of the circulatory model follow the fluid mechanic formulation and are under the control of the neural sub-model part. As typical examples of this class we can name the models by Hyndman, (1970), Leaning, Pullen, Carson, Finkelstein, (1983); Boyers, Guthbertsonand, (1972); Wesseling, Settles, (1992) [4]. The emphasis of this class of models is on the actual values of the parameters; arterial blood pressure, venous return, ventricular volume, vascular resistance, etc., through a set of pressure-volume-flow relationships combined with first and second order linear systems and a number of delays and sometimes nonlinearities. These models are divided into two groups of pulsatile and non-pulsatile models. In the pulsatile models the actual waveforms of the signals; instantaneous blood pressure and blood flow, time varying compliance of the heart chambers, etc., are of concern

[4] A detailed discussion and comparison of these models can be found in Chabbani (1990).

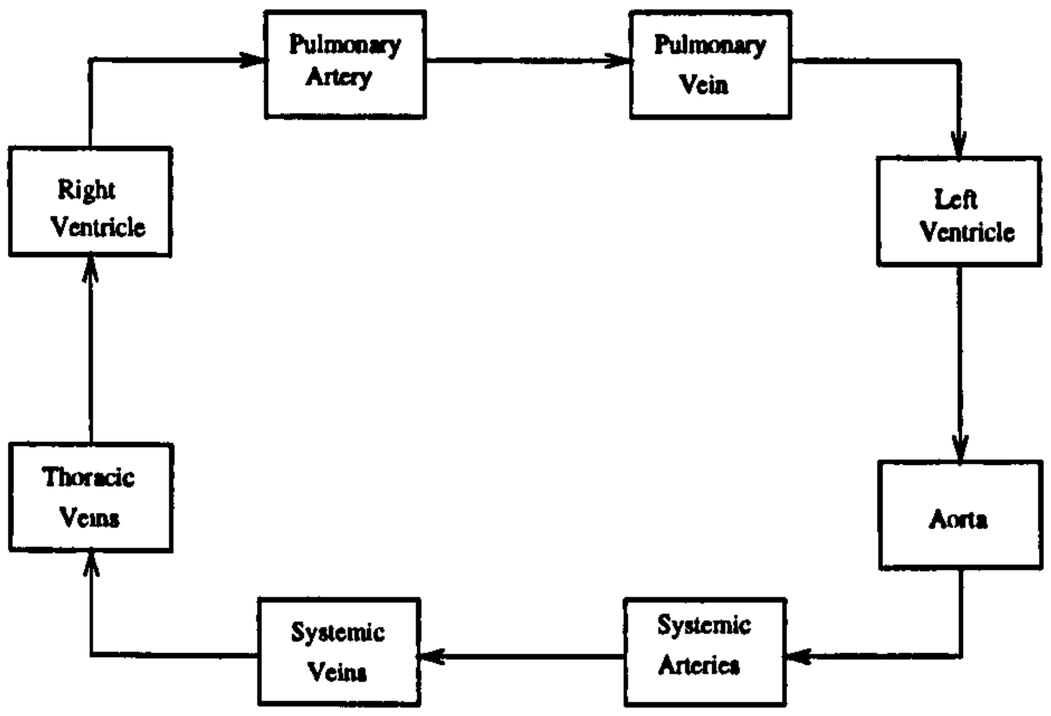


Figure 4.7: The eight segment model as an example of the circulatory model.

whereas in the non-pulsatile models a single value is attributed to each parameter in each cardiac cycle. Both of these models can be referred to as large signal models since they have been developed to deal with actual values of the parameters over a wide range of variations in different conditions (e.g. change in cardiac output or venous return following a postural change or blood loss).

In the context of heart rate variability and blood pressure variation, however, the emphasis is not on the actual values of the cardiovascular parameters but on their variations around their operating points (mean heart rate, mean blood pressure). That is why typical models of this class (Saul *et. al.*, 1991; Baselli *et. al.*, 1988; de Boer *et. al.*, 1987; Mullen *et. al.*, 1997) are concerned with modelling of the cardiovascular system in a small signal manner *i.e.*, variation in heart rate, fluctuation in blood pressure, etc.

There is indeed a close resemblance between large/small signal modelling of the cardiovascular system and the large/small signal modelling of a transistor amplifier circuit, for example (Fig. 4.8). Surely, the dominant and the comprehensive model is the large signal model from which the small signal model is extracted. Every conclusion achieved with the small signal model can of course be obtained from the large signal model, although with much more effort and complexity. The great benefit which is accrued from the small signal model, however, is its simplicity and scrutiny. The small signal model engenders a workspace for concentration on the small signal variations around the operating point (dc values) of the large signal model which is assumed to be constant. This concept can be extended to the cardiovascular system. Here

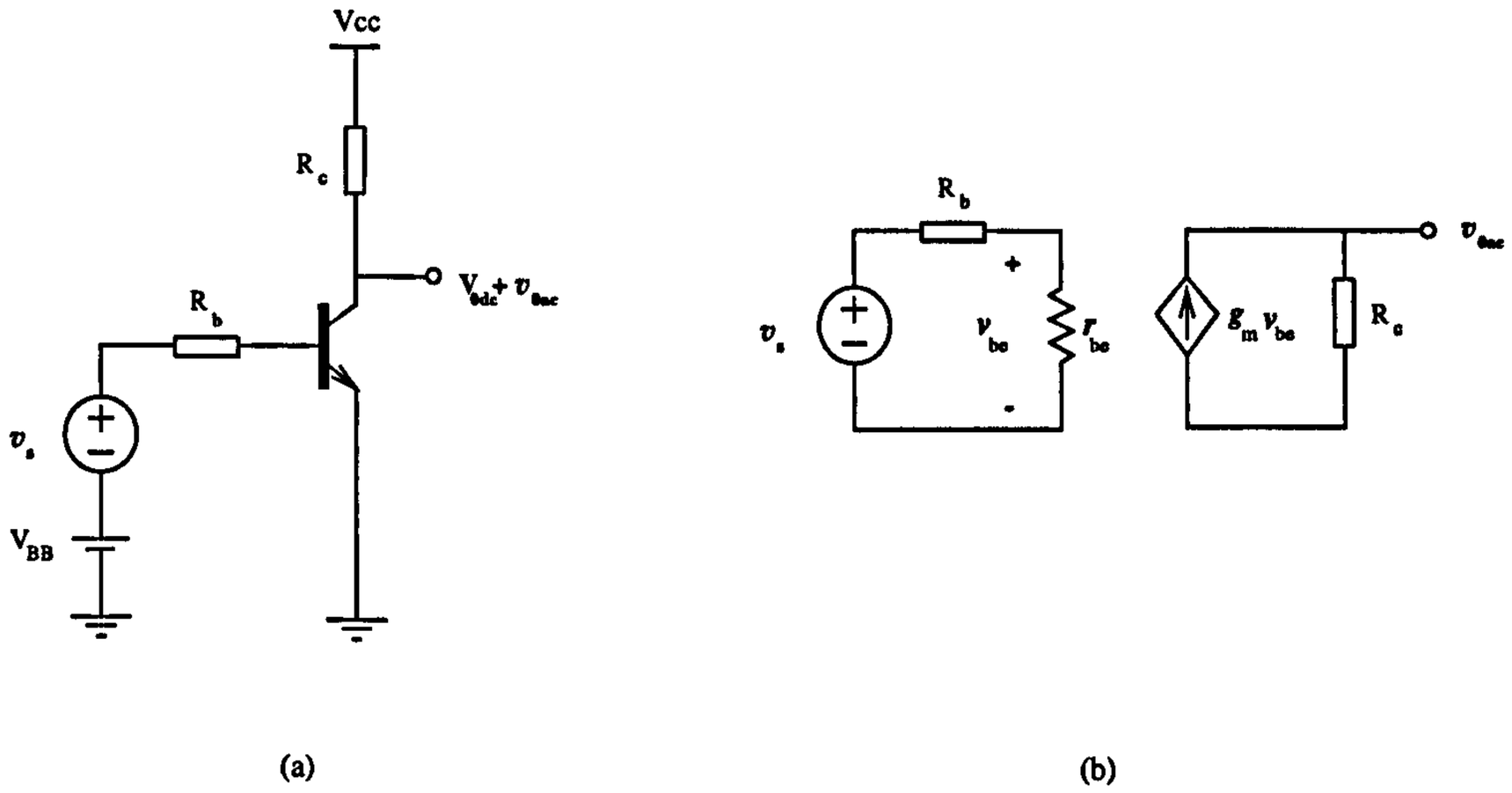


Figure 4.8: A transistor amplifier circuit as an example of the small and large signal modelling in system science. (a) Large signal model, (b) small signal model. The same concept can be extended to cardiovascular modelling.

the aim is to study the existing fluctuations in blood pressure and heart rate, with respiration as an exogenous input. If one were able to develop an exact large signal neuro-cardiovascular model then perfect analysis of the instantaneous values of the actual parameters including all the observed fluctuations in the whole frequency band would be conceivable. Since this is technically impossible one has to employ the small signal representation for the evaluation of HRV-BPV-ILV relationships. Furthermore, large signal representation would definitely need a distributed model [5], due to the respiratory influence. Pressure variation resulting from the respiratory activity has indeed a distributed effect on all the intrathoracic organs. Certainly, the describing set of equations used in the traditional representations (pressure-flow-volume relationships) is unable to capture this distributed effect. Therefore, the overall influence of respiration (distributed modelling) should be involved. That is why large signal models such as the T model lose their efficacy in variability (small signal) analysis. In contrast, small signal modelling (such as the S or B model) offers a reasonable compromise between mathematical complexity and neurophysiological relevance. The author, therefore, continues to adhere to small signal modelling to present a new model for the HRV-BPV-ILV relationships.

[5]Referring to the context of electric circuit analysis with lumped and distributed modelling (see also Section 7.6).

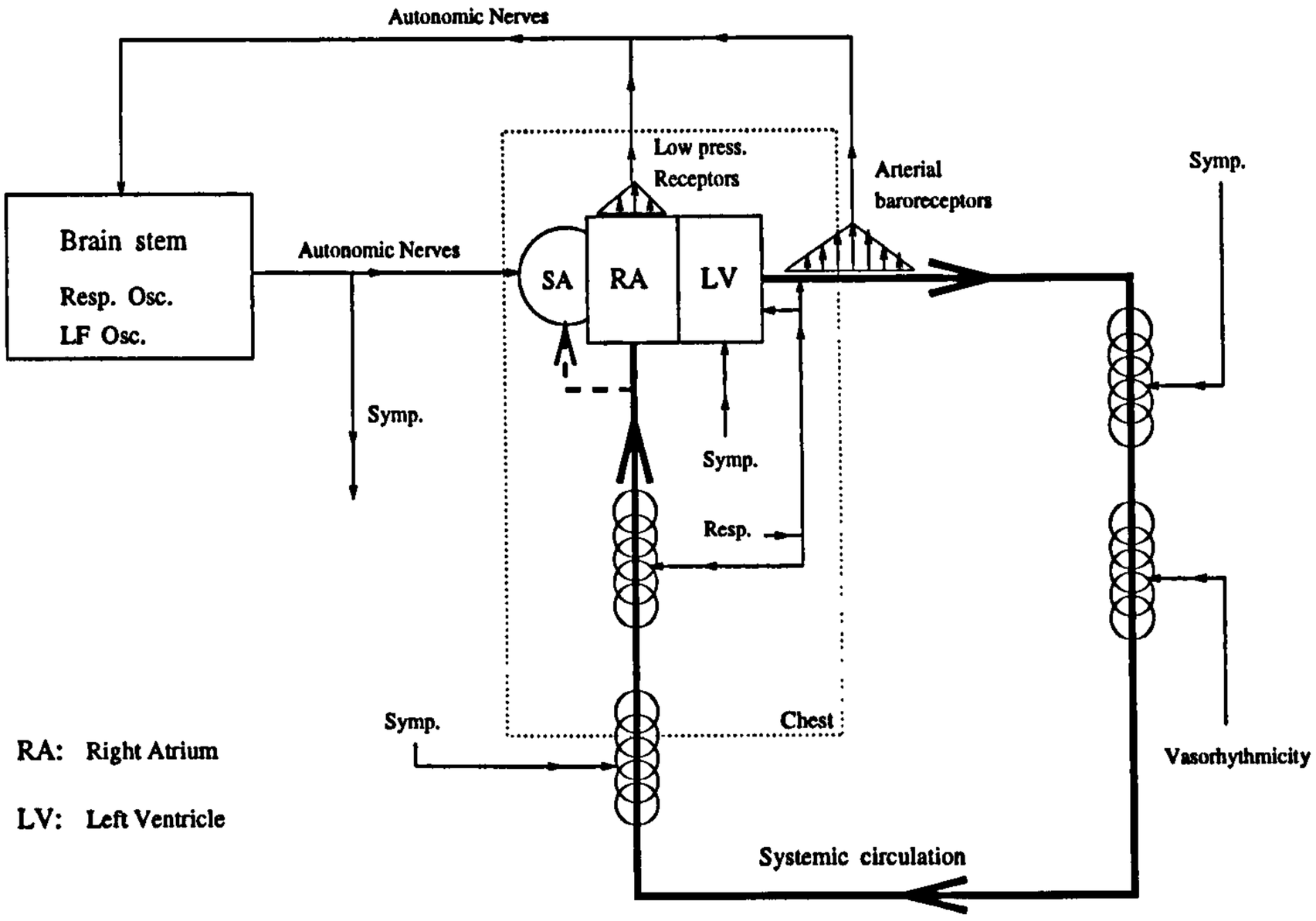


Figure 4.9: A physiological layout of the problem.

4.5 The Proposed Model

In this section the new model is presented. It will shortly be seen that the new model is more complete than the existing models and quite congruent with the underlying physiological phenomena. However, before illustrating the systemic diagram of the proposed model it is necessary to depict a conceptual layout of the relevant physiological bases. This layout, which is shown in Fig. 4.9, gives an insight into the delineation of the actual model and leads towards obtaining a block diagram of the system.

The heart (RA-LV) at the centre of the figure pumps the blood to the systemic circulation. Arterial blood pressure is continuously sensed by the arterial baroreceptors and the afferent signals are transmitted to the brain stem. The vascular system is under the influence of sympathetic stimulation which is shown at the right hand side of the figure. Sympathetic stimulation also affects the venous return by venoconstriction which returns the reserved blood into the systemic circulation. This effect is shown on the left hand side of the systemic circulation in Fig. 4.9. Endogenous vasorhythmicity which is assumed to produce the VLF component is also reflected in the model.

Mechanical respiratory modulation in the chest cage causes periodical changes in the venous return, ventricular loading and arterial pressure. This is illustrated in

the layout by two branches to the systemic veins and arteries inside the chest cage. Variations in the preload of the heart is transfered to the right atrium (RA) and is sensed by low pressure receptors. At the same time it affects the intrinsic rhythm of the SA node. The illustrated sympathetic branch to the left ventricle (LV) represents the alteration of the cardiac contractility under the influence of sympathetic excitation. All the efferent signals originate from the brain stem where the controlling centres, the respiratory oscillator and the centrogenic LF oscillator are placed.

Based on this general overview the proposed model can now be constructed as shown in Fig. 4.10. Different blocks and their interconnections in the model reflect the governing physiological phenomena. The heart in the middle of the figure produces the arterial blood pressure. Arterial blood pressure is affected by mechanical respiratory modulation on one hand, and peripheral resistance modulation on the other. The latter, in turn, is under the influence of the endogenous vasorhythmicity and sympathetic excitation, thereby transfers the corresponding variations to the arterial blood pressure. Based on the previous discussions, here we hypothesise that the VLF component is generated by intrinsic oscillation of the vascular smooth muscle.

Arterial blood pressure fluctuation is sensed by the baroreceptors. Afferent signals enter the brain stem. Fluctuations of the arterial blood pressure can also be transferred to the venous return by the vascular system. However, due to the large capillary resistance the transfer gain can be ignored in stationary conditions.

Block H_1 in the model, which is a multi-input single-output system, basically represents the mechanical thoracic coupling between respiration and vasculature and also sympathetic stimulation on venous return. The venous return fluctuation enters the heart and closes the systemic loop. The associated right atrium pressure fluctuation stimulates the low pressure receptors on one hand and affects, *via* block H_6, the intrinsic rate of the SA node on the other. The latter will be discussed with more details later.

Afferent signals from the peripheral receptors enter the cardiovascular centre in the brain stem. Satisfactory modelling of the brain stem is still very difficult. In spite of numerous anatomical and physiological study of the brain stem there is still a scarcity of information about the connections between the respiratory centre and groups of neurons controlling the cardiovascular system. Here it is assumed that afferent signals from different receptors, in the simplest form, add together. Furthermore, it is assumed

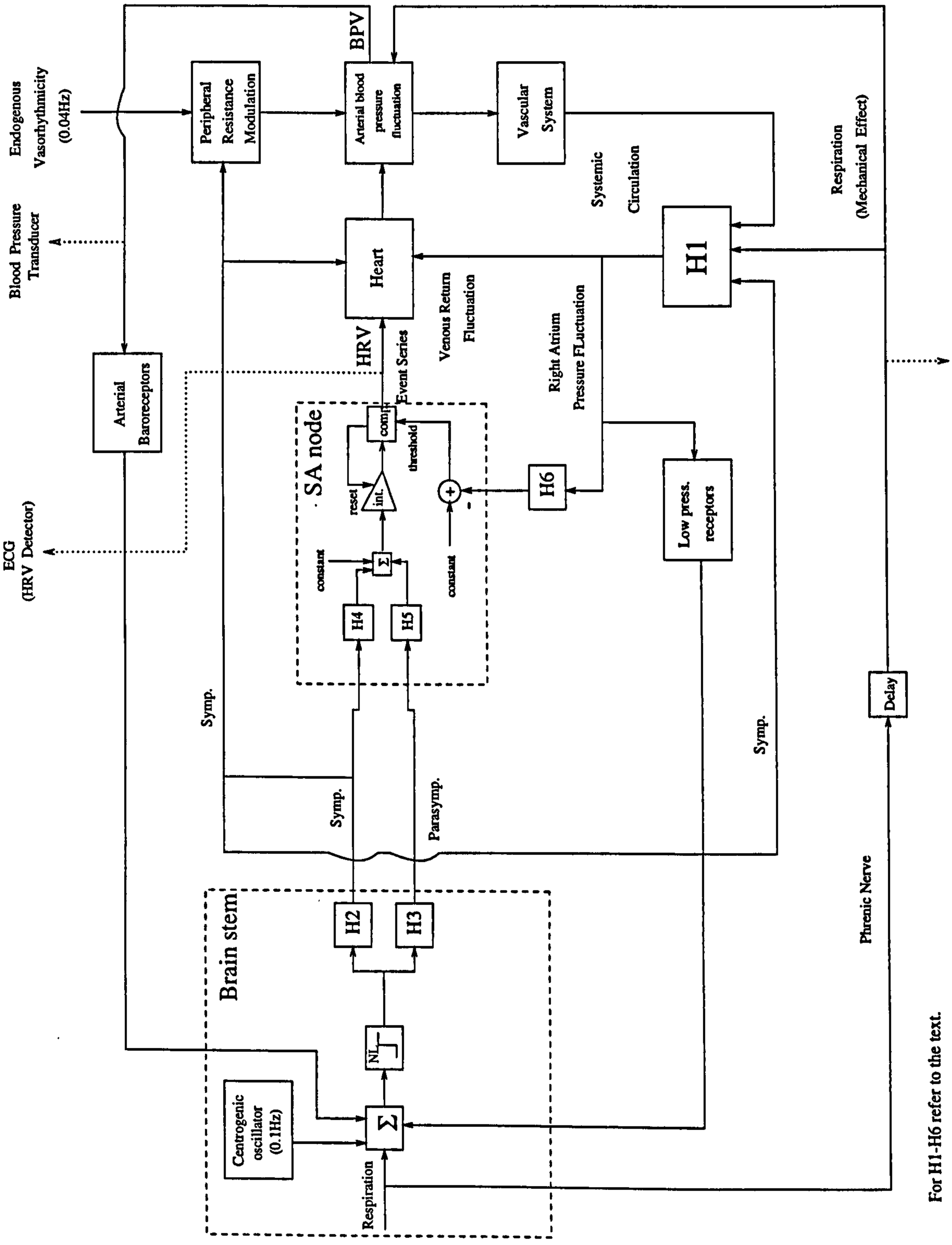


Figure 4.10: The proposed model.

that the direct link between the respiratory oscillator and the cardiovascular centre has also an additive property. Presence of the centrogenic LF oscillator completes the general view of the brain stem model and realizes the hypothesis of the central LF generating mechanism.

Frequency entrainment and pulling phenomena are exhibited by engaging a non-linear element in the brain stem. This nonlinear element together with the subsequent lowpass systems and the existing delays also guarantee the presence of a sustained LF oscillation through the feedback path as previously discussed. Characteristics of the nonlinear element and the feedback loop are detailed in Chapter 7. This oscillation satisfies the second hypothesis of the LF generation mechanism and completes the model in this sense.

Blocks H_2 and H_3 in the brain stem represent the loop controllers in the feedback system. The sympatho-vagal balance, central processing time delay and the modulation depth of vagal and sympathetic efferent activity are all aggregated in these blocks. Nevertheless, these transfer functions are allowed to change with postural change or in different physiological or pathological conditions.

Efferent signals are transmitted through sympathetic and vagus nerves. The sympathetic path innervates all parts of the cardiovascular system while vagal stimulation feeds only the SA node. The SA node comprises two parts, blocks H_4 and H_5 and a Time Varying Threshold IPFM (TVTIPFM) model. H_4 and H_5 illustrate the transfer functions of the sympathetic and vagal stimulation to the SA node, respectively. It has been shown that H_4 and H_5 have a lowpass filter characteristic with corresponding delays (Berger *et. al.*, 1989; Mokrane *et. al.*, 1995). Generation of the spike series signal is accomplished through an IPFM model. A thorough analysis of the IPFM was presented in Chapter 2. It was stated that the IPFM model is quite compatible with the physiological beliefs of the rhythmic generation mechanism of the SA node. However, the illustrated IPFM in the proposed model is slightly different. Instead of having a constant level, the threshold value now has a time dependent term which fluctuates around its mean value. This fluctuation is induced by the pressure variations in the right atrium. As previously explained, local stretching of the SA node increases the heart rate. If the right atrium pressure in the model increases, the threshold level decreases and therefore output frequency of the SA node (heart rate)

increases. Employing the TVTIPFM representation thus enables us to simultaneously model the autonomic stimulation and stretching effect of the SA node. Analysis of the TVTIPFM model through conventional methods, however, is a formidable task. In Chapter 6 a novel method to overcome this problem is presented.

The output signal of the SA node in the form of a cardiac event series is injected to the heart. The heart is also modelled by a multi-input single-output system. Besides the spike series and venous return inputs, a sympathetic branch to the heart alters the cardiac contractility and thereby arterial blood pressure. It is worth noting that in contrast to some of the existing models which simply recruit Windkessel and Starling equations, the heart model in Fig. 4.10 has a more complicated and more realistic structure. This is due to various factors which contribute to the performance of the heart. It does not seem that the simple beat-to-beat expressions such as equations (4.1) through (4.5) are able to present a satisfactory view of the true performance of the heart in the cardiovascular variability analysis. Furthermore, there are a number of phenomena which have to be considered in modelling. For instance, respiration affects pulmonary arterial blood flow and blood volume. However, the precise mechanisms that bring about these changes are still a matter of controversy (de Burgh Daly, 1986). It is known that the pulmonary vascular bed is very distensible therefore it is largely affected by intrapleural pressure variations which finally affect the arterial blood pressure. As another example, it is not definite yet which of the factors is more effective in transferring the venous return variations to the arterial side; blood volume change through pulmonary circulation or interventricular interdependence (Triedman & Saul, 1994). The heart in the proposed model is able to cover all these phenomena. If a multivariable identification method is applied, then a satisfactory model of the functional performance of the heart can be obtained. Although individual internal features can not be separated, all are included in the model. The details of the identification method and the pertinent results are presented in Chapters 7 and 8.

In our proposed model the mechanical respiratory input to the system has been discriminated from the central respiratory oscillator by the phrenic nerve and respiratory muscles transfer functions. It is quite reasonable not to assume the same shape for the respiratory drive in the brain stem and the mechanical influence through the chest movement. Respiratory signal, mainly through phrenic nerve, excites the inspiratory muscles. When inspiratory muscles contract the volume of thoracic cavity

increases and intrapleural pressure decreases. It is, therefore, this factor which affects the blood pressure in the chest cavity. Thus contribution of the chest movement to the mechanical respiratory modulation should be taken into account. In the simplest form, though, a pure delay due to the phrenic nerve transmission characteristic and lag of the inspiratory muscles can be considered.

For modelling and identification it is of the utmost importance to determine the location of the measured signals. In the study of the cardiovascular variabilities, the focus is on the signals that are most often and easily available in clinical studies and experimental protocols. These are ECG, arterial blood pressure and respiratory movement. Three dotted lines in the model illustrate the location of the corresponding measured signals.

The proposed model is basically a continuous state continuous time model and so the proposed sets of signal descriptors presented in Chapter 3 are well suited for the signal definitions. This is because the hemodynamic part of the model is well described on a continuous time basis rather than a beat-to-beat basis which poses problems both in combined analysis of the two signals and in the interpretation of the results (TenVoorde *et. al.*, 1995; de Boer, 1985b; Chapter 3). Above all there appears not to be any cogent reason for using a beat-to-beat approach, even for blood pressure variability. Clearly, baroreceptors continuously sense the instantaneous blood pressure. Although sensitive, they do not measure systolic, diastolic or pulse pressure which is assumed in some models. If we further notice that the pressure variation which is superimposed on the instantaneous blood pressure (Fig. 4.11) conveys the relevant information in our consideration then finding an appropriate definition for the blood pressure variability signal will not be difficult. This feature indeed resembles the pattern obtained when an audio frequency wave (slow variation) modulates a radio frequency carrier wave (fast instantaneous signal). Similarly, a continuous state time series blood pressure variability (BPV) signal can be obtained by preserving the desired low frequency band ($f < 0.5Hz$) simply by passing the instantaneous blood pressure signal through a lowpass filter. The characteristics of the filter can be adjusted in a similar way to the one used for the HRV. Moreover, continuous definition obviates the confusion which arises from the different results of the systolic, diastolic and pulse pressure considerations (de Boer, 1985b; Saul, *et. al.*, 1991). Consequently, three well defined continuous state time series variability signals, HRV, BPV and ILV, will be

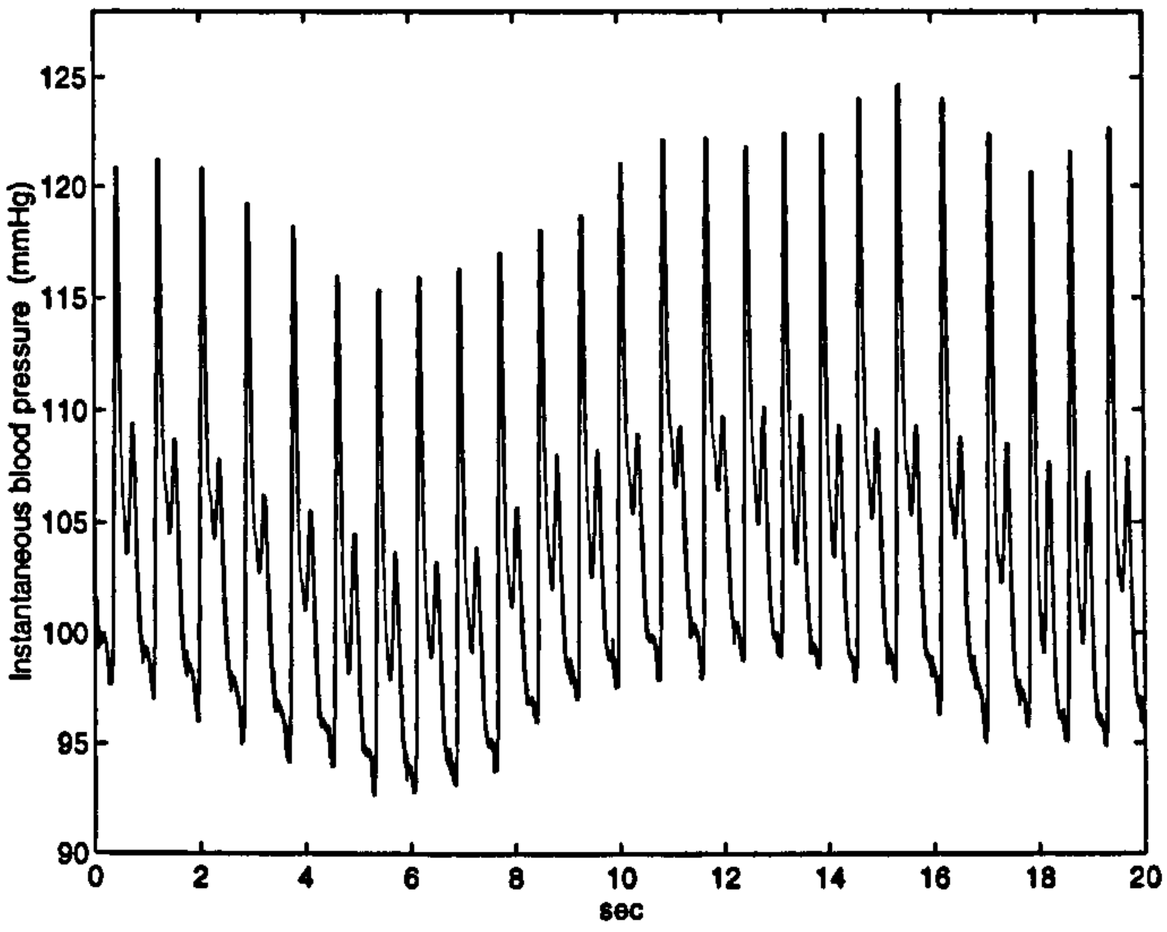


Figure 4.11: Superimposed slow variations on the instantaneous blood pressure signal.

provided, which are ideal for identification and model validation.

Since the proposed model tries to cover the widely-accepted physiological basis in a more realistic form it is more complicated than many of the existing models. Therefore, in Chapter 7 an attempt to simplify this model to make its mathematical treatment feasible is presented. However, to select the proper methodology for modelling and identification it is first necessary to determine linear or nonlinear property of the underlying system. This is detailed in the following chapter through a rigourous time domain technique which will show that the neuro-cardiovascular system exhibits Volterra type nonlinearity although it is studied in a small signal regime.

4.6 Conclusion

In this chapter a conceptual discussion of the origins of the heart rate variability and blood pressure variation in view of system engineering was illustrated. Fortified by the well-known physiological observations, an investigation into some of the popular HRV-BPV-ILV describing models, a distinct insight into the large signal and small signal cardiovascular modelling, and finally the proposal of a comprehensive model for further study of the HRV and BPV were presented.

The proposed model has many salient features while trying to keep the mathematical tractability. After presenting a detailed study of the physiological components

involved in the model, the proposed representation will be appropriately simplified in Chapter 7 and will be validated then by experimental results in Chapter 8.

Summary of the Chapter

The important achievement of this chapter was depicting a new model which reconciles the physiological beliefs of the rhythmical fluctuations with an appropriate block diagram representation in a more realistic form. Together with the proposed sets of signal descriptors presented in Chapter 3, this model seems to be able to give further insight into the rhythmical fluctuations in heart rate and blood pressure. For the time being the new model has an overly complex structure but it will be simplified later. Before that, however, it is necessary to concentrate on certain features of the model such as linearity or nonlinear properties. This is considered in the next chapter.

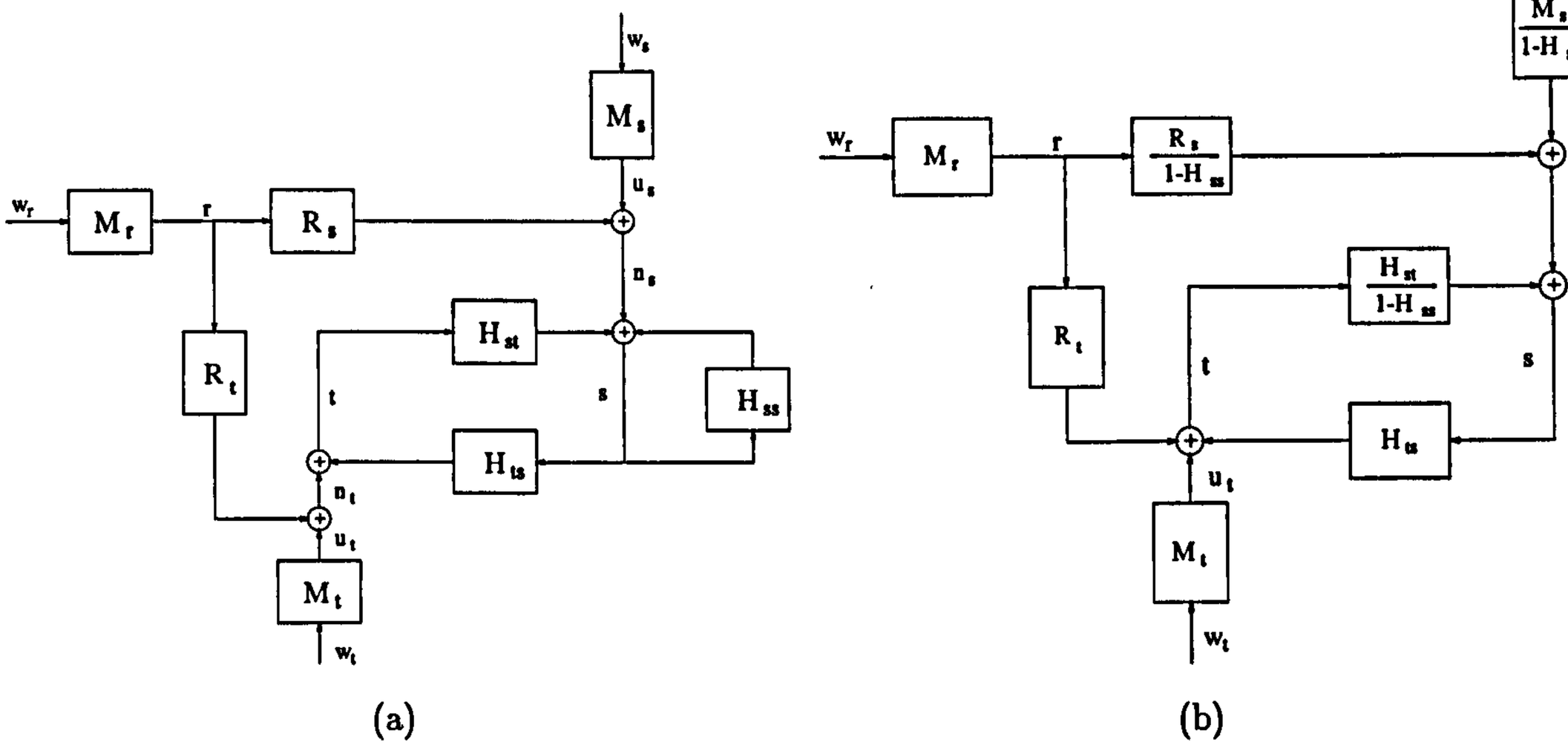


Figure 4.12: (a) The B model. (b) Alternative version of the B model which is used for identification of the neuro-cradiovascular system.

4.7 Appendix A: Baselli Model

A causal parametric model for HRV and BPV analysis has been presented by Baselli and his colleagues (1988, 1994, 1995) and is explained briefly here. Figure 4.12(a) shows this model. The kernel of the interactions between R-R interval (RRI) t, and systolic arterial blood pressure fluctuations (SAP) s, is represented by the $s-t-s$ loop including H_{st}, H_{ts} blocks. These two blocks are, respectively, the nonneural effects of RRI on SAP and the neurally-mediated responses stemming from arterial pressure receptors located in various sites. The inputs n_t and n_s to the loop represent the external disturbances independent from t and s, respectively. Respiratory signal r is injected to the model by passing the white noise w_r through the block M_r. In the same manner, u_s and u_t, which display any external or centrogenic input to the $s-t-s$ regulating loop, are generated by feeding white noise processes w_s and w_t through linear systems M_s and M_t, respectively. All white noise processes are assumed to be mutually independent. Blocks M_s, M_t and M_r describe the spectral properties of the respective outputs u_s, u_t and r, e.g., if a narrow band LF disturbance is supposed to enter the system through n_s (hypothesis of LF component of central origin) then M_s will exhibit a bandpass shape at the relevant frequency.

The pressure loop described by the H_{ss} block represents all arterial blood pressure

reflex regulating mechanisms *via* control variables different from HR (mainly peripheral vascular resistance, but also arterial compliances, heart contractility, venous return, etc.) which are considered non-measurable in the model. The $s-s$ closed loop gain $1/(1-H_{ss})$ may selectively amplify particular frequencies. The mechanical propagation of SAP variation from one beat to the next one, relevant to the Windkessel system properties, are also included in the H_{ss} block and are described by the first lag of its impulse response.

The direct effects of respiration on SAP are represented by R_s and involves different possible mechanisms, for instance, chest pressure changes transmitted to the vascular system, venous return changes induced by chest movements, etc. Mechanisms described by R_t may be reflexes on the sinus atrial node from lung receptors or from atrial receptors, central influences from respiratory centres, etc.

The mechanical effect between RRI and SAP is described by Windkessel and Starling equations and the result is given by the recursive equation,

$$s(i+1) = (k_2 - k_1)t(i) + ps(i)\cdot \tag{4.5}$$

in which k_1, k_2 and p are constants. Therefore the mechanical effect of t on s is modelled by a single lag in the block H_{st} and the recursive part of equation (4.5) is absorbed in the block H_{ss}.

Blocks M_s, M_r and M_t are assumed to be all pole filters while all other blocks are all zero transfer functions. Parametric multivariate closed loop identification based on the joint input-output method is employed for determining the characteristics of each block in the system in association with the alternative version of the model illustrated in Fig. 4.12(b). For the extracted signals r, s, t, the beat-to-beat method is employed (Chapter 3).

By using the model it was shown, for example, that for conscious dogs in the supine state, respiratory influence has the major effect *via* R_t on sinus node and then through mechanical effect on blood pressure. The opposite situation observed in hypertensive human subjects, R_s has the major role for the respiratory fluctuation of the SAP and then secondarily on RRI, while R_t has a minor role. Additionally, it was shown that in this case the LF component is induced *via* the resonance in the $s-s$ loop and not through the external influences to the system.

Chapter 5

Detection of Nonlinearity in Neuro-cardiovascular System

Objectives of the Chapter

A comprehensive block diagram representation for describing the HRV-BPV-ILV relationships based on the underlying physiological system was proposed in the previous chapter. The next stage in developing the final model is to determine whether the actual system exhibits only linear properties or nonlinearity is also involved. A simple algorithm for this purpose is to inject a sinusoidal function into the input of the system and then search for the appearance of new harmonics at the output. The system exhibits nonlinearity if higher order harmonics appear at the output. In spite of the simple concept, practical implementation of this algorithm needs special developments. The objective of this chapter is to determine whether HRV and BPV exhibit input-output nonlinearity by using this sinusoidal test. To do so, metronome breathing is employed to provide a sinusoidal input to the neuro-cardiovascular system in which HRV and BPV are considered as its outputs. Then the appearance of the new peaks in HRV and BPV is inspected to determine the presence of nonlinearity.

5.1 Introduction

The physiological aspects governing the neuro-cardiovascular system and some relevant models were presented in the previous chapter. The ultimate goal of this study is to find an appropriate systemic representation to describe the observed fluctuations in

the low frequency band ($f < 0.5Hz$) in heart rate and blood pressure. To achieve this goal, the linearity or nonlinear property of the system should be determined beforehand. As already illustrated most of the existing models postulate the linearity assumption. Even frequency entrainment and pulling phenomena characterise a specific type of nonlinearity. They only show up in a narrow band region; when the HF component approaches the LF component. This chapter examines the presence of input-output nonlinearity and its importance in the normal operating range of the neuro-cardiovascular system (supine resting position in this study). This examination will lead us towards selecting an appropriate identification method, namely linear or nonlinear identification, for proper modelling of the underlying physiological system.

Investigation of the input-output nonlinearity in the neuro-cardiovascular system except for a very few cases has not been considered yet. Christini *et. al.* (1995) have compared the results of the autoregressive moving average (ARMA) modelling with Nonlinear ARMA (NARMA) modelling. These authors have concluded that the HRV can be better fitted in a nonlinear framework. By derivation of the Volterra kernels, using the Laguerre expansion technique (Chapter 7), Chon, Mullen and Cohen (1996) have obtained the nonlinear interaction between ILV and BPV as inputs and HRV as the output of a nonlinear system. These workers showed that the second order kernels have significant contributions to the relationship between HRV, ILV and BPV. Interestingly, second order kernels also fade along with the first order kernels with autonomic blockade. By concentrating on higher order spectral analysis Calcagnini, Censi, Camera, Lino and Cerutti (1996) also have shown the presence of nonlinear terms in HRV and BPV.

Herein a robust sinusoidal test for detection of nonlinearity in the neurocardiovascular system based on cyclostationary analysis is introduced. The idea behind this test is to inject a sinusoidal input to the system. If the system is linear only the injected harmonic will appear in HRV and BPV whereas if nonlinearity is also involved then higher order harmonics will also appear. In practice respiration (ILV) is employed as the sinusoidal input. In the metronome breathing experiment the subject is instructed to breath with constant frequency. If the underlying physiological system exhibits nonlinearity then higher order harmonics of the respiratory input should effectively appear in HRV and BPV. Further the interaction between the HF and the LF components may also be observed and can be used as evidence of nonlinearity. Unfortunately the

power spectral density is not a suitable tool for the presence of nonlinearity as described below. Therefore, more complicated methods have to be employed.

The analysis commences with a brief explanation of some nonlinear specifications. Then advantages and disadvantages of higher order spectral analysis for nonlinearity detection are studied. Higher order spectral analysis has been the prevalent approach in various fields so far (Ning & Bronzino, 1989; Garello & Le Caillec, 1995; Sherman & Zoltowski, 1994; Zhou & Giannakis, 1995a and references therein). The suitability of the cyclostationary method for nonlinearity detection based upon a single record of data is considered next. Afterwards a systemic analysis of the cyclostationary approach which is quite realistic and more comprehensive than the existing signal processing counterpart is developed. This new approach is further used for nonlinearity detection in the variability signals. By illustrating the experimental results, it is finally concluded that a finite memory nonlinear representation is necessary for modelling of the underlying physiological system in its normal operating range.

5.2 Overview

Most physical and physiological systems encountered in practice have some nonlinear characteristics. Although it may be possible to represent systems which are excited over a restricted operating range by a linear model, in general, nonlinear processes can only be adequately characterised by a nonlinear model. It can be shown that for a system that is nonlinear, time invariant, has finite memory, and is analytic, the relationship between input $x(t)$ and output $y(t)$ can be written as the Volterra series expansion (Schetzen, 1989),

$$y(t) = K_0 + \int_{-\infty}^{+\infty} K_1(\tau)x(t-\tau)d\tau + \int_{-\infty}^{+\infty}\int_{-\infty}^{+\infty} K_2(\tau_1,\tau_2)x(t-\tau_1)x(t-\tau_2)d\tau_1 d\tau_2 +$$

$$\int_{-\infty}^{+\infty}\int_{-\infty}^{+\infty}\int_{-\infty}^{+\infty} K_3(\tau_1,\tau_2,\tau_3)x(t-\tau_1)x(t-\tau_2)x(t-\tau_3)d\tau_1 d\tau_2 d\tau_3 + \ldots \qquad (5.1)$$

where K_0, $K_1(\tau)$, $K_2(\tau_1,\tau_2)$,... are called Volterra kernels of the system.

Due to the diversity of nonlinear systems, there are numerous corresponding classifications. Among them, the instantaneous property of nonlinear systems is of

importance in this study. If a system acts instantaneously on the present input in a nonlinear fashion it is called a zero memory nonlinear system. In these systems the output $y(t)$ at any time t is a single-valued nonlinear function of the input $x(t)$ at the same time t. Zero memory nonlinear systems can be represented by

$$y(t) = g[x(t)], \tag{5.2}$$

where $g[x]$ is a single-valued nonlinear function of $x(t)$. Finite memory nonlinear systems (equation 5.1) can be obtained by inserting linear time invariant systems after and/or before zero memory nonlinear systems.

While mathematical tools for analysis of linear systems are well developed, the study of nonlinear systems is, often, very specific and cumbersome. Hence, before dealing with analysis of such systems, presence of nonlinearity should be assessed to determine a proper model order selection. This in turn means, applying an appropriate technique for the detection of nonlinearity and its hardness. Nonlinearity can simply be detected by using the superposition theorem (Marmarelis, 1978). However, if the input is not accessible or not controllable then other methods have to be found. Unfortunately, the number of nonlinearity detection techniques in this sense is very few.

At least in our case sinusoidal testing of the system seems to be straightforward. In the metronome breathing experiment, subjects are taught to breath with constant frequencies. If the breathing rate changes in discrete steps in separate experiments then the sweep of the whole range of interest ($0.1 < f < 0.5Hz$) will be possible. Clearly if a sinusoidal signal passes through a nonlinear system, given by equation (5.1), higher order harmonics will appear at the output. This gives a pointer for the detection of nonlinearity as will be considered throughout this chapter.

5.3 Phase and Frequency Coupling

Suppose the signal

$$x(t) = A_1 cos(2\pi f_1 t + \phi_1) + A_2 cos(2\pi f_2 t + \phi_2), \tag{5.3}$$

is passed through the following simple quadratic zero memory nonlinear system

$$y(t) = ax(t) + bx^2(t), \tag{5.4}$$

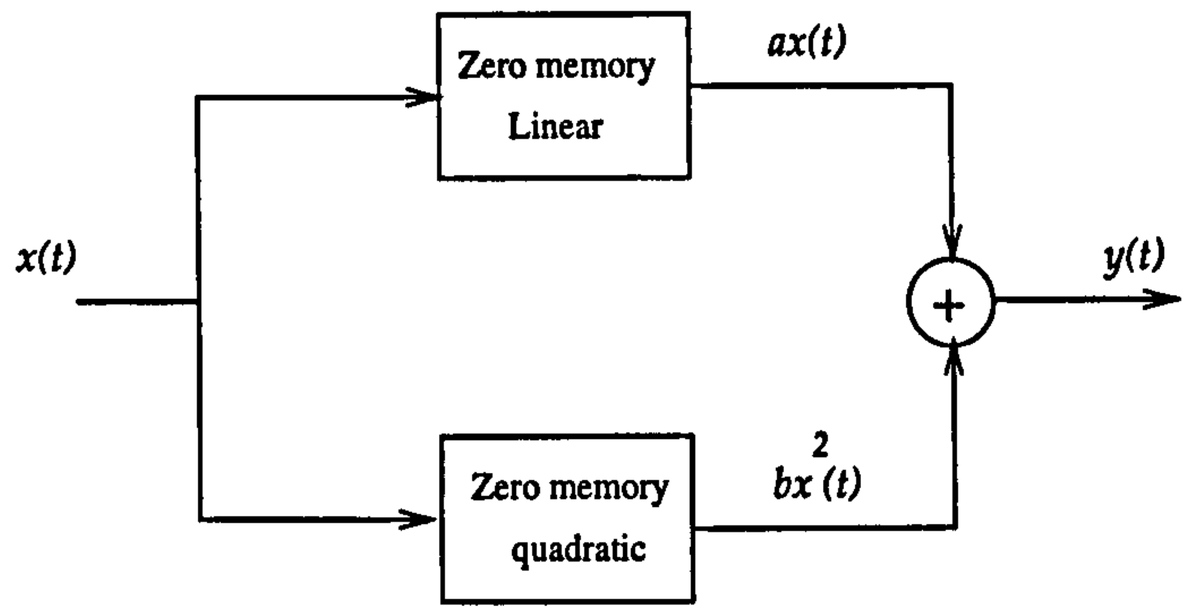


Figure 5.1: The nonlinear model when frequency coupling is accompanied by phase coupling.

in which a and b are constants. Therefore, $y(t)$ contains sinusoidal terms with corresponding phases at (f_1, ϕ_1), (f_2, ϕ_2), $(2f_1, 2\phi_1)$, $(2f_2, 2\phi_2)$,$(f_1 + f_2, \phi_1 + \phi_2)$,$(f_1 - f_2, \phi_1 - \phi_2)$. This means that for a quadratic nonlinear system the new components $(f_1 + f_2, \phi_1 + \phi_2)$,$(f_1 - f_2, \phi_1 - \phi_2)$ can be observed at the output. Such a phenomenon which gives rise to the sum or difference of phases with the same relationship to that of the frequencies is called phase coupling $(\phi_1 + \phi_2)$ and frequency coupling $(f_1 + f_2)$ (Nikias & Petropolu, 1993a, Nikias & Mendel, 1993b). If only one sinusoidal function is injected into the nonlinear system of equation (5.4) only the new component $(2f_1, 2\phi_1)$ will arise at the output. In this case it is said that $y(t)$ exhibits self phase $(2\phi_1)$ coupling and self frequency coupling $(2f_1)$ (Zhou & Giannakis, 1995a). It is, therefore, concluded that the presence of (self) frequency and (self) phase coupling can be an indicator of the nonlinearity. This also implies that detection of nonlinearity corresponds to retrieval of harmonics in the output signal.

If simultaneous (self) frequency and (self) phase coupling can be observed in a given signal then the simple model shown in Fig. 5.1 can be assumed to represent the underlying nonlinear system. In this case the identification procedure for finding the linear and nonlinear terms will be relatively simple (Bendat, 1990). However, if only (self) frequency coupling can be observed without (self) phase coupling then a nonlinear model in the form of equation (5.1) should be assumed which brings about more laborious work for characterising the underlying system. Clearly, the absence of (self) phase coupling and (self) frequency coupling renders the absence of nonlinearity in the underlying system.

Since power spectral density is phase blind, higher order statistics and cyclostationary analysis have been used for detection of nonlinearity in a signal (Nikias &

Petropulu, 1993a; Nikias & Mendel, 1993b; Zhou & Giannakis, 1994). In the following a brief review of the nonlinearity detection using higher order statistics will give a good insight to the application of the cyclostationary analysis as an appropriate tool for nonlinearity detection.

5.4 Frequency and Phase Coupling Detection Using Higher Order Spectra

Harmonic retrieval is one of the most frequently encountered problems in practice and constitutes a significant part of statistical signal processing research. Although the power spectrum is able to detect frequency coupling, it cannot be used for detection of phase coupling since the power spectrum suppresses all the phase relations. Higher order moment spectra, however, are capable of detecting and characterising frequency and phase coupling. To show this, assume the complex harmonic process

$$w(t) = y(t) + v(t) = \sum_{k=1} A_k e^{j(2\pi f_k t + \phi_k)} + v(t), \tag{5.5}$$

in which A_i, ϕ_i are constants and $v(t)$ is additive zero mean stationary mixing noise [1]. Then the scaled bispectrum of $w(t)$ is defined by (Zhou & Giannakis, 1993),

$$S_{3w}(\lambda_1, \lambda_2) = \lim_{T\to\infty} \frac{1}{T^3} E[W_T(\lambda_1) W_T(\lambda_2) W_T^*(\lambda_1 + \lambda_2)], \tag{5.6}$$

where $W_T(\lambda)$ is the discrete Fourier transform (DFT) of $w(t)$ and T is the data length. Since $S_{3v}(\lambda_1, \lambda_2) = 0$ (due to the properties of $v(t)$) it follows from equations (5.5) and (5.6) that (Zhou & Giannakis, 1993),

$$S_{3w}(\lambda_1, \lambda_2) = S_{3y}(\lambda_1, \lambda_2) = \sum_{k,l,m=1}^{3} A_k A_l A_m e^{j(\phi_k + \phi_l - \phi_m)} \delta(\lambda_1 - f_k) \delta(\lambda_2 - f_l) \delta(\lambda_1 + \lambda_2 - f_m), \tag{5.7}$$

in which $\delta(\lambda)$ denotes Kronecker's delta function,

$$\delta(\lambda) = \begin{cases} 1 & \lambda = 0 \ mod(2\pi) \\ 0 & \lambda \neq 0 \end{cases} \tag{5.8}$$

[1] By mixing property of a process, $x(t)$, the boundedness of the kth-order cumulant, $\sum_{\tau_i} |C_{kx}(\tau_1, \ldots, \tau_{k-1})| < \infty$ is meant. Mixing property is met by stable (non) stationary linear processes and it, for example, guarantees convergence of cumulant estimators to a finite value (Brillinger, 1973).

It follows from equation (5.7) that if $\lambda_1 = f_k, \lambda_2 = f_l, \lambda_1 + \lambda_2 = f_m$, then $S_{3y}(\lambda_1, \lambda_2)$ will show the corresponding peaks in the 2-D space of λ_1, λ_2 and $S_{3y}(\lambda_1, \lambda_2)$. This further means that frequency coupling can be detected by a peak-picking procedure in the bispectrum space.

Even though equation (5.7) shows the principal feature for frequency coupling detection, it does not provide a useful information for investigation of the phase coupling. This is because the presence of frequency coupling entails the appearance of the corresponding peaks in the bispectrum domain regardless of the presence or absence of phase coupling. Therefore, phase information in the form of equation (5.7) cannot be employed without subsequent assumptions.

In $y(t)$ of equation (5.5) the ϕ_k's were assumed to be constant deterministic values. If one supposes that the ϕ_k's are identically independent uniformly distributed random variables in the range $(-\pi, \pi]$ then the bispectrum will become,

$$S_{3y}(\lambda_1, \lambda_2) = \sum_{k,l,m=1}^{3} A_k A_l A_m E[e^{j(\phi_k + \phi_l - \phi m)}] \delta(\lambda_1 - f_k) \cdot \delta(\lambda_2 - f_l) \delta(\lambda_1 + \lambda_2 - f_m) \tag{5.9}$$

Since $\phi \triangleq \phi_k + \phi_l - \phi_m$ is a uniform random variable in the range $(-\pi, \pi]$, $S_{3y}(\lambda_1, \lambda_2)$ will be always zero except when

(i) $\lambda_1 = f_k, \lambda_2 = f_l, \lambda_1 + \lambda_2 = f_m$ which implies that $f_k + f_l = f_m$,

(ii) $\phi_k + \phi_l = \phi_m$.

Hence, it can be concluded that peaks in the ensemble bispectrum domain indicate both quadratic frequency coupling and phase coupling. In other words if the phase of the sinusoidal functions are assumed to be constant then nonzero peaks in the bispectrum domain indicate the presence of frequency coupling whereas if a uniform distribution for the phase values is assumed then appearance of the peaks in the bispectrum domain will show the presence of both phase and frequency coupling. Since in practice a single record of data is often available, ensemble averaging in equation (5.9) will not be (effectively) possible (it needs multiple independent records of data). Hence, phase coupling detection cannot be (effectively) checked. Recalling that the phase randomisation assumption demands a non-ergodic analysis (Zhou & Giannakis, 1996).

As an alternative solution to the problem of phase coupling detection using equation (5.7) with a single record of data, a deterministic approach together with

a phase estimation algorithm has been proposed by Zhou and Giannakis (1993). With $f_k + f_l = f_m$ it follows from (5.7) that,

$$arg\,[\lim_{T\to\infty} S_{3w}(f_k, f_l)] = \phi_k + \phi_l - \phi_m. \tag{5.10}$$

Hence, for T large enough and after identifying the bi-frequencies (f_k, f_l) from peak locations of $|S_{3w}(\lambda_1, \lambda_2)|$, one can estimate the phase of the bispectrum and perform a statistical test to check whether $\phi_k + \phi_l - \phi_m = 0$. If so, phase coupling can be declared in addition to frequency coupling.

Similar to the bispectrum method for detection of quadratic nonlinearity, the higher order spectrum can be employed for the kth-order nonlinearity detection of the form $y(t) = ax(t) + bx^k(t)$. To do so, the nonlinear system has to be excited by k separate components $(f_1, \phi_1), (f_2, \phi_2), \ldots, (f_k, \phi_k)$. Clearly at the output a new component with the sum frequency $\sum_{i=1}^{k} f_i$ and the sum phase $\sum_{i=1}^{k} \phi_i$ will appear. Next, kth-order frequency and phase coupling can be determined by observation of the $(k+1)$st-order moment spectrum (polyperiodogram). However, in practical situations injection of k separate harmonics may not be possible. Furthermore, the polyperiodogram has relatively high variance and the peak finding procedure is multi-dimensional. Importantly, the number of injected harmonics can be reduced to one if self phase and self frequency coupling is exerted instead of phase and frequency coupling. This, moreover, resolves the problem of the multidimensional peak-picking procedure as shown below.

5.5 k-th Order Self Phase and Self Frequency Coupling

It is well known that when a single harmonic (f_1, ϕ_1) is passed through the kth-order nonlinear system $y(t) = ax(t) + bx^k(t)$, harmonics at frequencies (f_1, ϕ_1) and $(kf_1, k\phi_1)$ are exhibited at the output. This suggests modification of the moment spectrum, discussed in the previous section, for detection of kth-order self phase and self frequency coupling. The time-averaged kth-order moment of the process $y(t)$ can now be defined as,

$$m_{ky}(\tau_1, \ldots, \tau_{k-1}) = \lim_{T\to\infty} \frac{1}{T} \sum_{t=0}^{T-1} E[y^*(t)y(t+\tau_1)\ldots y(t+\tau_{k-1})]. \tag{5.11}$$

If $y(t)$ consists only of sinusoidal functions then $m_{ky}(\tau_1,\ldots,\tau_{k-1})$ will be a periodic sequence of $[\tau_1,\ldots,\tau_{k-1}]$. Now by taking the kth-order Fourier series (FS) of m_{ky} one can get,

$$M_{ky}(\lambda_1,\lambda_2,\ldots,\lambda_{k-1}) = \lim_{T\to\infty}\frac{1}{T^{k-1}}\sum_{\tau_1,\ldots,\tau_{k-1}=-(T-1)}^{T-1} m_{ky}(\tau_1,\ldots,\tau_{k-1})e^{-j2\pi(\lambda_1\tau_1+\ldots+\lambda_{k-1}\tau_{k-1})} \tag{5.12}$$

It can be shown that (Zhou & Giannakis, 1995a).

$$M_{ky}(\lambda_1,\lambda_2,\ldots,\lambda_{k-1}) = \lim_{T\to\infty}\frac{1}{T^k}E[Y_T(\lambda_1)\ldots Y_T(\lambda_{k-1})Y_T^*(\sum_{i=1}^{k-1}\lambda_i)]. \tag{5.13}$$

where $Y_T(\lambda)$ is the DFT of $y(t)$. The diagonal slice of $M_{ky}(\lambda_1,\lambda_2,\ldots,\lambda_{k-1})$ is denoted by,

$$M_{ky}(\lambda) \triangleq M_{ky}(\lambda,\lambda,\ldots,\lambda). \tag{5.14}$$

Now assume that

$$y(t) = A_1e^{j(2\pi f_0t+\phi_1)} + A_2e^{j(2\pi kf_0t+\phi_2)} + v(t), \tag{5.15}$$

in which $v(t)$ is the additive noise process. Then the diagonal slice of the $(k+1)$st-order FS moment spectrum of $y(t)$ is given by (Zhou & Giannakis, 1994).

$$M_{(k+1)y}(\lambda) = A_1^kA_2e^{j(k\phi_1-\phi_2)}\delta(\lambda-f_0). \tag{5.16}$$

Equation (5.16) reveals that the kth-order self frequency coupling (kf_0) can be detected from the presence of the peak in $M_{(k+1)y}(\lambda)$. Next, self phase coupling ($\phi_2 = k\phi_1$) can be detected by checking the zeroness of $arg(M_{(k+1)y}(\lambda))$. In contrast to phase and frequency coupling detection, $M_{(k+1)y}(\lambda)$ here is a 1-D function which greatly simplifies the peak-picking procedure.

In an actual application ensemble averaging can be replaced by the following estimator for a single record of data (polyperiodogram).

$$\hat{M}_{(k+1)y}(\lambda) \triangleq \left(\frac{Y_T(\lambda)}{T}\right)^k\left(\frac{Y_T^*(k\lambda)}{T}\right). \tag{5.17}$$

It has been shown that $\hat{M}_{(k+1)y}(\lambda)$ is an asymptotically consistent estimator with the following properties [2] (Zhou & Giannakis, 1995a),

$$var(\hat{M}_{(k+1)y}(f_0)) = O(T^{-1}), \tag{5.18}$$

[2]By $h(T) = O(T^k)$ we mean $lim_{T\to\infty}h(T)/T^k = c$, where constant c satisfies $0 < |c| < \infty$.

$$var(\hat{f}_0) = \frac{1}{(k+1)^2} O(T^{-3}), \tag{5.19}$$

$$var(\hat{\phi}) = O(T^{-1}). \tag{5.20}$$

where

$$\hat{f}_0 = arg\ max_\lambda |\hat{M}_{(k+1)y}(\lambda)|, \tag{5.21}$$

$$\phi \triangleq k\phi_1 - \phi_2, \tag{5.22}$$

$$\hat{\phi} = arg\ (\hat{M}_{(k+1)y}(f_0)). \tag{5.23}$$

While f_0 can be estimated by finding the peak of $\hat{M}_{(k+1)y}(\lambda)$, a statistical test for zeroness of $\hat{\phi}$ based on chi-squared distribution can be used for phase coupling detection (Zhou & Giannakis, 1995a, 1996). It has also been shown that the scaled moment spectrum of equation (5.12) gives a good performance in the presence of additive noise regardless of its distribution (Zhou & Giannakis, 1995a).

5.6 Amplitude Modulated Signals Through Nonlinear Systems

Thus far only constant amplitude harmonics have been considered. However, in practice and particularly in the cardio-respiratory system, what exists is harmonics with fluctuating amplitudes. As an example, subjects in metronome breathing experiments exhibit random fluctuations in their tidal volumes (Fig. 5.2). Consequently, analysis of random amplitude harmonics or more technically amplitude modulated signals through nonlinear systems is essential.

If $y(t)$ is represented by,

$$y(t) = w(t)e^{j(2\pi f_0 t + \phi_1)} + z(t)e^{j(2\pi k f_0 t + \phi_2)} + v(t), \tag{5.24}$$

where $w(t)$ and $z(t)$ are mutually independent, real, stationary and mixing processes with nonzero mean values m_w and m_z, respectively, and also independent from $v(t)$, then it can be shown that (Zhou & Giannakis, 1993),

$$M_{(k+1)y}(\lambda) = m_w^k m_z e^{j(k\phi_1 - \phi_2)} \delta(\lambda - f_0). \tag{5.25}$$

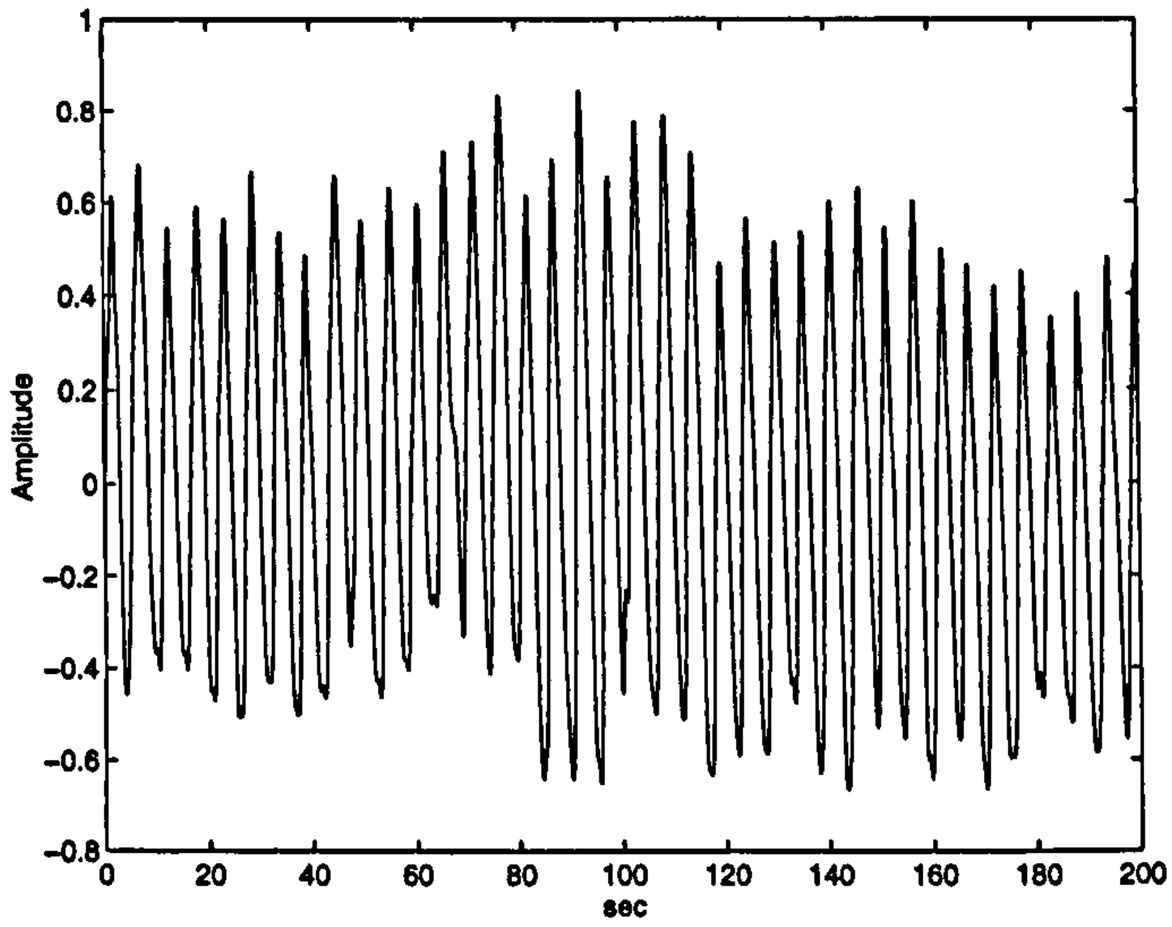


Figure 5.2: Random variation in respiratory amplitude in the metronome breathing pattern (12 breaths/min experiment).

Therefore, f_0 can still be estimated from the peak-picking procedure of $(k+1)$st-order polyperiodogram. Likewise a chi-squared based test can be presented for self phase coupling detection (Zhou & Giannakis, 1994). An analogous formula can also be obtained for phase and frequency coupling detection (Zhou & Giannakis, 1993).

Even though the polyperiodogram approach, described above, has many desired properties and has been used extensively in different areas, it has also some drawbacks such as:

(i) for the zero mean modulating signals $M_{(k+1)y}(\lambda)$ vanishes and hence self phase and frequency coupling can not be checked,

(ii) in the case of phase and frequency coupling, detection of nonlinearity using polyperiodogram imposes a multidimensional search $S_{ky}(\lambda_1, \lambda_2 \cdots \lambda_{k-1})$,

(iii) $(k+1)$st-order polyspectra can only detect kth-order coupling, thus for each order of nonlinearity a separate estimation and peak-picking procedure is required.

It will be shown shortly that the above mentioned problems are alleviated if the cyclostationary approach is invoked. Interestingly, higher order moment spectra can be expressed as a special case of higher order cyclic spectra (Appendix A). In the next section, (self) phase and (self) frequency coupling detection based on cyclic estimators are presented, followed by the development of a modified approach for nonlinearity detection which is more appropriate for system analysis.

5.7 The Cyclostationary Approach to Harmonic Retrieval

A nonstationary process, say $y(t)$, is called a strict sense cyclostationary process with period T if its statistical properties are invariant to a shift of the origin by integral multiples of T. This process is said to be cyclostationary in the wide sense if its mean and autocorrelation functions are periodic with period T (Gardner, 1988, 1995),

$$m_y(t) = m_y(t+T), \tag{5.26}$$

$$R_y(t+T+\frac{\tau}{2}, t+T-\frac{\tau}{2}) = R_y(t+\frac{\tau}{2}, t-\frac{\tau}{2}). \tag{5.27}$$

in which $m_y(t) = E(y(t))$, $R_y(t_1, t_2) = E(y(t_1)y(t_2))$. Due to the periodicity of the mean and autocorrelation functions, expansion in terms of Fourier series is possible. Thus,

$$R_{1y}(\alpha) \triangleq \lim_{T\to\infty} \frac{1}{T} \sum_{t=0}^{T-1} m_y(t) e^{-j2\pi\alpha t}, \tag{5.28}$$

$$R_{2y}^{\alpha}(\tau) \triangleq \lim_{T\to\infty} \frac{1}{T} \sum_{t=0}^{T-1} R_y(t,\tau) e^{-j2\pi\alpha t}. \tag{5.29}$$

Parameter α is called the cycle frequency while $R_{1y}(\alpha)$ and $R_{2y}^{\alpha}(\tau)$ are called cyclic mean and cyclic correlation functions, respectively. Noting that $R_{2y}^{\alpha}(\tau)$ is a 2D function of α and τ, however, as it will be seen subsequently only the slice $\tau = 0$ is indeed required for detection of nonlinearity.

Now, consider the amplitude modulated complex harmonics in the noise model,

$$y(t) = \sum_{i=1}^{L} z_i(t) e^{j(2\pi f_i t + \phi_i)} + v(t), \tag{5.30}$$

under the following assumptions:

(i) f_i's are distinct and nonzero and ϕ_i's are deterministic constants,

(ii) $v(t)$ is a stationary and mixing process,

(iii) $z_i(t)$ are stationary, mixing mutually independent processes and also independent of $v(t)$.

Then the cyclic mean will be given by,

$$\begin{aligned} R_{1y}(\alpha) &\triangleq \lim_{T\to\infty} \frac{1}{T} \sum_{t=0}^{T-1} E(y(t)) e^{-j2\pi\alpha t} \\ &= \sum_{i=1}^{L} m_{z_i} e^{j\phi_i} \delta(\alpha - f_i) + m_v \delta(\alpha). \end{aligned} \tag{5.31}$$

where $m_{z_i} = E(z_i(t))$ and $m_v = E(v(t))$. Further, the cyclic correlation will be given by:

$$R^{\alpha}_{2y}(\tau) \triangleq \lim_{T\to\infty} \frac{1}{T} \sum_{t=0}^{T-1} R_y(t,\tau) e^{-j2\pi\alpha t}$$

$$= \sum_{i=1}^{L} R_{z_i}(\tau) e^{j(2\phi_i)} \delta(\alpha - 2f_i) + R_v(\tau)\delta(\alpha)\cdot \tag{5.32}$$

in which $R_{z_i}(\tau) = E(z_i(t+\frac{\tau}{2}) z_i(t-\frac{\tau}{2}))$ and correspondingly for $R_v(\tau)$. From equations (5.31) and (5.32) it is concluded that the existence of harmonics can be detected by the peak-picking procedure in the cyclic mean or cyclic correlation domains ($R_{1y}(\alpha)$ or $R^{\alpha}_{2y}(0)$). Nevertheless, the phase value at each peak can be estimated and any possible (self) phase coupling between the detected harmonics can be inspected. If the modulating signals $z_i(t)$ have nonzero mean values then the cyclic mean is preferred and in the case of zero mean modulating signals cyclic correlation should be chosen. Consequently, a simple tool is provided to check the presence of (self) phase and (self) frequency coupling.

As already argued, with a single record of data, the expectation operator in equations (5.31) and (5.32) should be disregarded and the following temporal estimators ought to be used.

$$\hat{R}_{1y}(\alpha) = \frac{1}{T} \sum_{t=0}^{T-1} y(t) e^{-j2\pi\alpha t}, \tag{5.33}$$

$$\hat{R}^{\alpha}_{2y}(\tau) = \frac{1}{T} \sum_{t=0}^{T-1} \left(y(t+\frac{\tau}{2}) y(t-\frac{\tau}{2}) \right) e^{-j2\pi\alpha t}. \tag{5.34}$$

It has been proved that these estimators are asymptotically consistent with $var(\hat{R}^{\alpha}_{ky}(\tau_1, \tau_2, \ldots, \tau_{k-1})) = O(T^{-1})$, where $R^{\alpha}_{ky}(\tau_1, \tau_2, \ldots, \tau_{k-1})$ is the kth-order cyclic correlation (Dandawate & Giannakis, 1994a, 1994b). Despite the consistency of the cyclic correlation estimator, the phase and frequency estimators in the cyclic domain need specific consideration. Zhou and Giannakis (1995b) have shown that these estimators are also asymptotically consistent and close to the Cramer-Rao lower band and therefore almost efficient. Furthermore, they have proved that for both cyclic mean and cyclic correlation methods we have

$$var(\hat{f}_0) = O(T^{-3}), \tag{5.35}$$

$$var(\hat{\phi}_0) = O(T^{-1}), \tag{5.36}$$

It is worthwhile to point out that $\hat{R}_{1y}(\alpha)$ is nothing but the normalised DFT of $y(t)$ and can be implemented efficiently by using the FFT algorithm. Similarly, $\hat{R}^{\alpha}_{2y}(0)$ is nothing but the normalised DFT of $y^2(t)$ (Giannakis & Zhou, 1995). Therefore, implementation of the cyclic tools for detection of nonlinearity will be exceedingly simple.

5.8 Systemic Analysis of Nonlinearity Using Cyclostationary Properties

So far the major discussion has been given to the (self) phase and (self) frequency coupling detection of independent random amplitude harmonics (independent $z_i(t)$ in a given signal). In reality if a set of amplitude modulated signals (such as respiration or the LF component in HRV-BPV-ILV system) undergo a nonlinear operation, dependent random amplitude harmonics will appear at the output. This case needs special attention as explored below.

5.8.1 Self Frequency and Self Phase Coupling Detection

Assume signal $x(t) = z(t)cos(2\pi f_0 t + \phi_0)$, with $z(t)$ a stationary mixing random process, undergoes the nonlinear transformation $y(t) = ax(t) + bx^2(t)$, in which a and b are constant values. Then $y(t)$ is given by [3],

$$y(t) = \frac{b}{2}z^2(t) + az(t)cos(2\pi f_0 t + \phi_0) + \frac{b}{2}z^2(t)cos(2\pi(2f_0)t + 2\phi_0) \qquad (5.37)$$

In practice the true mean value of $y(t)$ is unknown and its statistical mean is removed prior to any processing. If $\langle y(t)\rangle$ denotes the statistical mean of $y(t)$ then,

$$\begin{aligned}\langle y(t)\rangle = \frac{1}{T}\int_{-T/2}^{T/2} y(t)dt &= \frac{b}{2T}\int_{-T/2}^{T/2} z^2(t)dt + \frac{a}{T}\int_{-T/2}^{T/2} z(t)cos(2\pi f_0 t + \phi_0)dt \\ &+\frac{b}{2T}\int_{-T/2}^{T/2} z^2(t)cos(2\pi(2f_0)t + 2\phi_0)dt\cdot \qquad (5.38)\end{aligned}$$

Therefore, $y_0(t)$ given by equation (5.39) is basically used for the cyclic analysis.

$$y_0(t) \triangleq y(t) - \langle y(t)\rangle = \frac{b}{2}z^2(t) - \langle y(t)\rangle$$

[3] In this section the effect of additive noise $v(t)$ is not considered. As stated before, stationary, independent (output) additive noise cannot perturb the cyclic analysis. Additive input noise, however, has destructive effect in the cyclic domain but theoretical study of this effect is quite cumbersome and is not considered here.

$$+az(t)cos(2\pi f_0 t+\phi_0)+\frac{b}{2}z^2(t)cos(2\pi(2f_0)t+2\phi_0))\cdot \tag{5.39}$$

Since the cyclic mean of $y_0(t)$ is expressed by

$$R_{1y_0}(\alpha)=\lim_{T\to\infty}\frac{1}{T}\int_{-T/2}^{T/2}E(y_0(t))e^{-j2\pi\alpha t}dt, \tag{5.40}$$

it follows that

$$\begin{aligned}R_{1y_0}(\alpha)&=\lim_{T\to\infty}\frac{1}{T}\int_{-T/2}^{T/2}E(y(t)-\langle y(t)\rangle)e^{-j2\pi\alpha t}dt\\&=\lim_{T\to\infty}\frac{1}{T}\int_{-T/2}^{T/2}[\frac{b}{2}m_{z^2}+am_z cos(2\pi f_0 t+\phi_0)\\&+\frac{b}{2}m_{z^2}cos(2\pi(2f_0)t+\phi_0)-\langle E(y(t))\rangle]e^{-j2\pi\alpha t}dt\\&=\lim_{T\to\infty}\frac{1}{T}\int_{-T/2}^{T/2}[\frac{b}{2}m_{z^2}+am_z cos(2\pi f_0 t+\phi_0)\\&+\frac{b}{2}m_{z^2}cos(2\pi(2f_0)t+\phi_0)-\frac{b}{2}m_{z^2}]e^{-j2\pi\alpha t}dt\cdot\end{aligned} \tag{5.41}$$

Consequently,

$$R_{1y_0}(\alpha)=\begin{cases}\frac{a}{2}m_z e^{j\phi_0}, & \alpha=f_0\\ \frac{b}{4}m_{z^2}e^{j2\phi_0}, & \alpha=2f_0\\ 0 & \text{otherwise and } \alpha\geq 0\end{cases} \tag{5.42}$$

As would be expected self frequency coupling can be detected by the peak-picking procedure (f_0, $2f_0$) on condition that $m_z\neq 0$. Next, self phase coupling (ϕ_0, $2\phi_0$) can be checked by phase estimation from the cyclic mean estimator. It is important to note that the statistical test based on the χ^2 distribution which has been suggested for phase coupling detection of independent random amplitude modulated harmonics is not applicable in this case (Zhou & Giannakis, 1994). This is because the random modulated harmonics at the output have dependent magnitudes [4].

If $m_z=0$ then cyclic correlation analysis has to be employed. It is proved in

[4] If $x(t)=z_1(t)e^{j(2\pi f_0 t+\phi_1)}+z_2(t)e^{j(2\pi k f_0 t+\phi_2)}+v(t)$ with $z_1(t)$ and $z_2(t)$ mutually independent stationary mixing processes and also independent from $v(t)$ and if there is kth-order self phase coupling then it can be shown that $\sqrt{T}(\hat{\phi}-\phi)$ is a normal distribution $\mathcal{N}(0,\sigma^2_{\hat{\phi}})$, where $\phi=k\phi_1-\phi_2$, $\hat{\phi}=k\hat{\phi}_1-\hat{\phi}_2$. Therefore $T(\hat{\phi}-\phi)^2/\sigma^2_{\hat{\phi}}$ is a $\chi^2(1)$ random variable.

Appendix B that,

$$R^{\alpha}_{2y_0}(\tau) = \begin{cases} \frac{b^2}{4}R_{h,h}(\tau) + \frac{a^2}{2}R_{z,z}(\tau)cos(2\pi f_0\tau) + \frac{b^2}{8}R_{z^2,z^2}(\tau)cos\left(2\pi(2f_0)\tau\right), & \alpha = 0 \\ \left[\frac{ab}{4}R_{h,z}(\tau)e^{j(2\pi(-\frac{f_0}{2})\tau)} + \frac{ab}{4}R_{z,h}(\tau)e^{j(2\pi(\frac{f_0}{2})\tau)} + \right. & \\ \left. \frac{ab}{8}R_{z,z^2}(\tau)e^{j(2\pi(-\frac{3f_0}{2})\tau)} + \frac{ab}{8}R_{z^2,z}(\tau)e^{j(2\pi(\frac{3f_0}{2})\tau)}\right] e^{j\phi_0}, & \alpha = f_0 \\ \left[\frac{b^2}{8}R_{h,z^2}(\tau)e^{j(2\pi(-f_0)\tau)} + \frac{b^2}{8}R_{z^2,h}(\tau)e^{j(2\pi(f_0)\tau)} + \right. & \\ \left. \frac{a^2}{4}R_{z,z}(\tau)\right] e^{j2\phi_0}, & \alpha = 2f_0 \\ \left[\frac{ab}{8}R_{z,z^2}(\tau)e^{j(2\pi(-\frac{f_0}{2})\tau)} + \frac{ab}{8}R_{z^2,z}(\tau)e^{j(2\pi(\frac{f_0}{2})\tau)}\right] e^{j3\phi_0}, & \alpha = 3f_0 \\ \frac{b^2}{16}R_{z^2,z^2}(\tau)e^{j4\phi_0}, & \alpha = 4f_0 \\ 0 & \text{otherwise and } \alpha > 0 \end{cases} \tag{5.43}$$

where $R_{g,u}(\tau) \triangleq E(g(t+\tau/2)u(t-\tau/2))$ and $h(t) \triangleq z^2(t) - \frac{2}{b}\langle y(t)\rangle$. It is deduced from equation (5.43) that in addition to the peaks at $\alpha = 2f_0$ and $\alpha = 4f_0$, two more peaks at $\alpha = f_0$ and $\alpha = 3f_0$ can be observed at $R^{\alpha}_{2y_0}(0)$ [5]. This is again due to the generation of dependent harmonics at the output and may complicate the detection of nonlinearity. Importantly, only lag $\tau = 0$ needs to be checked for the presence of nonlinearity in $R^{\alpha}_{2y_0}(\tau)$. This will greatly simplify the practical implementation of the algorithm (DFT of $y^2(t)$ as noted earlier).

It is worthwhile noting that simultaneous self frequency and self phase coupling shows the presence of a nonlinear transformation. However, a great majority of nonlinear systems are systems with memory which for them phase coupling does not arise. As an example consider the system $g(t) = x(t)x(t-t_0)$ with $x(t) = cos(2\pi f_0 t + \phi_0)$ then,

$$g(t) = \frac{1}{2}\left[cos(2\pi(2f_0)t - 2\pi f_0 t_0 + 2\phi_0) + cos(2\pi f_0 t_0)\right]\cdot \tag{5.44}$$

and

$$g_0(t) = g(t) - \langle g(t)\rangle = \frac{1}{2}cos(2\pi(2f_0)t - 2\pi f_0 t_0 + 2\phi_0)\cdot \tag{5.45}$$

Hence, the cyclic mean is given by

$$R_{1g_0}(\alpha) = \frac{1}{4}e^{j(-2\pi f_0 t_0 + 2\phi_0)}\delta(\alpha - 2f_0)\cdot \tag{5.46}$$

[5] $R^{\alpha}_{2y_0}(\tau)$ is in fact cyclic covariance of $y(t)$.

which does not exhibit the phase coupling phenomenon despite the presence of the second order nonlinearity. However, the presence of the self frequency coupling still indicates the existence of a nonzero memory nonlinear system.

5.8.2 Phase and Frequency Coupling Detection

Similar to the self phase and self frequency coupling, transmission of two random amplitude harmonics through a nonlinear system brings about the appearance of new peaks in the cyclic mean or cyclic correlation domains. If signal

$$x(t) = w(t)cos(2\pi f_1 t + \phi_1) + z(t)cos(2\pi f_2 t + \phi_2), \tag{5.47}$$

with $w(t)$ and $z(t)$ two random stationary mixing processes, is injected to the nonlinear system $y(t) = ax(t) + bx^2(t)$ then $y(t)$ will be given by,

$$\begin{aligned} y(t) &= \frac{b}{2}\left(w^2(t) + z^2(t)\right) + aw(t)cos(2\pi f_1 t + \phi_1) \\ &+ az(t)cos(2\pi f_2 t + \phi_2) + \frac{b}{2}w^2(t)cos\left(2\pi(2f_1)t + \phi_1\right) + \frac{b}{2}z^2(t)cos\left(2\pi(2f_2)t + \phi_2\right) \\ &+ bw(t)z(t)cos(2\pi(f_1 - f_2)t + \phi_1 - \phi_2) + bw(t)z(t)cos(2\pi(f_1 + f_2)t + \phi_1 + \phi_2)\cdot \end{aligned} \tag{5.48}$$

If,

$$y_0(t) \triangleq y(t) - \langle y(t)\rangle, \tag{5.49}$$

it follows then

$$R_{1y_0}(\alpha) = \begin{cases} \frac{a}{2}m_w e^{j\phi_1}, & \alpha = f_1 \\ \frac{a}{2}m_z e^{j\phi_2}, & \alpha = f_2 \\ \frac{b}{4}m_{w^2} e^{j2\phi_1}, & \alpha = 2f_1 \\ \frac{b}{4}m_{z^2} e^{j2\phi_2}, & \alpha = 2f_2 \\ \frac{b}{2}m_{w,z} e^{j(\phi_1+\phi_2)}, & \alpha = f_1 + f_2 \\ \frac{b}{2}m_{w,z} e^{j(\phi_1-\phi_2)}, & \alpha = |f_1 - f_2| \\ 0 & \text{otherwise and } \alpha \geq 0 \end{cases} \tag{5.50}$$

in which $m_{w,z} \triangleq E(w(t)z(t))$. As before, frequency and phase coupling can be checked by a peak-picking procedure and phase estimation in the cyclic mean domain. However,

for the appearance of the peaks in addition to the conditions $m_w \neq 0$ and $m_z \neq 0$, here, the extra condition $m_{w,z} \neq 0$ should also hold. If

$$w(t) = B + c(t), \tag{5.51}$$

$$z(t) = A + d(t), \tag{5.52}$$

with $c(t)$ and $d(t)$ two zero mean stationary mixing processes, and A,B constant values then we will have

$$m_{w,z} = E(w(t)z(t)) = AB + m_{c,d} \tag{5.53}$$

Hence, regardless of the dependency between $c(t)$ and $d(t)$, $m_{w,z}$ is always nonzero if $m_z \neq 0$ and $m_w \neq 0$. In other words, the existence of nonzero mean modulating signals is sufficient for the applicability of the cyclic mean method for nonlinearity detection.

One interesting inference which can be understood from equations (5.48) and (5.50) is the possibility of segregation between transmission of two components through a nonlinear system and transmission of each component through separate nonlinear systems by investigation of $y_0(t)$. This is because for the latter, peaks of the cyclic mean at $\alpha = f_1 + f_2$ and $\alpha = |f_1 - f_2|$ will vanish whereas for the former they can always be seen. This is of much importance in the present study. If frequency coupling is observed between HF and LF components then the existence of a common nonlinear system should be imagined, but if only self frequency coupling is exhibited then separate nonlinear systems have to be conceived.

If the nonlinear system is fed by zero mean modulating signals, cyclic correlation analysis is required. Derivation of cyclic correlation of $y_0(t)$ and its analysis is more complex in this case. It can be shown that [6],

[6]The proof is analogous to that of the Appendix B but it is not presented here.

$$
R^{\alpha}_{2y_0}(\tau) = \begin{cases}
\frac{a^2}{2}R_{w,w}cos(2\pi f_1\tau) + +\frac{b^2}{4}R_{h,h} + \frac{b^2}{8}R_{z^2,z^2}cos\left(2\pi(4f_2)\frac{\tau}{2}\right) + \\
\frac{b^2}{4}R_{w,z,\underline{w},\underline{z}}cos\left(2\pi(2f_1+2f_2)\frac{\tau}{2}\right) + \frac{b^2}{4}R_{w,z,\underline{w},\underline{z}}cos\left(2\pi(2f_1-2f_2)\frac{\tau}{2}\right) + \\
\frac{a^2}{2}R_{z,z}cos(2\pi f_2\tau) + \frac{b^2}{8}R_{w,w}cos\left(2\pi(4f_1)\frac{\tau}{2}\right), & \alpha = 0 \\
\\
\left\{\frac{ab}{8}R_{w,w^2}e^{j(2\pi(-3f_1)\frac{\tau}{2})} + \frac{ab}{4}R_{w,h}e^{j(2\pi(f_1)\frac{\tau}{2})} + \right. \\
\frac{ab}{4}R_{z,\underline{w},\underline{z}}e^{j(2\pi(-f_1-2f_2)\frac{\tau}{2})} + \frac{ab}{4}R_{z,\underline{w},\underline{z}}e^{j(2\pi(-f_1+2f_2)\frac{\tau}{2})} + \\
\frac{ab}{4}R_{h,w}e^{j(2\pi(-f_1)\frac{\tau}{2})} + \frac{ab}{8}R_{w^2,w}e^{j(2\pi(3f_1)\frac{\tau}{2})} + \\
\left.\frac{ab}{4}R_{w,z,\underline{z}}e^{j(2\pi(f_1+2f_2)\frac{\tau}{2})} + \frac{ab}{4}R_{w,z,\underline{z}}e^{j(2\pi(f_1-2f_2)\frac{\tau}{2})}\right\}e^{j\phi_1}, & \alpha = f_1 \\
\\
\left\{\frac{ab}{8}R_{z,z^2}e^{j(2\pi(-3f_2)\frac{\tau}{2})} + \frac{ab}{4}R_{z,h}e^{j(2\pi(f_2)\frac{\tau}{2})} + \right. \\
\frac{ab}{4}R_{w,\underline{w},\underline{z}}e^{j(2\pi(2f_1-f_2)\frac{\tau}{2})} + \frac{ab}{4}R_{w,\underline{w},\underline{z}}e^{j(2\pi(-2f_1-f_2)\frac{\tau}{2})} + \\
\frac{ab}{4}R_{h,w}e^{j(2\pi(-f_2)\frac{\tau}{2})} + \frac{ab}{8}R_{z^2,z}e^{j(2\pi(3f_2)\frac{\tau}{2})} + \\
\left.\frac{ab}{4}R_{w,z,\underline{w}}e^{j(2\pi(2f_1+f_2)\frac{\tau}{2})} + \frac{ab}{4}R_{w,z,\underline{w}}e^{j(2\pi(-2f_1+f_2)\frac{\tau}{2})}\right\}e^{j\phi_2}, & \alpha = f_2 \\
\\
\left\{\frac{b^2}{4}R_{w,z,\underline{w},\underline{z}}e^{j(2\pi(-2f_2)\frac{\tau}{2})} + \frac{a^2}{4}R_{w,w} + \right. \\
\frac{b^2}{4}R_{w,z,\underline{w},\underline{z}}e^{j(2\pi(2f_2)\frac{\tau}{2})} + \frac{b^2}{8}R_{h,w^2}e^{j(2\pi(-2f_1)\frac{\tau}{2})} + \\
\left.\frac{b^2}{8}R_{w^2,h}e^{j(2\pi(2f_1)\frac{\tau}{2})}\right\}e^{j2\phi_1}, & \alpha = 2f_1 \\
\\
\left\{\frac{b^2}{4}R_{w,z,\underline{w},\underline{z}}e^{j(2\pi(-2f_1)\frac{\tau}{2})} + \frac{a^2}{4}R_{z,z} + \right. \\
\frac{b^2}{4}R_{w,z,\underline{w},\underline{z}}e^{j(2\pi(2f_1)\frac{\tau}{2})} + \frac{b^2}{8}R_{h,z^2}e^{j(2\pi(-2f_2)\frac{\tau}{2})} + \\
\left.\frac{b^2}{8}R_{z^2,h}e^{j(2\pi(2f_2)\frac{\tau}{2})}\right\}e^{j2\phi_2}, & \alpha = 2f_2 \\
\\
\left\{\frac{a^2}{4}R_{w,z}e^{j(2\pi(f_1-f_2)\frac{\tau}{2})} + \frac{a^2}{4}R_{z,w}e^{j(2\pi(f_2-f_1)\frac{\tau}{2})} + \right. \\
\frac{b^2}{4}R_{h,\underline{w},\underline{z}}e^{j(2\pi(-f_1-f_2)\frac{\tau}{2})} + \frac{b^2}{4}R_{w,z,\underline{h}}e^{j(2\pi(f_1+f_2)\frac{\tau}{2})} + \\
\frac{b^2}{8}R_{w^2,\underline{w},\underline{z}}e^{j(2\pi(3f_1-f_2)\frac{\tau}{2})} + \frac{b^2}{8}R_{w,z,\underline{w^2}}e^{j(2\pi(-3f_1+f_2)\frac{\tau}{2})} + \\
\left.\frac{b^2}{8}R_{z^2,\underline{w},\underline{z}}e^{j(2\pi(-f_1+3f_2)\frac{\tau}{2})} + \frac{b^2}{8}R_{w,z,\underline{z^2}}e^{j(2\pi(f_1-3f_2)\frac{\tau}{2})}\right\}e^{j(\phi_1+\phi_2)}, & \alpha = f_1+f_2 \\
\\
\left\{\frac{a^2}{4}R_{w,z}e^{j(2\pi(f_1+f_2)\frac{\tau}{2})} + \frac{a^2}{4}R_{z,w}e^{j(2\pi(-f_2-f_1)\frac{\tau}{2})} + \right. \\
\frac{b^2}{4}R_{h,\underline{w},\underline{z}}e^{j(2\pi(f_1+f_2)\frac{\tau}{2})} + \frac{b^2}{4}R_{w,z,\underline{h}}e^{j(2\pi(f_1-f_2)\frac{\tau}{2})} + \\
\frac{b^2}{8}R_{w^2,\underline{w},\underline{z}}e^{j(2\pi(3f_1+f_2)\frac{\tau}{2})} + \frac{b^2}{8}R_{w,z,\underline{w^2}}e^{j(2\pi(-3f_1-f_2)\frac{\tau}{2})} + \\
\left.\frac{b^2}{8}R_{z^2,\underline{w},\underline{z}}e^{j(2\pi(-f_1-3f_2)\frac{\tau}{2})} + \frac{b^2}{8}R_{w,z,\underline{z^2}}e^{j(2\pi(f_1+3f_2)\frac{\tau}{2})}\right\}e^{j(\phi_1-\phi_2)}, & \alpha = |f_1-f_2|
\end{cases}
$$

$$
\begin{cases}
\left\{\frac{b^2}{16}R_{w^2,z^2}e^{j(2\pi(2f_1-2f_2)\frac{\tau}{2})}+\frac{b^2}{4}R_{w,z,\underline{w},\underline{z}}+\right. & \\
\left.\frac{b^2}{16}R_{z^2,w^2}e^{j(2\pi(2f_2-2f_1)\frac{\tau}{2})}\right\}e^{j(2\phi_1+2\phi_2)}, & \alpha=2f_1+2f_2 \\
\left\{\frac{b^2}{16}R_{w^2,z^2}e^{j(2\pi(2f_1+2f_2)\frac{\tau}{2}}+\frac{b^2}{4}R_{w,z,\underline{w},\underline{z}}\right. & \\
\left.\frac{b^2}{16}R_{z^2,w^2}e^{j(2\pi(-2f_2-2f_1)\frac{\tau}{2}}\right\}e^{j(2\phi_1-2\phi_2)}, & \alpha=|2f_1-2f_2| \\
\left\{\frac{b^2}{8}R_{w^2,\underline{w},\underline{z}}e^{j(2\pi(f_1-f_2)\frac{\tau}{2}}+\frac{b^2}{8}R_{w,\underline{z},\underline{w^2}}e^{j(2\pi(f_2-f_1)\frac{\tau}{2}}\right\}e^{j(3\phi_1+\phi_2)}, & \alpha=3f_1+f_2 \\
\left\{\frac{b^2}{8}R_{z^2,w,\underline{z}}e^{j(2\pi(f_2-f_1)\frac{\tau}{2}}+\frac{b^2}{8}R_{w,z,\underline{z^2}}e^{j(2\pi(f_2-f_1)\frac{\tau}{2}}\right\}e^{j(\phi_1+3\phi_2)}, & \alpha=3f_2+f_1 \\
\left\{\frac{ab}{8}R_{w,w^2}e^{j(2\pi(-f_1)\frac{\tau}{2})}+\frac{ab}{8}R_{w^2,w}e^{j(2\pi(f_1)\frac{\tau}{2})}\right\}e^{j3\phi_1}, & \alpha=3f_1 \\
\left\{\frac{ab}{8}R_{z,z^2}e^{j(2\pi(-f_2)\frac{\tau}{2})}+\frac{ab}{8}R_{z^2,z}e^{j(2\pi(f_2)\frac{\tau}{2})}\right\}e^{j3\phi_2}, & \alpha=3f_2 \\
\left\{\frac{b^2}{8}R_{w^2,\underline{w},\underline{z}}e^{j(2\pi(f_1+f_2)\frac{\tau}{2})}+\frac{b^2}{8}R_{w,z,\underline{w^2}}e^{j(2\pi(-f_1-f_2)\frac{\tau}{2})}\right\}e^{(3\phi_1-\phi_2)}, & \alpha=|3f_1-f_2| \\
\left\{\frac{b^2}{8}R_{z^2,\underline{w},\underline{z}}e^{j(2\pi(f_1+f_2)\frac{\tau}{2}}+\frac{b^2}{8}R_{w,z,\underline{z^2}}e^{j(2\pi(-f_1-f_2)\frac{\tau}{2}}\right\}e^{(3\phi_2-\phi_1)}, & \alpha=|3f_2-f_1| \\
\frac{b^2}{16}R_{w^2,w^2}e^{j(4\phi_1)}, & \alpha=4f_1 \\
\frac{b^2}{16}R_{z^2,z^2}e^{j(4\phi_2)}, & \alpha=4f_2 \\
0 & \text{otherwise and } \alpha>0
\end{cases}
\tag{5.54}
$$

where $R_{\eta,\beta,\underline{\gamma}}=R_{\eta,\beta,\underline{\gamma}}(\tau)\triangleq E\left[\eta(t+\tau/2)\beta(t+\tau/2)\gamma(t-\tau/2)\right]$, $R_{\eta,\beta,\underline{\gamma},\underline{\zeta}}=R_{\eta,\beta,\underline{\gamma},\underline{\zeta}}(\tau)\triangleq E\left[\eta(t+\tau/2)\beta(t+\tau/2)\gamma(t-\tau/2)\zeta(t-\tau/2)\right]$ and $h(t)\triangleq z^2(t)+w^2(t)-\frac{2}{b}\langle y(t)\rangle$. It is concluded from the above equation that in contrast to the independent modulating signals which are usually studied in the literature (and presented briefly in previous sections) special attention ought to be paid to the practical consideration of nonlinear systems. Appearance of several peaks causes the detection of nonlinearity to become more difficult. Particularly, the existence of more than two harmonics at the input of the system seriously affects the efficacy of the cyclic correlation analysis.

If $w(t)$ and $z(t)$ are dependent then the nonzero slices in $R^{\alpha}_{2y_0}(0)$ can be searched for frequency and phase coupling. In the case of independent zero mean modulating

signals all slices at $\alpha = 3f_1 + f_2, \alpha = 3f_2 + f_1, \alpha = |3f_1 - f_2|, \alpha = |3f_2 - f_1|$ become zero, but slices at $\alpha = f_1 + f_2, \alpha = |f_1 - f_2|, \alpha = 2f_1 + 2f_2, \alpha = |2f_1 - 2f_2|$ still exist (though with reduced magnitude) and can be used for phase and frequency coupling detection. As before, if these slices also fade in $R^{\alpha}_{2y_0}(0)$ then the existence of separate quadratic nonlinear systems is corroborated.

5.8.3 Detection of Higher Order Nonlinearities

If the nonlinear system is a third order system of the form $y(t) = ax(t) + bx^2(t) + cx^3(t)$ then self phase and self frequency coupling can be sought in the cyclic mean domain by using the following equation,

$$R_{1y_0}(\alpha) = \begin{cases} \left(am_z + \frac{3c}{4}m_{z^3}\right) e^{j\phi_0}, & \alpha = f_0 \\ \frac{b}{2}m_{z^2} e^{j2\phi_0}, & \alpha = 2f_0 \\ \frac{c}{4}m_{z^3} e^{j3\phi_0}, & \alpha = 3f_0 \\ 0 & \text{otherwise and } \alpha \geq 0 \end{cases} \tag{5.55}$$

Similarly, equation (5.56) presents the relevant formula for phase and frequency coupling detection.

$$R_{1y_0}(\alpha) = \begin{cases} \left(\frac{3c}{2}m_{w,z^2} + am_w + \frac{3c}{4}m_{w^3}\right)e^{j\phi_1}, & \alpha = f_1 \\ \left(\frac{3c}{2}m_{w,z^2} + am_z + \frac{3c}{4}m_{z^3}\right)e^{j\phi_2}, & \alpha = f_2 \\ bm_{w,z}e^{j(\phi_1+\phi_2)}, & \alpha = f_1 + f_2 \\ bm_{w,z}e^{j(\phi_1-\phi_2)}, & \alpha = |f_1 - f_2| \\ \frac{b}{2}m_{w^2}e^{j2\phi_1}, & \alpha = 2f_1 \\ \frac{b}{2}m_{z^2}e^{j2\phi_2}, & \alpha = 2f_2 \\ \frac{3c}{4}m_{w^2,z}e^{j(2\phi_1+\phi_2)}, & \alpha = 2f_1 + f_2 \\ \frac{3c}{4}m_{w^2,z}e^{j(2\phi_1-\phi_2)}, & \alpha = |2f_1 - f_2| \\ \frac{3c}{4}m_{z^2,w}e^{j(2\phi_2+\phi_1)}, & \alpha = 2f_2 + f_1 \\ \frac{3c}{4}m_{z^2,w}e^{j(2\phi_2-\phi_1)}, & \alpha = |2f_2 - f_1| \\ \frac{c}{4}m_{w^3}e^{j3\phi_1}, & \alpha = 3f_1 \\ \frac{c}{4}m_{z^3}e^{j3\phi_2}, & \alpha = 3f_2 \\ 0 & \text{otherwise and } \alpha \geq 0 \end{cases} \tag{5.56}$$

If modulating signals are zero mean, the cyclic correlation tool should be selected. However, derivation of the associated formula in this case as well as for higher order nonlinearities is very tedious and beyond the scope of this study. Furthermore, by virtue of the fact that the useful information in the variability signals is limited to $f < 0.5Hz$ and since nonlinearity detection in the normal respiratory rate between 7 to 15 breaths per minute is the objective, investigation of higher order nonlinearities does not seem to be necessary in this study.

5.9 Simulation Results

In this section it will be shown how second order nonlinearity can be detected in the synthetic data by cyclic mean and cyclic correlation analysis. Both self phase and self frequency coupling, and phase and frequency coupling will be examined for zero mean

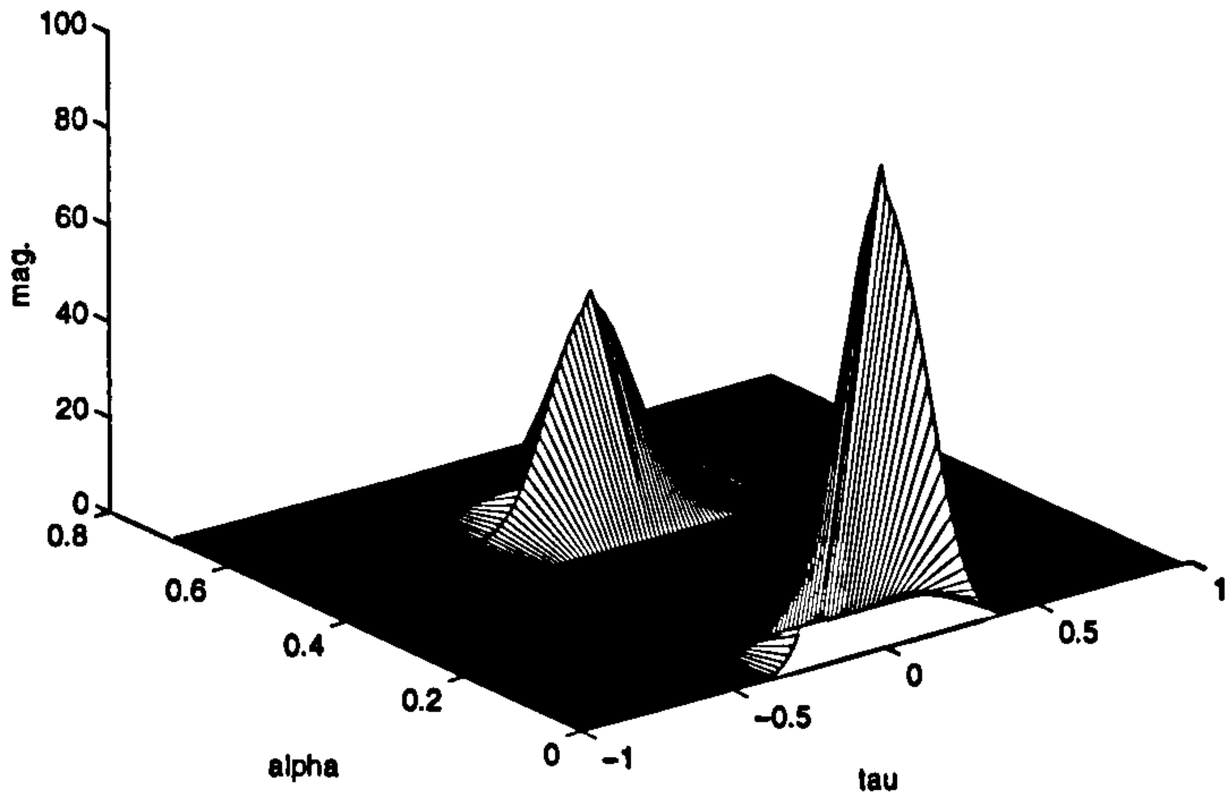


Figure 5.3: Magnitude of the cyclic correlation of signal $sin(2\pi 0.25t)$.

and nonzero mean signals. However, it will be useful if, prior to investigation of the slices, a plot of the two dimensional cyclic correlation of a sinusoidal signal is presented first.

Figure 5.3 illustrates the magnitude of the cyclic correlation of the signal $sin(2\pi 0.25t)$. The presence of the correlation at $\alpha = 0.5Hz$ indicates the existence of a harmonic at $f = 0.25Hz$. Although the cyclic correlation is a two dimensional function of α and τ, lag $\tau = 0$, due to the simplicity of the resulting statistic, was used here for nonlinearity detection.

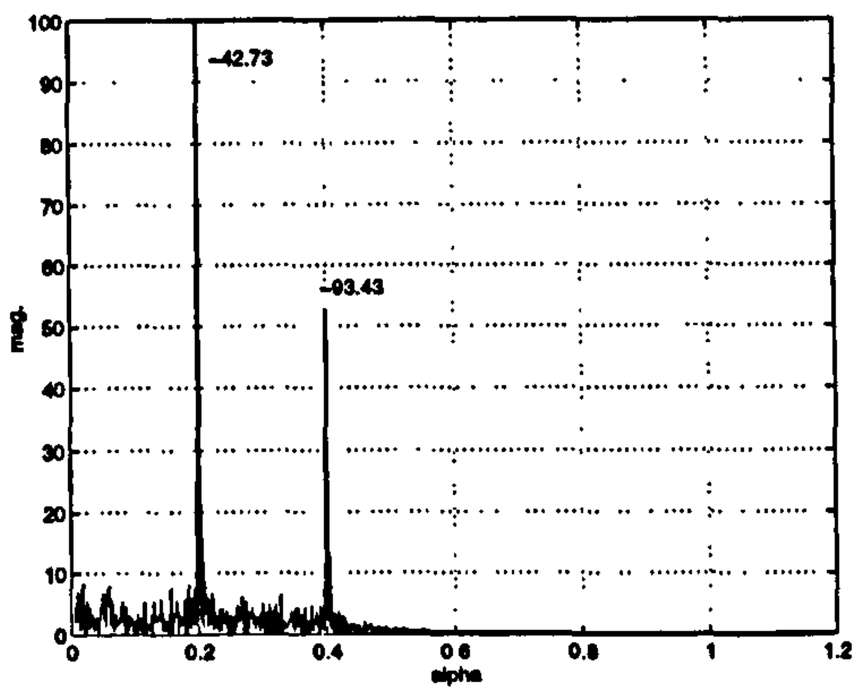
Figures 5.4(a) through 5.4(h) demonstrate the detection of nonlinearity by using cyclic mean ($R_{1y0}(\alpha)$) and cyclic correlation ($R^{\alpha}_{2y0}(0)$) analysis. The left hand column of the figure plots the cyclic mean estimations while the right hand column illustrates the corresponding cyclic correlation estimations. Since the components around $\alpha = 0$ do not have any benefit in the current study only the range $0.02Hz < \alpha < 1.2Hz$ has been covered in the figures.

For the cyclic estimations of Figs. 5.4(a) and 5.4(b) signal $x(t) = (A+d(t))sin(2\pi 0.2t)$ was passed through the system $y(t) = x(t) + x^2(t)$. The modulating signal $d(t)$ was created by filtering a zero mean uniform distributed white noise signal with cut off frequency $0.05Hz$. The amplitude of $d(t)$ was adjusted to obtain a 35% modulation index. To simulate the effect of the background noise a zero mean lowpass Gaussian

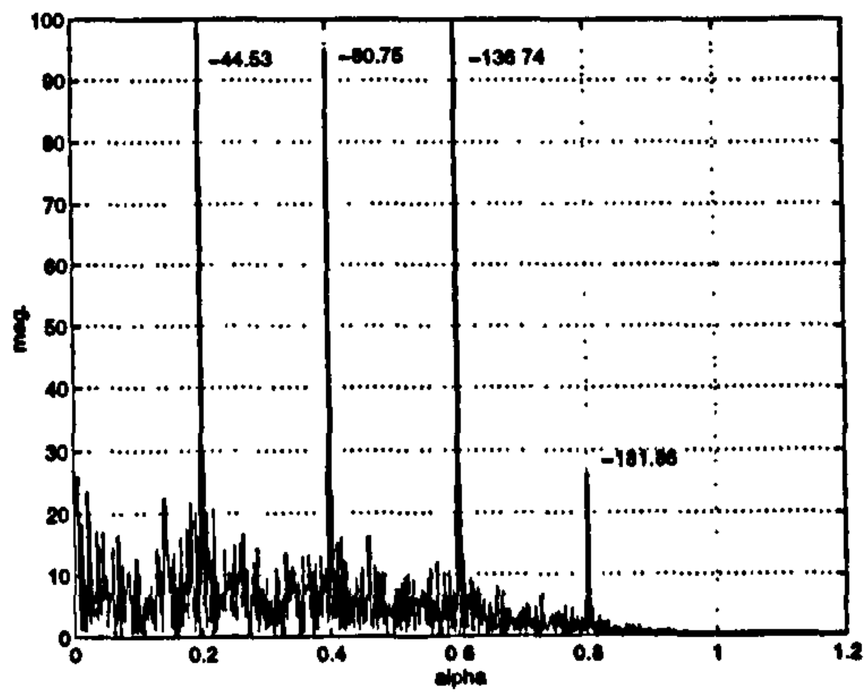
distributed process with cut off frequency $0.4Hz$ was added to $y(t)$. Signal to noise ratio of the output signal was adjusted to $10dB$. Cyclic mean and cyclic correlation were then estimated for 900 samples of the data. The magnitude of the cyclic mean estimator is shown in Fig. 5.4(a). Two peaks at $\alpha = 0.2Hz$ and $\alpha = 0.4Hz$ clearly indicate the presence of the self frequency coupling. The phase at each peak was also estimated and added to the figures at its location. The estimated phase values in Fig. 5.4(a) confirm the existence of self phase coupling. Interestingly, the phase values exhibit more deviation from their true ratio than the estimation of the frequencies. This can be explained based on the fact that variance of the frequency estimator is of $O(T^{-3})$ whereas the variance of the phase estimator is of $O(T^{-1})$. The result of the cyclic correlation along with the phase estimations is shown in Fig. 5.4(b). Again self phase and self frequency coupling can be assessed by the peak-picking procedure and phase analysis. The estimated phase and frequency values are equivalent with those predicted by equation (5.43).

If a zero mean modulating signal ($A = 0$ in the previous example) is passed through a quadratic nonlinear system the result will be different. This is shown in Figs. 5.4(c) and 5.4(d) for the cyclic mean and cyclic correlation estimation of the nonlinear system $y(t) = x(t)+2x^2(t)$. Although one peak can be observed at $f = 0.4Hz$ in the cyclic mean domain of Fig. 5.4(c), it might not be considered as evidence of nonlinearity (single component). However, self phase and self frequency coupling can easily be distinguished by the cyclic correlation analysis of Fig. 5.4(d). The presence of two peaks at $0.4Hz$ and $0.8Hz$ with coupled phases clearly indicates the existence of a quadratic system. The predicted peaks at $0.2Hz$ and $0.6Hz$ (equation 5.43) are in fact buried in the corrupting noise and cannot be seen in the cyclic correlation plot.

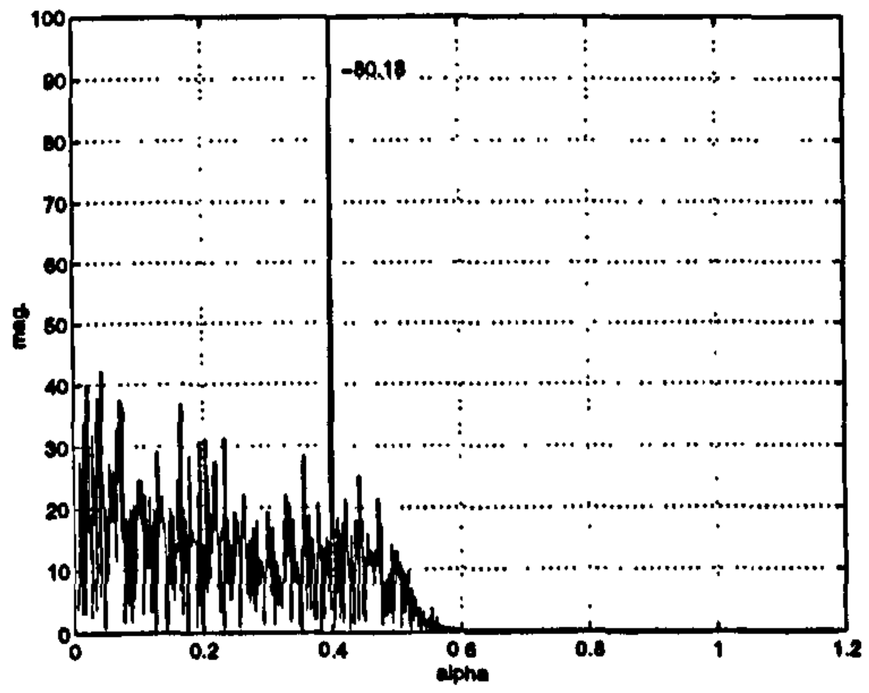
The number of the peaks in the cyclic domains tremondously increases if more than a single harmonic is fed to a nonlinear system (phase and frequency coupling detection). This is shown in Figs. 5.4(e) and 5.4(f) for nonzero mean amplitude modulated signals and in Figs. 5.4(g) and 5.4(h) for zero mean signals. Here, two dependent harmonics with amplitudes $A + d(t)$ and frequencies $f_1 = 0.1Hz$ and $f_2 = 0.25Hz$ with zero phase difference for Figs. 5.4(e) and 5.4(f) and with $\pi/4$ phase difference for Figs. 5.4(g) and 5.4(h) were employed. Now phase and frequency coupling can be distinguished by the peak-picking procedure and phase estimation. The estimated



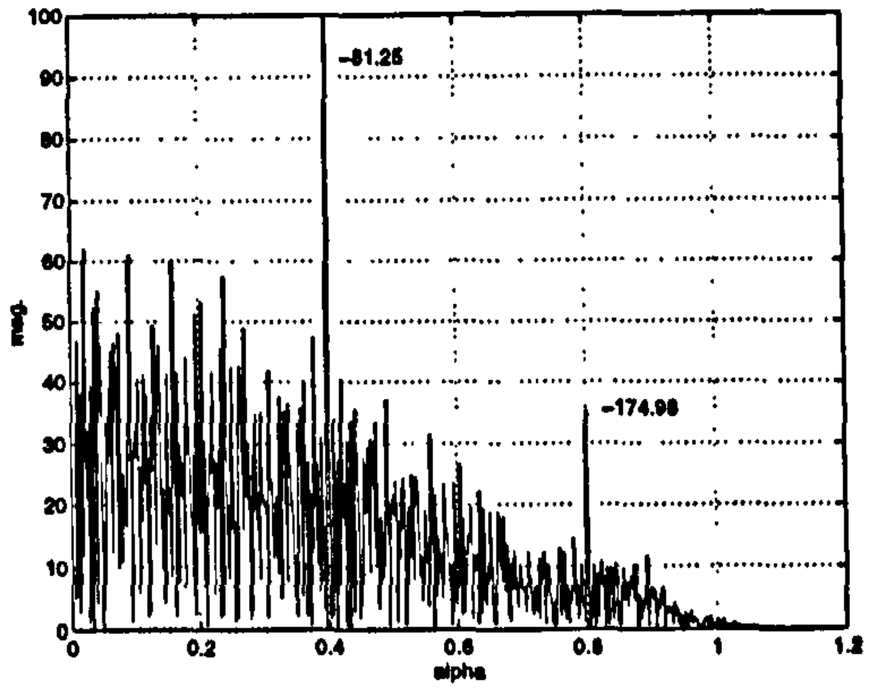
(a)



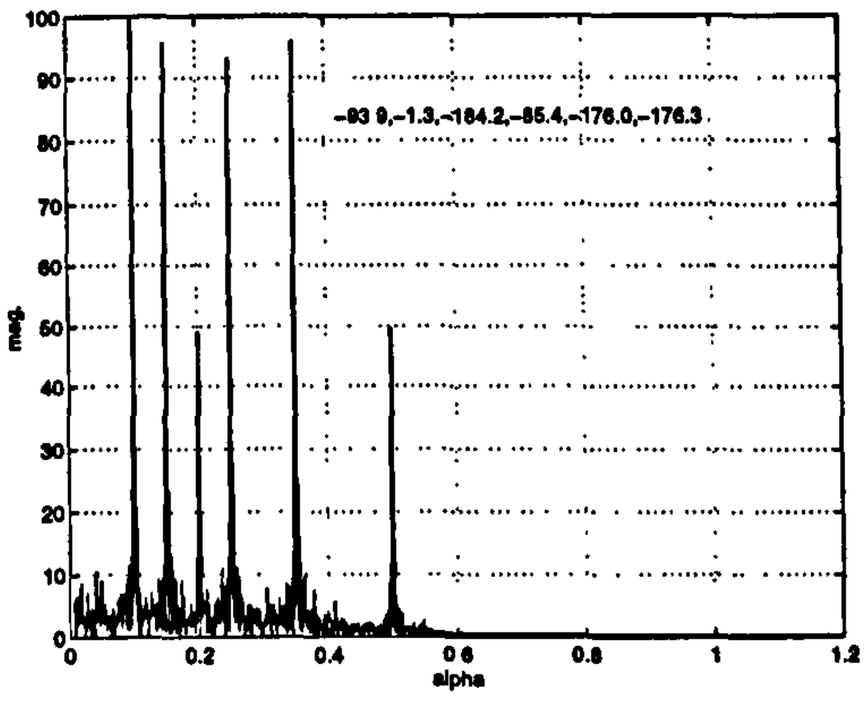
(b)



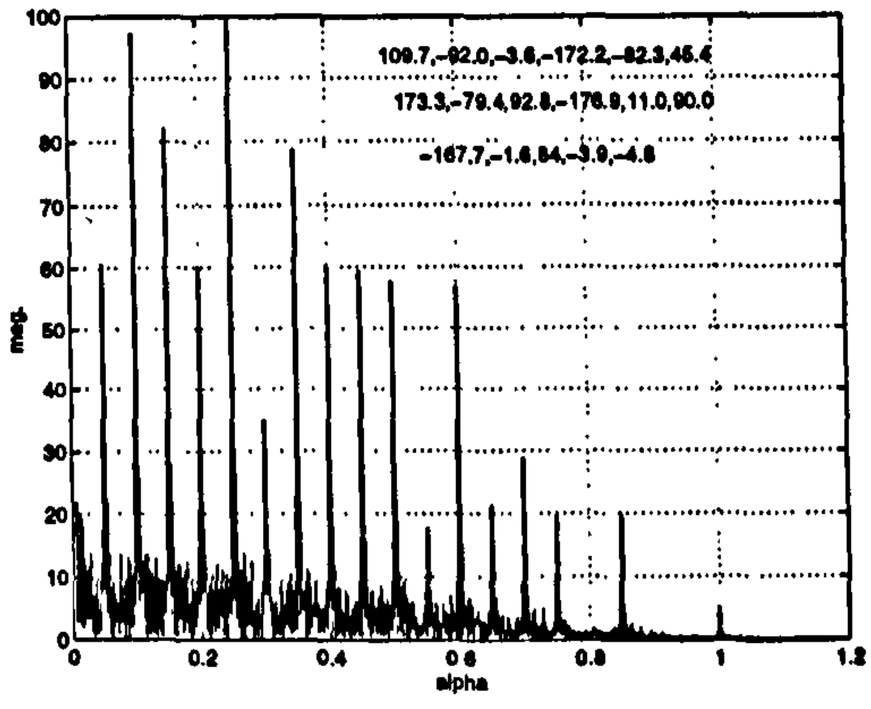
(c)



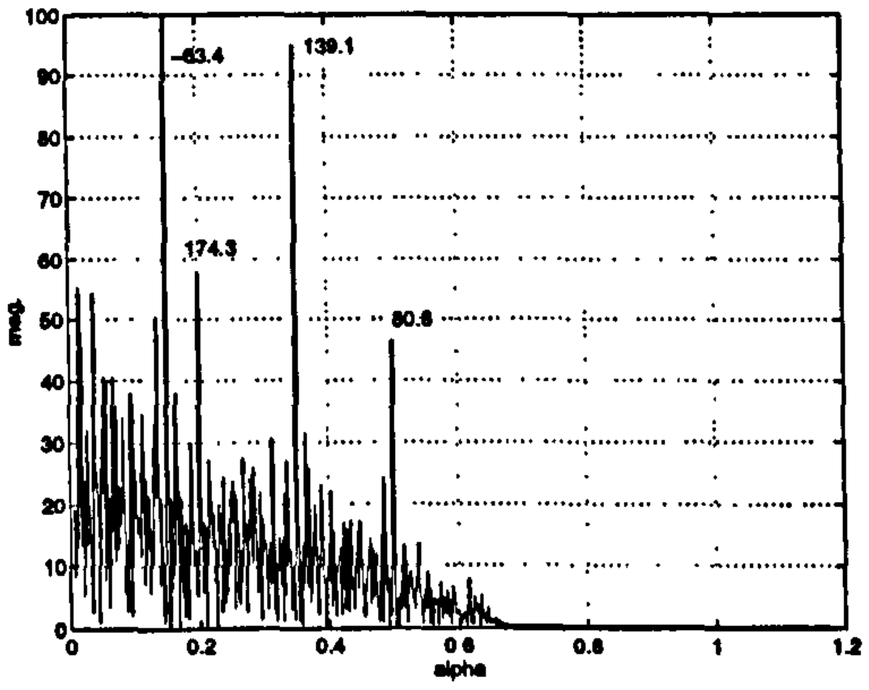
(d)



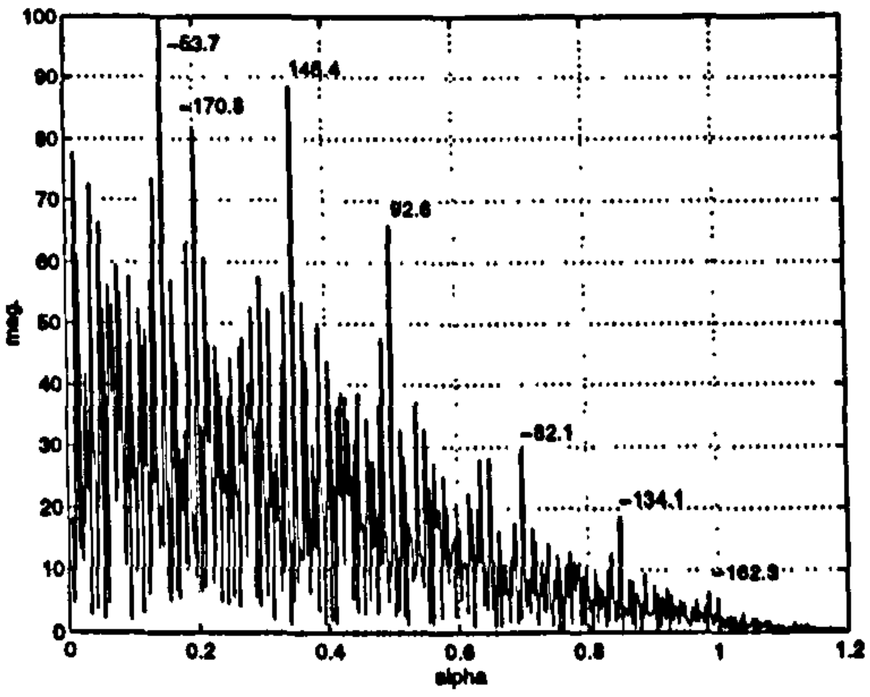
(e)



(f)



(g)



(h)

Figure 5.4: Normalized magnitude of the cyclic mean (left hand column) and cyclic correlation (right hand column) of the simulated signals. For the descriptions of the figures refer to the text.

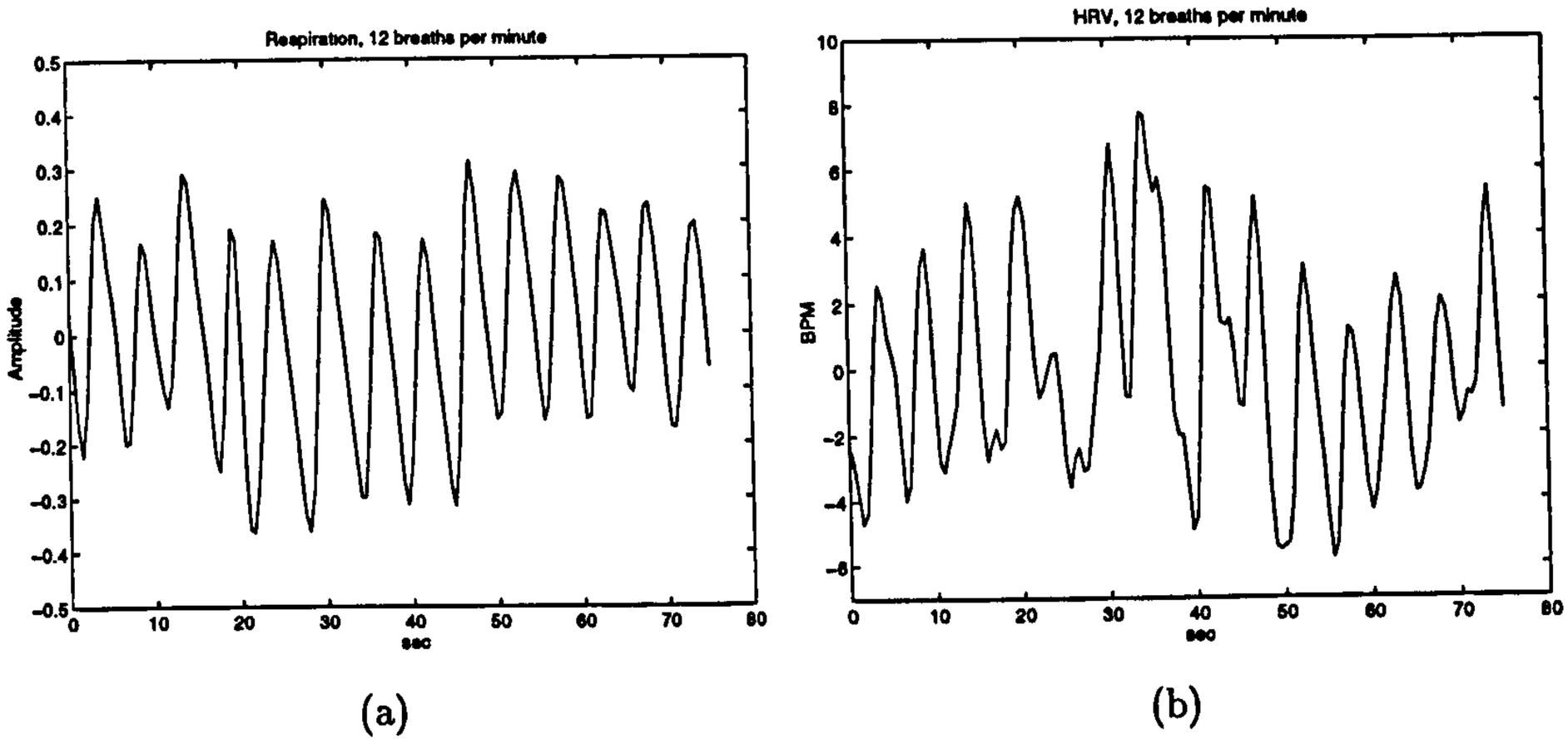
phase [7] and frequency values in this case are equivalent with those predicted by equations (5.50) and (5.54). Obviously detection of phase and frequency coupling is more difficult than self phase and self frequency detection. It is also worthwhile noting that due to the background noise and finite length of data, peaks in the case of zero mean signals are less pronounced than the nonzero mean case.

5.10 Experimental Results

As described throughout this chapter, the idea for nonlinearity detection in HRV and BPV is to inject a sinusoidal excitation, *via* the respiratory activity, to the neuro-cardiovascular system and then check whether any higher order harmonic (self frequency coupling) appears or not. If self phase coupling is also observed simultaneously then a nonlinear system in the form of Fig. 5.1 can be assumed. Otherwise, a Volterra type nonlinearity should be considered. Further evidence for the presence of nonlinearity can be given by detecting the frequency coupling between the LF and HF components. Likewise if frequency coupling is accompanied by phase coupling then the simple model of Fig. 5.1 can be assumed otherwise the Volterra type nonlinearity should be employed for HRV and BPV modelling. Clearly, the appropriate tool for this sinusoidal test is cyclostationary analysis of the HRV and BPV signals as presented in the previous sections.

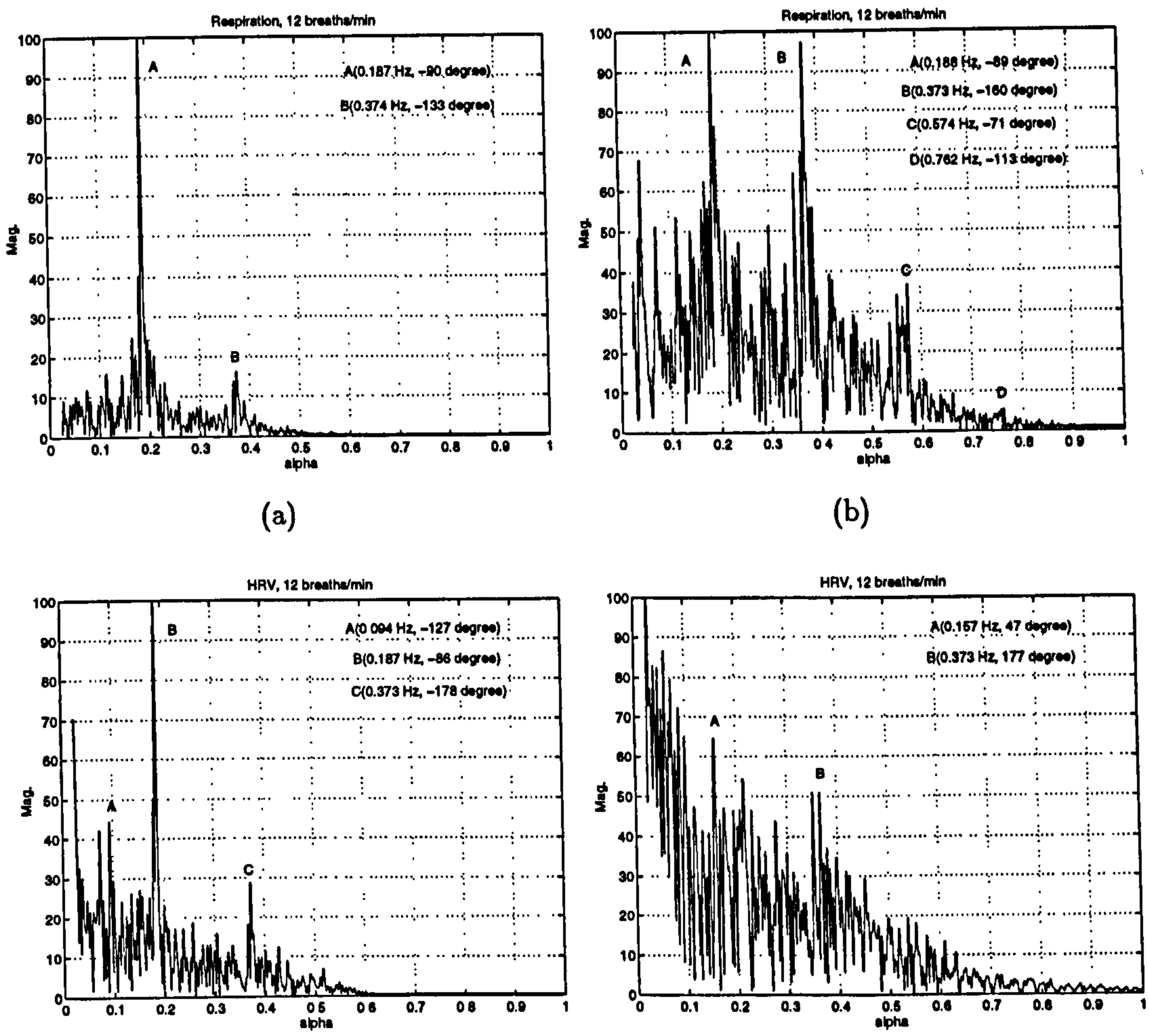
For the experimental study, the computer was programmed to produce auditory tones with constant intervals in each session and with different rates in different sessions. Respiratory movement, *via* the strain gauge plethysmography method, ECG, and noninvasive blood pressure, through a Finapres machine, were collected with sampling frequency $500Hz$ from seven healthy subjects aged between 21 and 29. The subjects were instructed to initiate a breath with each tone whilst trying to keep a sinusoidal respiratory pattern in the resting supine position. Data were collected for the range 15,12,10,8 breaths per minute from each subject for 8 minutes with 3 minutes resting gap following each session. HRV was extracted from the ECG using the KLPF algorithm with parameters $f_c = 0.5Hz$, $\beta = 4.5$, $d = 5$, $N = 250$ ($2Hz$ sampling frequency). The same filter was employed to obtain the respiratory signal from the

[7] The estimated phase values in Figs. 5.4(e) and 5.4(f) from left to right correspond to the observed peaks.



(a) (b)

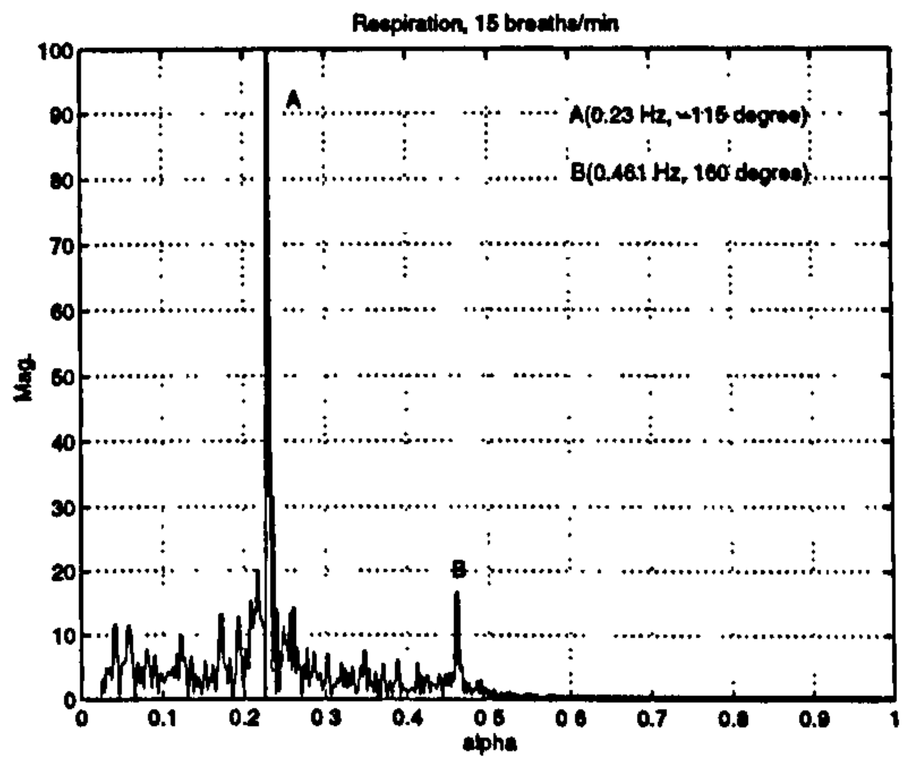
Figure 5.5: (a) Respiratory signal with 12 breaths/min, (b) the corresponding HRV signal.



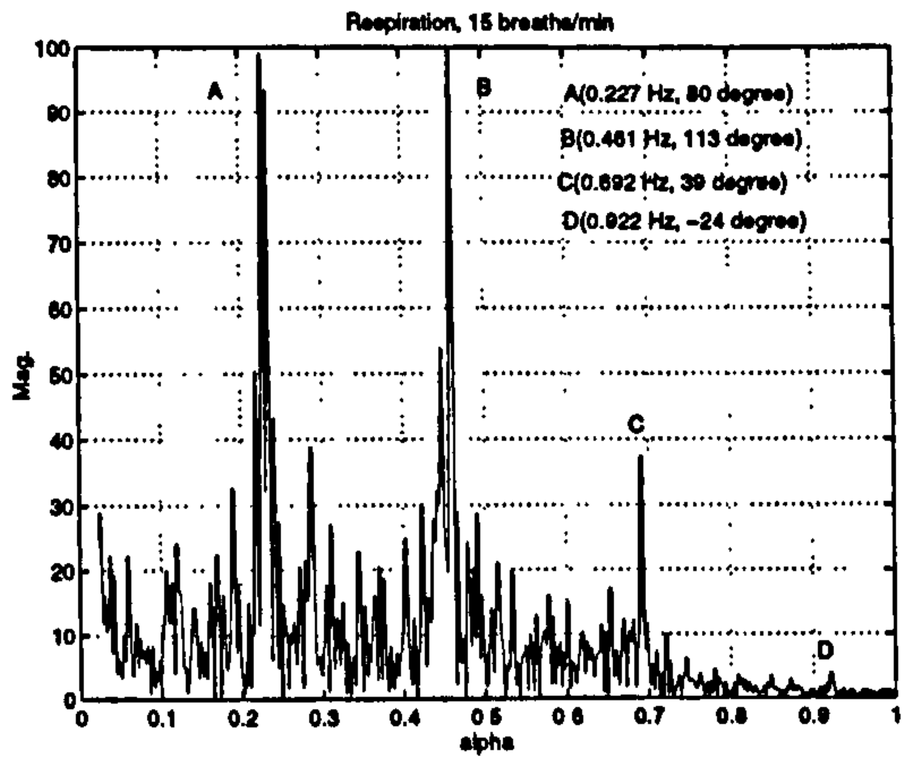
(a) (b)

(c) (d)

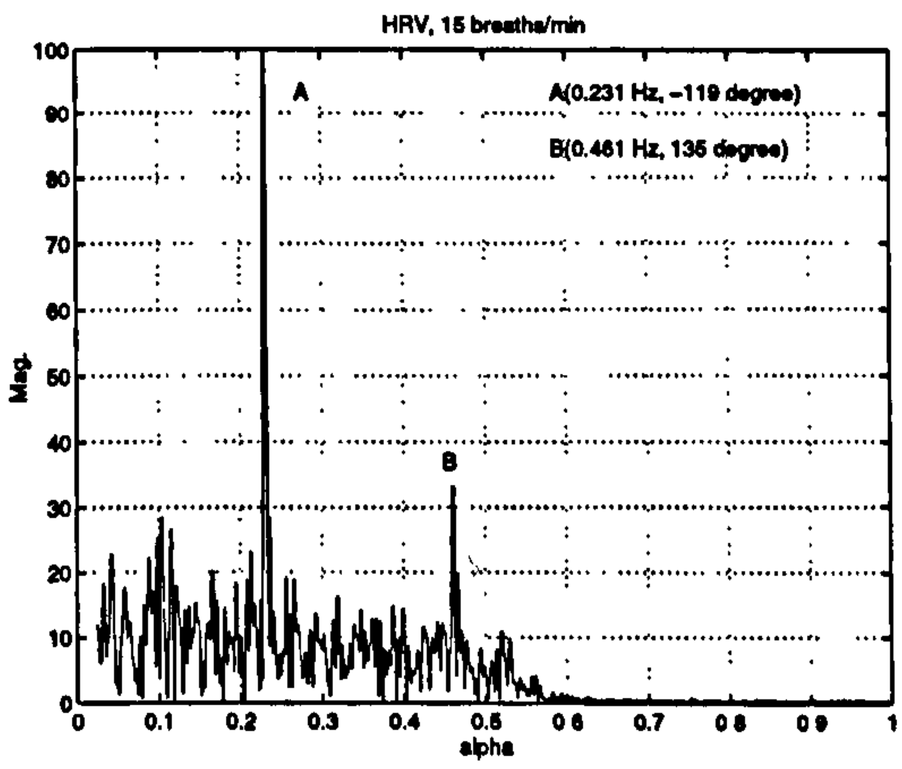
Figure 5.6: Cyclic mean (left hand column) and cyclic correlation (right hand column) of respiration (top panel) and HRV (bottom panel) in 12 breaths/min experiment (subject 1).



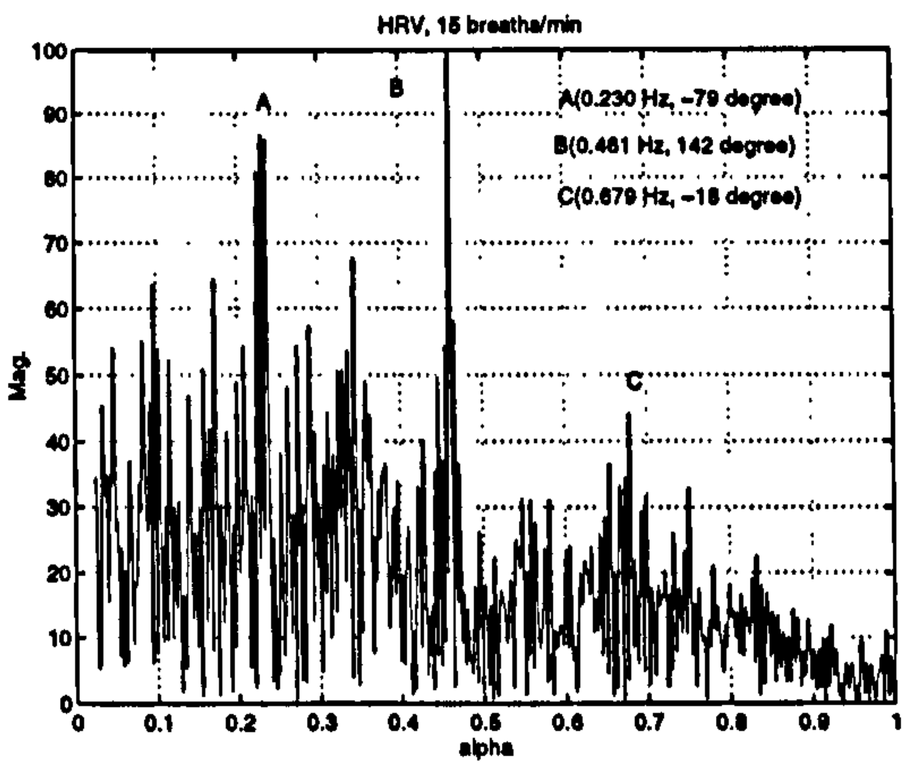
(a)



(b)



(c)



(d)

Figure 5.7: Cyclic mean (left hand column) and cyclic correlation (right hand column) of respiration (top panel) and HRV (bottom panel) in 15 breaths/min experiment (subject 2).

chest movement, and the BPV signal from the instantaneous blood pressure. A typical illustration of the variability signals for one subject in the 12 breaths per minute experiment is shown in Fig. 5.5.

For the cyclic analysis, 4 minutes (the stable sinusoidal part) of the extracted signals, equivalent to 480 samples, were selected. Cyclic mean and cyclic correlation of the HRV and BPV together with the respiratory signal were estimated (2^{14} points FFT) for each breathing rate. The existing harmonics in the variability signals were explored by finding the striking peaks in the cyclic plots. The phase value at each specific peak was estimated afterwards and added to the plots for further comparisons.

The cyclic mean plots of the respiratory and the HRV signals for one subject in

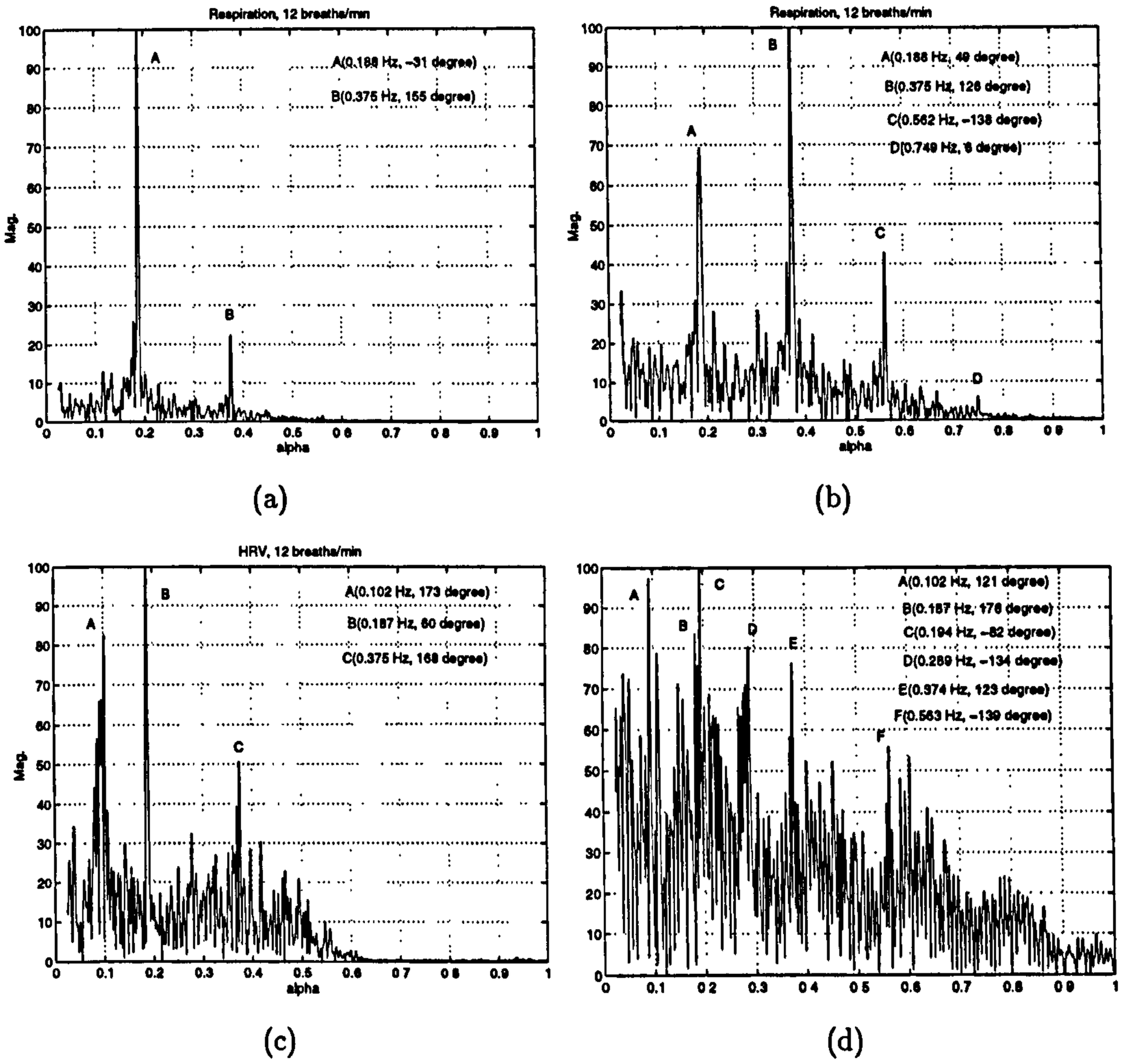


Figure 5.8: Cyclic mean (left hand column) and cyclic correlation (right hand column) of respiration (top panel) and HRV (bottom panel) in 12 breaths/min experiment (subject 2).

the 12 breaths/min experiment are displayed in Fig. 5.6. A dominant peak in the cyclic mean plot of Fig. 5.6(a) shows the presence of a major sinusoidal component in the respiratory signal. In an ideal case, this peak should be the only prominent peak in the cyclic mean domain since we wish to have a pure sinusoidal excitation. In actual applications, however, higher order components of the main respiratory component will appear in the cyclic plots, e.g. peak B in Fig. 5.6(a). The presence of these components in turn means that the respiratory signal deviates from being a single sinusoid either due to the nonlinear operation of the chest cage on the driving respiratory excitation or deviation of the central respiratory oscillator from an ideal sinusoid (nonlinearity in the central respiratory oscillator) or both. Apart from their origins, the presence of these higher order harmonics complicates the detection of nonlinearity in HRV and BPV. This is because if nonlinear systems are involved in producing the HRV and BPV, then

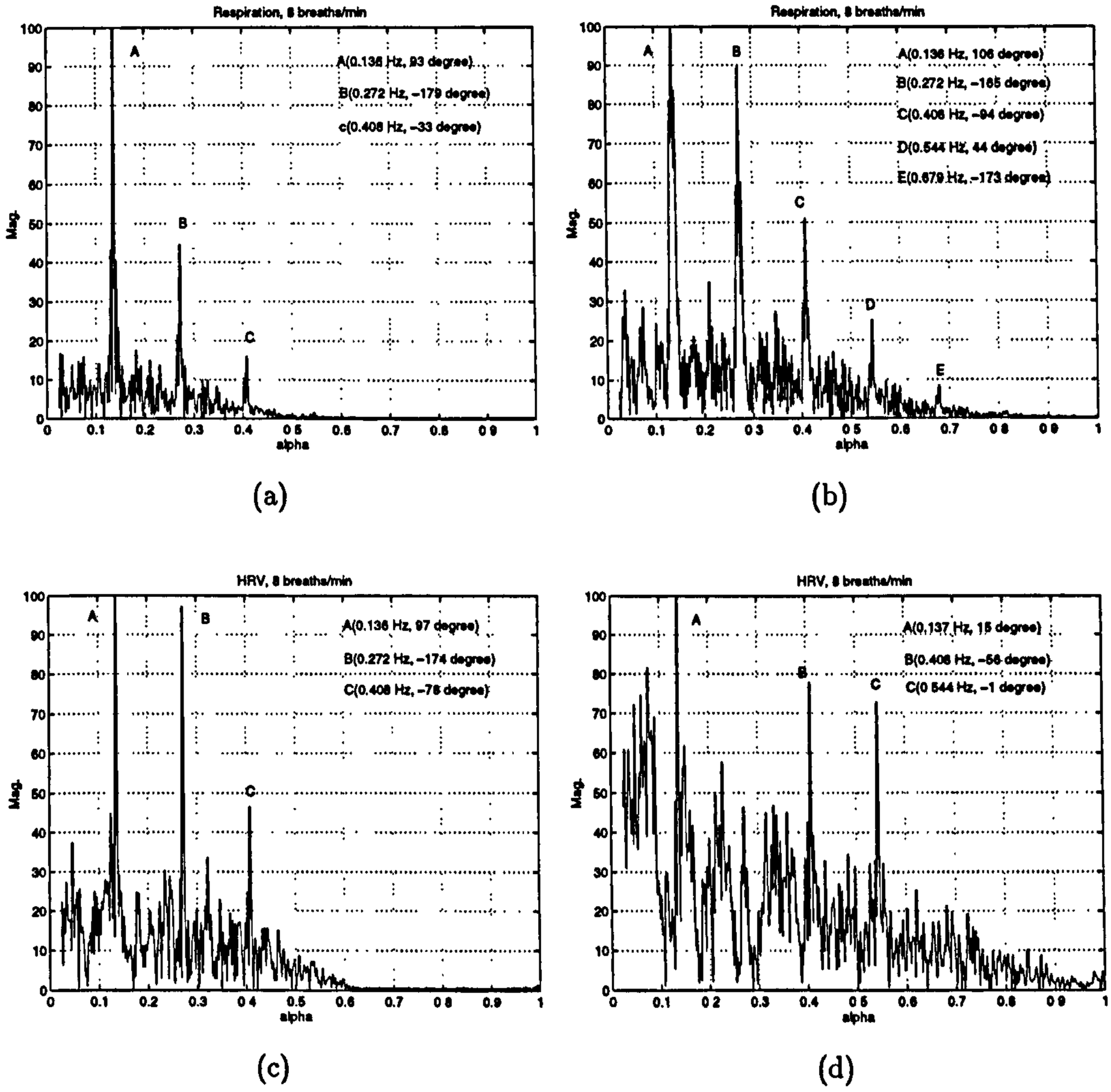


Figure 5.9: Cyclic mean (left hand column) and cyclic correlation (right hand column) of respiration (top panel) and HRV (bottom panel) in 8 breaths/min experiment (subject 2).

the higher order components of the respiratory signal will interfere with the emerging components of this nonlinear operation. Therefore, more attention should be paid to the detection of the harmonic coupling in HRV and BPV.

Three major components can be observed in the cyclic mean plot of the HRV in Fig. 5.6(c). The larger peak, labeled B, shows the dominance of the main respiratory component in the HRV. The self frequency coupling of this component is confirmed by the presence of the peak labeled by C at frequency $0.373Hz$. A larger ratio of the second order harmonic to the main respiratory component in the cyclic mean plot of the HRV ($\frac{C}{B}$ in Fig. 5.6(c)) compared to the respiratory plot ($\frac{B}{A}$ in Fig. 5.6(a)) indicates that a nonlinear system has contributed in producing the HRV. Otherwise the lowpass nature of the HRV (Saul *et. al.*, 1989; Hirsch & Bishop, 1981) should have decreased

the magnitude of the second order harmonic rather than causing it to increase.

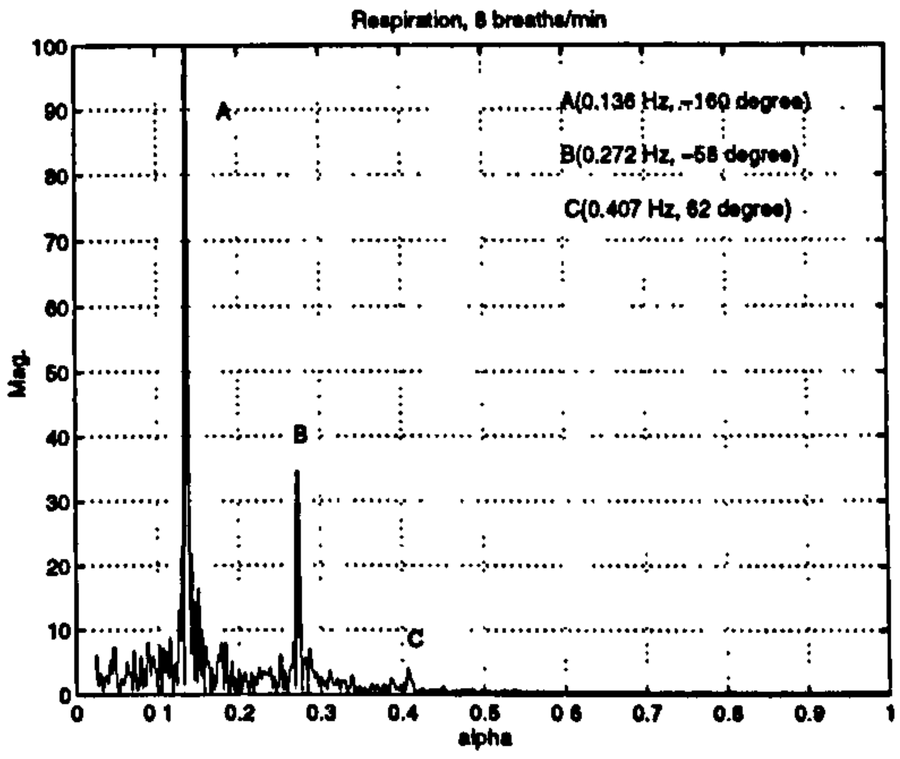
Unlike the self frequency coupling, no evidence of the self phase coupling can be observed from the estimated phase values. This can be suggestive of the presence of a finite memory nonlinear system in producing the heart rate and blood pressure fluctuations.

The results described above were also observed in the other subjects at the examined breathing rates, although the strength of the nonlinearity differed from subject to subject. Interestingly, the amount of nonlinearity increased with decreasing the breathing rate. This is shown in Figs. 5.7 through 5.9 for another subject in different breathing rates. As can be seen, by decreasing the breathing rate from 15 to 12 and then to 8, the ratio of the higher order components to the main respiratory component of the HRV in the cyclic mean plots increases more than the associated value in the respiratory signals, indicating that the higher order harmonics have been added to the HRV due to nonlinearity.

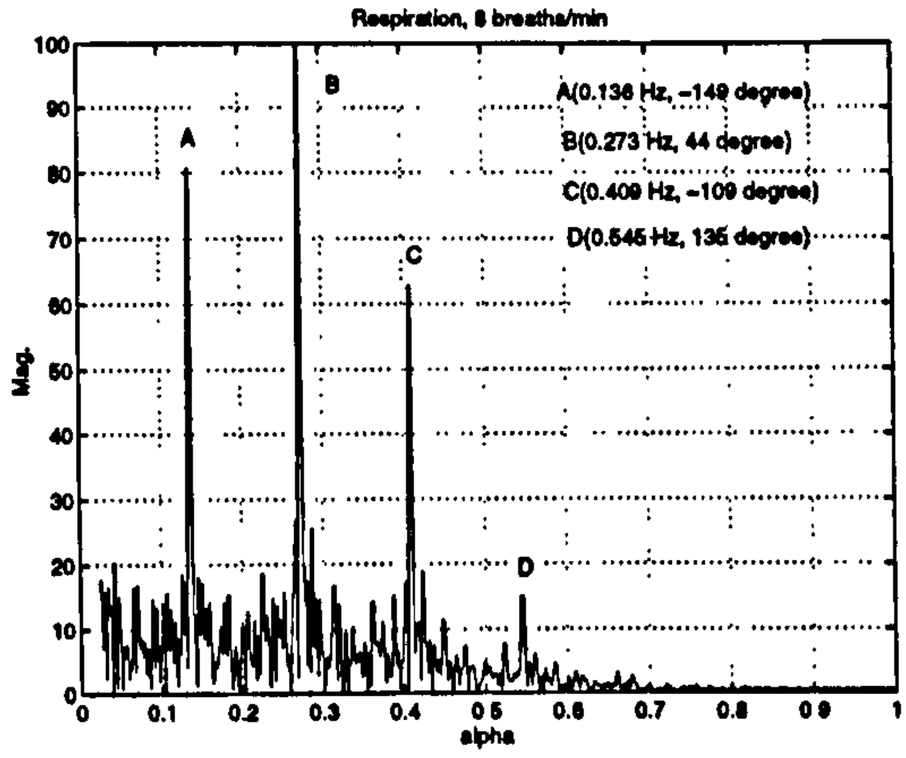
The presence of the harmonic coupling in the BPV was similar to the HRV but generally with less increase in the second order harmonics in the cyclic plots. Figure 5.10 illustrates the presence of the self frequency coupling in the BPV of another subject who was breathing with the rate of 8 per minute. In addition to the second order harmonic (peak B in Fig. 5.10(c)) a striking peak at the 3rd order harmonic of the respiratory signal (peak C in Fig. 5.10(c) strongly suggests the presence of a nonlinear system. Unfortunately, the cyclic correlation plots were too noisy in this set of data to be of any major use.

Out of seven subjects, only two of them showed a prominent LF component suitable for the phase and frequency coupling detection. The reason for having a low LF amplitude in this set of experiments might lie in the enhanced vagal stimulation in the metronome breathing experiment as suggested by some authors (Pagani *et. al.*, 1986; Malliani, *et. al.*, 1992). The cyclic plots of two subjects with frequency coupling between the LF and HF components are displayed in Figs. 5.11 and 5.12.

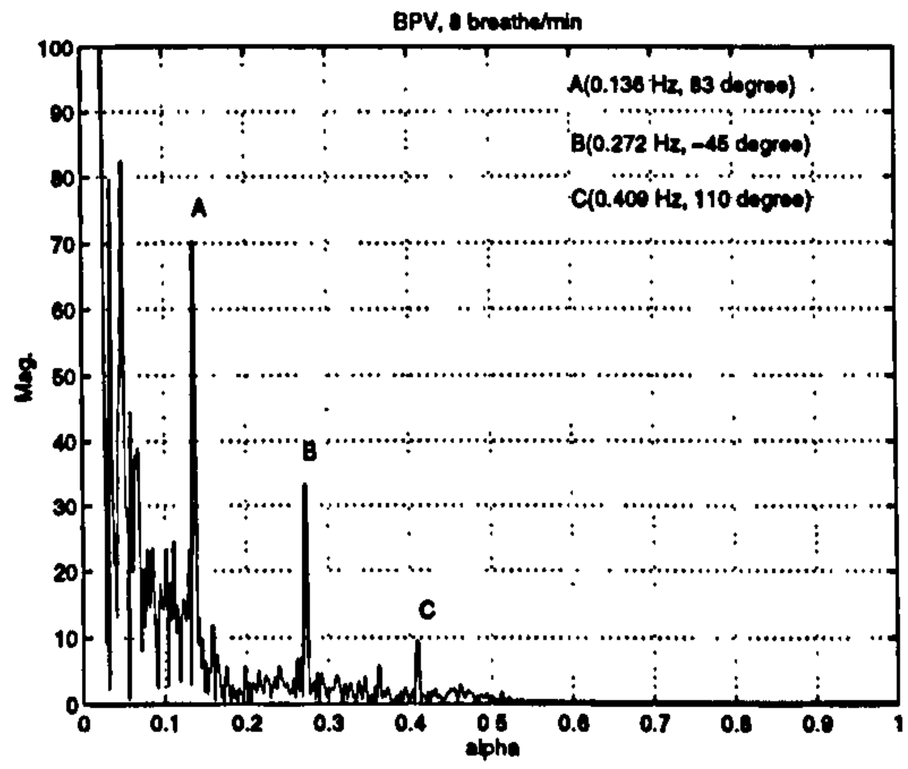
Figure 5.11(a),(b) illustrate the cyclic mean and cyclic correlation of the HRV of one of these subjects in the 12 breaths/min experiment. Peak A at $0.102Hz$ and peak C at $0.187Hz$ in Fig. 5.11(a) represent the presence of the LF and the HF components,



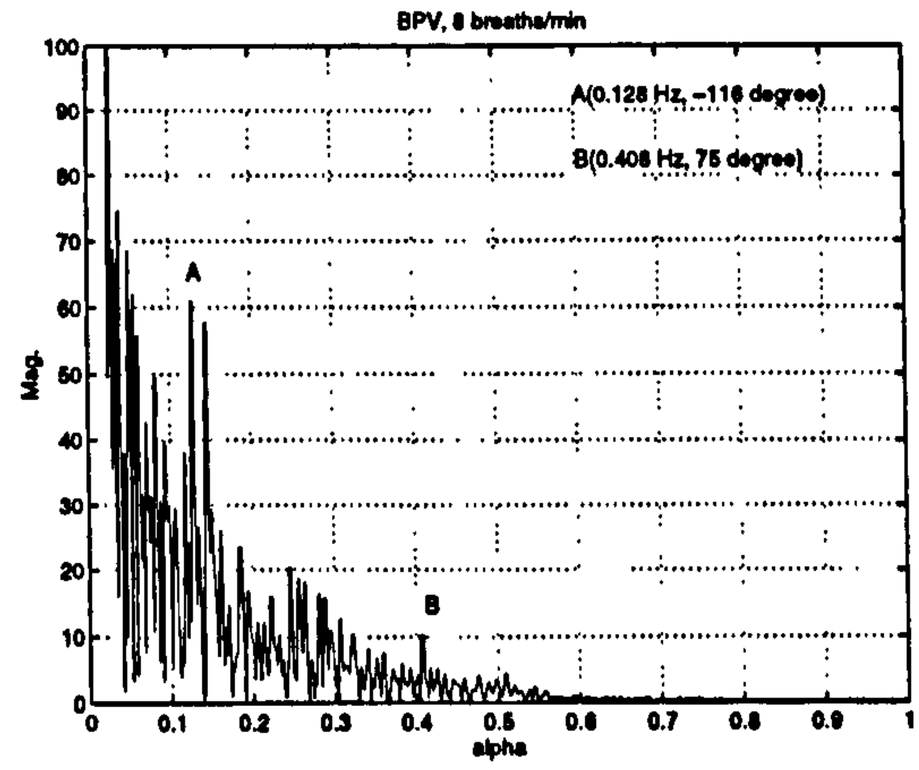
(a)



(b)

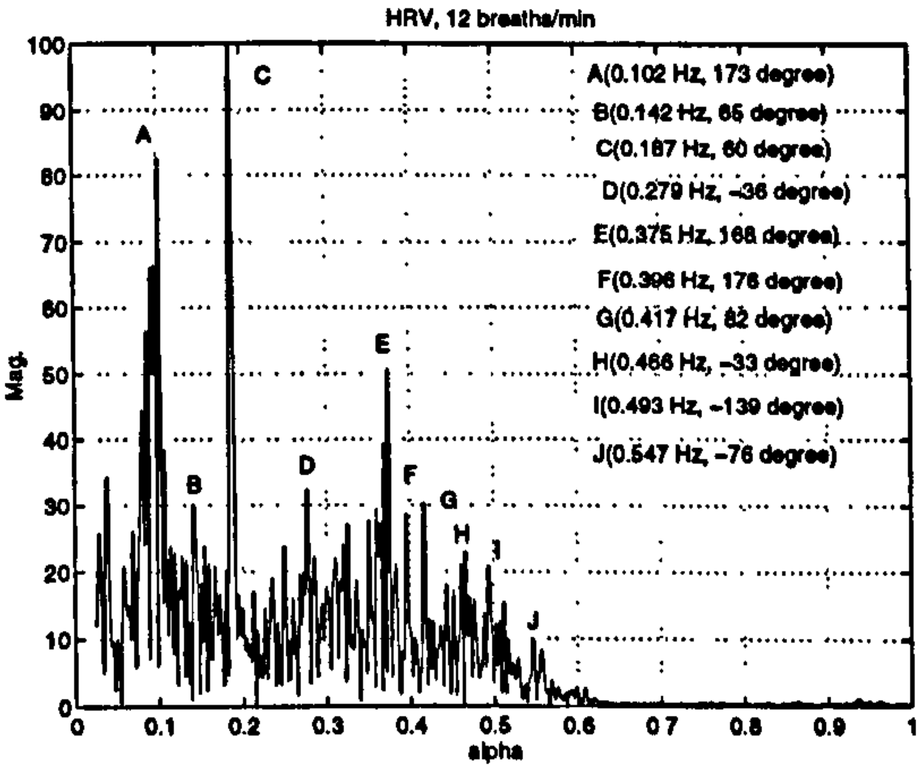


(c)

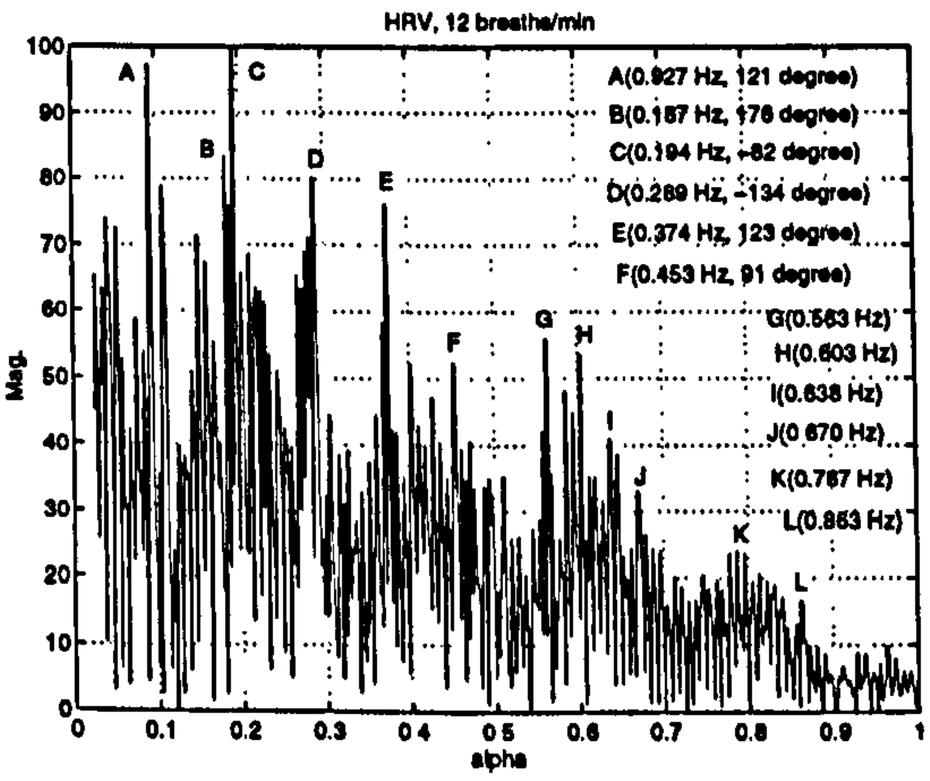


(d)

Figure 5.10: Cyclic mean (left hand column) and cyclic correlation (right hand column) of respiration (top panel) and BPV (bottom panel) in 8 breaths/min experiment (subject 3).

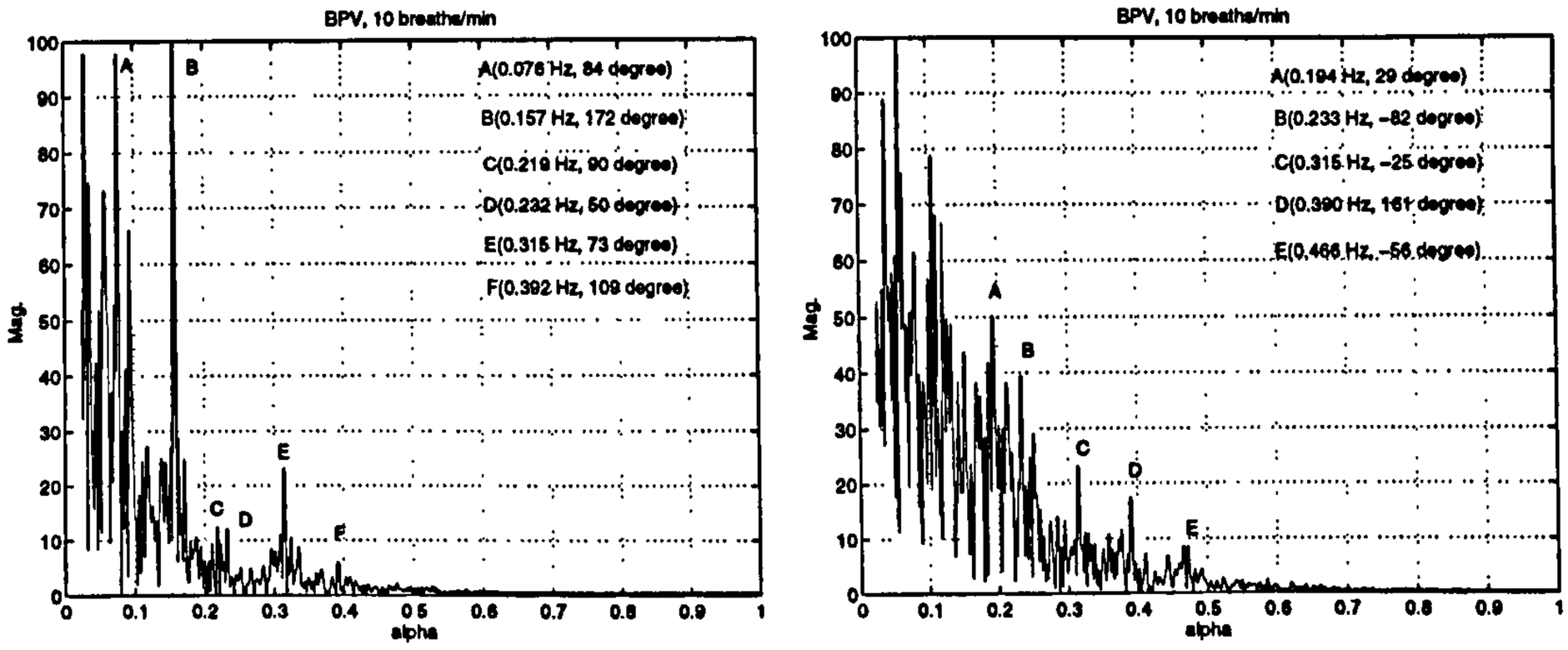


(a)



(b)

Figure 5.11: Cyclic mean (a) and cyclic correlation (b) of the HRV from a subject in 12 breaths/min experiment (subject 2).

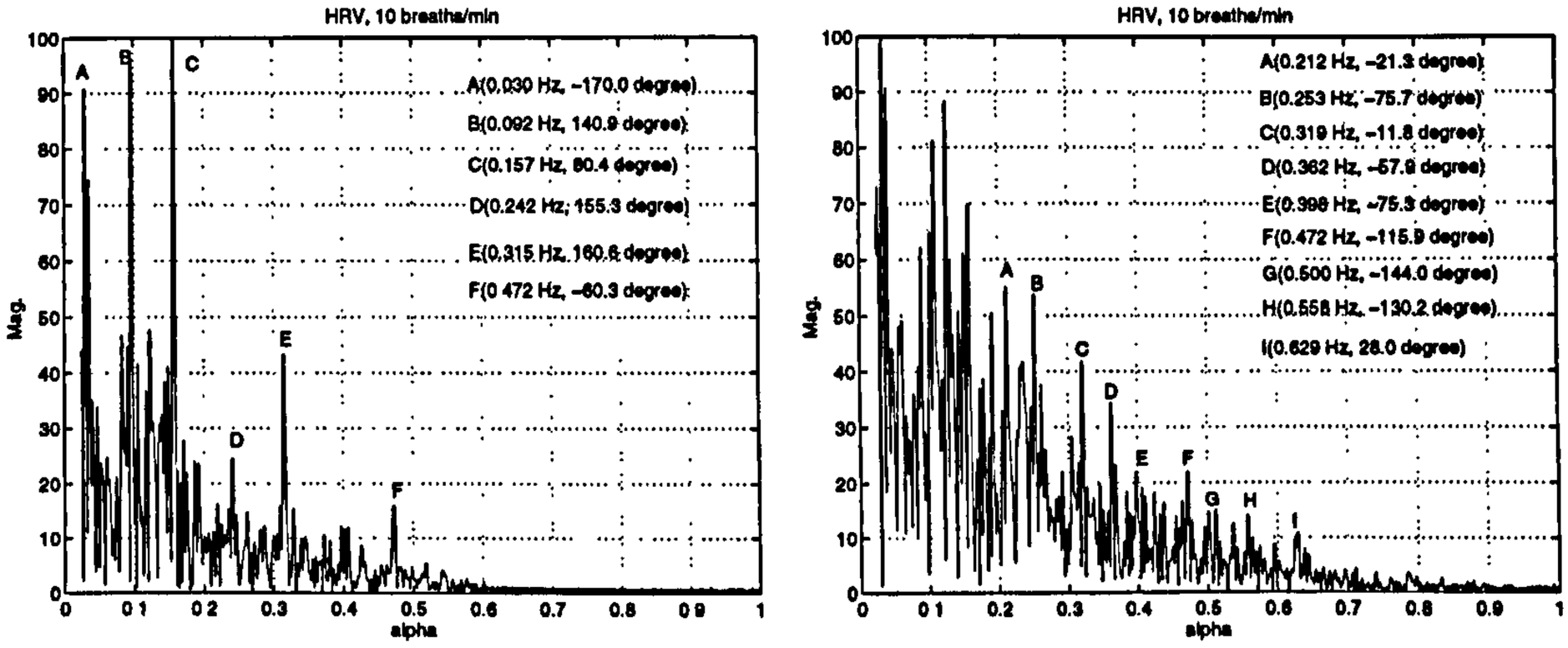


(a) (b)

Figure 5.12: Cyclic mean (a) and cyclic correlation (b) of the BPV from a subject in 10 breaths/min experiment (subject 4).

respectively. In addition to the 2nd order harmonic of the respiration at $0.375Hz$ (peak E), the frequency coupling between the LF and HF (LF+HF) at $0.279Hz$ (peak D) and the coupling 2HF+LF at $0.466Hz$ (peak H) are also distinguishable in the cyclic mean plot. However, no evidence of phase coupling between the LF and HF or between the LF and 2HF can be observed from the estimated phase values. In the cyclic correlation plot of Fig. 5.11(b) the estimated frequency of the LF component (peak C) is slightly less than that of the cyclic mean plot ($0.194/2 = 0.097Hz$ instead of $0.102Hz$). Phase coupling LF+HF at $0.289Hz$ (peak D), 2HF+LF at $0.453Hz$ (peak F), 3HF+LF at $0.67Hz$ (peak J) and 2HF+2LF at $0.563Hz$ can also be observed. Several other smaller peaks are also highlighted in the cyclic plots of Fig. 5.11. Although these peaks cannot be attributed to the interaction between the LF and HF components, they illustrate the variety of the existing components and the underlying physiological phenomena in the variability signals.

Figure 5.12(a) shows the cyclic mean plot of the BPV of the second subject in the 10 breaths/min experiment. Peaks A at $0.076Hz$ and B at $0.157Hz$ illustrate the LF and the HF components, respectively. The frequency coupling LF+HF at $0.232Hz$ (peak D) and LF+2HF at $0.392Hz$ (peak F) can be observed in the figure with small amplitudes. In the cyclic correlation plot of Fig. 5.12(b) the presence of dominant components at the VLF band has obscured the detection of the LF and HF components and their interactions. However, frequency coupling between the LF and



(a) (b)

Figure 5.13: Cyclic mean (a) and cyclic correlation (b) of the HRV for a subject who showed prominent LF component in the 10 breaths/min experiment (subject 5).

HF can be seen at peaks B (LF+HF), D (LF+2HF) and E (2HF+2LF), in addition to the 2nd order harmonic of the respiratory signal at C.

Figure 5.13 illustrates the cyclic plots of the HRV signal obtained from another subject who showed a prominent LF component only in the 10 breaths/min experiment.The VLF, LF and HF components appear at frequencies 0.03, 0.092, $0.157Hz$ in the cyclic mean plot, respectively. Frequency coupling LF+HF at $0.242Hz$ (peak D) clearly shows the nonlinear interaction between the LF and HF components. Self frequency coupling can also be observed at peaks E (2HF) and F (3HF) in the cyclic mean plot of Fig. 5.13(a). In the cyclic correlation plot of Fig. 5.13(b) the presence of the peaks at LF+HF (peak B), 2HF (peak C), 4LF (peak D), 2HF+LF (peak E), 3HF (peak F), 2HF+2LF (peak G), 4HF (peak I) consolidates the existence of nonlinearity.

5.11 Discussion and Conclusion

Unlike the power spectral density, retrieval of magnitude and phase of the harmonics for nonlinearity detection needs much more effort. Although bispectral analysis has been widely used for this purpose, cyclostationary analysis, due to its better performance, was employed in this study. Application of this method in the practical manner presented in this chapter can be advantegous in other areas as well.

The presence of (self) frequency coupling in HRV and BPV in different breathing rates demonstrates the contribution of the input-output Volterra type nonlinearity in the neuro-cardiovascular system. Indeed the purpose of this study was not to quantify the hardness of the nonlinearity, but to show its presence and its importance in the variability signals even in small signal regime (variation of heart rate and blood pressure around their mean values in supine resting position). For this purpose, the respiratory signal was exploited to behave as a sinusoidal input to the system. If the nonlinearity in the system was ignorable, neither amplification of the higher order harmonics nor interaction between the LF and HF components should be observed. Unlike the respiratory signal, no direct control over the LF component can be applied otherwise the frequency coupling between the LF and HF components could be more highlighted.

Although the subjects were instructed to carefully follow the auditory cues and only the best sinusoidal part of the recorded data were used for the cyclic domain analysis, small variations in the respiratroy frequency (or the LF component for phase coupling detection) could have had a deteriorating effect and degradation in the performance of the employed cyclic tools. The theoretical study which can be found in the literature and was further developed here are perfect for amplitude modulated signals. Deviation of the driving signals from this ideal case might bring about inaccuracies in the estimated frequencies and phase values or dissolution of the peaks in the background noise.

Even though some of the subjects did not show a very conspicuous peak at the 2nd order harmonic of the respiratory component, they exhibited a comparable ratio of the 2nd order to the first order harmonic in HRV and BPV with respect to that of the respiratory signal. If there was no sign of nonlinearity, one would expect to see always a reduced ratio instead. Nevertheless, no other reason can be conceived to explain this phenomenon over this sequence of experiments except the input-output nonlinearity. Appearance of a less conspicuous self frequency coupling at higher breathing rates does not mean a reduction in the amount of nonlinearity but it indicates that the higher order components are attenuated at the subsequent physiological systems which exhibit low pass characteristics.

One question which might arise in connection with the experimental procedure is whether the mandatory breathing pattern employed here imposes any nonlinearity

to the system or aggravates the influence of the nonlinearity or not. Unfortunately no clear answer can be given to this question due to the lack of avaliable information regarding the different effects of spontaneous and mandatory breathings.

It might be useful here to point out that the same set of experiments was applied for three subjects (different from the previous group) whose respiratory effort was measured by a spirometer instead of the strain gauge plethysmography method. The same observations was also obtained in these subjects.

Presence of (self) frequency coupling and absence of (self) phase coupling in the experimental data indicate that the underlying physiological system cannot be modelled as a parallel combination of zero memory linear and quadratic systems. Therefore, the Volterra type nonlinearity should be assumed for the development of the HRV-BPV-ILV model. This further means that the nonlinear system identification method based on the Volterra series representation should be studied in the following chapters.

In Chapter 8 the presence of the input-ouput nonlinearity is quantified in the random breathing experiment. However, the obtained nonlinearity is attributed to one specific part of the whole system due to the technical limitation of the existing methods.

Summary of the Chapter

Augmentation of the second order harmonic of the HF component in HRV and BPV in the metronome breathing experiment shows that a nonlinear system is actually involved in producing the rhythmical fluctuations in heart rate and blood pressure. Furthermore, observation of the frequency coupling between the LF and HF components, though less conspicuous than the self frequency coupling, can be referred to as further evidence. Unfortunately, the nonlinearity involved in HRV and BPV cannot be modelled as a parallel combination of zero memory linear and nonlinear systems. Therefore, the general class of Volterra type nonlinearity should be assumed for illustrating the HRV-BPV-ILV relationships.

5.12 Appendix A: Relation Between Higher Order Moment Spectra and Cyclic Spectra

As already argued the diagonal slice of the higher order moment spectra has been suggested by Zhou and Giannakis (1995a) for self frequency and self phase coupling detection. It is shown here that this slice is nothing but the (scaled) higher order cyclic spectra at slice $\alpha = 0$ and so their treatment can be fitted in the general class of cyclostationary analysis.

By definition, the kth-order correlation function is given by,

$$R_{kx}(t, \tau_1, \ldots, \tau_{k-1}) \triangleq E\left(x^*(t)x(t+\tau_1)\ldots x(t+\tau_{k-1})\right). \tag{5.57}$$

The kth-order cyclic correlation is the FS of R_{kx} hence,

$$R^{\alpha}_{kx}(\tau_1, \ldots, \tau_{k-1}) = \frac{1}{T}\sum_{t=0}^{T-1} R_{kx}(t, \tau_1, \ldots, \tau_{k-1})e^{-j2\pi\alpha t}. \tag{5.58}$$

and the kth-order cyclic spectra is the kth-order Fourier transform of R^{α}_{kx},

$$S^{\alpha}_{kx}(f_1, \ldots, f_{k-1}) = \sum_{\tau_i} R^{\alpha}_{kx}(\tau_1, \ldots, \tau_{k-1})e^{-j2\pi\left(\sum_{i=1}^{k-1} f_i\tau_i\right)}$$

$$= \sum_{\tau_i}\left\{\frac{1}{T}\sum_{t=0}^{T-1}\left[E\left(x(t+\tau_1)\ldots x(t+\tau_{k-1})x^*(t)\right)e^{-j2\pi\alpha t}\right]e^{-j2\pi\left(\sum_{i=1}^{k-1} f_i\tau_i\right)}\right\} \tag{5.59}$$

On the other hand,

$$M_{kx}(\lambda_1, \lambda_2, \ldots, \lambda_{k-1}) = \frac{1}{T^{k-1}}\sum_{\tau_i} m_{kx}(\tau_1, \ldots, \tau_{k-1})e^{-j2\pi(\lambda_1\tau_1+\ldots+\lambda_{k-1}\tau_{k-1})}$$

$$= \frac{1}{T^{k-1}}\sum_{\tau_i}\left\{\frac{1}{T}\sum_{t=0}^{T-1}\left[E\left(x(t+\tau_1)\ldots x(t+\tau_{k-1})x^*(t)\right)e^{-j2\pi\sum_{i=1}^{k-1}\lambda_i\tau_i}\right]\right\}. \tag{5.60}$$

From equations (5.59) and (5.60) we get,

$$M_{kx}(\lambda_1, \lambda_2, \ldots, \lambda_{k-1}) = \frac{1}{T^{k-1}} S^{\alpha}_{kx}(\lambda_1, \ldots, \lambda_{k-1})|_{\alpha=0}. \tag{5.61}$$

which is the required identity.

5.13 Appendix B: Proof of Equation (5.43)

If $h(t) = z^2(t) - \frac{2}{b}\langle y(t)\rangle$ is defined then from equation (5.39) we have

$$y_0(t) = \frac{b}{2}h(t) + az(t)cos(2\pi f_0 t + \phi_0) + \frac{b}{2}z^2(t)cos\,(2\pi 2 f_0 t + \phi_0)\cdot \tag{5.62}$$

Then,

$$R_{y_0}(t+\frac{\tau}{2}, t-\frac{\tau}{2}) = E\left(y_0(t+\frac{\tau}{2})y_0(t-\frac{\tau}{2})\right) =$$

$$E\left\{\frac{b^2}{4}h(t+\frac{\tau}{2})h(t-\frac{\tau}{2}) + \frac{ab}{2}h(t+\frac{\tau}{2})z(t-\frac{\tau}{2})cos(2\pi f_0(t-\frac{\tau}{2}) + \phi_0)\right.$$
$$+\frac{b^2}{4}h(t+\frac{\tau}{2})z^2(t-\frac{\tau}{2})cos\left(2\pi(2f_0)(t-\frac{\tau}{2}) + 2\phi_0\right)$$
$$+\frac{ab}{2}z(t+\frac{\tau}{2})h(t-\frac{\tau}{2})cos\left(2\pi f_0(t+\frac{\tau}{2}) + \phi_0\right)$$
$$+a^2z(t+\frac{\tau}{2})z(t-\frac{\tau}{2})cos\left(2\pi f_0(t+\frac{\tau}{2}) + \phi_0\right)cos\left(2\pi f_0(t-\frac{\tau}{2}) + \phi_0\right)$$
$$+\frac{ab}{2}z(t+\frac{\tau}{2})z^2(t-\frac{\tau}{2})cos\left(2\pi f_0(t+\frac{\tau}{2}) + \phi_0\right)cos\left(2\pi(2f_0)(t-\frac{\tau}{2}) + 2\phi_0\right)$$
$$+\frac{b^2}{4}z^2(t+\frac{\tau}{2})h(t-\frac{\tau}{2})cos\left(2\pi(2f_0)(t+\frac{\tau}{2}) + 2\phi_0\right)$$
$$+\frac{ab}{2}z^2(t+\frac{\tau}{2})z(t-\frac{\tau}{2})cos\left(2\pi(2f_0)(t+\frac{\tau}{2}) + 2\phi_0\right)cos\left(2\pi f_0(t-\frac{\tau}{2}) + \phi_0\right)$$
$$\left.+\frac{b^2}{4}z^2(t+\frac{\tau}{2})z^2(t-\frac{\tau}{2})cos\left(2\pi(2f_0)(t+\frac{\tau}{2}) + 2\phi_0\right)cos\left(2\pi(2f_0)(t-\frac{\tau}{2}) + 2\phi_0\right)\right\} =$$

$$E\left\{\frac{b^2}{4}h(t+\frac{\tau}{2})h(t-\frac{\tau}{2}) + \frac{ab}{2}h(t+\frac{\tau}{2})z(t-\frac{\tau}{2})cos\left(2\pi f_0(t-\frac{\tau}{2}) + \phi_0\right)\right.$$
$$+\frac{b^2}{4}h(t+\frac{\tau}{2})z^2(t-\frac{\tau}{2})cos\left(2\pi(2f_0)(t-\frac{\tau}{2}) + 2\phi_0\right)$$
$$+\frac{ab}{2}z(t+\frac{\tau}{2})h(t-\frac{\tau}{2})cos\left(2\pi f_0(t+\frac{\tau}{2}) + \phi_0\right)$$
$$+\frac{a^2}{2}z(t+\frac{\tau}{2})z(t-\frac{\tau}{2})\left[cos\,(2\pi(2f_0)t + 2\phi_0) + cos(2\pi f_0\tau)\right]$$
$$\left.+\frac{ab}{4}z(t+\frac{\tau}{2})z^2(t-\frac{\tau}{2})\left[cos\left(2\pi(3f_0)t - 2\pi f_0\frac{\tau}{2} + 3\phi_0\right) + cos(-2\pi f_0 t + 2\pi(3f_0)\frac{\tau}{2} - \phi_0)\right]\right.$$
$$+\frac{b^2}{4}z(t+\frac{\tau}{2})h(t-\frac{\tau}{2})cos\left(2\pi(2f_0)(t+\frac{\tau}{2}) + 2\phi_0\right)$$

$$+\frac{ab}{4}z^2(t+\frac{\tau}{2})z(t-\frac{\tau}{2})\left[cos\left(2\pi(3f_0)t+2\pi f_0\frac{\tau}{2}+3\phi_0\right)+cos(2\pi f_0 t+2\pi(3f_0)\frac{\tau}{2}+\phi_0)\right]$$
$$+\frac{b^2}{8}z^2(t+\frac{\tau}{2})z^2(t-\frac{\tau}{2})\left[cos\left(2\pi(4f_0)t+4\phi_0\right)+cos(2\pi(4f_0)\frac{\tau}{2})\right]\Big\}. \tag{5.63}$$

By applying

$$\frac{1}{T}\int_{-T/2}^{T/2} cos(2\pi f_1 t+2\pi f_2\tau+\phi_1)e^{-j2\pi\alpha t}dt =$$

$$\frac{1}{T}\int_{-T/2}^{T/2}\left[\frac{e^{j(2\pi f_1 t+2\pi f_2\tau+\phi_1)}+e^{-j(2\pi f_1 t+2\pi f_2\tau+\phi_1)}}{2}\right]e^{-j2\pi\alpha t}dt =$$

$$\begin{cases}\frac{1}{2}e^{j(2\pi f_2\tau+\phi_1)}, & \alpha=f_1\\ \frac{1}{2}e^{-j(2\pi f_2\tau+\phi_1)}, & \alpha=-f_1\\ 0 & \text{otherwise}\end{cases} \tag{5.64}$$

and definition of the cyclic correlation

$$R^{\alpha}_{2y_0}(\tau)=\frac{1}{T}\int_{-T/2}^{T/2}R_{y_0}(t+\tau/2,t-\tau/2)e^{-j2\pi\alpha t}dt, \tag{5.65}$$

the result expressed by equation (5.43) can be obtained.

Chapter 6

Time Varying Threshold Integral Pulse Frequency Modulation

Objectives of the Chapter

As detailed in Chapter 2 the IPFM model is an appropriate mathematical representation for the spike generation mechanism of the SA node. Although the IPFM model properly represents the conversion procedure of the autonomic nervous modulation to the interval variations, it is not capable of mediating the stretch induced modulation to the interval variations. The aim of this chapter is first to model the stretch induced modulation by including a time dependent term into the threshold level of the IPFM model and secondly to find an analytic solution to this modified model, namely the Time Varying Threshold IPFM (TVTIPFM) model. To analyse this model a parametric method will be presented which not only offers an appropriate solution to the TVTIPFM model but also gives further insight into the performance of the IPFM model.

6.1 Introduction

The atrial pressure and volume continuously change in each cardiac cycle. Superimposed on the filling and emptying sequence of the pressure and volume waveforms of the atria are lower frequency components due to respiratory fluctuations of intrathoracic pressure and changes in venous return. The variations in atrial pressure and volume can stimulate the low pressure receptors but in addition to that these variations certainly have a direct stretching effect on the sinus node.

There is abundant evidence that the basal rate of the cardiac pacemaker cells changes with stretching of the SA node (Lang, Lu, Chang, Brooks, 1966; Brooks, Lang, Mangel, Shaw, Geoly, 1966; Chiba, 1997; Ushiyama & Brooks, 1977). The results of extensive research have revealed that stretching of the SA node increases the rate of nodal firing *in vitro* whereas the natural rhythm is restored on release from the stretch. Lang *et. al.* (1966) have shown that the degree of acceleration in the firing rate is directly related to the magnitude of the stretch. Greater displacement results in greater acceleration up to a certain limit. Chiba (1977) has illustrated that the percentage increase in sinus rate is proportional to the amount of stretch (Fig. 6.1). The same result can also be observed in other investigations, particularly for a small amount of stretch.

The observations have suggested that the variation in the basal rate caused by stretching is a result of reactions within the node itself. A change in membrane potential is believed to be responsible for this effect. The ability of the stretch to initiate spontaneous firing of a quiescent nodal cell and the appearance of a progressive reduction (absolute value) in the resting membrane potential has consolidated the hypothesis that the stretch lowers the threshold requirements (Lang *et. al.*, 1966). Importantly, neurotransmitters such as epinephrine and blocking agents such as atropine and propranolol do not greatly modify responses to stretching (Lang *et. al.*, 1966; Chiba, 1977). This, in turn, implies that the variations in the sinus rhythm by the autonomic nerves, and stretch-induced variations are mediated through different mechanisms; the rate of depolarization for the former, and the threshold level for the latter.

The sinusoidal response of the nodal stretch has been studied by Ushiyama *et. al.* (1977). These authors showed that for low frequency of excitations ($f < 0.5Hz$), which is the area of interest in this study, sinusoidal stretching of the rabbit SA node induces the same sinusoidal variation in the sinus rhythm whereas by approaching the natural rhythm, the SA node promotes nonlinear phenomena such as frequency locking in the firing rate.

The results of the *in situ* study of the stretch on the SA node are also in general agreement with those found *in vitro*. The results obtained by Brooks and co-workers (1966) in dogs indicate that acceleration of the sinus rate depends on the degree of the stretch and not on the basal rate. The degree of acceleration in response to the stretch

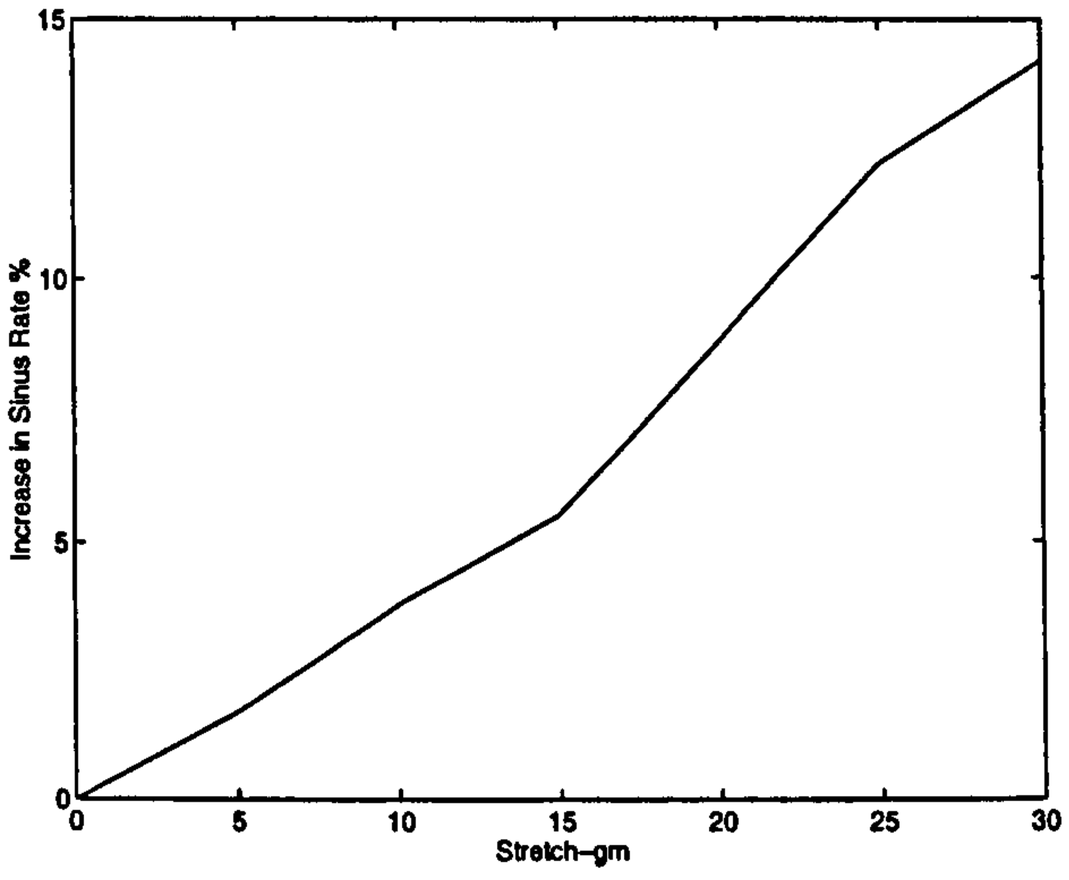


Figure 6.1: In an isolated blood-perfused SA node the sinus rate increases with increase in the nodal stretch. The degree of acceleration is directly related to the magnitude of stretch (Chiba, 1977).

differed somewhat from subject to subject but results were reasonably consistent in the same subject. These researchers also concluded that extrinsic cardiac nerves were not essential to the heart rate change produced by stretch of and release of tension on the SA node, however they were involved and modified these reactions.

The presence of nonautonomic RSA has also highlighted the participation of the nodal stretch in sinus arrhythmia. Evidence for a nonautonomic RSA mechanism in humans has been found in patients after cardiac transplant by Bernardi, Keller, Sanders, Reddy, Griffith, Neno and Pinsky (1989). These investigators used spectral estimation to quantify the amount of RSA and its relation to respiratory rate and tidal volume. Although the neuronal mechanism for heart rate control was demolished in these patients, Bernardi and his colleagues observed the presence of the HF component in synchrony with respiration for all the recordings but with a smaller amplitude compared to normal subjects (up to 15%). Much like in the normal subjects the observed HF component depends upon the breathing rate and tidal volume. Since changes in the level of circulating cathecolamines is very unlikely to be a determinant of cyclic changes in heart rate in synchrony with respiration, these researchers presumed that changes in the heart rate of the denervated heart are affected by changes or rate of changes in heart wall stretch.

That the residual RSA after abolishing the neuronal control of the heart is a consequence of the SA nodal stretching property has also been confirmed in a recent

study by Perlini *et. al.* (1995a) in anaesthetised vagotomized and mechanically ventilated rabbits. These workers observed a residual RSA in the PSD of the R-R interval fluctuations which persisted after atropine and propranolol administration. During positive pressure ventilation the R-R interval decreased with inflation and increased with deflation and it was directly dependent on respiratory frequency and tidal volume. Perlini *et. al.* concluded that the residual RSA cannot be attributed to a neuronal modulation of the sinus nodal discharge as far as cholinergic and β-adrenergic pathways are concerned and therefore changes in mechanical stretch imposed on the SA node by changes in venous return should be taken into account. This is in complete agreement with several other investigations (Triedman & Saul, 1994; Saul *et. al.*, 1991; Chon *et. al.*, 1996; Rimoldi *et. al.*, 1990).

Saul and coworkers (1991) have been able to characterise the transfer function between the residual RSA and respiration after combined sympathetic and parasympathetic blockade by random breathing pattern (Chapter 7). These investigators also attributed the observed residual RSA to the stretching property of the SA node.

In order to take the stretch induced modulation of the SA node into account, the IPFM model is considered when its threshold level is allowed to include a time varying term, namely the Time Varying Threshold IPFM (TVTIPFM) model. It was stated in Chapter 2 that the IPFM model is a satisfactory mathematical representation for the spike generation mechanism of the SA node. It was also shown that with certain conditions recovery of the modulating signal would be possible using the lowpass filtering technique. The involvement of the threshold signal will add more complexity to the mathematical analysis of the model and may suspend the efficacy of the LPF method. In this chapter a parametric approach for treating the TVTIPFM model is presented. The new method is simple for computer implementation yet powerful in signal reconstruction. Although the proposed parametric method is basically developed to contend with the TVTIPFM model, its utility for the IPFM model seems even more prominent. Like any other method, however, the proposed method suffers from certain limitations. Before scrutinising the parametric solution, a brief explanation of the TVTIPFM model together with some simple examples of its performance are given in the next section in order to give a good insight into the overall problem.

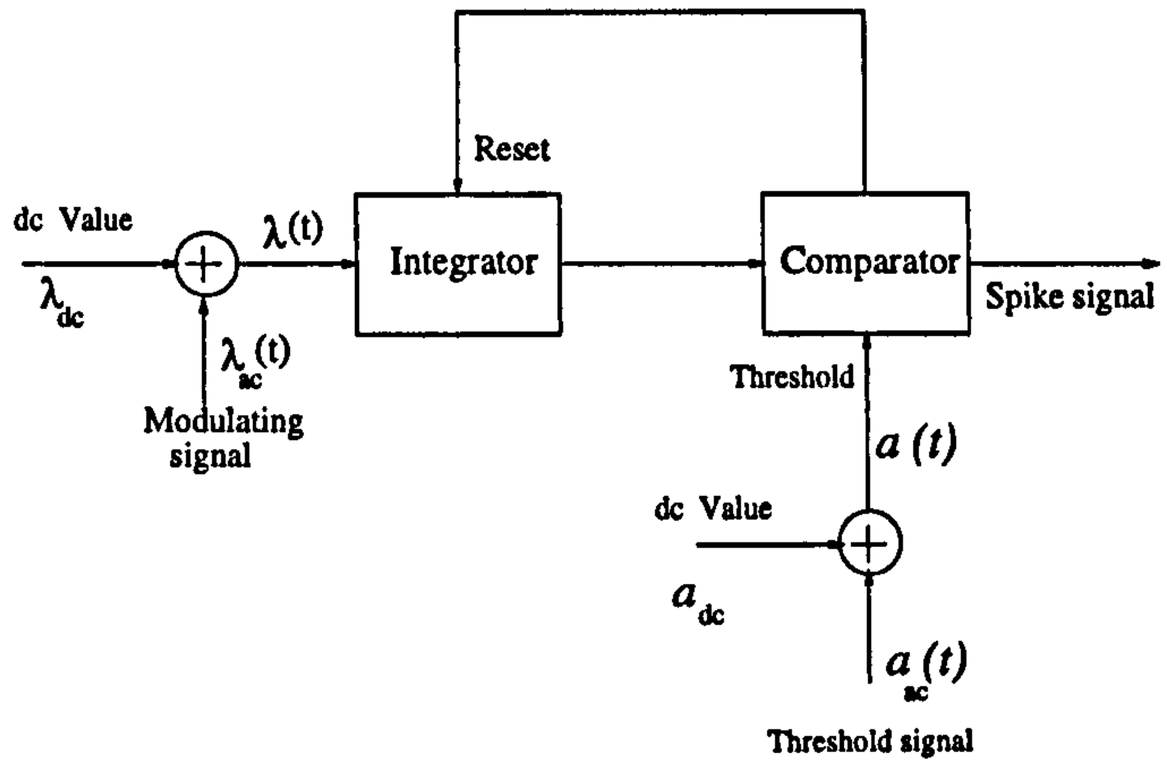


Figure 6.2: TVTIPFM model is the IPFM model with a varying threshold level.

6.2 TVTIPFM model

The TVTIPFM model is fundamentally the IPFM model of Fig. 2.2(a) with a time varying signal added to the dc value of the threshold level (Fig. 6.2). As before, the integral of $\lambda(t)$ is compared with the instantaneous value of the threshold signal $a(t)$. A spike is generated at time t_i when $\int_{t_{i-1}}^{t_i} \lambda(t)dt = a(t_i)$ with a subsequent reseting of the integrator. In fact, with this description the IPFM model can be regarded as a special case of the TVTIPFM model, when $a_{ac}(t) = 0$.
For the proper operation of the model we must have

$$\begin{aligned} |\lambda_{ac}(t)| &< \lambda_{dc} \\ |a_{ac}(t)| &< a_{dc} \\ a_{dc}, \lambda_{dc} &> 0. \end{aligned} \tag{6.1}$$

For the time being no constraint is placed upon the frequency content of the signals or the modulation depth.

Similar to the modulation signal, variation in the threshold signal has a direct influence on the interspike intervals. Figure 6.3 illustrates the modulating signal and the corresponding R-wave signal of the TVTIPFM model with no variation in the threshold level. Similar variations can be observed in the interspike intervals if the threshold level is varied while the modulating signal is kept constant (Fig. 6.4). If both signals are allowed to vary with time, as it is shown in Fig. 6.5, then they can amplify or attenuate their individual effects depending on their relative amplitudes. By mere measurements of the interspike intervals it might seem impossible to separate

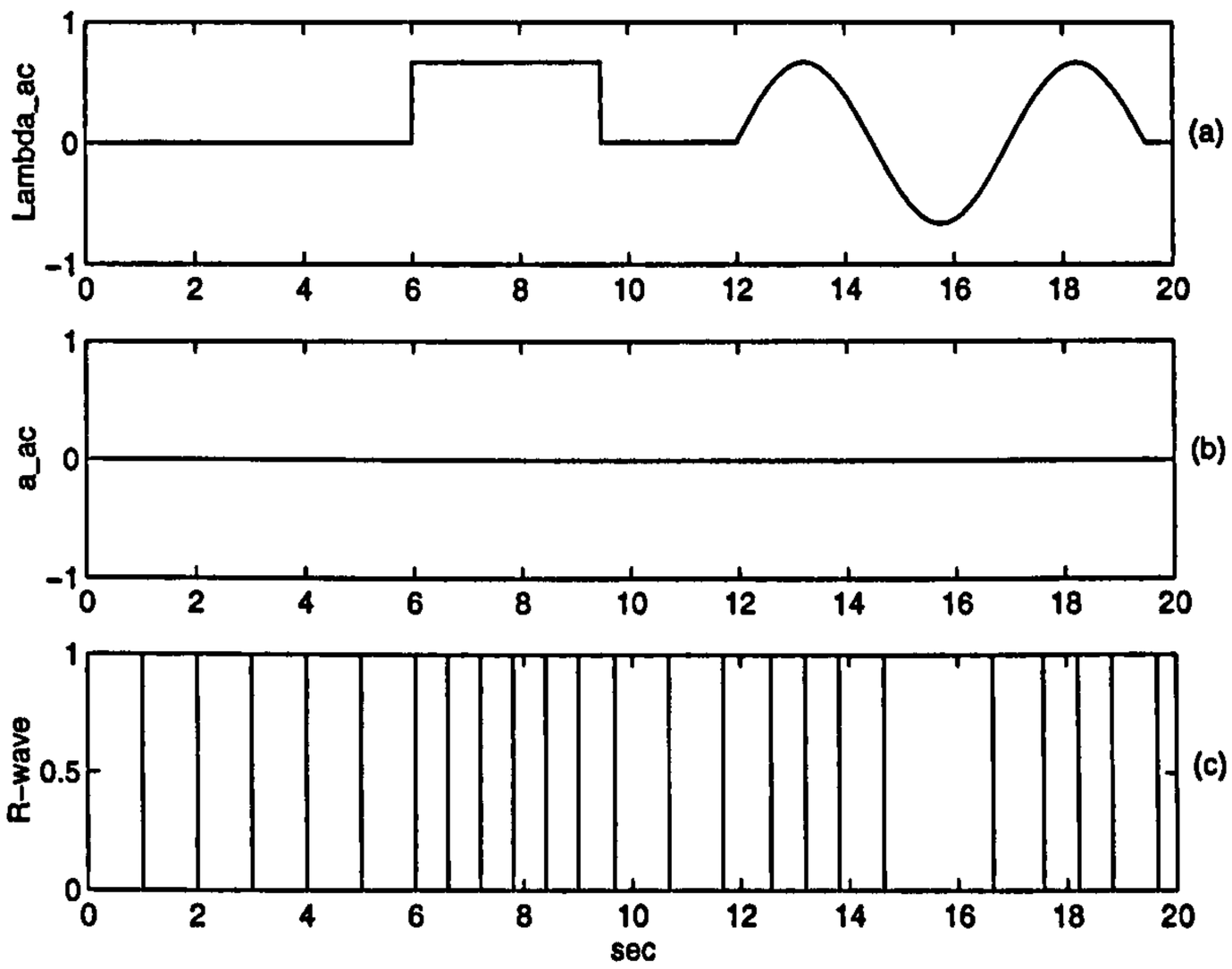


Figure 6.3: (a) The modulating signal $\lambda_{ac}(t)$. (b) Zero threshold signal $a_{ac}(t) = 0$. (c) The R-wave signal ($\lambda_{dc} = a_{dc} = 1$).

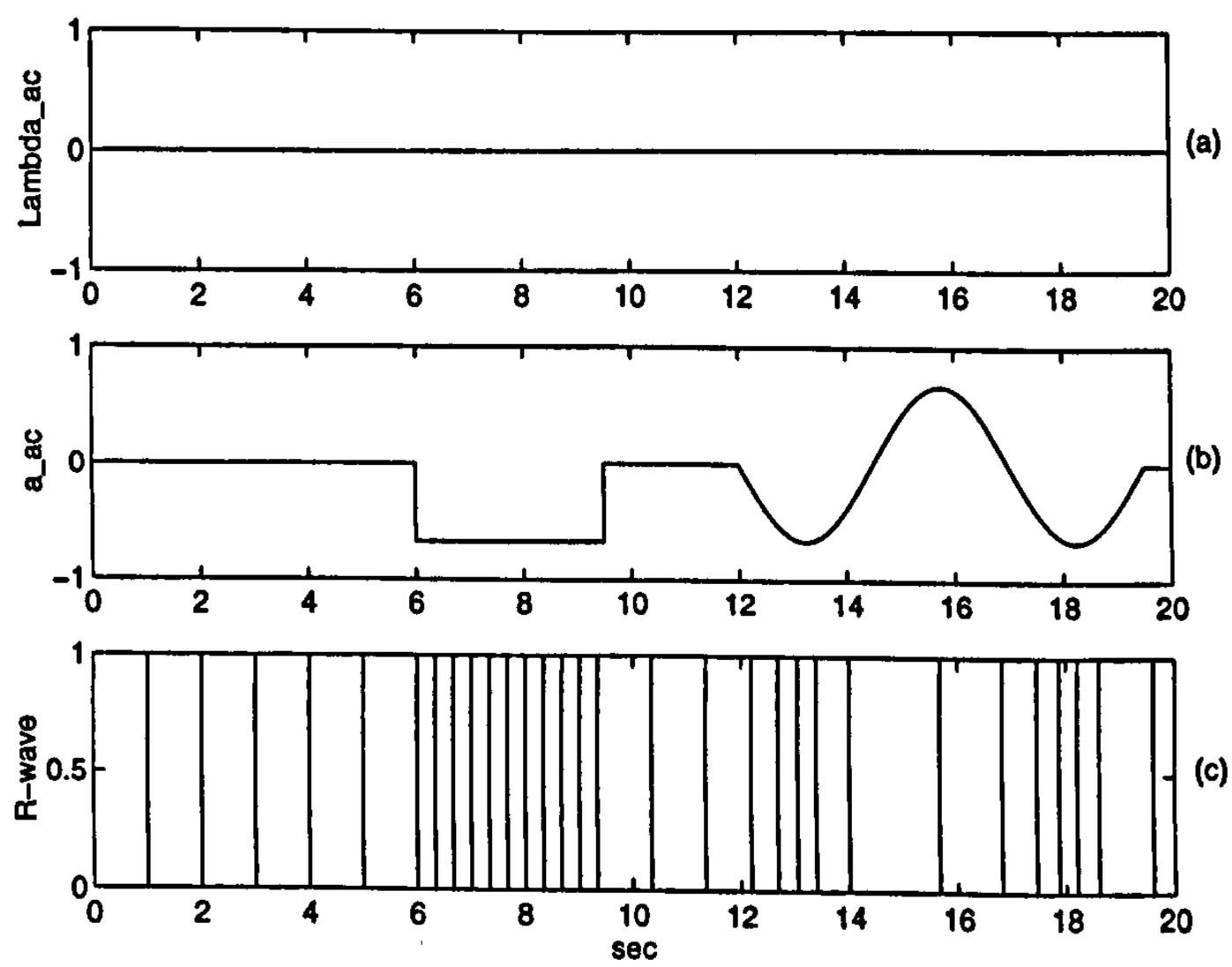


Figure 6.4: (a) Zero modulating signal $\lambda_{ac}(t) = 0$. (b) The threshold signal $a_{ac}(t)$. (c) The R-wave signal ($\lambda_{dc} = a_{dc} = 1$).

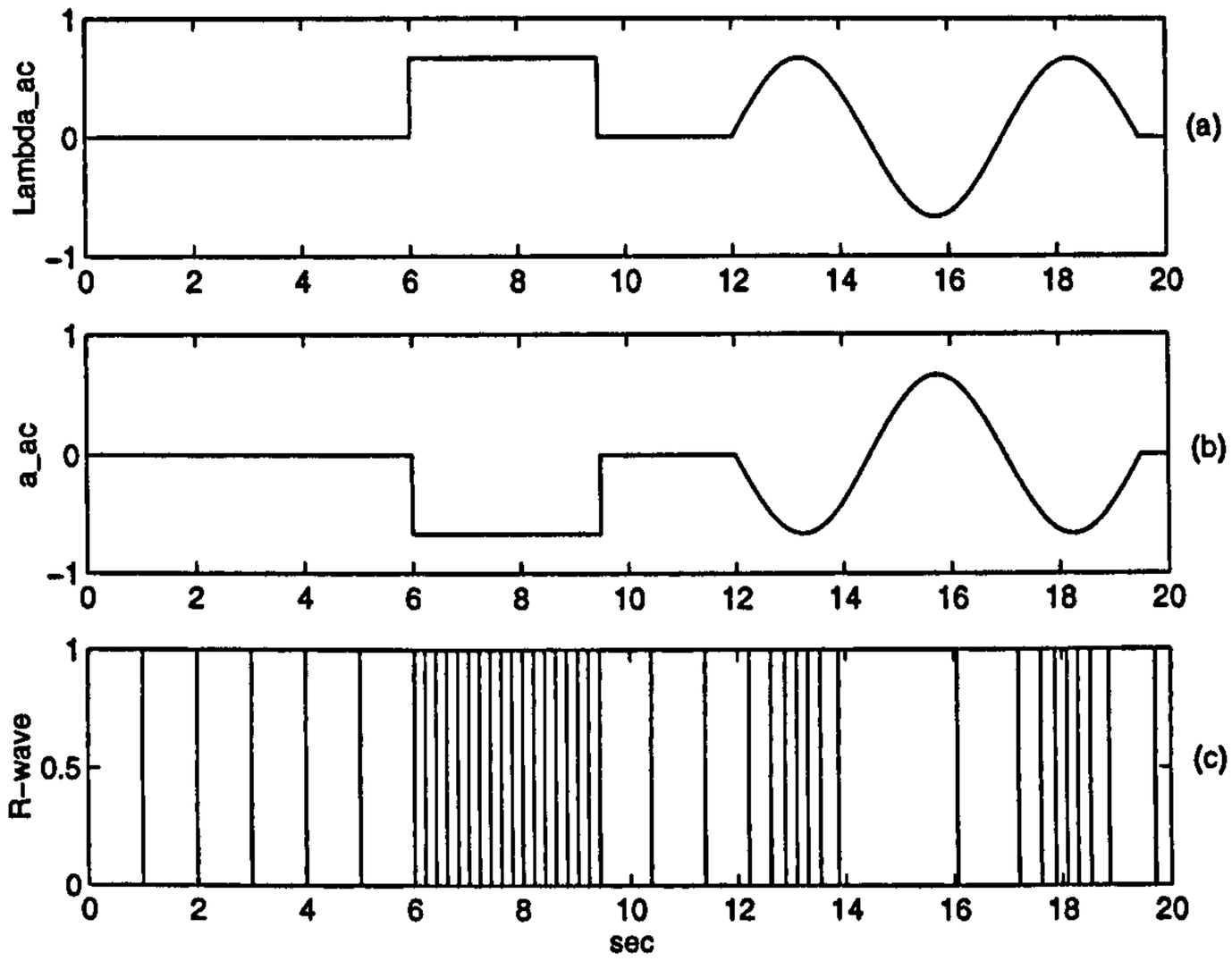


Figure 6.5: (a) The modulating signal $\lambda_{ac}(t)$. (b) The threshold signal $a_{ac}(t)$. (c) The R-wave signal ($\lambda_{dc} = a_{dc} = 1$).

the effect of the threshold signal from the modulating signal. It will be seen shortly that this is possible if certain conditions hold.

6.3 Parametric Solution of the TVTIPFM Model

6.3.1 Basic Concepts

Following on from the preliminary examples of the preceding section, a parametric method will now be developed for obtaining the modulating and the threshold signals of the TVTIPFM model based upon the knowledge of interspike intervals. In accordance with the definition presented in Chapter 2 and the notation in Fig. 6.2, the occurrence times, $t_1, t_2, \cdots, t_K$ of the generated spikes of the TVTIPFM model satisfy the following set of equations,

$$\int_0^{t_1} \lambda(t)dt = a(t_1)$$
$$\int_{t_1}^{t_2} \lambda(t)dt = a(t_2)$$
$$\int_{t_2}^{t_3} \lambda(t)dt = a(t_3)$$

$$\int_{t_{K-1}}^{t_K} \lambda(t)dt = a(t_K) \cdot \qquad (6.2)$$

or concisely,

$$\int_0^{t_k} \lambda(t)dt = \sum_{j=1}^{k} a(t_j), \qquad (6.3)$$
$$k = 1, 2, ..., K.$$

It is postulated that $\lambda(t)$ and $a(t)$ can be expanded in the forms of

$$\lambda(t) = \sum_{i=0}^{L} \alpha_i \varphi_i'(t), \qquad (6.4)$$

$$a(t) = \sum_{i=0}^{L} -\beta_i \theta_i(t), \qquad (6.5)$$

in which α_i and β_i are unknown parameters, $\varphi_i(t)$ and $\theta_i(t)$ are given functions [1], and $\varphi_i'(t) = \frac{d\varphi_i(t)}{dt}$. Substituting equations (6.4) and (6.5) in equation (6.3) yields,

$$\int_0^{t_k} \sum_{i=0}^{L} \alpha_i \varphi_i'(t)dt = \sum_{j=1}^{k} \left(\sum_{i=0}^{L} -\beta_i \theta_i(t_j) \right), \qquad (6.6)$$
$$k = 1, 2, ..., K.$$

Therefore,

$$\sum_{i=0}^{L} \alpha_i \int_0^{t_k} \varphi_i'(t)dt = \sum_{i=0}^{L} -\beta_i \left(\sum_{j=1}^{k} \theta_i(t_j) \right), \qquad (6.7)$$
$$k = 1, 2, ..., K.$$

If we define $\phi_i(t) = \varphi_i(t) - \varphi_i(0)$ then,

$$\sum_{i=0}^{L} \alpha_i \phi_i(t_k) = \sum_{i=0}^{L} -\beta_i \left(\sum_{j=1}^{k} \theta_i(t_j) \right), \qquad (6.8)$$
$$k = 1, 2, ..., K.$$

In matrix form, equation (6.8) can be written as:

[1] The number of $\varphi_i'(t)$ and $\theta_i(t)$ in equations (6.4) and (6.5), L, need not be equal. This is merely a convenience and brings about a unified approach for treating both signals. The extra coefficients can be equated to zero whenever appropriate.

$$\begin{bmatrix} \phi_0(t_1) & \phi_1(t_1) & \cdots & \phi_L(t_1) & \theta_0(t_1) & \theta_1(t_1) & \cdots & \theta_L(t_1) \\ \phi_0(t_2) & \phi_1(t_2) & \cdots & \phi_L(t_2) & \sum_{j=1}^{2}\theta_0(t_j) & \sum_{j=1}^{2}\theta_1(t_j) & \cdots & \sum_{j=1}^{2}\theta_L(t_j) \\ \phi_0(t_3) & \phi_1(t_3) & \cdots & \phi_L(t_3) & \sum_{j=1}^{3}\theta_0(t_j) & \sum_{j=1}^{3}\theta_1(t_j) & \cdots & \sum_{j=1}^{3}\theta_L(t_j) \\ \vdots & \vdots & \vdots & \vdots & \vdots & \vdots & \vdots & \vdots \\ \phi_0(t_K) & \phi_1(t_K) & \cdots & \phi_L(t_K) & \sum_{j=1}^{K}\theta_0(t_j) & \sum_{j=1}^{K}\theta_1(t_j) & \cdots & \sum_{j=1}^{K}\theta_L(t_j) \end{bmatrix} \begin{bmatrix} \alpha_0 \\ \alpha_1 \\ \vdots \\ \alpha_L \\ \beta_0 \\ \beta_1 \\ \vdots \\ \beta_L \end{bmatrix} = 0. \quad (6.9)$$

For notational brevity it is defined,

$$\Phi(t_1, t_K, 0, L) \triangleq \begin{bmatrix} \phi_0(t_1) & \phi_1(t_1) & \cdots & \phi_L(t_1) \\ \phi_0(t_2) & \phi_1(t_2) & \cdots & \phi_L(t_2) \\ \vdots & \vdots & \vdots & \vdots \\ \phi_0(t_K) & \phi_1(t_K) & \cdots & \phi_L(t_K) \end{bmatrix} \quad (6.10)$$

$$\Theta(t_1, t_K, 0, L) \triangleq \begin{bmatrix} \theta_0(t_1) & \theta_1(t_1) & \cdots & \theta_L(t_1) \\ \sum_{j=1}^{2}\theta_0(t_j) & \sum_{j=1}^{2}\theta_1(t_j) & \cdots & \sum_{j=1}^{2}\theta_L(t_j) \\ \vdots & \vdots & \vdots & \vdots \\ \sum_{j=1}^{K}\theta_0(t_j) & \sum_{j=1}^{K}\theta_1(t_j) & \cdots & \sum_{j=1}^{K}\theta_L(t_j) \end{bmatrix} \quad (6.11)$$

$$\underline{\alpha}_{0,L} \triangleq \begin{bmatrix} \alpha_0 \\ \alpha_1 \\ \vdots \\ \alpha_L \end{bmatrix} \quad (6.12)$$

$$\underline{\beta}_{0,L} \triangleq \begin{bmatrix} \beta_0 \\ \beta_1 \\ \vdots \\ \beta_L \end{bmatrix}. \quad (6.13)$$

Therefore the following simple identity will emerge,

$$\begin{bmatrix} \Phi(t_1, t_K, 0, L) & \Theta(t_1, t_K, 0, L) \end{bmatrix} \begin{bmatrix} \underline{\alpha}_{0,L} \\ \underline{\beta}_{0,L} \end{bmatrix} = 0 \quad (6.14)$$

$\Phi(t_1, t_K, 0, L)$ in equation (6.14) demonstrates the contribution of the modulating signal to the matrix identity. Likewise, the contribution of the threshold signal is represented by $\Theta(t_1, t_K, 0, L)$. In order to obtain a nontrivial solution for α_i and β_i, assuming $(2L+2)$ number of equations, the determinant of the data matrix in equation (6.14) must be zero,

$$\begin{vmatrix} \Phi(t_1, t_K, 0, L) & \Theta(t_1, t_K, 0, L) \end{vmatrix} = 0. \tag{6.15}$$

Due to numerical errors, however, equation (6.15) never holds in practice even if $\lambda(t)$ and $a(t)$ can be expressed exactly by equations (6.4) and (6.5). Resolution in localising the occurrence times of the spikes is a critical factor in deviation from this equality. This is so since continuous operators such as integration are replaced with their discrete counterparts. In an actual R-wave signal, sampling frequency of the ECG and performance of the R-peak detection algorithm are the crucial factors. To elucidate this matter we assume that $\lambda(t)$ and $a(t)$ consisting of the following sinusoidal functions

$$\lambda(t) = 1 + 0.4cos(2\pi 0.2t) - 0.2cos(2\pi 0.35t)$$

$$a(t) = 1 + 0.25cos(2\pi 0.15t) + 0.3sin(2\pi 0.25t)$$

are injected into the TVTIPFM model of Fig. 6.2. Three sampling frequencies $f_s = 100, 400, 800Hz$ are considered for the simulation together with the following basis functions,

$$\varphi_0(t) = t, \quad \varphi_1(t) = sin(2\pi 0.2t) \quad \varphi_2(t) = sin(2\pi 0.35t)$$
$$\theta_0(t) = 1, \quad \theta_1(t) = cos(2\pi 0.15t) \quad \theta_2(t) = sin(2\pi 0.25t)$$

The condition number of the data matrix, using the Singular Value Decomposition (SVD) method, is employed here as a criterion for singularity (Golub, 1996). The condition number is defined as the ratio of the largest to the smallest singular value. For a singular matrix the condition number is infinity in an exact arithmetic, and remarkably large in practice. The larger the condition number the closer the matrix is to singularity.

Table 6.1 displays the condition numbers and all the singular values of the data matrix for the presumed sampling frequencies. Deviation from singularity by decreas-

Singular Values	σ_1	σ_2	σ_3	σ_4	σ_5	σ_6	Condition Number $= \sigma_1/\sigma_6$
$f_s = 100$	13.6038	2.6170	1.6114	0.5367	0.3319	0.0016	8.502×10^3
$f_s = 400$	13.5815	2.6264	1.5926	0.5435	0.3230	3.089×10^{-4}	4.396×10^4
$f_s = 800$	13.5803	2.6261	1.5903	0.5439	0.3217	8.411×10^{-5}	1.614×10^5

Table 6.1: The effect of sampling frequency on singularity of the data matrix.

ing the sampling frequency can be inferred clearly from Table 6.1. We recall here that singularity of the coefficient matrix manifests the dependency of its constructing columns. Singularity of the data matrix of equation (6.14) becomes obvious following the identity (6.8) which imposes dependency between $\Phi(t_1, t_K, 0, L)$ and $\Theta(t_1, t_K, 0, L)$.

Deviation from singularity of the data matrix, though, unavoidable numerically, can be treated by the following corollary (Golub, 1996).

Corollary 6.1

Let M_0 denote an $n \times n$ nonsingular matrix, with its singular value decomposition $M_0 = U\Sigma_0 V^T$ in which $\Sigma_0 = diag(\sigma_1, \sigma_2, \cdots, \sigma_{n-1}, \sigma_n)$ is arranged in descending order. The closest singular matrix, say M_1, to M_0 in the sense of $\|M_1 - M_0\|_F$ [2] (or $\|M_1 - M_0\|_2$) is given by $M_1 = U\Sigma_1 V^T$ where $\Sigma_1 = diag(\sigma_1, \sigma_2, \cdots, \sigma_{n-1}, 0)$.

The attractive feature of the above corollary is that the associated singular matrix is achieved with only a slight perturbation to the original matrix. When the data matrix of the previous simulation, for example, is exposed to the above corollary the original data matrix

$$\begin{bmatrix} 5.7700 & 0.8235 & 0.1222 & 6.0000 & -1.2520 & 1.0212 \\ 4.7600 & -0.2970 & -0.8639 & 5.0000 & -1.9156 & 0.6677 \\ 3.9000 & -0.9823 & 0.7501 & 4.0000 & -1.6914 & -0.2620 \\ 2.9800 & -0.5673 & 0.2669 & 3.0000 & -0.8306 & -0.1056 \\ 2.0500 & 0.5358 & -0.9792 & 2.0000 & 0.1145 & 0.8939 \\ 1.1500 & 0.9921 & 0.5750 & 1.0000 & 0.4679 & 0.9724 \end{bmatrix}$$

[2] $\|\cdot\|_F^2$ denotes the Frobenius norm which is the sum of the squares of the entries of the matrix.

is converted to

$$\begin{bmatrix} 5.7699 & 0.8235 & 0.1222 & 6.0001 & -1.2519 & 1.0212 \\ 4.7603 & -0.2969 & -0.8640 & 4.9997 & -1.9157 & 0.6677 \\ 3.8994 & -0.9825 & 0.7502 & 4.0006 & -1.6912 & -0.2619 \\ 2.9806 & -0.5671 & 0.2668 & 2.9993 & -0.8308 & -0.1058 \\ 2.0496 & 0.5357 & -0.9792 & 2.0004 & 0.1146 & 0.8940 \\ 1.1502 & 0.9922 & 0.5750 & 0.9998 & 0.4679 & 0.9723 \end{bmatrix}.$$

Although the use of corollary 6.1 guarantees the existence of a nontrivial solution for the homogeneous system of equation (6.14) it does not help to capture a unique solution among an infinite number of possible solutions. To acquire unique values for the unknown parameters, *a priori* information should be involved. Knowing the contribution of one of the basis functions permits the transfer of the corresponding column to the right-hand side of equation (6.9), providing a nonhomogenous system of equations. Since in the IPFM model the modulating signal, $\lambda_{ac}(t)$, is always accompanied by a dc value, λ_{dc}, the linear function t is selected for $\phi_0(t)$ due to the differentiation operator of equation (6.4). Further, $\theta_0(t)$ is chosen to be a constant to handle the dc portion of the threshold input. Consequently, equation (6.9) is converted to

$$\begin{bmatrix} \phi_1(t_1) & \cdots & \phi_L(t_1) & \theta_1(t_1) & \cdots & \theta_L(t_1) \\ \phi_1(t_2) & \cdots & \phi_L(t_2) & \sum_{j=1}^{2}\theta_1(t_j) & \cdots & \sum_{j=1}^{2}\theta_L(t_j) \\ \phi_1(t_3) & \cdots & \phi_L(t_3) & \sum_{j=1}^{3}\theta_1(t_j) & \cdots & \sum_{j=1}^{3}\theta_L(t_j) \\ \vdots & \vdots & \vdots & \vdots & \vdots & \vdots \\ \phi_1(t_K) & \cdots & \phi_L(t_K) & \sum_{j=1}^{K}\theta_1(t_j) & \cdots & \sum_{j=1}^{K}\theta_L(t_j) \end{bmatrix} \begin{bmatrix} \alpha_1 \\ \alpha_2 \\ \vdots \\ \alpha_L \\ \\ \beta_1 \\ \beta_2 \\ \vdots \\ \beta_L \end{bmatrix} = - \begin{bmatrix} \alpha_0 t_1 + \beta_0 \\ \alpha_0 t_2 + 2\beta_0 \\ \vdots \\ \\ \vdots \\ \alpha_0 t_K + K\beta_0 \end{bmatrix} \tag{6.16}$$

or in simplified form to

$$\begin{bmatrix} \Phi(t_1, t_K, 1, L) & \Theta(t_1, t_K, 1, L) \end{bmatrix} \begin{bmatrix} \underline{\alpha}_{1,L} \\ \\ \underline{\beta}_{1,L} \end{bmatrix} = - \begin{bmatrix} \alpha_0 \Phi(t_1, t_K, 0, 0) + \beta_0 \Theta(t_1, t_K, 0, 0) \end{bmatrix} \tag{6.17}$$

β_0 in equation (6.16) is nothing but a_{dc}, the dc value of the threshold input. Likewise, α_0 is replaced with λ_{dc}, the dc value of the modulating input. Since α_0 and β_0 can be determined by the mean value of the interspike intervals and $t_1, t_2, \cdots, t_K$ are given,

the right hand side of equation (6.17) will be known. Therefore, a proper selection for $\phi_i(t)$ and $\theta_i(t)$ are required in order to attain a unique solution for the unknown parameters. Additionally, $\phi_i(t)$ and $\theta_i(t)$ must be able to satisfactorily represent $\lambda_{ac}(t)$ and $a_{ac}(t)$. The following section is dedicated to consider these important issues in detail.

6.3.2 Selection of the Basis Functions

Expressing $\lambda_{ac}(t)$ and $a_{ac}(t)$ in terms of the constructing functions $\phi_i(t)$ and $\theta_i(t)$ enables a new strategy to be established for considering the TVTIPFM model on the one hand and shifts the model to the vector space context on the other. Solving the problem in the function space gives a mathematically elegant solution. However, it would raise questions such as: is the problem solvable, is the solution unique, how accurate is the answer? To be more specific, equations (6.4) and (6.5) approximate $\lambda(t)$ and $a(t)$ in terms of the basis functions $\phi_i(t)$ and $\theta_i(t)$, respectively. Viewed in this perspective, the TVTIPFM model is indeed mapped to an approximation problem.

A large number of basis function sets exist, each having its own properties suitable for specific purposes (Davis, 1963). Among the various sets of basis functions, trigonometric polynomials are well suited to tackle our specific problem. There are important reasons behind this selection. First, trigonometric polynomials ensure an independent set of columns for the data matrix of equation (6.16) and hence a unique solution for α_i and β_i. Second, sin, (cos) functions convey the physical concept of the frequency contents of the excitation signals (recalling that this research is concerned with rhythmical fluctuations for $f < 0.5Hz$). Third, derivative of a sin (cos) function is a cos (sin) function, preserving all the appealing properties of the trigonometric polynomials. All these points will be clarified in the following sections.

Having provided the necessary framework, the following basis functions for $\varphi_i(t)$ and $\theta_i(t)$ are now introduced.

$$\begin{aligned} \varphi'_i(t) &= cos\,(2\pi(f_{low} + p\Delta f)t)\,, \\ \varphi'_{i+1}(t) &= sin\,(2\pi(f_{low} + p\Delta f)t)\,, \\ i = 1,3,5,\cdots,(L-1), \quad p = \frac{i-1}{2}, &\qquad L = Even \end{aligned} \tag{6.18}$$

$$\theta_i(t) = sin\,(2\pi(f_{low} + p\Delta f)t)\,,$$
$$\theta_{i+1}(t) = cos\,(2\pi(f_{low} + p\Delta f)t)\,,$$
$$i = 1,3,5,\cdots,(L-1), \quad p = \frac{i-1}{2}, \qquad L = Even \tag{6.19}$$

in which Δf denotes the frequency resolution between the successive basis functions and f_{low} represents the lowest frequency of the spanning functions. By this selection we obtain:

$\Phi(\mathrm{t_1}, \mathrm{t_K}, 1, \mathrm{L}) =$

$$\frac{1}{2\pi}\begin{bmatrix} \frac{1}{f_{low}}sin(2\pi f_{low}t_1) & \frac{-1}{f_{low}}\left(cos(2\pi f_{low}t_1)-1\right) & \cdots & \frac{-1}{2\pi(f_{low}+(\frac{L-2}{2})\Delta f)}\left(cos(2\pi(f_{low}+(\frac{L-2}{2})\Delta f)t_1)-1\right) \\ \frac{1}{f_{low}}sin(2\pi f_{low}t_2) & \frac{-1}{f_{low}}\left(cos(2\pi f_{low}t_2)-1\right) & \cdots & \frac{-1}{2\pi(f_{low}+(\frac{L-2}{2})\Delta f)}\left(cos(2\pi(f_{low}+(\frac{L-2}{2})\Delta f)t_2)-1\right) \\ \vdots & \vdots & \vdots & \vdots \\ \frac{1}{f_{low}}sin(2\pi f_{low}t_K) & \frac{-1}{f_{low}}\left(cos(2\pi f_{low}t_K)-1\right) & \cdots & \frac{-1}{2\pi(f_{low}+(\frac{L-2}{2})\Delta f)}\left(cos(2\pi(f_{low}+(\frac{L-2}{2})\Delta f)t_K)-1\right) \end{bmatrix} \tag{6.20}$$

and

$\Theta(\mathrm{t_1}, \mathrm{t_K}, 1, \mathrm{L}) =$

$$\begin{bmatrix} sin(2\pi f_{low}t_1) & cos(2\pi f_{low}t_1) & \cdots & cos(2\pi(f_{low}+(\frac{L-2}{2})\Delta f)t_1) \\ \sum_{j=1}^{2} sin(2\pi f_{low}t_j) & \sum_{j=1}^{2} cos(2\pi f_{low}t_j) & \cdots & \sum_{j=1}^{2} cos(2\pi(f_{low}+(\frac{L-2}{2})\Delta f)t_j)) \\ \vdots & \vdots & \vdots & \vdots \\ \sum_{j=1}^{K} sin(2\pi f_{low}t_j) & \sum_{j=1}^{K} cos(2\pi f_{low}t_j) & \cdots & \sum_{j=1}^{K} cos(2\pi(f_{low}+(\frac{L-2}{2})\Delta f)t_j)) \end{bmatrix} \tag{6.21}$$

Once the desired band of frequency is assumed and the appropriate number of spike intervals is given, the data matrix $[\Phi(t_1, t_K, 1, L) \;\; \Theta(t_1, t_K, 1, L)]$ will be known. Consequently, the unknown vectors $\underline{\alpha}_{1,L}$ and $\underline{\beta}_{1,L}$ will be obtained by solving the matrix identity (6.17). Next, $\lambda(t)$ and $a(t)$ can be reconstructed according to equations (6.4) and (6.5). It only remains to prove the uniqueness of the obtained solution. This is presented in Appendix A at the end of this chapter.

6.3.3 Properties of the Parametric Solution

The periodic nature of the trigonometric polynomials as the basis functions imposes a periodic solution to the reconstructed signals. Reconstruction based upon sinusoidal functions, for the first instant, brings to mind the well-known Fourier series expansion of a periodic function. However, beyond the similarity between the basis functions there is little resemblance between the two methods. Selection of the trigonometric polynomials is much in the spirit of the fundamental features of the heart rate variability signal. HRV is believed to be a bandlimited signal with certain rhythmical fluctuations. Spanning of this frequency band with sufficient frequency resolution will thus elicit the desired reconstructed signal. There is, however, a trade-off between frequency resolution, the frequency band of interest and the mean interspike intervals. To show this let $\hat{\lambda}_{ac}(t)$ and $\hat{a}_{ac}(t)$, respectively denote the reconstructed modulating signal and the reconstructed threshold signal, obtained by equations (6.4) and (6.5) with the parameters given by the matrix identity (6.17) over the length $T_l \triangleq t_K - t_1$. To avoid periodicity in the reconstructed signals T_l should be confined to $T_l \leq \frac{1}{\Delta f}$. If, as in Chapter 2, T_0 represents the mean interspike intervals then K, the number of spikes over the length T_l, will be given by $K \approx \frac{T_l}{T_0}$. The value of K indeed determines the amount of the available information and hence the number of equations in the matrix identity (6.17). The number of unknown parameters on the other hand is given by $\frac{4(f_{high}-f_{low})}{\Delta f} + 4$ where f_{high} illustrates the highest frequency of the spanning functions ($f_{high} = f_{low} + \frac{L-2}{2}\Delta f$). Therefore, the reconstruction algorithm encounters the following limitations:

$$\begin{aligned} \frac{1}{\Delta f} &\geq T_l \qquad (a) \\ \frac{4(f_{high} - f_{low})}{\Delta f} + 4 &\leq K \qquad (b) \\ \frac{T_l}{T_0} &\approx K \qquad (c) \end{aligned} \tag{6.22}$$

Consequently,

$$4(f_{high} - f_{low}) \leq (f_0 T_l \Delta f - 4\Delta f)\,, \tag{6.23}$$

in which $f_0 = \frac{1}{T_0}$ is the free running frequency. If $T_l = \frac{1}{\Delta f}$ is assumed and Δf is

selected sufficiently low then,

$$4(f_{high} - f_{low}) \leq f_0. \tag{6.24}$$

With $T_0 = 1sec$ as a typical value for the mean interspike intervals we thus obtain

$$(f_{high} - f_{low}) \leq 0.25Hz. \tag{6.25}$$

Equation (6.25) indicates that the frequency band of interest which can be covered by the spanning functions is limited to $0.25Hz$. For an IPFM model, with a constant threshold level, this range can be increased to $0.5Hz$. Surprisingly, the frequency resolution Δf does not participate in relation (6.25). This is because by decreasing Δf, K has to increase accordingly as a result of relation (6.22)(b). An increase in K demands a larger value for T_l, due to (6.22)(c). Therefore, a decrease in Δf which gives rise to an increase in the number of unknown parameters is compensated by an increase in the number of spikes over a larger period of time.

To establish a firm strategy while fulfilling all the limiting conditions, the following steps are suggested for the reconstruction procedure of the TVTIPFM model.

(i) Select the desired spanning band of frequency provided that $f_{high} - f_{low} = \frac{1}{4T_0}$, where T_0 is the mean interspike intervals.

(ii) Choose a desired value for the frequency resolution Δf. This value determines the accuracy in the reconstructed signals.

(iii) Select an appropriate length, T_l, from the spike series signal in which the number of spikes is equal to $\frac{4(f_{high}-f_{low})}{\Delta f} + 4$.

(iv) Construct the data matrix $[\Phi(t_1, t_K, 1, L) \;\; \Theta(t_1, t_K, 1, L)]$ by finding the occurrence times of the spikes within T_l.

(v) Construct the observation vector $[\alpha_0\Phi(t_1, t_K, 0, 0) + \beta_0\Theta(t_1, t_K, 0, 0)]$ by assuming $\alpha_0 = \frac{1}{T_0}$ and $\beta_0 = 1$

(vi) Solve the matrix identity (6.17) for the unknown parameters α_i and β_i.

(vii) Reconstruct the modulating signal $\hat{\lambda}(t)$ and the time varying threshold $\hat{a}(t)$ according to equations (6.4) and (6.5) and by using the parameters obtained from step (vi).

Before substantiating the above procedure by simulation results and experimental studies the closeness of the reconstructed signals, emerged from the proposed algorithm, to the actual signals should be considered. The following theorem deals with this problem.

Theorem 6.2

Let $\hat{\lambda}_{ac}(t)$ and $\hat{a}_{ac}(t)$ respectively, denote the reconstructed modulating signal and the reconstructed threshold signal obtained by equations (6.4) and (6.5) with the parameters given by the matrix identity (6.17) subject to equations (6.18) and (6.19). Then one of the following is true.

(i) $\hat{\lambda}_{ac}(t) = \lambda_{ac}(t)$ and $\hat{a}_{ac}(t) = a_{ac}(t)$, if

$$\lambda_{ac}(t) = \sum_{\substack{i=1,3,5,\cdots,(L-1) \\ p=\frac{i-1}{2},\ L=Even}} \mathrm{a}_i sin(2\pi(f_{low} + p\Delta f)t) + \mathrm{b}_i cos(2\pi(f_{low} + p\Delta f)t) \qquad (6.26)$$

$$a_{ac}(t) = \sum_{\substack{i=1,3,5,\cdots,(L-1) \\ p=\frac{i-1}{2},\ L=Even}} \mathrm{c}_i sin(2\pi(f_{low} + p\Delta f)t) + \mathrm{d}_i cos(2\pi(f_{low} + p\Delta f)t) \qquad (6.27)$$

for arbitrary values of $\mathrm{a}_i, \mathrm{b}_i, \mathrm{c}_i, \mathrm{d}_i$.

(ii) $\hat{\lambda}_{ac}(t) = \lambda_{ac}(t)$ and $\hat{a}_{ac}(t) = a_{ac}(t)$ if $\lambda_{ac}(t)$ and $a_{ac}(t)$ are limited to the frequency band $[f_{low} \quad f_{high}]$ $(f_{low} \neq 0)$ and $\Delta f \to 0, \quad L \to \infty, \quad T_l \to \infty$

(iii)

$$\int_0^{t_k} e_{\lambda_{ac}}(t)dt = \sum_{j=1}^{k} e_{a_{ac}}(t_j) \qquad (6.28)$$
$$k = 1, 2, \cdots, K.$$

in which

$$e_{\lambda_{ac}}(t) \triangleq \lambda_{ac}(t) - \hat{\lambda}_{ac}(t), \qquad (6.29)$$

$$e_{a_{ac}}(t) \triangleq a_{ac}(t) - \hat{a}_{ac}(t). \qquad (6.30)$$

are the error signals.

Proof

(i) This is the trivial part of the theorem. Conceptually, this part asserts that the actual signals are fully recoverable if they are trigonometric polynomials and the same basis functions are utilised for reconstruction. The proof is, therefore, very straightforward by noting the uniqueness of the obtained parameters as proved in Appendix

A and equations (6.4) and (6.5).

(ii) To prove this part $\lambda_{ac}(t)$ and $a_{ac}(t)$ are expressed in terms of their Fourier transforms,

$$\lambda_{ac}(t) = \int_{-\infty}^{\infty} \Lambda_{ac}(f) e^{j2\pi ft} df, \tag{6.31}$$

$$a_{ac}(t) = \int_{-\infty}^{\infty} A_{ac}(f) e^{j2\pi ft} df. \tag{6.32}$$

where

$$\Lambda_{ac}(f) \triangleq \mathcal{F}(\lambda_{ac}(t)),$$
$$A_{ac}(f) \triangleq \mathcal{F}(a_{ac}(t)). \tag{6.33}$$

Subsequently only $\lambda_{ac}(t)$ is dealt with. $a_{ac}(t)$ can be treated similarly. Equation (6.31) can be written as:

$$\lambda_{ac}(t) = \lim_{\Delta f \to 0} \sum_{r=-\infty}^{\infty} \Lambda_{ac}(r\Delta f) e^{jr2\pi\Delta ft} \Delta f =$$

$$\lim_{\Delta f \to 0} \sum_{r=1}^{\infty} [2Re(\Lambda_{ac}(r\Delta f))cos(2\pi r\Delta ft) - 2Im(\Lambda_{ac}(r\Delta f))sin(2\pi r\Delta ft)], \tag{6.34}$$

in which $Re(.)$ and $Im(.)$ denote the real and imaginary parts, respectively. Recalling the bandlimited property of $\lambda_{ac}(t)$ and invoking an appropriate change of variable yield,

$$\lambda_{ac}(t) = \lim_{\Delta f \to 0} \sum_{P=0}^{P_{high}} [2Re(\Lambda_{ac}(f_{low} + P\Delta f))cos(2\pi(f_{low} + P\Delta f)t)$$
$$-2Im(\Lambda_{ac}(f_{low} + P\Delta f))sin(2\pi(f_{low} + P\Delta f)t)], \tag{6.35}$$

where $f_{low} + P_{high}\Delta f = f_{high}$. Therefore, full recovery of the signals will ensue if $\Delta f \to 0$ and $L \to \infty$ ($T_l \to \infty$) for the basis functions of equations (6.18) and (6.19).

(iii) The actual signals which are encountered in practice often do not belong to the function space but they satisfy

$$\int_0^{t_k} \lambda(t)dt = \sum_{j=1}^{k} a(t_j), \tag{6.36}$$
$$k = 1, 2, ..., K.$$

Nevertheless, the reconstructed signals also satisfy

$$\int_0^{t_k} \hat{\lambda}(t)dt = \sum_{j=1}^{k} \hat{a}(t_j), \qquad (6.37)$$
$$k = 1, 2, ..., K\cdot$$

where $\hat{\lambda}(t) = \sum_{i=0}^{L} \alpha_i \varphi_i'(t)$ and $\hat{a}(t) = \sum_{i=0}^{L} -\beta_i \theta_i(t)$. Subtracting equation (6.37) from (6.36) yields

$$\int_0^{t_k} (\lambda(t) - \hat{\lambda}(t))dt = \sum_{j=1}^{k} (a(t_j) - \hat{a}(t_j)), \qquad (6.38)$$
$$k = 1, 2, ..., K$$

If

$$e_{\lambda_{ac}}(t) = \lambda_{ac}(t) - \hat{\lambda}_{ac}(t), \qquad (6.39)$$
$$e_{a_{ac}}(t) = a_{ac}(t) - \hat{a}_{ac}(t),$$

are defined as the error signals, then

$$\int_0^{t_k} e_{\lambda_{ac}}(t)dt = \sum_{j=1}^{k} e_{a_{ac}}(t_j), \qquad (6.40)$$
$$k = 1, 2, ..., K\cdot$$

Consequently,

$$\int_0^{t_1} e_{\lambda_{ac}}(t)dt = e_{a_{ac}}(t_1),$$
$$\int_{t_1}^{t_2} e_{\lambda_{ac}}(t)dt = e_{a_{ac}}(t_2),$$
$$.....$$
$$\int_{t_{K-1}}^{t_K} e_{\lambda_{ac}}(t)dt = e_{a_{ac}}(t_K). \qquad (6.41)$$

The above set of equations effectively illustrates the behaviour of the error signals over the entire length $[t_1\ t_K]$. The interesting property of the error signals is their specific characteristics in each interval, *i.e.*, integral of $e_{\lambda_{ac}(t)}$ over the ith interval is solely related to $e_{a_{ac}}(t_i)$. To have a better view of this error let us consider an IPFM model with a constant threshold level. In this case equation (6.41) becomes,

$$\int_{t_{i-1}}^{t_i} e_{\lambda_{ac}}(t) = 0\cdot \qquad (6.42)$$

This means that the positive and negative excursions of the error signal over each interval have compensating effects. Intuitively, one would expect to see a close fit

between the reconstructed signals and the actual signals if the major frequency band of the actual signals is spanned by the basis functions with sufficient accuracy, although neither equation (6.41) nor (6.42) is able to give a quantitative evaluation of this closeness.

6.4 Computational Aspects

Obtaining the parameter vector of equation (6.16) requires a $K \times K$ matrix inversion. Specifically, if a higher accuracy is requested Δf, and hence K, should be increased accordingly. This may give rise to a numerical instability in the matrix inversion process. Higher flexibility and better stability is obtained if equation (6.16) is treated in a Least Squares (LS) manner. This is achieved by imposing more equations than unknowns, namely by converting the square system to an overdetermined system. However, increasing K beyond necessity may violate the condition (6.22)(a). To take advantage of the LS solution while meeting all the limiting conditions, K can be increased slightly more than the number of unknowns. While the exact increase in K can be determined by considering the number of unknowns, the spanning band of frequency and the length of data, setting a $(K+2) \times K$ overdetermined set of equations is a wise selection for most practical cases.

Once the overdetermined system is constructed, one of the least squares methods can be employed to find the unknown parameters (Golub, 1996). Although computationally more expensive, the SVD method is used here due to its prominent features, specifically in manipulating the singular values. Based on this method the modified reconstruction algorithm is set forth in an iterative manner as follows:

(i) Select the desired spanning band of frequency provided that $f_{high} - f_{low} = \frac{1}{4T_0}$ where T_0 is the mean interspike intervals.

(ii) Choose a desired value for the frequency resolution Δf.

(iii) Select an appropriate length, T_l, from the spike series signal in which the number of spikes is equal to $\frac{4(f_{high}-f_{low})}{\Delta f} + 6$.

(iv) Construct the data matrix $[\Phi(t_1, t_{K+2}, 1, L) \;\; \Theta(t_1, t_{K+2}, 1, L)]$ by determining the occurrence times of the spikes within T_l, and compute its singular value decomposition in the standard form of $U\Sigma V^T$ where $\Sigma = diag(\sigma_1, \sigma_2, \cdots, \sigma_K) \in \mathcal{R}^{(K+2)\times K}$.

(v) Construct the observation vector $[\alpha_0\Phi(t_1, t_{K+2}, 0, 0) + \beta_0\Theta(t_1, t_{K+2}, 0, 0)]$ by assuming $\alpha_0 = \frac{1}{T_0}$, $\beta_0 = 1$.

(vi) Obtain the parameter vector

$$\begin{bmatrix} \underline{\alpha}_{1,L} \\ \\ \underline{\beta}_{1,L} \end{bmatrix} = -V\Sigma^{+}U^{T}\left[\alpha_0\Phi(t_1, t_{K+2}, 0, 0) + \beta_0\Theta(t_1, t_{K+2}, 0, 0)\right], \qquad (6.43)$$

in which $\Sigma^{+} = diag(\frac{1}{\sigma_1}, \frac{1}{\sigma_2}, \cdots, \frac{1}{\sigma_K}) \in \mathcal{R}^{K\times(K+2)}$.

(vii) Calculate $\hat{\lambda}(t)$ and $\hat{a}(t)$ using equations (6.4) and (6.5).

(viii) Inject $\hat{\lambda}(t)$ and $\hat{a}(t)$ to the TVTIPFM model and determine the occurrence times, $\hat{t}_1, \hat{t}_2, \cdots, \hat{t}_{K+2}$, of the spikes in the generated R-wave signal.

(ix) Define $\sum_{i=1}^{K}(t_i - \hat{t}_i)^2$ as the minimisation criterion. Go back to step (vi), set $\frac{1}{\sigma_K} = 0$ and iterate the procedure until all $\frac{1}{\sigma_i}$ are equated to zero.

(x) The reconstructed signals $\hat{\lambda}_{ac}(t)$ and $\hat{a}_{ac}(t)$ are those which produce the smallest minimisation criterion.

As an alternative option to the above exhaustive iterative procedure one can simply look for a break in the pattern of the singular values $\sigma_1, \sigma_2, \cdots, \sigma_K$; equating all $\frac{1}{\sigma_i}$ to zero for small σ_i and going through steps (vi)-(vii) only once. This latter procedure which is frequently used in other areas (Van Der Veen, Deprettere, Swindlehurst, 1993; Haykin, 1989) has been employed for the results displayed in the following sections.

6.5 Simulation Results

The simulation results are presented in three different cases:

(i) $a_{ac}(t) = 0$, $\lambda_{ac}(t) \neq 0$

(ii) $a_{ac}(t) \neq 0$, $\lambda_{ac}(t) = 0$

(iii) $a_{ac}(t) \neq 0$, $\lambda_{ac}(t) \neq 0$

6.5.1 Zero Threshold Signal

The TVTIPFM model with $a_{ac}(t) = 0$ is in fact the conventional IPFM model of Chapter 2. The parametric method for this special case finds the simplified form

$$\left[\ \Phi(t_1, \underset{+2}{t_K}, 1, L)\ \right]\left[\ \underline{\alpha}_{1,L}\ \right] = -\left[\ \alpha_0\Phi(t_1, \underset{+2}{t_K}, 0, 0) + \beta_0\Theta(t_1, \underset{+2}{t_K}, 0, 0)\ \right]. \qquad (6.44)$$

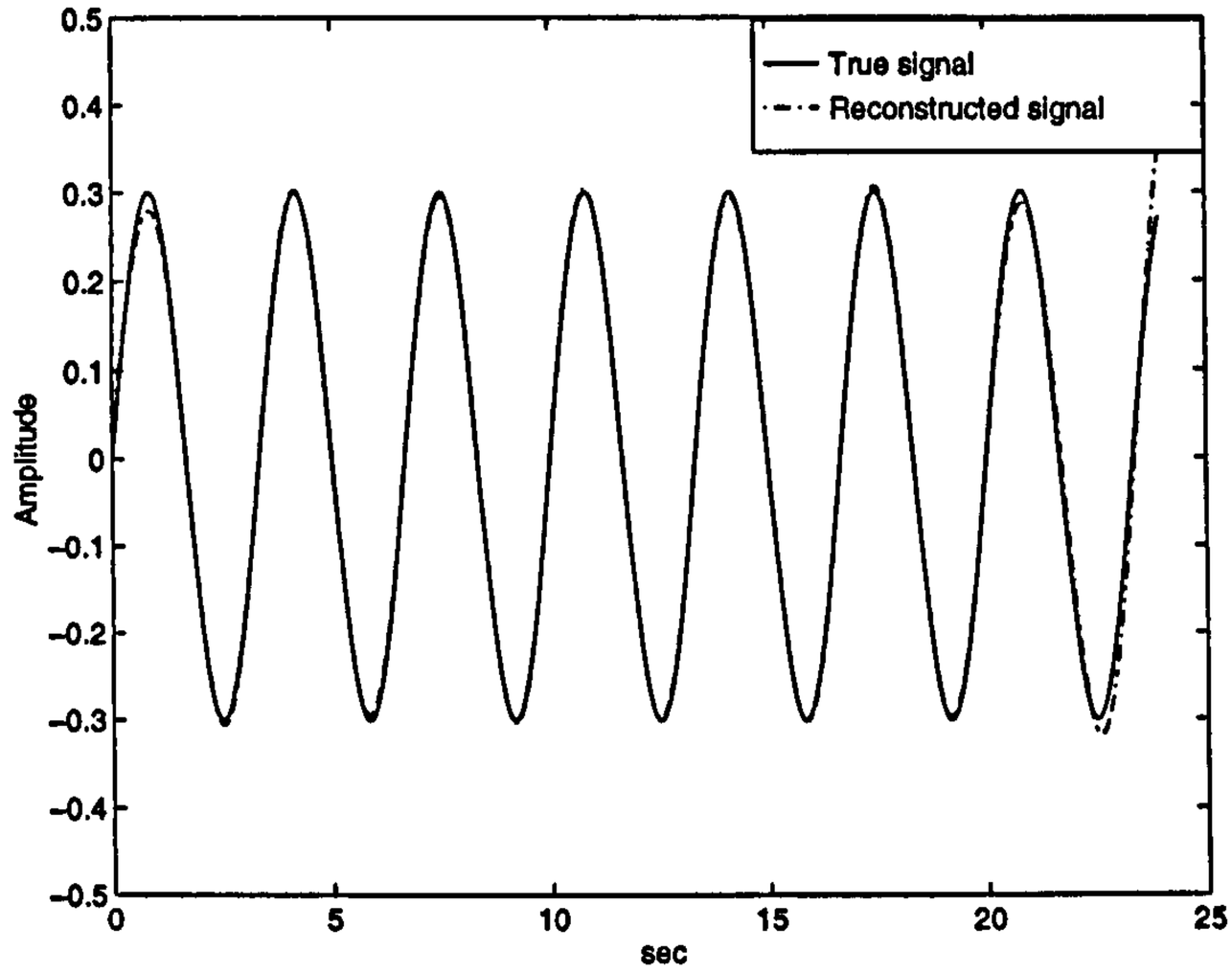


Figure 6.6: True and reconstructed signals for $\lambda_{ac} = 0.3sin(2\pi 0.3t)$ and $f_{low} = 0.2Hz$, $f_{high} = 0.4Hz, \Delta f = 0.02Hz$.

The simulation commences with selecting pure sinusoids as the input signals. First $\lambda_{ac}(t) = 0.3sin(2\pi 0.3t)$ was injected into the model excited with $\lambda_{dc} = a_{dc} = 1$ and sampling frequency $500Hz$. The data matrix was constructed by measuring the occurrence times of the generated spikes with the spanning range $f_{low} = 0.2Hz$, $f_{high} = 0.4Hz$, and resolution $\Delta f = 0.02Hz$. The modulating signal $\lambda_{ac}(t)$ was reconstructed according to the modified algorithm of Section 6.4. As is shown in Fig. 6.6, the reconstructed signal follows the actual signal quite well. This is because $0.3Hz \in [0.2, 0.22, 0.24, \cdots, 0.4]$, meaning that one of the basis functions captures the frequency of the actual signal. If this is not the case the reconstructed signal will be a further approximation to the original signal. This case is considered in Fig. 6.7 for the previous signal but with $f_{low} = 0.2 + 0.01Hz$, $f_{high} = 0.4 + 0.01Hz$ and $\Delta f = 0.02Hz$. The reconstructed signal still remains very close to the actual signal. If the gap between the true signal and the basis functions increases, a larger reconstruction error will arise as is displayed in Fig. 6.8(a) for $f_{low} = 0.12Hz$, $f_{high} = 0.52Hz$ and $\Delta f = 0.04Hz$. The relative contribution of the basis functions can be evaluated if the reconstructed signal is considered over a longer length and its Fourier transform is plotted for this length (Fig. 6.8(b),(c)). It is worthwhile noting that for the selected parameters the reconstruction algorithm only needs ≈ 22 seconds of the R-wave signal (equation 6.22). Therefore, the reconstructed signal is only valid for this length. However, if the reconstructed signal is plotted over a

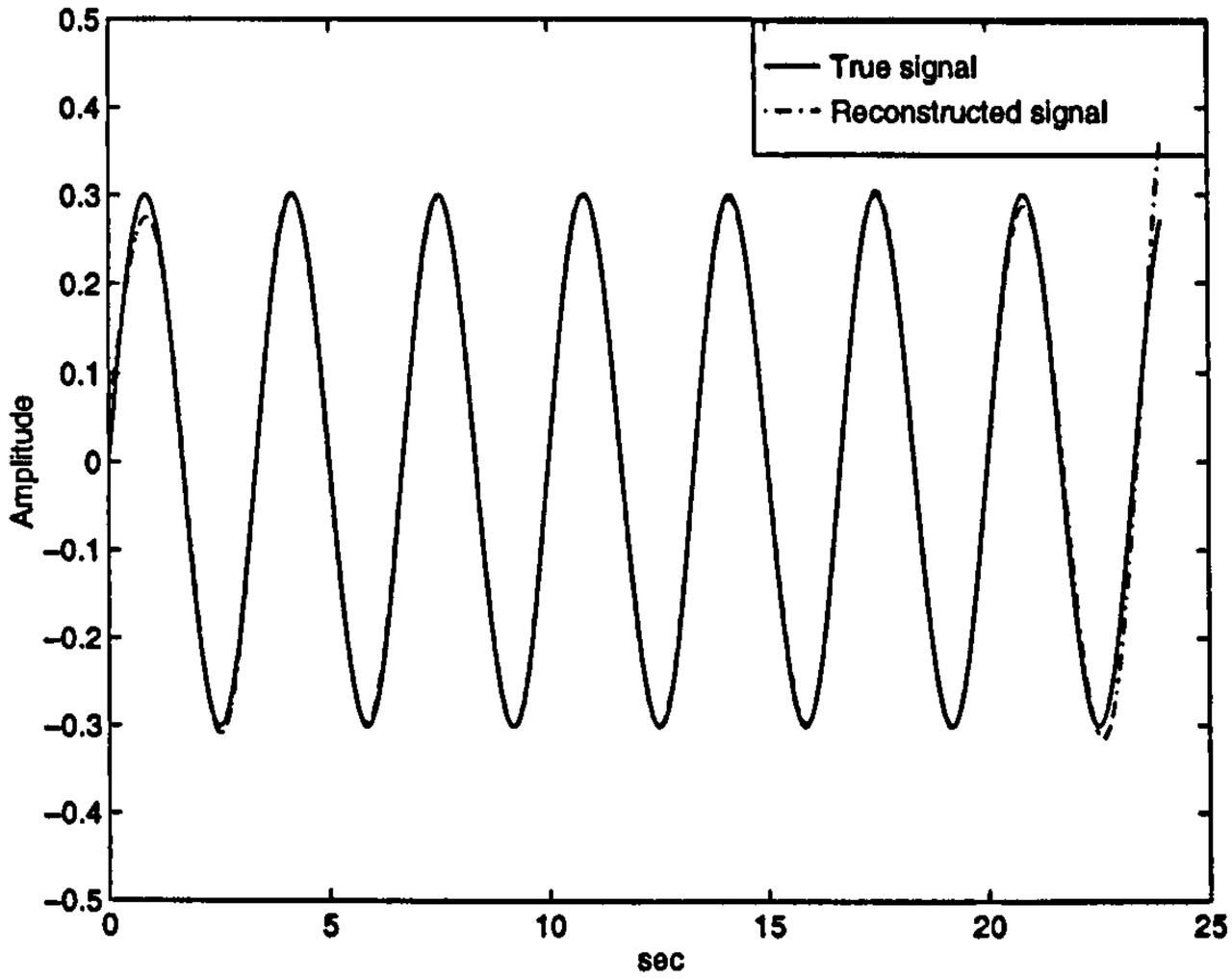
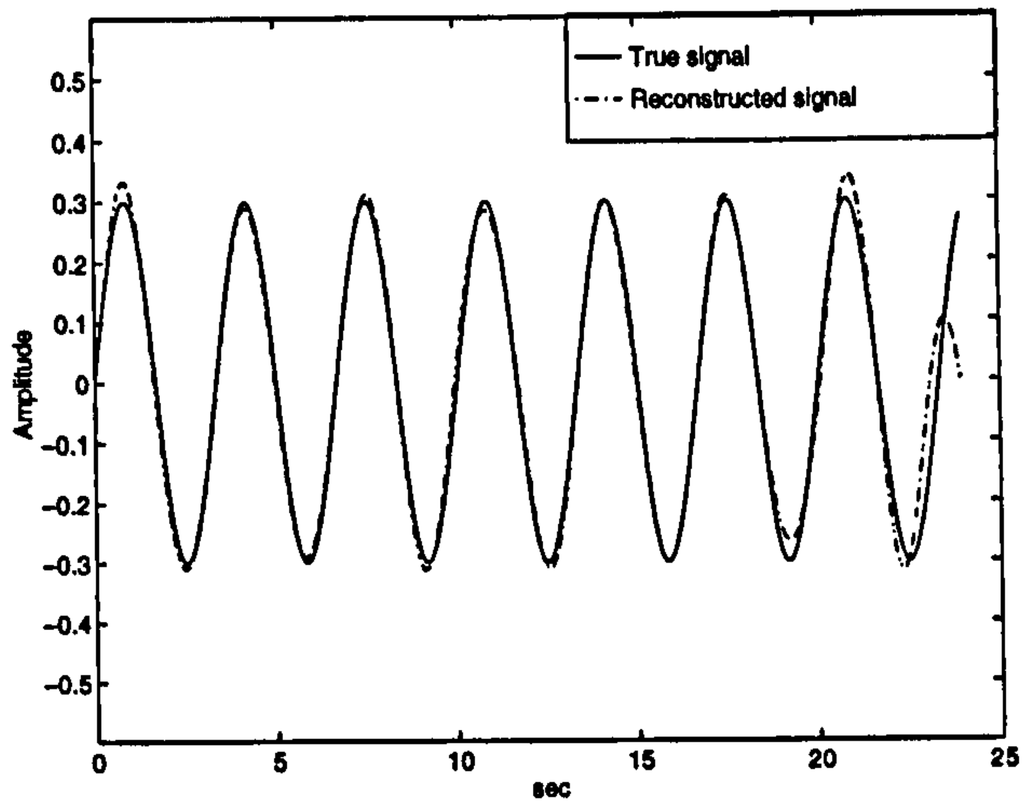


Figure 6.7: True and reconstructed signals for $\lambda_{ac} = 0.3sin(2\pi 0.3t)$ and $f_{low} = 0.2+0.01Hz, f_{high} = 0.4+0.01Hz, \Delta f = 0.02Hz$.

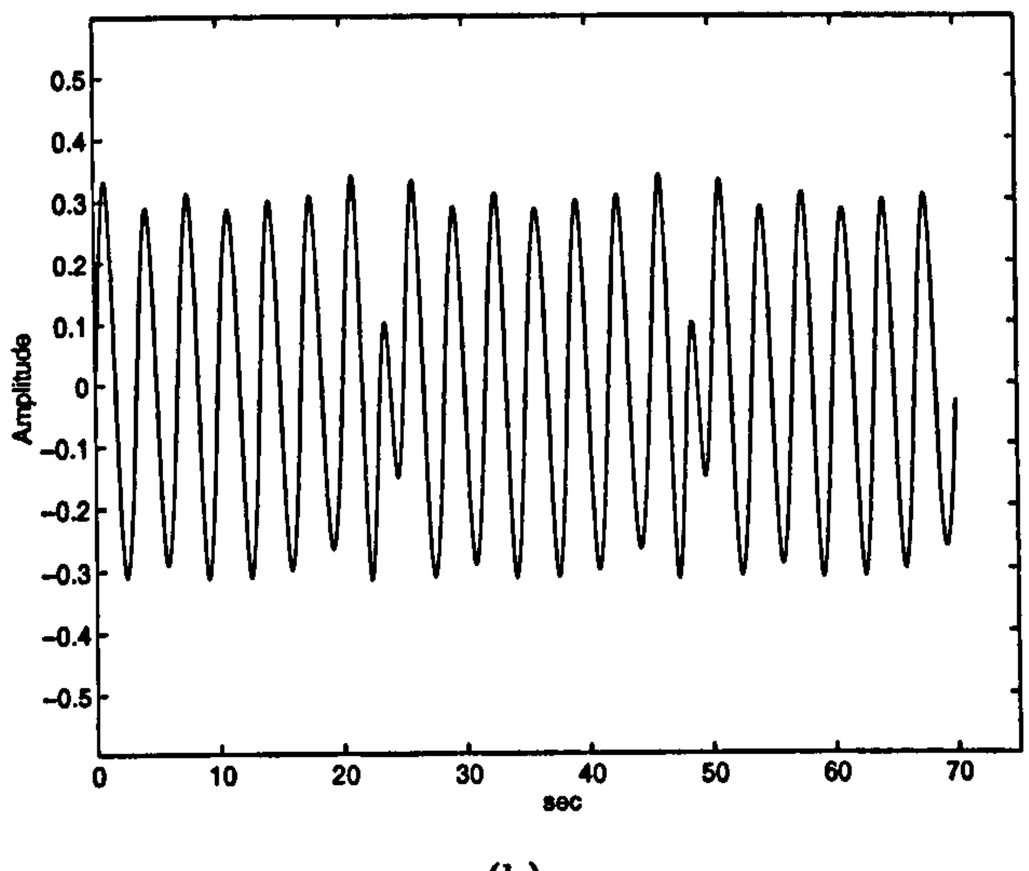
longer length then the deviation of the reconstructed signal from the actual signal will show up. If a longer length is required, then selected parameters should be modified accordingly. The Fourier transform of the reconstructed signal reveals that the basis functions close to the input signals have a much larger contribution than those further away. These components are adjusted by the parametric method in such a way that $\hat{\lambda}_{ac}(t)$ closely follows $\lambda_{ac}(t)$ in the sense of the introduced minimisation criterion over the considered length T_l.

Fig. 6.9 illustrates the performance of the reconstruction algorithm for the multiple sinusoidal signal $\lambda_{ac}(t) = 0.2sin(2\pi 0.1t) - 0.15cos(2\pi 0.25t) + 0.1cos(2\pi 0.35t - \pi/4)$ with $f_{low} = 0.08Hz$, $f_{high} = 0.4Hz$, $\Delta f = 0.02Hz$. A tight fit between the reconstructed signal and the true signal shows the ability of the parametric method to recover sinusoidal excitations. Importantly, none of the sinusoids can be exactly captured by the selected basis functions yet a complete overlap between the reconstructed signal and the original signal can be observed.

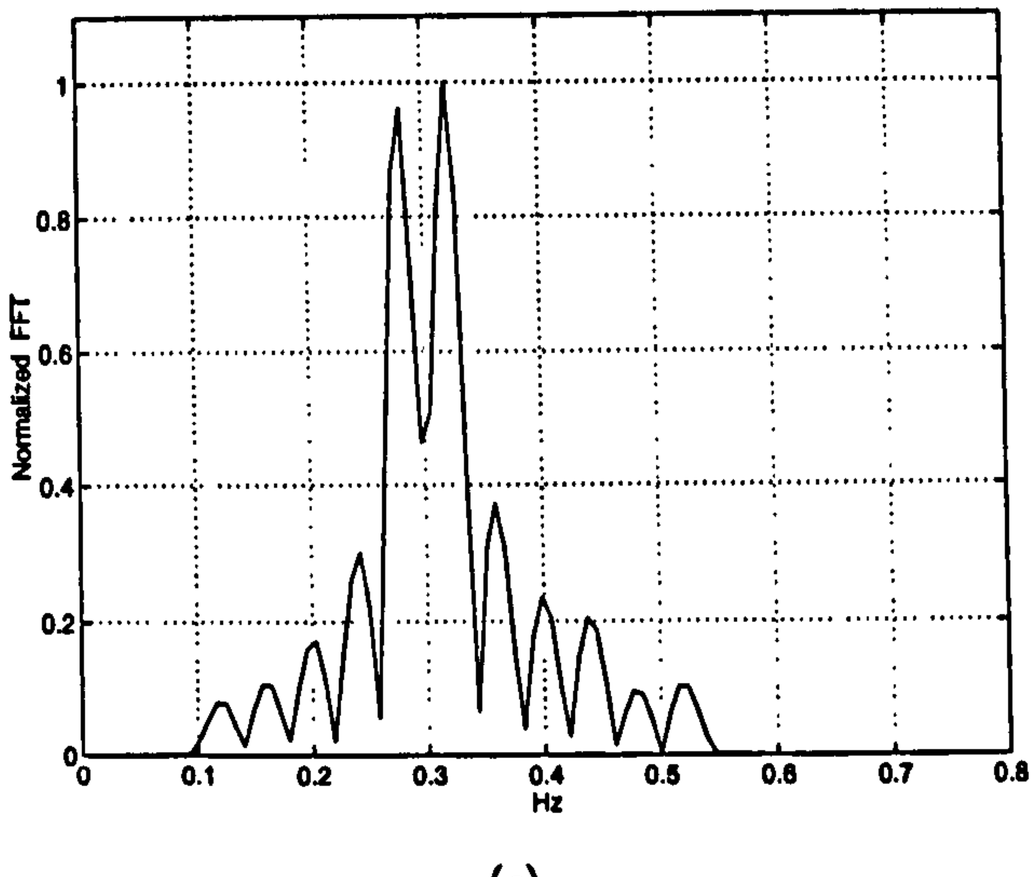
Before proceeding further and appraising the functionality of the parametric method for more realistic signals it would be very useful here to compare this method with the KLPF method. Recalling that in Chapter 2 the lowpass filtering method was introduced as an appropriate method for decoding the IPFM output signal contingent



(a)



(b)



(c)

Figure 6.8: True and the reconstructed signals for $\lambda_{ac} = 0.3sin(2\pi 0.3t)$ and $f_{low} = 0.12Hz, f_{high} = 0.52Hz, \Delta f = 0.04Hz$, (b) the reconstructed signal plotted over a longer length, (c) Fourier transform of the reconstructed signal.

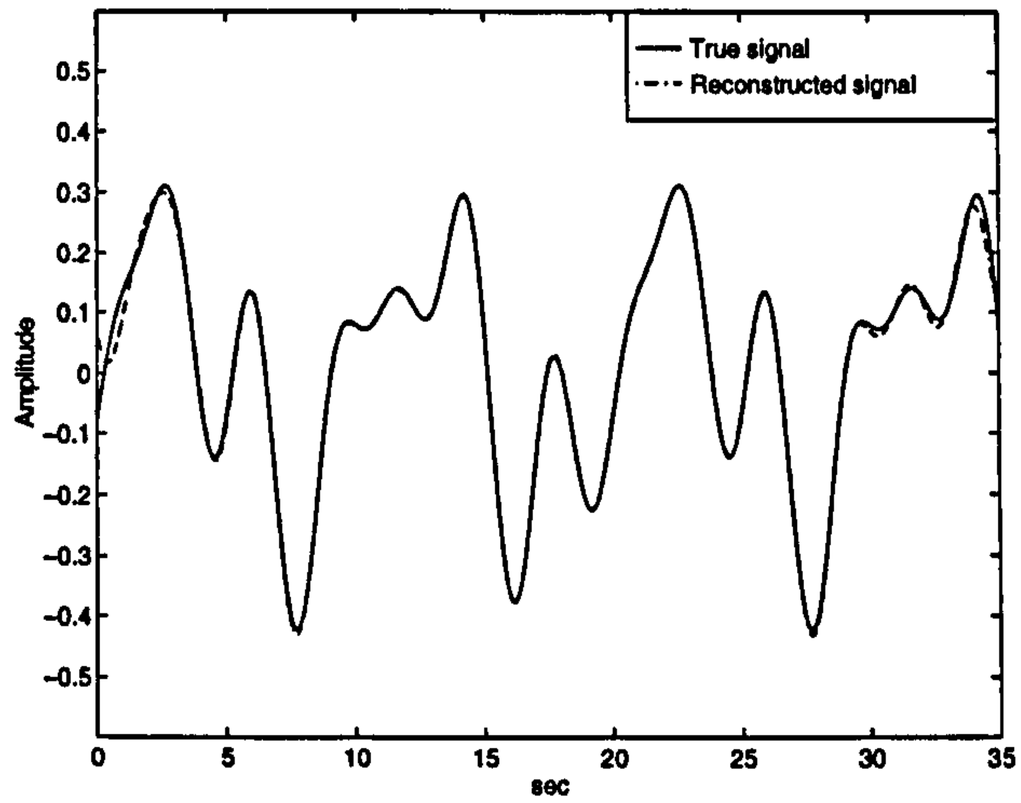
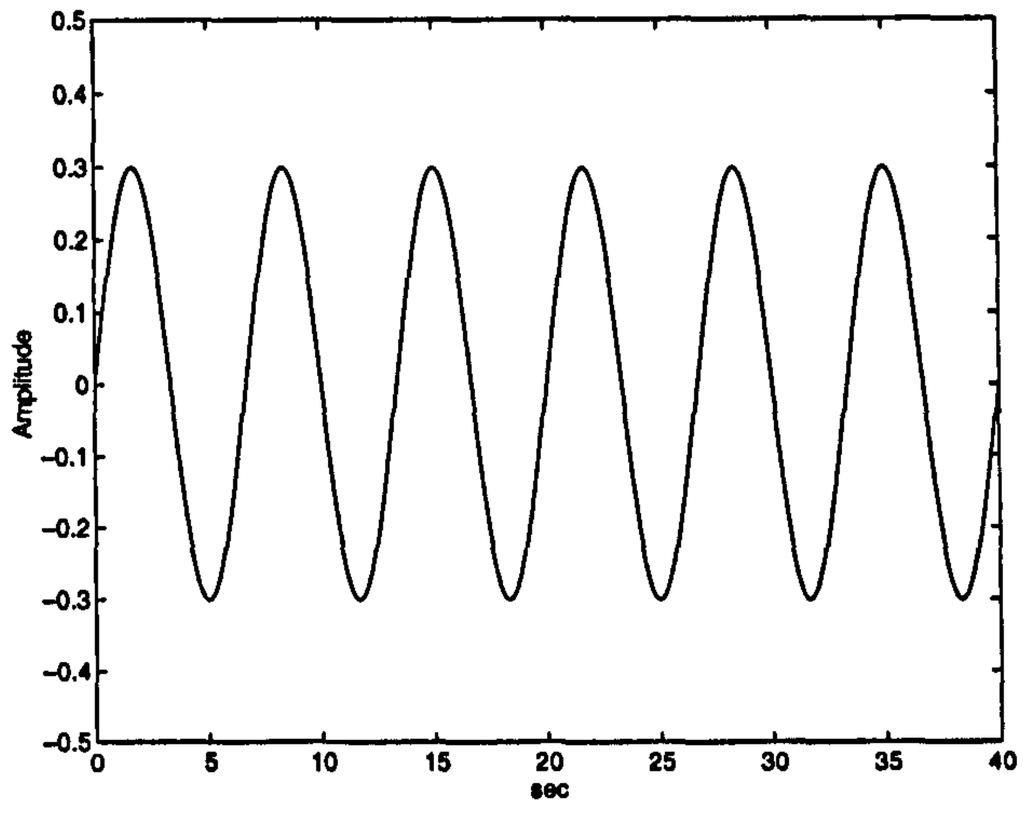


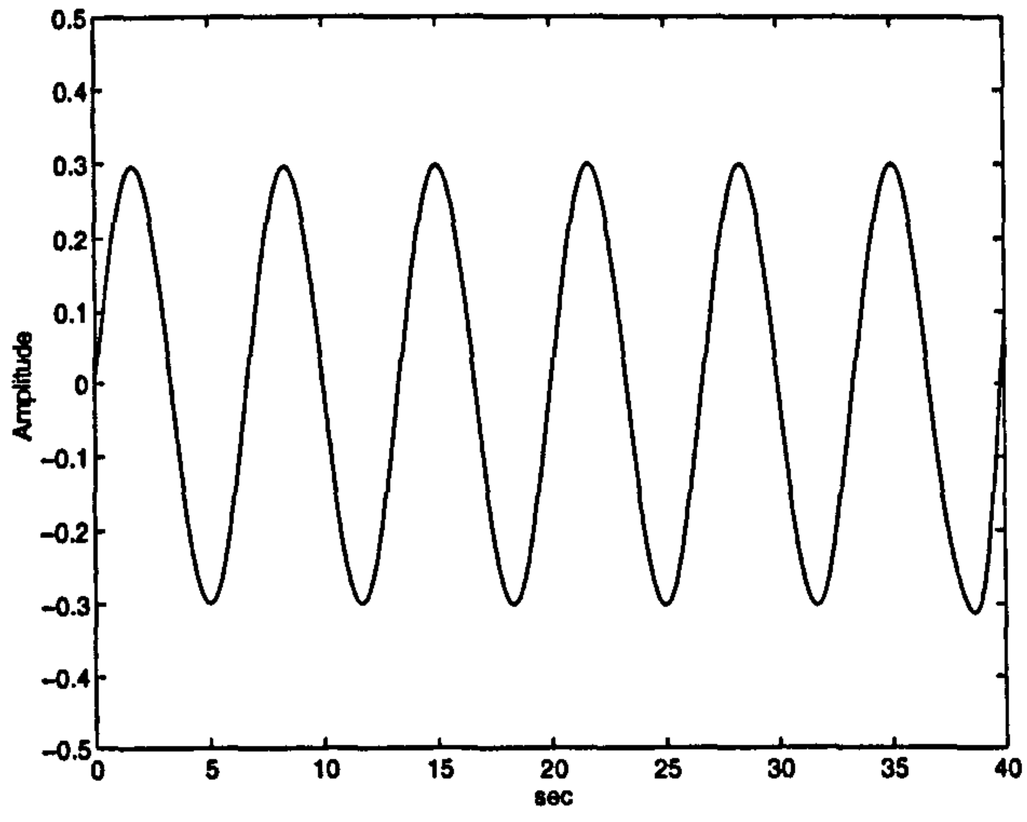
Figure 6.9: True and reconstructed signals for $\lambda_{ac} = 0.2sin(2\pi 0.1t) - 0.15cos(2\pi 0.25t) + 0.1cos(2\pi 0.35t - \pi/4)$ and $f_{low} = 0.08Hz$, $f_{high} = 0.4Hz, \Delta f = 0.02Hz$.

upon having low modulation depth and limited band of frequency for the excitation signal. The comparison begins with the single sinusoidal signal $\lambda_{ac}(t) = 0.3sin(2\pi 0.15t)$. Fig. 6.10(a),(b),(c) illustrate the actual signal, the reconstructed signal using the parametric method, and the reconstructed signal using the KLPF method, respectively. Both methods give satisfactory results in this case. However, if the required conditions for the KLPF method are violated with injection of signal $\lambda_{ac}(t) = 0.8sin(2\pi 0.29t)$ (high modulation depth) then superiority of the parametric method will appear as it is shown in Fig. 6.11. If the frequency of the sinusoid exceeds the cutoff frequency of the filter, the KLPF method will elicit a completely erroneous result whereas the parametric method is still able to recover the input signal quite well. The reconstructed signals along with the actual signals $\lambda_{ac}(t) = 0.4sin(2\pi 0.85t)$ and $\lambda_{ac}(t) = 0.8sin(2\pi 0.85t)$ and their Fourier transforms in Figs. 6.12 and 6.13 confirm this assertion. The small components in Fig. 6.12(f) and 6.13(f) are results of interference of the components according to equation (2.22) whereas the small components surrounding the major component of Fig. 6.12(e) and 6.13(e) arise as a result of the least squares minimisation algorithm. In spite of the superiority of the parametric solution for the IPFM model as considered in Fig. 6.10 through 6.13, the KLPF method can still play an important role in the context of heart rate variability as will be discussed shortly in the final section of this chapter.

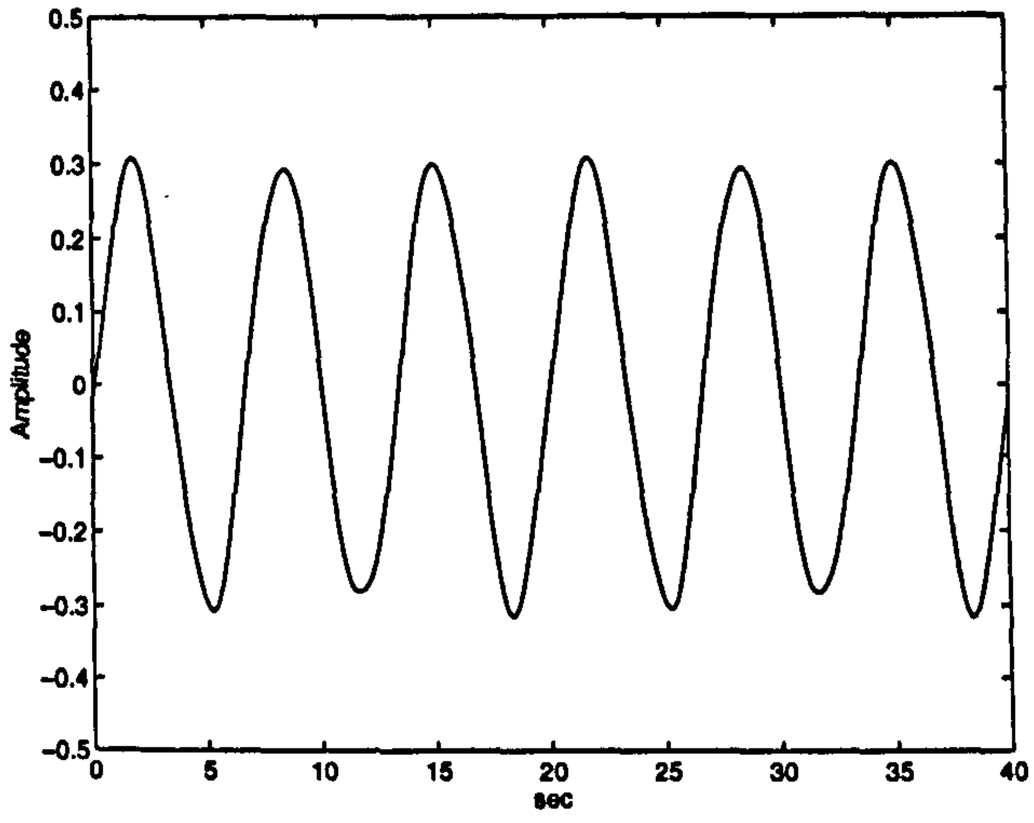
Non-sinusoidal signals can also be restored perfectly well by the parametric method.



(a)

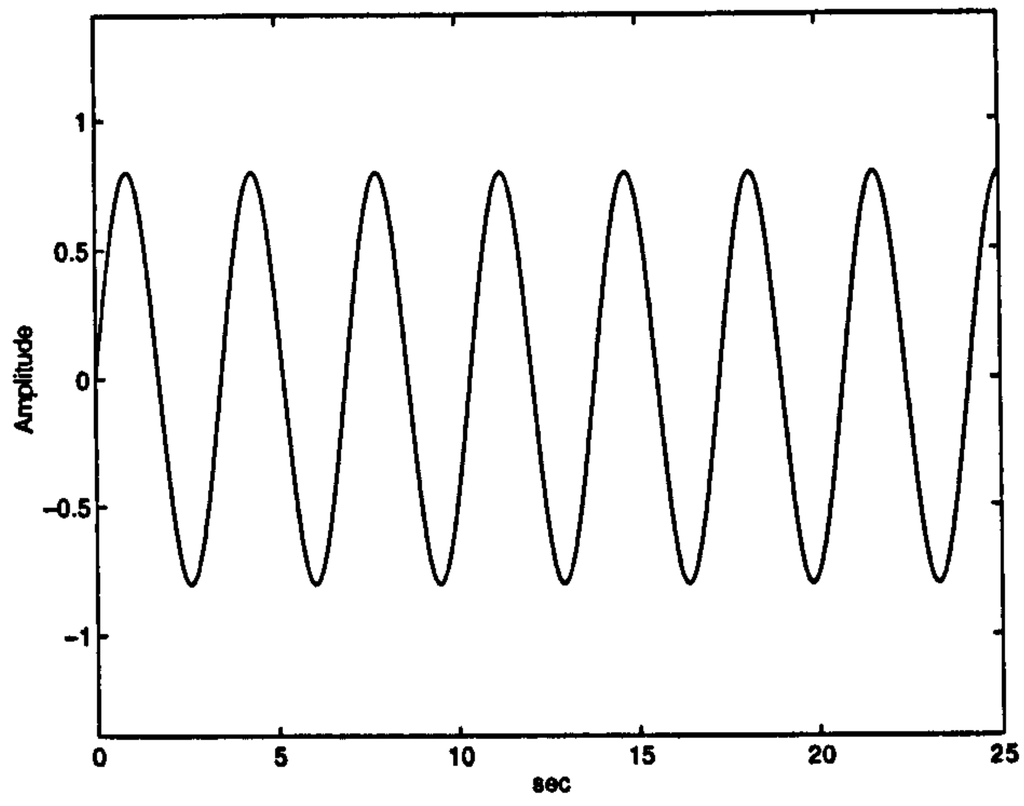


(b)

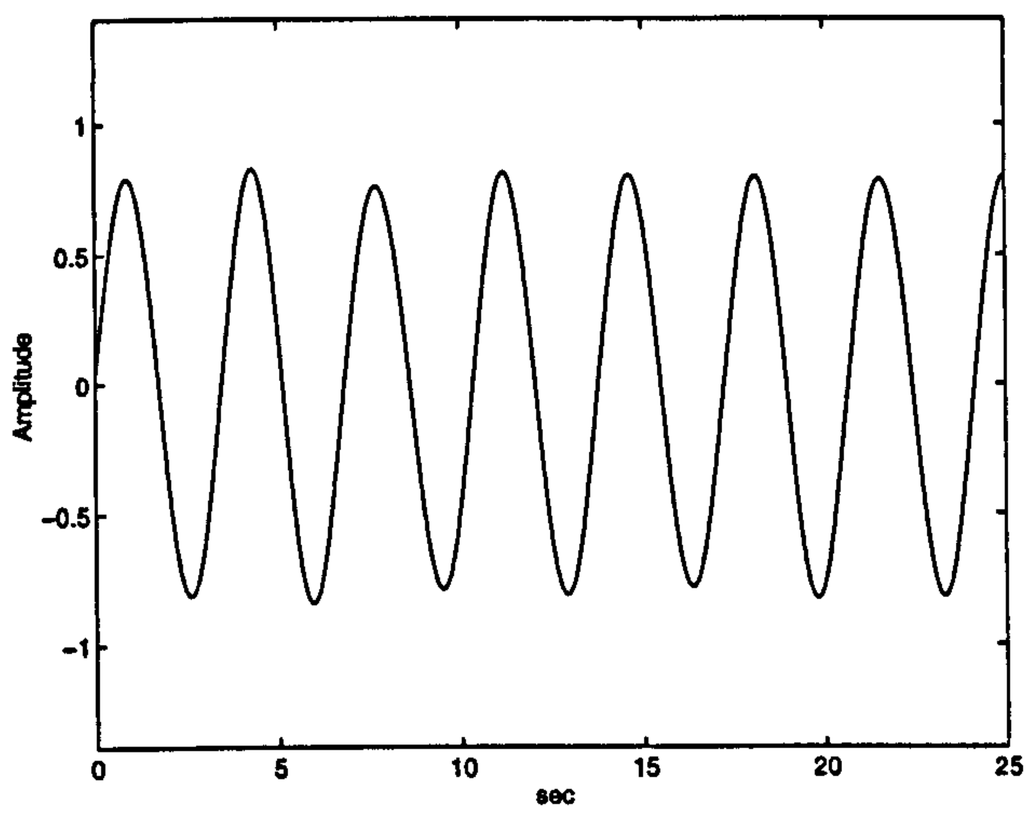


(c)

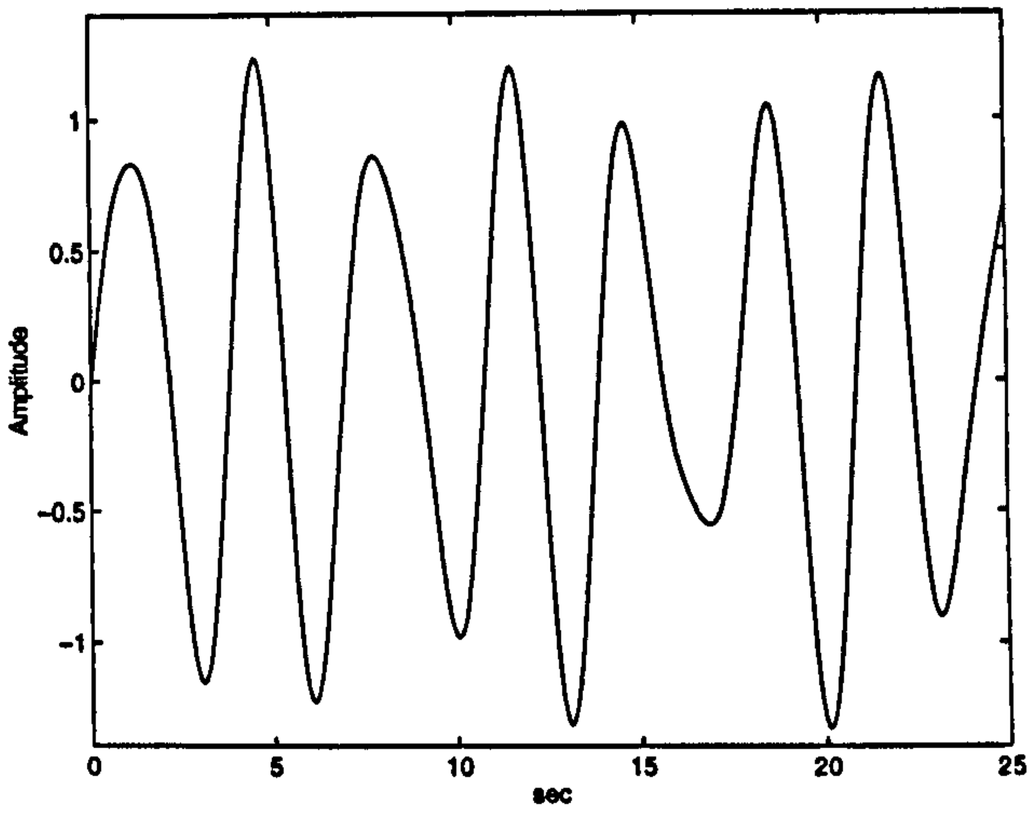
Figure 6.10: (a) The actual signal $\lambda_{ac}(t) = 0.3sin(2\pi 0.15t)$, (b) the reconstructed signal using the parametric method ($f_{low} = 0.04Hz$, $f_{high} = 0.4Hz$, $\Delta f = 0.02Hz$), (c) the reconstructed signal using the KLPF method ($f_c = 0.4Hz$, $\beta = 4.5$, $d = 5sec$).



(a)



(b)



(c)

Figure 6.11: (a) The actual signal $\lambda_{ac}(t) = 0.8sin(2\pi 0.29t)$, (b) the reconstructed signal using the parametric method ($f_{low} = 0.1Hz,\ f_{high} = 0.5Hz,\ \Delta f = 0.02Hz$), (c) the reconstructed signal using the KLPF method ($f_c = 0.45Hz,\ \beta = 4.5,\ d = 5sec$).

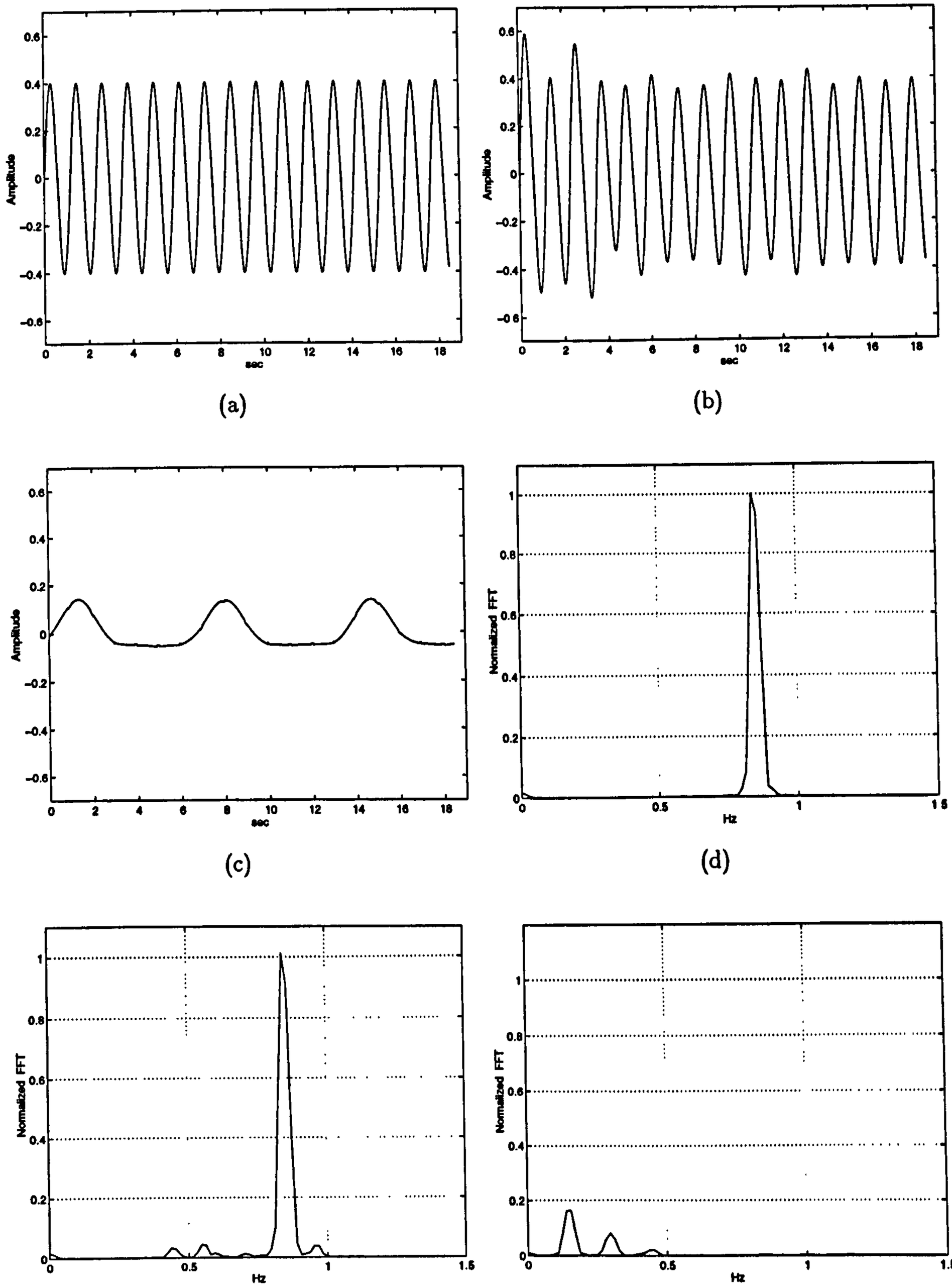
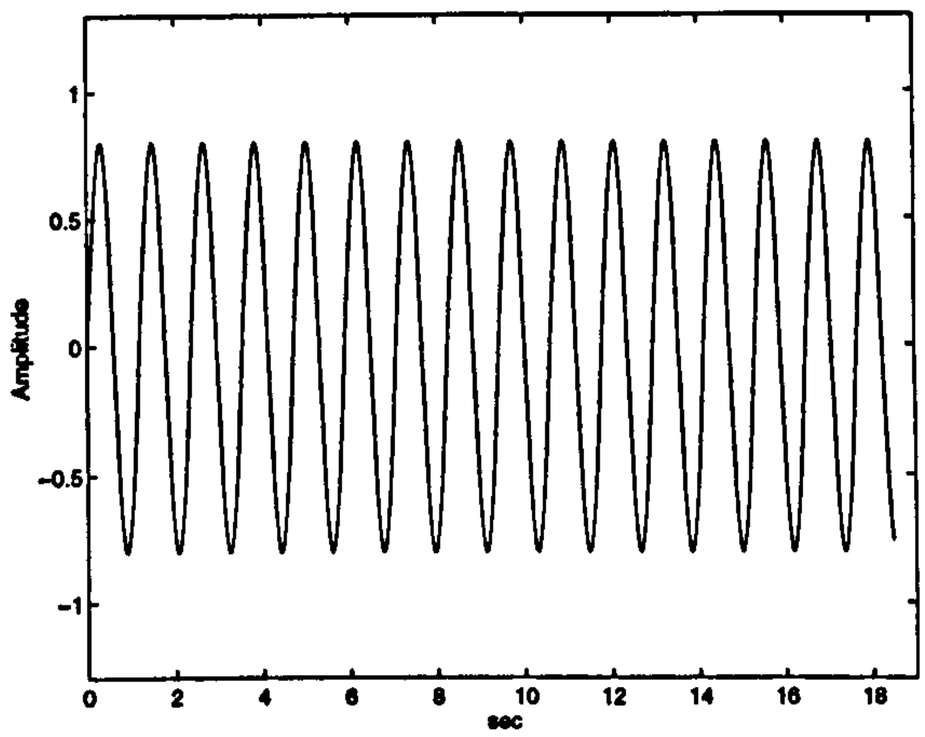
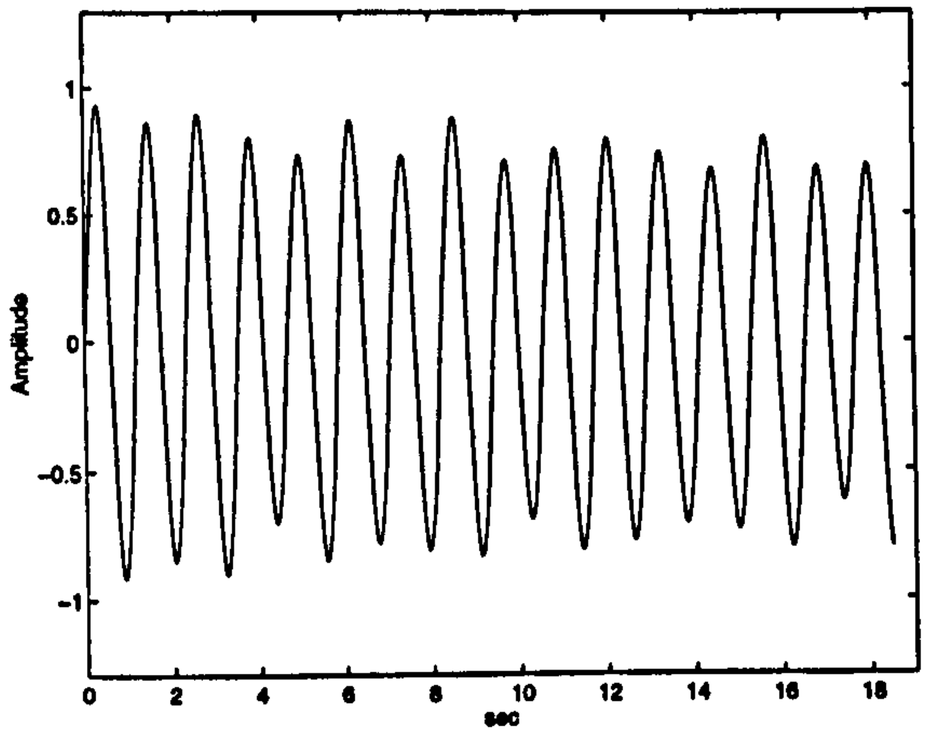


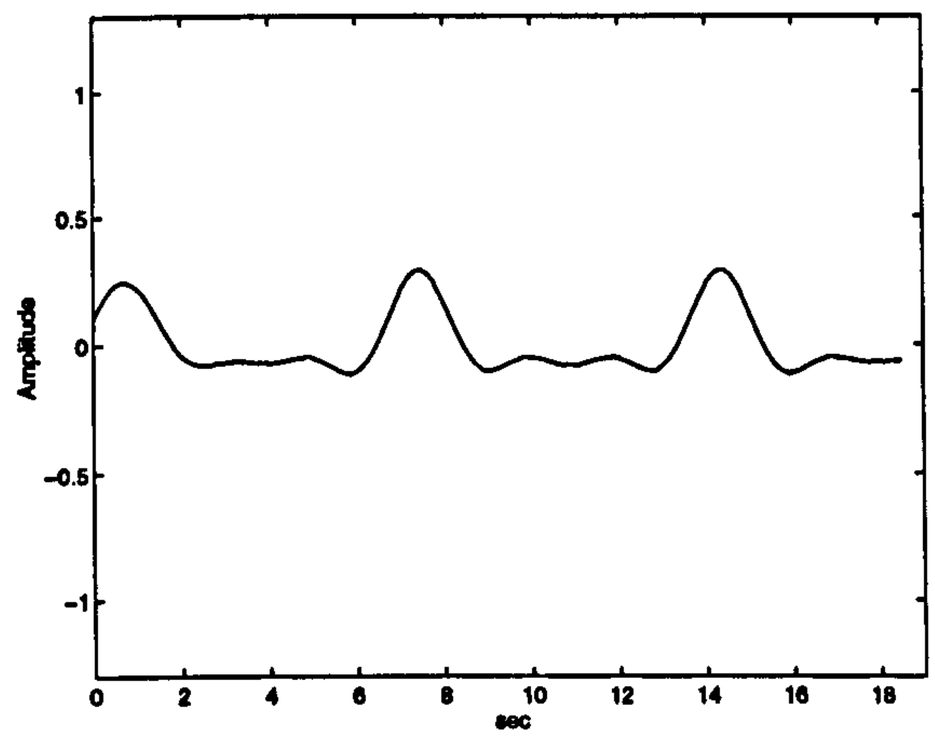
Figure 6.12: (a) The actual signal $\lambda_{ac}(t) = 0.4sin(2\pi 0.85t)$, (b) the reconstructed signal using the parametric method ($f_{low} = 0.45Hz$, $f_{high} = 0.95Hz$, $\Delta f = 0.02Hz$), (c) the reconstructed signal using the KLPF method ($f_c = 0.45Hz$, $\beta = 4.5$, $d = 5sec$), (d) Fourier transform of the actual signal, (e) Fourier transform of the signal of part (b), (f) Fourier transform of the signal of part (c).



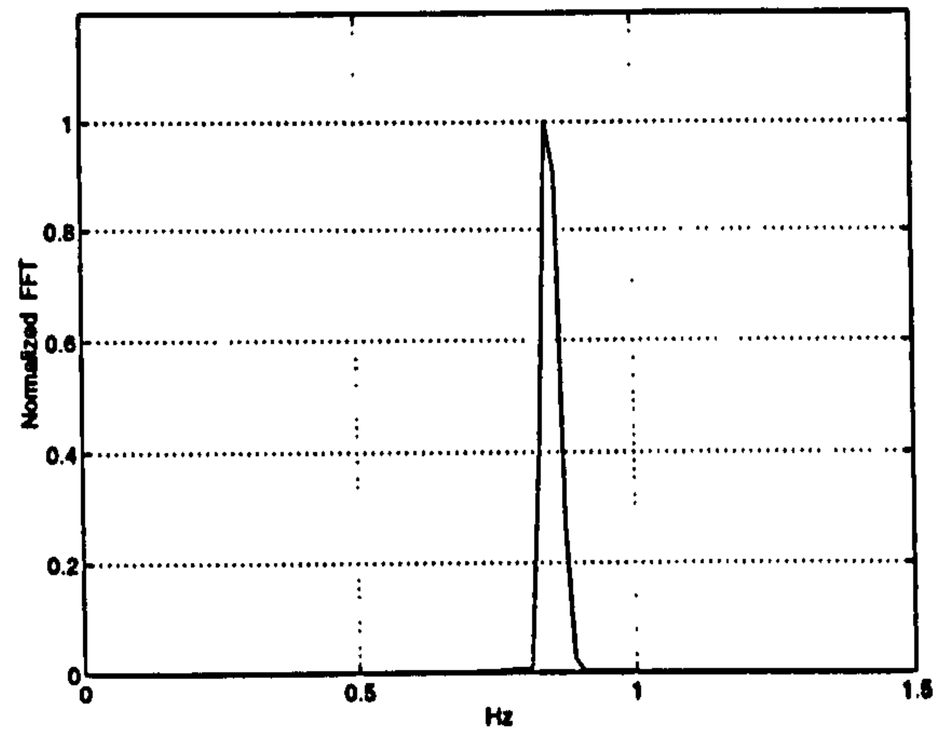
(a)



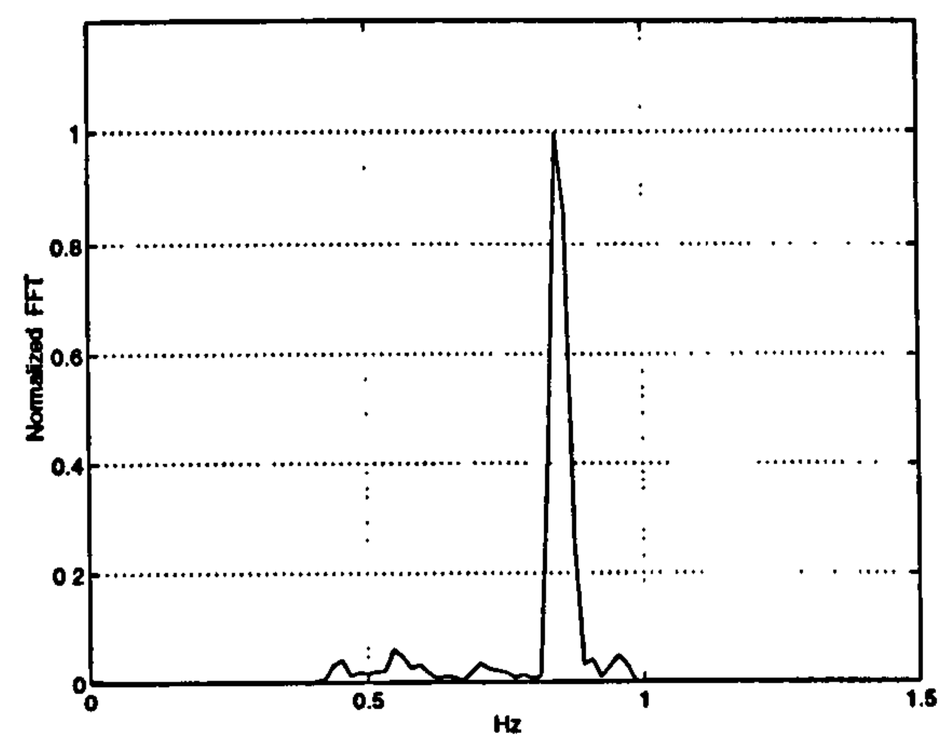
(b)



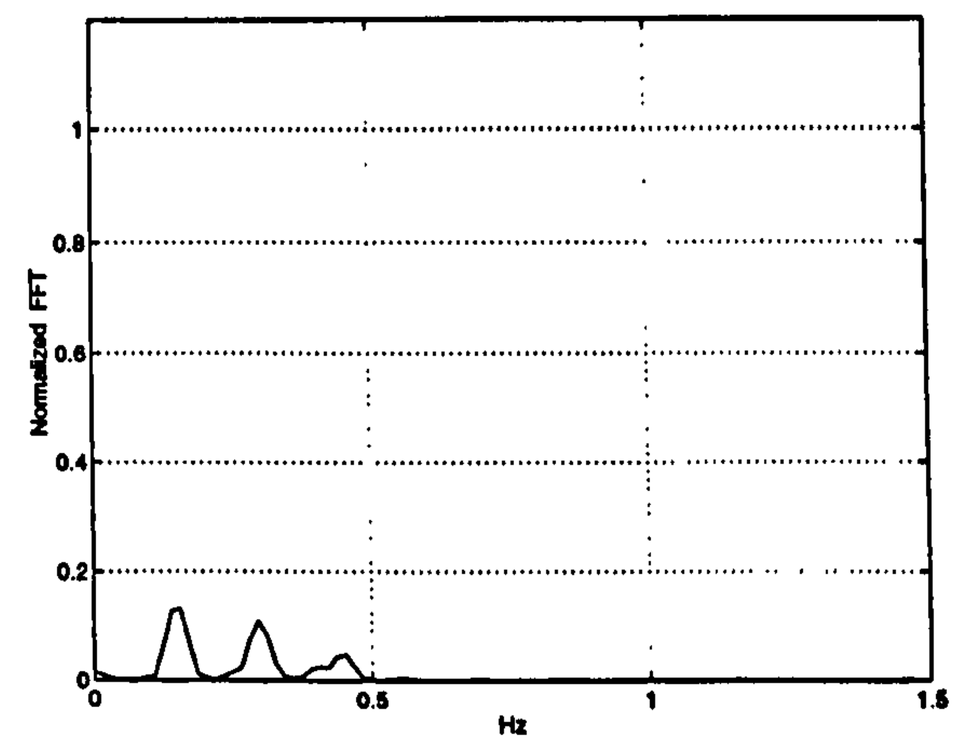
(c)



(d)

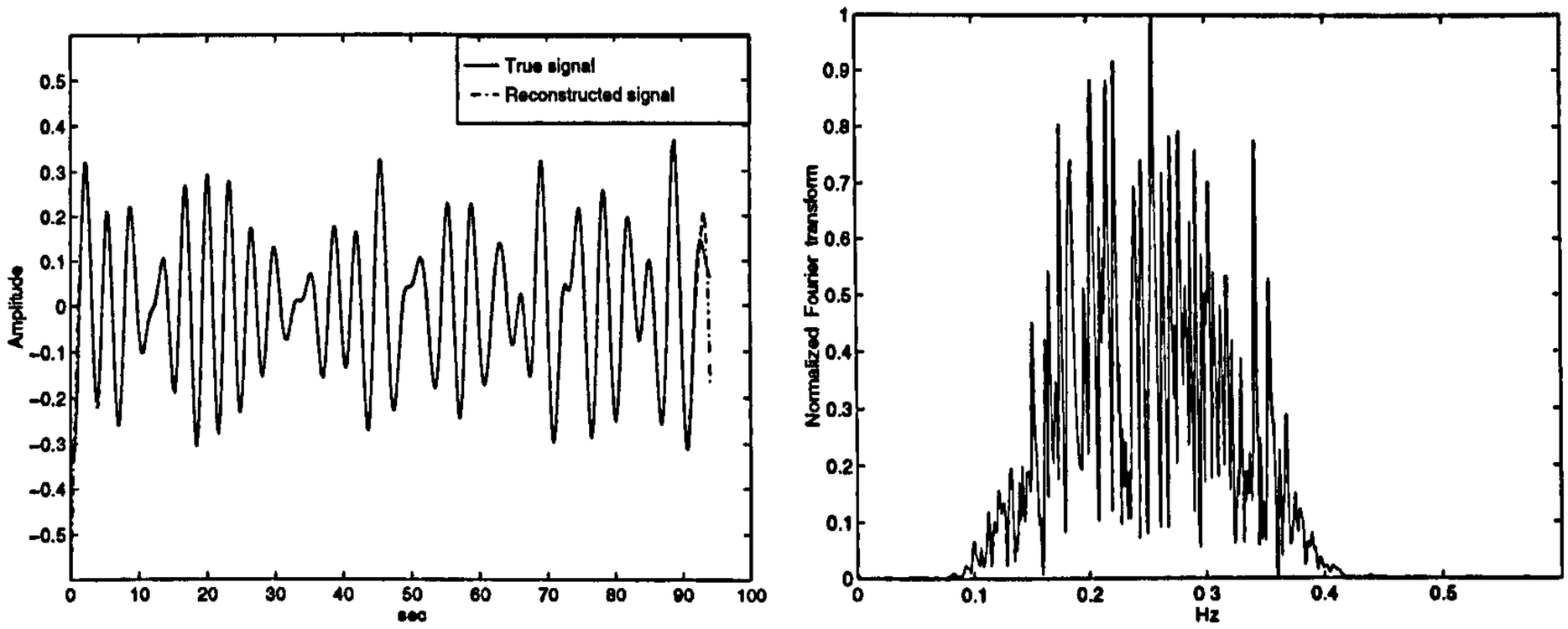


(e)



(f)

Figure 6.13: (a) The actual signal $\lambda_{ac}(t) = 0.8sin(2\pi 0.85t)$, (b) the reconstructed signal using the parametric method ($f_{low} = 0.45Hz$, $f_{high} = 0.95Hz$, $\Delta f = 0.02Hz$), (c) the reconstructed signal using the KLPF method ($f_c = 0.45Hz$, $\beta = 4.5$, $d = 5sec$), (d) Fourier transform of the actual signal, (e) Fourier transform of the signal of part (b), (f) Fourier transform of the signal of part (c).



(a) (b)

Figure 6.14: (a) True and reconstructed signals with a random input in the range $[0.1\ \ 0.4]Hz$, (b) Fourier transform of the random signal.

Fig 6.14 illustrates the result for a random signal (Gaussian zero mean) in the range $[0.1\ \ 0.4]Hz$ which recovered with frequencies $f_{low} = 0.08Hz$, $f_{high} = 0.44Hz$ and $\Delta f = 0.008Hz$. As it is seen in the figure there is a complete overlap between the actual and the reconstructed signal.

Fig. 6.15 shows the performance of the parametric method for a transient signal with sharp edges. For this signal the parametric method tries to fit a composite sinusoidal signal in the range $f_{low} = 0.005Hz, f_{high} = 0.3Hz, \Delta f = 0.005Hz$ to the transient signal. The reconstructed signal closely resembles the actual one over the whole range and shows clearly the robustness of the parametric method for the IPFM model.

6.5.2 Zero Modulating Signal

Assume now that the IPFM model is excited through its threshold input while the modulating signal is kept at zero. Equation (6.17) in this case simplifies to

$$\left[\ \Theta(t_1, \underset{+2}{t_K}, 1, L)\ \right]\left[\ \underline{\beta}_{1,L}\ \right] = -\left[\ \alpha_0 \Phi(t_1, \underset{+2}{t_K}, 0, 0) + \beta_0 \Theta(t_1, \underset{+2}{t_K}, 0, 0)\ \right]. \qquad (6.45)$$

To show the application of the parametric method when the TVTIPFM model is excited only through its threshold input, three different signals are assumed, starting from a pure sinusoid. Figures 6.16 and 6.17 illustrate the obtained results for the

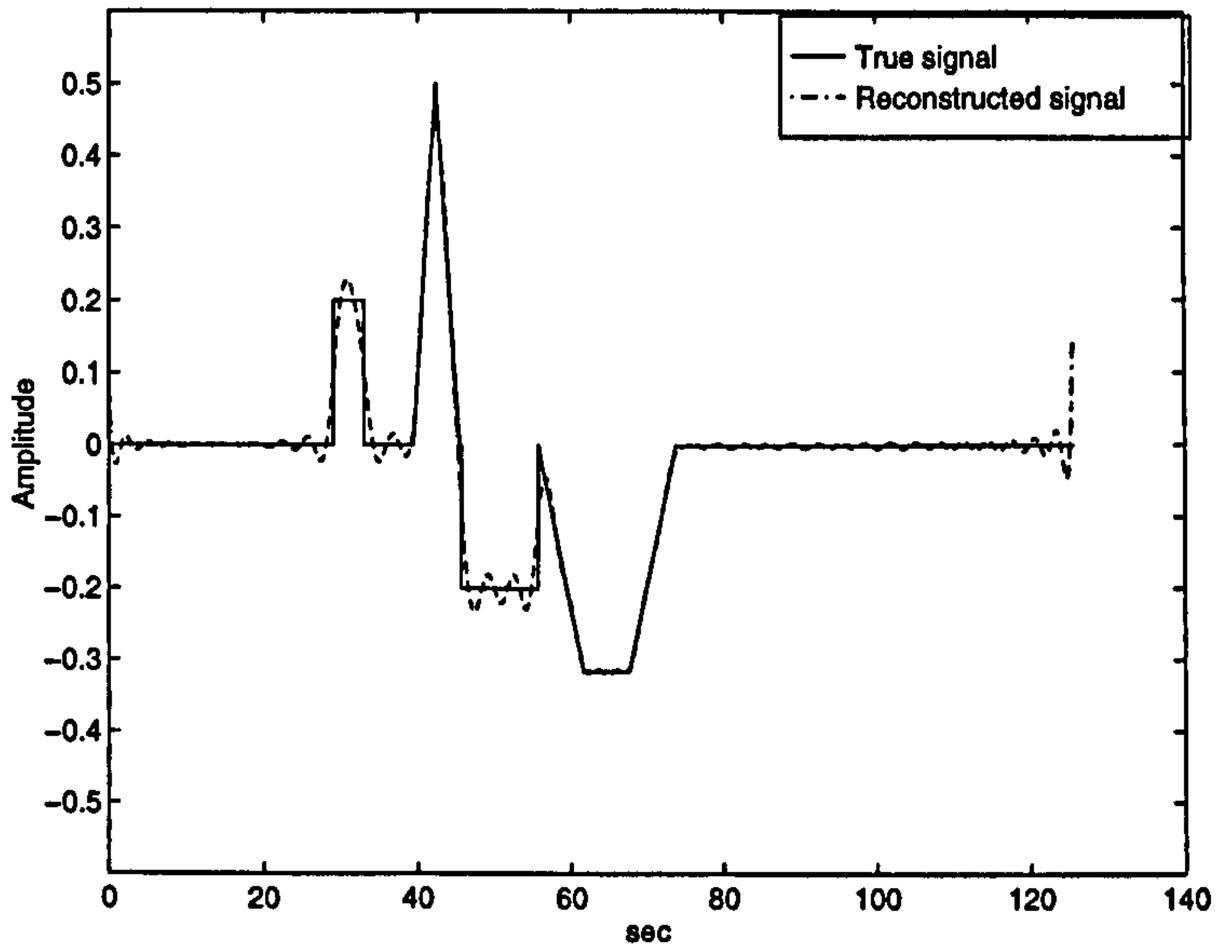


Figure 6.15: True and reconstructed signals for a transient input.

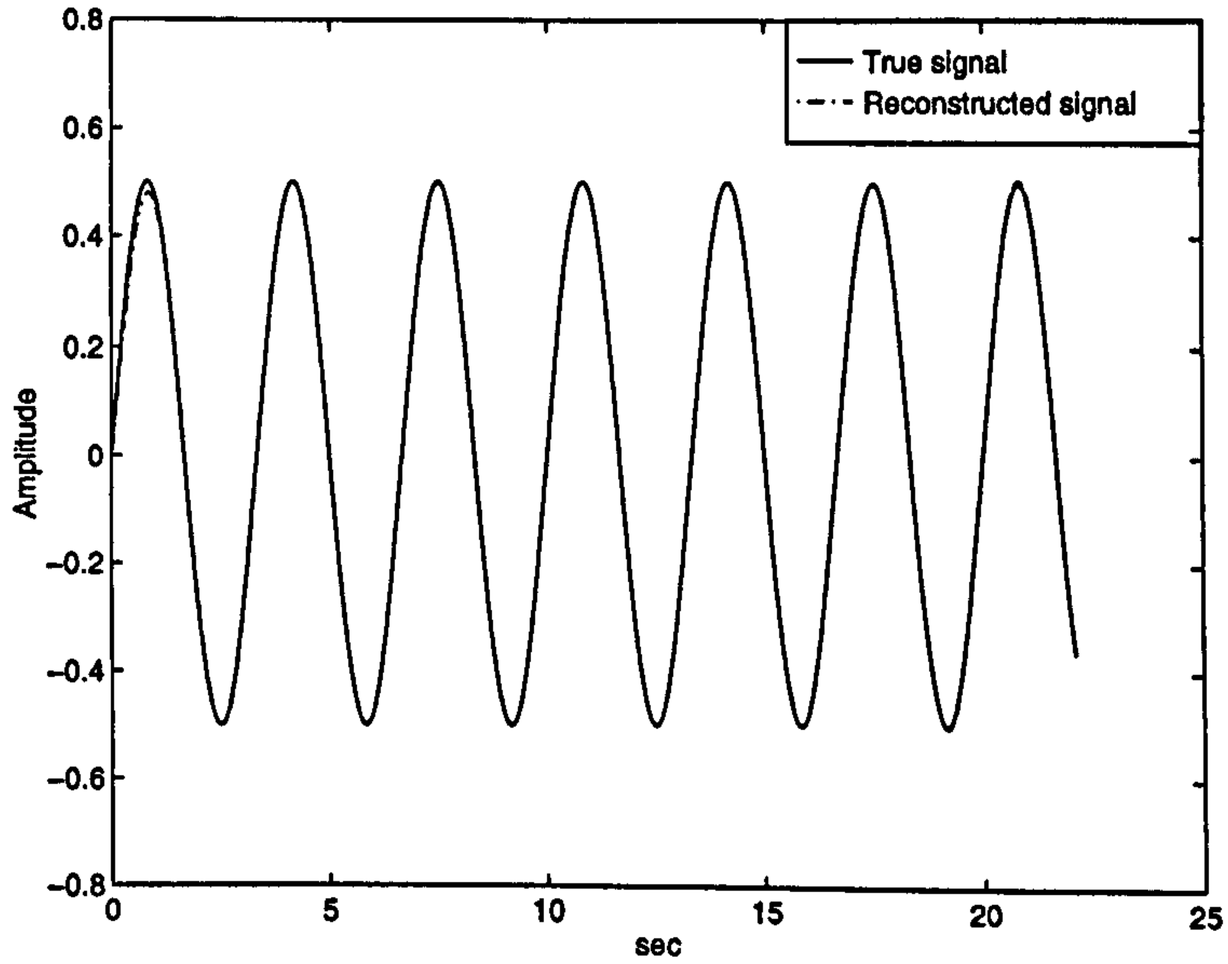


Figure 6.16: True and reconstructed signals for $a_{ac}(t) = 0.5sin(2\pi 0.3t)$ and $f_{low}(t) = 0.2Hz$, $f_{high} = 0.4Hz, \Delta f = 0.02Hz$.

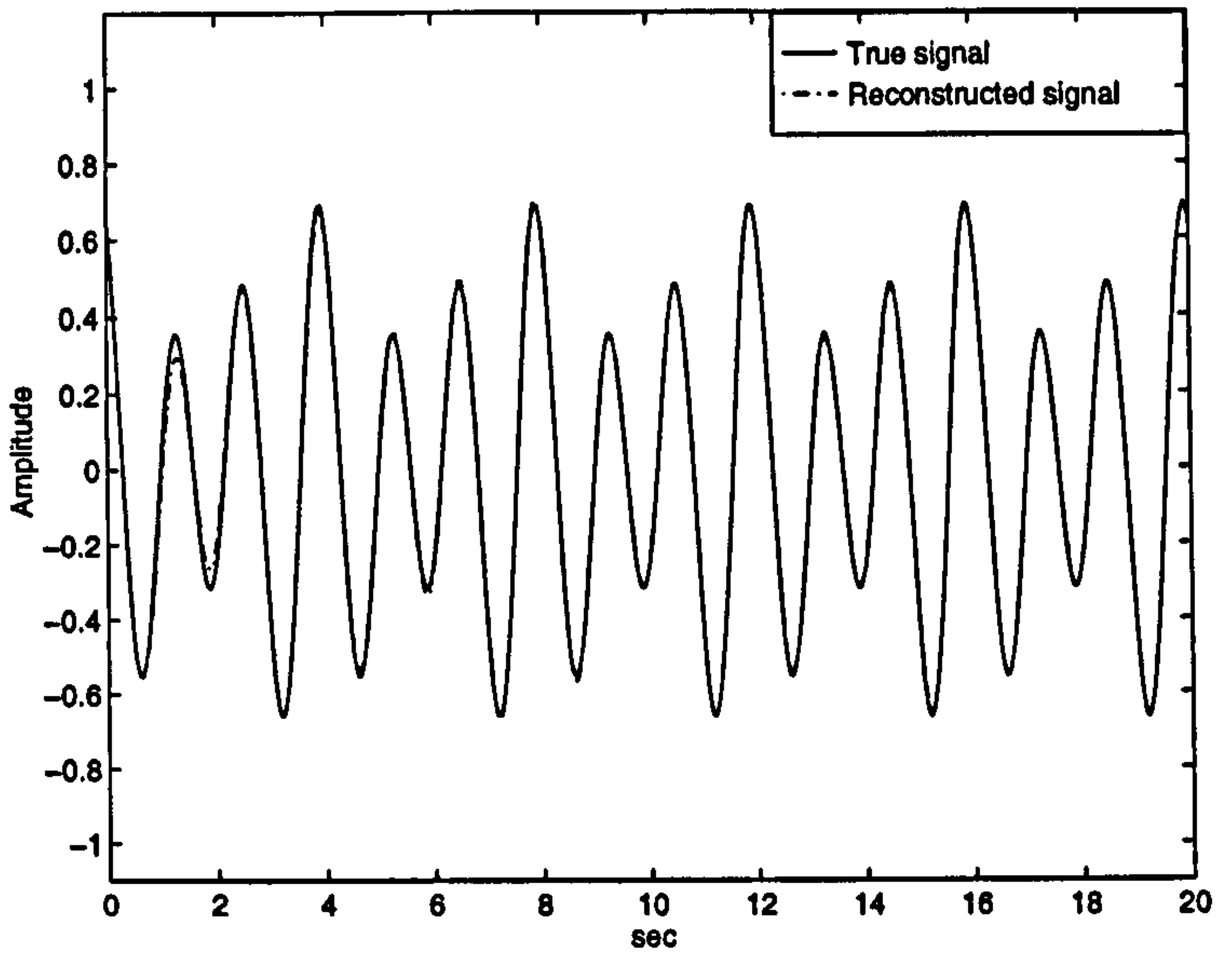


Figure 6.17: True and reconstructed signals for $a_{ac}(t) = 0.2cos(2\pi 0.5t) - 0.5sin(2\pi 0.75t - \pi/3)$ and $f_l(t) = 0.4Hz, f_h = 0.8Hz, \Delta f = 0.02Hz$.

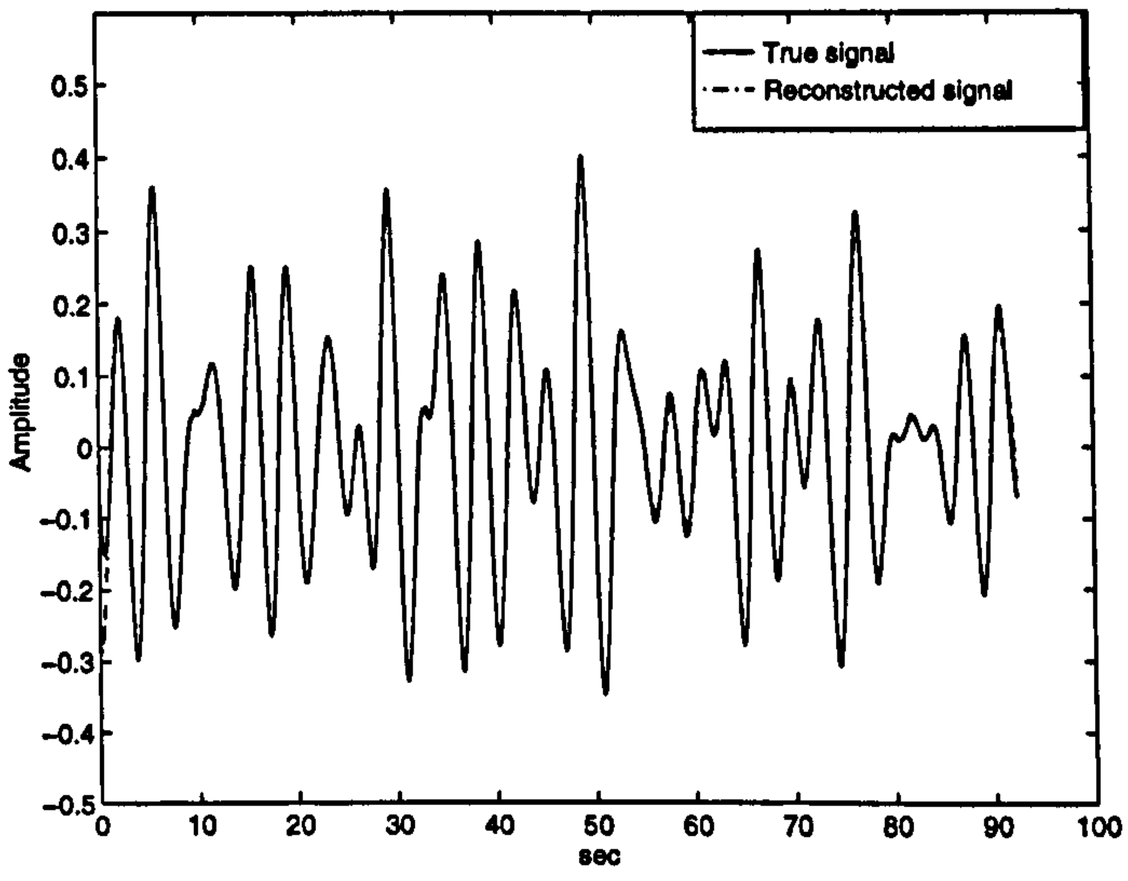


Figure 6.18: True and reconstructed signals for a random threshold input in the range $[0.1 \;\; 0.4]Hz$.

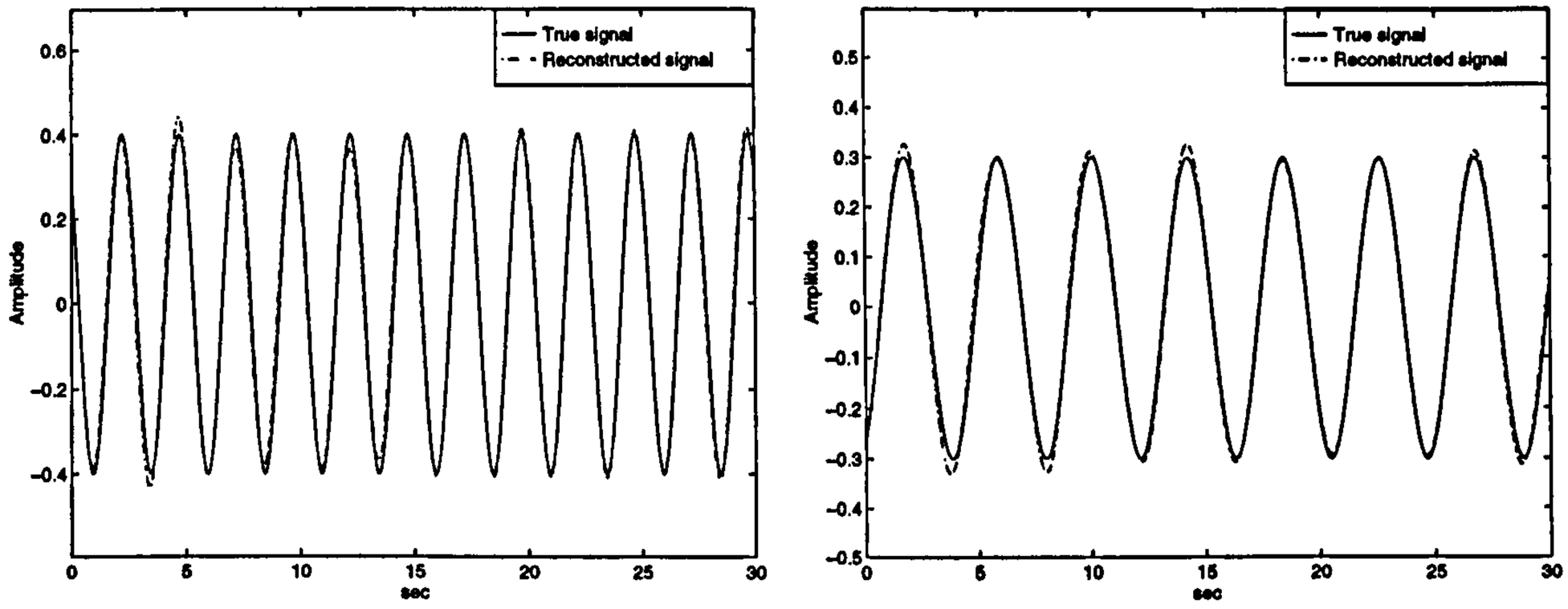


Figure 6.19: True and reconstructed signals with $f_{low} = 0.2Hz, f_{high} = 0.44Hz, \Delta f = 0.02Hz$, (a) $\lambda_{ac}(t) = 0.4cos(2\pi 0.4t + \pi/4)$, (b) $a_{ac}(t) = 0.3sin(2\pi 0.24t - \pi/3)$.

pure sinusoid $a_{ac}(t) = 0.5sin(2\pi 0.3t)$ and multiple sinusoids $a_{ac}(t) = 0.2cos(2\pi 0.5t) - 0.5sin(2\pi 0.75t - \pi/3)$, respectively. The close match between the reconstructed signals and the original signals shows the utility of the proposed method with zero modulation. In view of the parametric method reconstruction of $a_{ac}(t)$ is accomplished through an analogous way to that of $\lambda_{ac}(t)$. The tight fit between the reconstructed signal and the true signal remains unchanged if a nonsinusoidal signal such as the random signal of Fig. 6.14 is injected into the threshold input of the TVTIPFM model. This case is illustrated in Fig. 6.18 with $f_{low} = 0.08Hz$, $f_{high} = 0.44Hz$, $\Delta f = 0.008Hz$.

6.5.3 Nonzero Signals

Treating the TVTIPFM model is more challenging than the IPFM model. Firstly, the spanning band of frequency is reduced to half its size compared to the IPFM model. Secondly, the size of the data matrix and therefore the computational burden will increase (equation (6.17) instead of (6.44) or (6.45)).

As before the simulation begins with the injection of simple sinusoids to the inputs of the TVTIPFM model. Fig. 6.19 displays the results for $\lambda_{ac}(t) = 0.4cos(2\pi 0.4t + \pi/4)$, $a_{ac}(t) = 0.3sin(2\pi 0.24t - \pi/3)$, $f_{low} = 0.2Hz$, $f_{high} = 0.44Hz$, $\Delta f = 0.02Hz$. Clearly, both input signals are reconstructed quite well. Perfect recovery of the signals can also

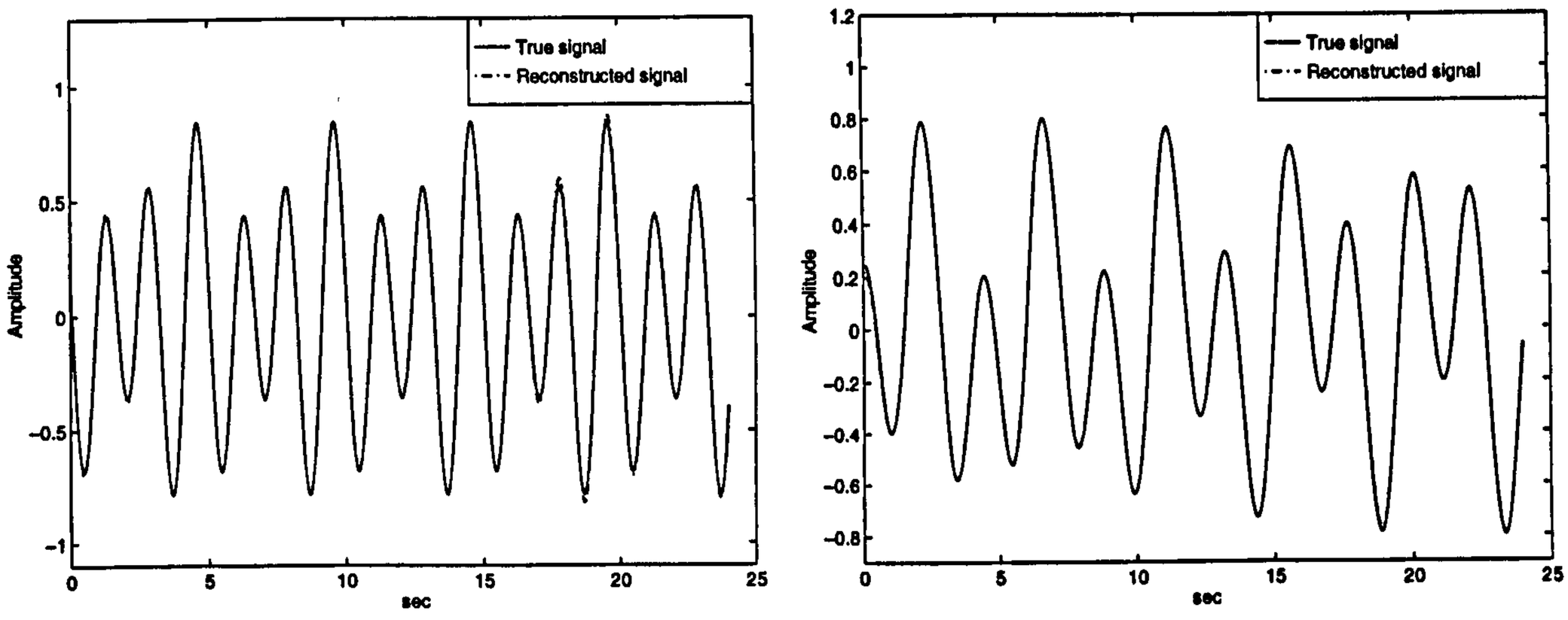


Figure 6.20: True and reconstructed signals with (a) $\lambda_{ac}(t) = 0.25cos(2\pi 0.4t + \pi/4) - 0.6sin(2\pi 0.6t)$, (b) $a_{ac}(t) = 0.3sin(2\pi 0.21t - \pi/3) + 0.5cos(2\pi 0.45t)$.

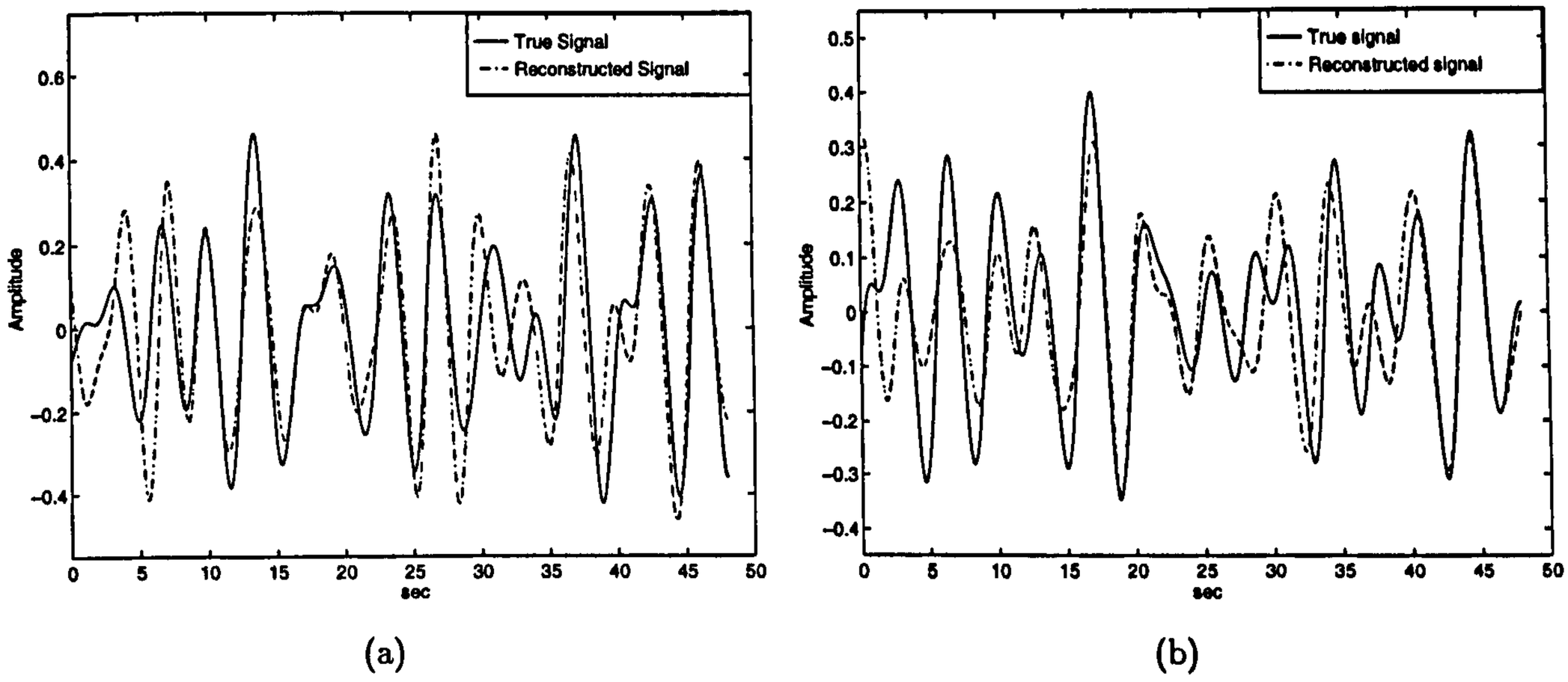


Figure 6.21: True and reconstructed signals for a TVTIPFM model with random signals at both inputs.

be achieved in the case of multiple sinusoids. This case is presented in Fig. 6.20 for $\lambda_{ac}(t) = 0.25cos(2\pi 0.4t + \pi/4) - 0.6sin(2\pi 0.6t)$ and $a_{ac}(t) = 0.3sin(2\pi 0.21t - \pi/3) + 0.5cos(2\pi 0.45t)$. In this example a different strategy for the reconstruction parameters was selected; $f_{low} = 0.4Hz$, $f_{high} = 0.64Hz$, $\Delta f = 0.02Hz$ for $\lambda_{ac}(t)$, and $f_{low} = 0.2Hz$, $f_{high} = 0.45Hz$, $\Delta f = 0.01Hz$ for $a_{ac}(t)$. Although this approach (different spanning range and different frequency resolution) was not considered theoretically, it would show the flexibility of the parametric method in recovering the input signals. As it is observed in Fig. 6.20 there is a complete overlap between the reconstructed signals and the actual ones.

An interesting example is depicted in Fig. 6.21 in which the inputs of the TVTIPFM model were excited with two different random signals similar to the one shown in Fig. 6.14. The reconstruction procedure was conducted with $f_{low} = 0.17Hz$, $f_{high} = 0.41Hz$ and $\Delta f = 0.008Hz$. The reconstructed signals follow the true signals fairly well although noticeable differences can also be observed in Fig. 6.21. The main reason for this difference lies in the fact that the spanning band of frequency is smaller than the actual band of the signals ($0.24Hz$ instead of $0.3Hz$) This is in contrast to the simulations presented before with a single input, in which we were able to cover the whole band of interest. The reconstruction algorithm tries to fit two signals by spanning the given band of frequency in order to give the desired time t_i for the R-peaks.

6.6 Experimental Results

The results obtained from two healthy subjects in three different breathing patterns are considered in this section. Subjects were examined in supine resting position with spontaneous and mandatory breathing patterns. Mean heart rates for the subjects were 65 and 78, respectively but it varied slightly in different breathing rates. For all the cases $f_{low} = 0.008Hz$, $f_{high} = 0.256Hz$ and $\Delta f = 0.008Hz$ were selected for the reconstruction procedure. This range covers the frequency band of interest in heart rate variability with adequate accuracy. Fourier transform (PSD) was invoked to characterise the observed components in the reconstructed signals $\lambda_{ac}(t)$ and $a_{ac}(t)$. Figs. 6.22(a)-(d) illustrate $\lambda_{ac}(t)$, $a_{ac}(t)$ and their PSD's (squared Fourier transform) for the first subject with spontaneous breathing in supine resting position. Figure 6.22(a) re-

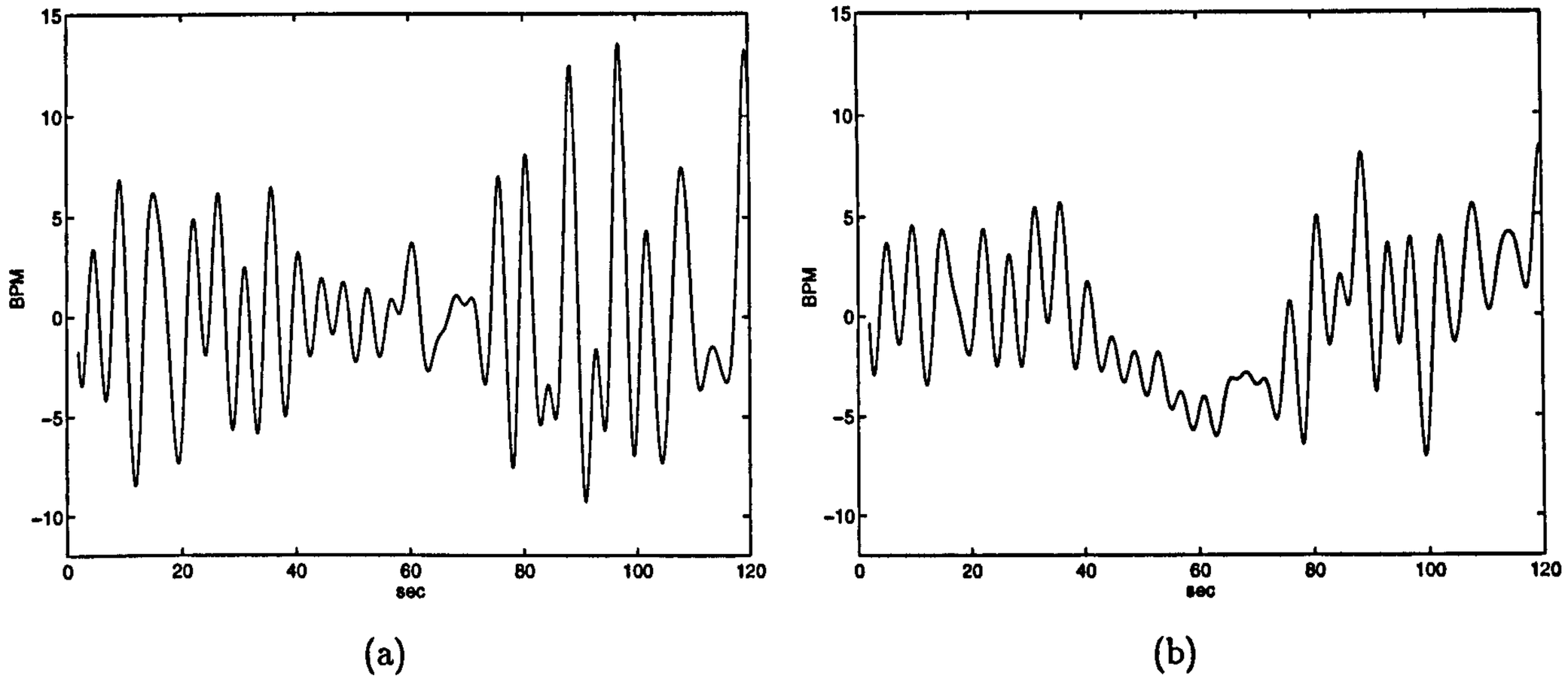
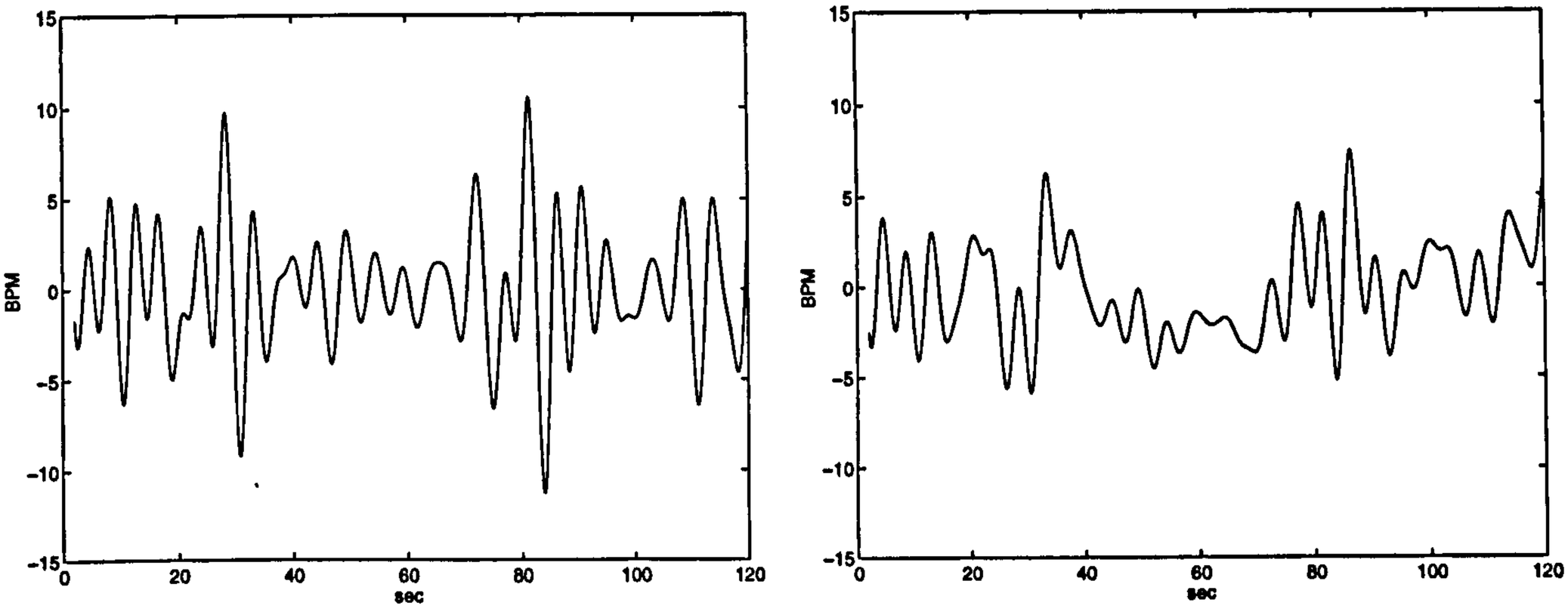


Figure 6.22: Spontaneous breathing experiment in resting supine position (subject 1). (a) $\lambda_{ac}(t)$, (b) $a_{ac}(t)$, (c) PSD of $\lambda_{ac}(t)$, (d) PSD of $a_{ac}(t)$.



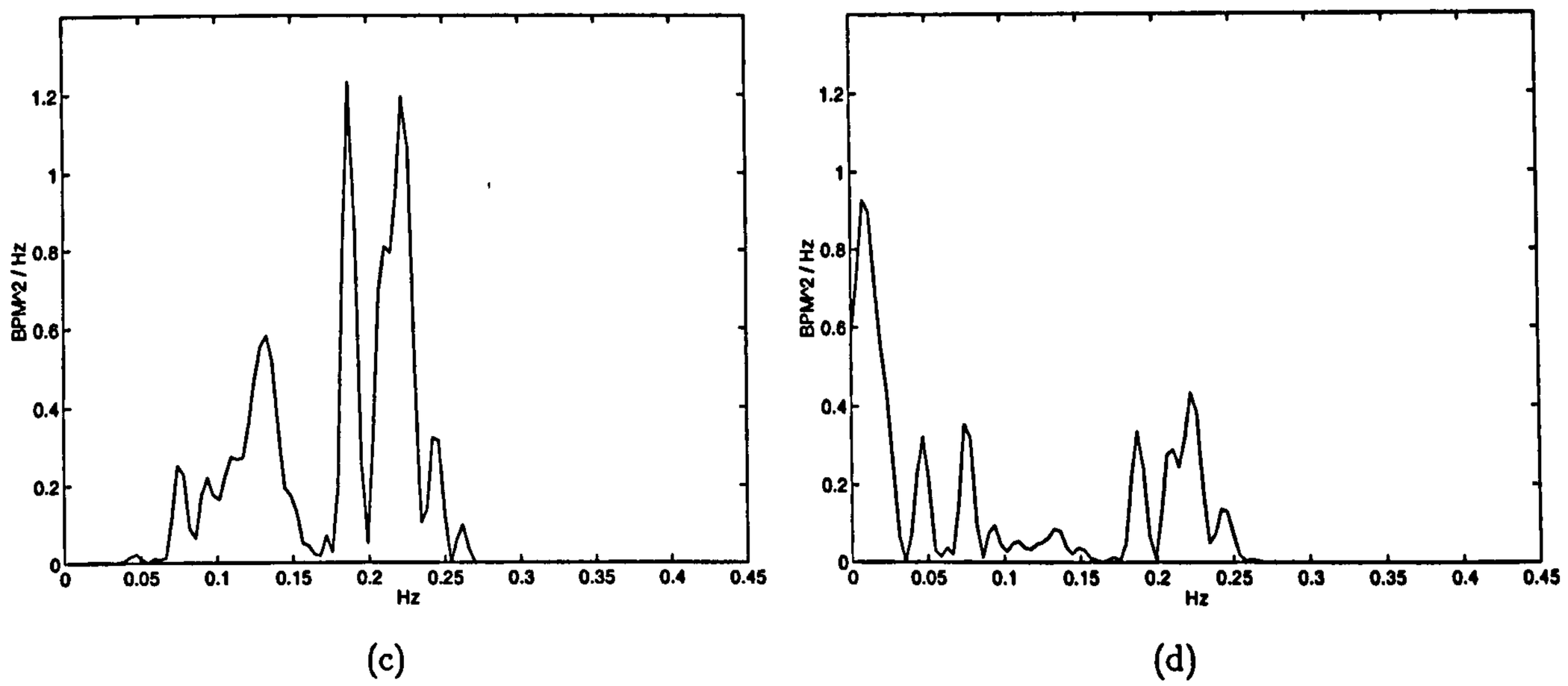


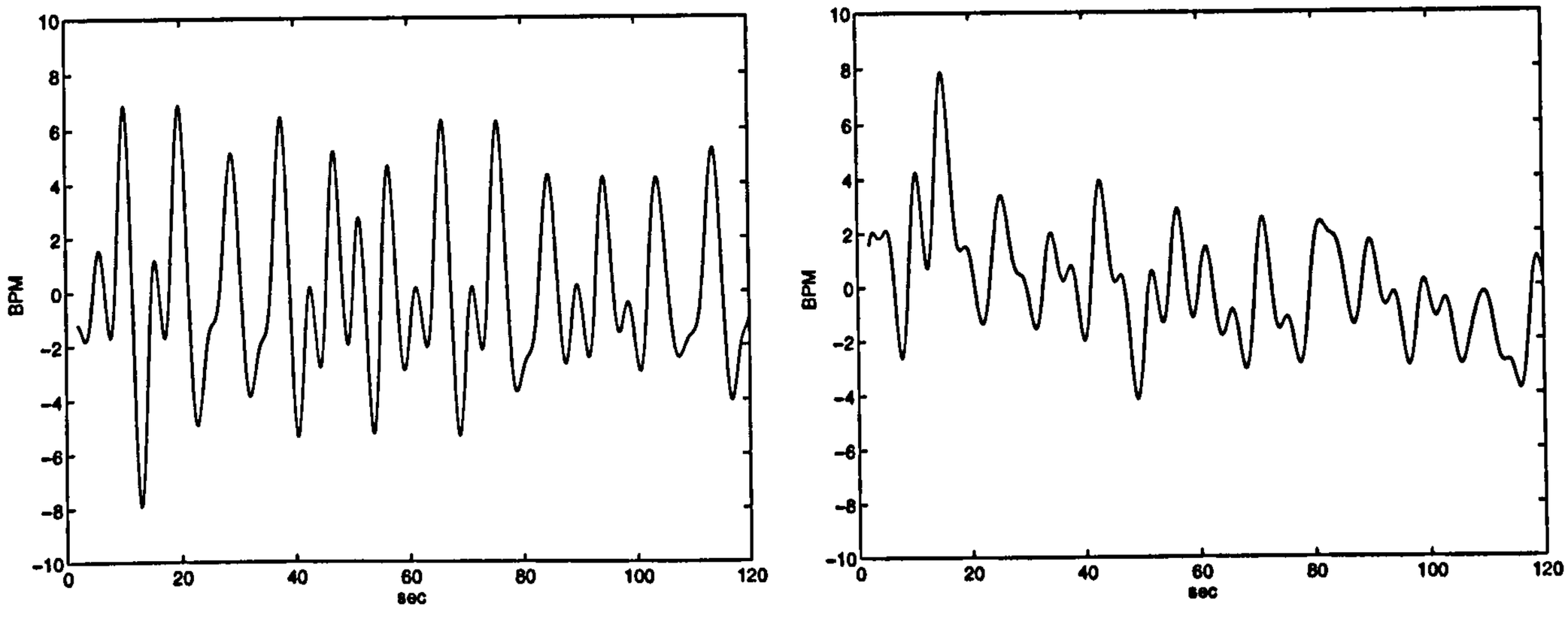
Figure 6.23: 12 breaths per minute experiment in resting supine position (subject 1). (a) $\lambda_{ac}(t)$, (b) $a_{ac}(t)$, (c) PSD of $\lambda_{ac}(t)$, (d) PSD of $a_{ac}(t)$.

veals that $\lambda_{ac}(t)$ has a larger amplitude in this experiment than $a_{ac}(t)$ which is displayed in Fig. 6.22(b). Frequency distribution of $\lambda_{ac}(t)$ in Fig. 6.22(c) is compatible with the frequency band which is normally observed in HRV in spontaneous breathing experiments using conventional methods. Unlike $\lambda_{ac}(t)$ in which the fluctuating components are distributed in a broad area, the components of $a_{ac}(t)$ are concentrated mostly in the very low frequency band. This feature can also be observed in Fig. 6.23 for which the subject was breathing with the rate of 12 breaths per minute. Fig. 6.23(c) shows two major components around $0.2Hz$ in synchrony with respiration. Smaller components with the same frequency can also be observed in the PSD of $a_{ac}(t)$. It is worthwhile noting that the displayed power spectral densities are in fact the squared magnitude of the constructing components of $\lambda_{ac}(t)$ and $a_{ac}(t)$. They differ from the PSD of the HRV signal which is obtained by other HRV detection methods and by treating the signal in frequency domain in a probabilistic (statistical) sense by for example smoothing the raw periodogram.

The major components of $\lambda_{ac}(t)$ and $a_{ac}(t)$ will shift to $\approx 0.11Hz$ if the subject starts breathing with 7 breaths per minute as shown in Fig. 6.24. The second order harmonic of the main component is also observed in both signals, reminding us the contribution of the nonlinear systems as discussed in Chapter 5. Like the previous figures the lower frequency components in this case are also concentrated in $a_{ac}(t)$, though with much less strength compared to the previous experiments.

Fig. 6.25 shows the time behaviour and PSD of the modulating signal $\lambda_{ac}(t)$ and the threshold signal $a_{ac}(t)$ for the second subject with the random breathing pattern (Section 3.6) in supine position. Distribution of the components over a broad area in both signals is quite clear. If the subject starts breathing with 15 breaths per minute the corresponding component will appear in the reconstructed signals as shown in Fig. 6.26. This subject obviously shows more regular fluctuation in constant frequency breathing compared to the previous subject. The impact of respiration on both signals ($\lambda_{ac}(t)$, $a_{ac}(t)$) will vary accordingly if the breathing rate changes to 8 breaths per minute. This is pictured in Fig. 6.27 by plotting the time behaviour and frequency distribution of the reconstructed signals. Like the previous subject the lower frequency components aggregate in $a_{ac}(t)$.

A few points should be raised here in connection with the experimental results.



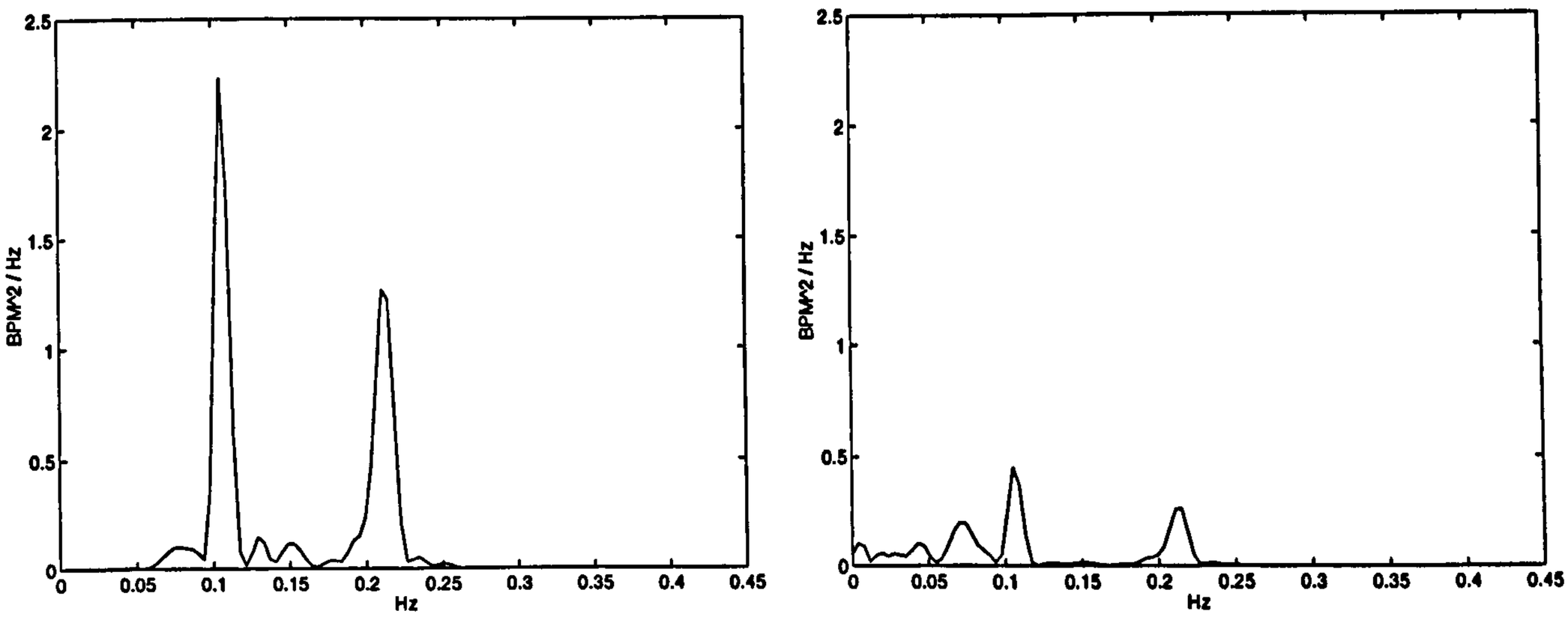
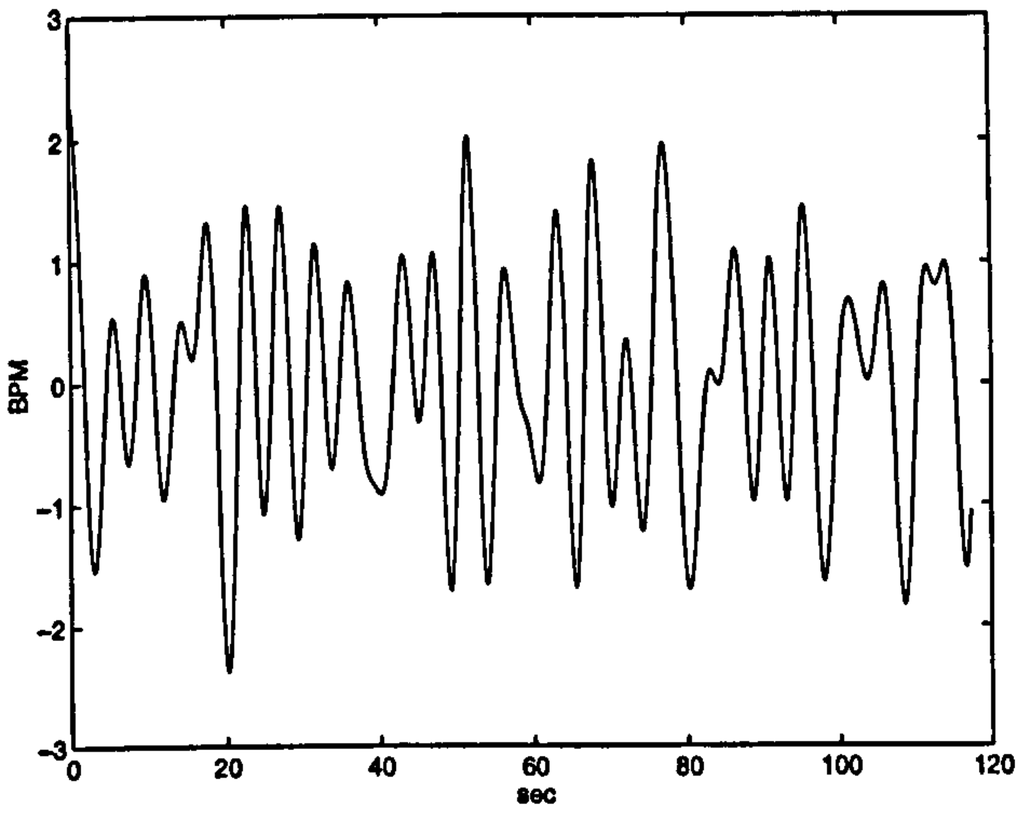
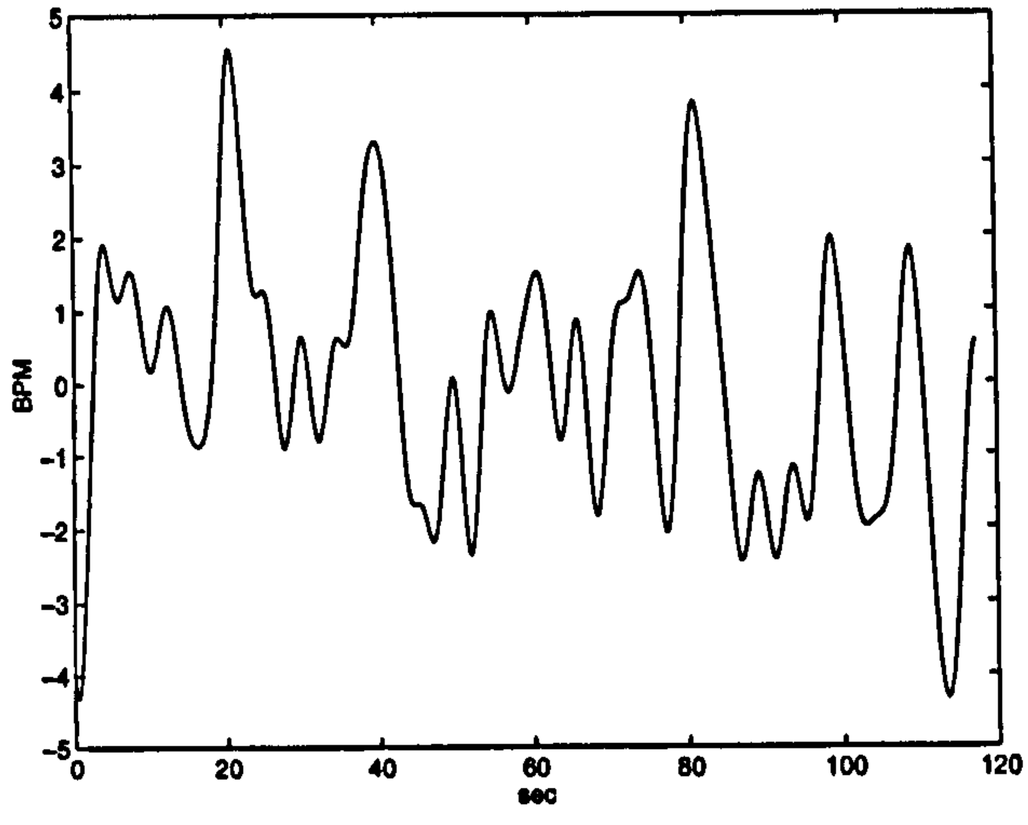


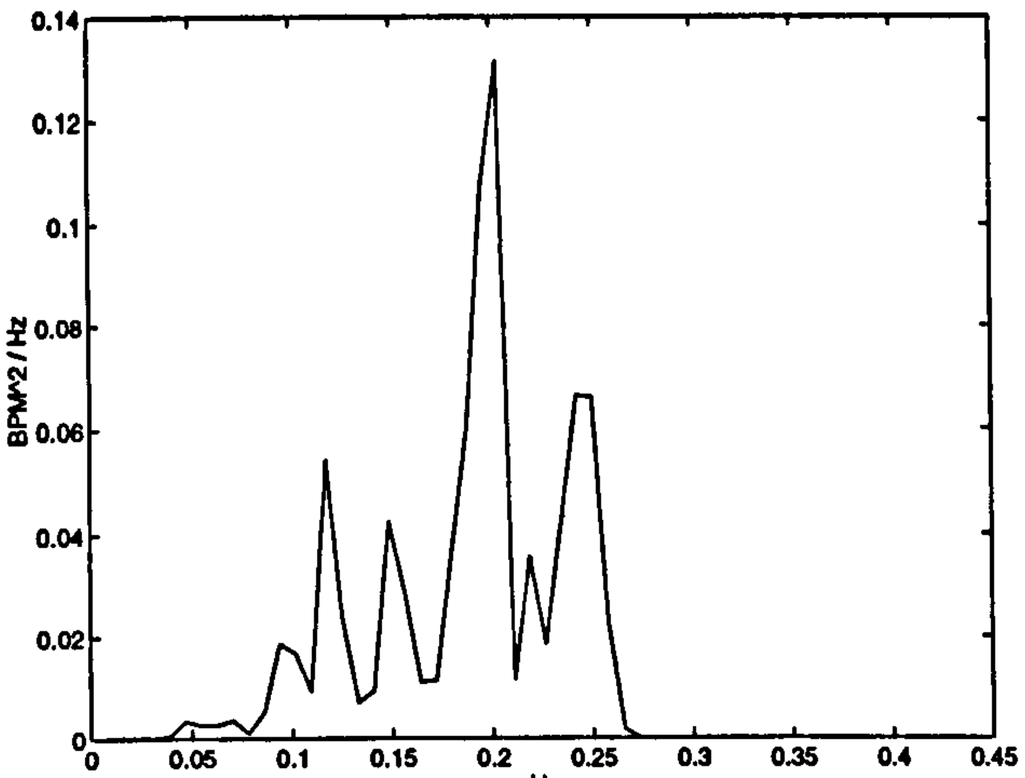
Figure 6.24: 7 breaths per minute experiment in resting supine position (subject 1). (a) $\lambda_{ac}(t)$, (b) $a_{ac}(t)$, (c) PSD of $\lambda_{ac}(t)$, (d) PSD of $a_{ac}(t)$.



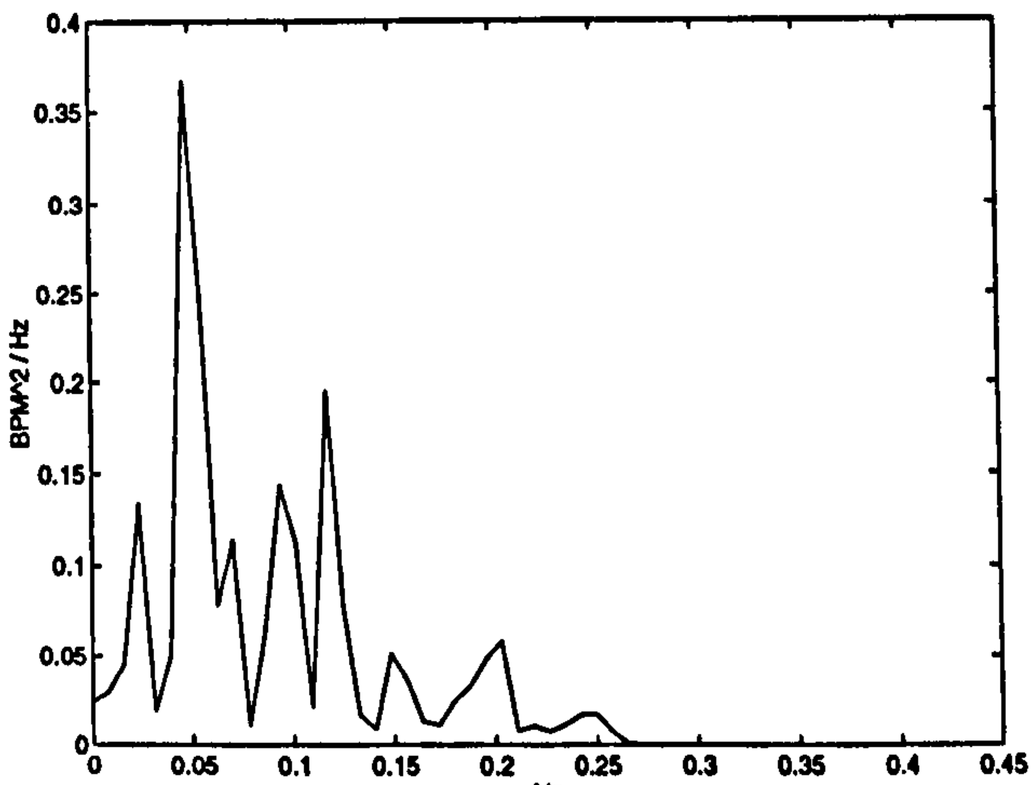
(a)



(b)

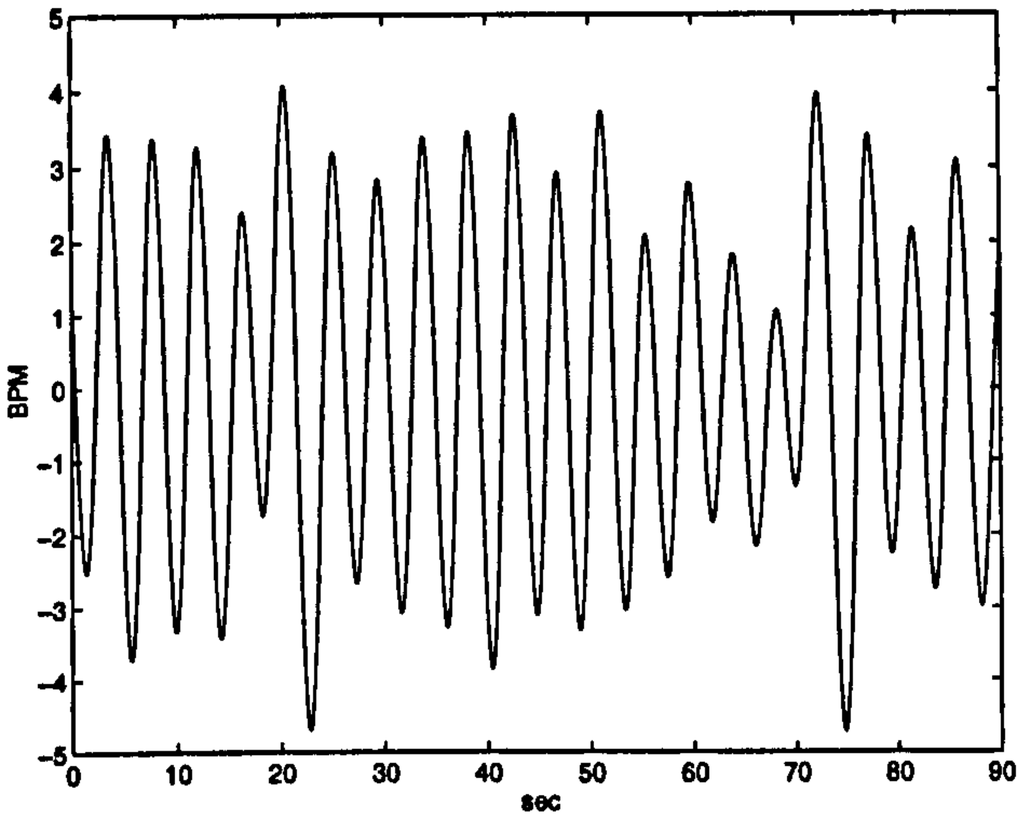


(c)

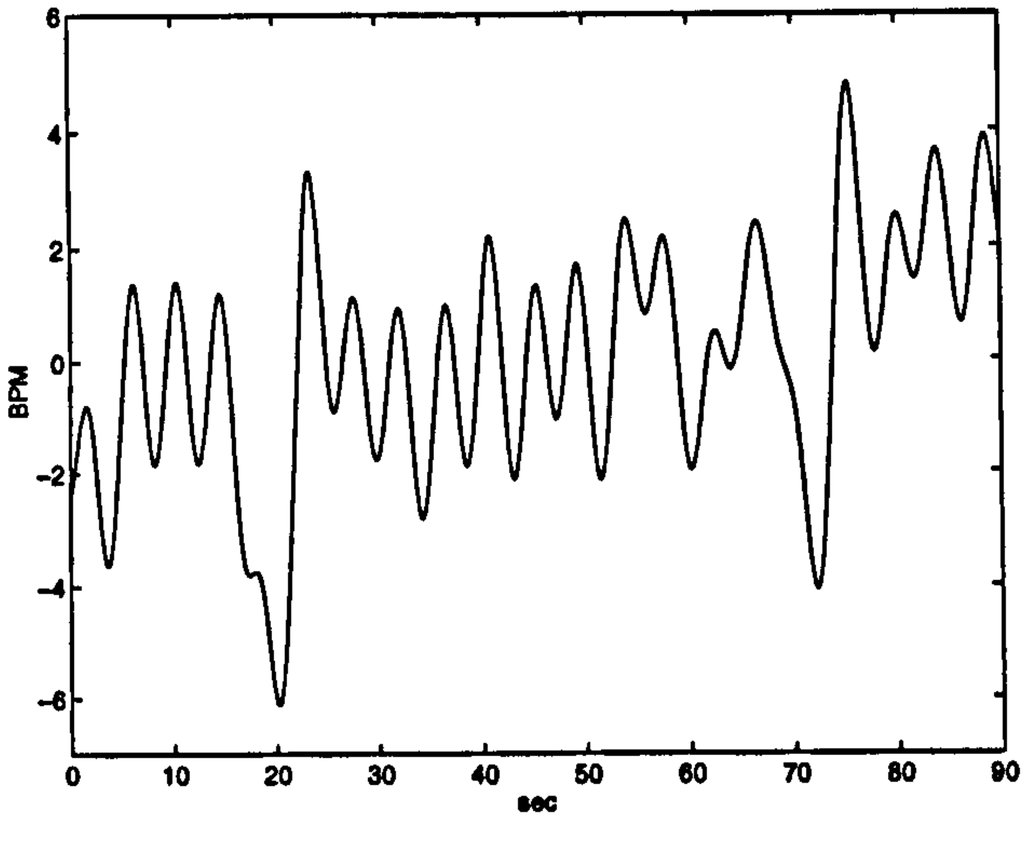


(d)

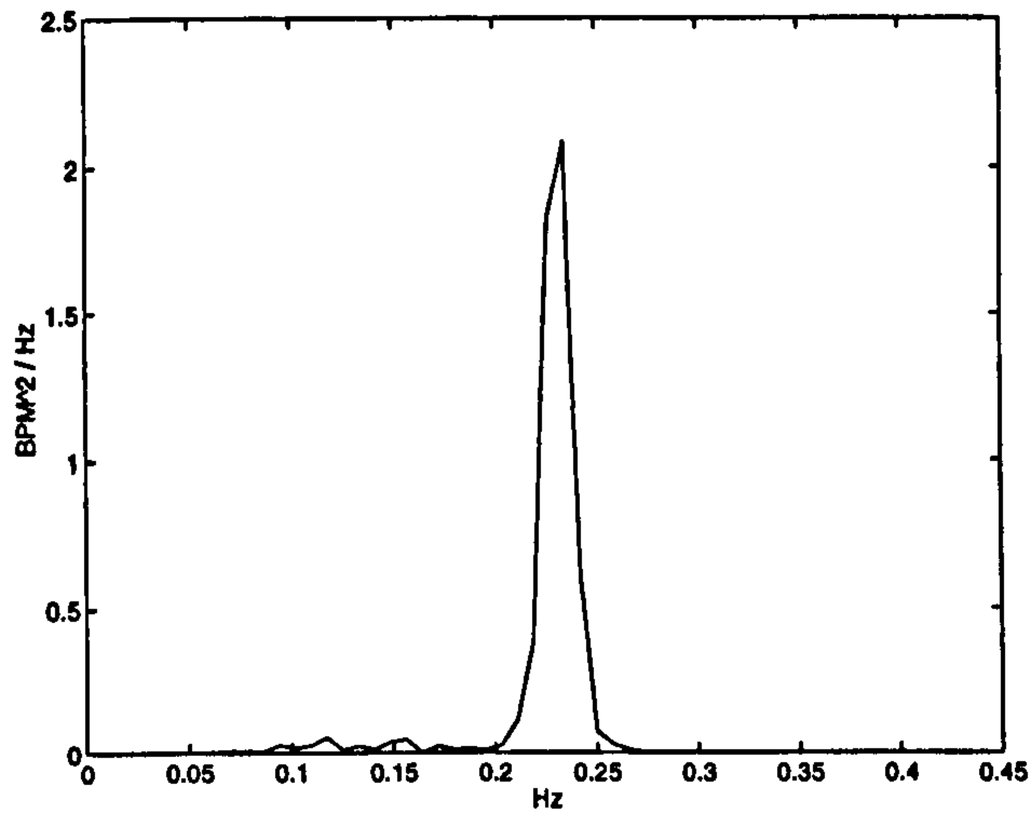
Figure 6.25: Random breathing experiment in resting supine position (subject 2). (a) $\lambda_{ac}(t)$, (b) $a_{ac}(t)$, (c) PSD of $\lambda_{ac}(t)$, (d) PSD of $a_{ac}(t)$.



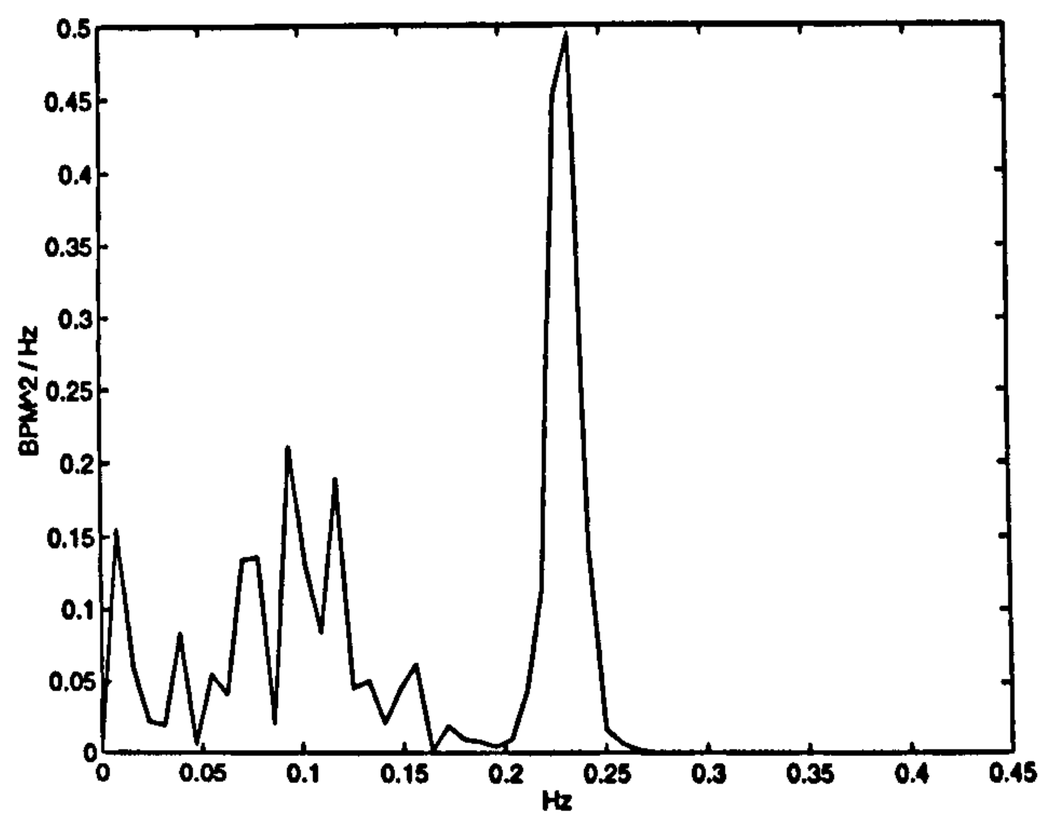
(a)



(b)

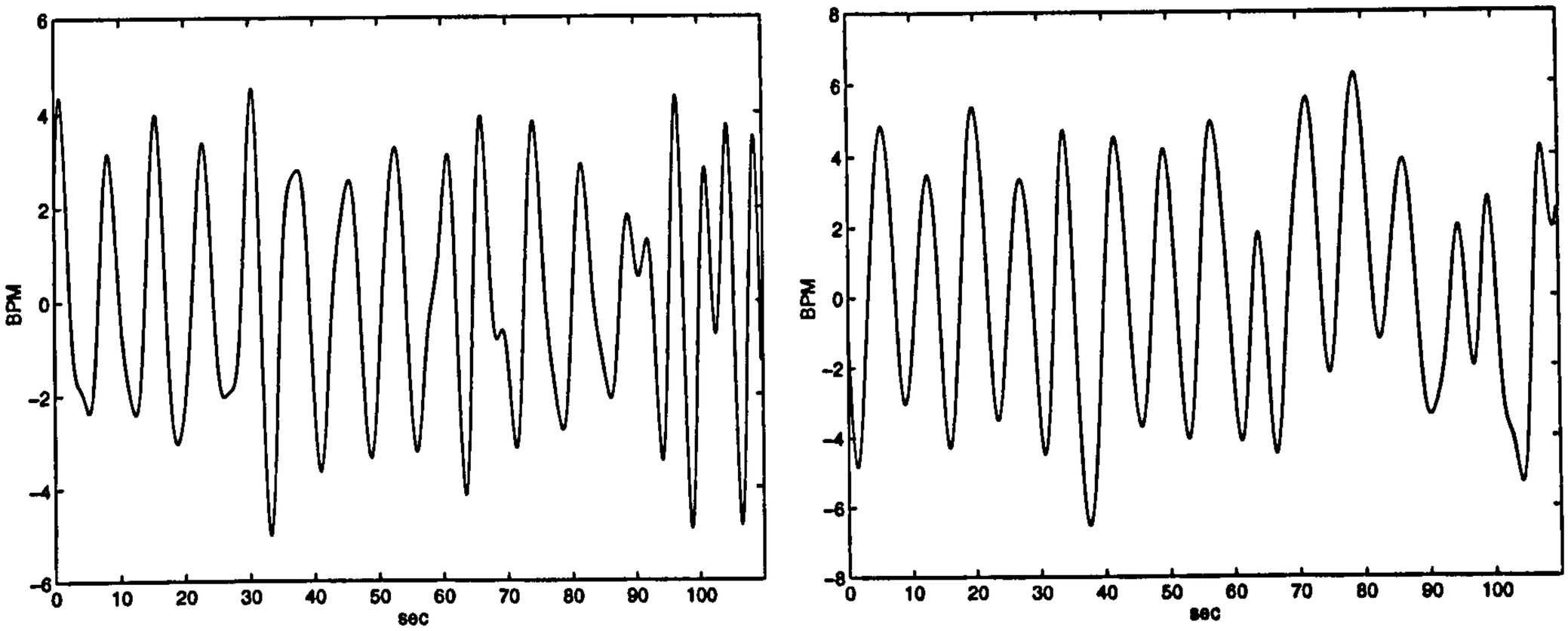


(c)

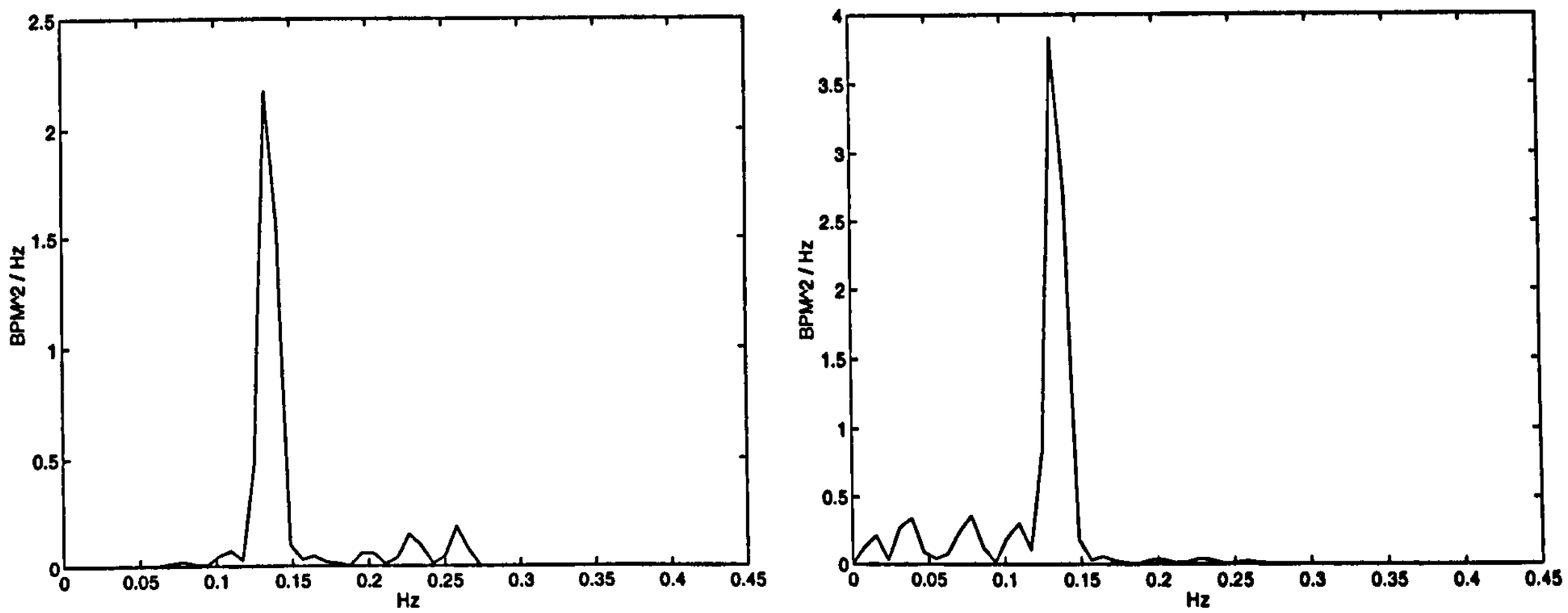


(d)

Figure 6.26: 15 breaths per minute experiment in resting supine position (subject 2). (a) $\lambda_{ac}(t)$, (b) $a_{ac}(t)$, (c) PSD of $\lambda_{ac}(t)$, (d) PSD of $a_{ac}(t)$.



(a) (b)



(c) (d)

Figure 6.27: 8 breaths per minute experiment in resting supine position (subject 2). (a) $\lambda_{ac}(t)$, (b) $a_{ac}(t)$, (c) PSD of $\lambda_{ac}(t)$, (d) PSD of $a_{ac}(t)$.

Firstly, contrary to the physiological observations (Saul *et. al.*, 1991; Perlini *et. al.*, 1995a) the magnitude of the estimated $a_{ac}(t)$, attributed to the mechanical stretching effect of the SA node, is not small compared to the modulating signal. No compelling reason can be offered for this difference. The augmented $a_{ac}(t)$ might be a result of interaction between the autonomic driving signal and the threshold level, a consequence of oversimplification of the complex nodal structure with the TVTIPFM model, or a compromise between the minimisation algorithm and the stimulating signals to achieve the minimisation criterion. Additionally, in the intact heart, other mechanisms are also involved which have not been included in the model. Brooks and his colleagues (1966) observed that the direct stretch of the SA node in anaesthetized dogs produced an initial acceleration of the heart rate followed by a gradual deceleration during maintenance of tension. Also, accomod ative reaction was seen by these authors in experiments in which the node was subjected repeatedly to equivalent stretch over a period of time; the first stretch always gave rise to a greater response. Moreover, these researchers showed that the response to stretch was reflex in part. The contribution of these factors might cause an erroneous augmentation of the estimated threshold signal.

Appearance of the low frequency components in $a_{ac}(t)$ and not in $\lambda_{ac}(t)$ in all the cases, however, is an interesting outcome. It can be interpreted as different mechanisms for inducing high and low frequency components in heart rate variability; high frequency components through autonomic nervous system and low frequency components *via* the stretching effect of the SA node, as a result of venous return fluctuations.

6.7 TVTIPFM Model with Small Threshold Signal

In this final section of the chapter the circumstances under which the IPFM model can be used as an approximation to the TVTIPFM model are described. This approximation is specifically important in practical applications. Physiological evidence indicates that the stretching effect of the SA node has a much smaller inducing effect on the interval variations than the autonomic modulating signal. If this is so, fitting the problem into a mathematical framework will enable us to find the required conditions.

Suppose the TVTIPFM model of Fig. 6.2 is excited by $\lambda_{dc}+\lambda_{ac}(t)$ and $a_{dc}+a_{ac}(t)$.

Then,

$$\int_0^{t_k}(\lambda_{dc}+\lambda_{ac}(t))dt = ka_{dc}+\sum_{j=1}^{k}a_{ac}(t_j), \tag{6.46}$$
$$k=1,2,.....,K.$$

Now if it is assumed that the input signal $\lambda_{dc}+\lambda_{ac}(t)+a_{ac}(t)$ is entered to an IPFM model with constant threshold a_{dc} then the occurrence times t'_k of the generated spikes will obey the following equation:

$$\int_0^{t'_k}(\lambda_{dc}+\lambda_{ac}(t)+a_{ac}(t))dt = ka_{dc}, \tag{6.47}$$
$$k=1,2,.....,K.$$

Equation (6.47) can be written as,

$$\int_0^{t'_k}(\lambda_{dc}+\lambda_{ac}(t)+a_{ac}(t))dt = \int_0^{t_k}(\lambda_{dc}+\lambda_{ac}(t)+a_{ac}(t))dt +$$
$$\int_{t_k}^{t'_k}(\lambda_{dc}+\lambda_{ac}(t)+a_{ac}(t))dt = ka_{dc}, \tag{6.48}$$
$$k=1,2,.....,K.$$

Therefore,

$$\int_0^{t_k}(\lambda_{dc}+\lambda_{ac}(t))dt+\int_0^{t_k}a_{ac}(t)dt+\int_{t_k}^{t'_k}(\lambda_{dc}+\lambda_{ac}(t))dt+$$
$$\int_{t_k}^{t'_k}a_{ac}(t)dt = ka_{dc}, \tag{6.49}$$
$$k=1,2,.....,K.$$

Using equation (6.46) it is obtained

$$\sum_{i=1}^{k}a_{ac}(t_i)+\int_0^{t_k}a_{ac}(t)dt+\int_{t_k}^{t'_k}(\lambda_{dc}+\lambda_{ac}(t))dt$$
$$+\int_{t_k}^{t'_k}a_{ac}(t)dt = 0, \tag{6.50}$$
$$k=1,2,.....,K.$$

By $a_{ac}(t)$ approaching zero in (6.50) we will have,

$$\int_{t_k}^{t'_k}(\lambda_{dc}+\lambda_{ac}(t))dt = 0 \tag{6.51}$$

The integrand of equation (6.51) is always positive because $|\lambda_{ac}(t)| < \lambda_{dc}$ and $\lambda_{dc} > 0$. Hence, equality with zero is obtained only when $t'_k = t_k$. In other words, if $a_{ac}(t) \to 0$

then $t'_k \rightarrow t_k$. This in turn implies that if the threshold signal in the TVTIPFM model is transferred to the modulating input of an IPFM model then the occurrence times of the spikes will deviate slightly, provided that $a_{ac}(t)$ remains small.

To obtain a quantitative evaluation, equation (6.50) is approximated with equation (6.52):

$$\sum_{i=1}^{k} a_{ac}(t_i) + \int_0^{t_k} a_{ac}(t)dt + [\lambda_{dc} + \lambda_{ac}(t_k) + a_{ac}(t_k)] \times (t'_k - t_k) = 0\cdot \qquad (6.52)$$

If $\Delta t_k \triangleq t'_k - t_k$ then equation (6.52) yields

$$\Delta t_k = -\frac{\sum_{i=1}^{k} a_{ac}(t_i) + \int_0^{t_k} a_{ac}(t)dt}{\lambda_{dc} + \lambda_{ac}(t_k) + a_{ac}(t_k)}\cdot \qquad (6.53)$$

To have a small Δt_k it is required that

$$a_{ac}(t_k) + \lambda_{ac}(t_k) + \lambda_{dc} >> \sum_{i=1}^{k} a_{ac}(t_i) + \int_0^{t_k} a_{ac}(t)dt, \qquad (6.54)$$
$$k = 1, 2, ..., K\cdot$$

or,

$$\lambda_{ac}(t_k) + \lambda_{dc} >> \sum_{i=1}^{k} a_{ac}(t_i) - a_{ac}(t_k) + \int_0^{t_k} a_{ac}(t)dt, \qquad (6.55)$$
$$k = 1, 2, ..., K$$

For $k \geq 2$ one can write,

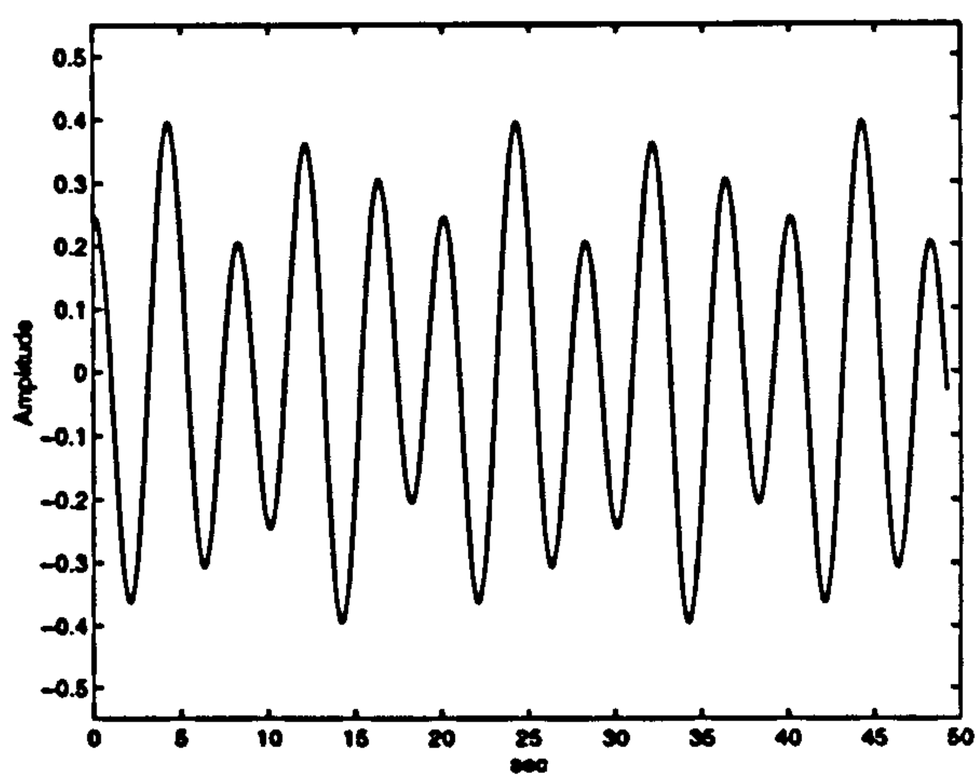
$$\lambda_{ac}(t_k) + \lambda_{dc} >> \sum_{i=1}^{k-1} a_{ac}(t_i) + \int_0^{t_k} a_{ac}(t)dt, \qquad (6.56)$$
$$k = 2, ..., K\cdot$$

In order to satisfy inequality (6.56) for all k, two conditions should be met,

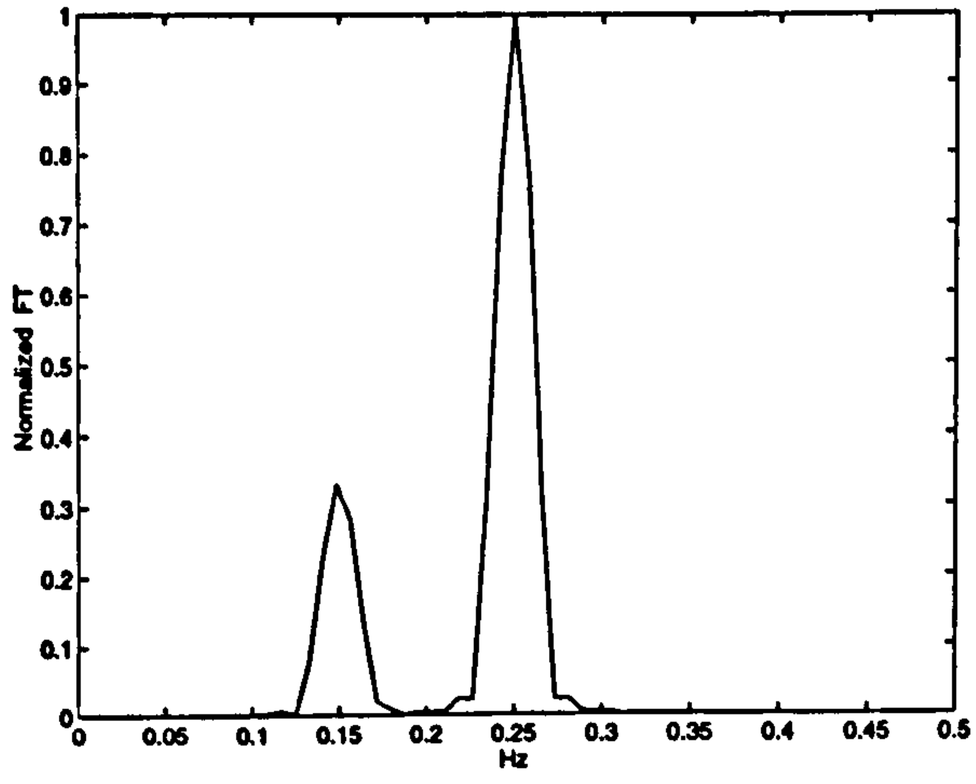
(i) $a_{ac}(t)$ must have a small amplitude,

(ii) $a_{ac}(t)$ must have a zero-mean value.

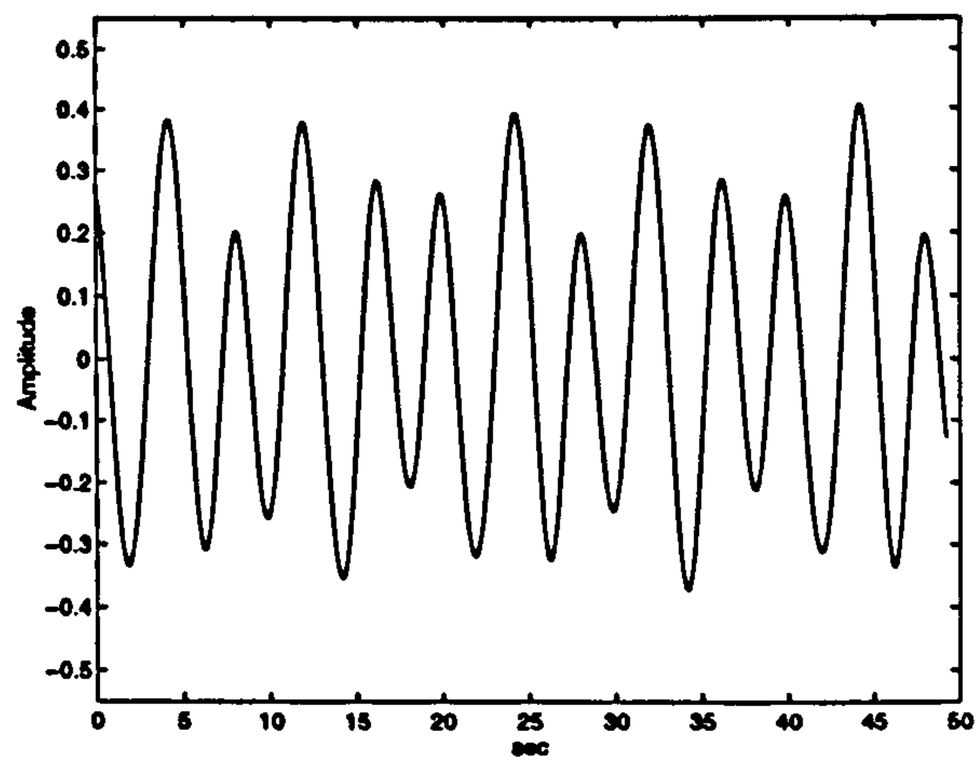
Condition (i) guarantees a small Δt_k for small values of k whereas condition (ii) becomes necessary for large values of k. Recalling that in an actual application $|\lambda_{ac}(t)| << \lambda_{dc}$, $|a_{ac}(t)| << a_{dc}$, $\lambda_{dc}, a_{dc} > 0$ and λ_{dc} remains close to a_{dc}. Further, since the dc part of $a_{ac}(t)$ (and also $\lambda_{ac}(t)$) is always zero by definition, only condition (i) is indeed required.



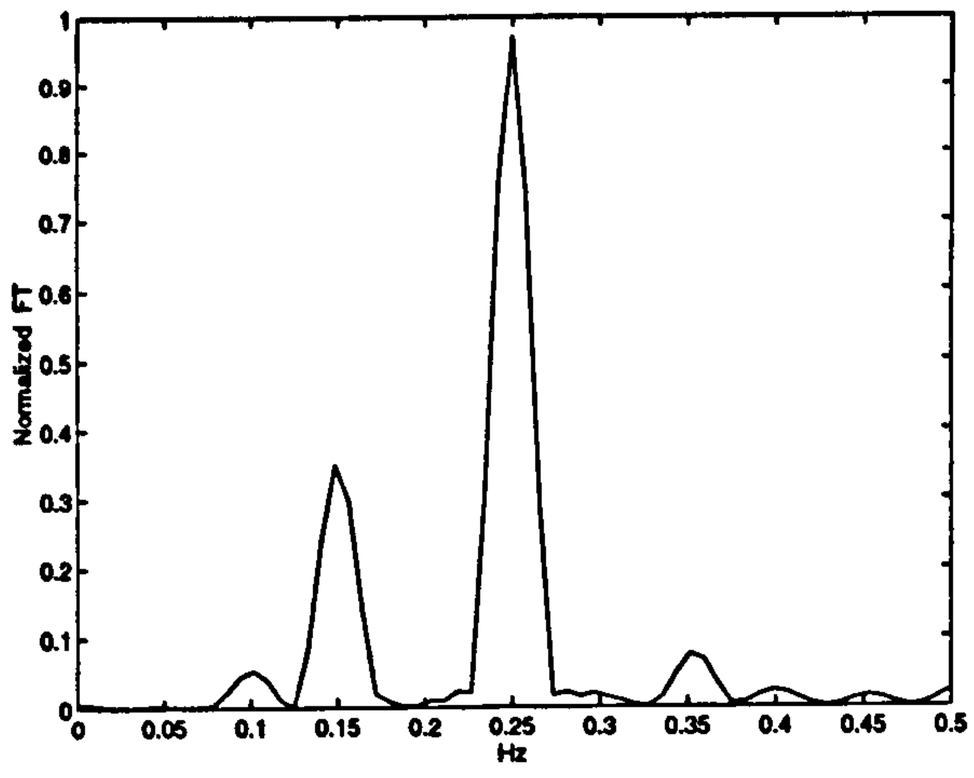
(a)



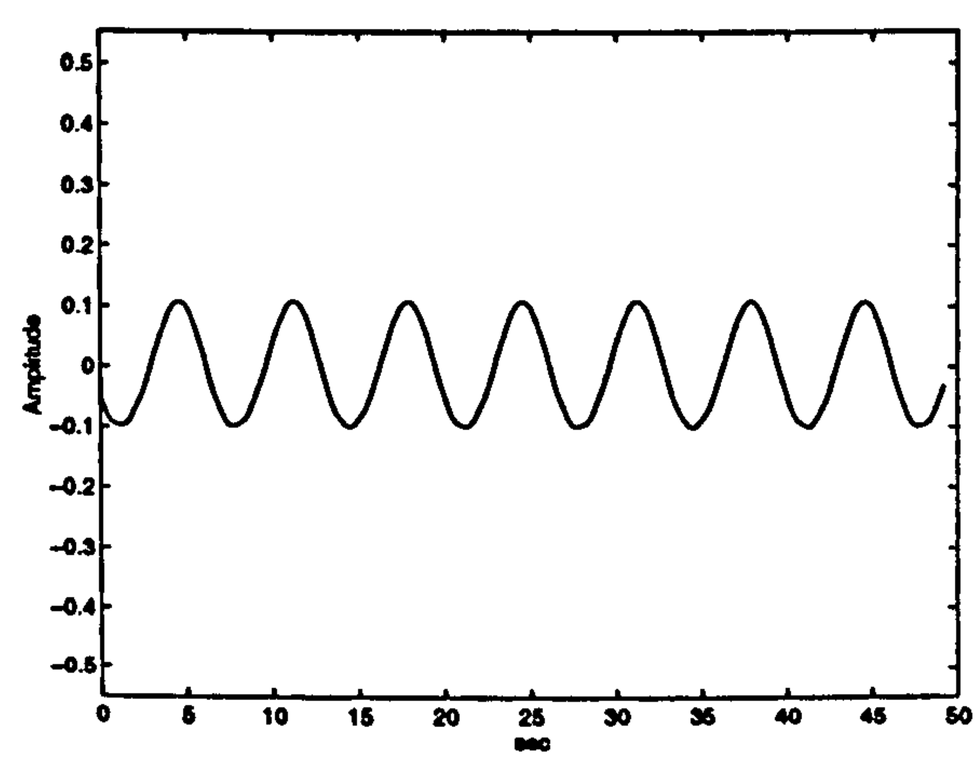
(b)



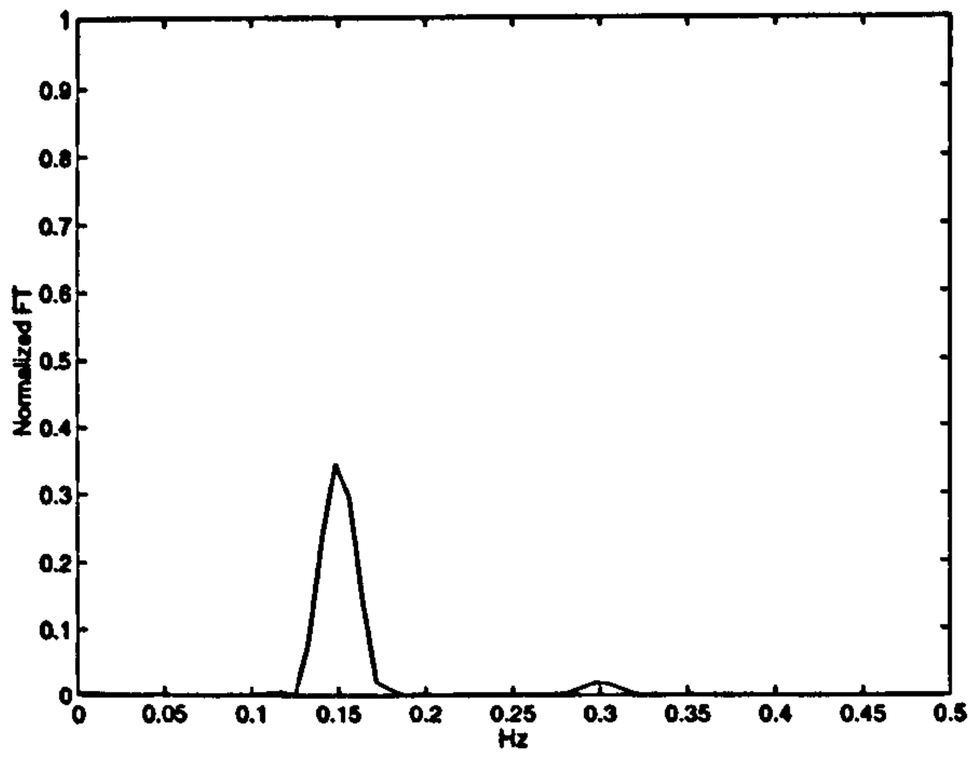
(c)



(d)



(e)



(f)

Figure 6.28: Small signal analysis of the TVTIPFM model. (a) $\lambda_{ac}(t) + a_{ac}(t) = 0.3cos(2\pi 0.25t) + 0.1sin(2\pi 0.15t)$, (b) Fourier transform of $\lambda_{ac}(t) + a_{ac}(t)$, (c) result of the KLPF method on t_i of the TVTIPFM model, (d) Fourier transform of the signal of part (c), (e) result of the KLPF method on t_i of the TVTIPFM model when $\lambda_{ac}(t) = 0$ and $a_{ac}(t) = 0.1sin(2\pi 0.15t)$, (f) Fourier transform of the signal of part (e).

The above analysis gives rise to the important conclusion that the TVTIPFM model can be treated as an IPFM model if condition (i) is satisfied. This greatly reduces the complexity of the problem; once the TVTIPFM model is approximated by an IPFM model either the parametric method or the KLPF method can be engaged to extract the excitation signal. The parametric method cannot offer the real-time property of the KLPF method, however, it provides other superior performances as discussed throughout this chapter. The KLPF method seems an easier task, however, when the relationship between signals or system analysis is the main purpose. This is because all the signals, *i.e,* HRV, BPV and ILV can be treated with the same filter. Furthermore, the KLPF method is length independent.

As a supportive example for the above results suppose a TVTIPFM model which is excited with $\lambda_{dc} = a_{dc} = 1$, $\lambda_{ac}(t) = 0.3cos(2\pi 0.25t)$ and $a_{ac}(t) = 0.1sin(2\pi 0.15t)$. Figures 6.28(a),(b) illustrate signal $\lambda_{ac}(t) + a_{ac}(t)$ and its Fourier transform, respectively. If the detected occurrence times t_k of the TVTIPFM model are used in the KLPF method (which assumes an IPFM model with constant threshold) with $f_c = 0.4$ and $\beta = 4.5$, the signal shown in Fig. 6.28(c) will emerge. Fig. 6.28(d) illustrates the Fourier transform of the signal of part (c). As would be expected, the LPF method simultaneously detects $\lambda_{ac}(t)$ and $a_{ac}(t)$ as if the modulating input of an IPFM model is excited with $\lambda_{ac}(t) + a_{ac}(t)$. The presence of small intermodulation components in Fig. 6.28(d) is indicative of the nonlinear operation of the TVTIPFM model on the input signals. If the modulating input, $\lambda_{ac}(t)$, of the TVTIPFM model becomes zeros then applying the LPF algorithm will detect $a_{ac}(t)$ as if it directly enters into the modulating input of an IPFM model. This case is displayed in Figs. 6.28(e),(f).

6.8 Conclusion

The issue of signal transformation and the coding mechanism of the IPFM model was considered in the context of vector space theory. The properties given by decomposition of the driving signals into basis functions enabled us to present a parametric approach for analysis of the IPFM model even when a fluctuating term was available in the threshold level. Specifically, the modulating signal and the time varying term of the threshold level can be well recovered by solving a simple matrix identity. Using the least squares method in conjunction with the proposed parametric procedure further

guarantee reaching the desired solution.

The flexibility, accuracy and versatility of the parametric solution draw a bright picture for the application of this method for the individual analysis of the HRV in future. In a similar manner, analysis of the neuronal discharge can take advantage of the presented method. However, reconciling the TVTIPFM model of the SA node and the solution offered by the parametric approach needs more speculation as it is made clear from the experimental results presented in this chapter. More work is required to determine why a relatively large amplitude for the threshold level is obtained in practical results.

Summary of the Chapter

The parametric approach presented in this chapter gives a new insight into analysing the IPFM model no matter whether its threshold level is constant or it can vary with time. Specifically, the parametric solution is able to reconstruct the excitation signals of the TVTIPFM model which takes the stretching effect of the SA node into account in addition to the autonomic modulation. It was also shown that if the stretch induced modulation of the SA node has a small amplitude then the simpler IPFM model can still be used to represent the SA node. In this case variation in heart rate due to the stretch will be added to the autonomic modulation of the heart rate.

6.9 Appendix A: Uniqueness of the Parametric Solution

It is first proved that matrix G given below is a nonsingular matrix in a parallel approach to that of Davis (1963).

$$G = \begin{bmatrix} 1 & cos(x_0) & sin(x_0) & cos(2x_0) & sin(2x_0) & \cdots & cos(nx_0) & sin(nx_0) \\ 1 & cos(x_1) & sin(x_1) & cos(2x_1) & sin(2x_1) & \cdots & cos(nx_1) & sin(nx_1) \\ \vdots & \vdots & \vdots & \vdots & \vdots & \vdots & \vdots & \vdots \\ 1 & cos(x_{2n}) & sin(x_{2n}) & cos(2x_{2n}) & sin(2x_{2n}) & \cdots & cos(nx_{2n}) & sin(nx_{2n}) \end{bmatrix} \tag{6.57}$$

In order to show this, G is first converted to complex form by multiplying the 3rd, 5th, ... columns by j and adding them respectively to the 2nd, 4th, ... columns. Therefore,

$$|G| = \begin{vmatrix} 1 & e^{jx_i} & sinx_i & e^{2jx_i} & sin2x_i & \cdots & e^{njx_i} & sinnx_i \end{vmatrix} \tag{6.58}$$

If the 3rd, 5th, ... columns are now multiplied by $-2j$ and the 2nd, 4th, ... columns are added to them respectively we obtain,

$$(-2j)^n|G| = \begin{vmatrix} 1 & e^{jx_i} & e^{-jx_i} & e^{2jx_i} & e^{-2jx_i} & \cdots & e^{njx_i} & e^{-njx_i} \end{vmatrix} \tag{6.59}$$

Interchanging the columns yields,

$$(-1)^{n(n+1)}(-2j)^n|G| = \begin{vmatrix} e^{-njx_i} & e^{-(n-1)jx_i} & \cdots & 1 & \cdots & e^{(n-1)jx_i} & e^{njx_i} \end{vmatrix} \tag{6.60}$$

By multiplying the ith row by $e^{njx_i}, i = 0, 1, \cdots, 2n$ we get,

$$e^{nj(x_0+x_1+\cdots+x_{2n})}(-1)^{n(n+1)}(-2j)^n|G| = \begin{vmatrix} 1 & e^{jx_i} & e^{2jx_i} & \cdots & e^{2njx_i} \end{vmatrix} \tag{6.61}$$

The right-hand side of equation (6.61) is the well-known Vandermonde determinant. Therefore,

$$e^{nj(x_0+x_1+\cdots+x_{2n})}(-1)^{n(n+1)}(-2j)^n|G| = \prod_{i>r}^{2n}(e^{jx_i} - e^{jx_r}) \tag{6.62}$$

which means $|G| \neq 0$ in view of $e^{jx_i} \neq e^{jx_r}$ *for* $i \neq r$. From $|G| \neq 0$ it ensues that $\Phi(t_1, t_K, 1, L)$ and $\Theta(t_1, t_K, 1, L)$ given by equations (6.20), (6.21) are full column rank matrices. Next it is shown that the data matrix $[\Phi(t_1, t_K, 1, L) \;\; \Theta(t_1, t_K, 1, L)]$ is also full rank. Owing to the orthogonality of *sin* (*cos*) functions it suffices to prove that,

$$G_1 \triangleq \begin{bmatrix} sin(2\pi f_a t_1) & cos(2\pi f_a t_1) & sin(2\pi f_a t_1) & cos(2\pi f_a t_1) \\ sin(2\pi f_a t_2) & cos(2\pi f_a t_2) & \sum_{i=1}^{2} sin(2\pi f_a t_i) & \sum_{i=1}^{2} cos(2\pi f_a t_i) \\ \vdots & \vdots & \vdots & \vdots \\ sin(2\pi f_a t_K) & cos(2\pi f_a t_K) & \sum_{i=1}^{K} sin(2\pi f_a t_i) & \sum_{i=1}^{K} cos(2\pi f_a t_i) \end{bmatrix} \tag{6.63}$$

or equivalently,

$$G_2 \triangleq \begin{bmatrix} e^{j2\pi f_a t_1} & e^{-j2\pi f_a t_1} & e^{j2\pi f_a t_1} & e^{-j2\pi f_a t_1} \\ e^{j2\pi f_a t_2} & e^{-j2\pi f_a t_2} & \sum_{i=1}^{2} e^{j2\pi f_a t_i} & \sum_{i=1}^{2} e^{-j2\pi f_a t_i} \\ \vdots & \vdots & \vdots & \vdots \\ e^{j2\pi f_a t_K} & e^{j2\pi f_a t_K} & \sum_{i=1}^{K} e^{j2\pi f_a t_i} & \sum_{i=1}^{K} e^{-j2\pi f_a t_i} \end{bmatrix} \tag{6.64}$$

is a full column rank matrix for an arbitrary frequency f_a.

Starting with the first four rows of G_2,

$$G_2(1,2,3,4) \triangleq \begin{bmatrix} e^{j2\pi f_a t_1} & e^{-j2\pi f_a t_1} & e^{j2\pi f_a t_1} & e^{-j2\pi f_a t_1} \\ e^{j2\pi f_a t_2} & e^{-j2\pi f_a t_2} & \sum_{i=1}^{2} e^{j2\pi f_a t_i} & \sum_{i=1}^{2} e^{-j2\pi f_a t_i} \\ e^{j2\pi f_a t_3} & e^{-j2\pi f_a t_3} & \sum_{i=1}^{3} e^{j2\pi f_a t_i} & \sum_{i=1}^{3} e^{-j2\pi f_a t_i} \\ e^{j2\pi f_a t_4} & e^{j2\pi f_a t_4} & \sum_{i=1}^{4} e^{j2\pi f_a t_i} & \sum_{i=1}^{4} e^{-j2\pi f_a t_i} \end{bmatrix} \tag{6.65}$$

It can easily be shown that

$$\begin{aligned} |G_2(1,2,3,4)| = 2 &- e^{j2\pi f_a(t_2-t_4)} + e^{j2\pi f_a(2t_1-t_2-t_4)} + e^{j2\pi f_a(-2t_1+t_2+t_4)} \\ &- e^{j2\pi f_a(t_4-t_2)} - e^{j2\pi f_a(2t_1-2t_3)} - e^{j2\pi f_a(-2t_1+2t_3)} - e^{j2\pi f_a(-2t_2+t_1+t_3)} \\ &+ e^{j2\pi f_a(t_1-t_3)} + e^{j2\pi f_a(-t_1+t_3)} - e^{j2\pi f_a(-t_1+2t_2-t_3)} \end{aligned} \tag{6.66}$$

If

$$t_1 = T_0 + \Delta t_1 \qquad t_2 = 2T_0 + \Delta t_2$$

$$t_3 = 3T_0 + \Delta t_3 \qquad t_4 = 4T_0 + \Delta t_4 \tag{6.67}$$

which means that the generated spike at time t_k is $\Delta t_k sec$ deviated from the free running position kT_0 then,

$$\begin{aligned}|G_2(1,2,3,4)| = 2 - e^{j2\pi f_a(-2T_0+(\Delta t_2-\Delta t_4))} + e^{j2\pi f_a(-4T_0+(2\Delta t_1-\Delta t_2-\Delta t_4))} \\ + e^{j2\pi f_a(4T_0-(2\Delta t_1-\Delta t_2-\Delta t_4))} - e^{j2\pi f_a(2T_0-(\Delta t_2-\Delta t_4))} - e^{j2\pi f_a(-4T_0+2(\Delta t_1-\Delta t_3))} - \\ e^{j2\pi f_a(4T_0-2(\Delta t_1-\Delta t_3))}) - e^{j2\pi f_a(-2\Delta t_2+\Delta t_1+\Delta t_3)} + e^{j2\pi f_a(-2T_0-\Delta t_3)} + \\ e^{j2\pi f_a(2T_0+\Delta t_3)} - e^{j2\pi f_a(-\Delta t_1+2\Delta t_2-\Delta t_3)}\end{aligned} \tag{6.68}$$

$|G_2(1,2,3,4)|$ will be zero only when $\Delta t_1 = \Delta t_2 = \Delta t_3 = \Delta t_4 = 0$. This in turn means that the determinant is zero only when the TVTIPFM model is working in the free running condition *i.e.*, $\lambda_{ac}(t)$, $a_{ac}(t) = 0$ [3].

Next assume $|G_2(1,2,3,r)| = 0$ where

$$\mathrm{G_2(1,2,3,r)} \triangleq \begin{bmatrix} e^{j2\pi f_a t_1} & e^{-j2\pi f_a t_1} & e^{j2\pi f_a t_1} & e^{-j2\pi f_a t_1} \\ e^{j2\pi f_a t_2} & e^{-j2\pi f_a t_2} & \sum_{i=1}^{2} e^{j2\pi f_a t_i} & \sum_{i=1}^{2} e^{-j2\pi f_a t_i} \\ e^{j2\pi f_a t_3} & e^{-j2\pi f_a t_3} & \sum_{i=1}^{3} e^{j2\pi f_a t_i} & \sum_{i=1}^{3} e^{-j2\pi f_a t_i} \\ e^{j2\pi f_a t_r} & e^{-j2\pi f_a t_r} & \sum_{i=1}^{r} e^{j2\pi f_a t_i} & \sum_{i=1}^{r} e^{-j2\pi f_a t_i} \end{bmatrix} \tag{6.69}$$

Then it will be shown that $|G_2(1,2,3,r+1)|$ will be zero only when $t_{r+1} = (r+1)T_0$ (*i.e.*, $\Delta t_{r+1} = 0$). Following the same steps for $|G_2(1,2,3,4)|$, $|G_2(1,2,3,r)|$ will be zero only when $\Delta t_1 = \Delta t_2 = \Delta t_3 = \cdots = \Delta t_r = 0$. Then,

$$|\mathrm{G_2(1,2,3,r+1)}| \triangleq \begin{vmatrix} e^{j2\pi f_a t_1} & e^{-j2\pi f_a t_1} & e^{j2\pi f_a t_1} & e^{-j2\pi f_a t_1} \\ e^{j2\pi f_a t_2} & e^{-j2\pi f_a t_2} & \sum_{i=1}^{2} e^{j2\pi f_a t_i} & \sum_{i=1}^{2} e^{-j2\pi f_a t_i} \\ e^{j2\pi f_a t_3} & e^{-j2\pi f_a t_3} & \sum_{i=1}^{3} e^{j2\pi f_a t_i} & \sum_{i=1}^{3} e^{-j2\pi f_a t_i} \\ e^{j2\pi f_a t_{r+1}} & e^{-j2\pi f_a t_{r+1}} & \sum_{i=1}^{r+1} e^{j2\pi f_a t_i} & \sum_{i=1}^{r+1} e^{-j2\pi f_a t_i} \end{vmatrix} =$$

[3] We discard the unrealistic case when $a_{ac}(t)$ counterbalances the effect of $\lambda_{ac}(t)$.

$$\begin{vmatrix} e^{j2\pi f_a t_1} & e^{-j2\pi f_a t_1} & e^{j2\pi f_a t_1} & e^{-j2\pi f_a t_1} \\ e^{j2\pi f_a t_2} & e^{-j2\pi f_a t_2} & \sum_{i=1}^{2} e^{j2\pi f_a t_i} & \sum_{i=1}^{2} e^{-j2\pi f_a t_i} \\ e^{j2\pi f_a t_3} & e^{-j2\pi f_a t_3} & \sum_{i=1}^{3} e^{j2\pi f_a t_i} & \sum_{i=1}^{3} e^{-j2\pi f_a t_i} \\ e^{j2\pi f_a t_r} & e^{-j2\pi f_a t_r} & \sum_{i=1}^{r} e^{j2\pi f_a t_i} & \sum_{i=1}^{r} e^{-j2\pi f_a t_i} \end{vmatrix} +$$

$$\begin{vmatrix} e^{j2\pi f_a t_1} & e^{-j2\pi f_a t_1} & e^{j2\pi f_a t_1} & e^{-j2\pi f_a t_1} \\ e^{j2\pi f_a t_2} & e^{-j2\pi f_a t_2} & \sum_{i=1}^{2} e^{j2\pi f_a t_i} & \sum_{i=1}^{2} e^{-j2\pi f_a t_i} \\ e^{j2\pi f_a t_3} & e^{-j2\pi f_a t_3} & \sum_{i=1}^{3} e^{j2\pi f_a t_i} & \sum_{i=1}^{3} e^{-j2\pi f_a t_i} \\ e^{j2\pi f_a t_{r+1}} & e^{-j2\pi f_a t_{r+1}} & e^{j2\pi f_a t_{r+1}} & e^{-j2\pi f_a t_{r+1}} \end{vmatrix} +$$

$$\begin{vmatrix} e^{j2\pi f_a t_1} & e^{-j2\pi f_a t_1} & e^{j2\pi f_a t_1} & e^{-j2\pi f_a t_1} \\ e^{j2\pi f_a t_2} & e^{-j2\pi f_a t_2} & \sum_{i=1}^{2} e^{j2\pi f_a t_i} & \sum_{i=1}^{2} e^{-j2\pi f_a t_i} \\ e^{j2\pi f_a t_3} & e^{-j2\pi f_a t_3} & \sum_{i=1}^{3} e^{j2\pi f_a t_i} & \sum_{i=1}^{3} e^{-j2\pi f_a t_i} \\ -e^{j2\pi f_a t_r} & -e^{-j2\pi f_a t_r} & 0 & 0 \end{vmatrix} \tag{6.70}$$

The first determinant is $|G_2(1,2,3,r)|$ which is zero according to the assumption. The second and the third determinant are zero only when $\Delta t_1 = \Delta t_2 = \Delta t_3 = \Delta t_{r+1} = 0$. Therefore, $G_2(1,2,3,\cdots,K)$ is a full rank matrix unless $\Delta t_1 = \Delta t_2 = \cdots = \Delta t_K = 0$. Finally, $[\Phi(t_1,t_K,1,L) \quad \Theta(t_1,t_K,1,L)]$ will be a full rank matrix if $\lambda_{ac}(t), a_{ac}(t) \neq 0$ *for* $0 \leq t \leq T_l$. This guarantees the uniqueness of the solution and completes the proof.

Chapter 7

Theoretical Development of the Proposed Model

Objectives of the Chapter

In the preceding chapters the basic steps required for modelling and identification of the neuro-cardiovascular system for analysing the HRV and BPV were taken. Based on the relevant physiological evidence an appropriate model was developed. Also general features of the proposed model and suitable analysis methods for investigation of the model were presented. Now the main objective is to give an exact mathematical form to each building block of the model, already sketched in Chapter 4, and then to connect all these blocks together to obtain the final mathematical representation of the system.

7.1 Introduction

The basis for creating a credible model structure is typically to decompose the actual sophisticated model into smaller identifiable components without affecting the existing interconnections. To achieve the above for the specific model of the present study, one has to use theoretical considerations together with animal or human experimentation. The approach selected in this chapter exactly follows this line. Using the well documented physiological evidence, each individual part of the proposed model, presented in Chapter 4 and reproduced here in Fig. 7.1 for convenience, finds a systemic representation. Next, by assembling all the individual parts and depicting the existing

interconnections in an appropriate manner a simpler topology of the model, suitable for identification and validation is obtained. In the following sections we focus on each constructing block of Fig. 7.1 one after the other and then present their mathematical counterparts. The required theories for the nonlinear parts of the model are also included in this chapter, leaving the next chapter entirely for the experimental results and illustrative discussions.

7.2 The SA Node

The SA node exhibits two fundamental properties, response characteristics to autonomic neural excitation and a spike generation mechanism. The latter was thoroughly investigated in previous chapters. It was shown that the TVTIPFM model adequately represents the spike generation mechanism of the SA node. The modulating signal of the TVTIPFM, however, is supplied by the autonomic nervous system. The SA node is under the dual control of the sympathetic and parasympathetic nerves (Fig. 7.1). While sympathetic excitation has an accelerating effect on the heart rate, parasympathetic stimulation causes a decelerating effect. Consequently, the first question is how the sympathetic and parasympathetic excitations interact in regulation of the heart rate (H_2, H_3, H_4, H_5 in Fig. 7.1).

7.2.1 Autonomic Response

Several investigations carried out in experimental animals and in man have demonstrated a reciprocal relationship between the sympathetic and parasympathetic nervous systems in response to changes in arterial blood pressure. When arterial pressure is altered, changes in heart rate are brought about not simply by an increase or a decrease in tone of one or the other but by reciprocal variations in the tone of both, meaning that the stimulation of one is associated with inhibition of the other. However, there are other experiments in which parasympathetic influence has been shown to be dominant in lowering the blood pressure whilst sympathetic influence has been effective in increasing the pressure (Glick & Braunwold, 1965; Robinson, Epstein, Beiser, Braunwold, 1966). The weight of evidence indicates that in the supine resting position parasympathetic restraint is the dominant influence on the heart rate in humans (Robinson *et.*

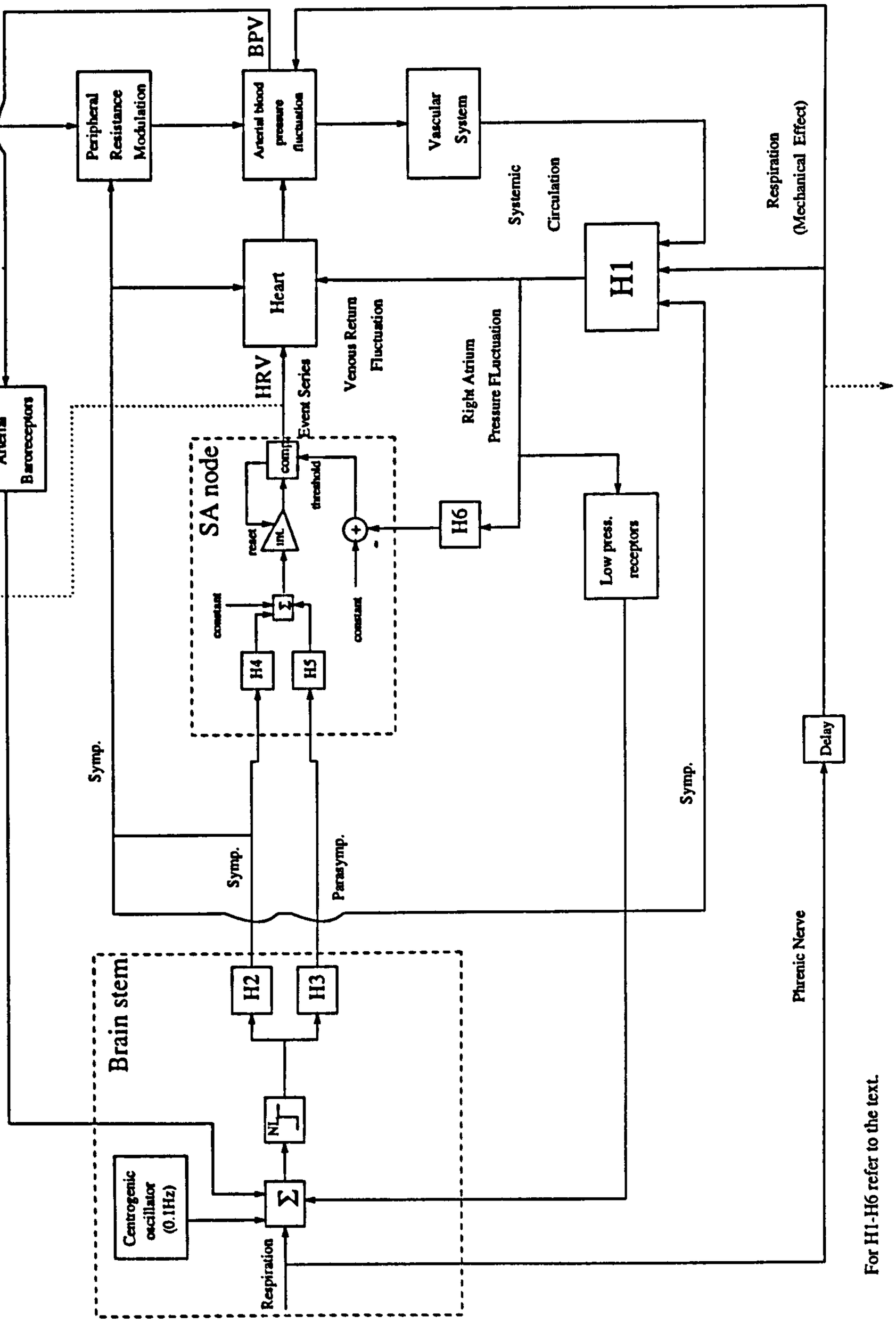


Figure 7.1: The proposed model.

al., 1966; Pickering, Gribbin, Strange Petersen, Cunningham, Sleight, 1972; Eckberg, Fletcher, Braunwald, 1972; Scher & Young 1979; Eckberg, 1980). Specifically, Eckberg *et. al.* (1972) have determined the relative role of the sympathetic and parasympathetic influences on heart rate by electrical stimulation of the carotid sinus nerve. By selective blockade of the adrenergic and parasympathetic systems these researchers showed that the parasympathetic influence is almost five times more effective than the sympathetic influence on prolongation of the R-R interval following carotid sinus nerve stimulation.

It has also been found by several investigators that the effects of the combined sympathetic and parasympathetic stimulation are not simply additive. As reviewed by Levy (1971), the result of these investigations shows that the parasympathetic effects not only predominate over the sympathetic influences, but that a given vagal response is enhanced in the presence of background sympathetic stimulation.

In an attempt to characterise the interaction between sympathetic and parasympathetic control of the heart rate, Rosenblueth and Simeone (1934) observed that in anaesthetised cats the absolute reduction in heart rate produced by a given vagal stimulus was greater when the response to the basal heart rate was increased by tonic sympathetic stimulation. However, when the responses to the vagal stimulation were expressed as fractions of the basal heart rates, the percent changes did not significantly differ with the sympathetic activity. These workers proposed a describing equation for the sympathetic and parasympathetic control of the heart rate which in its simplified form can be represented as:

$$R = (1 + m)(1 - n)R_0, \tag{7.1}$$

with m, n the characteristic factors of the sympathetic and parasympathetic activities, respectively ($0 \leq m, n \leq 1$) and R_0 the intrinsic rate of the denervated heart. This simple equation was later justified for humans by other researchers after several experiments (Katona & Jih, 1975a; Katona, Mclean, Dighto, Guz, 1982; TenVoorde *et. al.*, 1995).

The Rosenblueth equation, in fact, predicts a multiplicative interaction between sympathetic and parasympathetic excitations. As a result of this interaction, for example, the larger the sympathetic tone the larger the heart rate change, a constant parasympathetic activity produces. However, in the heart rate variability study small

variations of the heart rate around its normal operating point (mean heart rate) are assumed. Consequently, the differential change in the Rosenblueth equation can be written as:

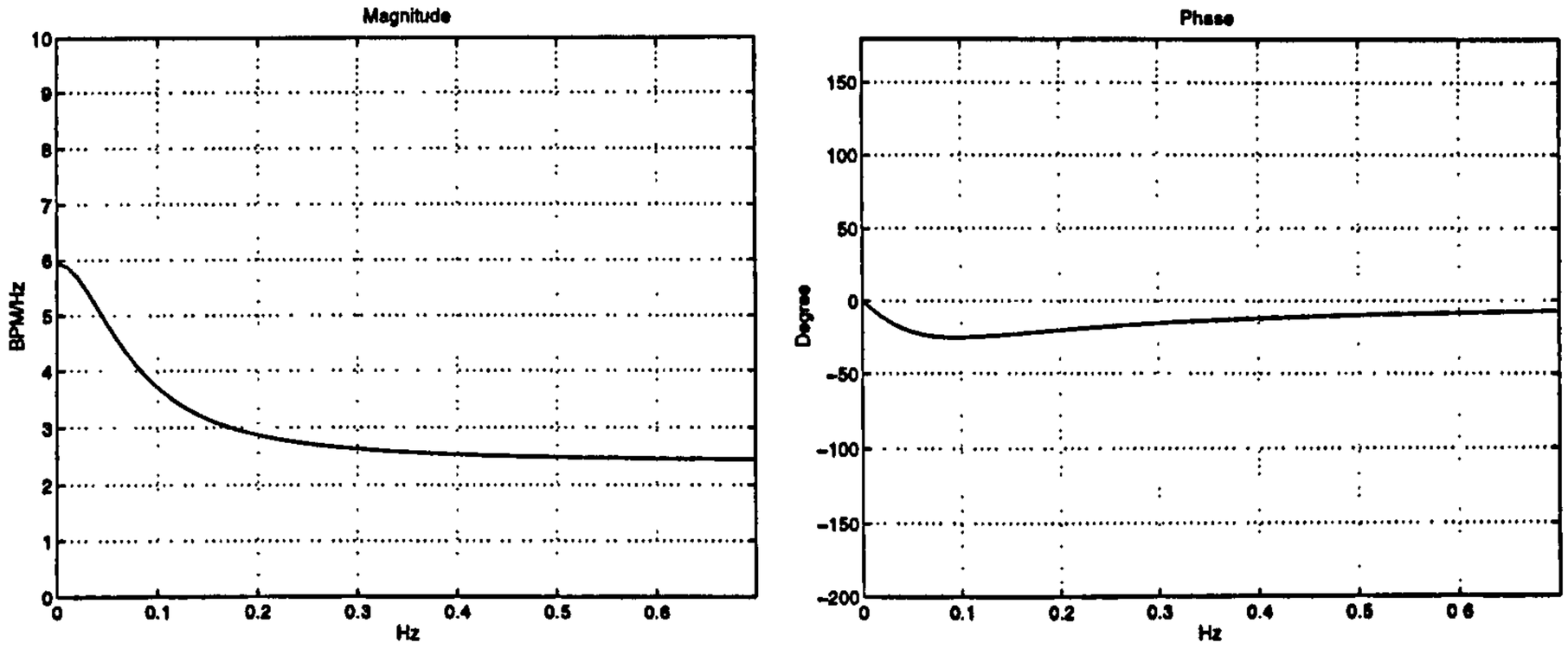
$$dR = [(1-n)dm + (-1-m)dn]R_0 = [dm - dn - ndm - mdn]R_0. \qquad (7.2)$$

The empirical values of $m = 0.2$ and $n = 0.5$ have been found for normal human subjects at rest (Katona *et. al.*, 1982). Since the vagal activity is dominant over the sympathetic activity, ratio $\frac{dn}{dm} = -5$ will be reasonable to consider the contribution of the nonlinear terms in equation (7.2) (Saul *et. al.*, 1989). If 10% (dR/R_0) variation in the heart rate is assumed (typical variation in heart rate), then differential values $dm = 0.0154$ and $dn = -0.077$ will be obtained by solving equation (7.2). It then follows that $dm - dn = 0.0924$, $ndm = 0.0077$ and $mdn = -0.0154$. Since the multiplicative term $ndm + mdn$ is much smaller than the additive term $dm - dn$, it is concluded that the sympathetic and parasympathetic influence of the heart rate can be modelled by a simple addition in the heart rate variability analysis. This feature although obtained for the Rosenblueth and Simone model, can be shown for the other SA characteristic equations as a result of small signal variations (Katona, Martin, Jih, 1975b; Chiu & Kao, 1997).

Vagal and Sympathetic Transfer Functions [1]

Although based on the above assumptions, sympathetic and parasympathetic control of the heart rate behave in an additive fashion, they exhibit different dynamic behaviours. It is well known that the heart rate shows a prompt change to vagal excitation whereas it illustrates a sluggish response to sympathetic stimulation (Eckberg, 1980, 1982). It is believed that the difference in the characteristics of the sympathetically and vagally mediated heart rate fluctuations is largely due to the response properties of the SA nodal cells to the respective neurotransmitters (Eckberg, 1980; Berger *et. al.*, 1989b). These characteristics have been enlightened by Berger and Saul (1989b) using spectral estimation. These investigators obtained the transfer functions between the heart rate and the cardiac sympathetic and vagal excitations using a white noise stimulus and pharmacological blocking agents. Their results indicate that the SA node behaves as a lowpass filter for both nerves but with corner frequency $f_c = 0.2Hz$ and zero delay for the vagus and $f_c = 0.015Hz$ and $1.7sec$ delay for the sympathetic

[1] H_4, H_5 in Fig. 7.1.



(a) (b)

Figure 7.2: (a) Magnitude, (b) phase of the SA node vagal transfer function given by equation (7.3).

nerve.

The Berger-Saul vagal transfer characteristic was later confirmed by Mokrane *et. al.* (1995) using a modified stimulation technique. They used a synchronous stimulation of the vagus nerve by applying random pulses at specific times in the cardiac cycle to mimic the physiological pattern of efferent vagal activity. In substantial agreement with the Berger-Saul transfer function these researchers also found a low pass filter characteristic with a decrease in magnitude and an increase in cutoff frequency by increasing the vagal tone. Besides the lowpass filter behaviour, Mokrane *et. al.* (1995) showed that the SA node exhibits an all pass filter property particularly in high vagal tones. This feature of the SA node had not been observed previously.

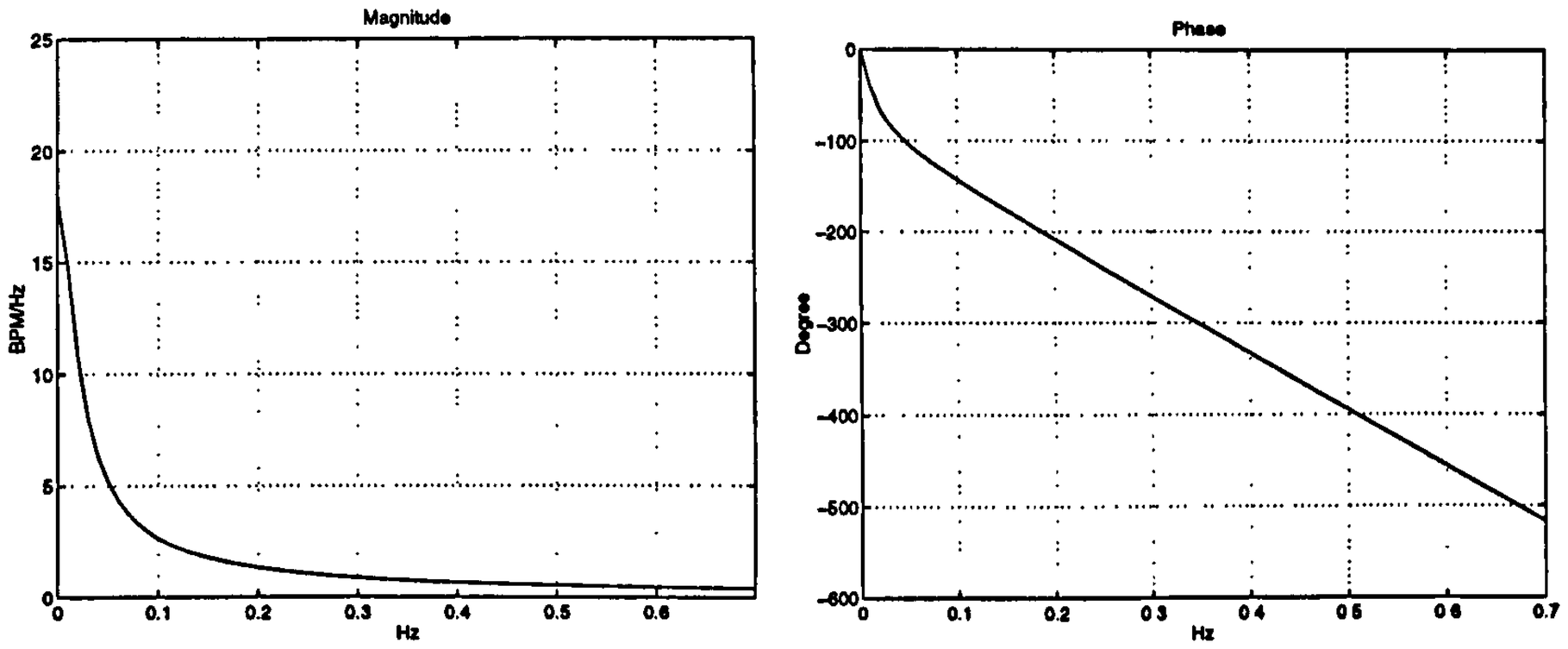
Fig. 7.2 displays the magnitude and phase of the vagal transfer function based on the results obtained by Mokrane and his colleagues. The transfer function is made up of a lowpass filter with cutoff frequency $0.06Hz$ in cascade with an allpass filter,

$$H_p(f) = -\frac{2.4s + 2.26}{s + 0.38}. \tag{7.3}$$

The SA node sympathetic transfer characteristic is based upon the Berger-Saul experiment and consists of a lowpass filter with cutoff frequency $0.015Hz$ and $1.7sec$ delay,

$$H_s(f) = \frac{1.7}{s + 0.095} e^{-1.7s}. \tag{7.4}$$

Fig. 7.3 illustrates the magnitude and phase plot of equation (7.4).



(a) (b)

Figure 7.3: (a) Magnitude, (b) phase of the SA node sympathetic transfer function given by equation (7.4).

Response to Blood Pressure Variation [2]

An important feature of the SA node which is mediated by the autonomic nervous system is its buffering effect on blood pressure *i.e.*, a decrease in heart rate following a rise in blood pressure and an increase in heart rate following a fall in blood pressure. Although it is still ongoing research, there is substantial agreement that the variation in R-R interval as a result of pressure change, namely the baroreflex sensitivity (α) lies in the range $5 - 15 msec/mmHg$ for normal human beings in the resting supine state (Mancia & Mark 1986; Parati, Di Rienzo, Castiglioni, Villani, Tortorici, Mancia, 1997).

By applying trains of repetitive, ramped, R-wave coupled neck suction and measuring the R-R prolongation, Eckberg and Eckberg (1982) obtained a baroreflex sensitivity of $5 msec/mmHg$. This value was measured as much as $13 msec/mmHg$ by de Boer (1985b) in his investigation for finding the short term relationships between the variability signals. Using a similar technique but by employing a random breathing pattern Saul *et. al.* (1991) determined the range $8-16 msec/mmHg$ $(1-2 BPM/mmHg)$ for α. Baselli *et. al.* (1988) estimated $5 msec/mmHg$ for the baroreflex sensitivity using the parametric approach. In a detailed study, Panerai, Martin, James and Potter (1997) compared the value of α obtained by estimating the impulse response between

[2] H_2, H_3 in Fig. 7.1.

the R-R interval variations and the blood pressure changes with the one obtained from spectral domain analysis as well as the sequence analysis method, following an injection of the pressor and depressor agents. These workers estimated a value very close to $10msec/mmHg$ for α.

In addition to the sensitivity of the heart rate to blood pressure changes, it is well known that blood pressure variation does not have an immediate impact on the heart rate. The conduction time of the baroreceptor-cardiac reflex has been measured by several researchers using different techniques. Katona *et. al.* (1970) using inflation and deflation of a balloon in the abdominal aorta of anaesthetised dogs measured $50 - 140msec$ delay between the beginning of the systolic pressure rise and the onset of the increased firing in the cervical vagus nerve. By injection of phenylephrine, Pickering and Davies (1973) estimated $470msec$ from the arrival of the stimulation at the carotid sinus to its effect on the P wave in humans. Since $70msec$ is assumed for the depolarization of the atria (Guyton, 1996), $400msec$ remains to be assigned for the delay between the change in pressure and the appearance of its influence in the efferent nerves. Almost the same result was obtained by Borst and Karemaker (1983) using low intensity electrical stimulation of the carotid sinus nerves in humans. They found that the PP-interval began to increase or decrease $0.5 - 0.6sec$ after the start or end of carotid sinus nerve stimulation.

7.2.2 Mechanical Stretching Effect of the SA Node [3]

Suppression of the autonomic influence on the SA node entails a considerable reduction in HRV (Saul *et. al.*, 1989; Triedman & Saul, 1994; Perlini *et. al.*, 1995a). The residual HRV is believed to be a result of mechanical stretching of the SA node induced by the blood volume change in the right atrium either by the mechanical effect of respiration or through modulation of the venous capacity.

Mechanical Effect of Respiration

With the aid of the random breathing pattern, Saul *et. al.* (1991) quantified the transfer relation between respiration and HRV when autonomically mediated heart rate fluctuations were eliminated by combined cardiac sympathetic and parasympathetic blockade. They found that the transfer function has a small magnitude that

[3] H_1, H_6 in Fig. 7.1.

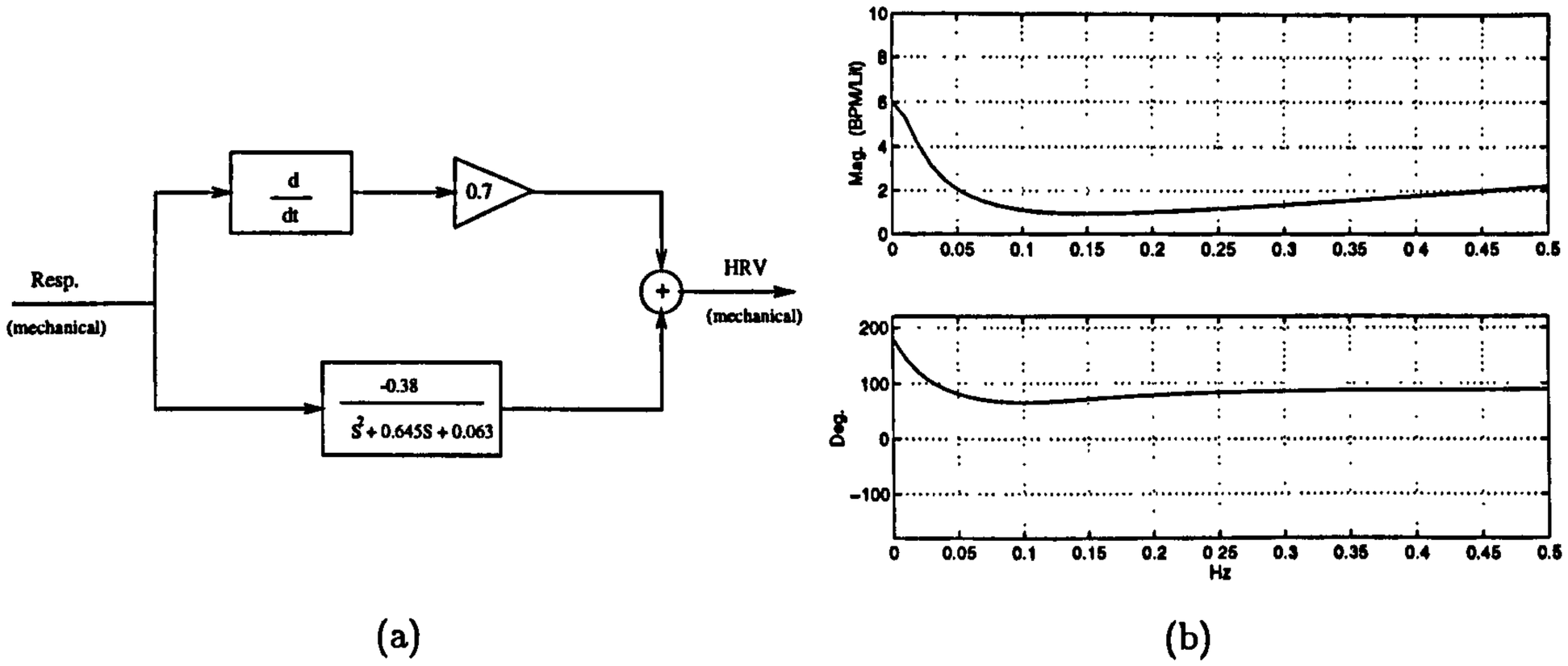


Figure 7.4: (a) Transfer function between respiration and nonautonomic response of the SA node, (b) frequency response of the transfer function.

increases linearly with frequency for $f > 0.15Hz$ accompanied with a 90° phase deviation. This characteristic resembles a positive differentiator for this frequency band. For lower frequencies ($f < 0.15Hz$), however, the transfer relation exhibits a lowpass filter characteristic.

The realization of this transfer function in a systemic form is shown in Fig. 7.4(a) by employing a second order lowpass filter in parallel with a differentiator. The input-output frequency response of this transfer function which is displayed in Fig. 7.4(b) closely mimics the experimental results given in Fig. 7 of the paper by Saul *et. al.* (1991).

Modulation by Venoconstriction

The role of baroreceptors in controlling the capacitive vessels and its important influence on haemostasis have been extensively studied by several researchers (Shoukas & Sagawa, 1973; Shoukas, Brunner, Greene, McAnespie, 1987; Bartelstone, 1960; Rothe, 1983). It has been shown that both the cardiac and aortic baroreceptors are capable of changing the venous capacity in anaesthetised vagotomized dogs (Shoukas, 1987). Bartelstone (1960) showed that carotid occlusion reflexly increases the tone of the venous reservoir, thereby increasing the quantity of the blood delivered to the heart. The

released blood causes an increase in the volume and hence the right atrial pressure with a consequent increase on the amount of SA nodal stretch.

Using a step change in intra-sinus pressure in anaesthetised vagotomized dogs Shoukas and Sagawa (1973) were able to determine the venous response characteristics to the baroreceptor reflex. They measured a 10-15 seconds time lag for the onset of the volume shift of the venous reservoirs following intra-sinus pressure change, and almost 2 minutes for observing the whole blood volume change. The sensitivity of the central venous pressure change to the carotid sinus pressure of 0.12 mmHg/mmHg can be obtained from their experiments.

By using the spectral estimation method and employing the random breathing pattern as well as the random variation in Lower Body Negative Pressure (LBNP), Triedman and Saul (1994) determined the response of the heart rate in humans with cardiac autonomic blockade. From their data the sensitivity of the heart rate to the central venous pressure change can be determined as 2.5 BPM/mmHg.

If a first order system between the arterial pressure change (measured by baroreceptors) and the change in the heart rate as a result of the venous return modulation by sympathetic stimulation is assumed then based on the results of Shoukas and Sagawa (1973) and Triedman and Saul (1994), equation (7.5) can be ascribed to the transfer function between arterial pressure change and the result of the stretching effect on the heart rate,

$$\frac{2.5 \times 0.12e^{-10s}}{24s+1}. \tag{7.5}$$

7.2.3 Overall Representation

The nonautonomic heart rate variability has a much smaller amplitude than the autonomically mediated variation. Recalling from Section 6.7 it can be concluded that the combined effect of the autonomic and nonautonomic modulations of the SA node has an additive property. Since it has already been assumed that the sympathetic and parasympathetic modulation also appear with an analogous additive feature, this means that the HRV is the summation of four inputs; direct sympathetic modulation, direct parasympathetic modulation, the stretching effect of respiration, and the stretching effect of venous modulation. This brings about the systemic representation shown

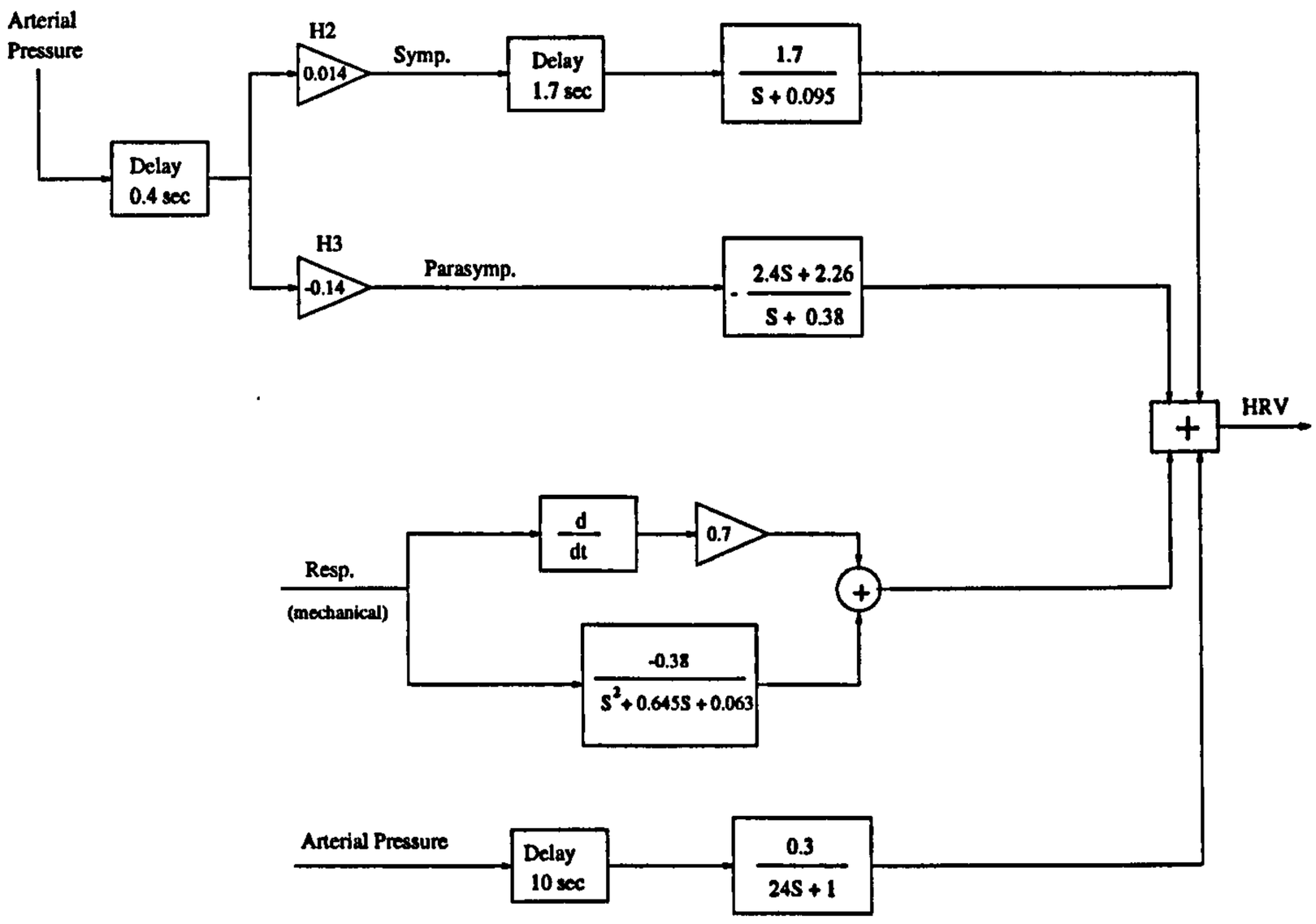


Figure 7.5: Complete model of the SA node.

in Fig. 7.5 for the model of the SA node. The first two branches from the top model the sympathetic and parasympathetic innervation of the SA node. The third branch represents the mechanical effect of respiration while the fourth branch illustrates the influence of venous modulation on the SA nodal rate.

Blocks H_2 and H_3 in the figure model the cardiac sympathovagal balance. These gain blocks have been tuned in order to give a $\approx 4/1$ static gain for the parasympathetic to sympathetic ratio (Eckberg *et. al.*, 1972) in the resting supine position while guaranteeing to have a baroreflex sensitivity of $10 msec/mmHg$ as described earlier. Furthermore, a delay of $0.4 sec$ has been assumed in the model to account for the latency of the change in the heart rate following the change in blood pressure through the vagal path.

7.3 Cardiopulmonary Baroreceptors [4]

CardioPulmonary (CP) baroreflexes, while not yet as well defined as the arterial baroreflexes, make a significant contribution to cardiovascular regulation. It is believed that the characteristics and general functions of the CP mechanoreceptors are similar to those of the arterial baroreceptors (Smith & Kampine, 1990). They elicit

[4]Low pressure receptors in Fig. 7.1.

circulatory responses that generally supplement the arterial baroreceptor reflexes with the ultimate result of buffering the arterial pressure changes. However, reflexes from the cardiopulmonary receptors and arterial baroreceptors cannot be regarded as parallel, since the arterial baroreceptors respond to changes in arterial pressure while the cardiopulmonary receptors respond to changes in central blood volume.

Similar to the arterial baroreceptors but to a much larger extent, CP receptors are different in terms of location and response features. Cardiopulmonary receptors can be divided into two major groups of receptors with vagal afferents and receptors with sympathetic afferents. The receptors of each group are distributed throughout the atria and ventricles with myelinated or unmyelinated fibres.

Paintal (1953) has divided the CP atrial receptors with myelinated vagal afferents into three different groups; type A which fire only during atrial systole, type B which fire only during atrial filling and an intermediate group which fire during both atrial systole and filling. Thus it is not surprising to observe that the B type receptors discharge shows a good correlation with changes in blood volume and central venous pressure. In fact, it has been shown that a small decrease in blood volume does not affect the aortic baroreceptors discharge whereas it reduces the mean firing rate of the B type receptors (Bishop, Malliani and Thoren, 1986). Recent studies, however, elucidate that the only difference between types A and B receptors lies in their location (Hainsworth, 1991). Type A receptors are located at the venoatrial junction and can be stimulated by atrial contraction whereas type B receptors are located in the walls of the atria and are influenced by atrial stretch.

In addition to the myelinated vagal fibres there is a dense population of receptors with unmyelinated vagal afferents (C fibres) also in the atria. These receptors have a higher threshold and considerably lower discharge frequencies than the myelinated endings. The atrial C fibres are activated during atrial filling and show a discharge during the V wave of the atrial pressure. The response of these receptors to spontaneous respiration has been considered by Thames, Donald and Shepherd (1977). These authors showed that the frequency and pattern of discharge of these receptors were altered during spontaneous respiration. The atrial C receptors discharged with cardiac rhythmicity during end inspiration and early expiration when transmural pressure was greatest, and were silent for the remainder of the respiratory cycle. These workers

also illustrated that when blood volume was increased or respiration was augmented by CO_2 breathing, the rate of discharge was a linear function of the atrial transmural pressure. Besides the unmyelinated C fibres, the discharge of the ventricular receptors with myelinated vagal afferents also exhibits marked variation with respiration (Bishop *et. al.*, 1986).

Receptors with sympathetic fibres also constitute an important part of the CP receptors. There are both myelinated and unmyelinated afferent fibres distributed throughout the atria and ventricles. It is known that the discharge of the afferent cardiac sympathetic fibres with atrial endings is increased during rises in atrial pressure (Bishop *et. al.*, 1986; Hainsworth, 1991). Conversely, the impulse activity of these receptors is reduced during reduction in atrial pressure. There is general agreement that ventricular sympathetic receptors with myelinated nerve fibres are sensitive to mechanical events of the cardiac cycle. The discharge of sympathetic ventricular receptive endings rises during increases in ventricular pressure, and decreases during reductions in ventricular pressure (Bishop *et. al.*, 1986; Hainsworth, 1991).

Besides the cardiac receptors explained above, the pressure change in the low pressure area of the circulatory system is also sensed by receptors located in the pulmonary artery. The impulse activity of these receptors is in phase with the upstroke of the pulmonary artery pressure (de Burgh Daly, 1986). An increase in the pulmonary arterial pressure increases the impulse firing of these receptors and a decrease in the pulmonary arterial pressure causes a reduction in their discharge rate. Thus these receptors appear to have the same general properties as the sympathetic mechanoreceptors. It has been shown that stimulation of these receptors increases vascular resistance and arterial blood pressure (Hainsworth, 1991).

In addition to the variety of the CP receptors and their associated responses, diversity in the effector responses is also noticeable. The observed effector responses also depend, at least partly, on the experimental techniques used (Hainsworth, 1991). It has been shown that, for instance, when there is a localised stretch of the region containing atrial receptors attached to the myelinated afferent nerves, there is a reflex tachycardia whereas a more diffuse stimulation, possibly stimulating nonmyelinated afferents, may result in a slowing of the heart rate (Hainsworth, 1991). On the other hand, experimental results have revealed important differences in the patterns of re-

sponses during activation of cardiopulmonary and arterial baroreflexes. It has been shown that by decreasing the central venous pressure, using the Lower Body Negative Pressure (LBNP) technique, the forearm vascular resistance increases with the associated decrease in the forearm blood flow (Zoller, Mark, Abboud, Schmidt, 1972; Abboud & Mark 1979a). Also application of the LBNP and rapid transfusion of blood have resulted in increase and decrease of the peroneal sympathetic nerve activity, respectively (Agewall, Rhea, Persson, Karlberg, Wallin, Anderson, 1990; Oren, Schobel, Weiss, Stanford, Ferguson, 1993). In both cases alteration in the central venous pressure was observed without concomitant change in the arterial blood pressure. These findings during low level LBNP indicate that decrease in venous return and central venous pressure can produce reflexogenic vasoconstriction without significant changes in the determinants of carotid and aortic baroreceptor activity. In contrast to the forearm response, the results of experiments suggest that the splanchnic vascular bed is much more sensitive to arterial than to CP receptors activities (Abboud & Mark 1979a; Abboud, Eckberg, Johanseen, Mark, 1979b). In a broader context these observations highlight the nonuniformity of the baroreceptor control of circulation emanating from the CP receptors versus high pressure receptors.

With regard to the effect of CP receptors on heart rate, the available information indicates that the issue is complex. Although the Bainbridge reflex, (increase in heart rate as a result of increase in cardiac filling) has been observed by different groups in dogs, several human studies have not successfully demonstrated the same effect (Mark & Mancia 1986; Desai, Collins, Snell, Mosqueda-Garcia, 1997). Moreover, the decrease in central venous pressure produced by LBNP does not alter the heart rate unless the stimulus is sufficient to decrease the arterial pressure and thereby engage the arterial baroreflexes (Zoller *et. al.*, 1972; Abboud *et. al.* 1979b). It is speculated that the increase in cardiac filling pressure stimulates several different cardiopulmonary sensory receptors and afferent pathways. Stimulation of some might promote reflex tachycardia (a Bainbridge effect) whereas stimulation of others might produce reflex bradycardia. The net effect could be a negligible change in the heart rate (Mark & Mancia, 1986). It is the general consensus that the arterial baroreceptors have a much more potent effect on the heart rate than the CP receptors.

Although all physiologists believe that the CP receptors participate in cardiovascular regulation, disparity between their observations has prevented them from assign-

ing a single functional role to these receptors. Some authors even disagree with the term "CP baroreflex" as there are many reflexes emanating from the heart and lungs, all with different characteristics and different time courses (Hainsworth, 1991).

Putting this controversial matter aside, the concern here is to consider the possible role of the CP receptors in rhythmical fluctuations of HRV and BPV. Respiration modulates the central venous pressure. In normal conditions the central venous pressure can fall to a few mmHg as a consequence of the inspiratory effort. Furthermore, respiration may have a direct stretching effect on the CP receptors. As already stated, the discharge rate of some types of receptors displays the respiratory pattern. But the question is whether this respiratory modulation influences the heart rate and blood pressure in the supine resting position assumed in this study. Indeed no definite answer can be offered to this question. The weight of evidence, however, indicates that the mild variation in the central venous pressure in normal resting conditions has no significant effect on the heart rate and arterial blood pressure (mean and systolic), even no transient change has been observed (Abboud *et. al.*, 1979b; Zoller *et. al.*, 1972; Oren *et. al.*, 1993; Agewall *et. al.*, 1990). Loading and unloading of the CP receptors by the LBNP technique, rapid blood transfusion or leg raising can greatly change the central venous pressure with no effect on the heart rate or arterial blood pressure. In agreement with the previous results but using more precise measuring techniques (cine computed tomography) Oren *et. al.* (1993) have examined the performance of the CP receptors in a recent study. They showed that a mild LBNP did not alter the heart rate, arterial blood pressure, cardiac output, right and left ventricular pressure and stroke volumes but it did produce a significant decrease in pulmonary artery and right and left atrial pressures. Forearm vascular resistance and efferent sympathetic (peroneal) nerve activity increased with LBNP, illustrating the influence of the CP receptors on muscular vessels. As further evidence Macov, Fagard, Mortelman, Claeys and Amery (1992) showed that loading and unloading of the CP receptors did not affect the mean R-R interval, LF component, HF component and LF/HF ratio in the PSD of the HRV, suggesting that that there is no direct neurally mediated effect on heart rate. As a result of these investigations it was decided not to give any role to the CP receptors in the variability analysis studied here.

7.4 Phrenic Nerves and the Diaphragm Transfer Functions

Normal quiet breathing is accomplished almost entirely by downward and upward movement of the diaphragm to lengthen or shorten the chest cavity. The inspiratory signal from the respiratory centre in the brain stem is transmitted mainly through the phrenic nerves to the diaphragm. While inspiration is an active movement, expiration results from elastic recoil of the lungs, chest wall and abdominal structures. Therefore, it can be assumed that the pressure changes inside the chest cavity will be different from the central respiratory drive signal by the phrenic nerves and the diaphragm transfer characteristics. This property has been considered in the proposed model by adding an individual path from the respiratory centre to the chest cavity and separating the effect of respiration from its mechanical influence as shown in Fig. 7.1.

Using a frequency analysis approach, Evanich and Lourenco (1976) studied the dynamic characteristics of the diaphragm by applying sinusoidally modulated pulse rate patterns to the phrenic nerves. They showed that the induced pressure changes inside the chest cavity illustrate a flat magnitude response and a linear phase with respect to the phrenic nerve excitation frequency up to twice the normal breathing rate.

Existence of a linear phase implies the presence of a constant time delay between the excitation and the pressure change. The total estimated delay is approximately $150msec$ (Evanich & Lourenco, 1976). This delay consists of two major parts; the conduction time of the phrenic nerves, and the delay in the transfer characteristic of the diaphragm. It has been shown that the conduction time of the phrenic nerves is only a small portion of the whole delay, almost $10msec$ (McKenzie & Gandevia, 1985; Davis, 1967). Hence, the major part of the delay is attributed to latency of the diaphragm muscle.

By joining the phrenic nerves and the diaphragm characteristics in one building block, the transfer function from the central respiratory signal to its mechanical influence through the chest movement can be modelled by a $150msec$ time delay system. The central respiratory drive signal, therefore, can be obtained by measuring the chest movement and applying a $150msec$ time shift.

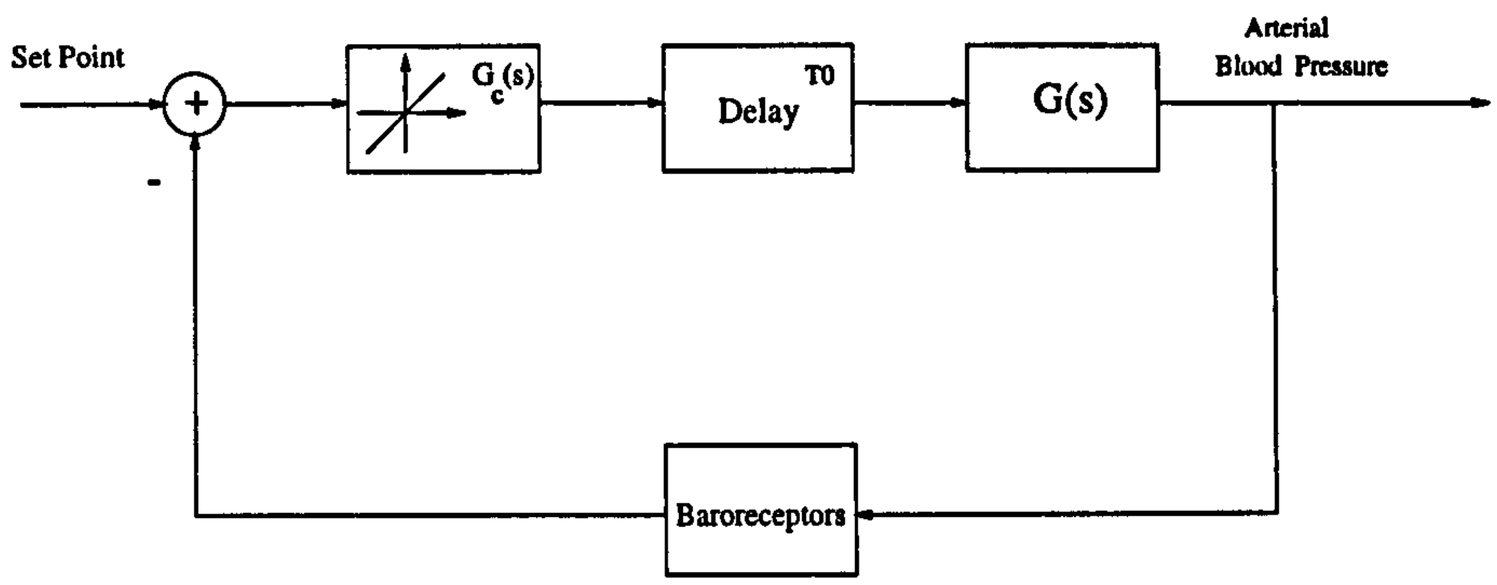


Figure 7.6: The feedback regulatory mechanism of the arterial blood pressure.

7.5 Mayer Waves Generation Mechanisms

As discussed in Chapter 4 there are three possible scenarios that might create the oscillation in the VLF and LF bands. Subsequently a systemic representation for each hypothesis is depicted along with more detailed discussions.

7.5.1 Feedback Mechanism [5]

The most prevalent opinion for the generation of the LF oscillation envisages an instability in the feedback regulatory mechanism of arterial blood pressure. The state of the circulation is continuously monitored by various receptors which send information to the brain over afferent neural pathways. The brain integrates the incoming information and generates the efferent signals to the active tissues of the cardiovascular system, namely the myocardium, the SA node and the smooth muscle of the blood vessels. In a simplified form, this regulatory mechanism can be modelled by a linear negative feedback system as shown in Fig. 7.6. $G(s)$ in the figure denotes the open loop dynamic behaviour of the feedback system. It incorporates the dynamic performance of the myocardial contractility, heart rate and vasoconstriction. Due to the latency of the different effectors the compensatory effect of the feedback loop is not immediate. The block denoted by delay T_0 in the figure models this latency. It comprises several delay mechanisms in the afferent-efferent pathways; neural pathways delay, central processing delay, effectors response delay, etc.

It has been shown that the latency in the blood pressure regulatory mechanism ranges from 2 to 5 seconds. Scher and Young (1963) illustrated that, in anaesthetised

[5]BPV-Symp-BPV loop in Fig. 7.1.

cats and dogs, when the pressure in the carotid sinus was changed in steps, 2 to 4.5 seconds elapsed before any response was seen. The same result was obtained by Shoukas and Sagawa (1973) in vagotomized dogs. By variation of intrasinus carotid pressure these investigators observed a 2 to 5 second time lag between the onset of the mean arterial blood pressure change and the sinus pressure change. Borst and Karemaker (1983) used direct carotid sinus nerve stimulation to measure the time delays in the human baroreceptor reflex. They observed that the decrease of arterial pressure started 2-3 seconds after the onset of the carotid sinus nerve stimulation following vagal blockade. Also the recovery of the pressure began with the same delay after cessation of the stimulation.

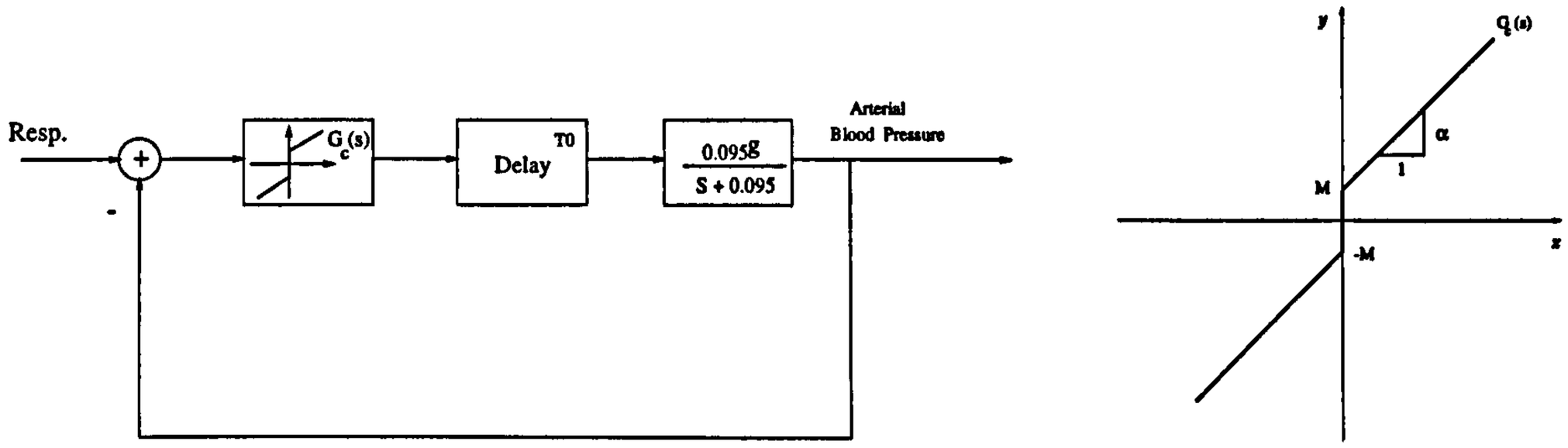
Inclusion of the delay in fact causes the feedback system to be susceptible to oscillation. Nevertheless, it has been demonstrated that the Bode diagram of the carotid sinus reflex system in dogs is only marginally stable around $0.1Hz$ (Scher & Young, 1963; Sagawa, 1983). Since an unstable linear system is unable to produce a sustained LF oscillation in practice (poles should be exactly on the imaginary axis), a resonant system around $0.1Hz$ has been employed by many investigators to describe the presence of the LF component (de Boer *et. al.* 1987; Baselli *et. al.*, 1988; TenVoorde *et. al.*, 1995; Madwed, Albrecht, Mark, Cohen, 1989; Mullen *et. al.*, 1997). de Boer *et. al.*, (1987) have shown that the $10sec$ variability of the HR and BP in their beat-to-beat model is due to the delay in the sympathetic path. In the de Boer model the LF component appears as a result of the noise amplified in the bandpass filter of the sympathetic regulatory mechanism. The same property has been recruited by Madwed *et. al.*, (1989) and Tenvoorde *et. al.*, (1995) by changing the peripheral resistance in the Windkessel equation through a feedback path. Similarly, in the model of Baselli *et. al.* (1988) a resonant circuit constitutes a path for amplifying the components in the LF band.

In summary, the premise based on the linear feedback theory relies upon some external input which is amplified in the resonant circuit and appears in BPV and then HRV. It has been assumed by some authors that respiration performs the role of this exogenous input for generation of the LF component (Bernardi, Passino, Spaducic, Valle, Leuzzi, Piepoli, Sleight, 1997; Sleight & Casadei, 1995). However, an increase or decrease in tidal volume does not induce the same change in the LF component. Furthermore, the Mayer waves do not disappear with apnea or by abolition of the

phrenic nerve activity following hyperventilation (Polosa, 1984b). Nonetheless, the presence of external noise, to be amplified in the resonant circuit, causes a perpetual LF component, and to be able to vary with the state of sympathetic provocation is not supported by physiological evidence. Instead, the LF component appears to emanate from an independent self sustained oscillatory system. This assumption inevitably needs nonlinear oscillating theory.

Linkens (1979b, 1979c) has studied the Van Der Pol oscillator as a possible explanation for the LF generation mechanism and the presence of frequency pulling and entrainment phenomena. A more meaningful feedback model has been detailed by Hyndman (1970) and Kitney (1979) by employing a bang-bang element as discussed in Chapter 4. It was argued there that the presence of the hard nonlinearity in the K model is not a physiologically well-established assumption. Subsequently the Kitney model will be modified not only to find a more realistic configuration but also to be able to describe some other aspects of the LF component.

To commence the analysis the simple linear feedback system of Fig. 7.6 is modified as shown in Fig. 7.7(a). As a preliminary representation, $G(s)$ in Fig. 7.7(a) is assumed to illustrate only the response of the cardiovascular effectors to sympathetic efferents. The study by Rosenbaum and Race (1968) has characterised the frequency response of resistance vessels to efferent sympathetic modulation and found that a lowpass filter with cutoff frequency of $0.017Hz$ describes the response. The filter shape and cutoff frequency were nearly identical to those of the cardiac sympathetic receptors derived later by Berger *et. al.* (1989b). Scher and Young (1963) also showed that at frequencies below $0.01Hz$ the response of the blood pressure to variation of the carotid sinus pressure in the open loop experiment was exactly out of phase whereas it found a lowpass filter characteristic beyond this frequency. As a consequence, a first order lowpass filter with cutoff frequency of $0.015Hz$ has been given to $G(s)$ in Fig. 7.7(a). Further, to incorporate the effect of the static open loop gain of the cardiovascular system and its consequence on the LF component, a constant parameter g has been added to $G(s)$. Many different methods have been used to measure g (Sagawa, 1983; Scher & Young 1963; Schmidt, Kumada, Sagawa 1971; Hosomi 1978; Burattini, Borgdorff, Westernhorf, 1987; Burattini, Socionovo, Bellocchi, 1994). In an open loop experiment Scher and Young (1963) obtained a mean static open loop gain of 4 for anaesthetised vagotomized cats and 2 for dogs in the normal operating range. In



(a) (b)

Figure 7.7: (a) Modified Kitney model, (b) modified nonlinear element.

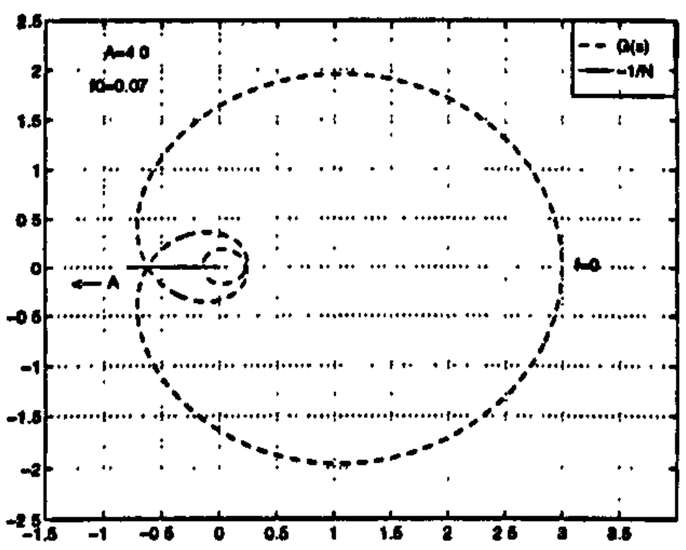
a similar experiment Schmidt and his colleagues (1971) obtained $g = 1$ for vagal intact dogs and $g = 2$ after vagotomy. In a close agreement with the previous results, Burattini *et. al.* (1987) calculated a value of 1.6 for g in a closed loop experiment in conscious dogs. In accordance with these results a static open loop gain $g = 2$ is assumed in this study for human beings in the normal operating range in the supine resting condition. A delay of $T_0 = 2.5sec$ is also allocated to represent the time required for the onset of the sympathetic influence following an arterial pressure change as previously described.

In the linear feedback hypothesis (Fig. 7.6), $G_c(s)$ has a linear characteristic. In the K model, $G_c(s)$ shows a significant nonlinear feature. In the modified model a mild nonlinearity as shown in Fig. 7.7(b) is employed. The proposed nonlinearity has a sharp sigmoid behaviour ($tanh(100x)$) around the origin and a linear characteristic everywhere else. This mild nonlinearity integrates any nonlinearity in the blood pressure regulatory mechanism and most likely is located in the brain stem. The appealing feature of this nonlinearity is its closeness to a linear characteristic, as assumed by many authors, while creating a sustained LF oscillation as well as the entrainment phenomenon. To make sure that this is indeed so, the describing function of $G_c(s)$ will be first obtained. Then the existence of the limit cycle and frequency entrainment in the modified K model (Fig. 7.7(a)) are examined.

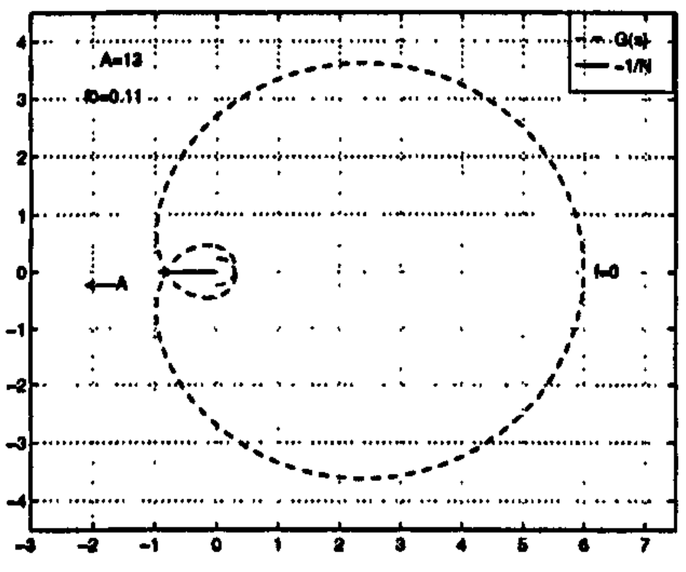
If A denotes the amplitude of an input sinusoidal function it is easy to show that the describing function of the nonlinearity depicted in Fig. 7.7(b) is approximated by (Slotine & Weipin, 1990)

$$N = \frac{4M + \alpha\pi A}{\pi A}. \tag{7.6}$$

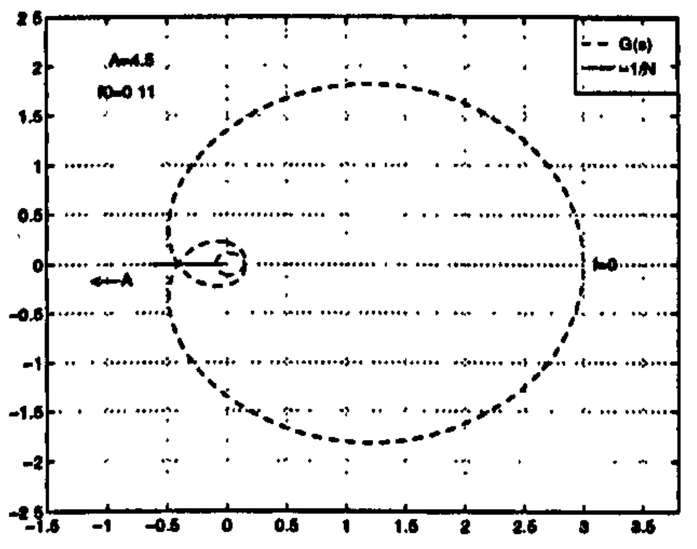
(a) (b) (c)



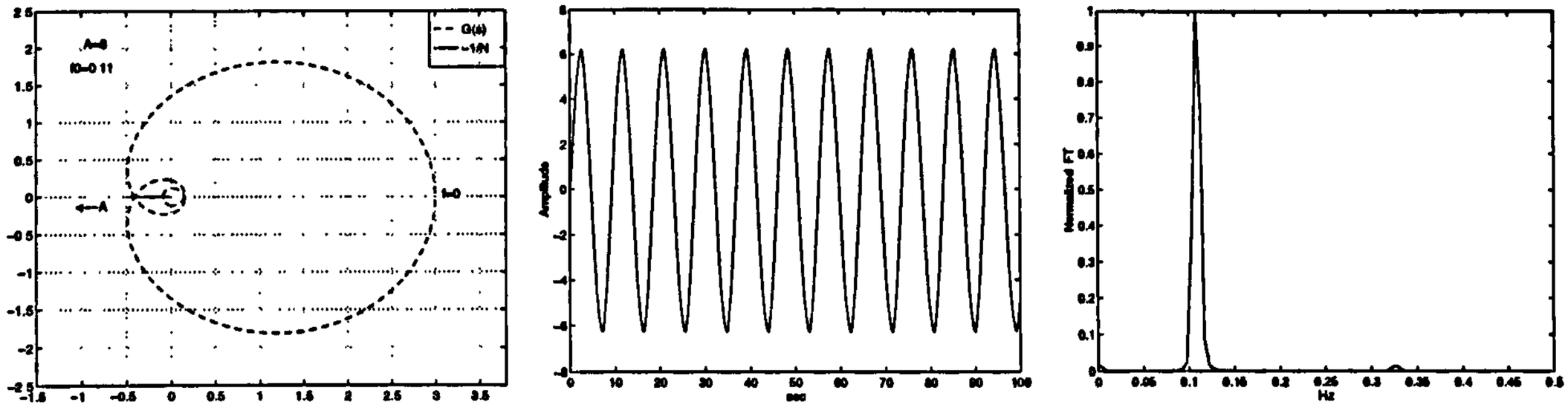
(d) (e) (f)



(g) (h) (i)



(j) (k) (l)

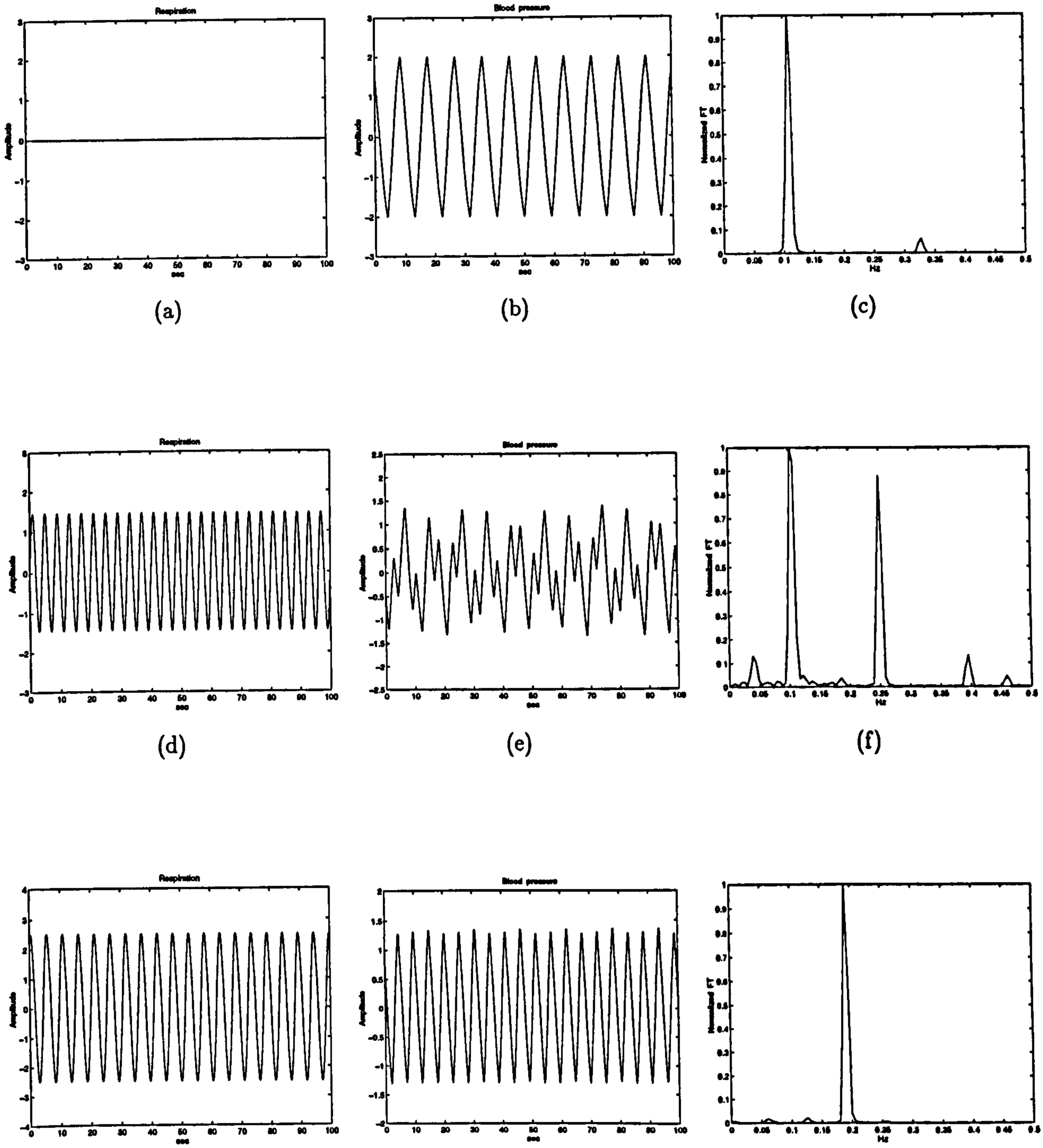


(m) (n) (o)

Figure 7.8: Analysis of the limit cycle in the modified K model with different selection of the parameters. The left hand column shows the Nyquist plot of $G(s)$ and $-\frac{1}{N}$. The amplitude and frequency of the oscillation can be determined by finding the intersection of these plots. The middle and the right hand columns illustrate the time behaviour and frequency analysis of the K model with the modified nonlinear element, respectively. (a),(b),(c) $M = 2, \alpha = 1, T_0 = 2.5, g = 3.0$, (d),(e),(f) $M = 2, \alpha = 1, T_0 = 4.0, g = 3.0$, (g),(h),(i) $M = 2, \alpha = 1, T_0 = 2.5, g = 6.0$, (j),(k),(l) $M = 4, \alpha = 1, T_0 = 2.5, g = 3.0$, (m),(n),(o) $M = 2, \alpha = 2, T_0 = 2.5, g = 3.0$.

The amplitude and frequency of the oscillation depends on the parameters of the feedback loop. Figures 7.8(a)-(o) illustrate the frequency and amplitude of the oscillation obtained by the Nyquist plot and also the simulation of the model for different selection of the parameters. Each horizontal panel displays the result of one specific set of parameters in Nyquist plot, time domain and frequency domain. Similar to the K model, increase or decrease in the delay causes a decrease or increase in the frequency of the oscillation, respectively (Figs. 7.8(c),(f)). The amplitude of the oscillation on the other hand depends on the hardness of the nonlinearity, M, and the open loop static gain, either through g or α (Figs. 7.8(h),(k),(n)). Increase of the static gain, however, has a more potent effect than M. This is an interesting feature. The LF component has been reported to increase after mild hemorrhage, during tilt, mental stress, mild physical exercise and generally on sympathetic provocation (Polosa, 1984b; Rimoldi *et. al.*, 1990; Pagani *et. al.*, 1986; Malliani, Pagani, Lombardi, Cerutti, 1991; Elghozi, Laude, Girard, Mounier-Vehier, 1997). The increase in sympathetic outflow is mediated by an increase in the open loop gain. In the model, this feature is reflected by a rise in g which entails an increase in the power of the LF component. Moreover, sympathetic excitation may increase the hardness of the nonlinearity with a further increase in the LF power.

The presence of frequency entrainment (Kitney, 1979) is displayed in Figs. 7.9(a) through 7.9(i) by injecting the respiratory input into the feedback loop of Fig. 7.7(a).



(a) (b) (c)

(d) (e) (f)

(g) (h) (i)

Figure 7.9: Frequency entrainment in the modified K model by increasing the amplitude and decreasing the frequency of the respiratory input. Left hand column shows respiration, middle blood pressure and the right hand column shows the normalised Fourier transform of the blood pressure. From top to bottom, zero respiratory input, respiration at $0.25Hz$, and respiration at $0.19Hz$, respectively.

It is clearly shown that by decreasing the frequency and increasing the amplitude of the respiratory input the LF component suddenly disappears.

Therefore, the modified K model appears to be a satisfactory representation to retain the well-known properties of the LF component while preserving the fundamental features of physiological relevance. In the following chapter this simple model will be extended by adding some further physiological blocks. It will be seen that the functionality of this model will not be violated by cooperation with the other neuro-cardiovascular components. In contrast, this cooperation will exhibit some attractive features of the LF oscillation which are observed experimentally.

7.5.2 Centrogenic Mechanism [6]

Unlike the feedback-based hypothesis which reckons on the instability of the afferent/efferent loop, in centrogenic theory the LF component is attributed to an inherent oscillation in the neuronal discharge patterns of the brain stem. In anaesthetised cats with carotid and aortic baro- and chemo-receptor denervation, Preiss (1974) and Polosa (1984b) showed that the temporal patterns of the sympathetic preganglionic neurons exhibit LF components essentially similar to those observed in non-deafferented animals. This observation was consistent with a cause-effect relationship between the rhythmic sympathetic activity and the corresponding blood pressure oscillation. Moreover, for deafferented animals the same procedure (mild hemorrhage) to that of the non-deafferented animals provoked the LF oscillation, suggesting that the feedback mechanism does not play a crucial role in inducing the LF component. Furthermore, these workers showed that periodic modulation of the neuronal firing patterns in decerebrated cats persisted when the systemic arterial pressure oscillation was abolished by means of a pressure-stabilising apparatus.

The results obtained by Polosa and Priess were also supported by other investigators (Langhorst *et. al.*, 1984; Montano, *et. al.* 1996). Langhorst *et. al.* showed that the LF rhythm of the neuronal activity of the brain stem can be observed in blood pressure variation in anaesthetised dogs. In vagotomized sinaortic denervated and decerebrated cats Montano *et. al.* illustrated that the LF oscillation ($0.12Hz$) in the discharge of the medullary neurones and the corresponding component in the

[6] Centrogenic oscillator in Fig. 7.1.

blood pressure variation were significantly correlated.

In an isolated perfused vascular bed in anaesthetised dogs, Cevese, Grasso, Poltronieri and Schena (1995) showed that the oscillation in the LF band in iliac arterial flow persisted and was in high correlation with arterial blood pressure. By considering the phase relationship between blood pressure, R-R interval and blood flow in the isolated limb these investigators concluded that spontaneous oscillation of peripheral resistance is mainly due to a rhythm of central origin leading to an oscillating sympathetic vasoconstrictor outflow.

If the LF fluctuations of blood pressure are emanating from the brain stem centres then blockade of the efferent arc should prevent these neuronal fluctuations from being transmitted to the vascular system. Just, Wagner, Ehmke, Kirchheim and Presson (1995) showed that after baroreceptor (chronic) denervation in conscious dogs the power spectral density of BPV was more than six times higher than in the non-deafferented animals for $f < 0.08Hz$. The high level of blood pressure variability after baroreceptor denervation was reduced by interruption of the efferent pathways by either α-adrenergic or ganglionic blockade; however, it was still larger than in the control dogs.

These lines of evidence are consistent with a central origin as the dominant mechanism underlying the Mayer waves. In order to realize this second hypothesis of the LF generation mechanism, an independent oscillator is simply assumed in the model of the brain stem (Fig. 7.10). This oscillator modulates the sympathetic and parasympathetic efferents through separate pathways. The gain of each pathway can be adjusted independently. In addition to the sympathetic efferents, the firing patterns of the parasympathetic nerves also exhibit oscillation in the LF band (Malliani, Pagani, Lombardi, 1992; Polosa 1984a), albeit less pronounced.

Besides the LF component, the neural firing patterns in the brain stem exhibit a simultaneous oscillation in the HF band, coherent with respiration (Montano *et. al.*, 1996; Langhorst *et. al.*, 1984). As argued in Chapter 4, there might be various kinds of interactions between the LF centrogenic oscillator and the respiratory oscillator. However, we avoid depicting any direct connection between these two oscillators due to their unclear relationships.

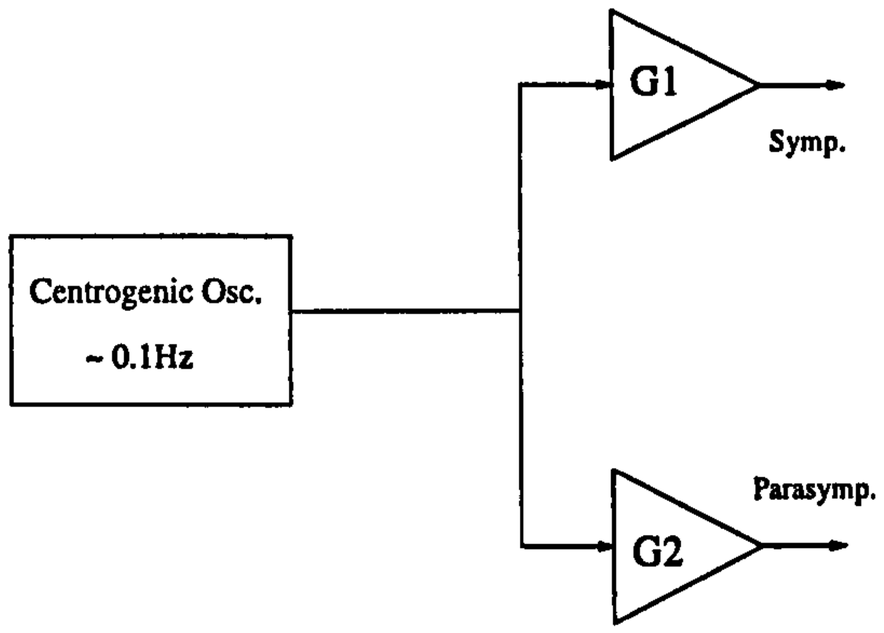


Figure 7.10: Model of the LF centrogenic oscillator and its influence on the autonomic nervous system.

7.5.3 The VLF Component [7]

It is most likely that the autorhythmicity of the vessels lies in the origin of the VLF component in the blood pressure. Small arteries and muscular venules often show spontaneous rhythmic contractions and relaxations, called vasomotion (Guyton, 1996; Milnor 1990). This rhythmical motion modulates the blood flow through the organ which may subsequently induce rhythmical fluctuations in blood pressure.

Barcroft (1932) and Nisimaru (1984) were among the first who raised the possibility of the blood pressure fluctuation as a result of a peripheral mechanism. They found that in cats and dogs rhythmical contraction of the spleen was present when blood pressure waves in a cycle of about $25 - 50sec$ appeared while if the spleen was closed with a clamp the blood pressure waves disappeared immediately. When the clamp was removed the blood pressure waves reappeared with the same cycle as rhythmical contractions of the spleen. The same phenomenon was also observed with rhythmical contraction of the intestinal tract and kidney. Later, it was shown that the induced VLF fluctuation in arterial blood pressure is due to the modulation of vascular resistance and not cardiac output (Iriuchijima, 1984).

In conscious resting rats, Janssen *et. al.* (1995) observed conspicuous VLF fluctuations in renal and mesenteric blood flow. While arterial blood pressure exhibited the same prominent VLF component there was little sign of the VLF in the PSD of the instantaneous cardiac output or stroke volume. These researchers argued that spontaneous fluctuations in arterial blood pressure in the VLF band originate from regionally specific oscillatory mechanisms contributing to flow resistance. These blood

[7] Endogenous vasorhythmicity in Fig. 7.1.

flow fluctuations were most pronounced in the mesenteric and renal vascular beds and were transmitted thence into the blood pressure.

Further evidence for vasorhythmicity and its influence on BPV can be obtained from the study by Yang, Terry, Kuo and Lin (1995) in cardiopulmonary bypass operations in human beings. While all higher components of the BPV effectively disappeared these authors observed that the VLF component persisted during hypothermic cardioplegia; that is when the heart was functionally disconnected from the blood vessels. Interestingly, persistence of the VLF component was accompanied by a maintained total peripheral resistance and systemic arterial pressure.

Although vasorhythmicity can be introduced as the origin of the VLF component, there is still uncertainty on the origin of the vasorhythmicity itself (Milnor, 1990). Some authors believe that the vasomotion originates from the activity of the smooth cells which show spontaneous oscillatory patterns and constitute a local pacemaker. Ionic pumps or rhythmical variation in permeability of the ionic channels of the smooth muscle cell membrane have been introduced as possible origins by these researchers (Siegel *et. al.*, 1984). Others have presumed that the vasorhythmicity arises from the actions of the local feedback regulatory mechanism that are either metabolic or myogenic in nature. Through subtle mathematical analysis Ursino, Fabbri and Belardinelli (1992) have shown that sustained rhythmic oscillation in the VLF band can occur in arterioles as a consequence of a myogenic response of the vascular smooth muscle.

Vasomotion is not a local property of the arterioles or venules only. Vascular rhythmicity has been observed even in large arteries with relatively large amplitude (Fuji, Heistad, Faraci, 1990). Furthermore, it can be assumed that the individual arterial or arteriolar rhythmicity can be synchronised or entrained and the vasomotion may spread over the whole organ blood flow and finally the arterial blood pressure (Siegel *et. al.*, 1984; Janssen *et. al.*, 1995).

In a systemic form the VLF component in the proposed model is simply imposed on the arterial pressure *via* an independent oscillator (Fig. 7.1). The power and frequency of the oscillation can be adjusted so as to create the same VLF component as that of the physiological experiments.

7.6 Overall Model

After detailing the individual performance of the governing components of the neuro-cardiovascular system and obtaining their specific characteristics all the constituting parts can now be assembled to depict a tractable mathematical form of the proposed model already sketched in Fig. 7.1. This is accomplished in two steps. In the first step all the segments of the model except the heart and sympathetic vascular modulation are substituted. The illustrative block for the combined heart and sympathetic vascular modulation will be added to the rest of the model after a conceptual description of its role in mediating the variability signals to the blood pressure variation.

Figure 7.11 illustrates the proposed model (Fig. 7.1) with each block replaced by its transfer relation. Starting from the right hand side, the blood pressure variation is sent to the brain stem *via* the baroreceptors following the VLF modulation. After sign inversion and central processing delay, the controlling signals (efferents) drive three parallel branches; cardiac autonomic nerves and sympathetic efferents. Meanwhile the centrogenic LF oscillator (Fig. 7.10) and the respiratory oscillator modulate the efferents *via* transfer gains $G1$ through $G4$ mediated by the vasomotor and cardiac control centres. The open loop gain g and the modified nonlinear element are also located in the vasomotor centre of the brain stem. The sympathovagal balance can be adjusted through transfer gains $H2$, $H3$ and g; $H3$ can weight the parasympathetic influence whereas $H2$ and g can be changed in favour of the sympathetic outflow. Therefore, the brain stem model which was already sketched in a simple form in Fig. 7.1 is now represented with mathematical details in Fig. 7.11.

The model of the SA node shown in Fig. 7.5 can now be seen in the centre of the detailed model in Fig. 7.11. This model in fact represents the SA node, $H6$ and (part of) $H1$ in Fig. 7.1, recalling that the blocks $H1$ and $H6$ in Fig. 7.1 transfer the sympathetic and respiratory modulation to the mechanical stretch of the SA node. The respiratory modulation originates from the brain stem respiratory oscillator. The respiratory drive signal in the brain stem traverses the phrenic nerves and distributes over the respiratory muscles with $0.2sec$ lag as shown by the lower part of Fig. 7.11. The BPV-Symp-BPV loop comprises sign inversion in the brain stem, $0.4 + 2.2 = 2.6sec$ delay, the modified nonlinear element, static open loop gain and the sympathetic

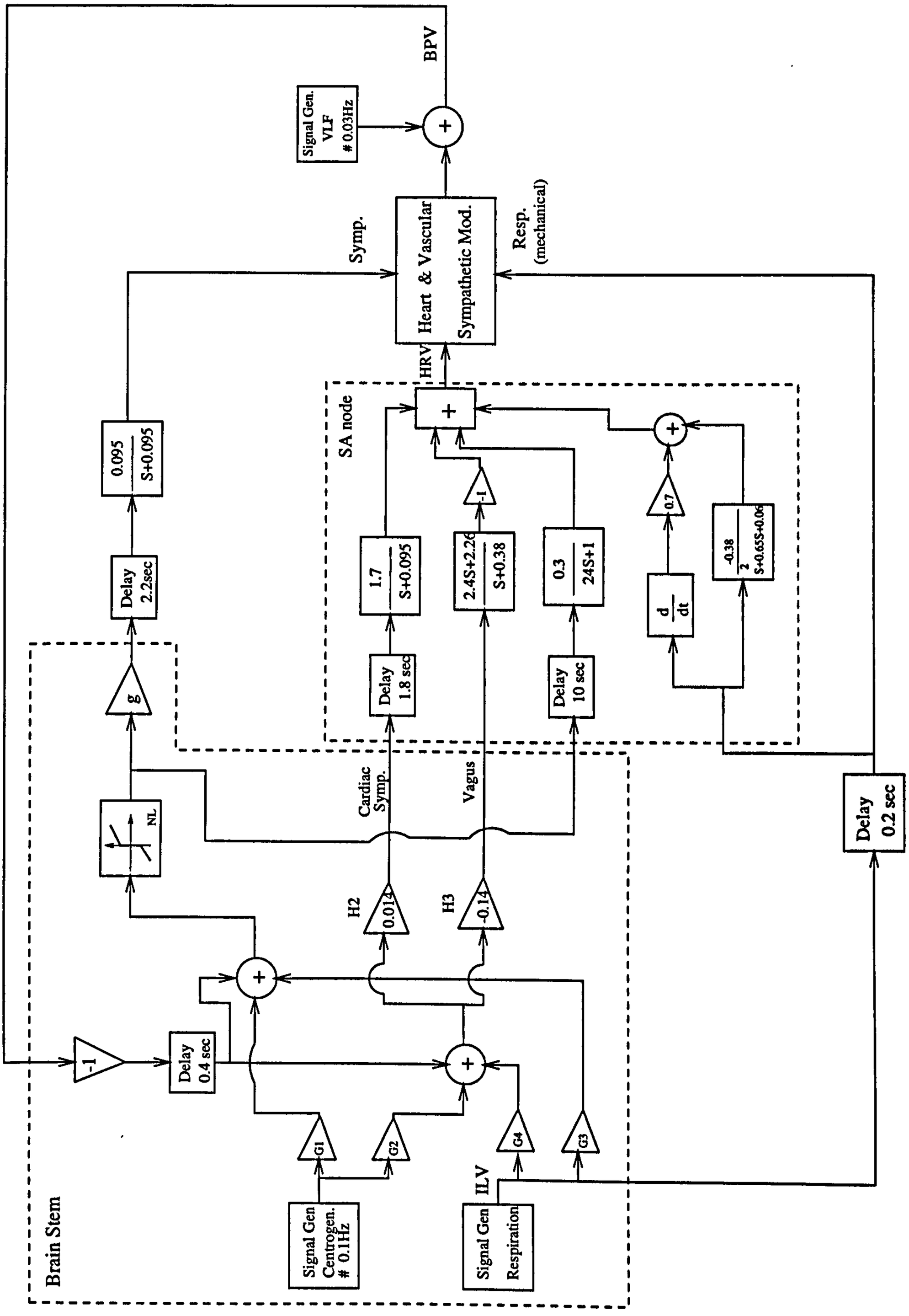


Figure 7.11: A detailed illustration of the proposed model.

effector response. This loop constructs a path for the generation of the LF component through the feedback mechanism.

Sympathetic influence (Symp.), heart rate variability (HRV) and the mechanical effect of respiration (Resp. mechanical) eventually produce the blood pressure variation (BPV) mediated through the heart and vascular modulation which is shown as a major block in the right hand side of Fig. 7.11. This block in fact integrates the heart, peripheral resistance modulation and H_1 in Fig. 7.1. As described in Section 7.3 the role of low pressure receptors in Fig. 7.1 is disregarded in Fig. 7.11. Furthermore, the transfer gain between the BPV and venous return fluctuation through the systemic circulation has been ignored in Fig. 7.11 due to the resting supine position assumed in this study.

Now in the second step, concentration is given to the heart and the vascular modulation as a complex medium which transfers the incoming variability signals (Symp., HRV, Resp.) to the arterial blood pressure variation (BPV). Variation in any of the inputs (Symp., HRV, Resp.) can induce a similar fluctuation, through the heart and the vascular system, to the BPV. The question is, therefore, how to model this complex behaviour in an appropriate manner. Let us first start with the mechanical influence of respiration. Figure 7.12 helps to clarify this influence. Pressure variation resulting from the respiratory activity has a distributed effect on all the organs residing in the intrathoracic space. It directly affects the left ventricular afterload, cardiac preload, pulmonary blood flow and pressure, and intrathoracic large arteries and veins. This distributed effect modulates the blood pressure in a sophisticated fashion. Hence, it is impractical to assume a lumped model [8] for each specific organ inside the chest cavity

[8]As described briefly in Chapter 4, lumped modelling means assuming a characteristic equation for each individual intrathoracic organ such as the right atrium, left ventricle, etc, in terms of pressure-volume-flow relationships and then trying to enter respiration as an input parameter to this equation (Hammer & Saul, 1996). Instead in distributed modelling the overall effect of respiration (mechanical effect) on the desired parameter (e.g. BPV here) is identified through an appropriate procedure. More precisely, in lumped modelling a large set of differential equations, describing the hemodynamic characteristics, collected from each individual organ in the circulation is developed (Chabbani, 1990). Respiration is then added to these equations as an exogenous input (Hammer & Saul, 1996). Therefore, the credibility of the respiratory modulation depends upon how precisely each individual equation has been obtained and how the respiratory input affects this equation. Clearly, to write each specific equation each intrathoracic organ should be examined separately, under the influence of respiration. Since this approach is practically impossible one has to use an approximation procedure (Hammer & Saul, 1996). Furthermore, there is no guarantee that the overall effect of respiratory modulation (Fig. 7.12) can be taken into account by aggregation of the limited number of organs studied normally in cardiovascular modelling. Instead in distributed modelling, which is undertaken here, the actual system between respiration as the input and BPV as the output, regardless of the individual effect of

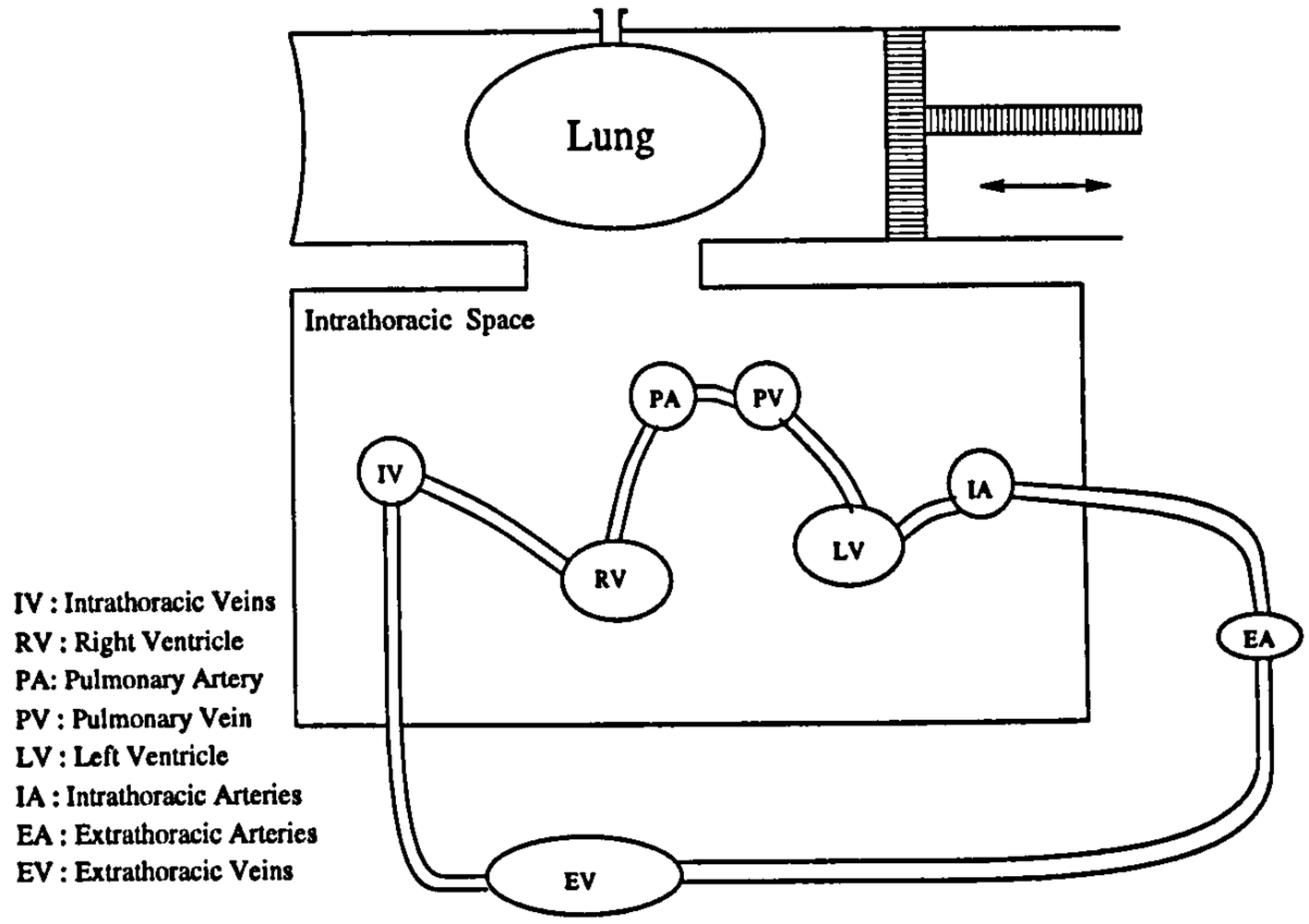


Figure 7.12: A sketch of the mechanical effect of respiration on intrathoracic circulation.

and still expect to cover the overall modulatory effect of respiration. The same situation exists for the sympathetic modulation and the influence of heart rate variability on blood pressure variation. Sympathetic excitation changes the cardiac contractility, vascular resistance and compliance, venous return and thereby the stroke volume and cardiac output and hence the blood pressure. The latter is concurrently influenced by the heart rate variability. Importantly, there is a joint functional relationship between each of these modulating factors. It is known that a change in the the heart rate causes a variation in cardiac contractility, the phenomenon which has been named the interval-force relationship (Smith & Kampine, 1990; Nobel & Seed 1992). This means that the heart rate variability simultaneously affects the cardiac contractility while it directly affects the blood pressure. On the other hand the strength of the heart in pumping the blood is a function of the venous return (Starling effect). This in turn means that the modulation of the venous return by respiration also changes the cardiac contractility. Even interaction between HRV and the mechanical effect of respiration through modulation of the venous return by variation in the diastolic filling time is conceivable.

This complex functional behaviour of respiration, sympathetic influence and HRV

---

respiration on each individual organ, is identified. Therefore, no *a priori* assumption or information is required. Indeed, distributed modelling has already been used in cardiovascular variability modelling without an explicit statement (Baselli *et. al.*, 1988; Mullen *et. al.*, 1997; Saul *et. al.*, 1991).

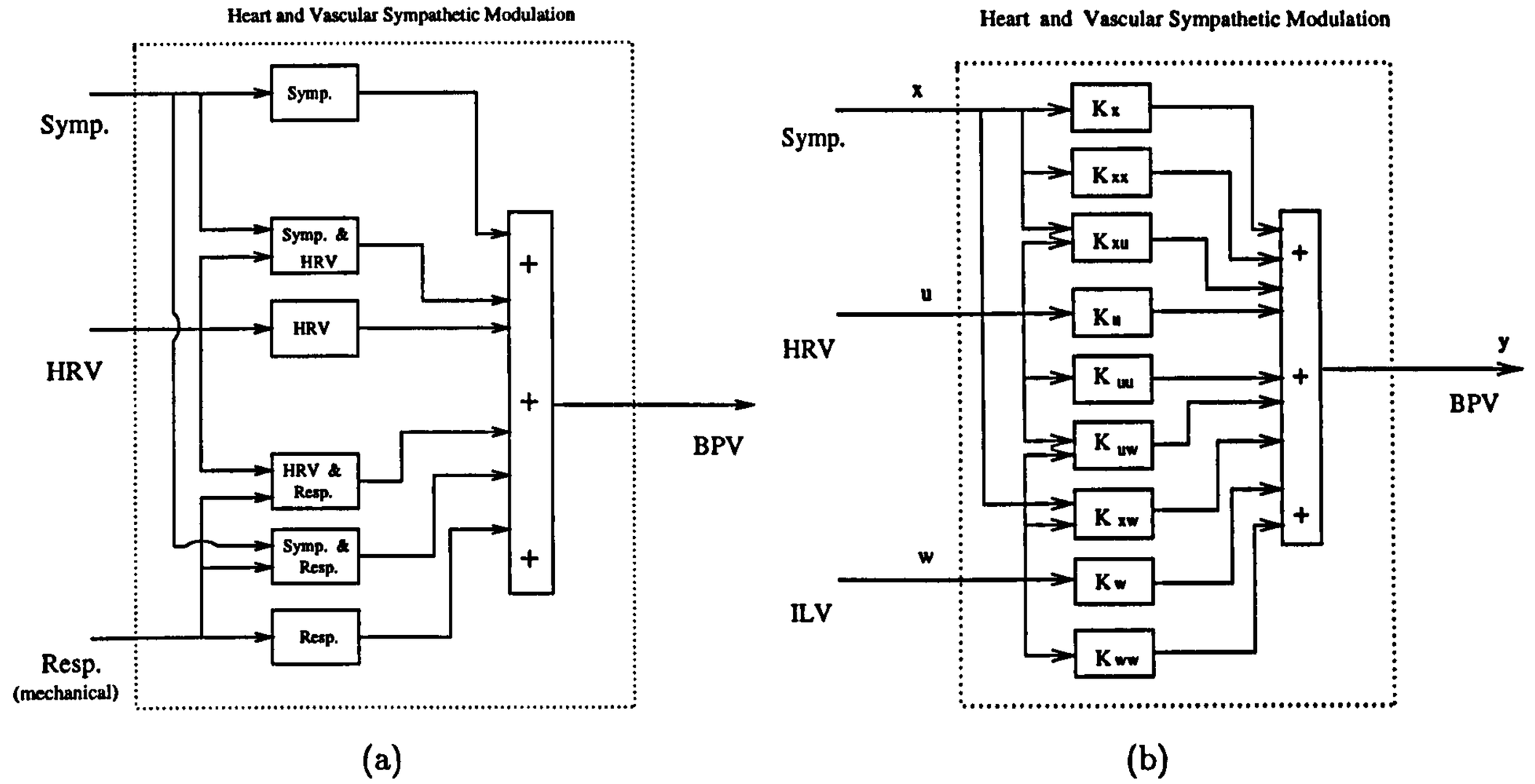


Figure 7.13: (a) The model of the individual influence and the interaction between Symp, HRV and ILV on BPV. Each input has a direct effect as well as a joint effect with the other inputs on BPV. (b) The equivalent mathematical representation of the model of part (a) in the nonlinear system identification context.

in producing BPV necessitates the use of a complex structure to properly represent the joint relationship as well as the individual influence of each of these inputs. Figure 7.13(a) displays a schematic illustration of this structure.

Fortunately, an analogous structure to that of Fig. 7.13(a) has been studied extensively in the field of nonlinear system identification (Fig. 7.13(b)). Specifically, this structure can also include the nonlinear features of the variability signals as highlighted in Chapter 5. By combining this overall model of the heart and vascular modulation with the rest, the proposed model now finds a well-established systemic representation as shown in Fig. 7.14. In the following section the required theory for identification of the block representing the heart and vascular modulation by the proposed structure of Fig. 7.13 is detailed. In Chapter 8 this theory will be used to identify the experimental transfer functions between Symp., HRV, ILV and BPV.

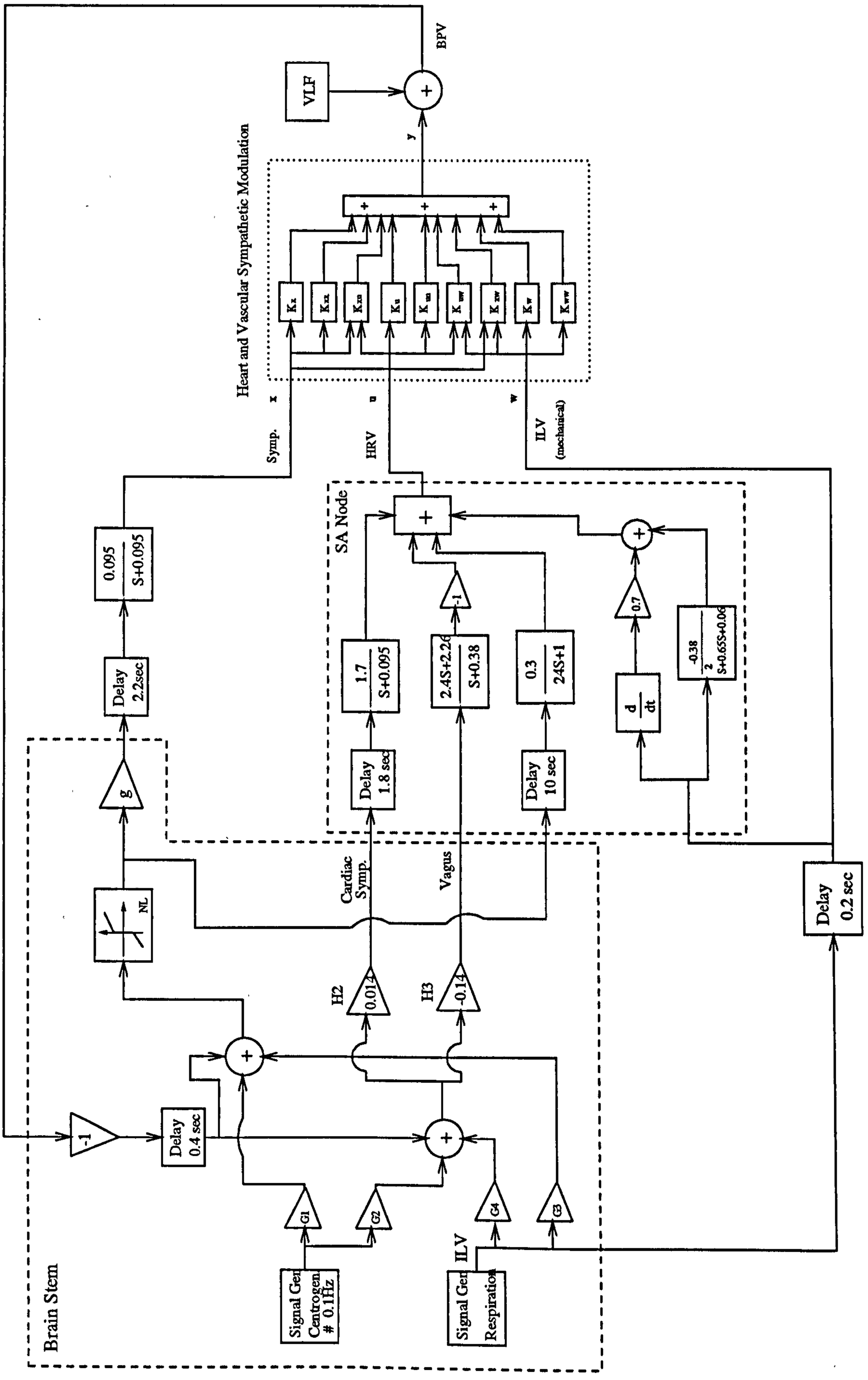


Figure 7.14: The final model of the neuro-cardiovascular system for variability analysis (see also conclusion).

7.7 Nonlinear Identification Methodology

Nonlinearities abound in physiology. However, effective methodologies for nonlinear modelling and analysis have been slow to develop and be adopted by physiologists, owing to the complexity associated with the study of nonlinear dynamics. Each specific identification methodology exhibits certain advantages together with confining drawbacks. There is no single methodology that is globally superior to the others. The ultimate selection of a particular methodology hinges upon the specific characteristics of the application at hand (Marmarelis, 1987b).

In the context of nonlinear identification of the physiological systems, the existing methods fall into three major categories (Marmarelis, 1987b):
(i) Block structured models,
(ii) Difference equation models,
(iii) Volterra-Wiener functional expansion.

In block structured models the underlying system is modelled by connections of a limited number of simple linear and nonlinear blocks (Hunter & Korenberg, 1986; Westwick & Korenberg, 1994; Chen, 1995; Haber & Unbehauen, 1990). The topology of the selected structure, however, must be based on *a priori* information which is not normally available.

In the difference equation method, models are sought in the form of difference equations with unknown parameters which should be estimated from the input-output data (Billings & Voon, 1984; Billings, Chen, Korenberg, 1989; Chen & Billings 1989; Korenberg, 1987; Korenberg & Paarman, 1991). This method is in fact a generalisation of linear parametric identification methods such as AR, MA and ARMAX (Ljung, 1987) to the nonlinear case; NAR, NMA, NARMAX. Although it has been shown that this method can model a very broad class of nonlinear systems, it has found a limited application in physiological systems due to the difficulties in the model order selection and bulk of computation.

Among the most efficient methodological approaches for physiological system identification, methods based on Volterra-Wiener theory have made considerable progress recently (Korenberg, 1989; Marmarelis, 1993a, 1993b, 1994; Chon *et. al.*, 1996). The

new methods are more robust and more flexible than their older versions. In these methods, the response $y(t)$ of a nonlinear time invariant continuous time system can be expressed in terms of a series of functionals (Volterra series) that represent multiple convolutions of the stimulus $x(t)$,

$$y(t) = \sum_{n=0}^{\infty} \int_0^{\infty} \cdots \int_0^{\infty} K_n(\tau_1, \cdots, \tau_n) x(t-\tau_1) \cdots x(t-\tau_n) d\tau_1 \cdots d\tau_n. \qquad (7.7)$$

The multiple convolution integrals of the Volterra series involve high-order kernel functions $K_n(\tau_1, \cdots, \tau_n)$ which constitute the descriptors of the system nonlinear dynamics. The set of kernels, K_i, can be considered as generalised impulse responses of the system much in the same way that $h(t)$ is the impulse response of a linear system. The nth-order Volterra kernel $K_n(\tau_1, \cdots, \tau_n)$ is in fact the pattern of interaction among n samples of the past stimulus on the current value of the output (Marmarelis, 1987b). Consequently, the system identification task is to obtain estimates of these kernels from the input-output data.

A practical scheme for identifying the system kernels can be obtained by making the terms of the Volterra series orthogonal to each other for a specific input $x(t)$. When the input is Gaussian White Noise (GWN) then the well-known Wiener series approach is obtained (Schetzen, 1989),

$$y(t) = \sum_{n=0}^{\infty} G_n[h_n; x(t'), t' \leq t] = \sum_{n=0}^{\infty} \sum_{n=0}^{[n/2]} \frac{(-1)^m n! P^m}{(n-2m)! m! 2^m} \int_0^{\infty} \cdots \int_0^{\infty}$$

$$h_n(\tau_1, \cdots, \tau_{n-2m}, \lambda_1, \lambda_1, \cdots, \lambda_m, \lambda_m) x(t-\tau_1) \cdots x(t-\tau_{n-2m}) d\tau_1 \cdots d\tau_{n-2m} d\lambda_1 \cdots d\lambda_m. \qquad (7.8)$$

where P is the power of the GWN input and h_i denotes the ith-order Wiener kernel. Once the Wiener kernels are identified the Volterra kernels can be calculated (Schetzen, 1989; Marmarelis, 1978).

The most commonly used technique for Wiener kernel estimation has been the cross-correlation technique proposed by Lee and Schetzen (1965),

$$h_n(\tau_1, \cdots, \tau_n) = \frac{1}{n! P^n} E\left[\left(y(t) - \sum_{k=0}^{n-1} G_k(t)\right) x(t-\tau_1) \cdots x(t-\tau_n)\right]. \qquad (7.9)$$

In practice, though, use of Wiener's functionals and the Lee-Schetzen cross-correlation formula can lead to significant errors in the estimated kernels. Such errors occur

even when the estimation is free of input and output noise corruption. One reason for this is the difficulty in producing an ideal GWN. Furthermore, the infinite time average (replacing the E operator) required in the Lee-Schetzen algorithm must be approximated by a finite average, which leads to additional errors. This in turn means that the G-functionals ($G_n(t)$ in equation 7.8) are not quite orthogonal over the actual data record and this causes inaccuracy in the estimated kernels (Marmarelis, 1978).

Introduction of the Laguerre Expansion Technique (LET), however, has alleviated most of the deficiencies which inherently exist in the cross-correlation technique (Korenberg, 1987; Marmarelis, 1993a). In LET, Volterra kernels are expressed as a series of Laguerre orthogonal basis functions (Davis, 1963) with unknown parameters. These parameters can then be found by Least Squares Minimisation (LSM) algorithms as described subsequently.

If a three input single output model encountered in this study is assumed (Fig. 7.13(b)) and the nonlinearity is limited to the second order then the Volterra expansion is given by ($K_0 = 0$),

$$\begin{aligned} y(t) = & \int_0^\infty K_x(\tau)x(t-\tau)d\tau + \int_0^\infty K_u(\tau)u(t-\tau)d\tau + \int_0^\infty K_w(\tau)w(t-\tau)d\tau \\ & + \int_0^\infty \int_0^\infty K_{xx}(\tau_1,\tau_2)x(t-\tau_1)x(t-\tau_2)d\tau_1 d\tau_2 + \int_0^\infty \int_0^\infty K_{uu}(\tau_1,\tau_2)u(t-\tau_1)u(t-\tau_2)d\tau_1 d\tau_2 \\ & + \int_0^\infty \int_0^\infty K_{ww}(\tau_1,\tau_2)w(t-\tau_1)w(t-\tau_2)d\tau_1 d\tau_2 + \int_0^\infty \int_0^\infty K_{xu}(\tau_1,\tau_2)x(t-\tau_1)u(t-\tau_2)d\tau_1 d\tau_2 \\ & + \int_0^\infty \int_0^\infty K_{xw}(\tau_1,\tau_2)x(t-\tau_1)w(t-\tau_2) + \int_0^\infty \int_0^\infty K_{uw}(\tau_1,\tau_2)u(t-\tau_1)w(t-\tau_2)d\tau_1 d\tau_2 \cdot \end{aligned} \tag{7.10}$$

Kernels K_x and K_{xx} (along with K_u, K_{uu} and K_w, K_{ww}) are called self-kernels since they represent the effect of a single input on the output. These kernels correspond to the individual transfer functions from Symp., HRV and ILV to BPV in Fig. 7.13. K_x represents the linear contribution of $x(t)$ to the output whereas K_{xx} illustrates its quadratic contribution, and correspondingly for others. The cross-kernels denoted by K_{xu}, K_{xw} and K_{uw} demonstrate the joint contribution of the inputs to the output. The cross-kernels represent the simultaneous influence of Symp., HRV and ILV on BPV in Fig. 7.13. If equation (7.10) is exposed to the Laguerre expansion technique it yields

(Marmarelis, 1993a)

$$y(t) = \int_0^l \sum_{i=1}^{M} c_{xi} L_i(\tau) x(t-\tau) d\tau + \int_0^l \sum_{i=1}^{M} c_{ui} L_i(\tau) u(t-\tau) d\tau + \int_0^l \sum_{i=1}^{M} c_{wi} L_i(\tau) w(t-\tau) d\tau$$
$$+ \int_0^l \int_0^l \sum_{i=1}^{M}\sum_{j=1}^{M} c_{xxij} L_i(\tau_1) L_j(\tau_2) x(t-\tau_1) x(t-\tau_2) d\tau_1 d\tau_2 + \int_0^l \int_0^l \sum_{i=1}^{M}\sum_{j=1}^{M} c_{uuij} L_i(\tau_1) L_j(\tau_2)$$
$$u(t-\tau_1) u(t-\tau_2) d\tau_1 d\tau_2 + \int_0^l \int_0^l \sum_{i=1}^{M}\sum_{j=1}^{M} c_{wwij} L_i(\tau_1) L_j(\tau_2) w(t-\tau_1) w(t-\tau_2) d\tau_1 d\tau_2$$
$$+ \int_0^l \int_0^l \sum_{i=1}^{M}\sum_{j=1}^{M} c_{xuij} L_i(\tau_1) L_j(\tau_2) x(t-\tau_1) u(t-\tau_2) d\tau_1 d\tau_2 + \int_0^l \int_0^l \sum_{i=1}^{M}\sum_{j=1}^{M} c_{xwij} L_i(\tau_1) L_j(\tau_2)$$
$$x(t-\tau_1) w(t-\tau_2) d\tau_1 d\tau_2 + \int_0^l \int_0^l \sum_{i=1}^{M}\sum_{j=1}^{M} c_{uwij} L_i(\tau_1) L_j(\tau_2) u(t-\tau_1) w(t-\tau_2) d\tau_1 d\tau_2, \tag{7.11}$$

in which c_* are unknown parameters, l denotes the extent of the system memory, M determines the number of basis functions and $L_i(\tau)$ represents the ith Laguerre function. To obtain equation (7.11), it has been assumed that each kernel can be expanded as a series of Laguerre functions, e.g. $K_x(\tau) = \sum_{i=1}^{M} c_{xi} L_i(\tau)$ or $K_{xx}(\tau_1, \tau_2) = \sum_{i=1}^{M}\sum_{j=1}^{M} c_{xxij} L_i(\tau_1) L_j(\tau_2)$. If

$$\mu_i(t) \triangleq \int_0^l L_i(\tau) x(t-\tau) d\tau, \tag{7.12}$$

$$\nu_i(t) \triangleq \int_0^l L_i(\tau) u(t-\tau) d\tau, \tag{7.13}$$

$$\xi_i(t) \triangleq \int_0^l L_i(\tau) w(t-\tau) d\tau, \tag{7.14}$$

then

$$y(t) = \underline{V}^T(t) \cdot \underline{C} \tag{7.15}$$

where

$$\underline{V}^T(t) = [\mu_1(t) \cdots \mu_M(t) \;\; \nu_1(t) \cdots \nu_M(t) \;\; \xi_1(t) \cdots \xi_M(t) \;\; \mu_1(t)\mu_1(t) \;\; \mu_1(t)\mu_2(t)$$
$$\cdots \mu_M(t)\mu_M(t) \;\; \nu_1(t)\nu_1(t) \;\; \cdots \nu_M(t)\nu_M(t) \cdots \mu_1(t)\nu_1(t) \cdots \nu_M(t)\xi_M(t)], \tag{7.16}$$

and

$$\underline{C}^T = [c_{x1} \cdots c_{xM} \;\; c_{u1} \cdots c_{uM} \;\; c_{w1} \cdots c_{wM} \;\; c_{xx11} \;\; c_{xx12} \cdots c_{xxMM}$$
$$c_{uu11} \cdots c_{uuMM} \cdots c_{xu11} \;\; c_{uwMM}] \cdot$$

(7.17)

Equation (7.15) can be used to construct a matrix identity through which the unknown parameters c_* and therefore the Volterra kernels can be identified,

$$\begin{bmatrix} y(1) \\ \cdots \\ y(N) \end{bmatrix} = \begin{bmatrix} \underline{V}^T(1) \\ \cdots \\ \underline{V}^T(N) \end{bmatrix} \cdot \underline{C} \tag{7.18}$$

The use of LET as presented above offers important practical advantages. Specifically, accurate kernel estimates can be obtained from short experimental data even if the experimental inputs deviate from the whiteness property. Furthermore, the LET is remarkably robust in the presence of contaminating noise. Nonetheless, the structure of the Laguerre functions *i.e.*, exponentially weighted polynomials (Davis, 1963) makes it suitable for most physical and physiological systems whose kernels usually exhibit an asymptotically exponential structure (Marmarelis, 1993a).

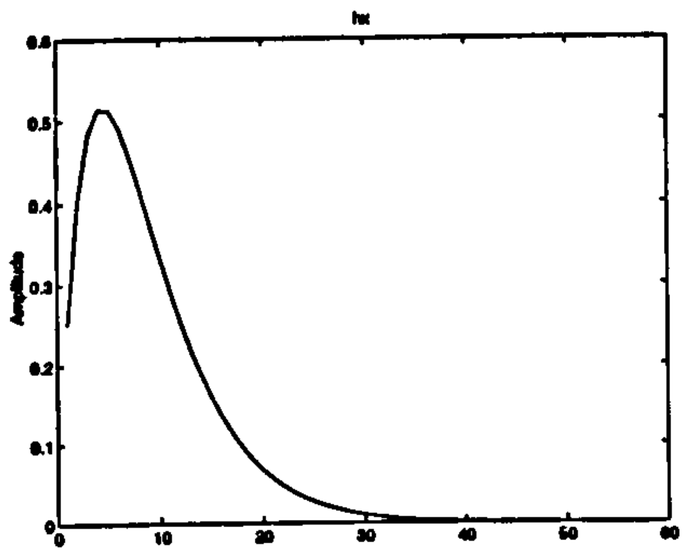
7.7.1 Simulation Results

To illustrate the efficacy of the LET, three arbitrary first order kernels and six second order kernels were generated in the discrete time domain as shown in Fig. 7.15 [9]. Exponential functions were assumed for these kernels to mimic the behaviour of the physiological systems. As the first trial, three independent zero mean uniform distributed ([−0.5 0.5]) white noise signals were assumed as the inputs. 1000 samples of the input-output data were selected for the kernel reconstruction which are now assumed to be unknown. A set of $M = 9$ discrete time Laguerre functions in the form of (Marmarelis, 1993a),

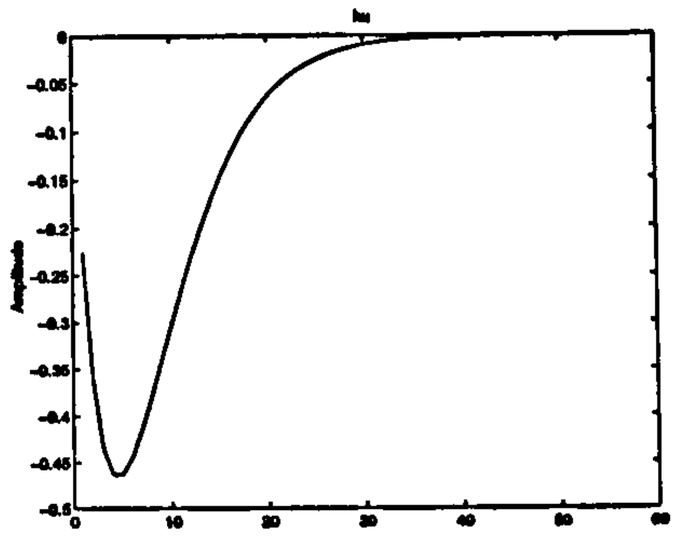
$$L_j(\tau) = \alpha^{(\tau-j)/2}(1-\alpha)^{1/2}\sum_{k=0}^{j}(-1)^k \binom{\tau}{k}\binom{j}{k}\alpha^{j-k}(1-\alpha)^k, \tag{7.19}$$

was chosen with $\alpha = 0.6$ and $l = 60$. The criterion for selection of M, α (the discrete time Laguerre parameter) and l (kernels memory) is based on the distribution of the kernels in time and the trade-off between accuracy and computational burden (Marmarelis, 1993a). The identified kernels are shown in Fig. 7.16. No difference can be observed between these estimated kernels and the original kernels of Fig. 7.15.

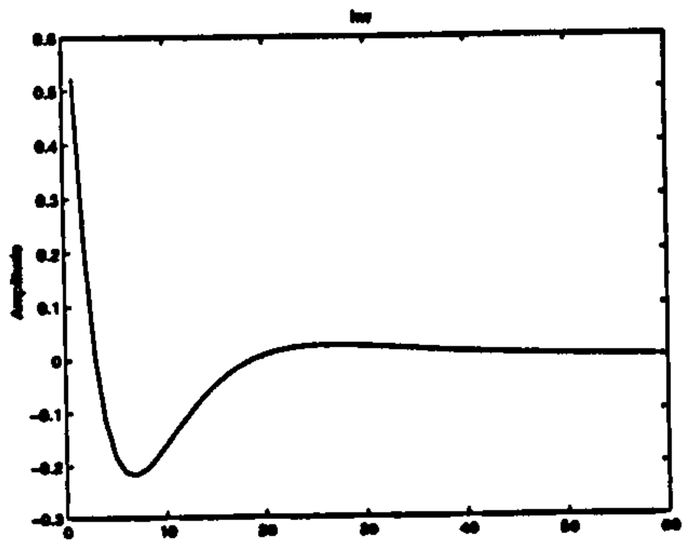
[9] $h_i = K_i$, $h_{ii} = K_{ii}$.



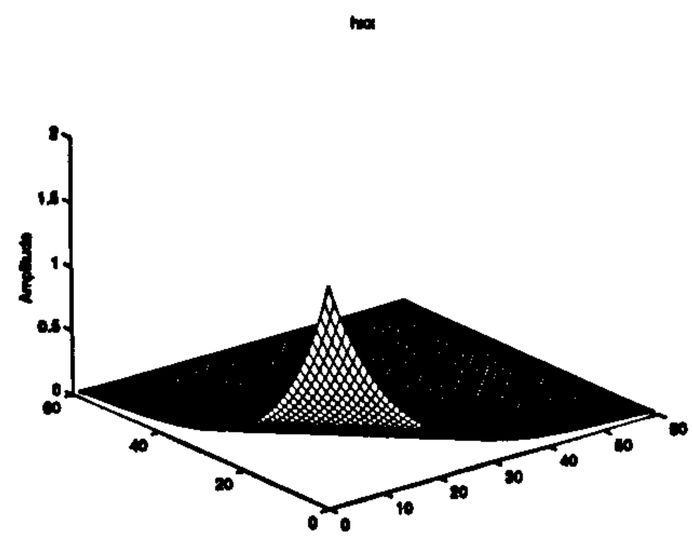
(a)



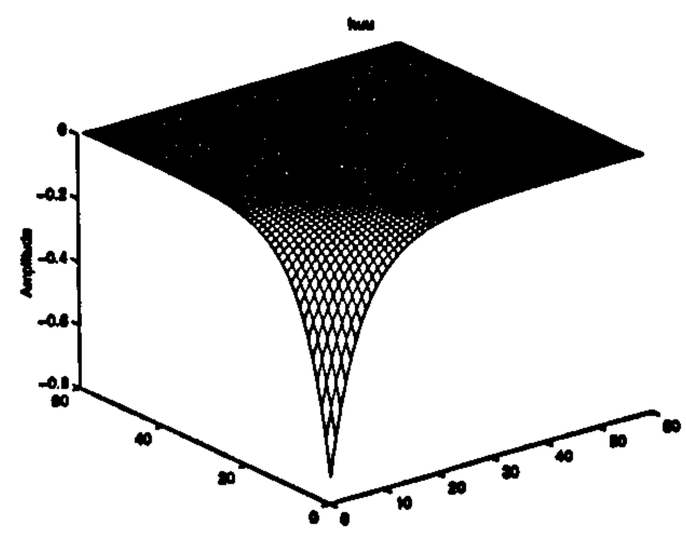
(b)



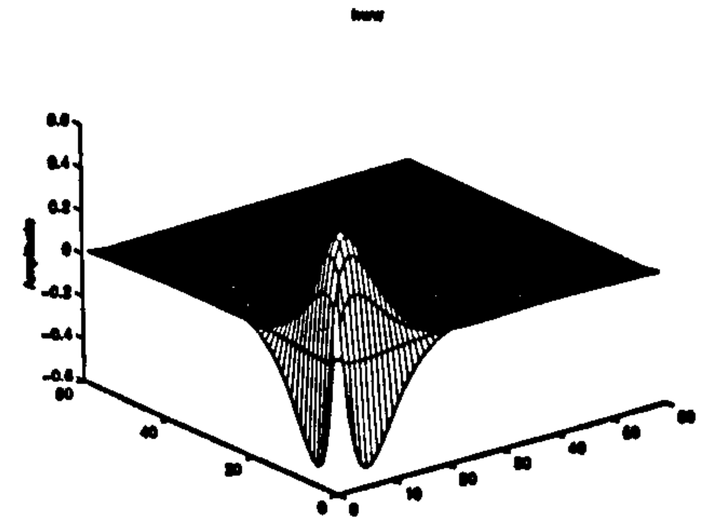
(c)



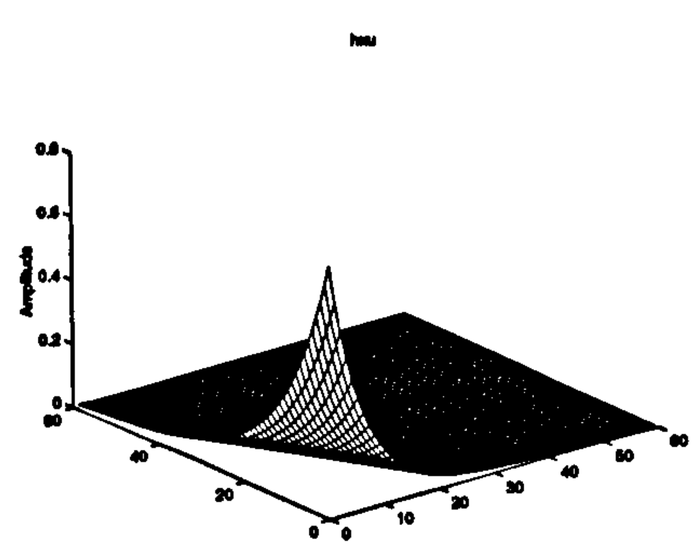
(d)



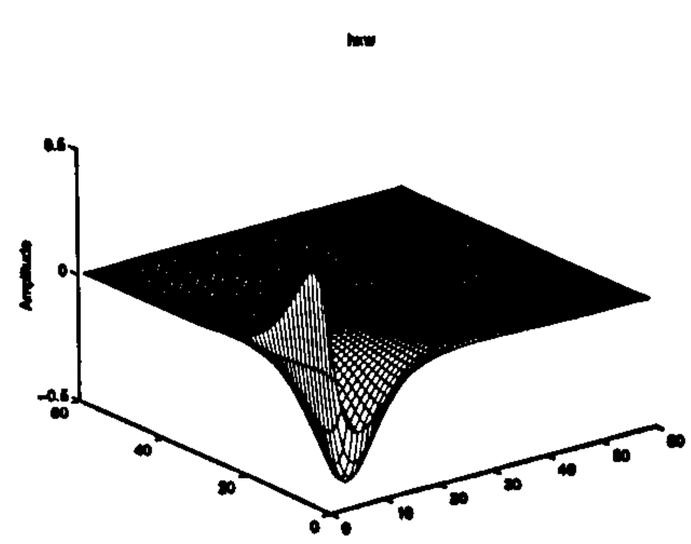
(e)



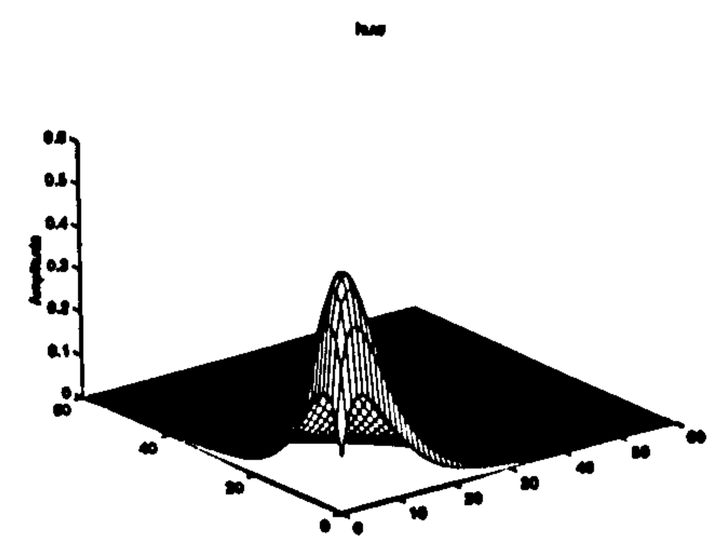
(f)



(g)

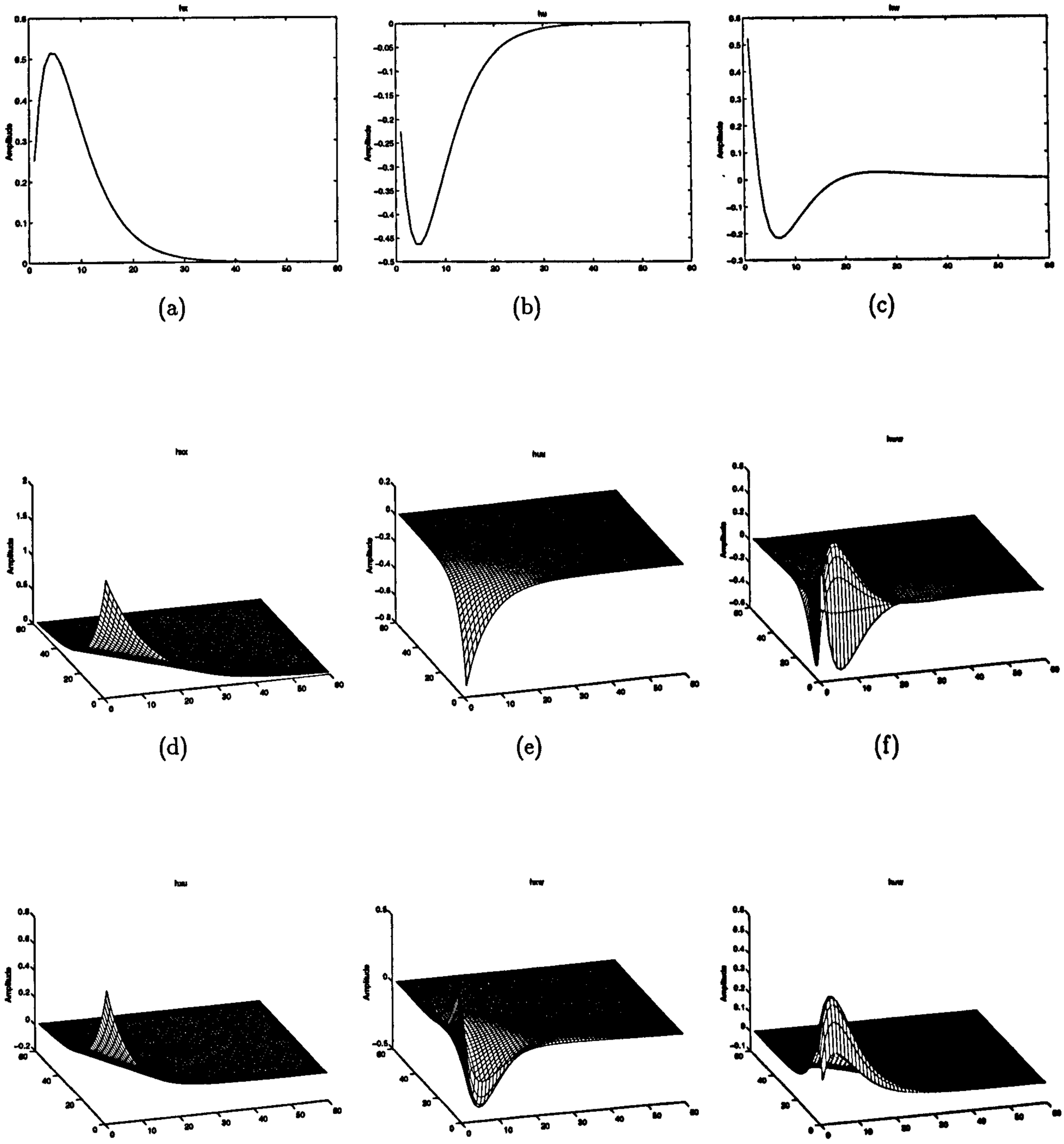


(h)



(i)

Figure 7.15: The original kernels used for evaluating the nonlinear identification procedure.



(a) (b) (c)

(d) (e) (f)

(g) (h) (i)

Figure 7.16: The identified kernels with $x(t)$, $u(t)$, and $w(t)$ three independent white noise signals.

Although the LET relaxes the whiteness property of the input signals, it still demands broadband stimuli, otherwise ill-conditioning will appear in the LSM algorithm. Specifically, the HRV, ILV and Symp. signals involved in the present study are band limited signals ($f_{max} = 0.5Hz$). The ill-conditioning in the LSM, however, can be treated by employing the SVD algorithm as described in Chapter 6. In the same manner, if the data matrix of equation (7.18) is decomposed as $[\underline{V}^T(i)] = U\Sigma P^T$, then the unknown parameters c_* will be found by taking the pseudo inverse solution (Golub, 1996)

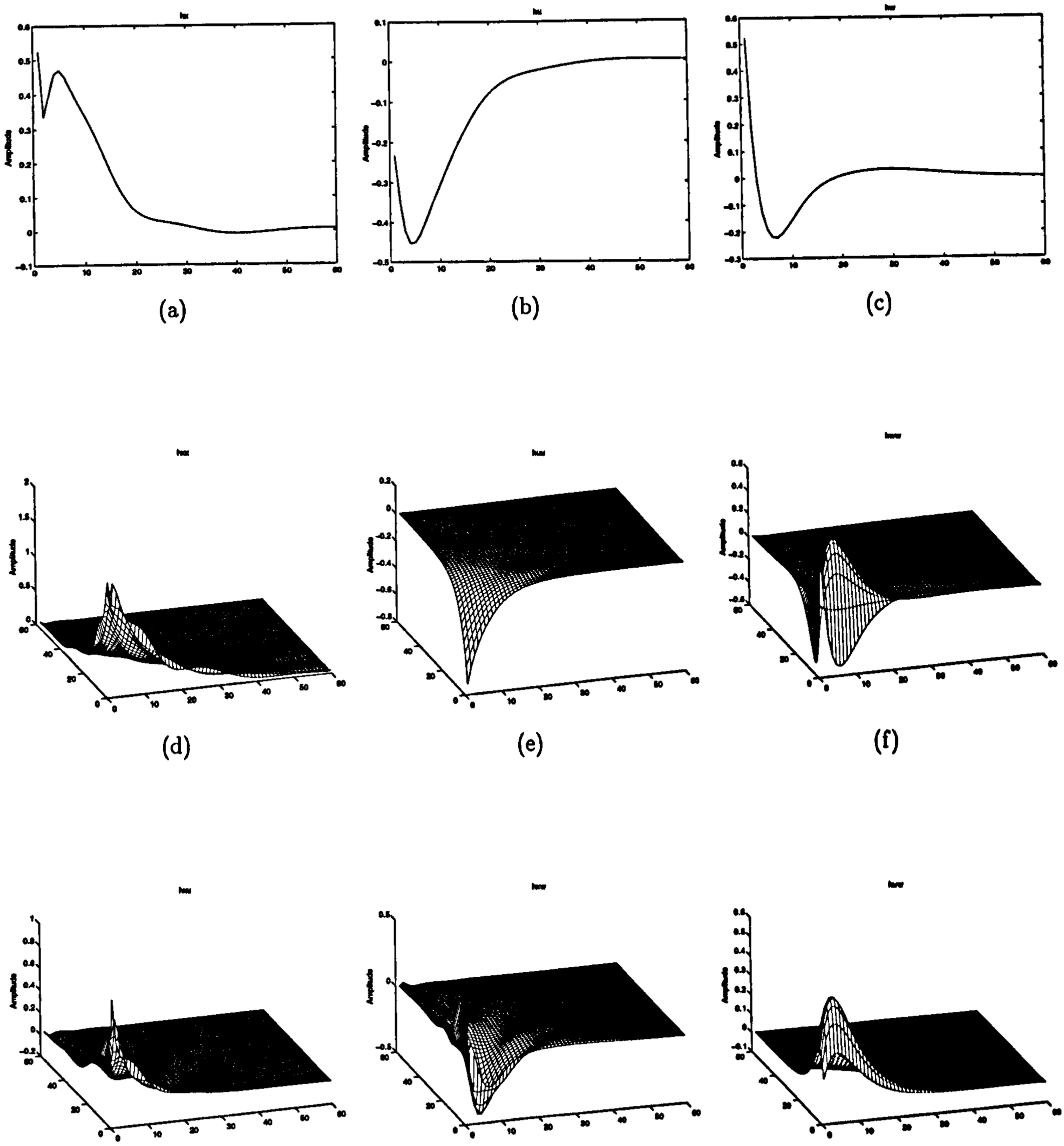
$$\underline{C} = P\Sigma^+ U^T \underline{Y}, \tag{7.20}$$

and discarding the small singular values. This procedure has been shown to be very successful in system identification algorithms particularly in the presence of noise (Westwick & Korenberg, 1997; Carrette, Bastin, Genin, Gevers, 1996; Van der Veen *et. al.*, 1993).

To evaluate the identifiability of the kernels using this algorithm, the white noise inputs of the previous example were replaced with the actual HRV, ILV and Symp. signals. HRV was obtained by the KLPF method of Chapter 2 with parameters $d = 5$, $f_c = 0.4Hz$, $\beta = 4.5$. The same filter was applied to provide the BPV and ILV signals from the instantaneous blood pressure and respiratory movement as described in Chapter 3. All the signals were resampled with sampling frequency $2.5Hz$. Then they were passed through a 2nd-order polynomial trend removal algorithm. The Symp. signal was extracted afterwards by applying a first order low pass filter with cutoff frequency $0.015Hz$ to the BPV signal to mimic the sympathetic effector response as described in Section 7.5. Figure 7.17 displays the estimated kernels with these inputs using $\alpha = 0.6$, $M = 9$, $l = 60$ and 1000 samples of each data record. The closeness of the estimated kernels to the actual ones is evident from this figure. This moreover shows the eligibility of the LET for the identification procedure with actual signals.

In real conditions the Symp. signal is not available independently from the other signals; it is obtained from the output through a feedback path as shown in the actual model of Fig. 7.14. To ensure that the identifiability of the kernels is still preserved under this condition a closed loop simulation was carried out by implementing the block diagram shown in Fig. 7.18.

$u(t)$ and $w(t)$ were obtained by generating two independent GWN signals with



(a) (b) (c)

(d) (e) (f)

(g) (h) (i)

Figure 7.17: The estimated kernels with actual HRV, ILV and Symp. signals as inputs.

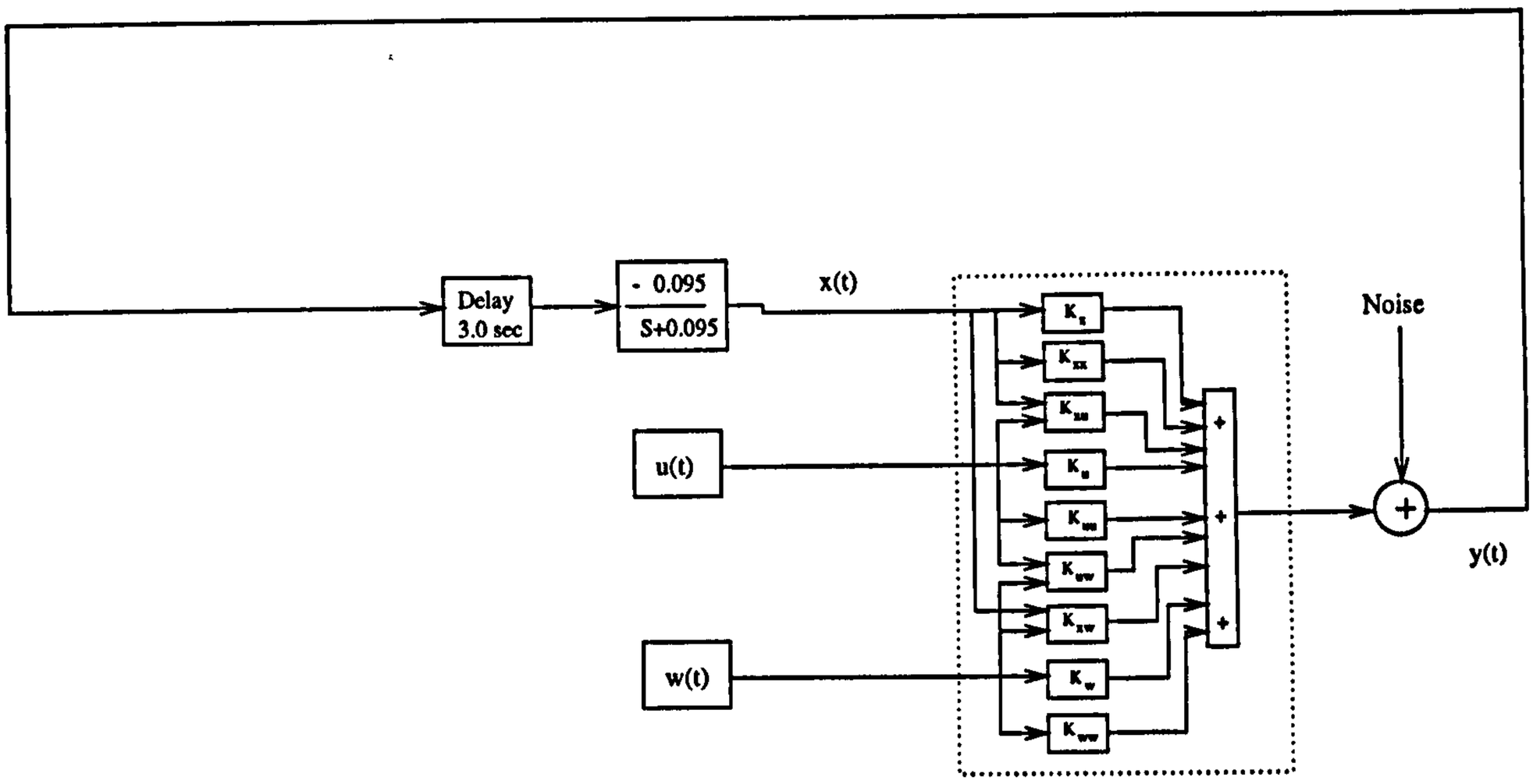


Figure 7.18: The simulated model for the closed loop experiment.

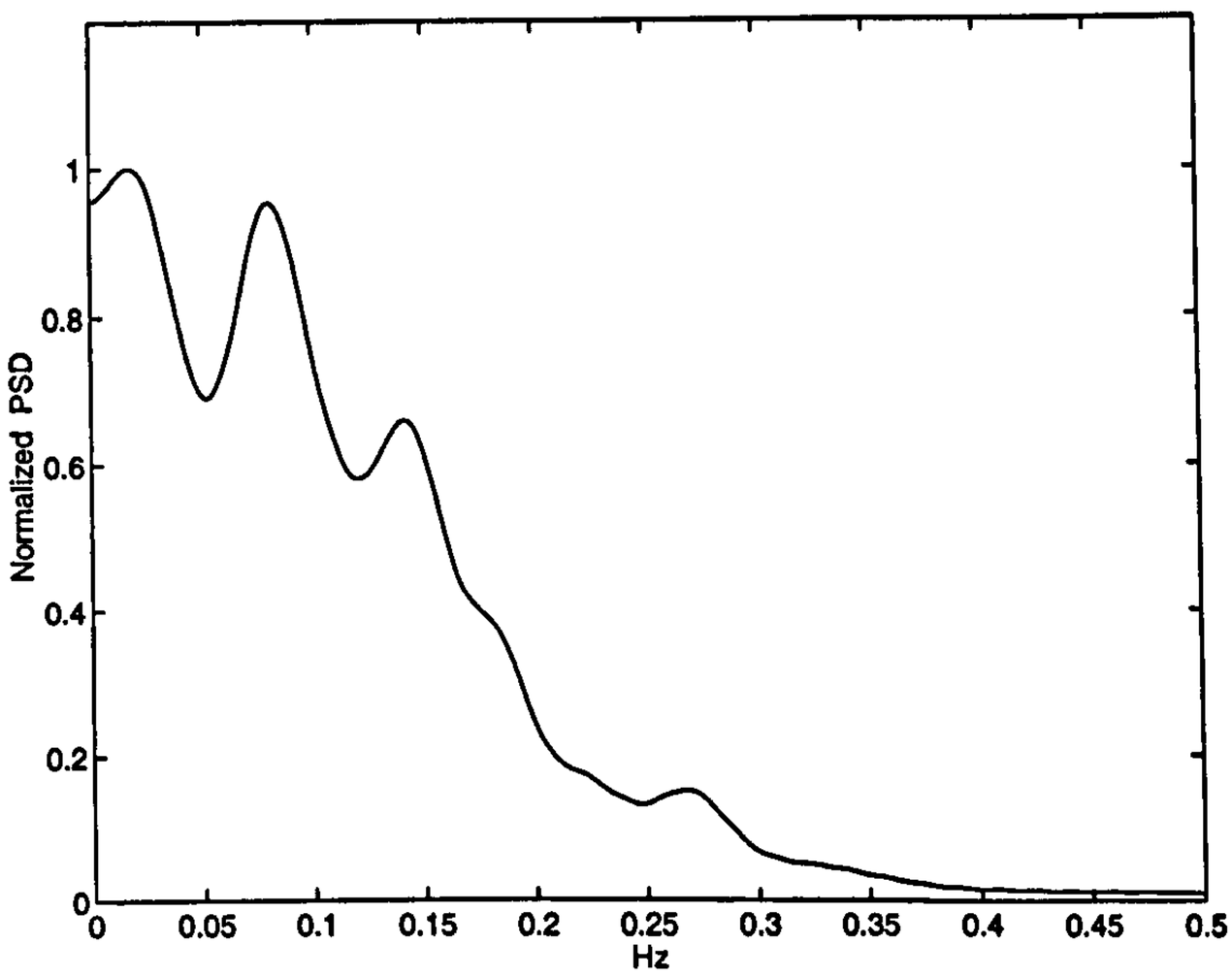
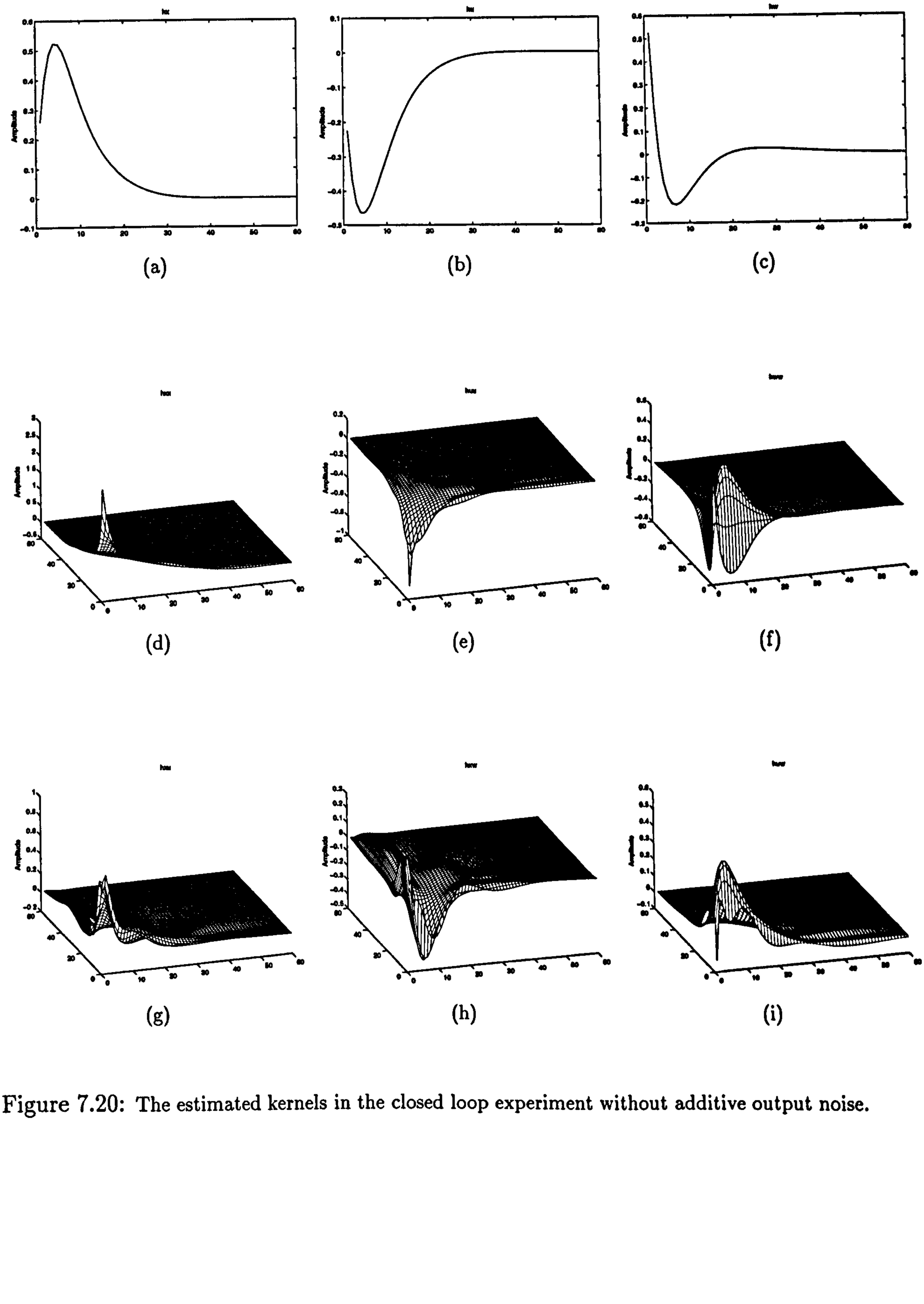


Figure 7.19: Power spectral density of the signals ($u(t)$, $w(t)$) which were used for the simulation in the closed loop condition (Fig. 7.18).

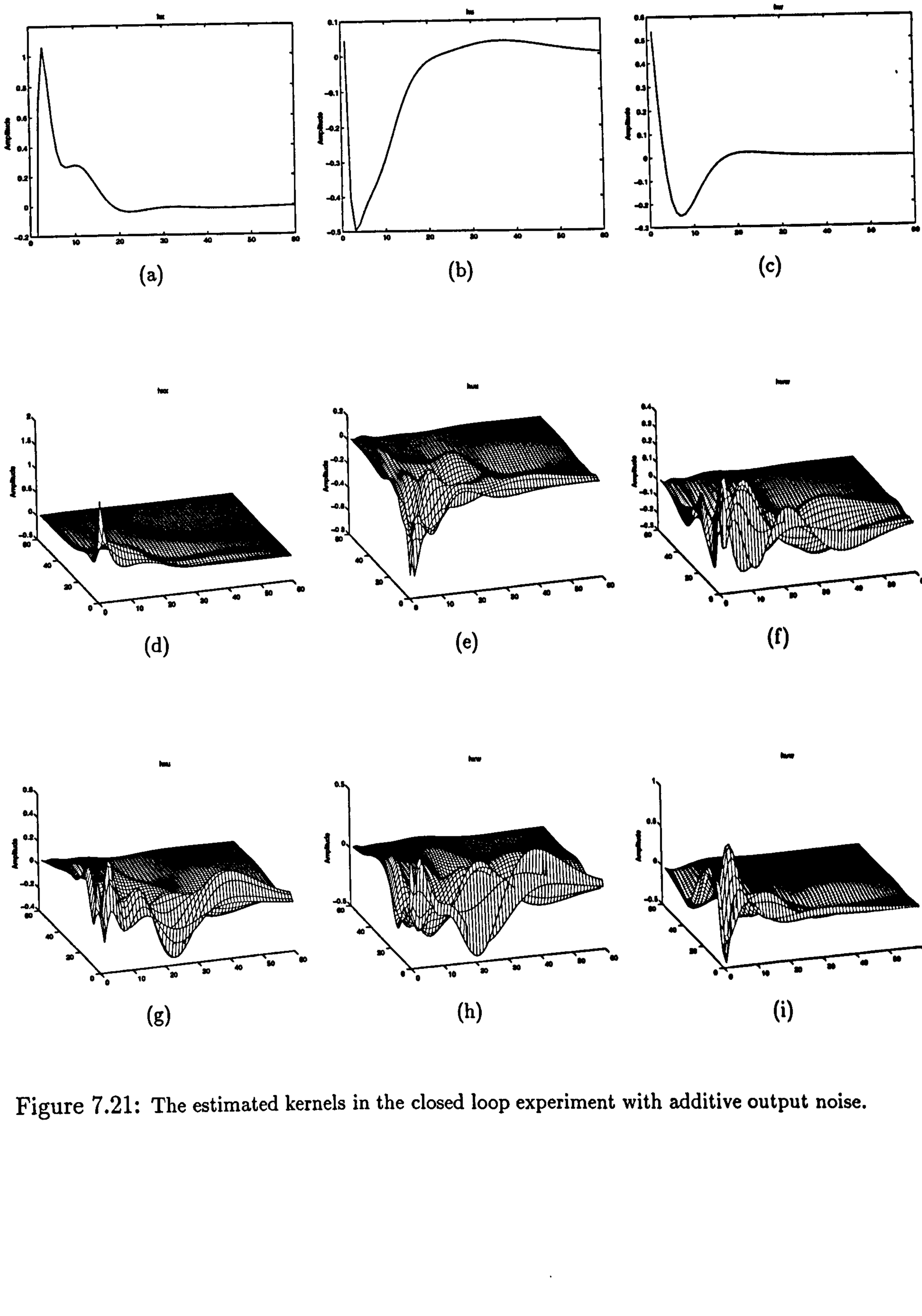


(a) (b) (c)

(d) (e) (f)

(g) (h) (i)

Figure 7.20: The estimated kernels in the closed loop experiment without additive output noise.



(a) (b) (c)

(d) (e) (f)

(g) (h) (i)

Figure 7.21: The estimated kernels in the closed loop experiment with additive output noise.

sampling frequency $2.5Hz$ and a two step filtering procedure. In the first step the GWN signals were passed through an FIR (Hamming) lowpass filter with order 36 and cutoff frequency $0.4Hz$ to produce two bandlimited signals. In the second step another FIR lowpass filter with cutoff frequency $0.05Hz$ and order 10 was employed to create the input signals with a decaying spectral content as observed experimentally for ILV and HRV (Chapter 3, Fig. 3.7; Chapter 8, Figs. 8.2, 8.3). The PSD of a typical synthetic signal is shown in Fig. 7.19.

The simulation was conducted in two situations; with and without additive output noise [10]. For the former, an independent zero mean Gaussian coloured noise ($[0\ 0.4Hz]$) with SNR $12dB$ was mixed with the output. The results of kernel estimations are illustrated in Fig. 7.20 and 7.21, with the same data lengths and parameters as those used in the previous simulations. As it can be seen in Fig. 7.20 the kernels can be identified quite well in the absence of the output noise. Although addition of the noise degrades the identifiability of the kernels, the main features of the kernels are still preserved under this severe condition (Fig. 7.21). Importantly, the first order kernels are more tolerant than the second order kernels against noise corruption.

The results demonstrated above support the robustness of the kernel estimation using the Laguerre expansion technique and the resilience of this modelling approach in the case of noise-corrupted data. To the author's knowledge no identification technique is available with a better performance than the LET algorithm in these restricted conditions. In the next chapter this identification procedure will be invoked to characterise the transfer function of the heart and vasculature from the experimental data. The obtained kernels will then be joined with the rest of the model to fulfil the validation stage.

7.8 Conclusion

The specific contribution of this chapter was to create a tractable mathematical form of the HRV-ILV-BPV model presented in Chapter 4. Of course, as Wesseling (1992)

[10]The Simulink software (Ver. 1.3 MathWorks Inc.) was employed for the simulation at this stage. This software was also used for the simulation of the proposed model and the results presented in Chapter 8. The sampling frequency for running the programs was fixed at $5Hz$ ($0.2sec$ computing interval). This selection caused a slight change in the delay values *i.e.*, $200msec$ instead of $150msec$ and $1.8sec$ instead of $1.7sec$.

states "a model of a biological system is a sketchy, incomplete, inaccurate image of the real system that can give a user important, remarkable, quantitative and decisive insights". It is hoped that the new model manifests a reasonable resemblance to the actual system in its behaviour, and even more, gives fruitful explanations for those phenomena which cannot be inspected practically. However, it should be noticed that the final model of Fig. 7.14 is a collection of various blocks each obtained from a different experiment and under a different condition. Even more, some blocks are based on human data whereas others are based on animal experimentation. This causes to oberve more error between the actual data and the results predicted by the model. All these points will be examined in the following chapter which is devoted to model validation using the experimental data.

Summary of the Chapter

A schematic illustration of the HRV-BPV-ILV relationships in the form of a block diagram representation had been developed in Chapter 4. In the present chapter this model was first simplified. Then a mathematical representation was given to each specific block of the model based upon its physiology. What we have obtained at this point is an exact description of the model under study. This model is ready to be examined with experimental data in the following chapter.

Chapter 8

Validation of the Proposed Model by Comparison with Experimental Results

Objectives of the Chapter

A block diagram representation for describing the rhythmical fluctuations in heart rate and blood pressure was developed in Chapter 4. Later in Chapter 7 this block diagram was converted to an appropriate mathematical form by replacing each physiological block with its systemic counterpart. All the constructing blocks were properly characterised except the model of the heart and vascular sympathetic modulation. The objective of this chapter is first to identify the transfer function representation of the block denoted by the heart and vascular sympathetic modulation and second to evaluate the performance of the proposed model in predicting the rhythmical fluctuations in HRV and BPV by comparing the results obtained from the model with the experimental observations.

8.1 Introduction

After dedicating several chapters to the quest for a decent HRV-BPV-ILV model it is now time to find out how successful these efforts have been. Utilising the experimental data, in this chapter a validation procedure will be applied to justify the proposed model, which is reproduced here in Fig. 8.1. Important features of the new model will be shown by comparison of the simulation results with the practical data. The reasons

for the observed discrepancies will also be explained and their conceivable treatments will be discussed. A step by step approach will be pursued to address some of the fundamental questions relating to the variability signals by investigating the results obtained from the new model.

The experimental evaluation of the model begins with identifying the performance of the heart and vascular sympathetic modulation, represented by a three input single output system in Fig. 8.1. All the experimental first and second order kernels K_* will be characterised by using the Laguerre expansion technique which was detailed in the previous chapter. Next, the existence of respiratory sinus arrhythmia in the model will be investigated. It will be shown that the central link between the respiratory oscillator and cardiac control centres plays an important role in producing the RSA. In the next step the presence of the LF component and the contribution of the different mechanisms will be inspected and compared with experimental results. The validity of the model in predicting the variability signals is also investigated in time and spectral domains. Finally a thorough discussion of the obtained results will conclude the chapter.

8.2 Experimental Procedure and Data Collection and Analysis

Experiments were performed on seven healthy adult subjects of both sexes, aged between 21-29. All subjects were free of medication and had no history of cardiovascular disease. They were asked to avoid beverages containing caffeine for at least three hours before experiment. To effectively broaden the spectral content of the respiratory signal, required for the identification algorithm, the random breathing pattern was employed as described in Chapter 3. All subjects were carefully instructed to breathe as directed by random auditory cues generated by a dedicated computer. Respiratory movement, *via* the strain gauge plethysmography method, ECG, and noninvasive blood pressure through a Finapres machine (Ohmeda, Englewood, Colo.) were collected from the subjects in the supine resting position for 8 minutes. The respiratory signal was later converted to lung volume using a calibration factor provided by a flowmeter instrument. All the signals were digitised with sampling frequency 500Hz and 12 bit resolution.

To obtain the variability signals a two step filtering procedure was employed.

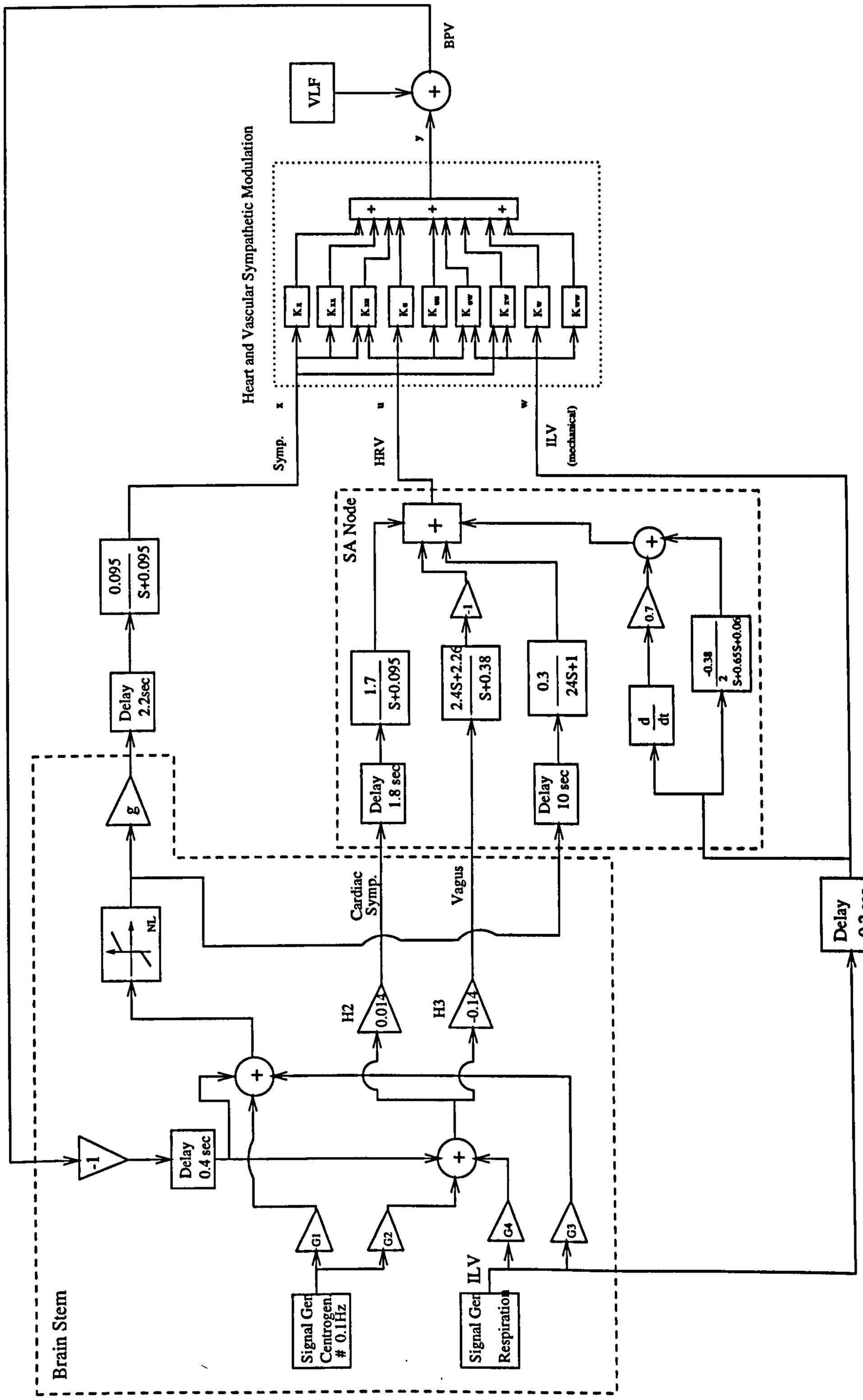


Figure 8.1: The final model of the neuro-cardiovascular system.

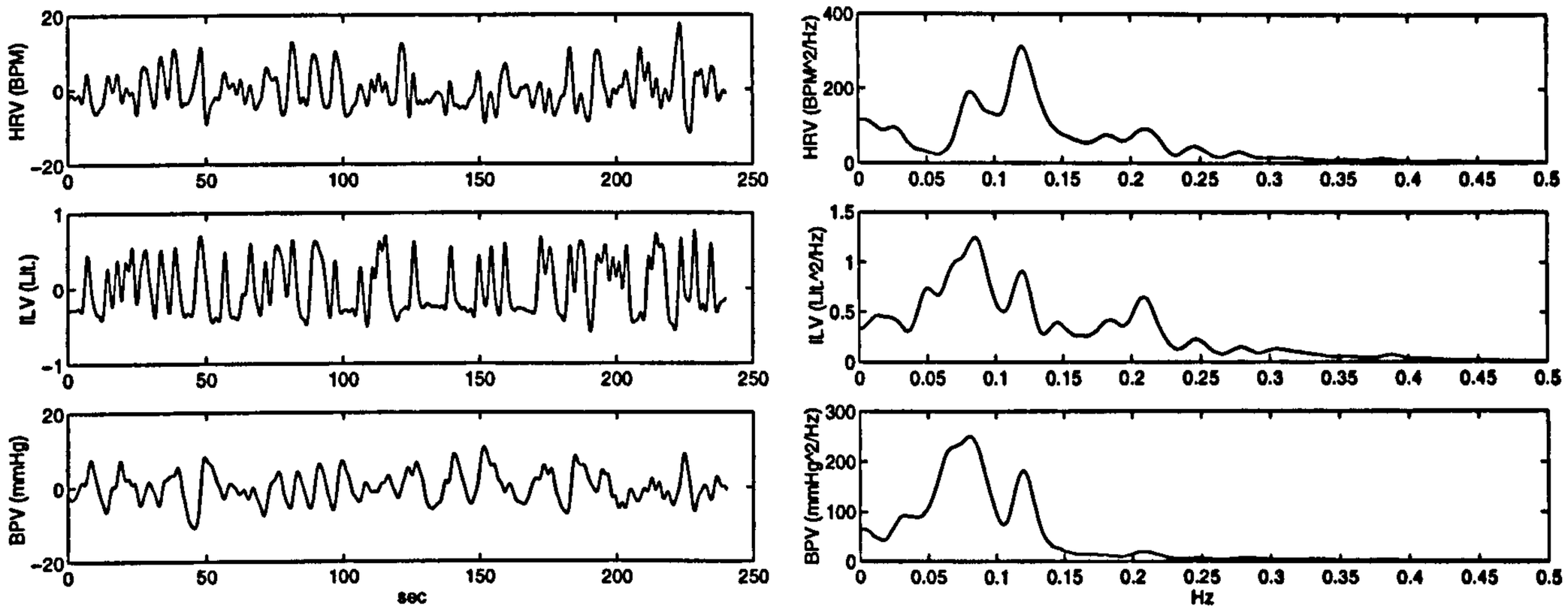


Figure 8.2: Time behaviour (left hand column) and power spectral density (right hand column) of the variability signals for subject 1.

After extracting the R-wave signal from the ECG, all the signals were subjected to the KLPF method of Chapter 2 with parameters $f_c = 1Hz$, $\beta = 4.5$, $d = 5$ and $N = 50$ (equivalent to 10Hz sampling frequency). In the second step the KBPF method with parameters $f_l = 0.02Hz$, $f_h = 0.45Hz$, $\beta = 3.4$, $d = 10$ and $N = 4$ (equivalent to 2.5Hz sampling frequency) was employed. This procedure was selected in order to extract the frequency band of interest while suppressing low frequency artifacts in the signals. Consequently, three variability signals, HRV, BPV and Instantaneous Lung Volume (ILV), distributed over the same frequency band ($[0.02Hz \;\; 0.45Hz]$) and synchronous with each other were provided (Chapter 3). The first minute of all the signals were discarded due to the transient period of the filters, leaving 1050 samples for each record. A 2nd-order polynomial trend removal was applied to the signals afterwards.

Time behaviour and power spectral density of the variability signals for two subjects are shown in Figs. 8.2 and 8.3, respectively. Broadening of the respiratory signal is evident in both subjects, although the major part of the power is concentrated between $f = 0.05Hz$ and $f = 0.15Hz$. In fact Figs. 8.2 and 8.3 reveal that the ILV contains the highest frequency components followed by HRV and then BPV.

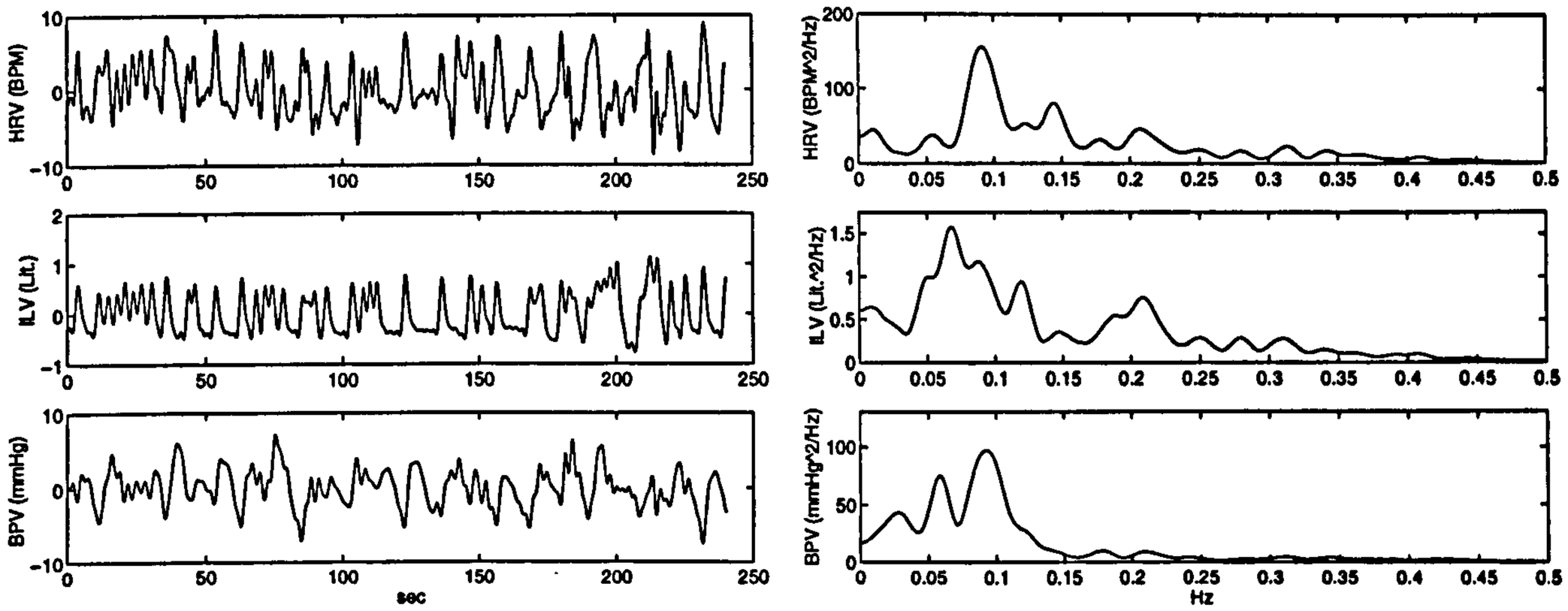


Figure 8.3: Time behaviour (left hand column) and power spectral density (right hand column) of the variability signals for subject 5.

8.3 Identifying the Experimental Kernels

To identify the Volterra kernels of the heart and vasculature block shown in Fig. 8.1 the multi input single output identification procedure described in Section 7.7 was applied to the variability signals. Out of the three inputs two of them, HRV and ILV, are directly accessible. The sympathetic excitatory signal (Symp. in Fig. 8.1) however, must be acquired through an indirect procedure by considering the sympathetic regulatory loop. Referring to Fig. 8.1, variation in the blood pressure is reflected to the brain stem where a compensatory sympathetic signal is produced by a sequence of sign inversion, nonlinearity transformation, delay and the sympathetic receptor characteristic. Therefore, to obtain this sympathetic compensatory signal, the blood pressure variability was injected into the analogous path shown in Fig. 8.4. The sympathetic signal which emerges at the output drives the cardiovascular effectors in the opposite direction to that of the blood pressure change. The open loop gain of the sympathetic path, g, has been normalised to one in Fig. 8.4 but will be scaled later in the actual model.

To guarantee a safe identification procedure, tolerant against computational errors which might arise as a result of different amplitudes, all the signals involved with the identification algorithm were normalised by dividing by their RMS (Root Mean Squared) values (Marmarelis *et. al.*, 1993b). Thus, regardless of the actual magnitudes, all the analysed data were converted to zero mean unit variance signals, resulting in

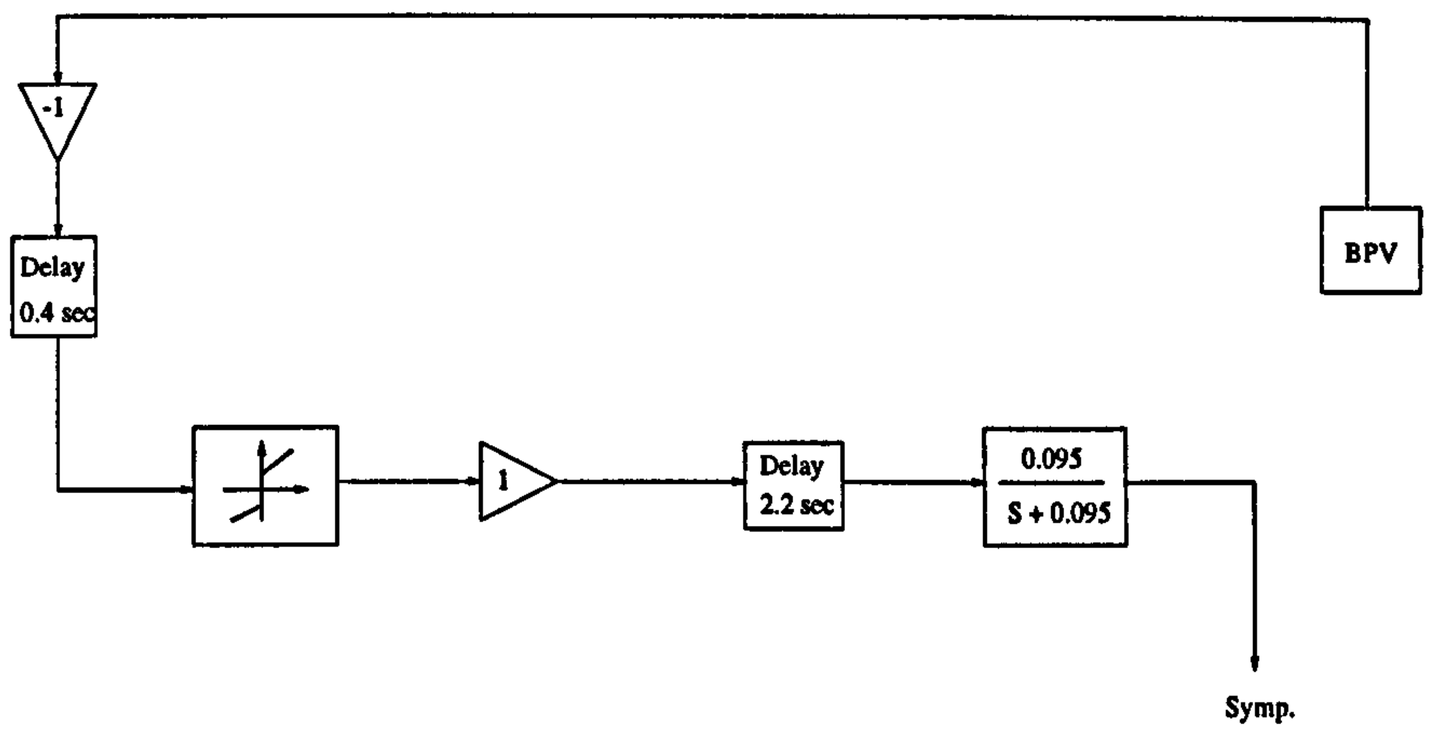


Figure 8.4: Extraction of the sympathetic influence from the blood pressure variability signal.

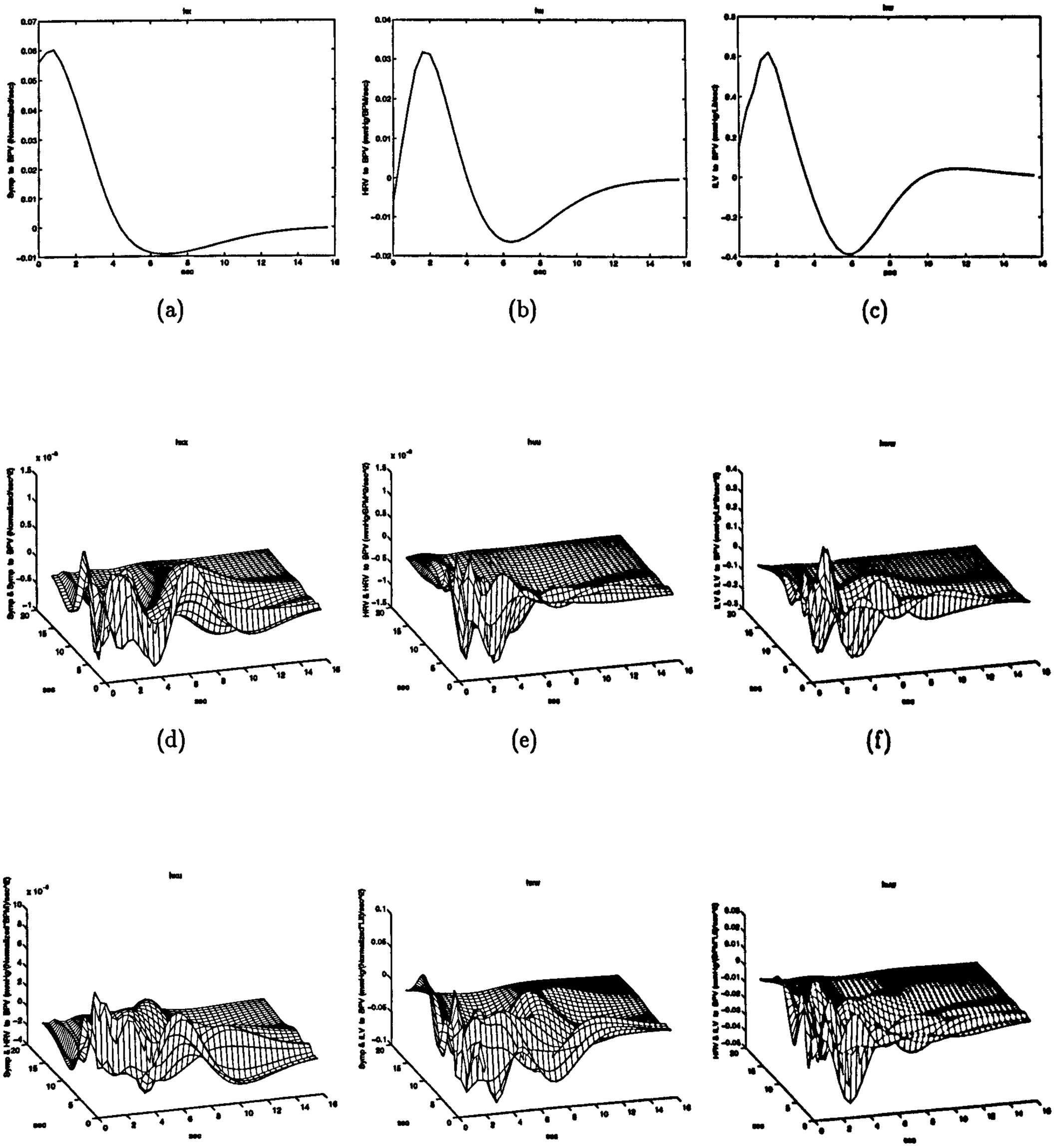
normalised kernels. The identified kernels can easily find their actual values by scaling them with these RMS values after the identification procedure.

Eight Laguerre basis functions with $\alpha = 0.4$ and memory length $M = 40$ $(16sec)$ were selected for the nonlinear identification algorithm as detailed in the previous chapter. The identified linear and nonlinear kernels for five subjects are illustrated in Figs. 8.5 through 8.9 [1]. The top panel of the figures displays the first order kernels; Symp. to BPV, HRV to BPV, and ILV to BPV, from left to right, respectively. As can be seen, there is a close similarity between the estimated first order kernels of all the subjects. The first order kernels have the straightforward meaning of the consequent change at the output for a sudden change in the inputs. Therefore, the shapes of these kernels are expected to be consistent with the physiological observations.

The first order kernel from the sympathetic influence to the blood pressure variation, h_x, demonstrates a positive decaying effect. If the entire loop from BPV to the sympathetic, to the BPV is considered, the positive decaying behaviour of h_x shows that a sudden positive change (impulse) in blood pressure produces a mild negative (sign inversion in brain stem) compensatory effect, imposed on the blood pressure *via* the sympathetic path. This behaviour is clearly in agreement with what is known of the sympathetic blood pressure regulatory mechanism through the peripheral resistance, venous return and cardiac contractility *i.e.*, a rise in pressure should be compensated through the effector response in the opposite direction.

The first order kernel between HRV and BPV, h_u, exhibits a sharp positive peak,

[1] $h_* = K_*$



(a) (b) (c)

(d) (e) (f)

(g) (h) (i)

Figure 8.5: The identified kernels for subject 1.

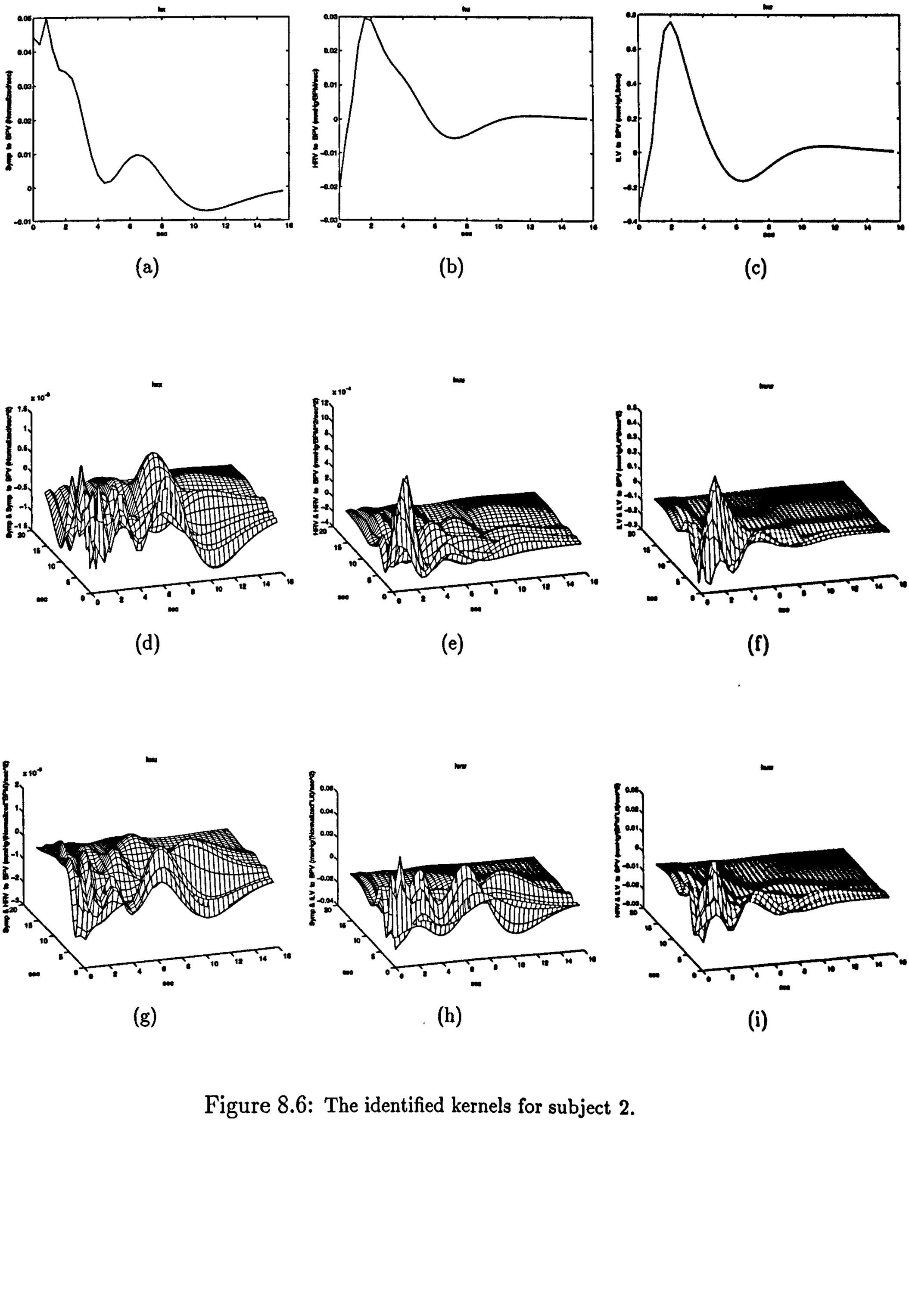
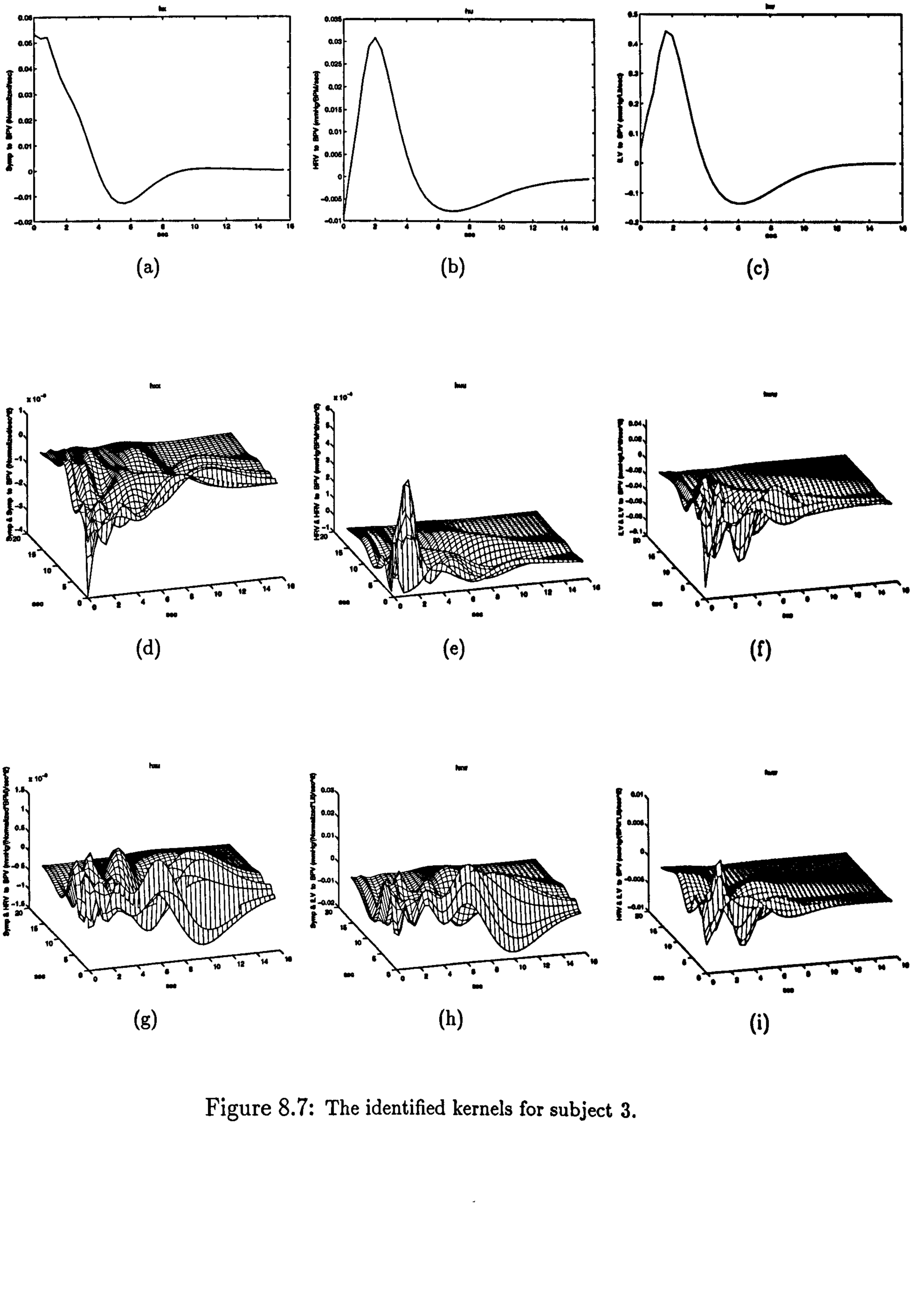


Figure 8.6: The identified kernels for subject 2.

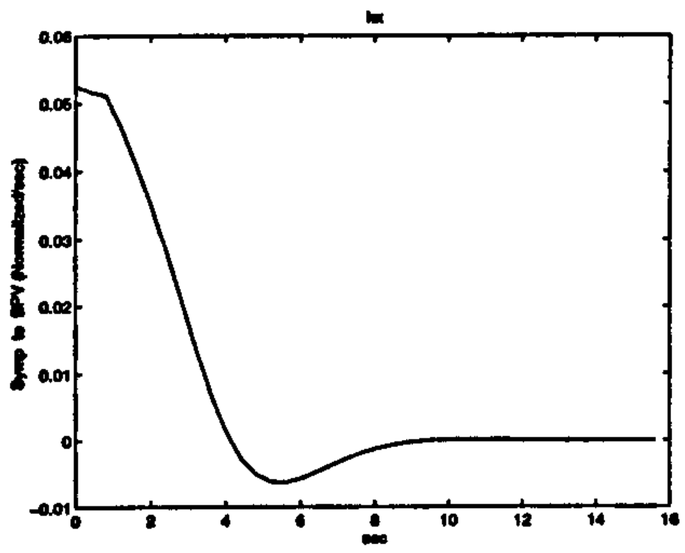


(a) (b) (c)

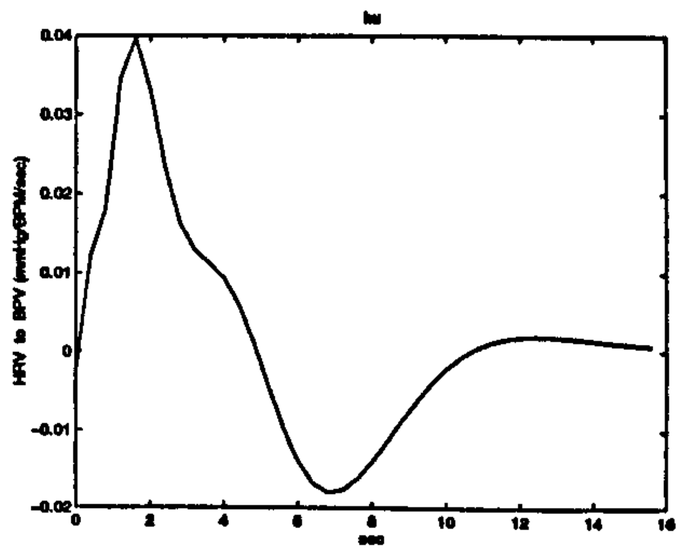
(d) (e) (f)

(g) (h) (i)

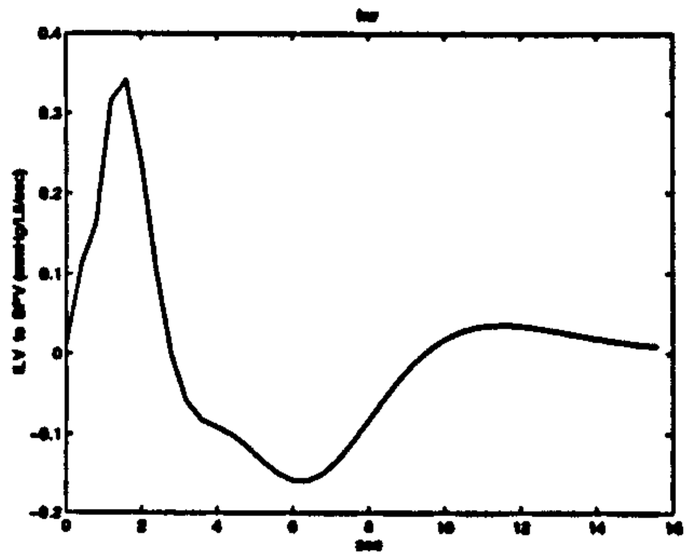
Figure 8.7: The identified kernels for subject 3.



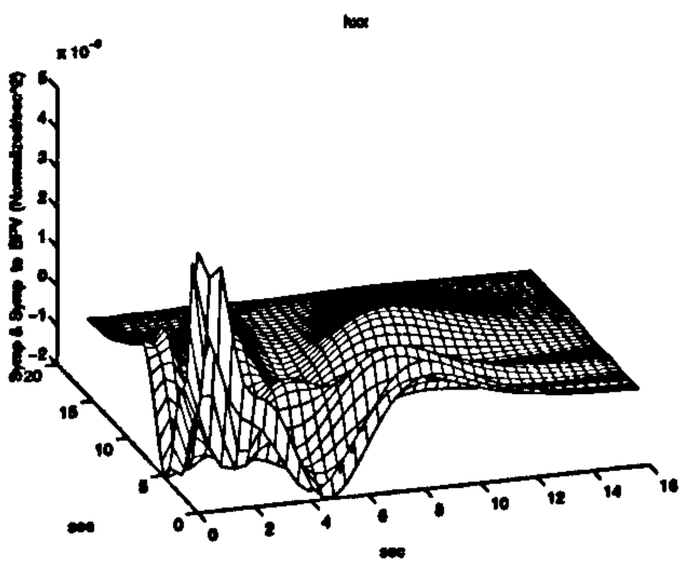
(a)



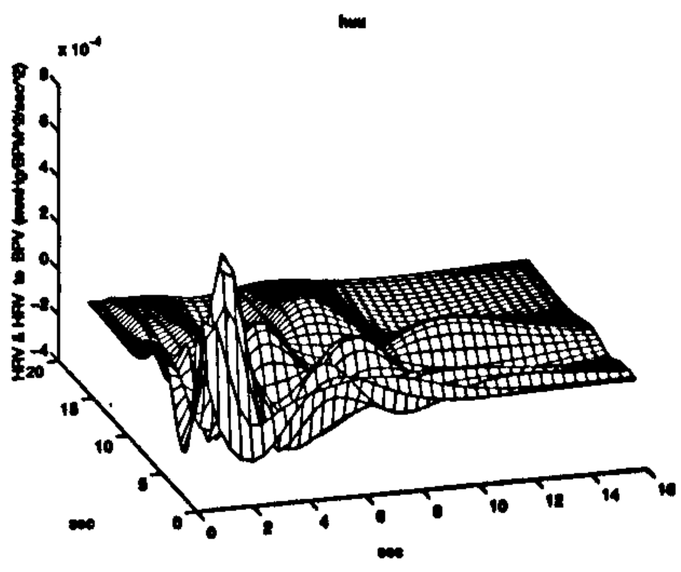
(b)



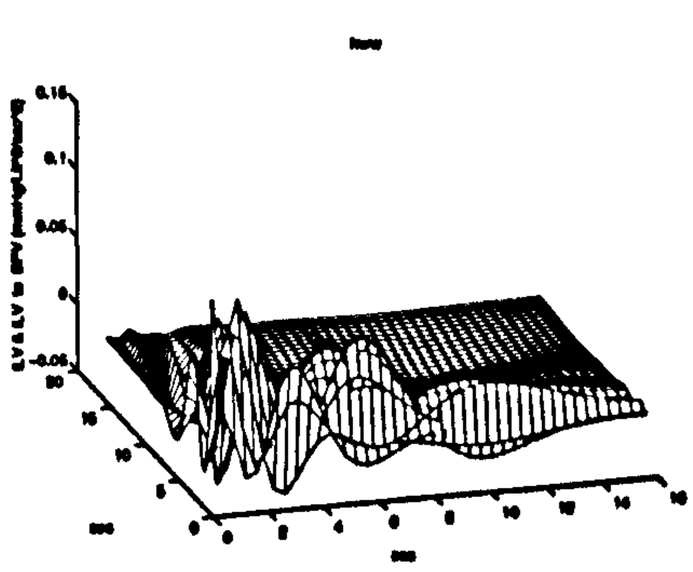
(c)



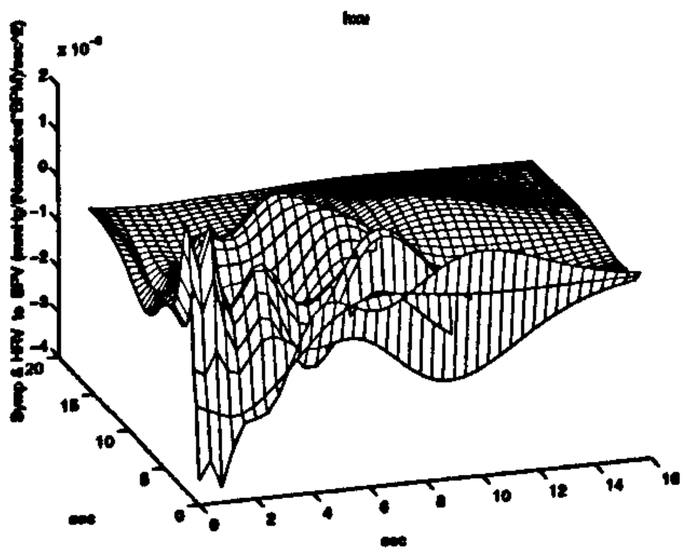
(d)



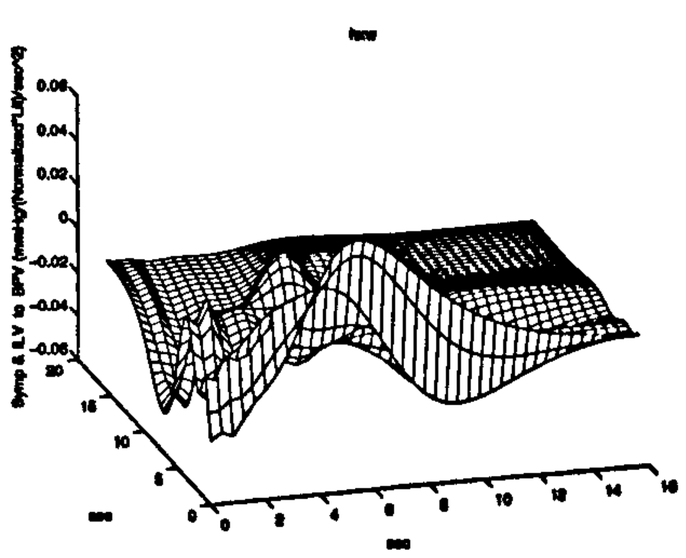
(e)



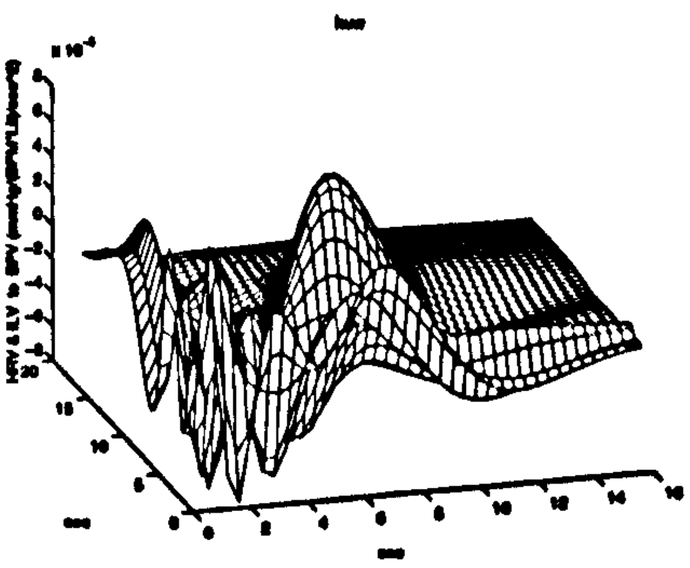
(f)



(g)

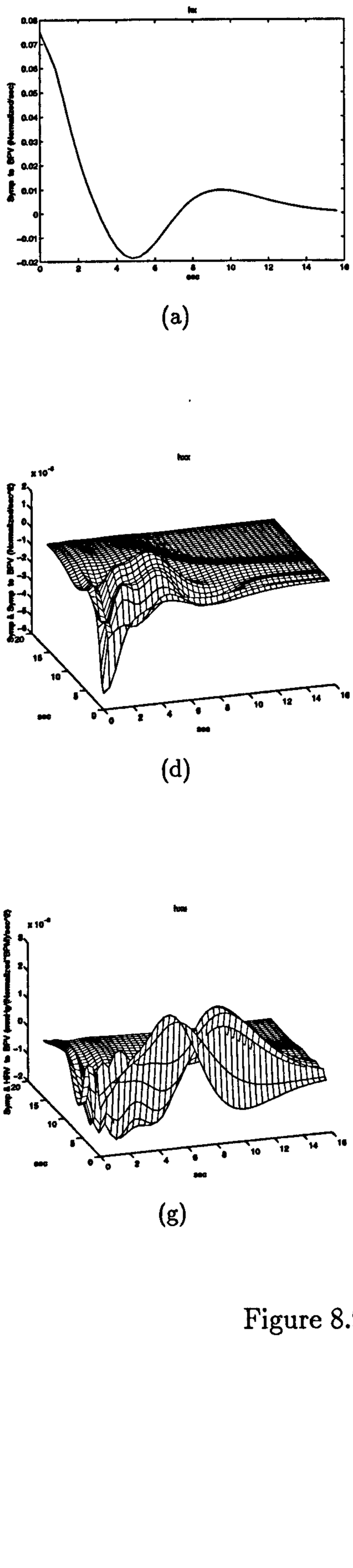


(h)

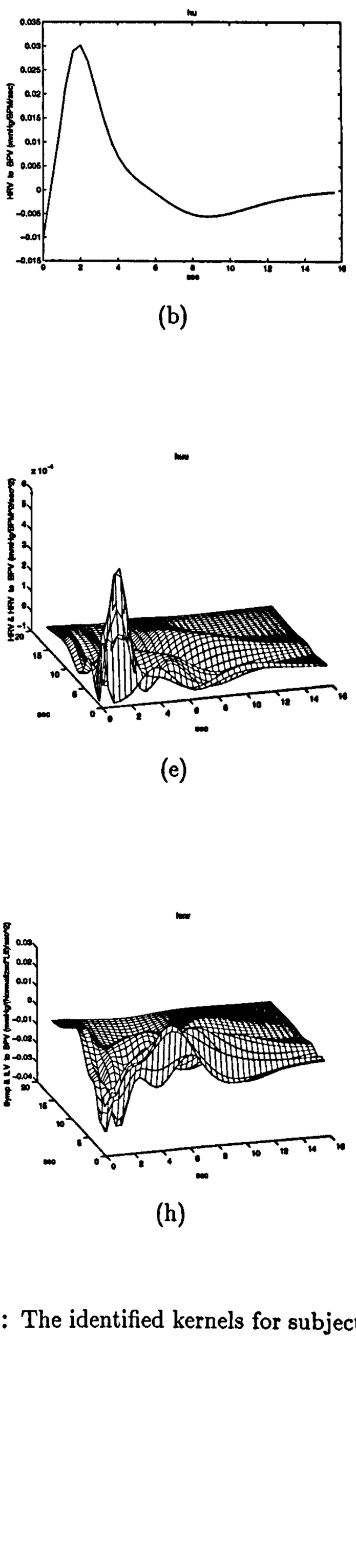


(i)

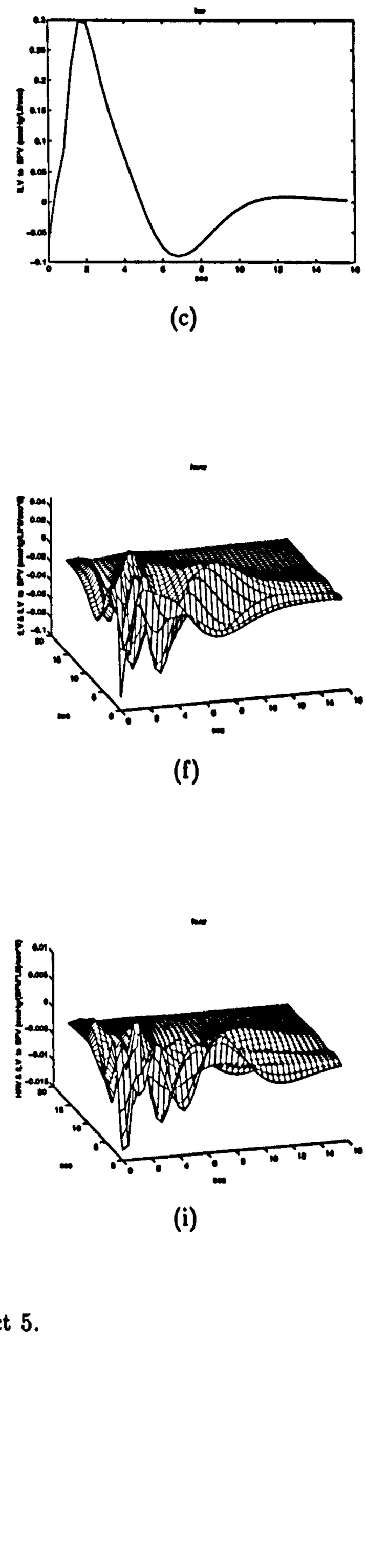
Figure 8.8: The identified kernels for subject 4.



(a)



(b)



(c)

(d)

(e)

(f)

(g)

(h)

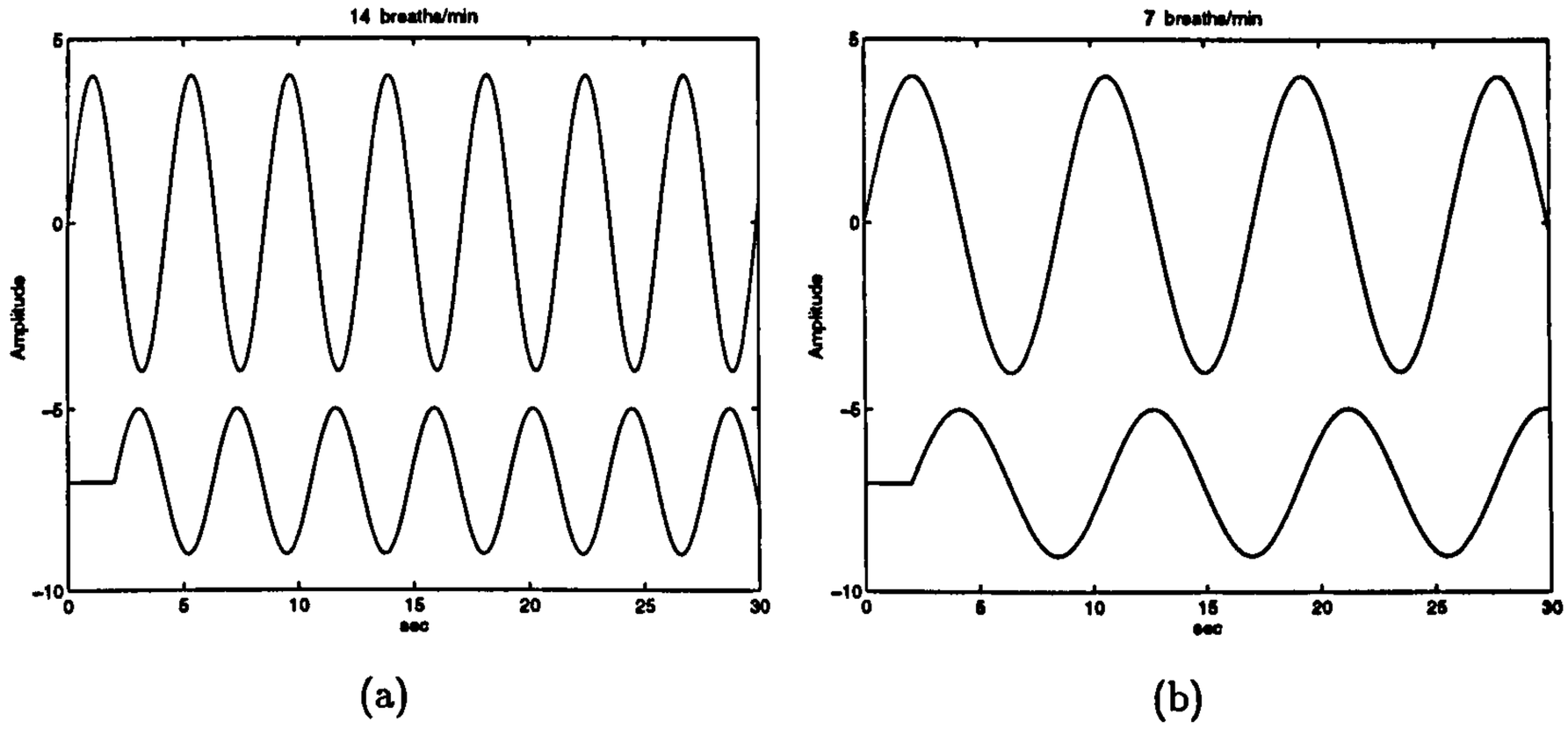
(i)

Figure 8.9: The identified kernels for subject 5.

meaning that a change in the heart rate induces an almost simultaneous change in the same direction in blood pressure. This behaviour is also acknowledged within the physiological understanding of the influence of the heart rate on blood pressure. It is well-known that if the heart rate increases (within a certain limit), blood pressure will also increase and a decrease in heart rate causes a decrease in blood pressure. Nonetheless, a sudden change in blood pressure entails a rapid but opposite change in heart rate, following the sign inversion in the brain stem, and consequently a compensatory effect on blood pressure through h_u in the present model.

In contrast to h_x and h_u, the behaviour of h_w, the first order kernel from ILV to BPV needs more discussion. Figures 8.5 through 8.9 illustrate a positive prompt change in BPV as a result of inspiration. As stated in Chapter 4, no fixed relationship between respiration and blood pressure has been observed. It has been shown that for high respiratory rates (12 breaths/min) arterial blood pressure falls during inspiration whereas at low respiratory rates (6 breaths/min) blood pressure rises with inspiration (Laude *et. al.*, 1993; Dornhorst *et. al.*, 1952). The obtained kernel h_w seems to be consistent with this observation. The PSD of the respiratory signal shown in Figs. 8.2 and 8.3 is concentrated on the low respiratory rates. Since the identification procedure also elicits the global behaviour of the kernels, the estimated h_w shows a rise in blood pressure with inspiration. This is further regarded if the two seconds delay at the peak of h_w is taken into account. If a pure delay between ILV and BPV is assumed then at higher breathing rates a reverse relationship between ILV and BPV can be observed (Fig. 8.10(a)) whereas at lower breathing rates the blood pressure will exhibit an increase during the inspiratory period (Fig. 8.10(b)). The illustrated results in Fig. 8.10 are indeed in striking agreement with the experimental observations obtained by Laude *et. al.* (1993) and Dornhorst *et. al.* (1952). Laude *et. al.* found exactly the same relationship between BPV and ILV using a set of metronome breathing experiments in healthy adult subjects in the supine position. Similar results were also obtained by Dornhorst *et. al.* by comparing the fluctuations in instantaneous blood pressure and lung volume.

These results are also in substantial agreement with the results obtained by Saul *et. al.* (1989, 1991) and Triedman and Saul (1994). Through extensive research performed in humans, Saul *et. al.* observed that the effect of respiration on arterial blood pressure is strongest during maximal respiratory flow, when intrathoracic pressure is

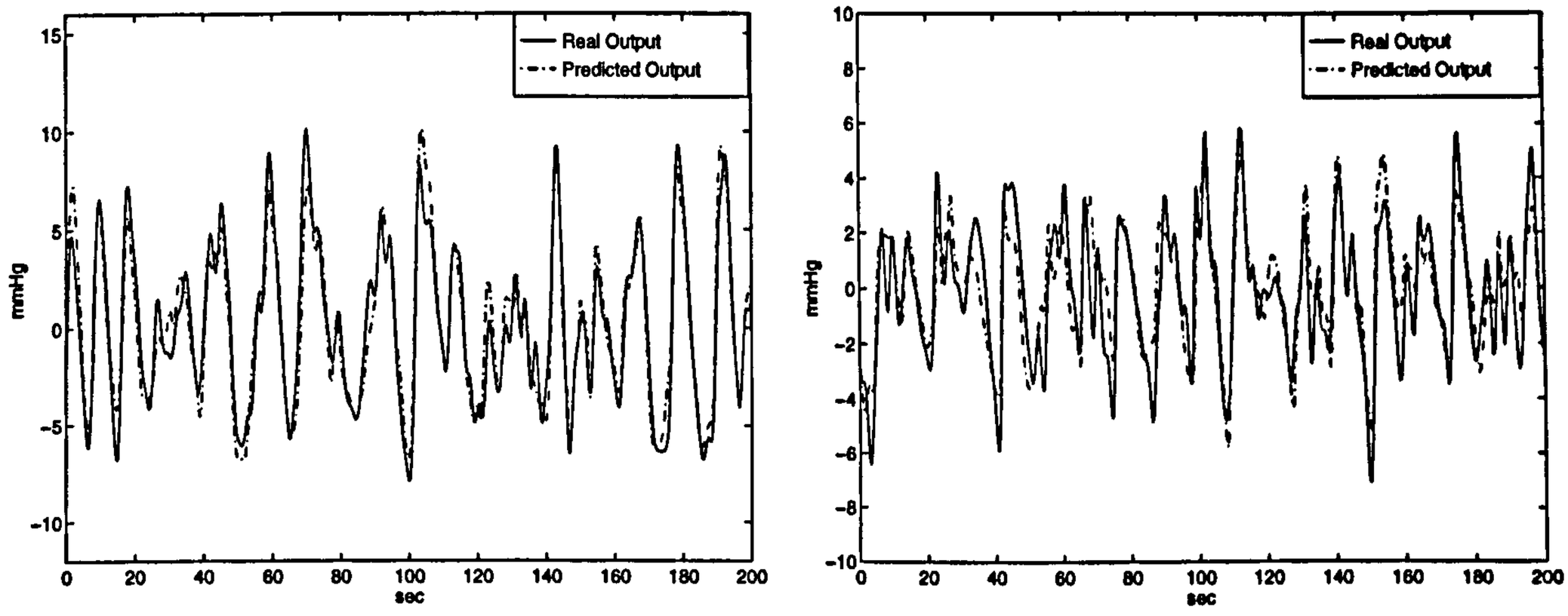


(a) (b)

Figure 8.10: Phase relationship between ILV (top trace) and BPV (bottom trace) for two different breathing rates if a pure delay (two seconds) system is assumed.

changing most rapidly. These authors, therefore, hypothesised a type of capacitive coupling between the lung volume and the arterial blood pressure. This in turn means that the arterial pressure changes are most closely related to the rate of change of lung volume; slow deep breaths are less effective than fast respiration in inducing corresponding fluctuations in blood pressure. On the other hand, by using a random breathing pattern together with a random LBNP technique in humans, Triedman and Saul (1994) showed that the variation in central venous pressure is transmitted to the arterial side with a delay of about 2 seconds and only up to a frequency of $0.1Hz$. These authors concluded that the respiratory modulation of venous return is actually mediated by movement of the blood through the pulmonary vasculature to the left ventricle and thus arterial blood pressure, and not by propagation of pressure waves or ventricular interdependence. The breathing pattern used in the current study is concentrated on low respiratory rates. Therefore, it appears that the presumed capacitive coupling of respiration on blood pressure contributes only a negligible amount when compared to the more potent effect of the direct mechanical movement of the blood from the venous side to the arterial side, thereby increasing the blood pressure during inspiration.

Unlike the first order kernels, the second order kernels exhibit less similarity between different subjects. It was shown in Chapter 7 that the second order kernels are more vulnerable to noise corruption and reconstruction errors than the first order



(a) (b)

Figure 8.11: The actual and the predicted BPV for two subjects, (a) subject 1, (b) subject 5.

kernels. In addition to that, the amount of nonlinearity and/or interactions between inputs might differ from subject to subject (Chapter 5). As a matter of fact due to the complexity of the second order kernels it is not easy to give them a direct physiological interpretation. In nonlinear physiological system identification these kernels are used in order to segregate the linear characteristics from the nonlinear contribution without offering an explicit interpretation or direct application (Marmarelis *et. al.*, 1993b).

Next, to technically justify the authenticity of the identified kernels, the actual BPV signal was compared with the predicted BPV obtained by injecting the Symp., HRV, and ILV inputs into the identified nonlinear system. The results for two subjects are shown in Figs. 8.11(a),(b). The relative mean squared error defined by $\frac{Power(BPV_{actual}-BPV_{predicted})}{Power(BPV_{actual})}\%$ was relatively high (10-60%). However, in such a complex system with multiple interfering inputs this amount of error could be expected. This residual error can also be ascribed to the corrupting output noise since the Volterra identification algorithm is inherently unable to identify the noise model.

Although not very easy to interpret in the physiological context, the existence of the second order kernels verifies the presence of considerable nonlinearity in the actual model. Otherwise, the second order kernels should be zero. Table 8.1 illustrates that the output power due to the nonlinearity is between $20-50\%$ of the total power. This further implies that reliance solely on linear modelling might cause significant bias in the determination of the transfer functions (Marmarelis, 1993a, 1994).

Subject	1	2	3	4	5	6	7
Sex	*M*	*M*	*M*	*M*	*F*	*F*	*M*
Mean HR (BPM)	73	75	73	65	61	81	76
$\frac{Nonlinear\ Power}{Total\ power}$ %	32	36	23	38	45	43	52
G_4	30	28	24	32	14	62	12

Table 8.1: Central respiratory gain G_4 and percentage contribution of the nonlinear power for the examined subjects.

8.4 Respiratory Sinus Arrhythmia in the Model

The arterial blood pressure information is continuously gathered by the arterial baroreceptors. This information is sent to the brain stem centres and is analysed there whereupon the appropriate controlling commands are issued to the various organs. Therefore, it seems reasonable to see that one of the principal explanations for the respiratory R-R interval fluctuations is that they represent baroreflex buffering of arterial pressure changes induced by the mechanical effects of breathing on intrathoracic pressure, venous return and ventricular preload and afterload. However, the results of extensive experiments have revealed that the interaction between HRV and BPV is more complex than a simple buffering relationship. If HRV has only a stabilising effect on BPV, fixing the heart rate will evoke larger fluctuations of blood pressure. In contrast, reduced BPV with fixed heart rate suggests an augmenting feature for the influence of HRV on BPV.

Akselrod *et. al.* (1985) examined the HRV-BPV relationship in conscious dogs by cardiac pacing as well as using parasympathetic blocking agents. Cardiac pacing eliminates the heart rate variability and thereby opens the closed loop path between HRV and BPV. Akselrod *et. al.* observed that the pacing caused a dramatic decrease in the respiratory fluctuation of the BPV. Similar results obtained in the parasympathetic blockade condition showed that the blood pressure variation in the respiratory band decreased largely together with heart rate variability. These workers concluded that in normal dogs respiratory variation in BPV is secondary to the heart rate variability at that frequency.

Contrary to the above results Kardos, Rudas, Gingel, Szabados and Simon (1995) showed that the amplitude of the systolic blood pressure fluctuation during spontaneous

breathing increased significantly in patients with a fixed ventricular pacemaker rhythm in comparison with normal sinus rhythm subjects with the same conditions. However, there was only a mild increase in the LF, HF and total power of the PSD of the BPV in the pacemaker subjects. Lack of the smoothing effect of the HRV on systolic blood pressure was introduced by these investigators as the main reason.

In agreement with Akselrod *et. al.*, but in freely behaving rats, Perlini, Giangregorio, Coco, Radaelli, Solda, Bernardi and Ferrari (1995b) observed that the power of the blood pressure variation in the respiratory band was halved after administration of cardiac autonomic blocking agents. These investigators therefore concluded that the mechanical factor accounts for only 50% of the HF blood pressure fluctuations, whereas the remaining 50% should be ascribed to respiratory-synchronous vagally mediated HRV.

By injection of parasympathetic blocking agents Parati and his colleagues (1987) focussed on alteration of the BPV in human beings. They observed that the marked reduction in HRV as a result of parasympathetic blockade is accompanied by a small reduction in BPV in resting supine (mild hypertensive) subjects.

In a recent study in healthy subjects, Taylor and Eckberg (1996) compared the change in HRV and BPV before and after atrial pacing with an esophageal electrode. Their results demonstrated that the R-R interval fluctuations at the respiratory frequency do not dampen and in fact can augment the arterial pressure fluctuations in the supine position. They reasoned that the positive phase relation obtained between the R-R intervals and systolic blood pressure in their experiment indicates that the latter follows the former. In contrast, they observed that in the tilt position elimination of sinus arrhythmia by cardiac pacing increased the respiratory dependent arterial pressure variability, suggesting a buffering role for the HRV. Based on these observations, Taylor and Eckberg concluded that the respiratory sinus arrhythmia buffers the respiratory arterial pressure oscillations in upright humans but augments the arterial pressure oscillations in supine humans.

These conflicting results for the interaction between HRV and BPV might depend on the fact that the role of the heart rate and cardiac output variations in producing the BPV is different in different species or varies with the degree of physical activity as Parati *et. al.* (1987) have argued. They showed that although in the resting supine

subjects vagal blockade imposes a reduction in BPV, mild physical activity causes a significant rise in BPV following vagal blockade. Therefore, they concluded that in the resting supine position HRV participates in production of BPV and has an oscillatory influence whereas during physical activity heart rate opposes the blood pressure changes and exhibits an anti-oscillatory role. This seems to be in good agreement with the results obtained by Taylor and Eckberg in the tilt experiment.

It should be pointed out, however, that cardiac pacing or vagal blockade not only suppresses the buffering role of the heart rate on blood pressure but also blocks the transmission of the central respiratory modulation of the heart rate to the BPV. Therefore, fixing the heart rate can suspend the buffering role of the heart rate with a consequent increase in BPV whilst it may also cause a decrease in BPV due to the suppression of the central respiratory modulation. A delicate test in the proposed model seems to be able to unravel the role of the HRV on BPV. If HRV has only a stabilising effect on BPV then transmission of BPV to the brain stem and then to the heart rate in the model must create the same HRV as that of the actual one. However, if the predicted HRV differs considerably from the experimentally observed HRV then the existence of a central link between the respiratory oscillator and the cardiac control centre is corroborated.

To test this hypothesis the model of Fig. 8.12 was first simulated with the injection of the actual BPV while $G_4 = 0$ was assumed (no central link). This model in fact comprises those components of the proposed model (Fig. 8.1) which are believed to contribute in producing RSA; the SA node, blood pressure influence on heart rate and central respiratory oscillator. Then the obtained HRV from Fig. 8.12 was compared with the actual HRV. The results for two subjects are shown in Figs. 8.13 and 8.14.

Figures 8.13(a),(b),(c) and 8.14(a),(b),(c) depict the actual ILV, BPV and HRV signals, respectively. If no central link between the respiratory oscillator and the cardiac control centre is assumed ($G_4 = 0$), then the predicted HRV in the model will be much less than the actual HRV as shown in Figs. 8.13(d) and 8.14(d). This means that the simple buffering relationship between the BPV and HRV cannot explain the presence of the much larger fluctuations observed experimentally in heart rate.

In order for the predicted HRV to closely follow the actual HRV and specifically exhibit synchronous fluctuations with respiration, the existence of a central link with

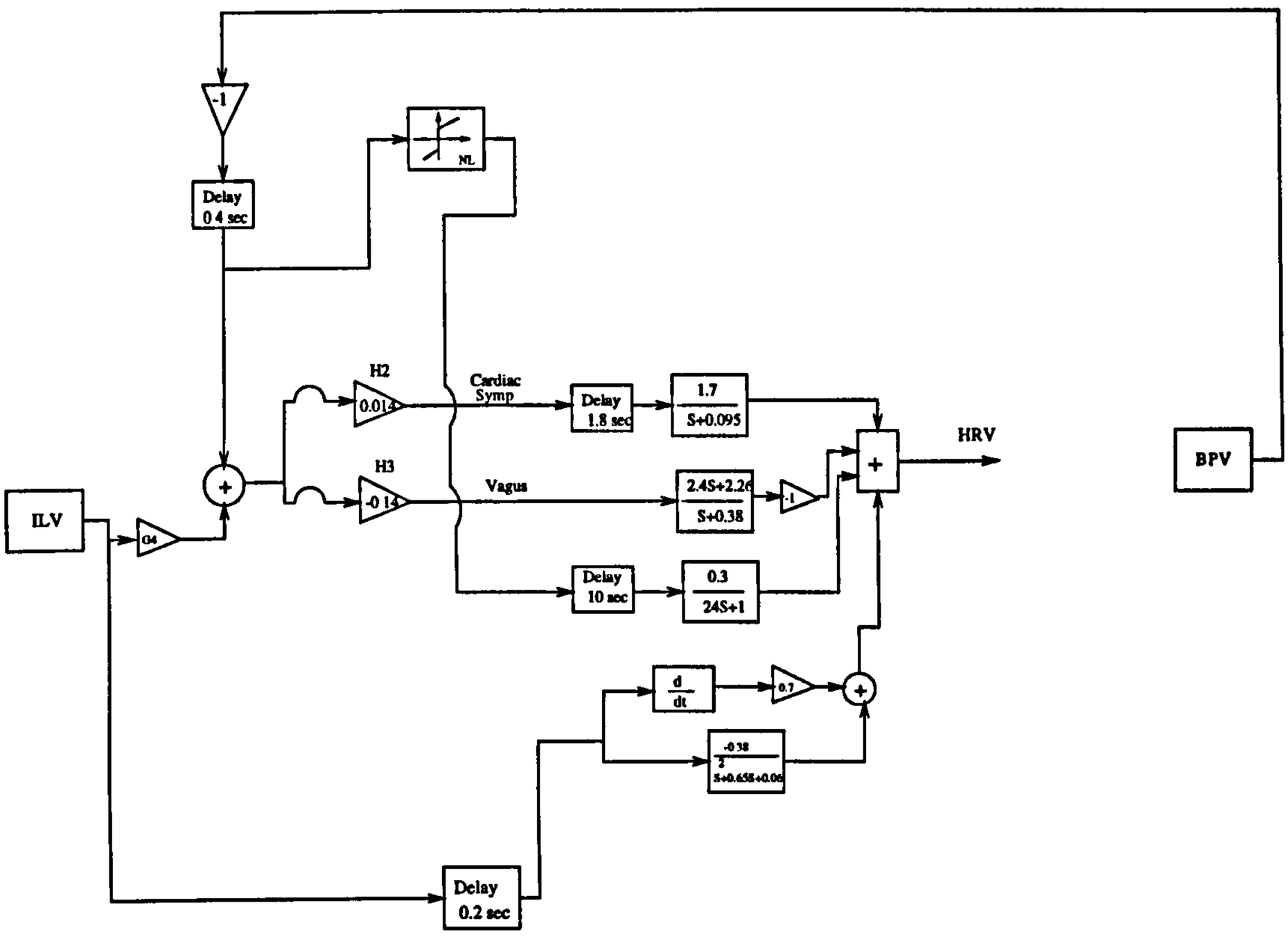
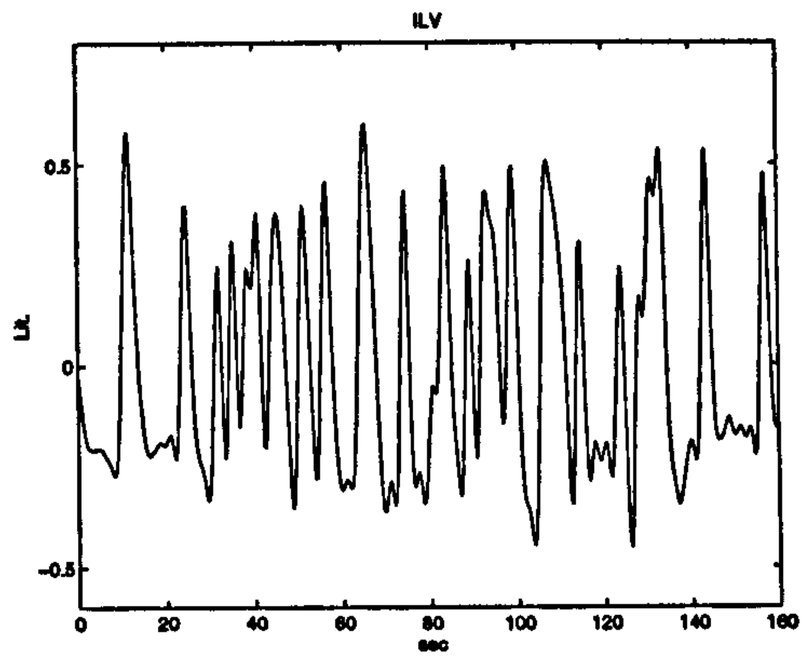


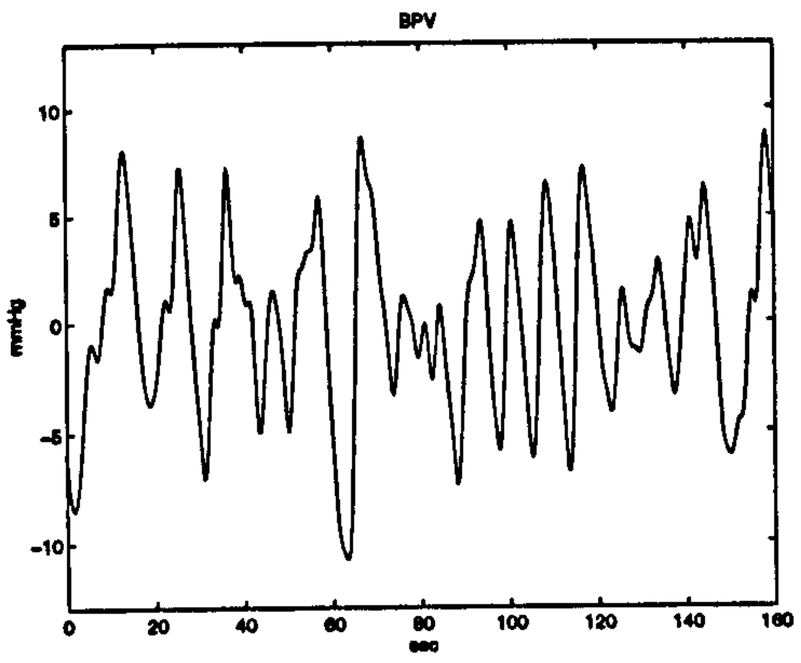
Figure 8.12: The assumed model for determining the central respiratory gain G_4 to the cardiac control centres.

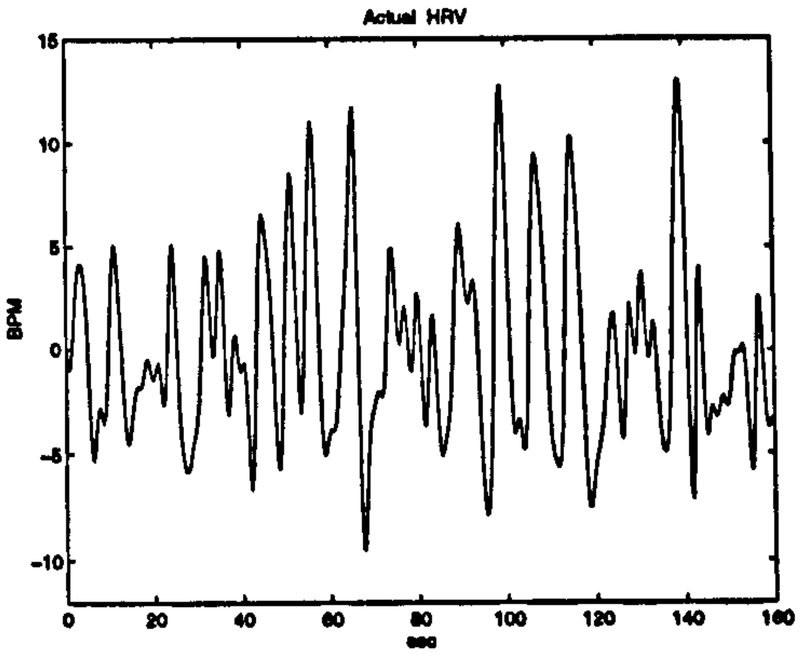
the respiratory oscillator seems imperative. To show this, the model of Fig. 8.12 was simulated again with different values of G_4. This gain was increased in steps of 2 units from zero until the difference between the power of the predicted HRV and the actual HRV finds a local minimum. Figures 8.13(e),(f),(g) and 8.14(e),(f),(g) illustrate the predicted HRV for increasing values of G_4. An optimum value of $G_4 = 30$ for the first subject and 14 for the second were obtained. The predicted HRV of Figs. 8.13(f) and 8.14(f) now exhibit a close resemblance to the actual HRV shown in Figs. 8.13(c) 8.14(c), confirming the presence of a central link between the respiratory oscillator and the group of neurones responsible for regulating the heart rate. Interestingly, the strength of this central modulation shows a satisfactory correlation between different subjects as depicted in Table 1.

Further support for the models relying on the central link theory can be provided by investigating the time behaviour and the PSD of the HRV and BPV shown in Figs. 8.2 and 8.3. While the HRV signal demonstrates fast fluctuations synchronous with respiration, BPV components are concentrated in the lower band of the frequency

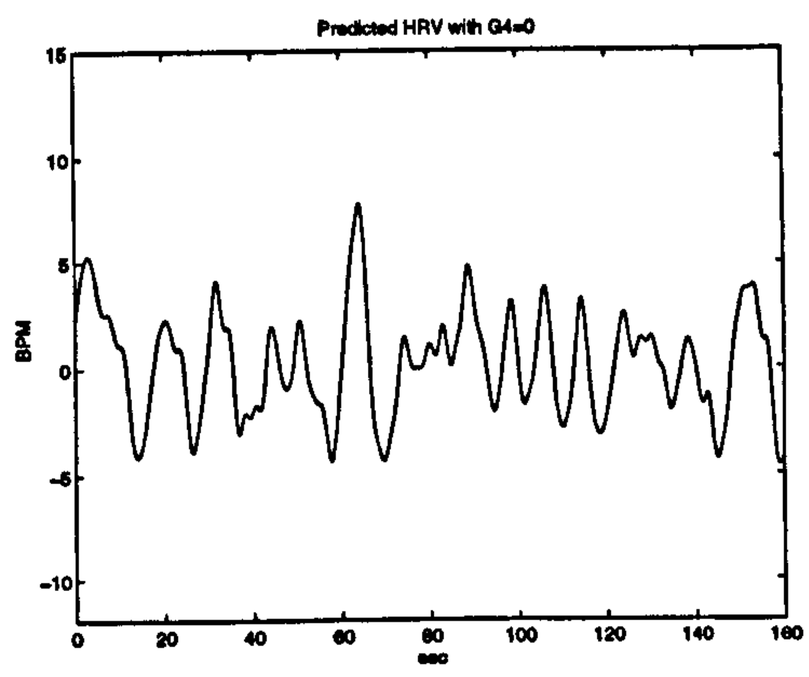


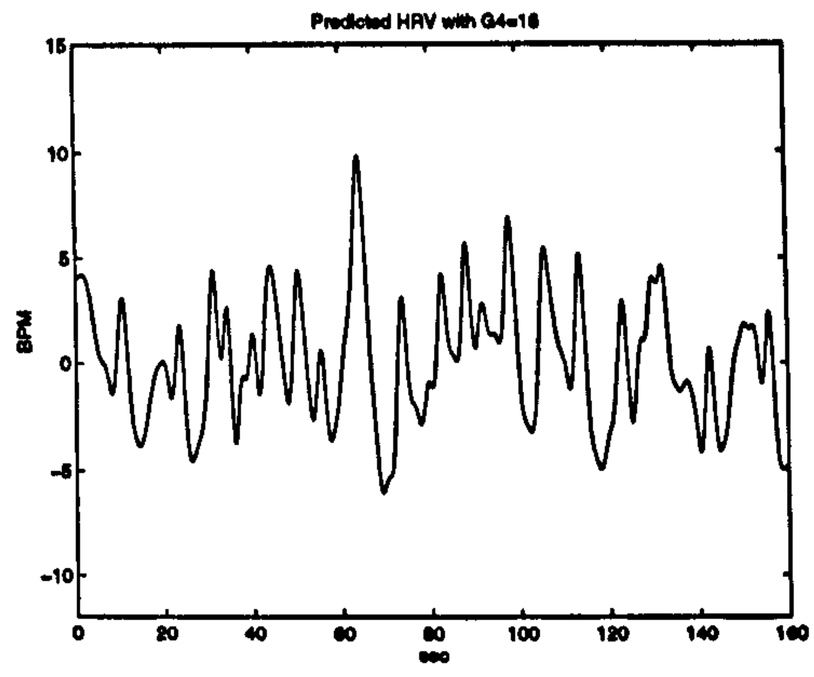
(a)



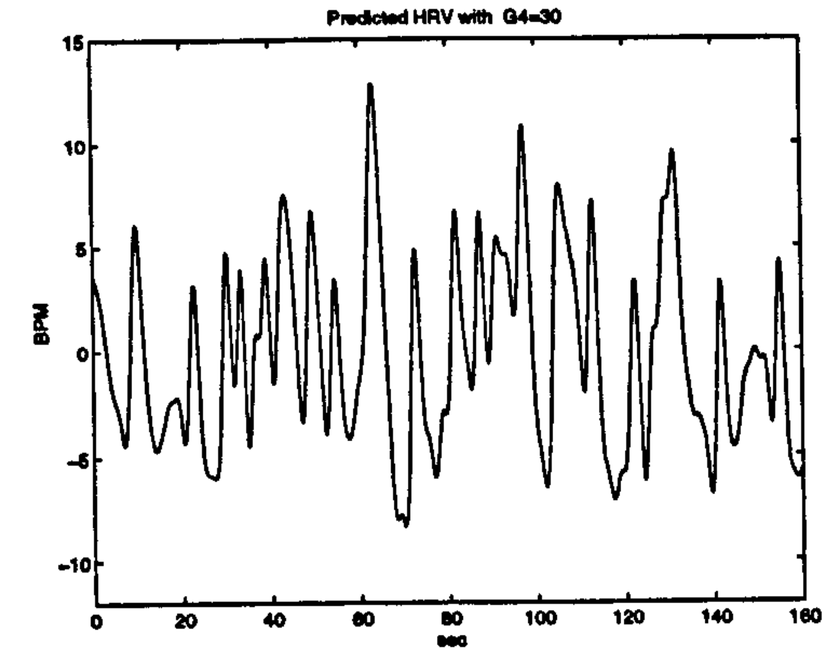


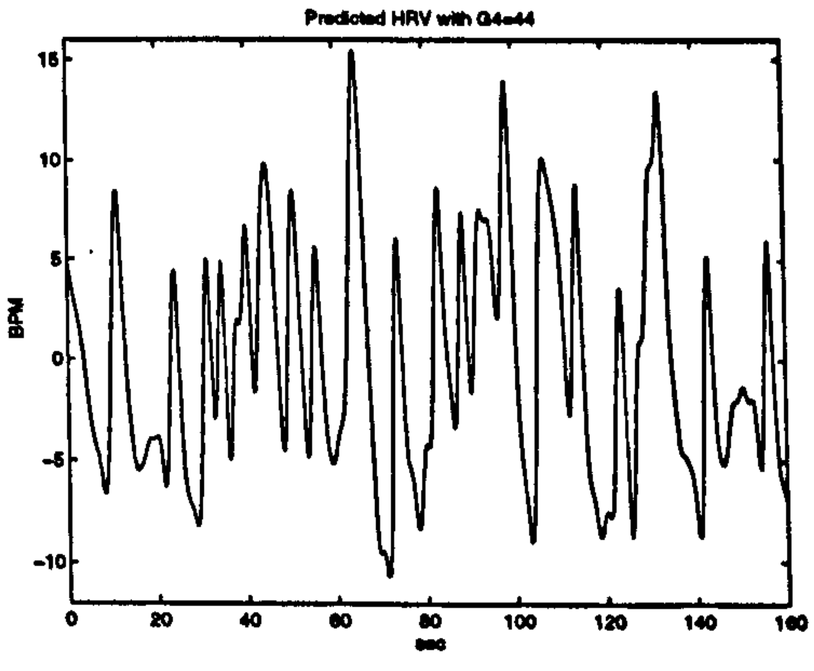
(b) (c)





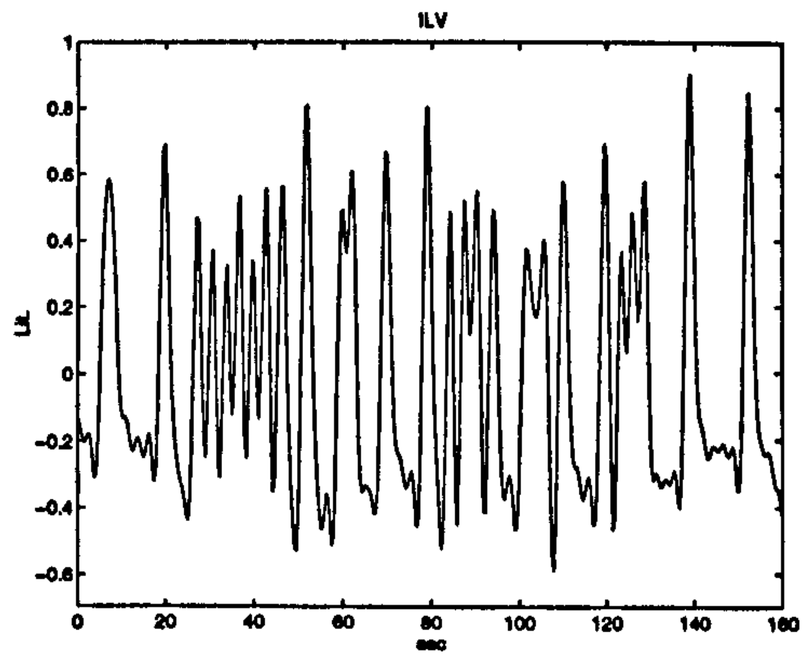
(d) (e)



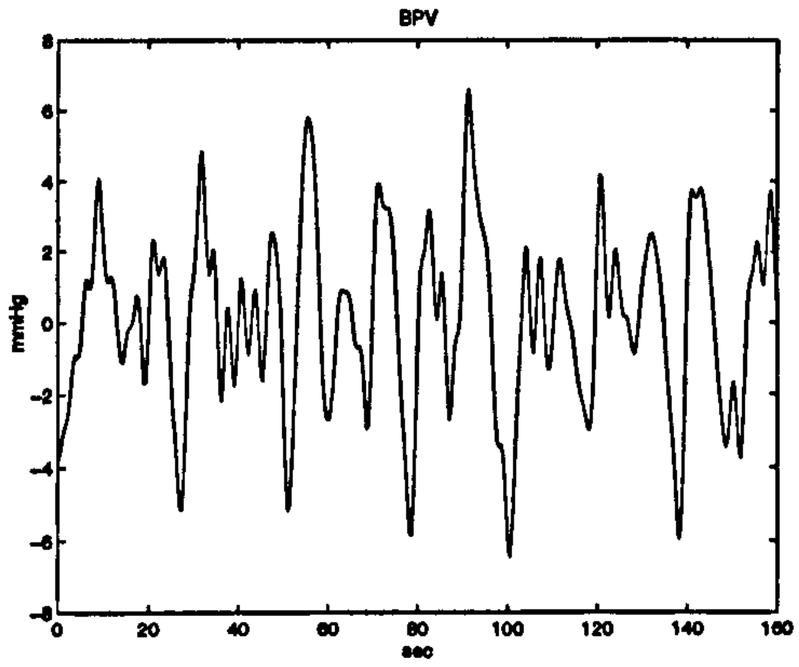


(f) (g)

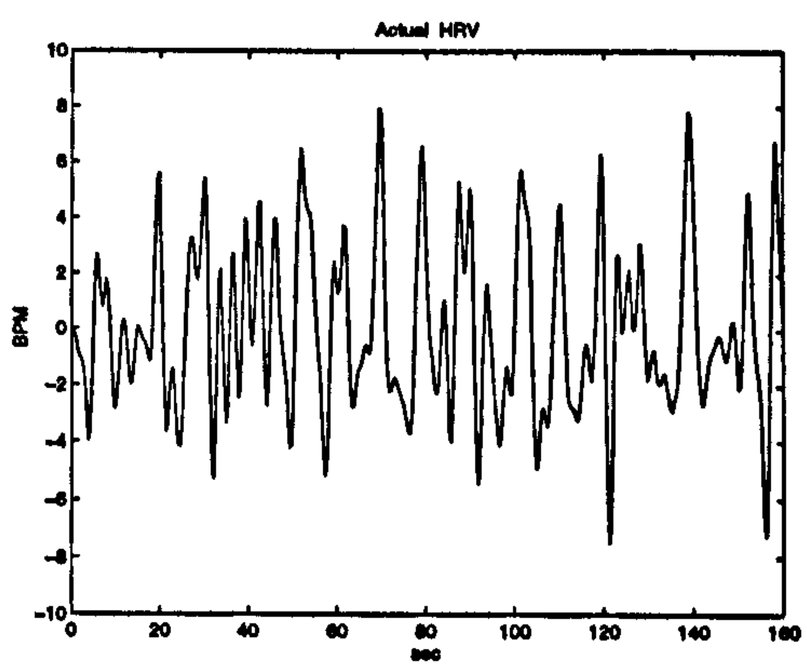
Figure 8.13: Simulation results of Fig. 8.12 with different values of G_4 for subject 1.



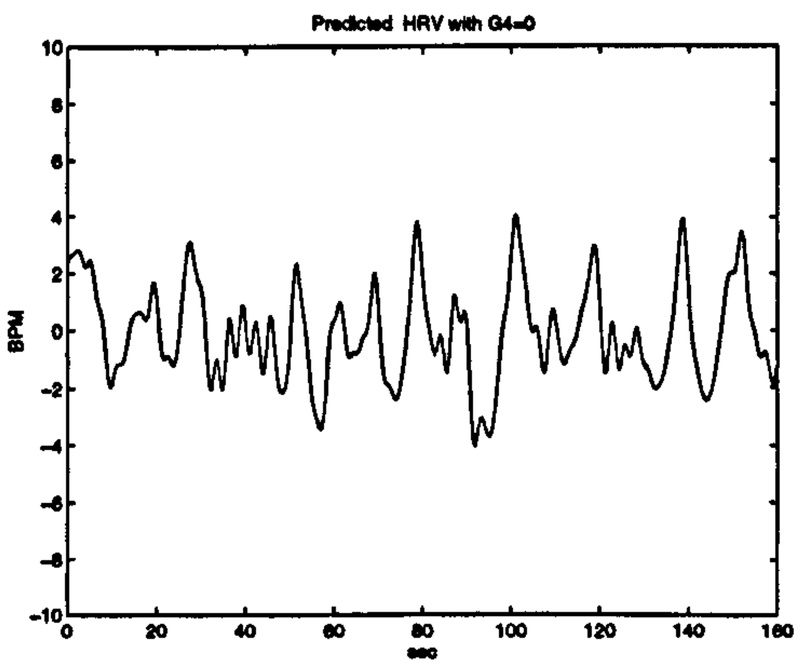
(a)



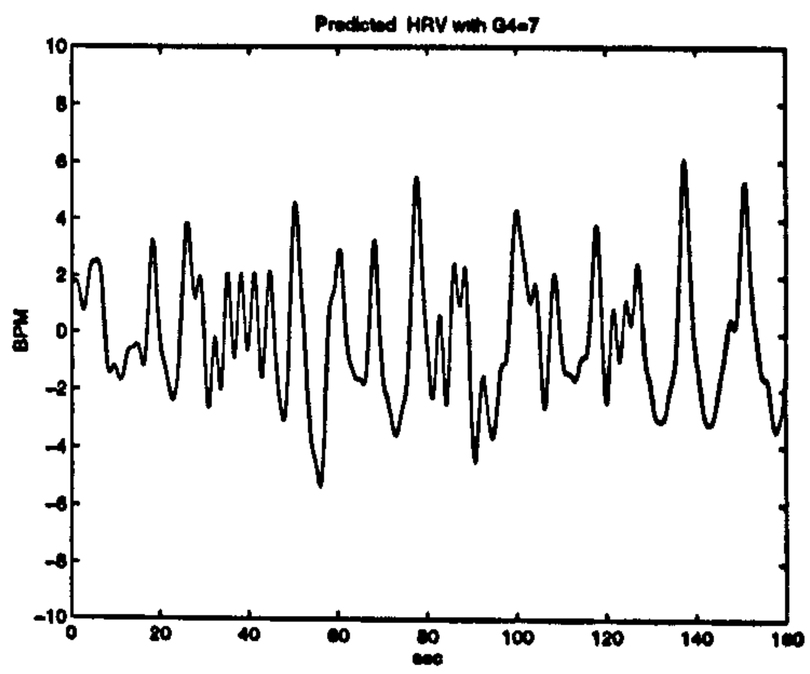
(b)



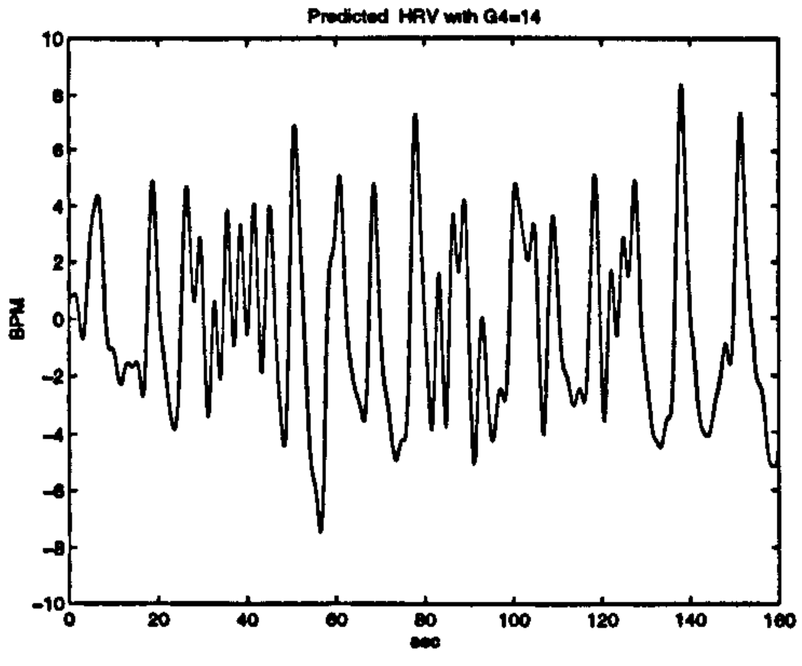
(c)



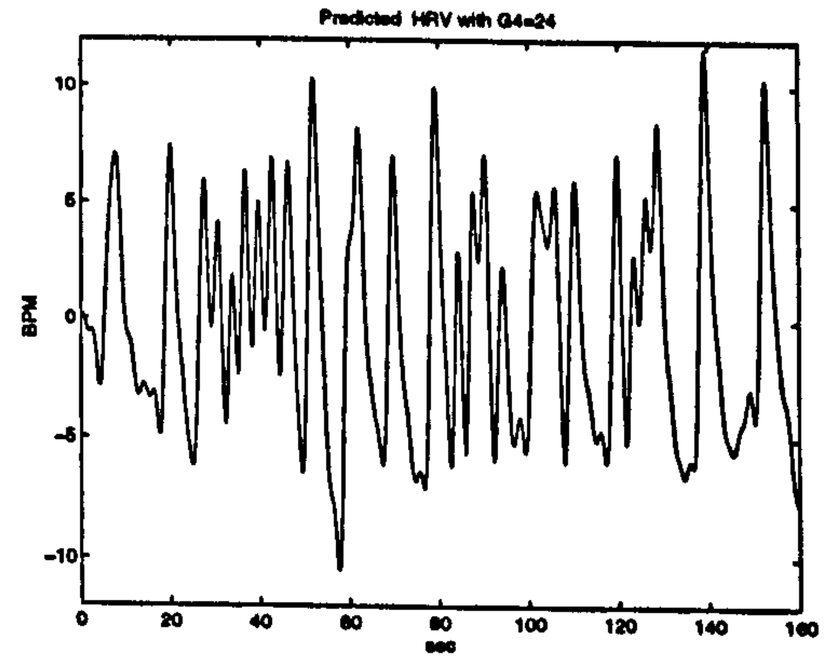
(d)



(e)



(f)



(g)

Figure 8.14: Simulation results of Fig. 8.12 with different values of G_4 for subject 5.

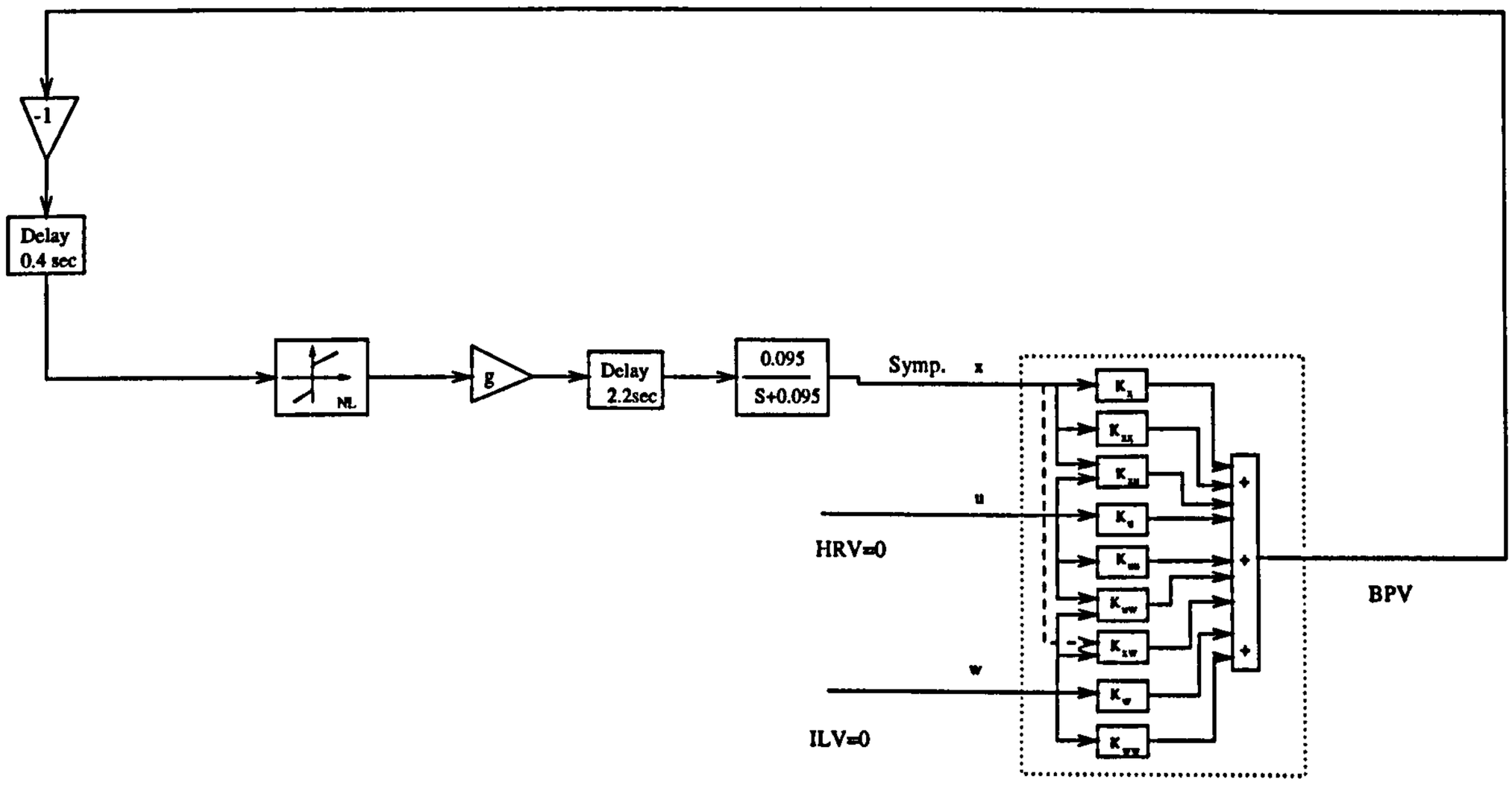


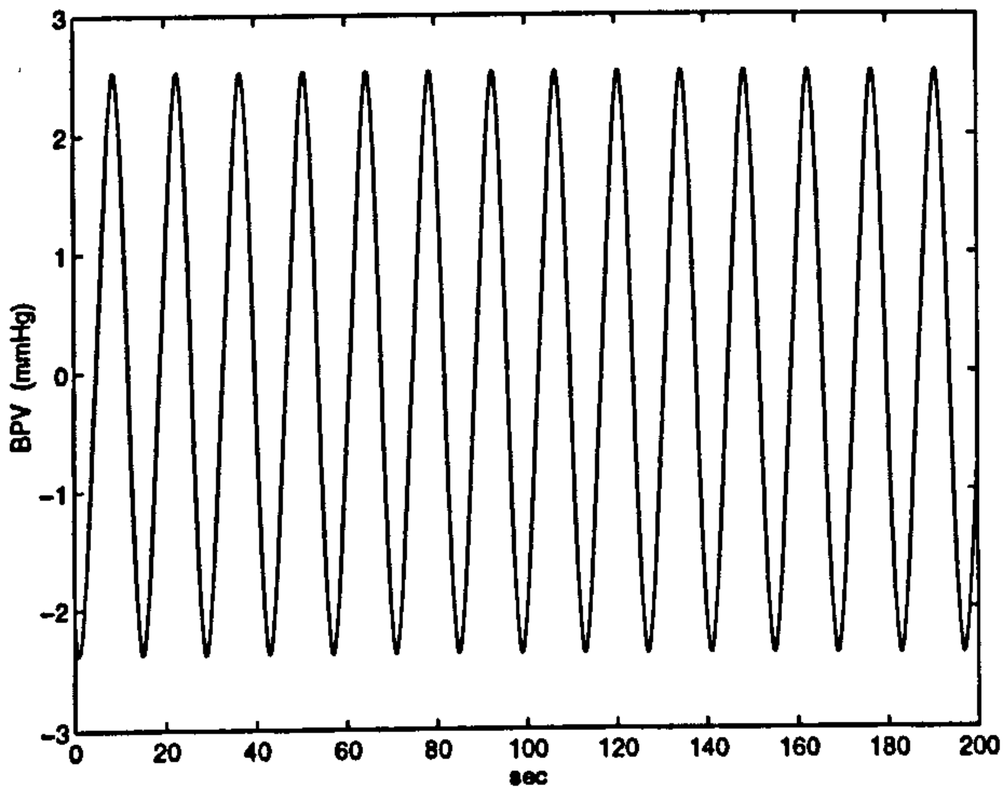
Figure 8.15: The simulated model for observing the LF component ($M = 2, \alpha = 1$ for the NL).

spectrum. If no direct modulation of the heart rate by respiration is assumed then no convincing reason for this observation can be raised. A mere buffering effect of the HRV on BPV is not able to draw a satisfactory picture of the characteristics seen in the HRV over the respiratory band.

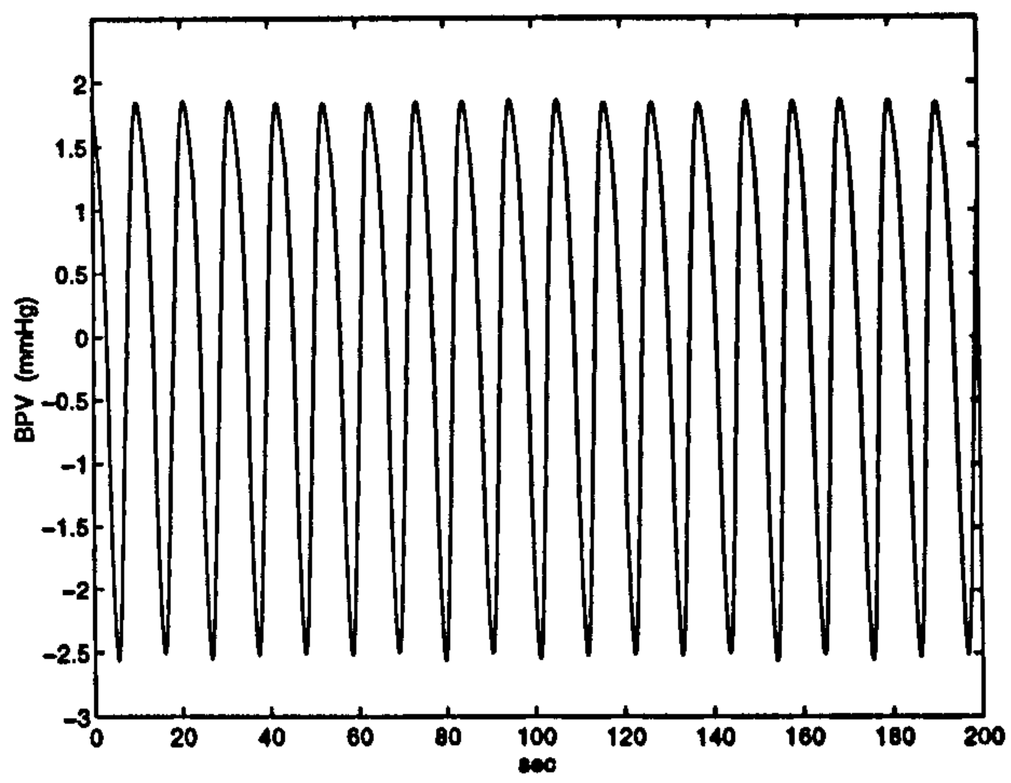
If the central respiratory modulation is mediated to the BPV *via* HRV then fixing the heart rate may evoke a reduction in BPV. This statement will be examined in Section 8.8 after further justification of the new model. It will be shown that constraining the HRV to zero brings about a reduction in BPV in the supine resting condition.

8.5 The LF Component in the Model

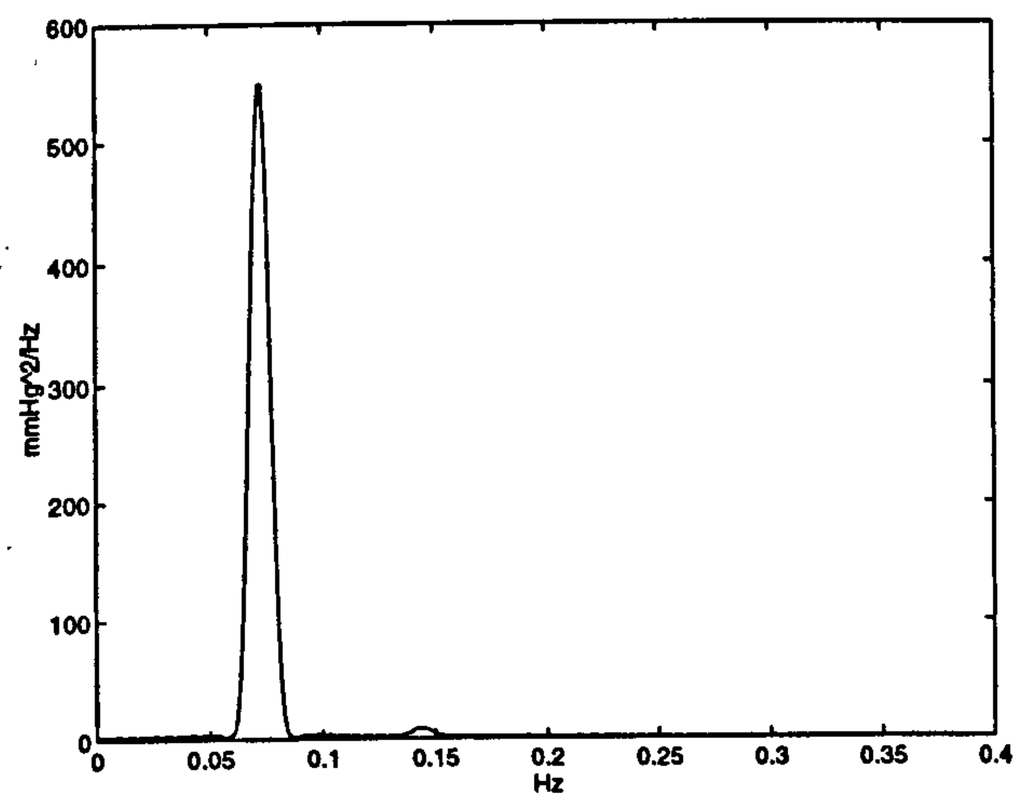
The simulation results of the proposed model in the LF band are very promising. If in the model of Fig. 8.1 only the sympathetic blood pressure regulatory mechanism is simulated (Fig. 8.15), with the identified kernels engaged, then a clear LF component can be observed in blood pressure. The results for two subjects are displayed in Fig. 8.16 in time and frequency domains. Before running the simulation, gain g of the model was adjusted in order to have a static open loop gain 2 for both subjects



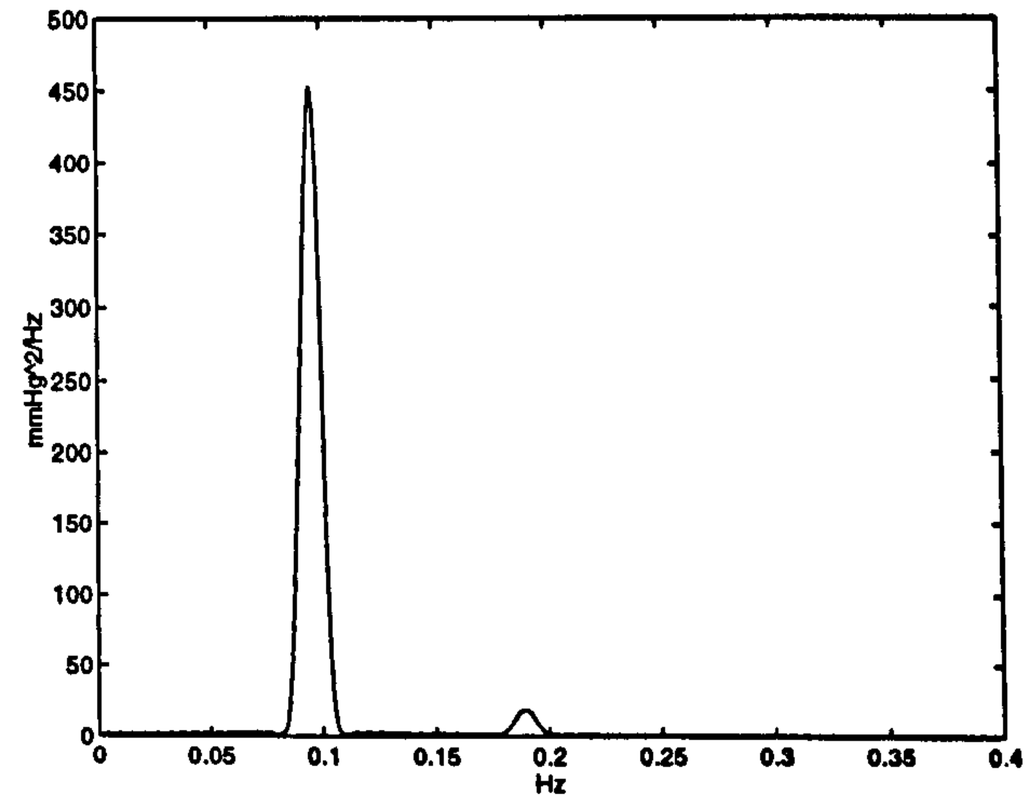
(a)



(b)

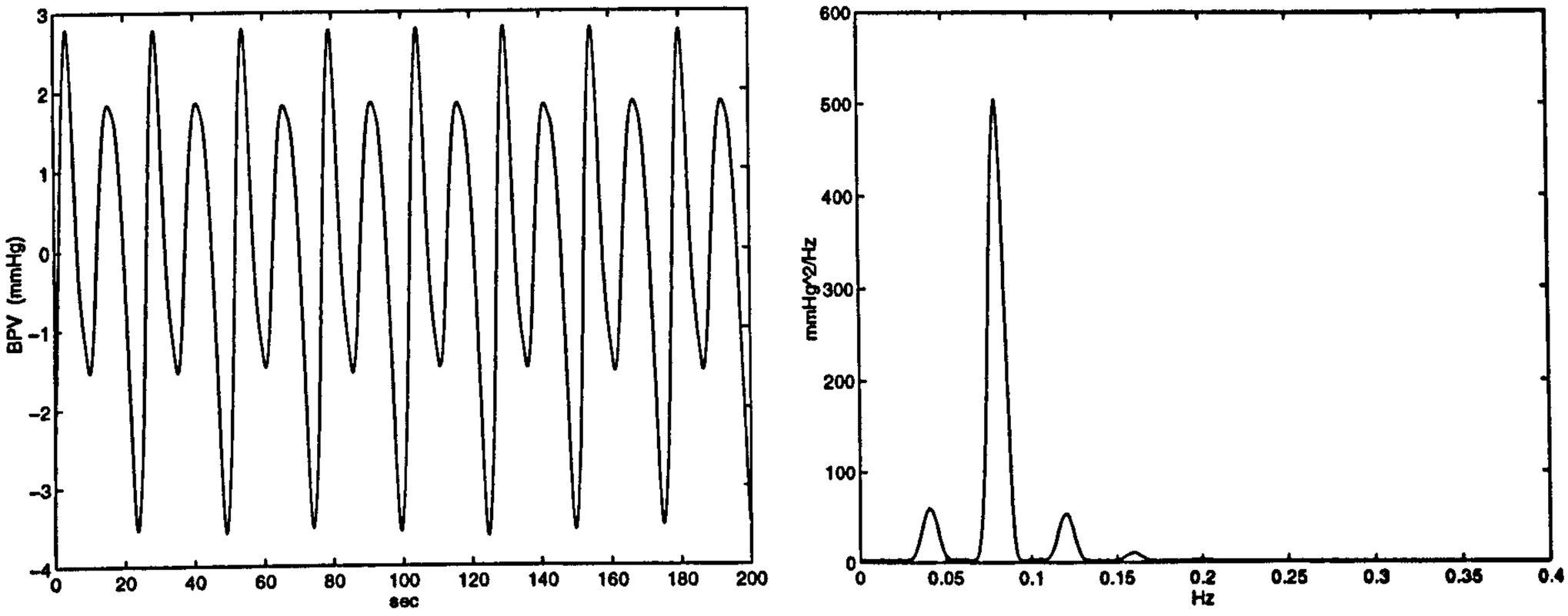


(c)



(d)

Figure 8.16: The LF oscillation in the model. Right hand column subject 1 and left hand column subject 5. (a),(b) time behaviour (c),(d) power spectral density.



(a) (b)

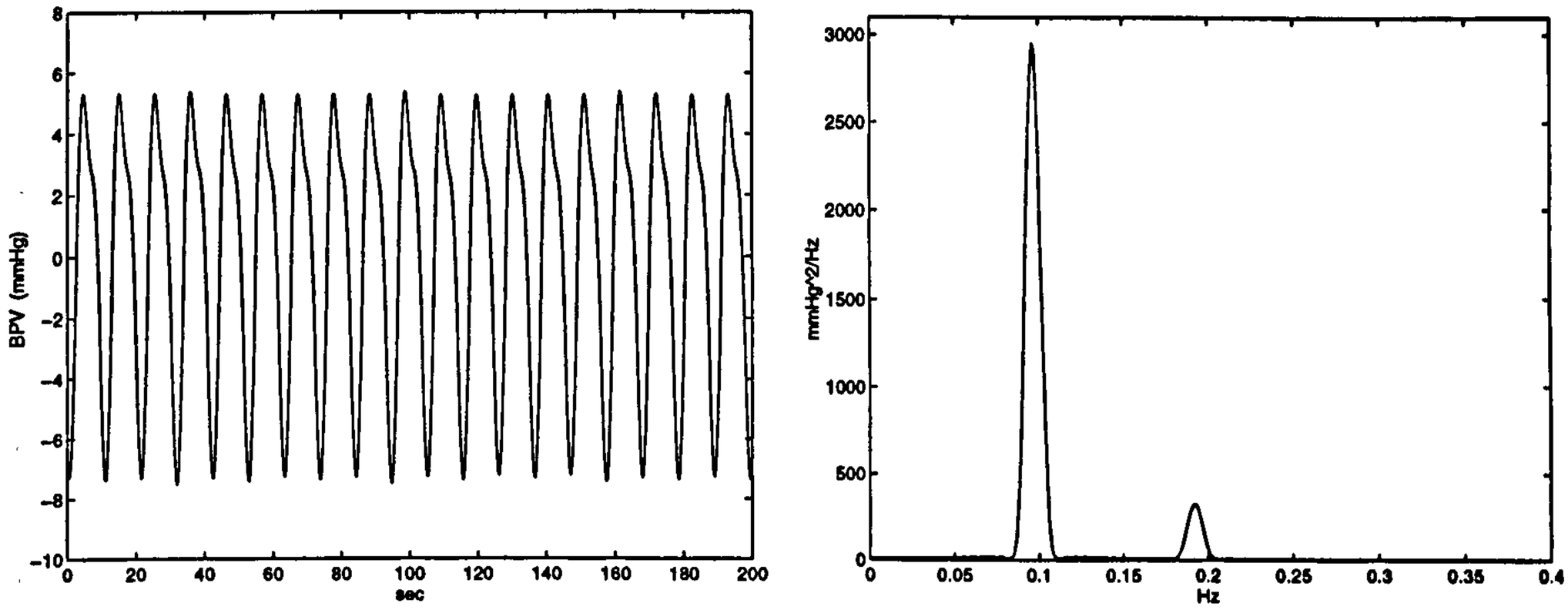
Figure 8.17: The LF oscillation for subject 3, (a) in time and, (b) in frequency domain.

$(g_1 = 1.2, g_5 = 2.2)$ [2]. Interestingly, the frequency of the LF component slightly varies from subject to subject in the obtained results. This is quite compatible with the physiological observations; different people exhibit the LF component with different power and at somewhat different frequency. Since in the model of Fig. 8.15 the identified kernels constitute the varying part of the model, it can be concluded that the shape of the sympathetic kernels are responsible for this discrepancy. However, variation in the delay of the sympathetic loop can also have a significant effect in practice (Section 7.5.1). Specifically, the time behaviour of the LF oscillation also depends on the identified kernels. Figure 8.17 displays a higher amount of nonlinearity in the LF oscillation for subject 3.

The power of the LF component greatly depends on the static open loop gain. If the gain g in the model increases (e.g g_5 from 2.2 to 2.8) the magnitude of the LF oscillation will also increase. This is also in accordance with the physiological observations as discussed in Chapter 7 and is further pictured here in Fig. 8.18 by taking the Volterra kernels into consideration [3].

[2] An additional block for removing the mean was also employed for the simulation to suppress any dc value produced in the BPV as a result of the Volterra nonlinearity. We recall that the operating point of the modified nonlinear element is zero. This block was also employed for all the simulations from now onward.

[3] A large increase in g causes instability in the model.



(a) (b)

Figure 8.18: Augmentation of the LF oscillation by increasing the open loop static gain for subject 5 ($g_5 = 2.8$).

Injection of the respiratory signal into the model also exhibits interesting features. If the entire model shown in Fig. 8.1 is excited by a sinusoidal respiratory signal with frequency $0.25Hz$ (15 breaths/min) and parameters $G_1 = G_2 = G_3 = 0$, $G_4 = 30$, $g = 1.5$ for subject 1 and $G_1 = G_2 = G_3 = 0$, $G_4 = 14$, $g = 2.3$ [4] for subject 5 then both the LF and HF components in the variability signals will appear. Together with the VLF component with frequency $0.02Hz$ and amplitude $3mmHg$, the presence of these components in Figs. 8.19 and 8.20 reveals that the simulated model behaves closely like the underlying physiological system. Figs. 8.21 and 8.22 display the distribution of the components in the actual variability signals when the subjects were breathing at a rate of 15 breaths per minute.

Further comparison of the actual results of Figs. 8.21 and 8.22 with the simulated results of Fig. 8.19 and 8.20 seems to be beneficial. Firstly, the respiratory component in all the BPV signals has a smaller amplitude than the LF component but with a smaller ratio in the simulated signals than the actual ones. Assuming $G_3 = 0$ in the model might be one reason. If a neuronal connection between the respiratory centre and the cardiac control centres exists, a similar link to the vasomotor centre can also be conceived. However, the lowpass nature of the sympathetic effector response might considerably weaken the appearance of this component in blood pressure. Following

[4] G_1, G_2 are assumed to be zero at this stage to exclude the LF centrogenic mechanism.

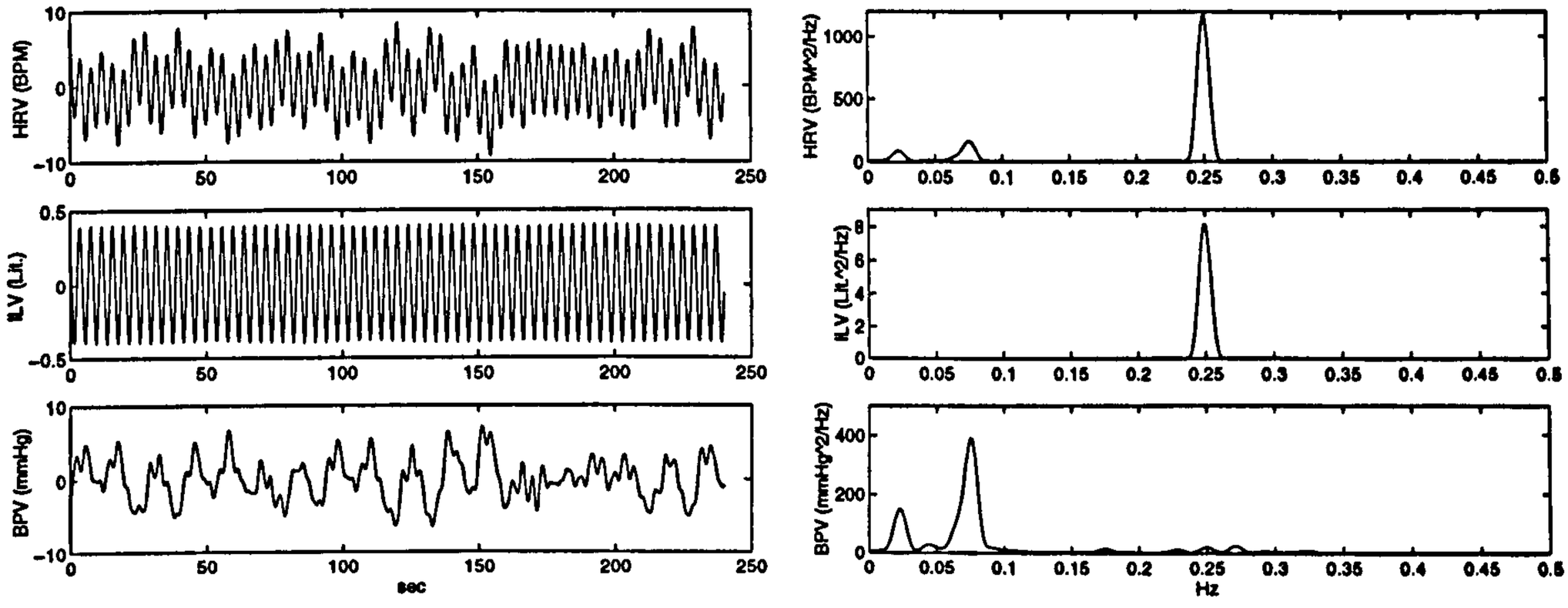


Figure 8.19: Presence of the HF, LF and VLF components in the simulated variability signals of the model of subject 1. Left hand column time behaviour, right hand column PSD. From top to bottom HRV, ILV and BPV.

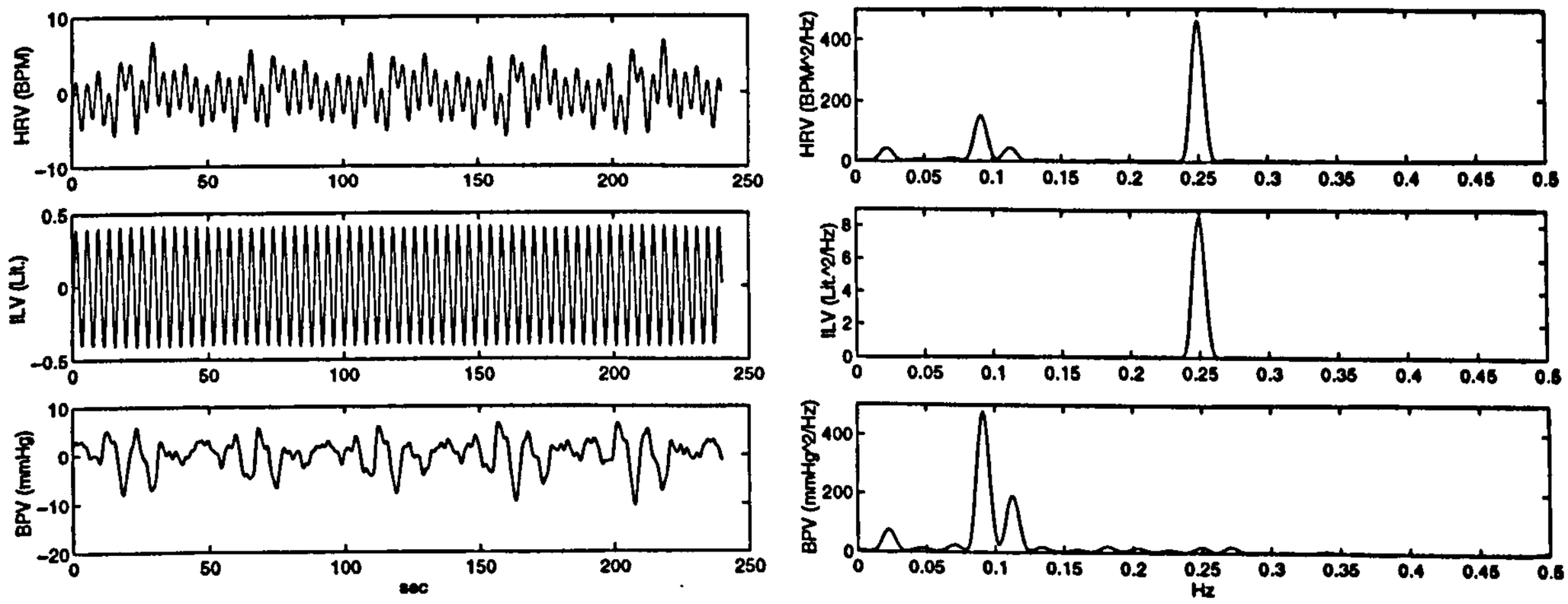


Figure 8.20: Presence of the HF, LF and VLF components in the simulated variability signals of the model of subject 5. Left hand column time behaviour, right hand column PSD. From top to bottom HRV, ILV and BPV.

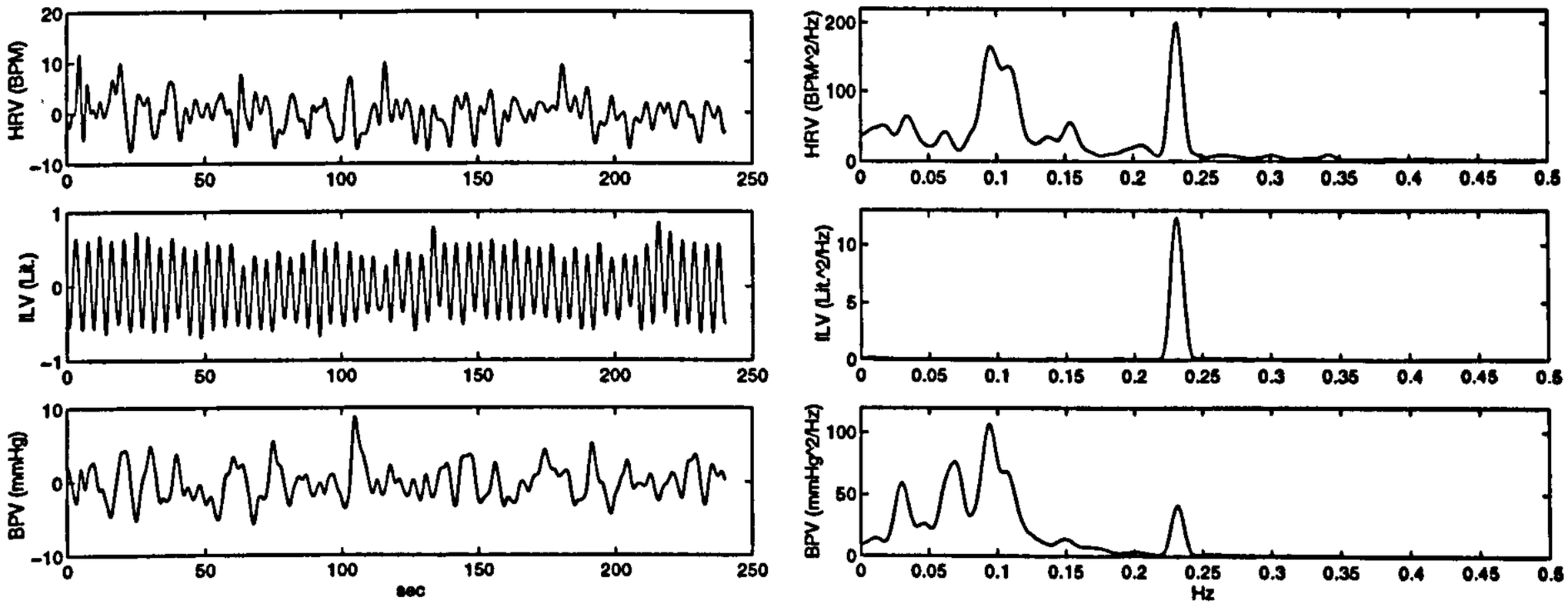


Figure 8.21: Time behaviour (left hand column) and PSD (right hand column) of the actual variability signals when subject 1 was breathing with rate 15 breaths/min. From top to bottom HRV, ILV and BPV.

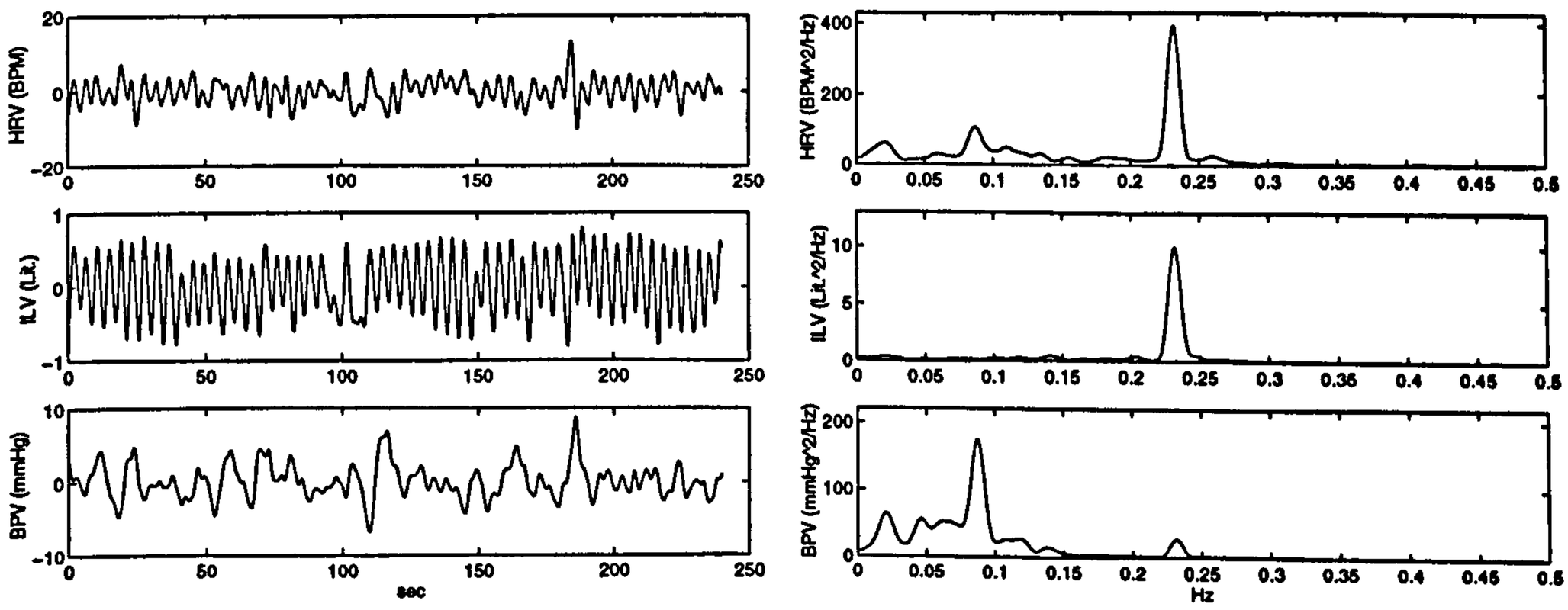


Figure 8.22: Time behaviour (left hand column) and PSD (right hand column) of the actual variability signals when subject 5 was breathing with rate 15 per minute. From top to bottom HRV, ILV and BPV.

the results obtained by Rosenbaum and Race (1968) it has been the general view that the sympathetic nervous system is too sluggish to transmit frequencies above $0.15Hz$. However, recent studies have shown that the vascular resistance can oscillate even in the respiratory band (Stauss & Kregel, 1996). This in turn means that the respiratory fluctuations can be directly induced by the vascular muscles to the blood pressure. Unfortunately, no specific value can be given for G_3 due to the lack of physiological data in this area.

While the simulated LF component for subject 5 has a frequency very close to the actual one, for subject 1 the dominant LF component in the actual signals shows a slightly higher frequency than the predicted result. A slight change in the parameters of the sympathetic loop from a random breathing pattern to a metronome breathing with a fixed frequency may explain this. An analogous change has been observed in response to a manoeuver from supine to tilt (Raymond, Mazumdar, Nandagapol, 1997). Another possibility might be the contribution of the centrogenic LF oscillator. To elucidate this latter hypothesis, the model of Fig. 8.1 was simulated with parameters $G_1 = 1$, $G_2 = 1$, $G_3 = 0$, $G_4 = 30$, $g = 1.4$, VLF: (Amp=0,f=0Hz), Centrogenic: (Amp=5,f=0.1Hz), Respiration: (Amp=0.35,f=0.25Hz) for subject 1 and $G_1 = 1$, $G_2 = 0$, $G_3 = 0$, $G_4 = 14$, $g = 2.3$, VLF: (Amp=0,f=0Hz), Centrogenic: (Amp=3,f=0.1Hz), Respiration: (Amp=0.4,f=0.25Hz) for subject 5 [5]. The results showing the presence of a new LF component are illustrated in Figs. 8.23 and 8.24. Interestingly, the feedback LF component is entrained by the centrogenic LF component. Whether this phenomenon happens in practice or not is still unclear but it has been anticipated by some authors (Koepchen, 1984; Langhorst *et. al.*, 1984). This observation is at least in favour of those physiologists who believe in the centrogenic LF oscillator rather than the feedback mechanism (Section 7.5.2). It can also be concluded that if the required conditions for producing the LF component through the feedback path are not available then the centrogenic mechanism may take over. On the other hand under circumstances in which the sympathetic regulatory mechanism is more active and/or the discharge pattern of the medullary neurones in the LF band is less pronounced then the feedback mechanism might be more effective. This feature of the model seems to be congruent with the physiological evidence on both sides; observation of the centrogenic

[5]The amplitude of the centrogenic oscillator has an arbitrary unit in the model. In the simulation its value has been selected in order to yield a relative power distribution between the observed components close to the experimental results.

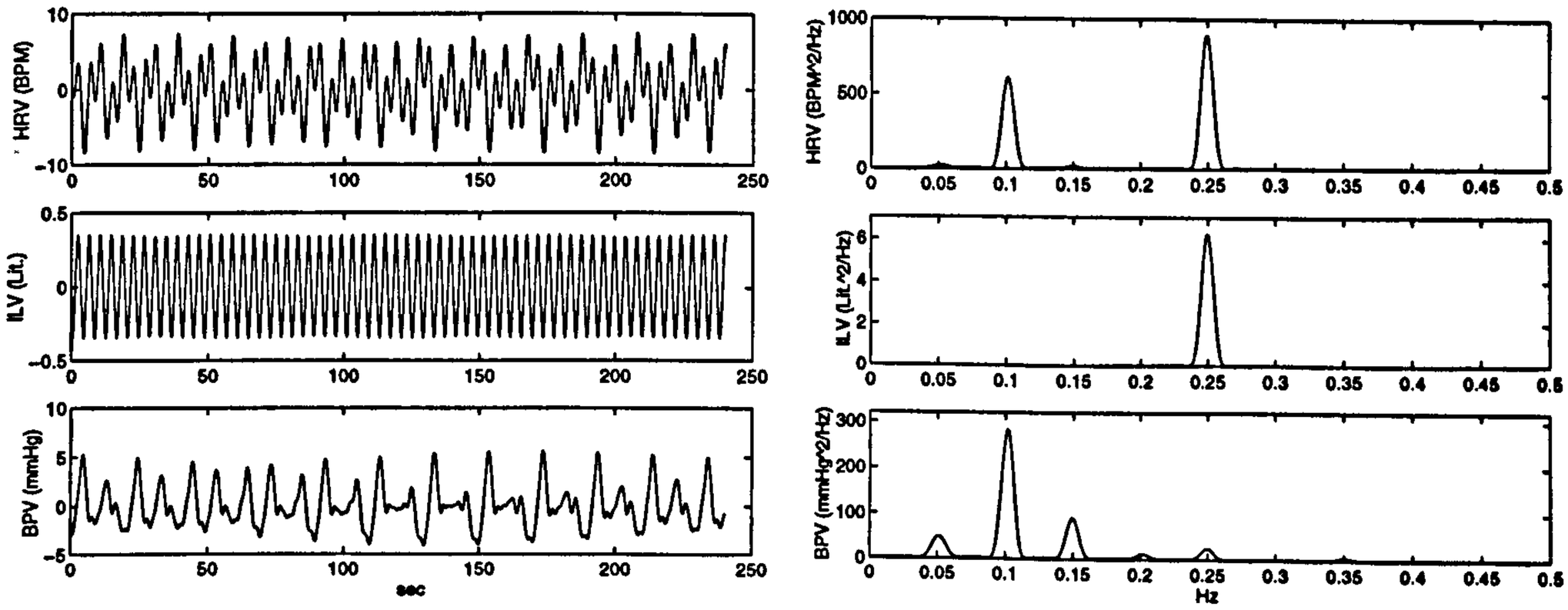


Figure 8.23: Time behaviour (left hand column) and PSD (right hand column) of the simulated signals for subject 1 when the centrogenic LF oscillator is active. From top to bottom HRV, ILV and BPV.

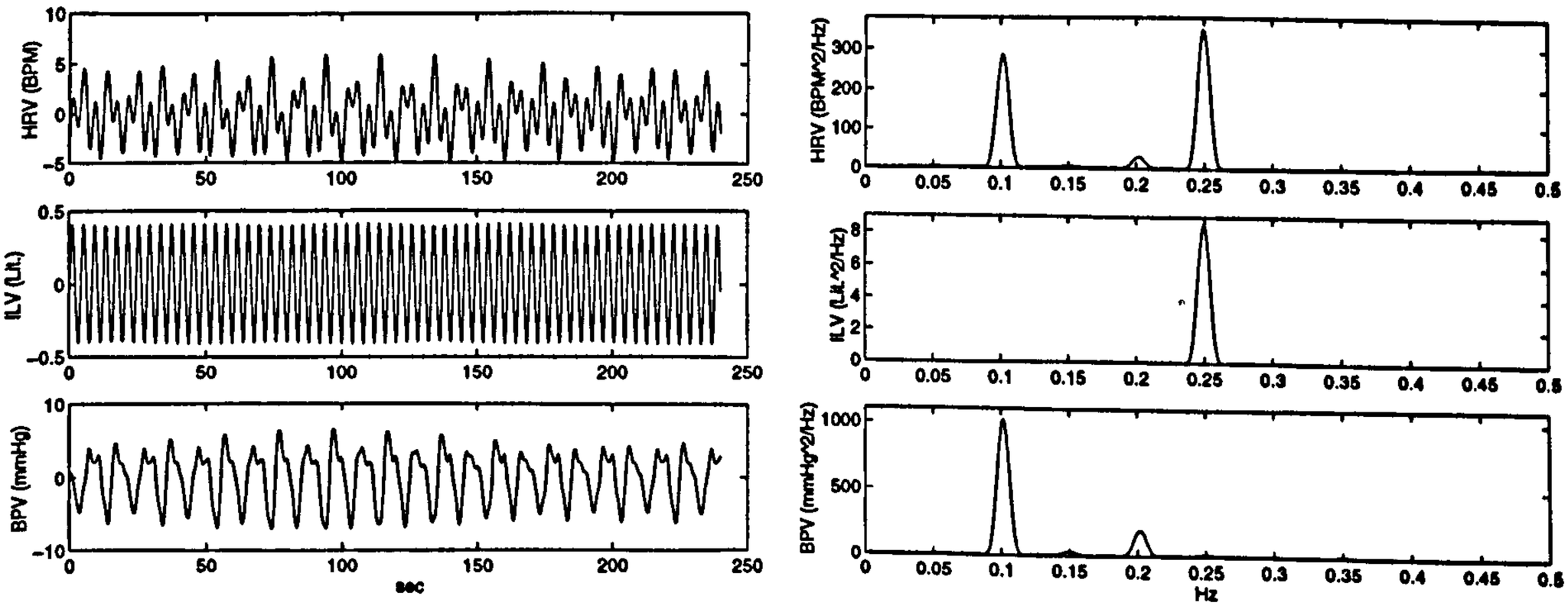


Figure 8.24: Time behaviour (left hand column) and PSD (right hand column) of the simulated signals for subject 5 when the centrogenic LF oscillator is active. From top to bottom HRV, ILV and BPV.

LF in some conditions and the feedback mechanism on other occasions, although no definite value can be offered for G_1 or G_2 at this stage due to the lack of physiological information.

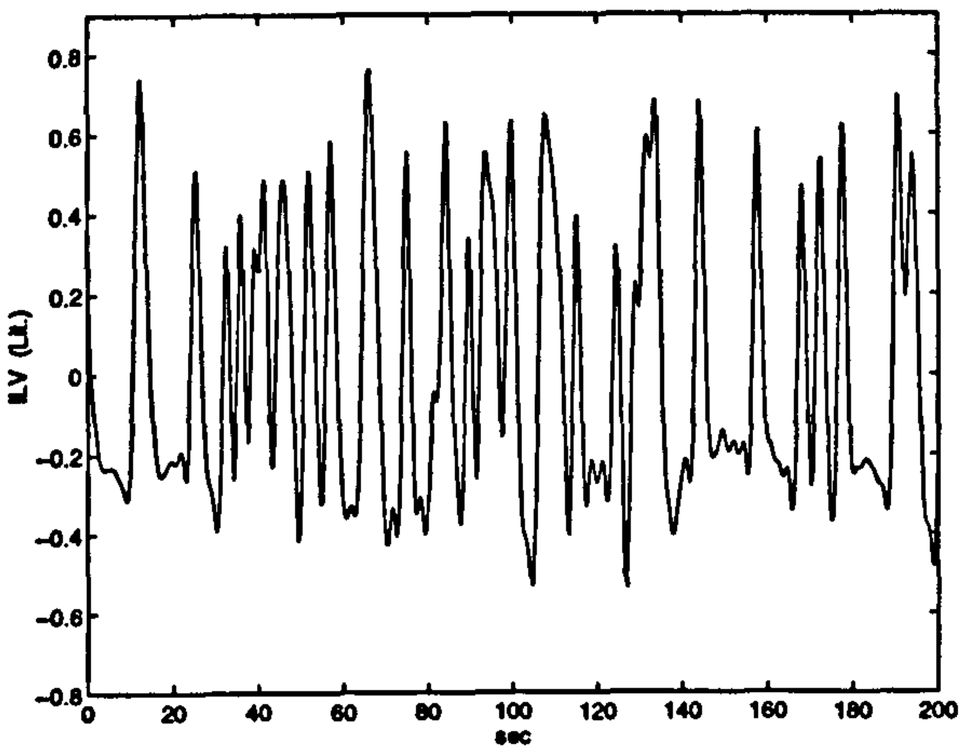
8.6 Simulation of the Model with the Actual ILV Signal

If the proposed model is a satisfactory representation of the interaction between the variability signals, it should be able to reproduce the experimentally observed fluctuations in HRV and BPV by injection of the actual ILV signal. This is indeed a tough challenge for the new model as the predicted signals are compared with the actual ones on an individual basis rather than on global behaviour. For this purpose, the model of Fig. 8.1 with parameters $G_1 = G_2 = G_3 = 0$, $G_4 = 30$, $g = 1.1$ for subject 1 and $G_1 = G_2 = G_3 = 0$, $G_4 = 14$, $g = 2.1$ for subject 5 was simulated with injection of the actual respiratory signal (random breathing pattern) for each subject, respectively. Since no *a priori* information about the activity of the centrogenic oscillator or the VLF component was available all the corresponding gains were assumed to be zero. The predicted signals superimposed on the actual signals are shown in Fig. 8.25. As can be seen the predicted signals generally follow the actual ones fairly well although considerable differences can also be observed. Needless to say, numerous disturbances not included in the model but present in the actual system, together with the existence of unmodelled parts of the system are responsible for the observed differences. In such a complex model, reaching this level of agreement may still be regarded as a satisfactory achievement.

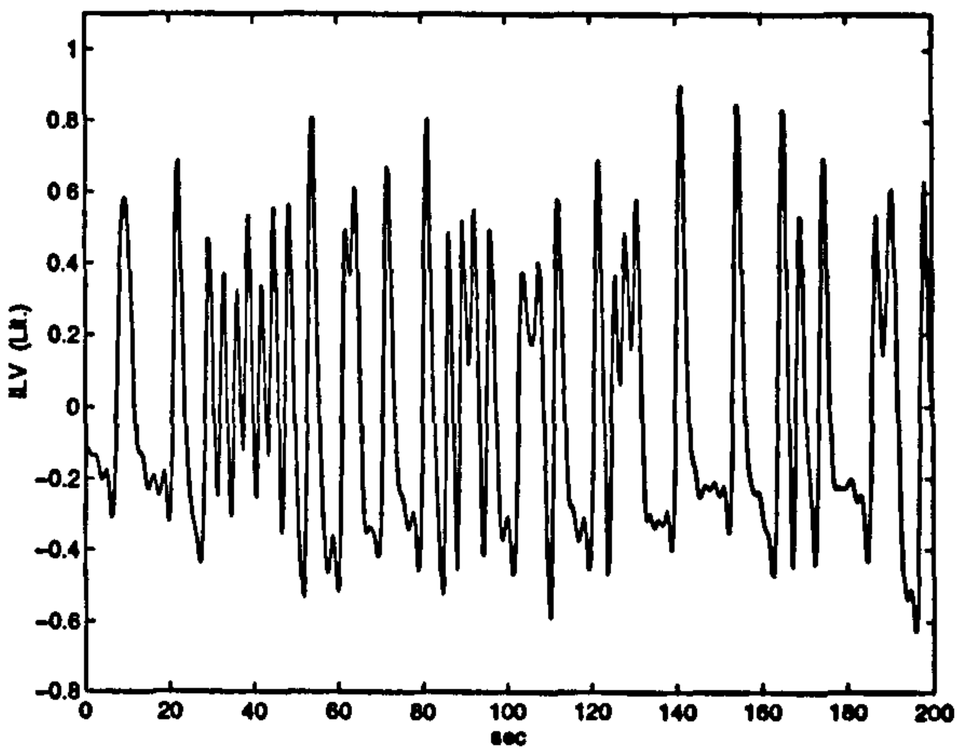
8.7 Performance of the Model in Spectral Domain

Since inspection in the spectral domain has been the major source for previous investigations of the HRV-ILV-BPV relationships, it would be advantageous here to evaluate the performance of the proposed model in the frequency domain, although the identification method used in this study is basically a time domain technique.

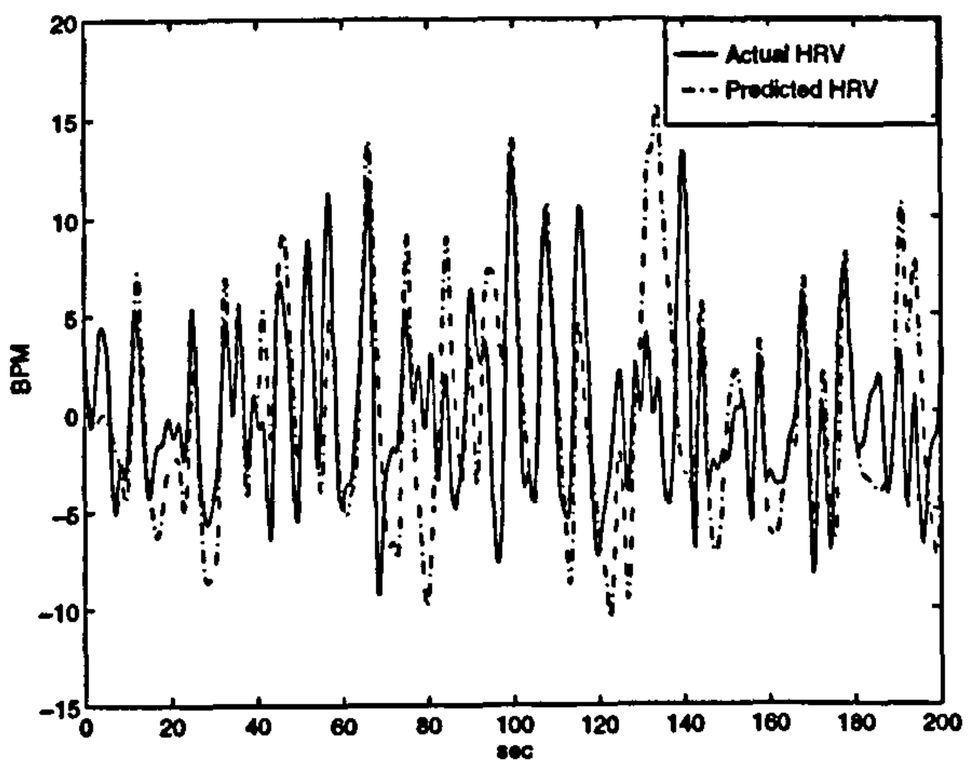
In order to produce a broad band synthetic respiratory signal close to the actual



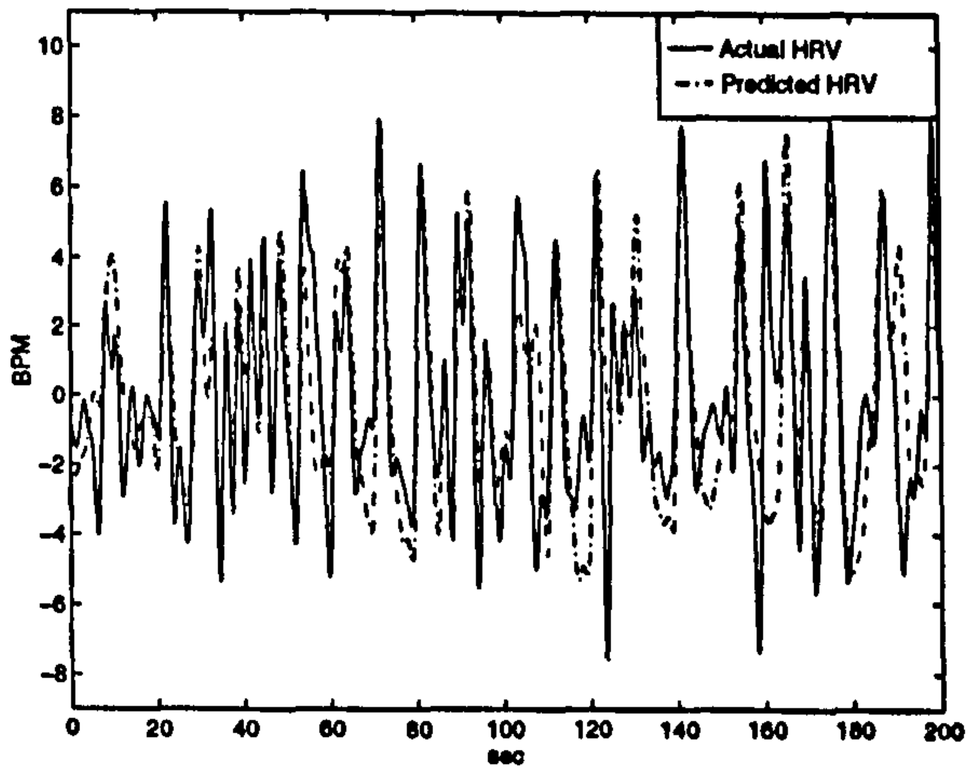
(a)



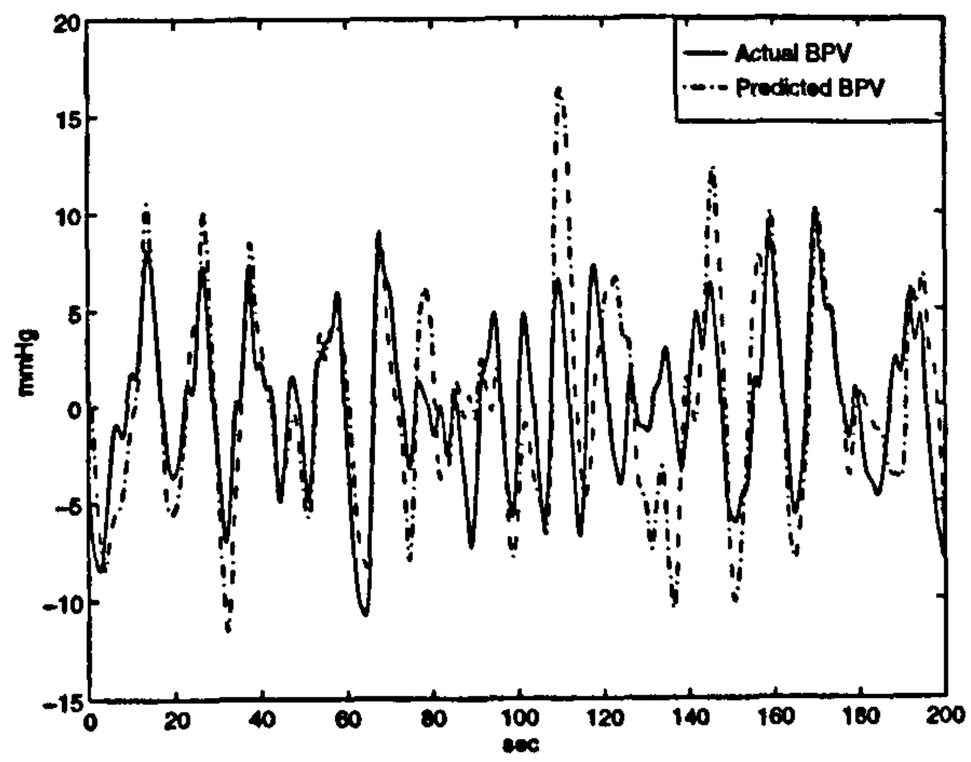
(b)



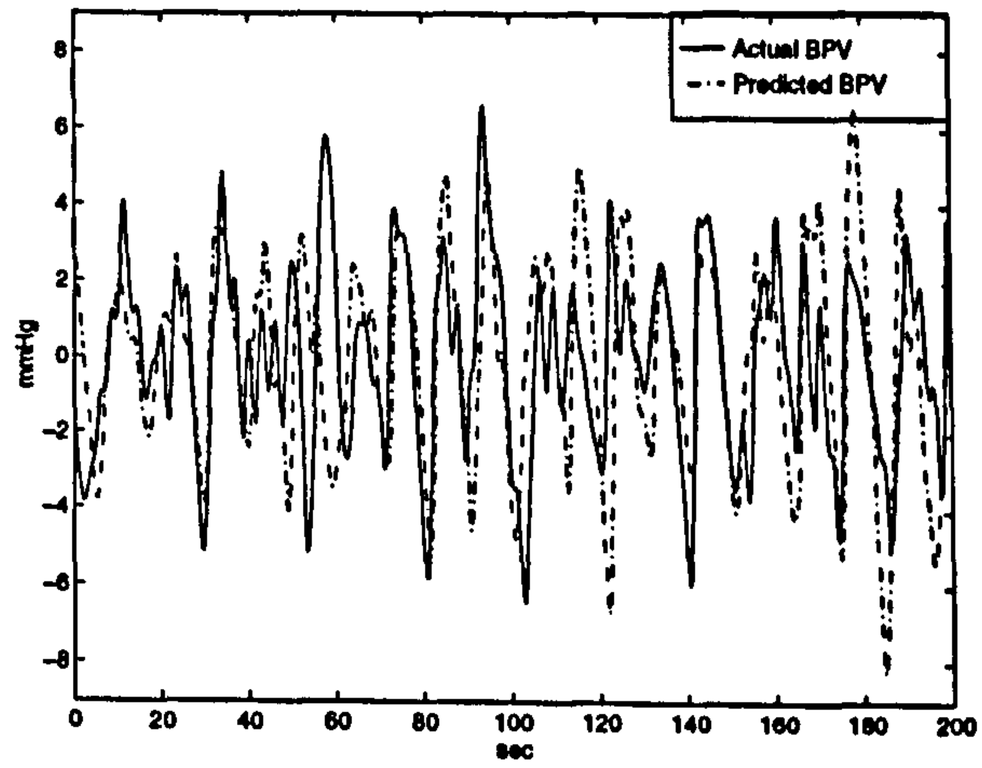
(c)



(d)



(e)



(f)

Figure 8.25: Simulation of the proposed model with the actual ILV signal. Left hand column subject 1, right hand column subject 5. From top to bottom ILV, HRV, BPV.

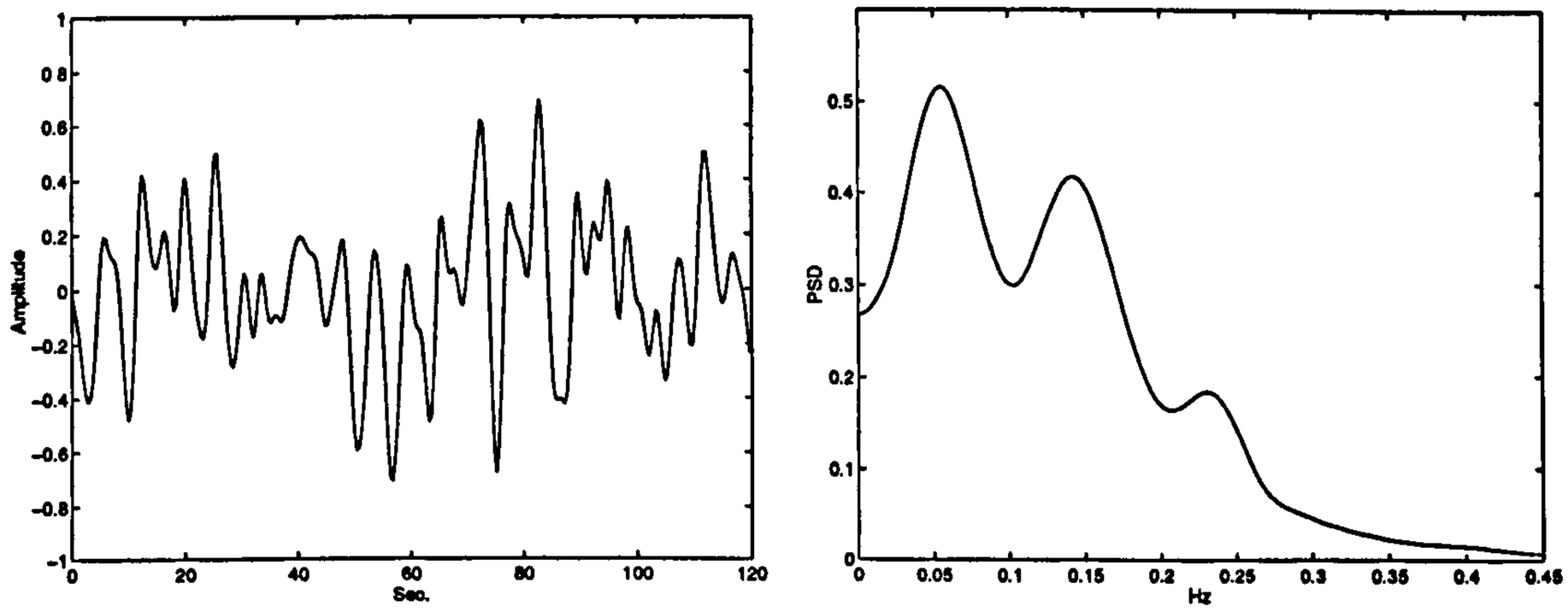
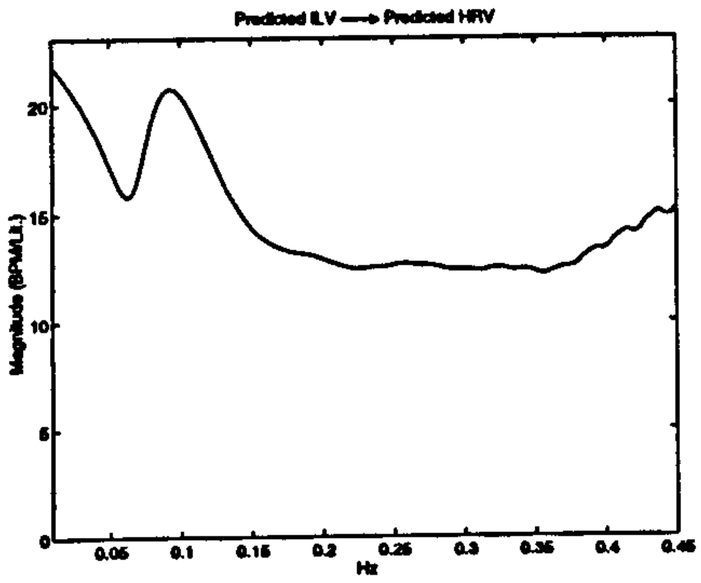


Figure 8.26: Time behaviour and power spectral density of the synthetic respiratory signal used for the simulation in spectral domain.

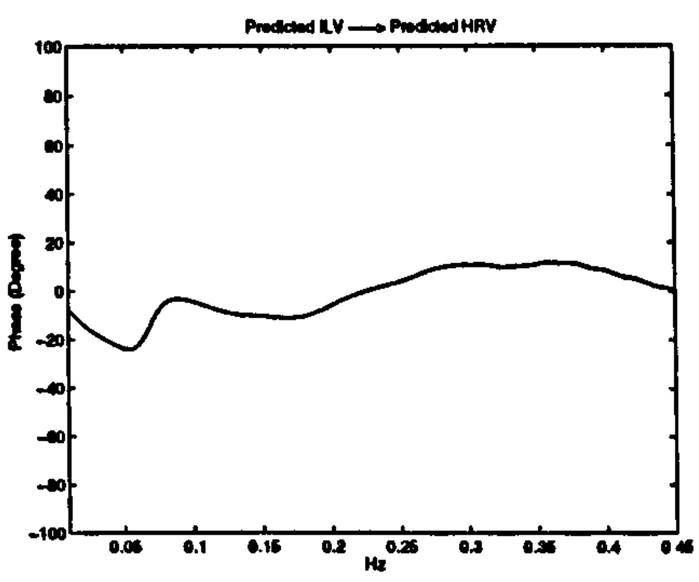
one, a uniform distributed random process in the range $[-0.5 \;\; 0.5]$ was passed through an FIR filter (Hamming) with order 40 and pass band $[0.02Hz \;\; 0.45Hz]$. Since the actual respiratory signal exhibits a decreasing magnitude with increasing frequency (Figs. 8.2(a) and 8.3(a)) the output signal of the above filter was subsequently fed to a second FIR lowpass filter with order 10 and cutoff frequency $0.1Hz$. Figure 8.26 displays this simulated signal along with its PSD. The obtained signal was then rescaled to mimic the actual respiratory signal. The proposed model of Fig. 8.1, with the parameters assumed in Section 8.6, was simulated with this synthetic respiratory signal. The transfer functions between each two variability signals (HRV,BPV,ILV) was estimated according to equation (3.10) together with the coherence function. For the sake of comparison similar procedures were employed for both the simulated (predicted) signals and the actual signals. Figures 8.27, 8.29 and 8.28, 8.30 depict the estimated (predicted) and the actual transfer functions for subject 1 and subject 5, respectively.

A close similarity between the simulation results and the experimental results can be observed in most cases. Specifically, the experimental results in Figs. 8.28 and 8.30 are quite consistent with the results obtained by Saul *et. al.* (1989, 1991) [6]. These authors also employed the random breathing pattern for the same purpose. However, unlike them, there is no intention here to present any conclusion about the relationships between ILV, HRV and BPV from the spectral estimations, since identification in the spectral domain poses severe limitations in closed loop systems (Söderstrom & Stoica

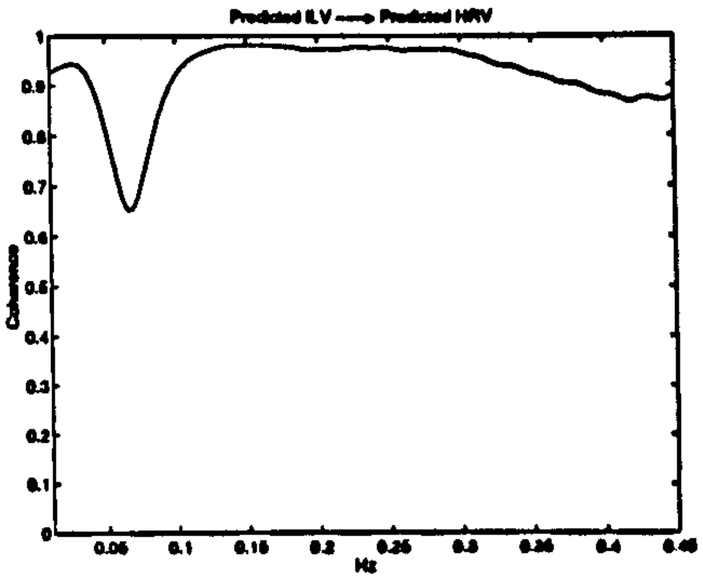
[6] A detailed discussion about the interpretation of these transfer functions can be found in the paper by Saul *et. al.* (1991). Here the aim is only to evaluate the performance of the proposed model in predicting the experimental results in the spectral domain.



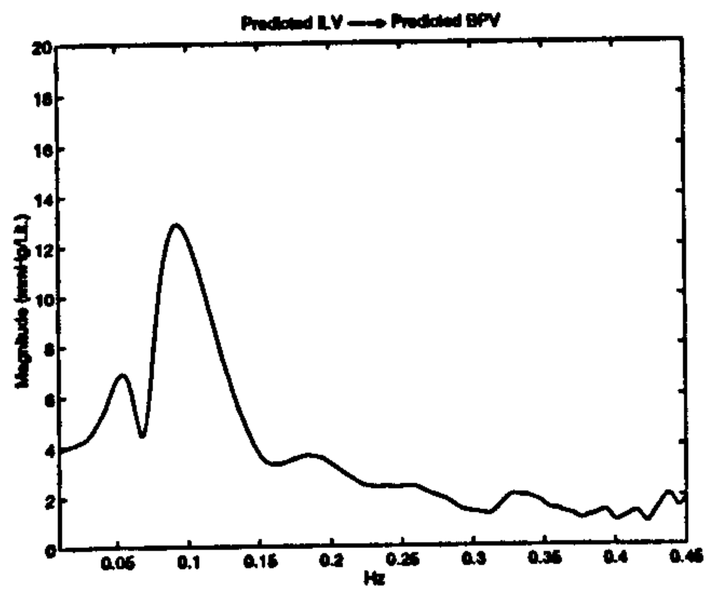
(a)



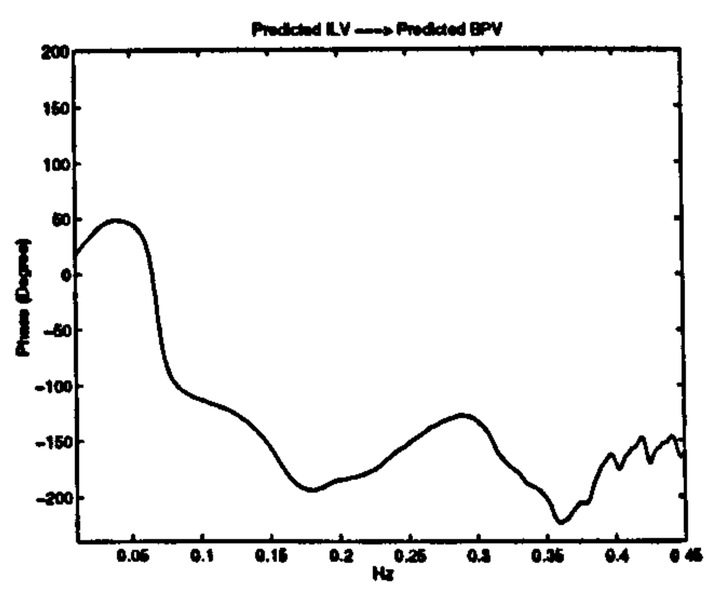
(b)



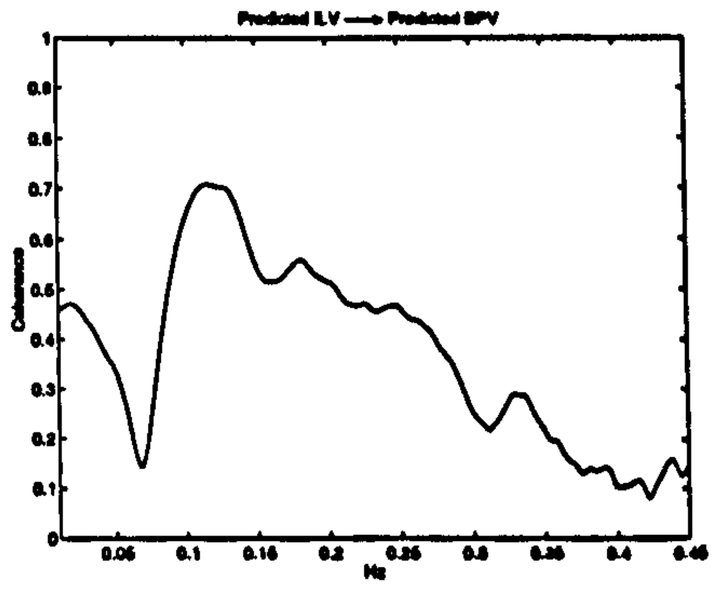
(c)



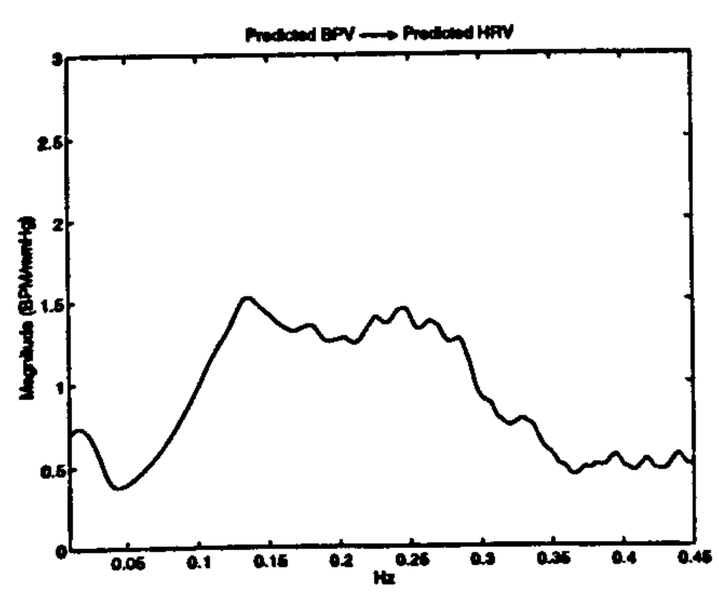
(d)



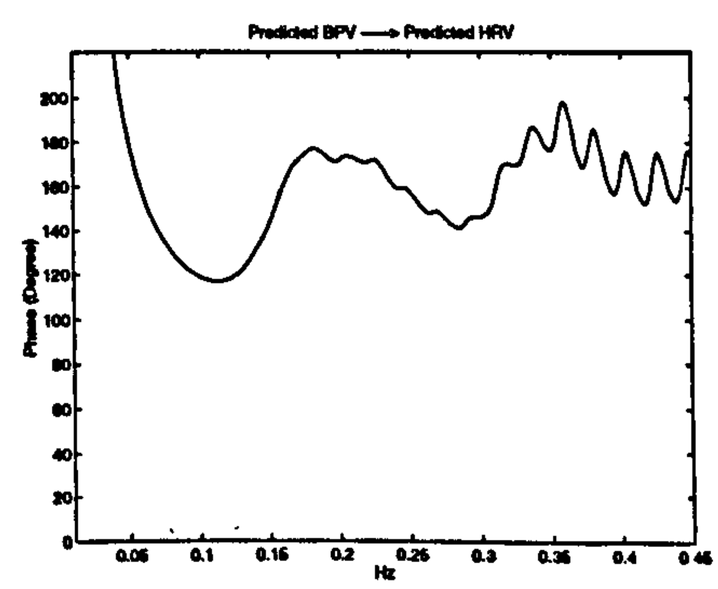
(e)



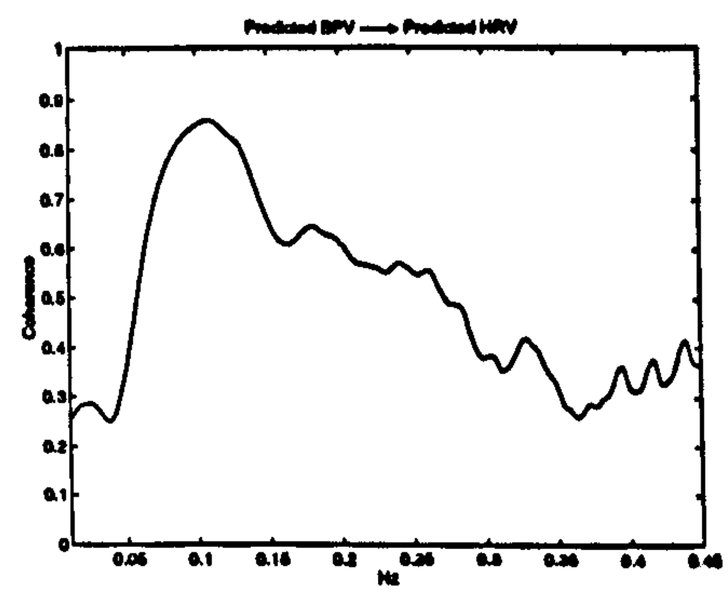
(f)



(g)

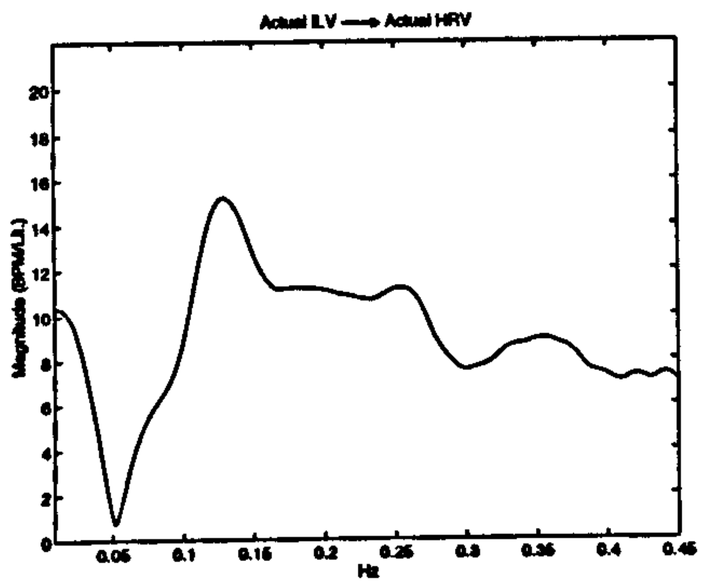


(h)

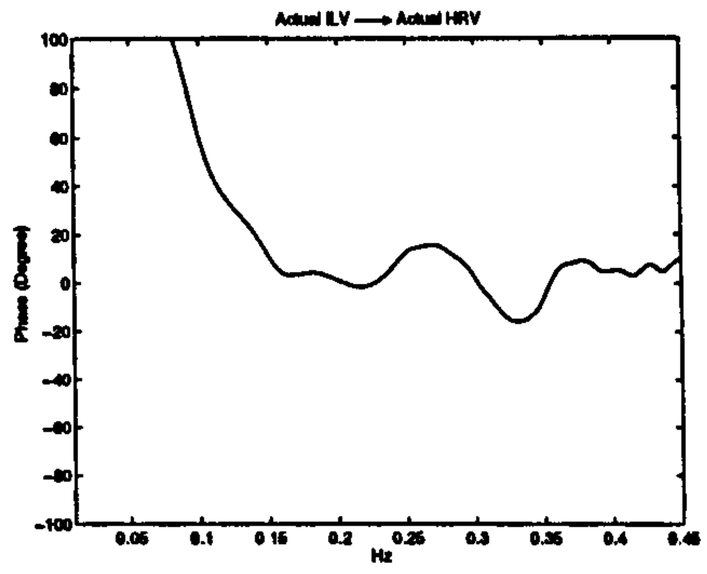


(i)

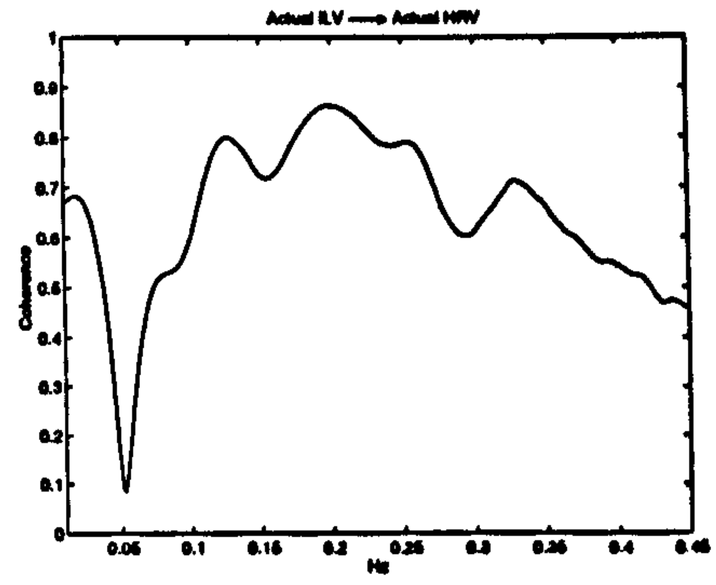
Figure 8.27: Predicted transfer functions for subject 1. Left hand column magnitude, middle column phase and right hand column coherence function. From top to bottom (ILV to HRV), (ILV to BPV), (BPV to HRV).



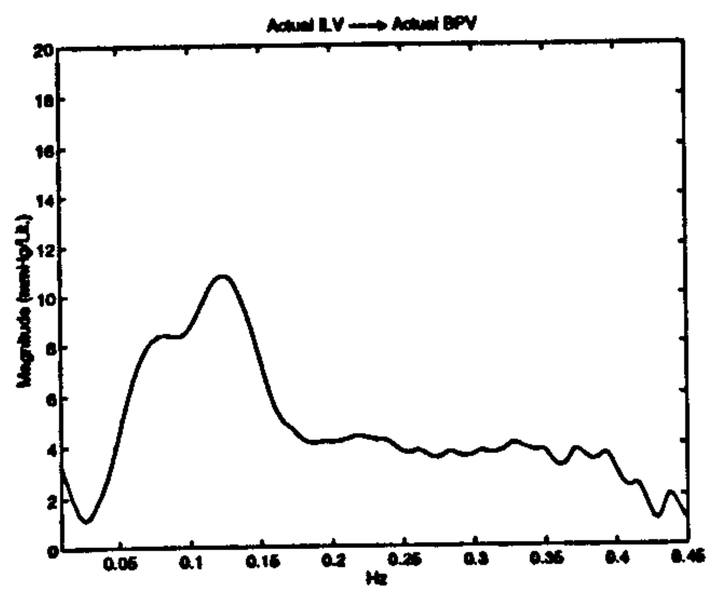
(a)



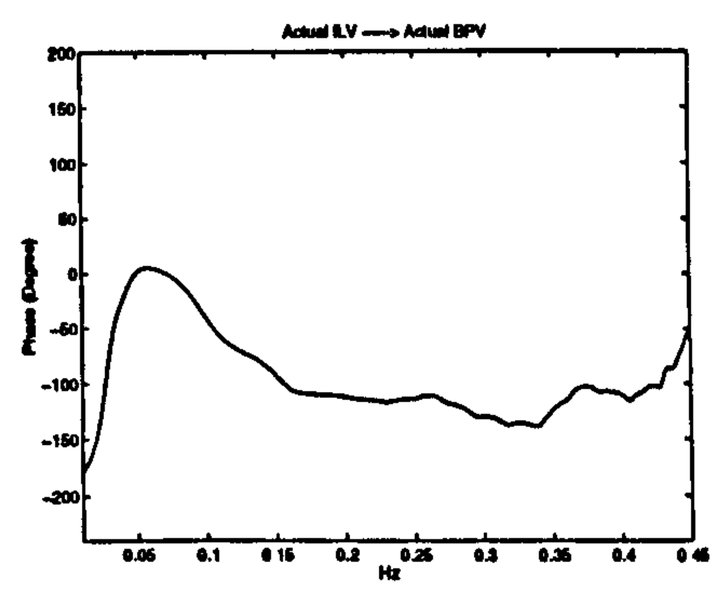
(b)



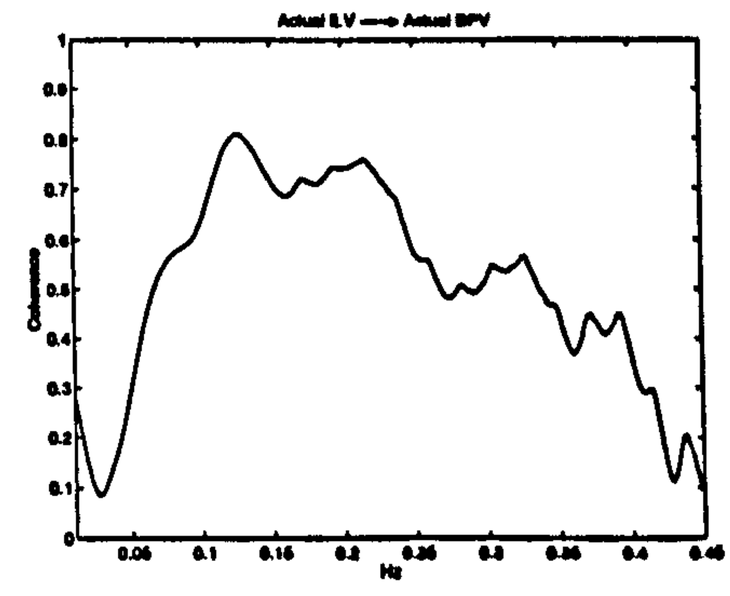
(c)



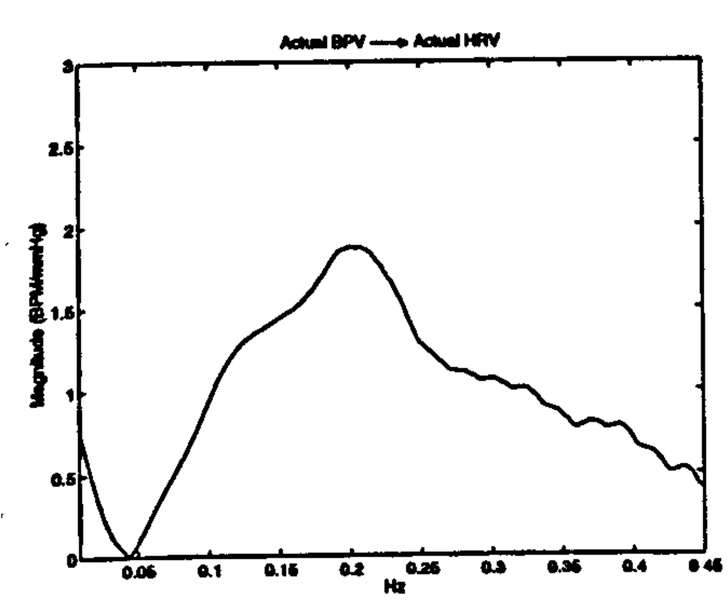
(d)



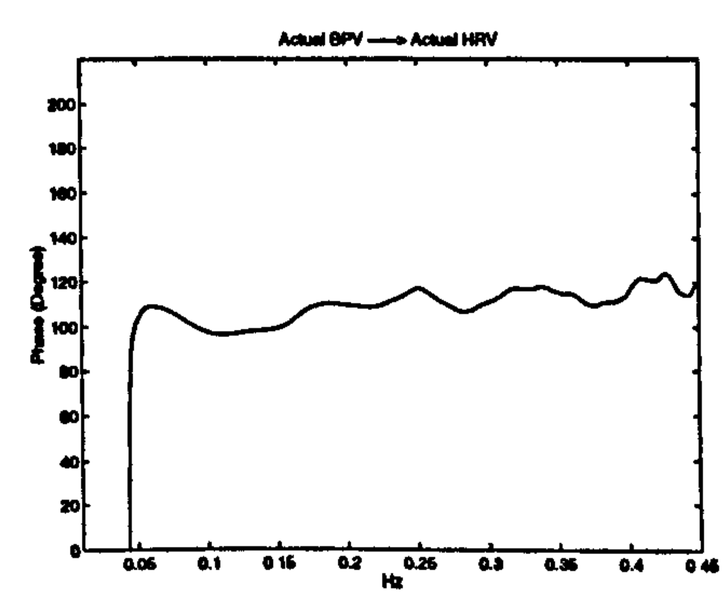
(e)



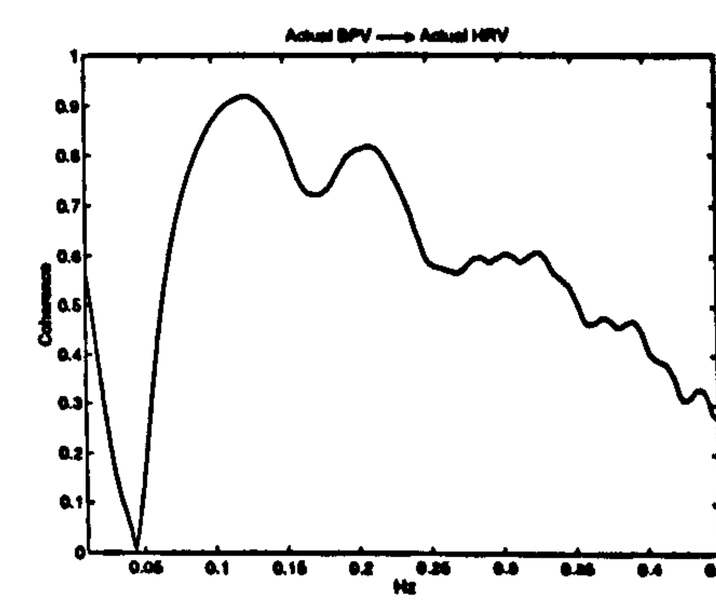
(f)



(g)

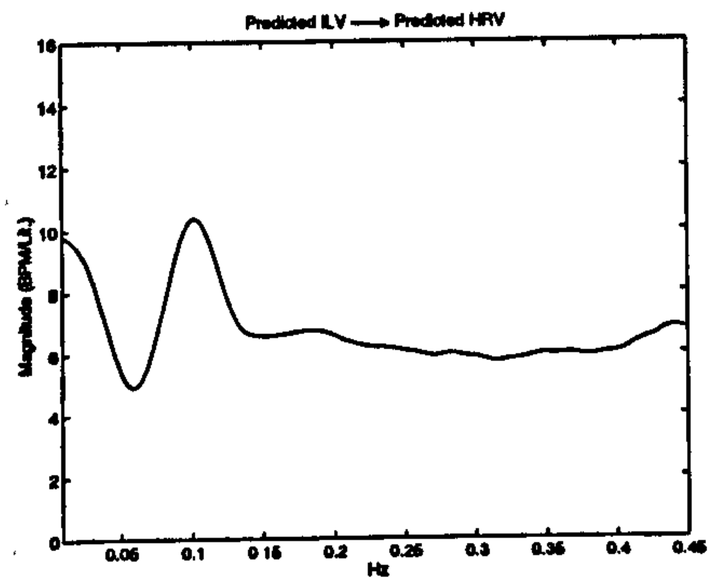


(h)

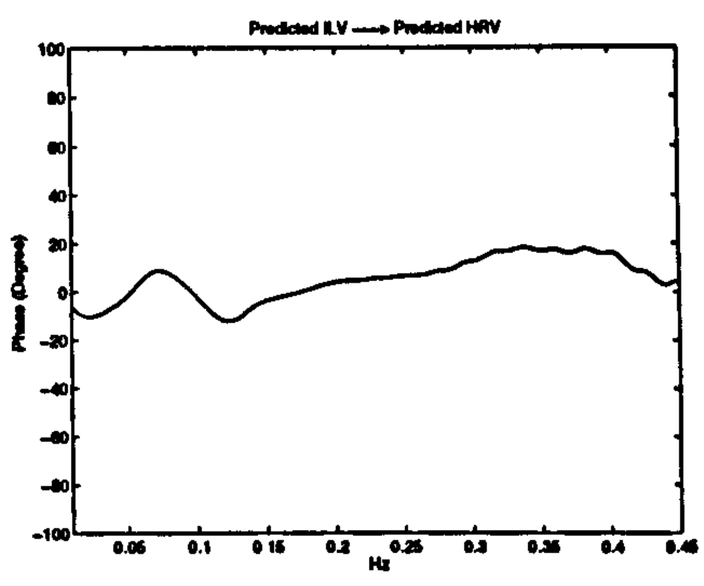


(i)

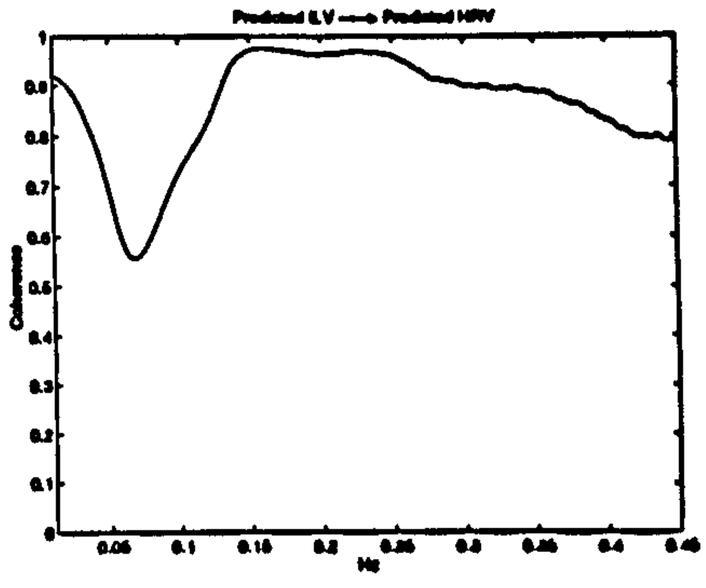
Figure 8.28: Actual transfer functions for subject 1. Left hand column magnitude, middle column phase and right hand column coherence function. From top to bottom (ILV to HRV), (ILV to BPV), (BPV to HRV).



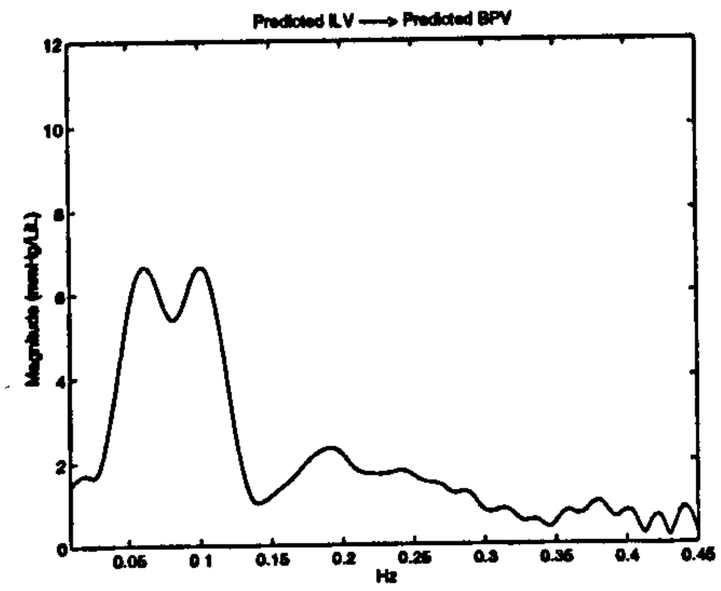
(a)



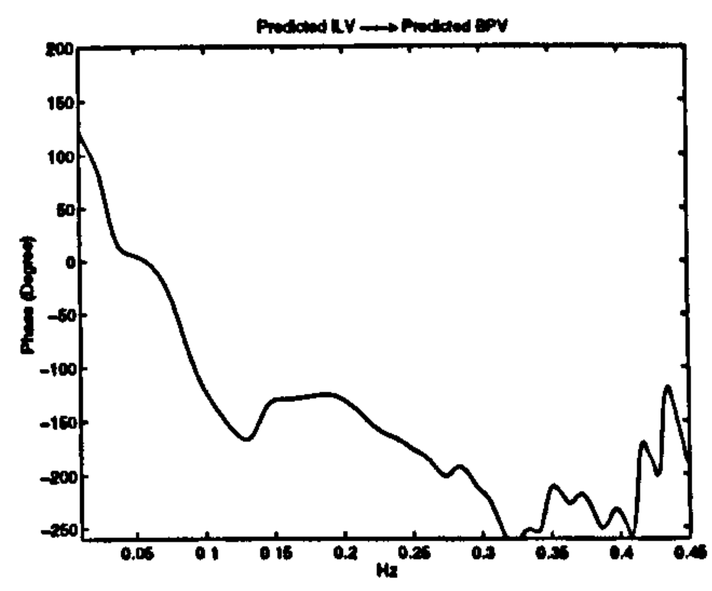
(b)



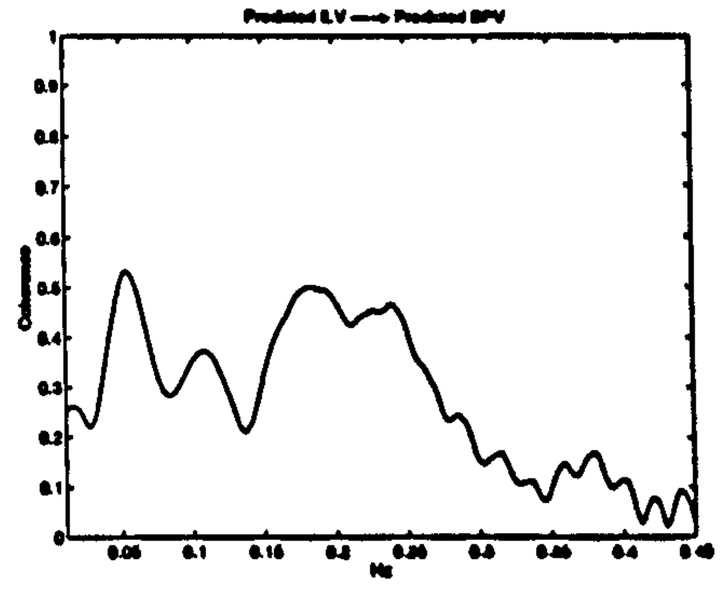
(c)



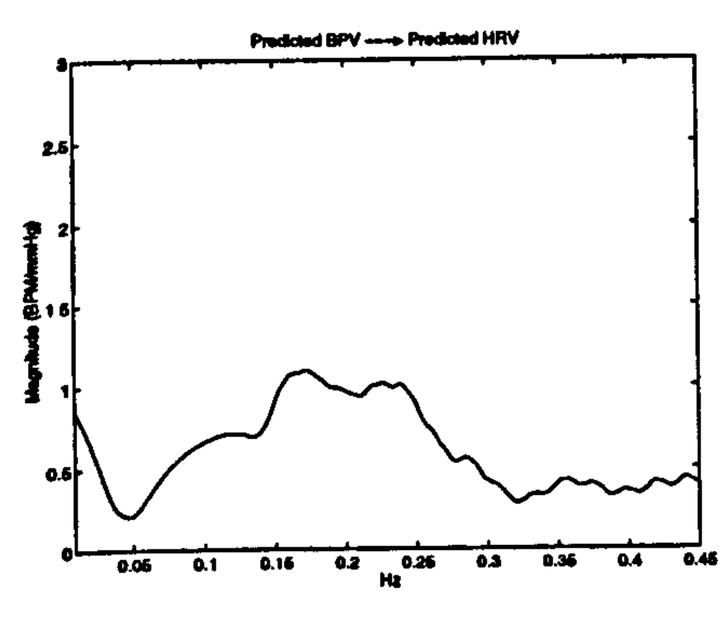
(d)



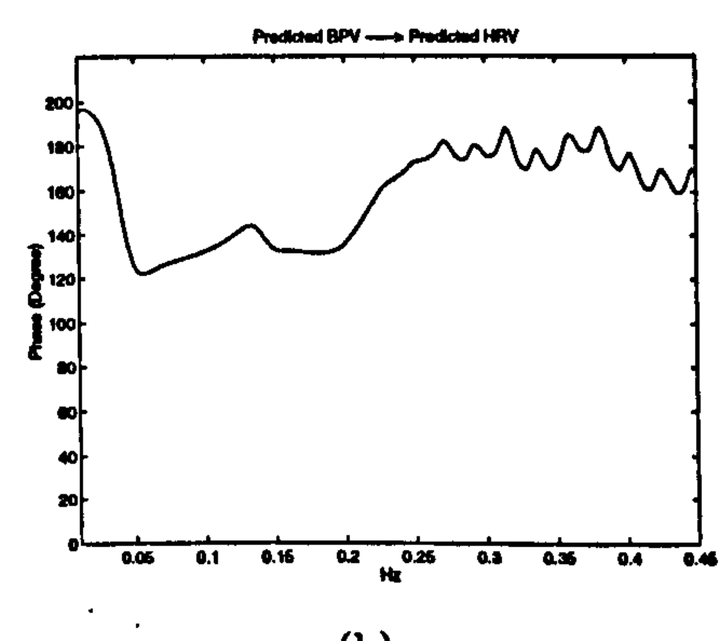
(e)



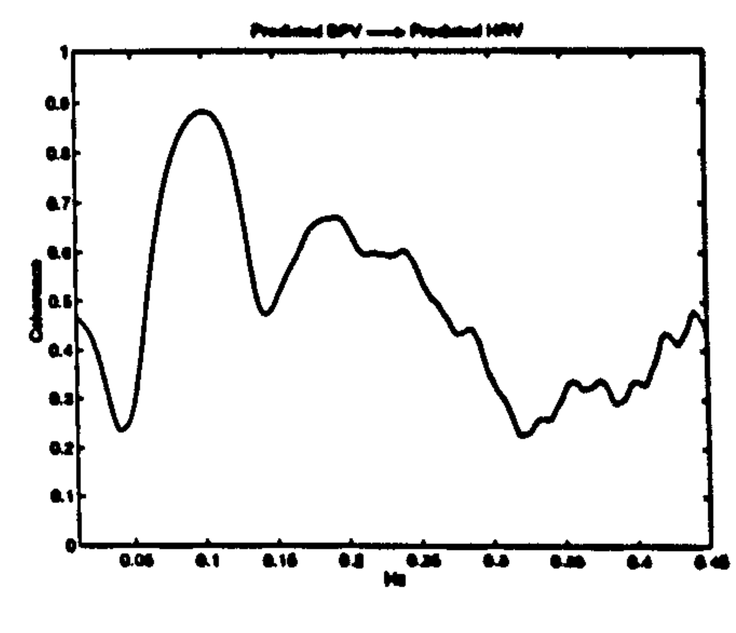
(f)



(g)

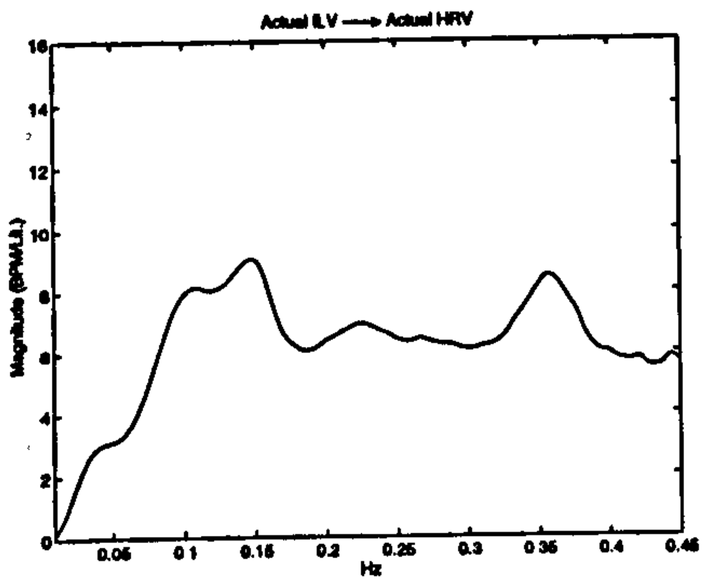


(h)

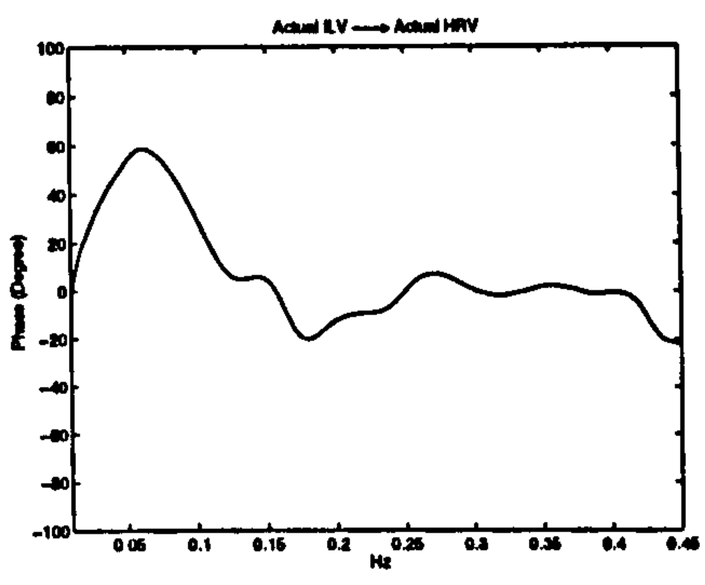


(i)

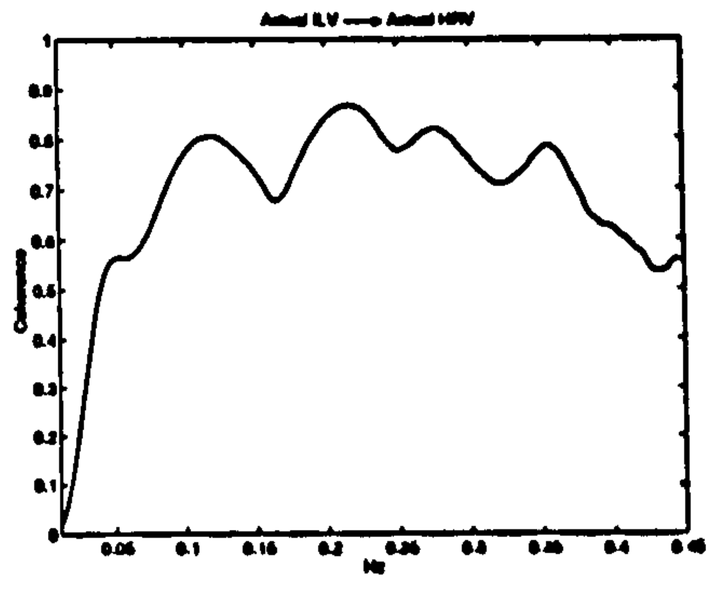
Figure 8.29: Predicted transfer functions for subject 5. Left hand column magnitude, middle column phase and right hand column coherence function. From top to bottom (ILV to HRV), (ILV to BPV), (BPV to HRV).



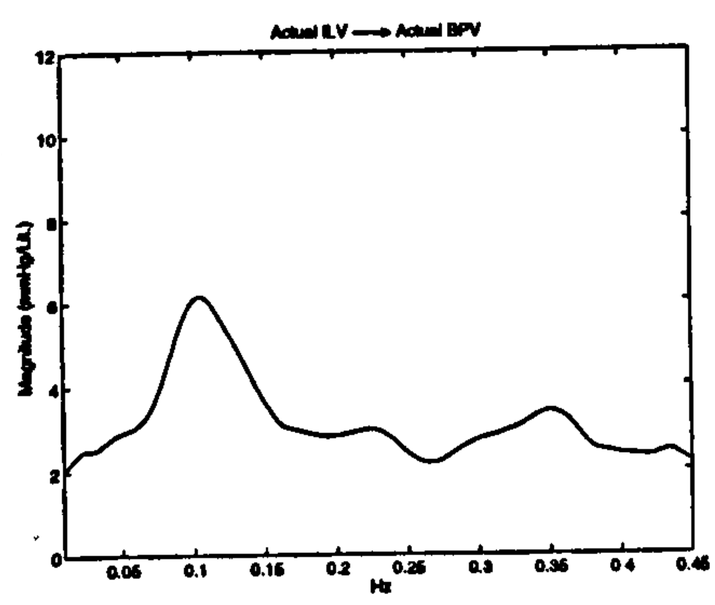
(a)



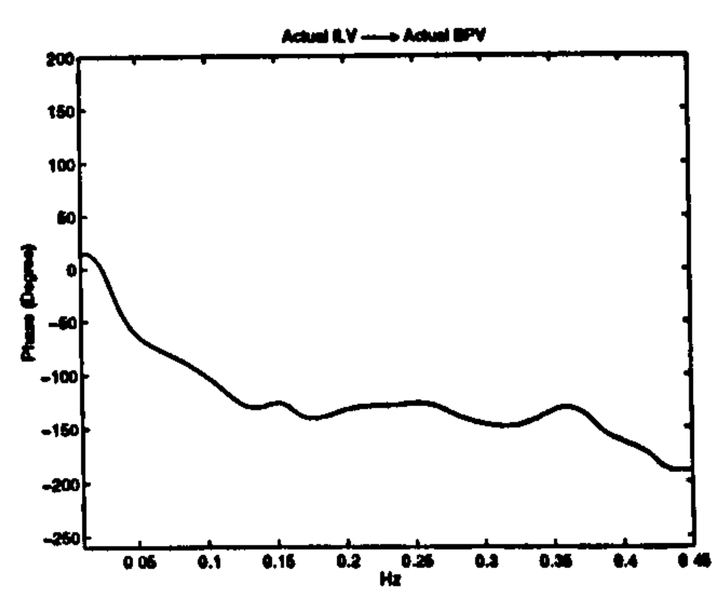
(b)



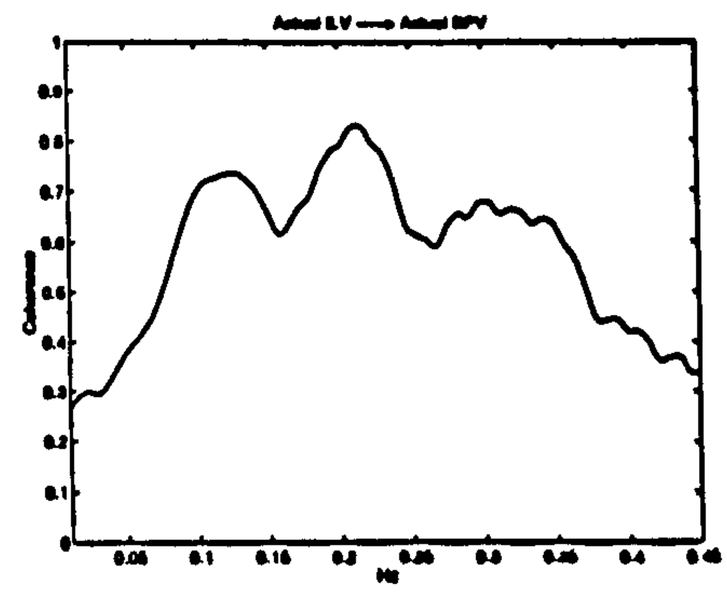
(c)



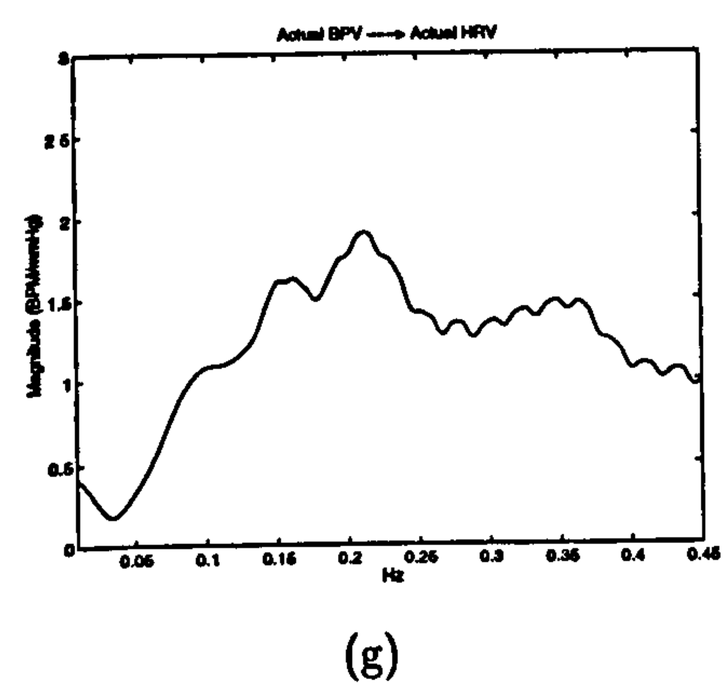
(d)



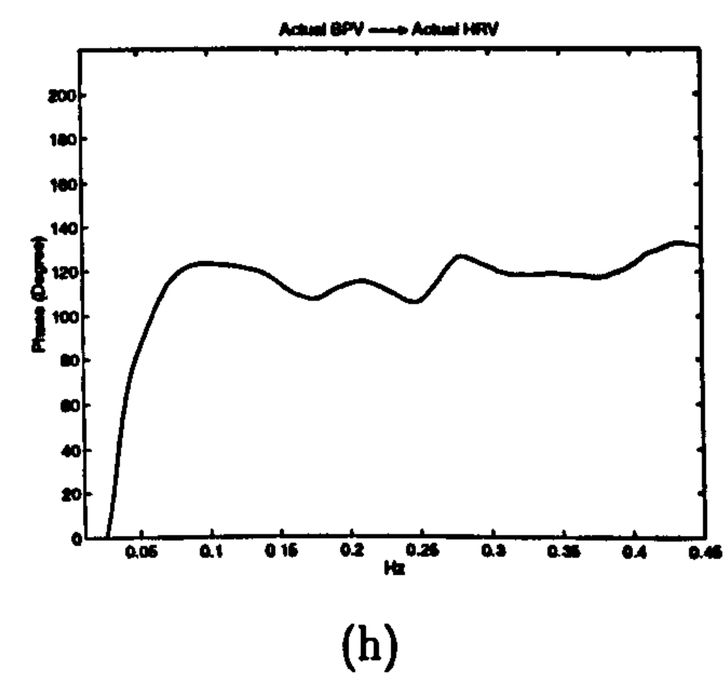
(e)



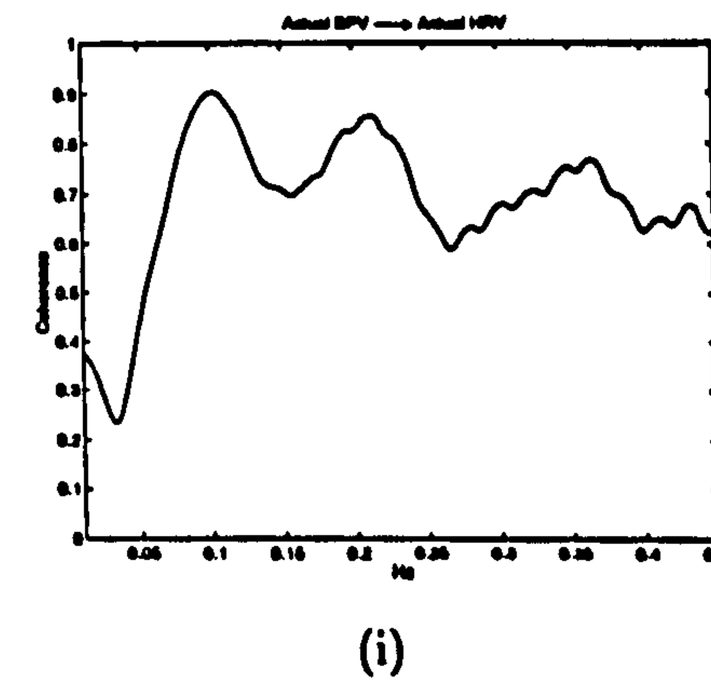
(f)



(g)



(h)



(i)

Figure 8.30: Actual transfer functions for subject 5. Left hand column magnitude, middle column phase and right hand column coherence function. From top to bottom (ILV to HRV), (ILV to BPV), (BPV to HRV).

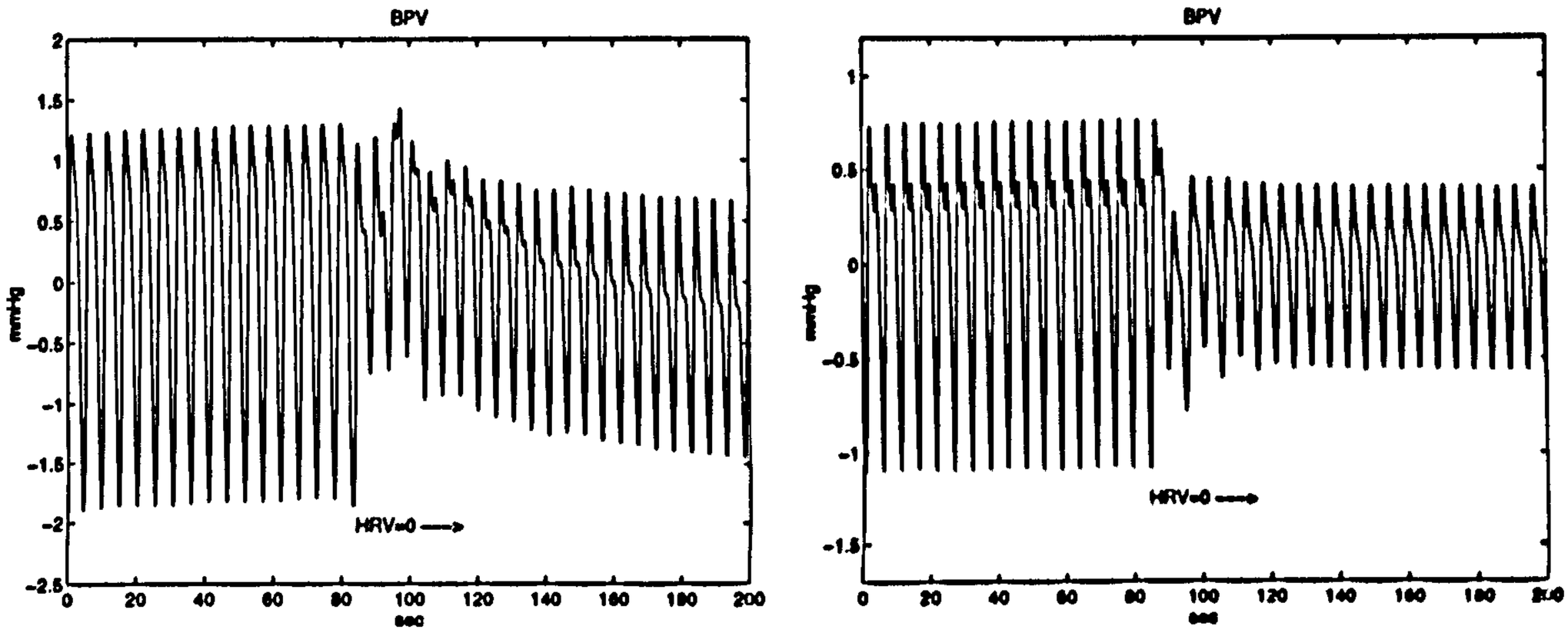
1989).

The lowpass filter characteristic in the magnitude response of all the transfer functions is evident from the figures. This property has also been reported by many other investigators among them Triedman & Saul (1994); Hirsch & Bishop (1981) and Eckberg (1983). The magnitude of the predicted transfer function between ILV and HRV, however, has a less steep slope than the actual magnitude and it even increases in slope at the end. This might indicate that the actual vagal transfer function differs from the one estimated by Mokrane *et. al.* (1995) which was used in this study. It might even suggest that a second order transfer function should be employed instead of having an all pass feature for higher frequencies as described in Section 7.2.

Investigation of the phase plot also seems to be important. While the actual phase plot demonstrates a negative phase, very close to zero for the ILV-HRV relationship, the predicted phase plot illustrates a positive phase very close to zero. The presumed central link between the respiratory oscillator and the cardiac control centre can be introduced for this small, but debatable, difference. In the proposed model a straight path *via* the gain G_4 has been assumed to transfer the respiratory modulation to the cardiac centre. However, if a small delay between the respiratory oscillator and the cardiac control centre exists then the predicted phase plot will shift slightly downward.

Although not entirely supported by the experimental results in Fig. 8.28 and 8.30, a small positive phase has been obtained between ILV and HRV by Saul and Berger and other researchers in the MIT group (Triedman & Saul, 1994; Saul *et. al.*, 1991; Yana, Saul, Berger, Perrot, Cohen, 1993; Chon *et. al.*, 1996). These investigators believe that there is an anticausal relationship between the respiratory oscillator and the associated variation in the heart rate *i.e.*, the HRV leads the ILV in the respiratory band. The proposed model seems to give a solution to this controversial matter. Clearly, no anticausal system has been employed in the proposed model [7]. Hence, there is no need for having an anticausal system in the brain stem to produce a slight positive phase. Furthermore, it is hard to believe that the HRV has an anticipatory feature with respect to respiration.

[7] Even by disconnecting the mechanical modulation of the SA node to suppress the influence of the differentiator no significant change in the phase plot was observed.



(a) (b)

Figure 8.31: Fixing the heart rate in the model causes a reduction in the respiratory fluctuation of the BPV. (a) Subject 1, (b) subject 5.

8.8 Influence of HRV on BPV in the Respiratory Band

To complete the earlier discussion about the relationship between HRV and BPV in the respiratory band, the blockade of the SA node was simulated in the proposed model with the parameters employed in Section 8.6. A sinusoidal respiratory signal with frequency $0.2Hz$ (12 breaths/min) was injected into the model while the nonlinearity of the NL element was eliminated ($M = 0$) to suppress the interference of the LF component. After recording the blood pressure variability in the steady state condition, the connection of the HRV to the heart and vasculature block was broken to imitate the cardiac pacing experiment. The change in the BPV for two subjects following this manoeuver is illustrated in Fig. 8.31. Reduction of BPV to almost half its size shows that the HRV participates in inducing the respiratory fluctuation in BPV. Although in the intact state any fluctuation in BPV produces a compensatory effect on the SA node through the baroreceptors and the sign inversion in the brain stem (blood pressure regulatory mechanism), the net effect of the SA node appears to be augmentation of the respiratory component in BPV due to the central respiratory modulation of the cardiac control centres. This prediction of the model favours those physiologists who believe in modulation of the cardiac centres by the respiratory oscillator rather than

the secondary effect following the mechanical modulation of BPV by respiration.

8.9 Discussion and Conclusion

The purpose of implementing the combined theoretical and experimental approach outlined in this chapter and the previous chapter was to construct a mathematical model for describing the observed fluctuations in the variability signals and their mutual interactions. With the aid of the random breathing pattern a nonlinear identification procedure was applied to the heart and vasculature to determine the linear as well as the nonlinear interactions between Symp., BPV, HRV and ILV. The employed Laguerre expansion technique (LET) revealed the contribution of second order nonlinearity in the underlying physiological system. Although the presence of higher order nonlinearities is also possible (Chapter 5), they were ignored in this study due to their much smaller contributions and the computational load.

In an earlier study by Chon and Cohen, the LET was employed to identify the Volterra kernels of a hypothetical system with ILV and BPV as inputs and HRV as the output (Chon *et. al.*, 1996). However, this configuration contradicts the physiological dictation of the actual system (Fig. 8.1). Instead, the structure which was assumed in this study for the heart and vascular sympathetic modulation in cooperation with the closed loop regulatory mechanism of the blood pressure as well as the contribution of the brain stem factors would lead us to a much more realistic form of the problem.

The question which naturally arises in connection with the nonlinear identification approach is whether it is worth tolerating the cost of a laborious procedure instead of using a much simpler linear methodology. Certainly, ignoring the significant nonlinear terms will cause significant bias in the estimated linear transfer functions. It may appear even worse if any physiological interpretations are to be inferred from the obtained results. It has been the intention of this study to employ the nonlinear analysing methods to alleviate this problem. On the other hand the prominent features of the LET greatly mitigate the overwhelming work normally required by other nonlinear methods.

In regard to the influence of respiration on HRV and BPV, the findings of the

proposed model indicate that the central respiratory oscillator plays a great role. Modulation of the heart rate *via* the neuronal pathways in the brain stem (denoted by G_4 in the model) is eventually transmitted to the blood pressure and is added to the direct mechanical modulation of respiration. This result is entirely consistent with Saul *et. al.*'s conclusion (1989, 1991). These investigators found that the fluctuations of the arterial blood pressure which occur with respiration are due to both the mechanical thoracic coupling and the effects of respiratory induced fluctuations of the heart rate. With elimination of HRV, these authors observed a reduction in the transfer magnitude between ILV and blood pressure indices for most of the frequency band.

One reason for this same outcome might stem from utilising a random breathing pattern in both experiments. It has been shown that mandatory breathing shifts the sympathovagal balance towards the vagal side (Pagani *et. al.*, 1988; Malliani *et. al.*, 1991). However, this assertion has been opposed by some authors (Patwardhan, Evans, Bruce, Eckberg, Knapp, 1995). The contribution of the cerebral centres in mandatory breathing might also be important in augmenting the central respiratory modulation (de Burgh Daly, 1995). In summary, it can be concluded that when HR fluctuations arise from direct central nervous modulation of autonomic activity and are large, such as occurs in the normal resting dog (Akselrod *et. al.*, 1985) or in mandatory breathing in humans, the feedforward from heart rate to arterial pressure has an important role in BPV whereas when the mechanical influence of respiration is larger, such as occurs in the standing position, then the HRV finds only a secondary role (Taylor & Eckberg, 1996; Parati *et. al.*, 1987).

Whether the central respiratory influence is simply mediated through constant gains as assumed here (G_4, G_3) or *via* more complex structures, cannot be easily determined. In the linear parametric models, the transfer relation between HRV and ILV is obtained by finding a set of unknown parameters (Mullen *et. al.*, 1997; Baselli *et. al.*, 1988; Mainardi *et. al.*, 1997). However, this transfer function models the entire path including the autonomic efferent pathways and the SA node. Moreover, the result is dependent upon the employed technique (bi-variate, tri-variate) and the configuration and the number of parameters (Barbieri, Bianchi, Triedman, Mainardi, Cerutti, Saul, 1997; Matsukawa & Wada, 1997).

It is also useful here to point out that although the influence of lung stretch

receptors on RSA was not included in the model, their integrative mechanism could have contributed to the respiratory modulation in the brain stem (de Burgh Daly, 1995). If so, G_4 could not only represent the depth of central respiratory modulation but also could denote the strength of vagal inhibition following lung inflation (de Burgh Daly, 1995; Hainsworth, 1974). This can also present a satisfactory explanation for the observation of a large central modulation of the RSA for this set of experiments.

In the LF band the proposed model exhibits very attractive features. It can explain the presence of a sustained LF oscillation, the alteration of the LF power with the state of the autonomic response, the entrainment phenomenon, and the alternating role of the centrogenic oscillator and the LF feedback mechanism, all without employing a bizarre structure.

The results predicted by the model are also in substantial agreement with the physiological observations obtained in unanaesthetised cats by Di Rienzo, Parati, Castiglioni, Omboni, Ferrari, Ramirez, Pedotti and Mancia (1991) and Di Rienzo, Castiglioni, Parati, Mancia and Pedotti (1996). These investigators found that sinoaortic denervation increased total BPV power and decreased total HRV power. The reduction of HRV power was paralleled by significant reductions in all the frequency components. In contrast, the increase in BPV power was accompanied by a marked increase in the VLF power, a decrease in LF power and almost no change in HF power. According to our proposed model sinoaortic denervation has three major effects. It breaks the LF feedback generating mechanism, blocks the transmission of the VLF component from the BPV to the other parts, and prevents the respiratory fluctuation of blood pressure from reaching the SA node. As a result, the model predicts a marked decrease in all the components of the HRV. However, part of RSA will still remain due to central respiratory modulation. On the other hand, it is predicted by the model that the lack of the buffering effect of heart rate on blood pressure will cause a large increase in the VLF band and a mild decrease in the HF band on BPV. In the mean time the LF component in the BPV should decrease greatly due to suspension of the feedback loop particularly when no contribution from the LF centrogenic oscillation is assumed. All these results are quite close to what have been obtained by Di Rienzo *et. al.* as described above.

Benefits aside, there are also some drawbacks in the proposed model. Firstly, the

model allocates most of the existing nonlinearity in the actual system to the heart and vascular sympathetic modulation; nonlinearities in the other segments are not taken into account (except the modified nonlinear element in the brain stem). This may cause bias in the estimated kernels, particularly in a feedback nonlinear system. Secondly, the model is very sensitive to the static open loop gain; a small increase in g (3 instead of 2 for example) may produce instability in the system ($BPV >\approx 8mmHg$). One reason for this observation might lie in the fact that the operating range of the model is limited to this amount of BPV and that the kernels were identified within this range ($HRV_{max} \approx \pm 10BPM$, $BPV_{max} \approx \pm 10mmHg$). Another conceivable reason might be the linear range of the modified nonlinear element (NL) in the brain stem model. For larger values of BPV (e.g. $|BPV| > 10mmHg$) a decrease in the slope of the linear part (α in Fig. 7.7(b)) towards saturation limits the BPV and gives better stability to the system. However, this behaviour needs physiological justification. Furthermore, the model does not assume separate mechanisms for the central respiratory modulation and the reflex from the lung stretch receptors.

Comparison of the experimental results with their counterparts obtained from the computer simulations is also promising. While certain features of the model are kept fixed, a reasonable adjustment in the other components is allowed in order for the model to adapt itself to the physiological differences observed in different subjects. However, the presented model is certainly not the final word on this topic and more aspects should be added when new ideas in physiological experimentation or modelling techniques are made available.

Summary of the Chapter

Having been examined by different procedures, the proposed model appears to be a valid mathematical representation for the physiological system underlying the generation of the rhythmical fluctuations in heart rate and blood pressure. Validated by the experimental results, the model

(i) exhibits the presence of significant nonlinear interaction between the variability signals,

(ii) shows that the central link between the respiratory oscillator and cardiac control centres plays an important role in producing RSA as well as the respiratory fluctua-

tions in BPV,

(iii) illustrates that both the feedback mechanism and the centrogenic LF oscillator can be responsible for generation of the LF component in HRV and BPV,

(iv) demonstrates the complexity involved in the brain stem in generating and mediating the variability signals.

These achievements were obtained at the operating point assumed in this study, namely resting supine position in a mandatory random breathing experiment.

Chapter 9

Overall Conclusions and Future Work

The observed fluctuations in heart rate and blood pressure are not random; they are meaningful rhythmical fluctuations which reflect useful information about autonomic regulation. The objective of this study was to present a mathematical representation to describe these rhythmical fluctuations in terms of the interconnections of appropriate systems. Like any other model, the aim of the presented model was to obtain a deeper understanding of the underlying physiological system, together with providing convincing explanations for the origin of the observed fluctuations and their relationships in a structured manner.

Confined by the technical methods available, the approach taken here was to employ suitable methods of analysis without sacrificing the realistic features of the problem in hand. This approach dictated the specific tools utilised here, although they were mostly involved with sophisticated concepts imposed by the nature of the underlying system. The employed techniques were chosen following a conceptual consideration of the problem. This strategy prompted us to begin the analysis with some preliminary steps such as definition of the variability signals. One needs to have a clear definition of the involved signals before applying any method of analysis. Most of the signal processing and system identification techniques rely on continuous state time series signals. It would be, therefore, a great benefit if all the variability signals could be defined in this form. Unlike the respiratory signal, heart rate needs an appropriate operation for conversion to such form. Even extraction of the blood pressure variation from the instantaneous arterial blood pressure requires some care.

In Chapter 2 the IPFM model was invoked to obtain a continuous state time series signal for the HRV. The IPFM representation for modelling of the SA node and specifically the lowpass filtering method for extracting the HRV signal have already been used by previous authors. However, the approach presented in Chapter 2 was a rigorous analysis to describe the coding and decoding mechanism of the IPFM model and its features. Using this model, a general scheme for extraction of the HRV from the R-wave signal was presented. It was clearly shown why the lowpass filtering method can elicit a well defined HRV signal. This analysis further provided a real-time algorithm not only for detection of HRV but also for other linear operations on the R-wave signal. The KLPF algorithm developed in this chapter is just a manifestation of such operations which delineates an appropriate way to deal with spike series signals. It is particularly useful for tracking the transient behaviour of the HRV. Once a well defined continuous state time series HRV signal is obtained, further steps can be taken towards finding the relationships between the variability signals.

Bandpass filtering of the R-wave signal was also developed in Chapter 2 based on the same concept of the KLPF algorithm. The KBPF method provides the opportunity to consider the constituent components of the HRV simultaneously and in real time. Specifically, the application of this method in analysis of the sympathovagal balance following a postural change or autonomic blockade, or in different physiological or pathological conditions, can be useful for clinical purposes and is suggested for future work. By assigning different bandpass filters within the HF, LF and even VLF bands, variations of these components in different conditions can be monitored and used as assessment criteria.

The aim of Chapter 3 was to verify that the proposed definition for the HRV signal would guarantee a reliable identification procedure. Moreover, other protocols for obtaining the variability signals were examined and compared with the presented method in this respect. It was shown that the definition of the variability signals based on the continuous state time series representation is indeed able to identify an unknown system in the frequency band assumed for the variability signals. Although this conclusion was based on the IPFM representation for the SA node, the definition presented for the variability signals is straightforward enough to be used even without this assumption. It was also demonstrated that the beat-to-beat method, despite its simplicity and popularity, is not an appropriate method for cardiovascular variability

modelling. This does not mean that all the results obtained by the beat-to-beat method are biased, but when it comes to cardiovascular variability modelling more effective signal descriptors can be used.

The analysis in Chapter 3 was confined to the process of identification between a spike series signal and continuous signals and namely identification of continuous input spike output (CISO) systems. Though it remains to be verified as future work, the proposed signal descriptors show a considerable promise for system identification between two spike series signals or even more. In this manner all event series signals can be converted to their continuous state time series counterparts. Consequently, the identification procedure can be easily applied to these continuous signals to characterise their transfer relations. This conclusion is particularly important in specifying the relationships between neuronal discharge patterns.

The major outcome of Chapter 4 was a block diagram representation for cardiovascular variability modelling based on the physiology of the system. An important concept highlighted in this chapter was the small signal and large signal cardiovascular modelling. In system science this concept is well known. Whenever small variations are superimposed on large fixed quantities and the dynamic behaviour of the system against these small variations is of interest, the small signal representation takes over. In Chapter 4 the same concept was extended to the cardiovascular system. This view, consequently, enabled us to better focus on cardiovascular variability modelling and to propose a new model which was used afterwards as a basis for investigation of HRV and BPV. However, the presented model in its basic form could not be used without further investigations which were presented in the subsequent chapters.

To check the presence of nonlinearity in the underlying system a novel approach was employed in Chapter 5. The usual method for detection of nonlinearity in a given signal is to use bispectral analysis for detection of harmonic coupling. Unfortunately this approach might give an erroneous result for a single record of data. Hence, it was replaced by an analysis based on cyclostationarity. Moreover the shortcomings of the available methods for detection of nonlinearity based upon the presence of two independent harmonics in a given signal were obviated by injecting sinusoidal functions into a nonlinear system and evaluating the performance of the cyclostationary method on the output signal. This theoretical development of the cyclostationary analysis can

be equivalently used for nonlinearity detection in other areas. For the experimental procedure, respiration was exploited to provide a sinusoidal excitation to the neuro-cardiovascular system. Analysis of the HRV and BPV by the cyclostationary tools revealed that input-output nonlinearity is indeed involved in producing the rhythmical fluctuations in heart rate and blood pressure. In the metronome breathing experiments, second or sometimes higher order harmonics of the HF component effectively appear in the HRV and BPV. Additionally, if the subject shows a large LF component, frequency coupling between this component and the HF component can be observed in HRV and BPV, indicating that both components undergo a common nonlinear operation. It was further illustrated that this nonlinearity could be classified as a Volterra type nonlinearity.

Since in this study modelling of the variability signals only in supine resting position was the aim, the nonlinearity test was solely applied for this case. As future work, detection of nonlinearity for the data in the tilt position can be suggested. It is known that the tilt manoeuver causes an augmentation in the LF power. Therefore, harmonic coupling between the LF and HF components can be better characterised. Moreover, the change in the amount of nonlinearity from supine to tilt position may be able to give further information about the behaviour of the neuro-cardiovascular system in normal and pathological conditions.

To improve the performance of the nonlinearity test a double frequency breathing pattern can also be devised. In the current study subjects were breathing at a single frequency in each session. If they breath according to a summation of two sinusoidal functions then the nonlinear feature of the neuro-cardiovascular system can be better evaluated by detection of the coupling between these two mandatory components. For this purpose, the composite breathing pattern can be displayed on a computer monitor to provide visual guidance for the subjects. Sweeping of the frequency band of interest will determine the strength of the nonlinearity in different frequency areas.

As a further development to the IPFM model, in Chapter 6, a time dependent term was added to its threshold level. The so-called TVTIPFM model, obtained by this modification, appears to be a suitable mathematical representation for the stretch induced modulation of the SA node in addition to its spike generation mechanism. Accordingly, a parametric solution was developed to concurrently recover the autonomic

modulation and the stretch induced effect. This method is indeed the first parametric method for analysing the popular IPFM model. Not only does this method give a broader insight into the behaviour of the IPFM model but also it opens a new chapter in its theoretical analysis and computational implementation. Decomposing the autonomic modulation and the threshold signal into basis functions offered by this method converts the treatment of the TVTIPFM model to an approximation problem. Hence, the powerful vector space and approximation theories can be invoked to analyse the IPFM model in an appropriate manner. Despite the strong theory, however, the presented parametric method was not very successful in recovering the stretch induced modulation from the practical data, perhaps due to the simplicity of the model. As a future perspective of the parametric method, development of an IPFM model with refractory period and leaky integrator, which reflect more realistic features of the SA node, can be envisaged. Furthermore, employing alternative sets of orthogonal functions or minimisation criteria can also be suggested.

The small effect of stretch induced modulation on heart rate, compared with the autonomic modulation, was also demonstrated in Chapter 6. Even though the stretch induced modulation and the autonomic modulation are mediated through different mechanisms, it was shown that they can exhibit an additive property once the former has a small amplitude.

In Chapters 7 and 8 we exclusively dealt with establishing the new HRV-BPV-ILV model. Preceded by a discussion about the functional performance of each individual block, an appropriate mathematical representation was developed to describe the specific behaviour of each building block of the proposed model. While each individual block had a simple representation, when all together they demonstrated a complex interaction. Specifically, the model demonstrated a satisfactory resemblance to the actual data.

The simplest rhythmical generation mechanism in the model belongs to the VLF component. A simple oscillator has been employed to model the periodic contraction of the vascular smooth muscles. This rhythmical fluctuation can modulate the arterial blood pressure and thereby the whole cardiovascular system. In this frequency band it is, perhaps, more judicious not to assume one specific source; other mechanisms such as the thermoregulatory system or chemoreceptor regulatory mechanisms might

equally contribute. However, for the purpose of HRV-BPV-ILV modelling, all of them can simply be modelled by one VLF oscillator affecting the arterial blood pressure as employed in the presented model.

In the LF band the model gives equal weight to the LF centrogenic mechanism and baroreceptor feedback mechanism. If the LF centrogenic mechanism is not active then the feedback mechanism will be dominant. Loop delay and the nonlinearity in the closed loop path are responsible for producing a sustained LF oscillation in blood pressure and consequently in heart rate. Specifically, this mechanism does not need an exogenous input to produce a perpetual LF component. The frequency of the LF component depends on the delay of the loop and the transfer characteristics of the sympathetic effectors. Importantly, the model shows that an increase in the gain of the blood pressure regulatory mechanism causes an augmentation of the LF power in this case. This rhythm can be entrained when the centrogenic LF oscillator becomes more active.

For the fluctuations in the HF band, the model shows that the direct influence of the respiratory oscillator in the brain stem makes a significant contribution. The mechanical effect of respiration on the heart and intrathoracic vessels induces rhythmical fluctuations in the BPV over the HF band. These fluctuations are reflected in the heart rate through the blood pressure regulatory mechanism and produce the HF component in the HRV. This is added to the HF fluctuations imposed as a result of the direct respiratory influence on the cardiac control centres in the brain stem. This result, however, was obtained in the mandatory random breathing experiment. Therefore, it might be claimed that the importance of the central respiratory modulation is a result of this mandatory pattern; the impact of the central respiratory modulation might be less effective in a spontaneous breathing experiment. The restriction to using a mandatory breathing pattern was in fact imposed by the requirements of the system identification procedure for having a rich signal.

The identification of the heart and vascular sympathetic modulation was quite specific here. The sympathetic modulation, heart rate variability and respiration were used as inputs to characterise the performance of the heart and vascular sympathetic modulation in producing the blood pressure variation. Aside from the current study, the presented identification method can have a potential application in determining the

performance of the heart in general. If the response of the heart is obtained through this method by measuring the blood pressure variation following the stimulation of the heart rate and/or variation of the venous return with a broad band stimulus then its performance and strength can be evaluated and perhaps used as an assessment tool for pathological conditions.

As a further study, modification of the model for the tilt position can also be suggested. The tilt manoeuver causes a change in sympathovagal balance; furthermore, the mechanical effect of respiration on the intrathoracic organs is altered. Comparison of the results in the tilt position with the obtained results in the resting supine position could give a broader view of the variability signals and their clinical applications. The time varying representation of the model presented in this study can also be developed in future for analysing the neuro-cardiovascular system during postural change or drug injection.

The presented model is a coarse representation of the actual physiological system. However, it exhibits the main features of the variability signals which are experimentally observed. The model reconciles reasonable simplicity with sufficient reality. As the first comprehensive nonlinear HRV-BPV-ILV model, it paves the way for developing more sophisticated nonlinear models by illustrating a new approach to cardiovascular variability modelling.

Bibliography

[1] Abboud F.M. and Mark A.L., "Cardiac baroreceptors in circulatory control in humans", in *Cardiac Receptors*, R. Hainsworth Eds. Cambridge University Press, pp. 437-461, 1979a.

[2] Abboud F.M., Eckberg D.L., Johannsen U.J. and Mark A.L., "Carotid and cardiopulmonary baroreceptor control of splanchnic and forearm vascular resistance during venous pooling in man", *J. of Physiol. London*, Vol. 286, pp. 173-184, 1979b.

[3] Agewall S., Rhea B.,Persson B., Karlberg B., Wallin G. and Anderson O.K., "Reflexogenic neuronal and humoral to selective stimulation of low-pressure cardiopulmonary receptors in man", *J. Internal Medicine*, Vol. 228, pp. 151-158, 1990.

[4] Akselrod S., Gordon D. and Madwed J.B., "Hemodynamic regulation: Investigation by spectral analysis" *Am. J. Physiol.*, Vol. 249, H867-H875, 1985.

[5] Barbieri R., Bianchi A.M., Triedman J.K., Mainardi L.T., Cerutti S. and Saul J.P., "Model dependency of multivariate autoregressive spectral analysis", *IEEE Eng. Med. Biol. Mag.*, Vol. 16, No. 5, pp. 74-85, 1997.

[6] Barcroft J. and Nisimaru Y., "Rhythmical contraction of the spleen", *J. Physiol.*, Vol. 74, pp. 294-298, 1932.

[7] Barman S.M. and Gebber G.L., "Basis for synchronisation of sympathetic and phrenic nerve discharge", *Am. J. Physiol.*, Vol. 231, pp. 1601-1607, 1976.

[8] Bartelstone H.J., "Role of the veins in venous return", *Circ. Res.*, Vol. VIII, pp. 1059-1076, Sept. 1960.

[9] Baselli G., Cerruti S. and S. Civardi, "Cardiovascular variability signals: Towards the identification of a closed loop model of the neuronal control mechanisms", *IEEE Trans. Biomed. Eng.*, Vol. 35, No. 12, pp. 1033-1046, Dec. 1988.

[10] Baselli G., Cerutti S., Badilini F., Biancardi L., Porta A., Pagani M., Lombardi F., Rimoldi O., Furlan R. and Malliani A., "Model for the assessment of heart period and arterial pressure variability interactions and of respiration influences", *Med. & Biol. Eng. & Comp.*, Vol. 32, pp. 143-152, March 1994.

[11] Baselli G., Porta A., Ferrari G., Cerutti S., Rimoldi O. and Pagani M., "Multi-variate identification and spectral decomposition for the assessment of cardiovascular control", in *Computer Analysis of Cardiovascular Signals*, Chapter 7, Eds. M. Di Rienzo et. al., IOS press, 1995.

[12] Bayly E.J., "Spectral analysis of pulse frequency modulation in the nervous systems", *IEEE Trans. Biomed. Eng.*, Vol. BME-15, No.4, pp. 257-265, 1968.

[13] Bendat J.S., "Nonlinear system analysis and identification from random data", John Wiley & Sons Pub. Co. 1990.

[14] Berger R.D., Akselrod S., Gordon D. and Cohen J., "An efficient algorithm for spectral analysis of heart rate variability", *IEEE Trans. Biomed. Eng.* Vol. BME-33, No.9, pp. 900-904, Sept. 1986.

[15] Berger R.D., Saul J.P. and R.J. Cohen, "Assessment of autonomic response by broad-band respiration", *IEEE Trans. Biomed. Eng.*, Vol. BME-36, pp. 1061-1065, 1989a.

[16] Berger R.D., Saul J.P. and Cohen R.J. , "Transfer function analysis of autonomic regulation, I. canine atrial rate response", *Am. J. Physiol.*, Vol. 256, pp. H142-H152, 1989b.

[17] Bernardi L., Keller F., Sanders M., Reddy P.S., Griffith B., Meno F. and Pinsky M. R., "Respiratory sinus arrhythmia in the denervated human heart", *J. Appl. Physiol.*, Vol. 67(4), pp. 1447-1455, 1989.

[18] Bernardi L., Passino C., Spadacini G., Valle F., Leuzzi S., Piepoli M. and Sleight P., "Arterial baroreceptors as determinant of $0.1Hz$ and respiration-related changes in blood pressure and heart rate spectra", in *Frontiers of Blood Pressure and Heart Rate Analysis*, M. Di Rienzo, *et. al.* Eds. pp. 241-252, IOS Press, 1997.

[19] Billings S.A. and Voon W.S.F., "Least squares parameter estimation algorithms for nonlinear systems", *Int. J. Systems*, Vol. 15, pp. 601-615, 1984.

[20] Billings S.A., Chen S. and Korenberg M.J., "Identification of MIMO nonlinear systems using a forward-regression orthogonal estimator", *Int. J. Control*, Vol. 49, pp. 2157-2189, 1989.

[21] Bishop V.S., Malliani A. and Thoren P., "Cardiac mechanoreceptors", Chapter 15 in Handbook of Physiology, section 2, The Cardiovascular System, Vol. III, Peripheral Circulation and Organ Blood Flow part 2, J.T. Shepherd, F.M. Abboud Eds. American Physiological Society, Bethesda, MD USA, 1986.

[22] Borst C. and Karemaker J.M., "Time delays in the human baroreceptor reflex", *J. Autonom. Nerv. Syst.*, Vol. 9, pp. 399-409, Nov. 1983.

[23] Boyers D.G. and Guthbertsonand M.D., "Simulation of the cardiovascular system: A model with normal response to changes of posture, blood losses, transfusion and autonomic blockade", *Simulation*, Vol. 18, pp. 197-205, 1972.

[24] Brillinger D.R., "Time series: data analysis and theory", Halt Rienhart and Winston, 1973.

[25] Broersen P.M.T., "A comparison of transfer function estimators", *IEEE Trans. Instrum. & Meas.* , Vol. 44, No.3, pp. 657-661, June 1995.

[26] Brooks C.McC., LU H., Lang G., Mangel R., Shaw R.B. and Geoly K., "Effects of localised node region of the dog heart", *Am. J. Physiol.*, Vol. 211, pp. 1197-1202, 1966.

[27] Bruckstein A.M. and Zeevi Y.Y., "Analysis of integral-to-threshold Neural coding schemes", *Biol. Cyber.*, Vol. 34, pp. 63-70, 1979.

[28] Burattini R., Borgdorff P. and Westerhorf N., "Short-Term regulation of artificial pressure and the calculation of open-loop gain in the intact anaesthetised dog", *Ann. Biomed. Eng.*, Vol. 15, pp. 427-441, 1987.

[29] Burattini R., Socionovo G. and Bellocchi F. , " On the approximation of static open-loop characteristics of baroreceptor reflex", *Am. J. Physiol.*, Vol.267, pp. H267-H275, 1994.

[30] Calcagnini G., Censi F., Camera A., Lino S. and Cerutti S. , "Interference and phase locking patterns between low and high frequency rhythms of cardiovascular variability signals in normal subjects", *Proc. of 18th Ann. Int. Conf. IEEE-EMBS*, Vol. 1 pp.730-731, 1996.

[31] Carrette P., Bastin G., Genin Y.Y. and Gevers M., "Discarding data may help in system identification", *IEEE Trans. Signal Proc.*, Vol. 44, pp. 2300-2310, Sept. 1996.

[32] Cerutti S., Bianchi A.M. and Mainardi L.T., "Spectral analysis of heart rate variability signal", in *Heart Rate Variability*, M. Malik and A.J. Camm Eds. Futura Pub. Co. pp. 63-74, 1995.

[33] Cevese A., Grasso R., Poltronieri R. and Schena F., "Vascular resistance and arterial pressure low-frequency oscillations in the anesthetized dog", *Am. J. Physiol.*, Vol. 268, pp. H7-H16, 1995.

[34] Chabbani M.A., "A validation study of mathematical models of the human cardiovascular system for short term regulation", PhD Thesis, Imperial College, University of London, 1990.

[35] Chen H-W, "Modelling and Identification of parallel nonlinear systems: Structural classification and parameter estimation methods", *Proc. IEEE*, Vol. 83, pp. 39-66, 1995.

[36] Chen S. and Billings S.A., "Representation of nonlinear systems: The NARMAX model", *Int. J. Control*, Vol. 49, pp. 1013-1032, 1989.

[37] Chiba S., "Pharmacological analysis of stretch-induced sinus acceleration of the isolated dog atrium", *Japanese Heart Journal*, Vol. 18, No. 3, pp.398-405, May 1977.

[38] Chiu H-W and Kao T., "A mathematical model of sinus node and heart rate variability analysis", *Proc. of IFAC Modelling and Control in Biomedical Systems*, Warwick UK, pp. 1-6, 1997.

[39] Chon K.H., Mullen T.J. and Cohen R.J. , "A dual input nonlinear system analysis of autonomic modulation of heart rate", *IEEE Trans. Biomed. Eng.*, Vol. 43, No. 5, May 1996.

[40] Christini D.J., Bennette M.F., Lutchen K.K., Ahmed H.M., Hansdorff J.M. and Oriol N., "Application of linear and nonlinear time series modelling to heart rate dynamics analysis", *IEEE Trans. Biomed. Eng.* , Vol. 42, No. 4, pp. 411-415, April 1995.

[41] Coenen A.J.R.M., Rompelman O. and Kitney R.I., "Measurement of heart rate variability: Part 2- Hardware digital device for the assessment of heart rate variability", *Med. Biol. Eng. Comp.* , Vol. 15, pp. 423-430, 1977.

[42] Coggshall J.C., "Linear models for biological transducers and impulse train spectra: general formulation and review", *Kybernetic*, Vol. 13, pp. 30-37, 1973.

[43] Craelius W., "Rhythm analysis of arterial blood pressure", *IEEE Trans. Biomed. Eng.* , Vol. BME-33, No.12, pp. 1166-1172, Dec. 1986.

[44] Dandawate A.V. and Giannakis G.B., "Nonparametric polyspectral estimators", *IEEE Trans. Inform. Theor.* Vol. 40, No. 1, pp. 67-84, Jan. 1994a.

[45] Dandawate A.V. and Giannakis G.B., "Statistical tests for presence of cyclostationarity", *IEEE Trans. Signal Proc.* Vol. 42, No. 9, pp. 2355-2369, Sept. 1994b.

[46] Davis J.N., "Phrenic nerve conduction in man", *J. Neurol. Neurosurg. Psychia.*, Vol. 30, pp. 420-426, 1967.

[47] Davis P.J., "Interpolation and approximation", Blaisdell Pub. Co. 1963.

[48] de Boer R.W., Karemaker J.M. and Strackee J., "Comparing spectra of a series of point events, particularly for heart-rate variability spectra", *IEEE Trans. Biomed. Eng.* , Vol. BME-31, pp. 384-387, April 1984.

[49] de Boer R.W., Karemaker J.M. and Strackee J., "Spectrum of a series of point events generated by the integral pulse frequency modulation model", *Med. & Biol. Eng. & Comp.* , Vol. 23, pp. 138-142, 1985a.

[50] de Boer R.W., "Beat-to-Beat blood pressure fluctuations and heart rate variability in man: Physiological relationships, analysis techniques and a simple model", PhD Thesis, University of Amsterdam, 1985b.

[51] de Boer R.W., Karemaker J.M. and Strackee J. , "Hemodynamic fluctuations and baroreflex sensitivity in humans: a beat-to-beat model", *Am. J. Physiol.*, Vol. 253, pp. H680-H689, 1987.

[52] de Burgh Daly M., "Interactions between respiration and circulation", in Handbook of Physiology, Section 3, The Respiratory System, Vol. II, Control of Breathing Part 2, N.S. Cherniack Eds. American Physiological Society, Bethesda, MD USA, 1986.

[53] de Burgh Daly M., "Aspects of the integration of the respiratory and cardiovascular systems", in *Cardiovascular Regulation*, D. Jordan and J. Marshall Eds, Chapter 2, Portland Press, 1995.

[54] Desai T.H., Collins J.C., Snell M. and Mosqueda-Garcia R., "Modelling of arterial and cardiopulmonary baroreflex control of the heart rate", *Am. J. Physiol.*, Vol. 272, pp. H2343-H2352, 1997.

[55] Di Rienzo M., Parati G., Castiglioni P., Omboni S., Ferrari A.U., Ramirez A.J., Pedotti A. and G. Mancia, "Role of sinoaortic afferents in modulating BP and pulse-interval: spectral characteristics in unanesthetized cats", *Am. J. Physiol.*, Vol. 261, H1811-H1818, 1991.

[56] Di Rienzo M., Castiglioni P., Parati G., Mancia G. and Pedotti A., "Effects of sinoaortic denervation on spectral characteristics of blood pressure and pulse interval- a wide-band approach", *Med. & Biol. Eng. & Compu.*, Vol. 34, No. 2, pp. 133-141, 1996.

[57] Dornhorst A.C., Howard P. and Leathart G.L., "Respiratory variations in blood pressure", *Circ.* Vol. 6, pp. 553-558, 1952.

[58] Eckberg D.L., Fletcher G.F. and Braunwald E., "Mechanism of prolongation of the R-R interval with electrical stimulation of the carotid sinus nerves in man", *Circ. Res.* , Vol. XXX, pp. 131-138, Jan. 1972.

[59] Eckberg D.L., "Nonlinearities of the human carotid baroreceptor-cardiac reflex", *Circ. Res.*, Vol. 47, pp. 208-216, 1980.

[60] Eckberg D.L., Eckberg M.J., "Human sinus node responses to repetitive, ramped carotid baroreceptor stimuli", *Am. J. Physiol.*, Vol. 242, pp. H638-H644, 1982.

[61] Eckberg D.L., "Human sinus arrhythmia as an index of vagal cardiac outflow", *J. Appl. Physiol.*, Vol. 54, pp. 961-966, 1983.

[62] Elghozi J.L, Laude D., Girard A. and Mounier-Vehier C., "Heart rate and blood pressure spectra during mental stress", in M. Di Rienzo, *et. al.* Eds. *Frontiers of Blood Pressure and Heart Rate Analysis*, pp. 143-153, IOS Press, 1997.

[63] Evanich M.J. and Lourenco R.V., "Frequency response analysis of the diaphragm in vivo", *J. Applied Physiol.* , Vol. 40, pp. 729-735, 1976.

[64] French A.S. and Holden A.V., "Alias-Free sampling of Neuronal spike trains", *Kybernetic*, Vol. 8, pp. 165-175, May, 1971.

[65] Fuji K., Heistad D.D. and F.M. Faraci, "Vasomotion in basilar arteries in vivo", *Am. J. Physiol.*, Vol. 258, pp. H1829-H1834, 1990.

[66] Gardner W.A., "Statistical spectral estimation, A nonprobabilistic approach", Prentice Hall, 1988.

[67] Gardner W.A., "Cyclostationarity in communication and signal processing", IEEE Press, 1995.

[68] Garello R., Le Caillec J.M., "Estimation of the phase content of SAR images of the ocean using 2D bispectrum estimation", *IEEE Proc. Int. Geoscience & Remote Sensing Symp. IGARSS95*, Vol. 2, pp. 1075-1077, 1995.

[69] Gebber G.L., " Central oscillators responsible for sympathetic nerve discharge", *Am. J. Physiol.*, Vol. 239, pp. H143-H155, 1980.

[70] Gestri G., "Pulse frequency modulation in neural systems", *Biophysical J.*, Vol. 11, pp. 98-109, 1971.

[71] Giannakis G.B. and Zhou G., "Harmonics in multiplicative and additive noise: parameter estimation using cyclic statistics", *IEEE Trans. Signal Proc.* Vol. 43, No.9, pp. 2217-2221, Sept. 1995.

[72] Golub G.H. and Van Loan C.F., "Matrix Computations", The Johns Hopkins University Press, 3rd Ed. 1996.

[73] Glick G. and Braunwold E., "Relative roles of the sympathetic and parasympathetic nervous system in the reflex control of heart rate", *Circ. Res.*, Vol. XVI, pp. 363-375, April 1965.

[74] Guyton A.C., "Textbook of Medical Physiology", Saunders Pub. Co. 1996.

[75] Haber R. and Unbehauen H., "Structure identification of nonlinear dynamic systems: A survey on input/output approaches", *Automatica*, Vol. 26, pp. 651-677, 1990.

[76] Hainsworth R., "Circulatory responses from lung inflation in anesthetized dogs", *Am. J. Physiol.*, Vol. 226, pp. 247-255, 1974.

[77] Hainsworth R., "Reflexes from the heart", *Physiol. Rev.*, Vol. 71, No. 3, pp. 617-658, July 1991.

[78] Hales S., "Statistical essays: containing haemastaticks", London, Innings and Manby, Vol. 2, 1733.

[79] Hammer P. and Saul J.P., "Can sympathetic modulation of arterial smooth muscle produce the 10-seconds rhythm? Analysis with a computer model of blood pressure control", *Proc. IEEE Comp. in Cardiol.*, pp. 93-96, 1996.

[80] Haykin S., "Modern Filters", Macmillan Pub. Co. 1989.

[81] Hirsch J.A. and Bishop B., "Respiratory sinus arrhythmia in humans: how breathing pattern modulates heart rate", *Am. J. Physiol., Vol. 241, pp. H620-629, 1981.*

[82] Hosomi H., "Overall characteristics of arterial pressure control system studied by mild hemorrhage", *Am. J. Physiol.* Vol. 234, pp. R104-R109, 1978.

[83] Hosomi H. and Hayashida Y., "Systems analysis of blood pressure oscillation", in *Mechanisms of Blood Pressure Waves*, K. Miyakawa, H.P. Koepchen, and C. Polosa, Eds. New York, Springer-Verlag, pp. 215-229, 1984.

[84] Hunter I.W. and Korenberg M.J., "The identification of nonlinear biological systems: Wiener and Hammerstein cascade models", *Biol. Cyber.* Vol. 55, pp. 135-144, 1986.

[85] Hyndman B.W., "A digital simulation of the human cardiovascular system and its use in the study of sinus arrhythmia", PhD Thesis, Imperial College, University of London, 1970.

[86] Hyndman B.W. and Mohn R.K., "A model of the cardiac pacemaker and its use in decoding the information content of cardiac intervals", *Automedica*, Vol. 1, pp. 239-252, 1975.

[87] Iriuchijima J., "Role of cardiac output and total peripheral resistance in the generation of splenic blood pressure wave", in *Mechanisms of Blood Pressure Waves*, K. Miyakawa, H.P. Koepchen, and C. Polosa, Eds. New York, Springer-Verlag, pp. 347-348, 1984.

[88] Janssen B.J.A., Oosting J., Sloaf D.W., Persson P.B. and Struijker-Boudier H.A.J., "Hemodynamic basis of oscillations in systemic arterial pressure in conscious rats", *Am. J. Physiol.*, Vol. 269, pp. H62-H71, 1995.

[89] Just A., Wagner C.D., Ehmke H., Kirchheim H.R. and Presson P.B., "On the origin of low-frequency blood pressure variability in the conscious dog", *J. Physiol.*, Vol. 489.1, pp. 215-223, 1995.

[90] Kanoh H., "Analysis by mathematical model", in *Mechanisms of Blood Pressure Waves*, K. Miyakawa, H.P. Koepchen, and C. Polosa, Eds. New York, Springer-Verlag, pp. 241-254, 1984.

[91] Kardos A., Rudas L., Gingel Z., Szabados S. and Simon J., "The mechanism of blood pressure variability study in patients with fixed ventricular pacemaker rhythm", *European Heart J.* Vol. 16, pp. 545-552, 1995.

[92] Katona P.G., Poitras J.W., Barnett G.O. and Terry B.S., "Cardiac vagal efferent activity and heart period in the carotid sinus reflex", *Am. J. Physiol.* Vol. 218, pp. 1030-1037, 1970.

[93] Katona P.G. and Jih F., "Respiratory sinus arrhythmia: noninvasive measure of parasympathetic cardiac control", *J. Appl. Physiol.* Vol. 39, No. 5, pp. 801-805, 1975a.

[94] Katona P.G., Martin P.J. and Jih F., "Neural control of heart rate: A conciliation of models", *IEEE Trans. Biomed. Eng.* Vol. 23, pp. 164-166, March 1976. 801-805, 1975b.

[95] Katona P.G., Mclean M., Dighton D.H. and Guz A., " Sympathetic and parasympathetic cardiac control in athletes and nonathletes at rest", *J. Appl. Physiol.* Vol. 52, No. 6, pp. 1652-1657, 1982.

[96] Kitney R.I., "The analysis and simulation of the human thermoregulatory control system", *Med. & Biol. Eng.* , Vol. 12, pp. 57-65. 1974.

[97] Kitney R.I., "An analysis of nonlinear behaviour of the human vasomotor control system", *J. Theor. Biol.*, Vol. 52, pp. 231-248, 1975.

[98] Kitney R.I., "A nonlinear model for studying oscillation in the blood pressure control system", *J. Biomed. Eng.*, Vol. 1, No. 2, pp. 89-99, April 1979.

[99] Kitney R.I. and Rompelman O., "The study of heart rate variability", Oxford, Clarendon Press, 1980.

[100] Kitney R.I. and Rompelman O., "The beat-to-beat cardiovascular function", Oxford science publications, 1987.

[101] Koepchen H.P., "History of studies and concepts of blood pressure waves", in *Mechanisms of Blood Pressure Waves*, K. Miyakawa, H.P. Koepchen, and C. Polosa, Eds. New York, Springer-Verlag, pp. 3-27, 1984.

[102] Koizumi K., Terui N. and Kollai M., "Relationship between vagal and sympathetic activities in rhythmic fluctuations", *Mechanisms of Blood Pressure Waves*, K. Miyakawa, H.P. Koepchen, and C. Polosa, Eds. New York, Springer-Verlag, pp. 40-63, 1984.

[103] Korenberg M.J., "Functional expansions, parallel cascades and nonlinear difference equations", in *Advanced Methods of Physiological System Modelling*, V.Z. Marmarelis Eds. Biomedical Simulation Resource, USC Press, Vol. 1 pp. 221-240, 1987.

[104] Korenberg M.J., "A robust orthogonal algorithm for system identification and time series analysis", *Biol. Cyber.*, Vol. 60, pp. 267-276, 1989.

[105] Korenberg M.J. and Paarmann L.D., "Orthogonal approaches to time series analysis and system identification", *IEEE Signal. Proc. Mag.*, Vol. pp. 29-43, July 1991.

[106] Langhorst P., Schulz G. and Lambertz M., "Oscillating neuronal network of the common brainstem system", in *Mechanisms of Blood Pressure Waves*, K. Miyakawa, H.P. Koepchen, and C. Polosa, Eds. New York, Springer-Verlag, pp. 257-277, 1984.

[107] Lang G., Lu H., Chang A. and Brooks C.McC., "Effect of stretch on the isolated cat sinoatrial node", *Am. J. Physiol.*, Vol. 211, pp. 1191-1196, 1966.

[108] Laude D., Goldman M., Escourrou P. and Elghozi J-L , "Effect of breathing pattern on blood pressure and heart rate oscillations in humans", *Clin. Exp. Pharmac. Physiol.*, Vol. 20, pp. 619-626, 1993.

[109] Lee Y.W. and Schetzen M., "Measurement of the Wiener kernels of a nonlinear system by cross-correlation", *Int. J. Control*, Vol. 2, pp. 237-254, 1965.

[110] Leaning M.S., Pullen H.E., Carson E.R. and Finkelstein L., "Modelling a complex biological system: the human cardiovascular system, 1. Methodology and model description", *Trans. Inst. M. C.* , Vol. 5, No. 2, pp. 71-86, 1983.

[111] Levick J.R., "An introduction to the cardiovascular physiology", Butterworth & Co. Pub. 1991.

[112] Levy M.N., Degeest H. and Zieske H., "Effect of respiratory centre activity on the heart", *Circ. Res.*, Vil 18, pp. 67-78, 1966.

[113] Levy M.N., "Sympathetic-Parasympathetic interaction in the heart", *Circ. Res.*, Vol. XXIX, No. 5, pp. 437-445, Nov. 1971.

[114] Lindqvist A., "Noninavsive methods to study autonomic nervous control of circulation", *Acta Physiologica Scandinavica*, Vol. 138, Supplement 588, 1990.

[115] Linkens D.A., "Biological system modelling and control", IEE control Engineering series 11, Peter Peregrinus LTD, 1979a.

[116] Linkens D.A., "Modulation analysis of forced nonlinear oscillators for biological modelling", *J. Theor. Biol.*, Vol. 77, pp. 235-251, 1979b.

[117] Linkens D.A., "Theoretical analysis of beating modulation phenomena in weakly intercoupled Van Der Pol oscillator systems for biological modulating", *J. Theor. Biol.*, Vol. 79, pp. 31-54, 1979c.

[118] Ljung L., "System identification: Theory for the user", Prentice Hall Inc. 1987.

[119] Macov F., Fagard R., Mortelman L., Claeys K. and Amery A., "Effects of baroreceptor and cardiopulmonary reflexes on neural control of heart rate in normal man, as assessed by power spectral analysis", *Clinic. Autonom. Res.*, Vol. 2 pp. 367-371, 1992.

[120] Madwed J.B., Albrecht P., Mark R.G. and Cohen R.J., "Low-frequency oscillations in arterial pressure and heart rate: A simple computer model", *Am. J. Physiol.*, H1573-H1579, Vol. 256, 1989.

[121] Mainardi L.T., Bianchi A.M., Barbieri R., Di Virgilio V., Piazza S., Furlan R., Baselli G. and Cerruti S., "Multivariate time-variant identification of cardiovascular variability signals: A beat-to-beat spectral parameter estimation in vasovagal syncope", *IEEE Trans. Biomed.*, Vol. 44, pp. 978-989, 1997.

[122] Malliani A., Pagani M., Lombardi F. and Cerutti S., "Cardiovascular neural regulation explored in the frequency domain", *Circulation*, Vol. 84, No. 2, pp. 482-492, Aug. 1991.

[123] Malliani A., Pagani M. and Lombardi F. , "Low frequency oscillation of heart rate and arterial pressure variabilities as a marker of sympathetic modulation of cardiovascular function", in *Blood Pressure and Heart Rate Variability* , M. Di Rienzo *et. al.* Eds. IOS Press, pp. 215-227, 1992.

[124] Mancia G. and Mark A., "Arterial baroreflex in humans", Chapter 20 in Handbook of Physiology, Section 2, The Cardiovascular System, Vol. III, Peripheral Circulation and Organ Blood Flow part 2, J.T. Shepherd, F.M. Abboud Eds. American Physiological Society, Bethesda, MD USA, 1986.

[125] Mark A. and Mancia G., "Cardiopulmonary baroreflexes in humans", Chapter 21 in Handbook of Physiology, Section 2, The Cardiovascular System, Vol. III, Peripheral Circulation and Organ Blood Flow part 2, J.T. Shepherd, F.M. Abboud Eds. American Physiological Society, Bethesda, MD USA, 1986.

[126] Marmarelis V.Z., "Analysis of physiological systems, the white noise approach", Plenum press, 1978.

[127] Marmarelis V.Z., Citron M.C. and Vivo C.P., "Minimum-order Wiener modelling of spike-output system", *Biol. Cyber.* , Vol. 54, pp. 115-123, 1986.

[128] Marmarelis V.Z., "Recent advances in nonlinear and nonstationary analysis", in *Advanced Methods of Physiological System Modelling*, Vol. 2, V.Z. Marmarelis Eds. Biomedical Simulations Resource, USC Press, pp.323-336, 1987a.

[129] Marmarelis V.Z., "Nonlinear and nonstationary modelling of physiological systems: An overview", in *Advanced Methods of Physiological System Modelling*,Vol. 1, V.Z. Marmarelis Eds. Biomedical Simulation Resource, USC Press, pp. 1-24, 1987b.

[130] Marmarelis V.Z., "Identification of nonlinear biological systems using Laguerre expansions of kernels", *Ann. Biomed. Eng.*, Vol. 21, pp. 573-589, 1993a.

[131] Marmarelis V.Z., Chon K.H., Chen Y-M, Marsh D.J. and Holstein-Rathlou N-H, "Nonlinear analysis of renal autoregulation under broadband forcing conditions", *Ann. Biomed. Eng.*, Vol. 21, pp. 591-603, 1993b.

[132] Marmarelis V.Z., "Nonlinear modelling of physiological systems using principal dynamic modes", in *Advanced methods of physiological system modelling*, V.Z. Marmarelis Eds. Plenum Press, Vol. 3, pp. 1-27, 1994.

[133] Mathias C. J., Bannister R. "Investigation of autonomic disorders", in *Autonomic Failure: A Textbook of Clinical Disorders of the Autonomic Nervous System*, R. Bannister and C. J. Mathias Eds, Oxford: OUP Pub, pp. 255-290, 1992.

[134] Matsukawa S. and Wada T., "Vector autoregressive modelling for analysing feedback regulation between heart rate and blood pressure", *Am. J. Physiol.*, Vol. 273, pp. H1478-H486, 1997.

[135] McCrady J.D., Vallbona C. and Hoff H.E., "Neural origin of the respiratory-heart rate response", *Am. J. Physiol.*, Vol. 211, pp. 323-328, 1966.

[136] McKenzie D.K. and Gandevia S.C., "Phrenic nerve conduction time and twitch pressures of the human diaphragm", *J. Applied Physiol.*, Vol. 58, pp. 1496-1504, 1985.

[137] Merri M., Farden D.C., Mottley J.G. and Titlebaum E.L., "Sampling frequency of the electrocardiogram for spectral analysis of the heart rate variability", *IEEE Trans. Biomed. Eng.*, Vol. 37, No. 1, pp. 99-105, Jan. 1990.

[138] Milnor W.R., "Cardiovascular Physiology", Oxford University Press, 1990.

[139] Mokrane A., LeBlanc A.R. and Nadeau R., "Transfer function analysis of vagal control of heart rate during synchronised vagal stimulation", *Am. J. Physiol.*, Vol. 269, pp. H1931-H1940, 1995.

[140] Montano N., Gnecchi-Ruscone T., Porta A., Lombardi F., Malliani A. and Barman S. M., "Presence of vasomotor and respiratory rhythms in the discharge of single medullary neurones involved in the regulation of cardiovascular system", *J. Auto. Nerv. Sys.*, Vol. 57, pp. 116-122, 1996.

[141] Mullen T.J., Appel M.L., Mukkamala R., Matias J.M. and Cohen R.J., "System identification of closed-loop cardiovascular control: effects of posture and autonomic blockade", *Am. J. Physiol.*, Vol. 272, pp. H448-H461, 1997.

[142] Nikias C.L. and Petropulu A.P., "Higher order spectral analysis, a nonlinear signal processing", Prentice Hall, 1993a.

[143] Nikias C.L. and Mendel J.M, "Signal processing with higher order spectra", *IEEE Signal Proc. Mag.*, pp. 10-37, July 1993b.

[144] Ning T., Bronzino J.D., "Bispectral analysis of the rat EEG during various vigilance states", *IEEE Trans. Biomed. Eng.*, Vol. 36, pp. 497-499, 1989.

[145] Nisimaru Y., "A story of the spleen, the fourth grade blood pressure change", in *Mechanisms of Blood Pressure Waves*, K. Miyakawa, H.P. Koepchen, and C. Polosa, Eds. New York, Springer-Verlag, pp. 341-346, 1984.

[146] Nobel M.I.M. and Seed W.A., "The interval-force relationship of the heart", Cambridge Univ. Press, 1992.

[147] Noguchi Y., Hataoka H., Sugimoto S., Kobayashi H. and Kobayashi M., "Integral function method, a new analysing method for heart rate variability", *Proc. of 9th IEEE Ann. Conf. EMB.* , pp-1056-1057, 1987.

[148] Oppenheim A.V., Schafer R.W., "Discrete time signal processing", 2nd Ed. Prentice Hall, 1989.

[149] Oren R.M., Schobel H.P., Weiss R.M., Stanford W. and Ferguson D.W., "Importance of left atrial baroreceptors in the cardiopulmonary baroreflex of normal humans", *J. Appl. Physiol.*, Vol. 74(6), pp. 2672-2680, 1993.

[150] Pagani M., Lombardi F., Guzetti S.,Rimoldi O., Furlan R.,Pizzinelli P., Sandone G., Malfatto G., Dell'Orto S., Piccaluga E., Turiel M., Baselli G., Cerutti S. and Malliani A., "Power spectral analysis of heart rate and arterial pressure variabilities as a marker to sympatho-vagal interaction in man and conscious dog", *Circ. Res.*, Vol. 59, pp. 178-193, 1986.

[151] Paintal A.S., "A study of right and left atrial receptors", *J. Physiol. Lond.*, Vol. 120, pp. 596-610, 1953.

[152] Panerai R.B., Martin M.A., James A. and Potter J.F., "Impulse response analysis of baroreceptor sensitivity", *Am. J. Physiol.*, Vol. 272, pp. H1866-H1875, 1997.

[153] Parati G., Pomidossi G., Casadei R., Groppelli A., Trazzi S., Di Rienzo M. and Mancia G., "Role of heart rater variability in the production of blood pressure variability in man", *J. Hypertension*, Vol. 5, pp. 557-560, 1987.

[154] Parati G., Di Rienzo M., Castiglioni P., Villani A., Tortorici E. and Mancia G., "Spontaneous baroreflex sensitivity: From the cardiovascular laboratory to patient's bedside", in *Frontiers of Blood Pressure and Heart Rate Analysis*, M. Di Rienzo, *et. al.* Eds., pp. 219-240, IOS Press, 1997.

[155] Patwardhan A.R., Evans J.M., Bruce E.N., Eckberg D.L. and Knapp C.F., "Voluntary control of breathing does not alter vagal modulation of heart rate", *J. Appl. Physiol.*, Vol. 78, pp. 2087-2094, 1995.

[156] Paulin M.G., "Digital filters for firing rate estimation", *Biol. Cyber.* Vol. 66, pp. 525-531, 1992.

[157] Paulin M.G., "A method for constructing data-based models for spiking neurones using a dynamic linear-static nonlinear cascade", *Biol. Cyber.* Vol. 69, pp. 67-76, 1993.

[158] Perlini S., Solda P.L., Piepoli M., Sala-Gallini G., Calciati A., Finardi G. and Bernardi L., "Determinants of respiratory sinus arrhythmia in the vagotomized rabbit", *Am. J. Physiol.*, Vol. 269, pp. H909-H915, 1995a.

[159] Perlini S., Giangregorio F., Coco M., Radaelli A., Solda P.S., Bernardi L. and Ferrari A.U., "Autonomic and ventilatory components of heart rate and blood pressure variability in freely behaving rats", *Am. J. Physiol.*, Vol. 269, pp. H1729-H1734, 1995b.

[160] Pickering T.G., Gribbin B., Strange Petersen E., Cunningham D.J.C. and Sleight P., "Effects of autonomic blockade on the baroreflex in man at rest and drug exercise", *Circ. Res.* , Vol. XXX pp. 177-185, Feb. 1972.

[161] Pickering T.G. and Davies J., "Estimation of the conduction time of the baroreceptor-cardiac reflex in man", *Cardiovasc. Res.*, Vol. 7, pp. 213-219, 1973.

[162] Polosa C., "Rhythms in the activity of the autonomic nervous system, their role in the generation of systemic arterial pressure waves", in *Mechanisms of Blood Pressure Waves*, K. Miyakawa, H.P. Koepchen, and C. Polosa, Eds. New York, Springer-Verlag, pp. 27-43, 1984a.

[163] Polosa C., "Hemorrhage and blood pressure waves", in *Mechanisms of Blood Pressure Waves*, K. Miyakawa, H.P. Koepchen, and C. Polosa, Eds. New York, Springer-Verlag, pp. 147-166, 1984b.

[164] Ponikowski P., Chua T.P., Piepoli M., Amadi A.A., Harrington D., Webb-Peploe K., Volterrani M., Colombo R., Mazzeuero G., Giordano A. and Coats A.J.S., "Chemoreceptor dependence of very low frequency rhythms in advanced chronic heart failure", *Am. J. Physiol.* Vol. 272, pp. H438-H447, 1997.

[165] Preiss G. and Polosa C., "Patterns of sympathetic neuron activity associated with Mayer waves", *Am. J. Physiol.*, Vol. 226, pp. 724-739, 1974.

[166] Raymond B., Mazumdar J. and Nandagopal D., "Modelling the shift of the low frequency component of heart rate variability", *Proc. IEEE Comp. Cardi. Conf.*, pp. 407-410, 1997.

[167] Rimoldi O., Pierini S., Ferrari A., Cerutti S., Pagani M. and Malliani A., "Analysis of short-term oscillations of R-R and arterial pressure in conscious dogs", *Am. J. Physiol.*, Vol. 258, pp. H967-H976, 1990.

[168] Robinson B.F., Epstein S.E., Beiser G.D. and Braunwold E., "Control of heart rate by the autonomic nervous system", *Circ. Res.* Vol. XIX, pp. 400-411, Aug. 1966.

[169] Rompelman O., Coenen A.J.R.M. and Kitney R.I., "Measurement of heart rate variability: Part 1-Comparative study of heart-rate variability analysis methods", *Med. Biol. Eng. Comp.* pp. 233-239, May 1977.

[170] Rompelman O., Snijders J.B.I.M. and Van Spronsen C.J.V., "The measurement of heart rate variability spectra with the help of a personal computer", *IEEE Trans. Biomed. Eng.*, Vol. BME-29, No.7, pp. 503-510, July 1982.

[171] Rompelman O., "Spectral analysis of fluctuations in heart rate and blood pressure", in *Computer Analysis of Cardiovascular Signals*, M. Di Rienzo Eds. IOS Press, pp. 3-15, 1995.

[172] Rosenbaum M. and Race D., "Frequency-response characteristics of vascular resistance vessels", *Am. J. Physiol.*, Vol. 215, pp. 1397-1402, 1968.

[173] Rosenblueth A. and Simeone F.A., "The interrelations of vagal and accelerator effects on the cardiac rate", *Am. J. Physiol.*, Vol. 110, pp. 42-55, 1934.

[174] Rothe C.F., "Venous system", in Handbook of Physiology, Chapter 13, Section 2, The Cardiovascular System, J.T. Shepherd Eds. American Physiological Society, Bethesda, MD USA, 1983.

[175] Rowe H.E., "Signals and noise in communication systems", D. Van Nostrand Co., Princeton, 1965, Chap V.

[176] Sagawa K., "Baroreflex control of blood pressure", in Handbook of Physiology, Chapter 14, Section 2, The Cardiovascular System, J.T. Shepherd Eds. American Physiological Society, Bethesda, MD USA, 1983.

[177] Sakai H.M., "White-Noise analysis in neurophysiology", *Physiological Reviews*, Vol. 72, pp. 491-505, April 1992.

[178] Sanderson A.C., "Input-Output analysis of an IPFM neural model: effects of spike regularity and record length", *IEEE Trans. Biomed. Eng.*, Vol. BME-27, pp. 120-131. March 1980

[179] Saul J.P., Berger R.D., Chen M.H. and Cohen R.J., "Transfer function analysis of automatic regulation, II. Respiratory sinus arrhythmia", *Am. J. Physiol.*, Vol. 256, pp. H153-H161, 1989.

[180] Saul J.P., Berger R.D., Albrecht P., Stein S.P., Chen M.H. and Cohen R.J., "Transfer function analysis of the circulation: Unique insights into cardiovascular regulation", *Am. J. of Physiol.* , Vol. 91, pp. H1231-H1245, 1991.

[181] Saul J.P. and Cohen R.J., "Respiratory sinus arrhythmia", in *Vagal Control of Heart, Experimental Basis and Clinical Implications*, M.N. Levy and P.J. Schwartz Eds., Futura Pub. Co. Chapter 30, 1994.

[182] Scher A.M. and Young A.C., "Servoanalysis of carotid sinus reflex effects on peripheral resistance", *Circ. Res.*, Vol. 12, pp. 152-162, 1963.

[183] Scher A.M. and Young A.C., "Reflex control of heart rate in the unanesthetized dog", *Am. J. Physiol.*, Vol. 218 (3), pp. 780-789, 1979.

[184] Schetzen M., "The Volterra and Wiener theories of nonlinear systems", Robert E. Krieger Pub. Co., 1989.

[185] Schmidt R.M., Kumada M. and Sagawa K., "Cardiac output and total peripheral resistance in carotid sinus reflex", *Am. J. Physiol.*, Vol. 221, pp. 480-487, 1971.

[186] Sherman D.L., Zoltowski M.D., "Mixed-Based higher order spectral analysis for three-wave coupling processes", *IEEE Trans. Signal Proc.*, Vol. 42, pp. 32-348, 1994.

[187] Shin S.J., Tapp W.N., Resiman S.S. and Natelson B.H., "Assessment of autonomic regulation of heart rate variability by the method of complex demodulation", *IEEE Trans. Biomed. Eng.* , Vol. 36, No.2, pp. 274-283, Feb. 1989.

[188] Shoukas A.A. and Sagawa K., "Control of total systemic vascular capacity by the carotid sinus baroreceptor reflex", *Circ. Res.*, Vol. XXXIII, pp. 22-33, July 1973.

[189] Shoukas A.A., Brunner M.J., Greene A.S. and McAnespie C.L., "Aortic arch reflex control of total systemic vascular capacity", *Am. J. Physiol.*, Vol. 253, pp. H598-H603, 1987.

[190] Siegel G., Ebeling H.W., Hofer H.W., Nolte J., Roedel H. and Klubendorf D., "Vascular smooth muscle rhythmicity", in *Mechanisms of Blood Pressure Waves*, K. Miyakawa, H.P. Koepchen, and C. Polosa, Eds. New York, Springer-Verlag, pp. 319-340, 1984.

[191] Sleight P. and Casadei B., "Relationships between heart rate, respiration and blood pressure variabilities", in *Heart Rate Variability*, M. Malik and A.J. Camm Eds. Futura Pub. Co. pp. 311-327, 1995.

[192] Slotine J-J E. and Weipin L., "Applied nonlinear control", Prentice Hall, 1990.

[193] Smith J.J. and Kampine J.P., "Circulatory Physiology, the Essentials", 3rd Edition, Williams & Williams Pub. 1990.

[194] Söderstrom T. and Stoica P., "System identification", Prentice Hall Inc, 1989.

[195] Stauss H.M. and Kregel K.C., "Frequency response characteristic of sympathetic mediated vasomotor nerves in conscious rats", *Am. J. Physiol.* Vol. 271, pp. H1416-1422, 1996.

[196] Taylor J.A. and Eckberg D.L., "Fundamental relation between short-term RR interval and arterial pressure oscillations in humans", *Circulation* Vol. 93, pp. 1527-1532, 1996.

[197] TenVoorde B.J., Faes Th.J.C. and Rompelman O., "Spectra of data sampled at frequency modulated rates in application to cardiovascular signals: part 1, analytical derivation of the spectra", *Med. & Biol. Eng. & Comp.*, Vol. 32, pp. 63-70, 1994.

[198] TenVoorde B.J., Faes Th.J.C., Janssen T.W.J., Scheffer G.J. and Rompelman O., " Respiratory modulation of blood pressure and heart rate studied with a computer model of baroreflex control", in *Computer Analysis of Cardiovascular Signals*, Chapter 9, Eds. M. Di Rienzo et. al., IOS press, 1995.

[199] Thames M.D., Donald D.E. and Shepherd J.T., "Behaviour of cardiac receptors with nonmyelinated vagal afferents during spontaneous respiration in cats", *Circ. Res.* , Vol. 41, No. 5, pp. 694-701, Nov. 1977.

[200] Triedman J.K. and Saul J.P., "Blood pressure modulation by central venous pressure and respiration, buffering effects of the heart rate reflexes", *Circulation*, Vol. 89, pp. 169-179, 1994.

[201] Ursino M., Fabbri G. and Belardinelli E., "A mathematical analysis of Vasomotion in the peripheral vascular bed", *Cardioscience*, Vol. 3, No. 1, pp. 13-25, March 1992.

[202] Ushiyama J. and Brooks C.McC., "Interacting of oscillators: effect of sinusoidal stretching of the sinoatrial node on nodal rhythm", *J. Electrocardiography*, Vol. 10, No. 1, pp. 39-44, 1977.

[203] Van Der Veen A.J., Deprettere E.F. and Swindlehurst L., "Subspace-Based signal analysis using singular value decomposition", *IEEE Proceeding*, Vol. 81, No. 9, pp. 1277-1308, 1993.

[204] Wesseling K.H. and Settels J.J., "Circulatory model of baro- and cardio-pulmonary reflexes", in *Blood Pressure and Heart Rate Variability* , M. Di Rienzo *et. al.*, Eds. IOS Press 1992.

[205] Westwick D.T. and Korenberg R.E., "Identification of multiple-input nonlinear systems using non-white test signals", in *Advanced Methods of Physiological System Modelling*, V.Z. Marmarelis Eds. Plenum Press, Vol. 4, pp.163-178, 1994.

[206] Westwick D.T. and Korenberg R.E., "Identification of physiological systems: A robust method for non-parametric impulse response estimation", *Med. & Biol. Eng. & Comput.*, Vol. 35, pp. 83-90, 1997.

[207] Yana K., Saul J.P., Berger R.D., Perrot M.H. and Cohen R.J., "A time domain approach for the fluctuation analysis of heart rate related to instantaneous lung volume", *IEEE Trans. Biomed. Eng.* , Vol. 40, No.1, pp. 74-81, Jan. 1993.

[208] Yang M.W., Terry B.J., Kuo S.M., Lin K.H., "Continuous on-line, real-time spectral analysis of SAP signals during cardiopulmonary bypass", . *Am. J. Physiol.*, Vol. 268, pp. H2329-2335, 1995.

[209] Zeevi Y.Y. and Bruckstein A.M., "A note on single signed integral pulse frequency modulation", *IEEE Trans. Sys. Man. Cyb.* , Vol. SMC-7, No.12, pp. 875-877, Dec. 1977.

[210] Zhou G. and Giannakis G.B., "Estimating coupled harmonics in additive and multiplicative noise", *IEEE Annual Conf. Signal Proc.*, pp. 1250-1254, 1993.

[211] Zhou G. and Giannakis G.B., "Self coupled harmonics: Stationary and cyclostationary approach", *IEEE Ann. Conf. on Signal Proc.*, pp. 153-156, 1994.

[212] Zhou G. and Giannakis G.B., "Retrieval of self coupled harmonics", *IEEE Trans. Signal Proc.*, Vol. 43, No. 5, pp. 1173-1186, May 1995a.

[213] Zhou G. and Giannakis G.B., "Harmonics in multiplicative and additive noise: Performance analysis of cyclic estimators", *IEEE Trans. Signal Proc.* Vol. 43, No.6, pp. 1445-1460, June 1995b.

[214] Zhou G. and Giannakis G.B., "Polyspectral analysis of mixed processes and coupled harmonics", *IEEE Trans. Infor. Theor.* Vol. 42, No.3, pp. 943-958, May 1996.

[215] Zoller R.P., Mark A.L., Abboud F.M., Schmidt P.G. and Heistad D.D., "The role of low pressure baroreceptors in reflex vasoconstrictor responses in man", *J. Clinical Investigation*, Vol. 51, pp. 2967-2972, 1972.

BIBL
LONDON
UNIV.